

---

Electronic Thesis and Dissertation Repository

---

7-14-2017 2:00 PM

## Enstatite achondrites as indicators of processes and environments in the early solar system

Diego David Uribe, *The University of Western Ontario*

Supervisor: Dr. Phil McCausland, *The University of Western Ontario*

Joint Supervisor: Dr. Matthew Izawa, *The University of Western Ontario*

Co-Supervisor: Dr. Roberta Flemming, *The University of Western Ontario*

A thesis submitted in partial fulfillment of the requirements for the Master of Science degree in Geology

© Diego David Uribe 2017

Follow this and additional works at: <https://ir.lib.uwo.ca/etd>

 Part of the [Cosmochemistry Commons](#), [Geochemistry Commons](#), and the [Geology Commons](#)

---

### Recommended Citation

Uribe, Diego David, "Enstatite achondrites as indicators of processes and environments in the early solar system" (2017). *Electronic Thesis and Dissertation Repository*. 4817.  
<https://ir.lib.uwo.ca/etd/4817>

This Dissertation/Thesis is brought to you for free and open access by Scholarship@Western. It has been accepted for inclusion in Electronic Thesis and Dissertation Repository by an authorized administrator of Scholarship@Western. For more information, please contact [wlsadmin@uwo.ca](mailto:wlsadmin@uwo.ca).

## **Abstract**

This thesis investigates the processes and environments of formation of the anomalous enstatite achondrites NWA 4301, Zakłodzie, and NWA 8173 to determine how they relate to other enstatite meteorites (chondrites, impact melt rocks, aubrites, and so-called “primitive enstatite achondrites”). Observations of Zakłodzie and NWA 4301 showed that both meteorites may share a common parent body, but have experienced different metamorphic conditions. Different zonation patterns in plagioclase, silica polymorphs and associations, and sulfide assemblages indicate that Zakłodzie experienced higher metamorphic temperatures and cooled faster than NWA 4301, therefore NWA 4301 was buried deeper in the parent body relative to Zakłodzie. In NWA 8173, mineral assemblages and textures indicate that it formed at high temperatures, and underwent subsolidus annealing. Detailed mineral, chemical and structural classification of fluorophlogopite in NWA 8173 was made, to determine the role of halogens in formation mechanisms of enstatite meteorites. Overall findings showed that incipient partial melting and annealing following impact melting can each form the anomalous enstatite meteorites. However, a model is proposed where halogens can act as a fluxing agent in the melt as represented by NWA 8173 and can cause a thermally metamorphosed rock such as Zakłodzie and NWA 4301 to melt, fractionally crystallize and ultimately differentiate.

**Keywords:** Enstatite, Achondrite, primitive, differentiation, environments, EBSD, X-Ray diffraction, formation processes



## **Acknowledgements**

Foremost I would like to dedicate this work to my parents. For whom sacrifice and unconditional support has allowed me to get this far in life and to whom I owe everything that I am. I thank them for having left everything in hopes that one day I may be successful and have the best opportunities available to me. To my brother, I thank him for his friendship and support throughout this journey and I hope I can remain an example for you to follow. I would also like to thank my uncles, cousins and close family for believing in me and always supporting me.

Secondly, I would also like to thank, but mostly dedicate this work to my supervisors, whom above all, have become an integral part of my life and from whom I have learned a great deal not only scientifically, but also the various life lessons I have learned from them. I am proud to have been your student and to have been able to work and get to know you for all these years. Thank you for all your guidance, and unconditional support. Phil, Matt and Robbie, I will always have the utmost respect and admiration for you and I hope that we may cross paths sometime again.

To my friends, whom have put up with my endless life and science rambles, I thank you and am grateful to have been able to spent the last few years with such an amazing group of people. To my posse, and one direction crew, thank you for all the great moments spend, they will always be remembered and specially for your friendship.

I would like to thank each of the members of the faculty of Earth Sciences because I have learned valuable skills that have prepared me for the professional world as well as contributed to my personal growth.

Finally, would also like to thank my collaborators for all the technical advice provided. Marc Beauchamp, thank you for all the technical help and helpful advice on EPMA instrumentation and interpretation. I would like to thank Ivan Barker for his guidance and technical assistance with EBSD. Dr. Des Moser thank you allowing me use of the EBSD instrument. I also would like to acknowledge Joseph Umoh for all his assistance with  $\mu$ CT instrumentation. To all of you, thank you for your receptiveness when I approached you about using each of your instruments and providing advice.

Finally, I thank my examination committee for taking the time and interest in looking at this work.

<b>Table of Contents</b>	<b>Page</b>
Abstract and Keywords	ii
Acknowledgements	iii
Table of Contents	v
List of Figures	ix
List of Appendices	xii
<b>Chapter 1: Introduction and General outline</b>	<b>1</b>
1.1 Preamble	1
1.2 Context for this study	1
1.3 Enstatite Meteorites	2
1.3.1 EH and EL chondrites	3
1.3.2 Aubrites	7
1.3.3 Anomalous enstatite-rich meteorites	9
1.3.4 Primitive Enstatite achondrites	9
1.4 Processes of formation	10
1.5 Implications for planetary differentiation	10
1.6 References	13
<b>Chapter 2: Methods</b>	<b>15</b>
2.1 Introduction of Methodology	15
2.2 Samples selected	15
2.2.1 Sample preparation	15
2.3 Non-destructive X-ray techniques	16
2.3.1 Introduction to Micro-CT	16
2.3.2 Theoretical Overview of computed tomography (CT)	17
2.3.3 Operating conditions	19
2.3.4 Modal abundance determination from threshold limit selection	20
2.3.5 An introduction into micro X-ray diffraction ( $\mu$ XRD)	22

2.3.5.1 Typical $\mu$ XRD operating parameters	24
2.4 Electron microbeam methods	25
2.4.1 Mineral Chemistry via EPMA	25
2.4.2 EPMA operating conditions	26
2.5 Electron Backscatter Diffraction (EBSD)	28
2.5.1 EBSD mineral phase index preparation	30
2.5.2 EBSD Sample preparation	30
2.5.3 EBSD operating conditions	32
2.6 Micro Raman spectroscopy	33
2.6.1 Raman Operating Parameters	34
2.7 References	35
<b>Chapter 3: Insights on early parent body processes through mineralogical and textural investigation of the anomalous enstatite achondrite NWA 8173</b>	<b>38</b>
3.1 Introduction	38
3.2 Methods	39
3.3 Results	40
3.3.1 Petrography (EPMA and $\mu$ CT)	41
3.3.2 Mineral Chemistry	51
3.3.3 Crystal structure ( $\mu$ XRD and EBSD)	55
3.4 Discussion	61
3.4.1 Enstatite	61
3.4.2 What do the silica polymorphs tell us about thermal history of NWA 8173?	64
3.4.3 Chemical reactions and geothermometry from sulfides	65
3.4.4 Metal	68
3.4.5 Silicon content in the metal	69
3.4.6 Fluorophlogopite and presence of halogens in NWA 8173	70

3.4.7 Petrogenetic sequence of NWA 8173	73
3.5 References	74
<b>Chapter 4: Extensively metamorphosed anomalous Enstatite</b>	<b>79</b>
<b>Achondrites Zakłodzie and NWA 4103 and insights on early solar system processes</b>	
4.1 Introduction	79
4.2 Methods	80
4.3 Results	81
4.3.1 Micro computed tomography ( $\mu$ CT)	81
4.3.1.1 Zakłodzie	81
4.3.1.2 NWA 4301	82
4.3.2 Petrography (BSE imaging)	83
4.3.2.1 Zakłodzie	83
4.3.2.2 NWA 4301	90
4.3.3 Mineral Chemistry	97
4.3.3.1 Zakłodzie	97
4.3.3.2 NWA 4301	100
4.3.4 Mineralogy and crystal structure based on $\mu$ XRD and EBSD	100
4.3.4.1 Enstatite and Plagioclase	100
4.3.4.2 Sulfides	105
4.3.4.3 Silica	108
4.3.4.4 Sinoite	110
4.3.4.5 Graphite	112
4.4 Discussion	113
4.4.1 Petrographical interpretation from silicates	113
4.4.2 Thermal history from silica polymorphs	114
4.4.3 Sinoite	117
4.4.4 Are these meteorites paired?	119

4.4.5 Formation mechanism (Impact vs internal heating)	121
4.4.5.1 Impact melt	121
4.4.5.2 Internal heating	122
4.5 Summary	122
4.5.1 Arguments for pairing	122
4.5.2 Evidence for different metamorphic histories	122
4.5.2.1 Zakłodzie	122
4.5.2.1 NWA 4301	123
4.6 Concluding Remarks	123
4.7 References	125
<b>Chapter 5: Synthesis, General Conclusions and Future Research</b>	<b>129</b>
5.1 Summary of findings in NWA 8173	129
5.2 Formation mechanisms for NWA 8173	130
5.2.1 Impact melting	131
5.2.2 Internal heating	132
5.3 Zakłodzie and NWA 4301	132
5.3.1 Impact heating source	133
5.3.2 Internal heating source	133
5.3.3 Do Zakłodzie and NWA 4301 share a common parent body?	134
5.4 Linkages with enstatite meteorites	134
5.5 Concluding statement	136
5.6 Ideas for future work	137
5.7 References	139

## List of Figures

<b>Figure 1.1:</b> Si vs Ni % content in metal in enstatite meteorites	5
<b>Figure 1.2:</b> Ternary diagram of FeS-MgS-MnS in enstatite meteorites	6
<b>Figure 1.3:</b> Bulk composition plot of Fe/Si vs Mg/Si for enstatite meteorites	8
<b>Figure 1.4:</b> Oxygen isotopic composition of enstatite chondrites and aubrites	11
<b>Figure 2.1:</b> A) photoelectric and B) Compton effects in CT	18
<b>Figure 2.1:</b> GE eXplore Locus $\mu$ CT scanner used for meteorite scans	19
<b>Figure 2.2:</b> Cone beam configuration in CT scanning	20
<b>Figure 2.3:</b> $\mu$ CT histogram of NWA 8173	21
<b>Figure 2.5:</b> $\mu$ XRD Schematic diagram	22
<b>Figure 2.6:</b> Bragg's Law schematic	23
<b>Figure 2.7:</b> Internal EPMA structure	25
<b>Figure 2.8:</b> JEOL JXA-8530F field emission electron microprobe	27
<b>Figure 2.4:</b> Schematic diagram of EBSD setup in a SEM	30
<b>Figure 2.5:</b> EBSD diffraction patterns of SiO <sub>2</sub> grain in NWA 8173	31
<b>Figure 2.6:</b> Hitachi SU 6600 FEG-SEM at the ZAPLab at Western University	32
<b>Figure 2.7:</b> Schematic diagram of various types of photon scattering	33
<b>Figure 2.8:</b> Renishaw InVia Reflex Raman Spectrometer	34
<b>Figure 3.1:</b> NWA 8173 samples slabs context image	41
<b>Figure 3.2:</b> Micro-CT images of Zakłodzie	42
<b>Figure 3.3:</b> Elemental X-ray maps of Mg, Si and Al of NWA 8173	43
<b>Figure 3.4:</b> Myrmekitic texture in NWA 8173	44
<b>Figure 3.5:</b> BSE images of reaction bands in sulfides with EDS spectra	46
<b>Figure 3.6:</b> Graphite inclusions in metal	47
<b>Figure 3.7:</b> Sulfide exsolution in NWA 8173	48
<b>Figure 3.8:</b> BSE image and EDS spectra possible oldhamite	49
<b>Figure 3.9:</b> F-bearing mica association in NWA 8173	50
<b>Figure 3.10:</b> Plagioclase ternary compositional diagram for NWA 8173	51

<b>Figure 3.11:</b> Ternary diagram of (MgS-FeS-MnS) system for NWA 8173	53
<b>Figure 3.12:</b> Raman spectra of F-bearing mica grain in NWA 8173	54
<b>Figure 3.13:</b> Raman spectra test for OH in NWA 8173 fluorophlogopite	55
<b>Figure 3.14:</b> EBSD of host and exsolved lamellae NWA 8173	56
<b>Figure 3.15:</b> X-ray diffractogram of NWA 8173 "a" sulfide target	58
<b>Figure 3.16:</b> EBSD of silica polymorphs in NWA 8173	58
<b>Figure 3.17:</b> X-ray diffractogram of F-bearing mica grain in NWA 8173	59
<b>Figure 3.18:</b> EBSD of F-bearing mica grain in NWA 8173	60
<b>Figure 3.19:</b> Metal surrounding enstatite in Y-92189 and NWA 8173	63
<b>Figure 3.20:</b> Troilite exsolution in niningerite in Y-82189 and NWA 8173	67
<b>Figure 3.21:</b> Sulfide composition ternary with isotherms	68
<b>Figure 4.1:</b> $\mu$ CT images of Zakłodzie and NWA 4301	82
<b>Figure 4.2:</b> High contrast BSE context image of Zakłodzie	84
<b>Figure 4.3:</b> BSE image and CL map of Zakłodzie	85
<b>Figure 4.4:</b> BSE context image Si and X-ray elemental maps	86
<b>Figure 4.5:</b> Silica grain associations in Zakłodzie	87
<b>Figure 4.6:</b> BSE images of graphite in Zakłodzie	88
<b>Figure 4.7:</b> BSE image of sulfides in Zakłodzie	89
<b>Figure 4.8:</b> SEI image and EDS spectra of sinoite in Zakłodzie	90
<b>Figure 4.9:</b> CL context image of NWA 4301	91
<b>Figure 4.10:</b> X-ray elemental maps showing zoning in NWA 4301	92
<b>Figure 4.11:</b> BSE and X-ray element maps of silica in NWA 4301	93
<b>Figure 4.12:</b> BSE context images of graphite in NWA 4301	94
<b>Figure 4.13:</b> BSE and EDS of sinoite in NWA 4301	95
<b>Figure 4.14:</b> BSE montage and EDS maps of NWA 4301	96
<b>Figure 4.15:</b> Ternary diagram of plagioclase in Zakłodzie and NWA 4301	97
<b>Figure 4.16:</b> BSE images and EDS spectra of oldhamite in NWA 4301	99
<b>Figure 4.17:</b> X-ray diffractograms of Zakłodzie and NWA 4301	101



<b>Figure 4.18:</b> EBSD maps of Zakłodzie	103
<b>Figure 4.19:</b> EBSD maps of NWA 4301	104
<b>Figure 4.20:</b> EBSD phase and Euler map of NWA 4301	105
<b>Figure 4.21:</b> EBSD of sulfides in Zakłodzie and NWA 4301	106
<b>Figure 4.22:</b> SEI and EBSD of silica in Zakłodzie and NWA 4301	108
<b>Figure 4.23:</b> EBSD map and image of sinoite in Zakłodzie and NWA 4301	110
<b>Figure 4.24:</b> EBSD of graphite in NWA 4301	112
<b>Figure 4.25:</b> Phase diagram of the MgO-SiO <sub>2</sub> system showing evolution of silicate melt in Zakłodzie	115
<b>Figure 5.1:</b> Meteorite parent body schematic model	136

**List of Appendices**

<b>Appendix 1:</b> EPMA conditions and standards	141
<b>Appendix 2.1:</b> WDS raster of sulfides	144
<b>Appendix 2.2:</b> WDS peak position of standards vs samples	148
<b>Appendix 2.3:</b> WDS Raster of F-mica	154
<b>Appendix 2.4:</b> Raman Operating conditions	160
<b>Appendix 3.1:</b> NWA 8173 X-Ray Elemental Maps	161
<b>Appendix 3.3:</b> EBSD map of sulfide	255
<b>Appendix 4.1:</b> Zakłodzie X-Ray Elemental maps	256
<b>Appendix 4.2:</b> NWA 4301 X-Ray Elemental Maps	290
<b>Curriculum Vitae:</b> Diego Uribe	340

## **Chapter 1: Introduction and General outline**

### **1.1 Preamble**

Since antiquity, humans have been trying to understand how we came into existence as well as what lies beyond our planet. What processes formed the solar system and the planet we call Earth? Given that technology has always been a major limiting factor in allowing us to learn more about the cosmos, we have not until the last few decades been able to directly sample material that lies outside Earth. Beyond these still-limited sample return missions to a few bodies, meteorites and interplanetary dust remain the only representative samples of extraterrestrial material we can study to learn about the environments and processes that formed our solar system (McSween, 1999).

The study of planetary materials relies on identifying the spatial, textural, mineralogical and chemical relationships present in meteorites, which in turn, may allow us to understand the conditions and processes that took place in the early solar system. Combining the above aspects allows scientists to not only provide insight about the formation conditions of meteorites in the early solar system but also expand on the current knowledge that we have about the early processes that formed the planets in the early solar system.

### **1.2 Context for this study**

This thesis will attempt to combine textural, mineralogical and geochemical investigation of anomalous enstatite achondrites in order to provide information about the formation mechanisms of these meteorites in the early solar system. This work will also attempt to investigate the role of reservoir distribution in the solar nebula in the formation of these meteorites and hence, their role during early differentiation and accretion of terrestrial planets, in particular, the role of volatiles in highly reducing magmatic systems. The anomalous enstatite meteorites studied here will be compared with other enstatite meteorites to determine if these might serve as the missing link between enstatite chondrites and aubrites, therefore resembling the evolutionary history from nebular accretion, and partial melting up to planetary differentiation.

The meteorites selected for this thesis contain unique textural and chemical features that may provide information about planetary differentiation processes and environments in the early solar system. This chapter will provide context about the environments of formation of enstatite meteorites, types of enstatite meteorites, importance and implications of enstatite meteorites in representing early stages of planetary differentiation of terrestrial planets. Chapter 2 provides a detailed description of the methodology used in this thesis as well as the theoretical background for each method. Using the methods described in Chapter 2, Chapter 3 will provide detailed descriptions of the petrography, mineral chemistry and structural phase identification of the anomalous enstatite achondrite North West Africa (NWA 8173) to establish its petrogenetic sequence as well as determine the possible mechanisms of formation in the early solar system. It will provide detailed description of a F-bearing mica phase, which will be discussed in terms of environments of formation and the role fluorine may have in highly reducing systems during the formation of NWA 8173. Chapter 4 will provide an investigation that is similar to that in Chapter 3, but will instead focus on samples of highly metamorphosed, ungrouped, enstatite meteorites, Zakłodzie and NWA 4301. Additionally, a comparison between these meteorites will be made to determine if they are in fact paired (from the same fall event, despite being found in very different places on Earth) or if they are samples of the same parent body. An important constraint on pairing and commonality of source body is the metamorphic history experienced by each meteorite, which is recorded by the mineral compositions and textures in each. Chapter 5 will summarize the findings from Chapter 3 and 4 and will discuss the overall evolutionary history of enstatite meteorites, returning to discuss the hypothesis stated in Chapter 1. Chapter 5 will also describe ideas for possible future work which may contribute to the overall understanding of planetary differentiation processes in the early solar system.

### **1.3 Enstatite meteorites**

The unique mineral and chemical assemblages seen in enstatite meteorites are the result of having formed under highly reducing conditions. That is, there was very little oxygen present and sulfur fugacity was significantly high. These unique features distinguish the

enstatite meteorites from any other group of meteorites. Enstatite meteorites are predominantly composed of Fe-free enstatite, with Fe only present in metal or sulfide species. They notably contain Si in the FeNi metal and contain an array of exotic sulfides such as oldhamite (CaS), niningerite (Mg,Fe,Mn)S, alabandite (Mn,Fe,Mg)S, keilite (Fe,Mg,Mn)S, daubréelite (FeCr<sub>2</sub>S<sub>4</sub>) as well as nitrides, carbides, silicides and fluorine-rich mica and amphibole (Keil, 1965; Rubin, 1997; Hutchison, 2004; Rubin, 2015; Uribe et al., 2017). The exotic sulfide minerals form because normally lithophile elements behave as chalcophile elements during extremely reducing conditions and ultimately bind with sulfur (Rubin, 1997). Compared to other meteorite groups, enstatite meteorites have a low Mg/Si ratio of the silicate fraction (~0.85; Shirley and Fairbridge, 1997) and combined with the low oxidation state the main silicate present is enstatite.

Enstatite meteorites are thought to have formed in the inner region of the solar nebula where conditions were highly reducing at about ~10 Ma after the beginning of the solar system. Enstatite meteorites are further subdivided into E-chondrites, with subtypes EH and EL and differentiated enstatite achondrites (aubrites). Differences between the EH and EL types have been determined based on the amount of metal, mineral assemblages and bulk compositions. The following sections will address each subtype in detail to provide context for this study.

### *1.3.1 EH and EL chondrites*

Chondrites are rocks that contain early solar system material which demonstrate that the rock has experienced little alteration by geological processes since its formation.

Chondrites are composed of chondrules, which are essentially molten droplets of silicates that formed in microgravity early in the solar system over the span of a few minutes to hours and therefore represent some of the most primitive material in the solar system.

Earlier classification schemes of the enstatite meteorites by Anders (1964), proposed a subdivision of the enstatite chondrites class into type I (high Fe, and S, showing little evidence for recrystallization) and type II (low Fe and S, and high recrystallization). This classification scheme was then replaced by Van Schmus and Wood (1967), who classified them according to meteorite group and petrologic type, where increasing

petrologic type reflects increased metamorphic conditions. Petrologic types 1-2 are not present in enstatite meteorites as these reflect aqueous alteration, which is not present in any enstatite meteorite. Later work by Sears et al. (1981), proposed to classify the enstatite chondrites into EH (high Fe, high siderophile) and EL (low Fe, low siderophile). It was later observed that these two-distinct groups have unique chemical and mineralogical differences or represent different metamorphic conditions in their parent body. The EH type contains an average of 3.3 wt% Si in metal and EL 1.3 wt% Si in metal (Rubin, 1997; Fig. 1.1). EH chondrites contain djferfisherite ( $K_6Na(Fe,Cu,Ni)_{25}S_{26}Cl$ ) and niningerite ( $Mg,Fe,Mn$ )S, higher metal and sulfide content and more albitic plagioclase ( $NaAlSi_3O_8$ ) compositions whereas EL chondrites contain sinoite ( $Si_2N_2O$ ), alabandite ( $Mn,Fe,Mg$ )S and plagioclase with a more anorthitic ( $CaAl_2Si_2O_8$ ) composition (Keil, 1968). The distinction of each enstatite chondrite subtype can be observed in FeS-MgS-MnS ternary compositional diagram (Fig. 1.2). Modern classification of enstatite chondrite subtypes is therefore defined as EH/EL, depending on compositional and mineral features mentioned above, and petrologic type ranges (3-6) depending on the level of metamorphic alteration on their parent body, where 3 represents the most pristine (~400-600°C), unaltered material and grade 6 (~750-950°C) (Mc Sween, 1999) indicates a high degree of thermal metamorphism.

Schneider et al. (2002), suggest that there is no need to sub- classify the EH and EL meteorites further based on textural investigation of chondrules in EH/EL types respectively. The study by Schneider et al. (2002) describes the apparent differences in chondrules in EH and EL types as being due to rapid cooling of EH chondrites, whereas EL chondrites cooled slowly, explaining the textural variability of chondrules in the EH and EL chondrite types. A few meteorites such as QUE 94204 and Zakłodzie have been proposed as possible type E7 chondrites (McBride and Mason 1996; Stepniewski et al., 2000; Manecki and Lodzinski 2000), implying that despite having relict chondrules and chondritic compositions, high degree of thermal metamorphism causes near complete solid state recrystallization. Overall, enstatite chondrites are divided in EH and EL subtypes depending on their chemical and mineral composition and in petrologic type depending on the degree of thermal metamorphism experienced.

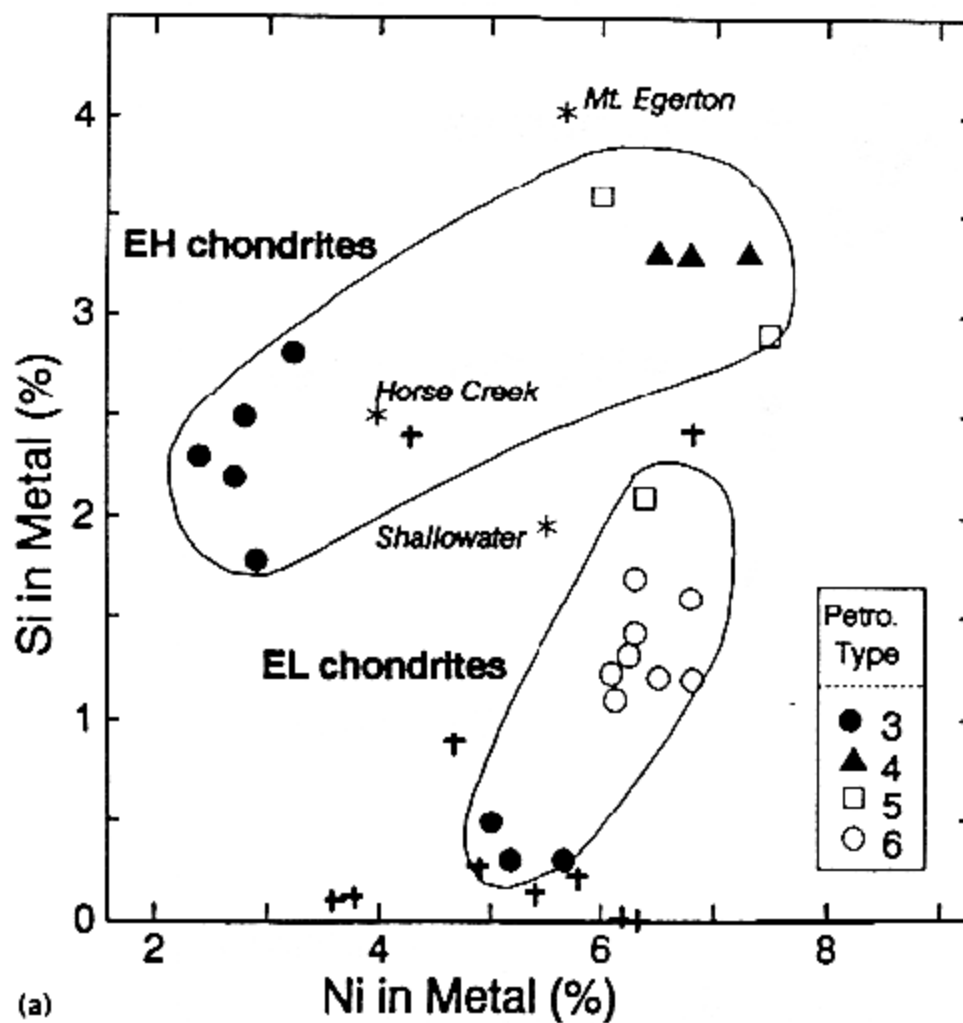


**Figure 1.1:** Si vs Ni % content in metal, distinguishing the enstatite meteorite types. The EH chondrites have a generally higher amount of Si in the metal compared to the EL group (Shirley and Fairbridge, 1997).

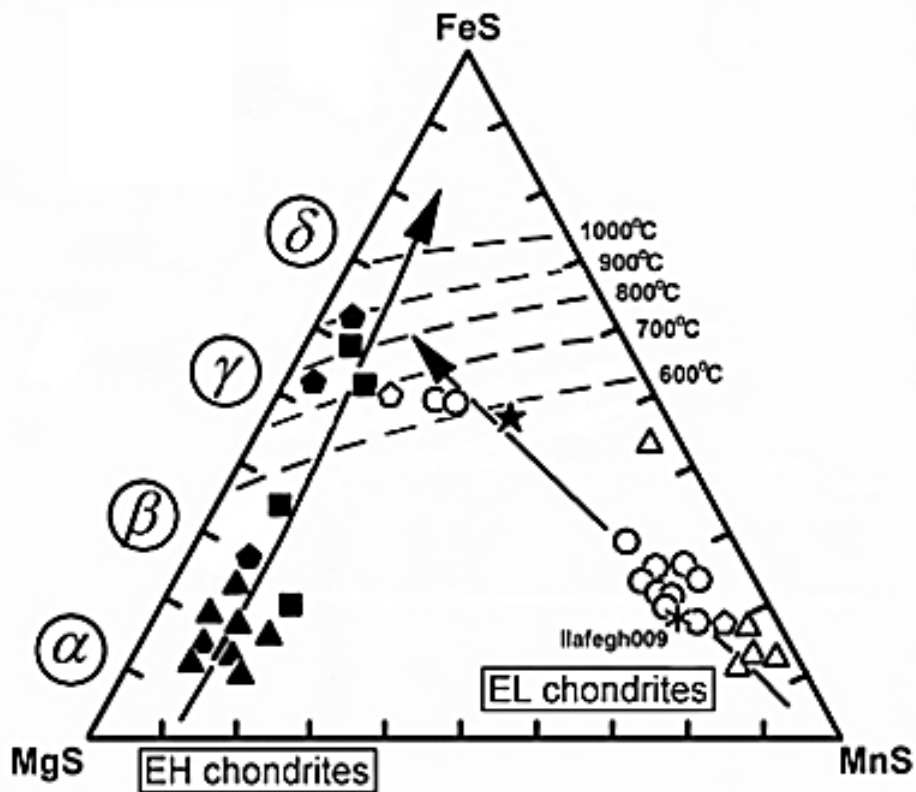


**Figure 1.2:** Ternary diagram of FeS-MgS-MnS sulfide compositions in enstatite meteorites. EL chondrites contain more alabandite (MnS) compared to EH chondrites. Dashed lines represent experimentally determined formation temperatures of sulfides (Przylibski et al., 2005).



It was initially thought that EH and EL chondrites types shared a common parent body but most now accept a model where each subtype represents a distinct parent body that formed at similar distances from the sun (Sears et al., 1981). This view is supported by bulk compositional differences in non-volatile major elements that were established by nebular processes and despite many of them being brecciated, no EL clasts are found in EH chondrites and vice versa, which suggest they represent two separate parent bodies (Keil, 1989). The relevance of this section, arises from the hypothesis posed earlier. Is it possible that the anomalous enstatite meteorites studied here represent a continuum between increasingly metamorphosed E chondrites (type 3-6) up to the point of partial melt, therefore representing the early stages of planetary differentiation?

### *1.3.2 Aubrites*

Aubrites are achondritic, igneous rocks which are the product of partial melting and crystallization and are composed of Fe-free enstatite, small but variable amounts of Fe-Ni metal, olivine, troilite and an array of exotic sulfides similar to those previously described in section 1.3.1. Most aubrites are fragmental or regolith breccias (apart from Shallowater, which is unbrecciated) where most of the clasts contain large enstatite phenocrysts of cumulate origin and other minerals such as plagioclase, augite and silica, phases not commonly ascribed to aubrites (McSween, 1999). Rare earth element patterns for aubrites show a negative europium anomaly, which is characteristic of there having been a plagioclase fractionation from aubritic magma. Additionally, their mineralogy is reflected in their bulk compositions where Mg/Si ratios are lower than that of the sun and are highly depleted in siderophile and chalcophile elements (Fig. 1.3), forming the low Fe/Si values compared to EH and EL chondrites (Shirley and Fairbridge, 1997). The low Fe/Si bulk ratios result from depletion of sulfide and metal in the aubrite source material as it fractionated after melting. Biswas et al. (1980), describe that aubrites reflect material deficient in metal compared with enstatite chondrites due to processes involving secondary separation of aubrite-forming magma from chondritic parent material.

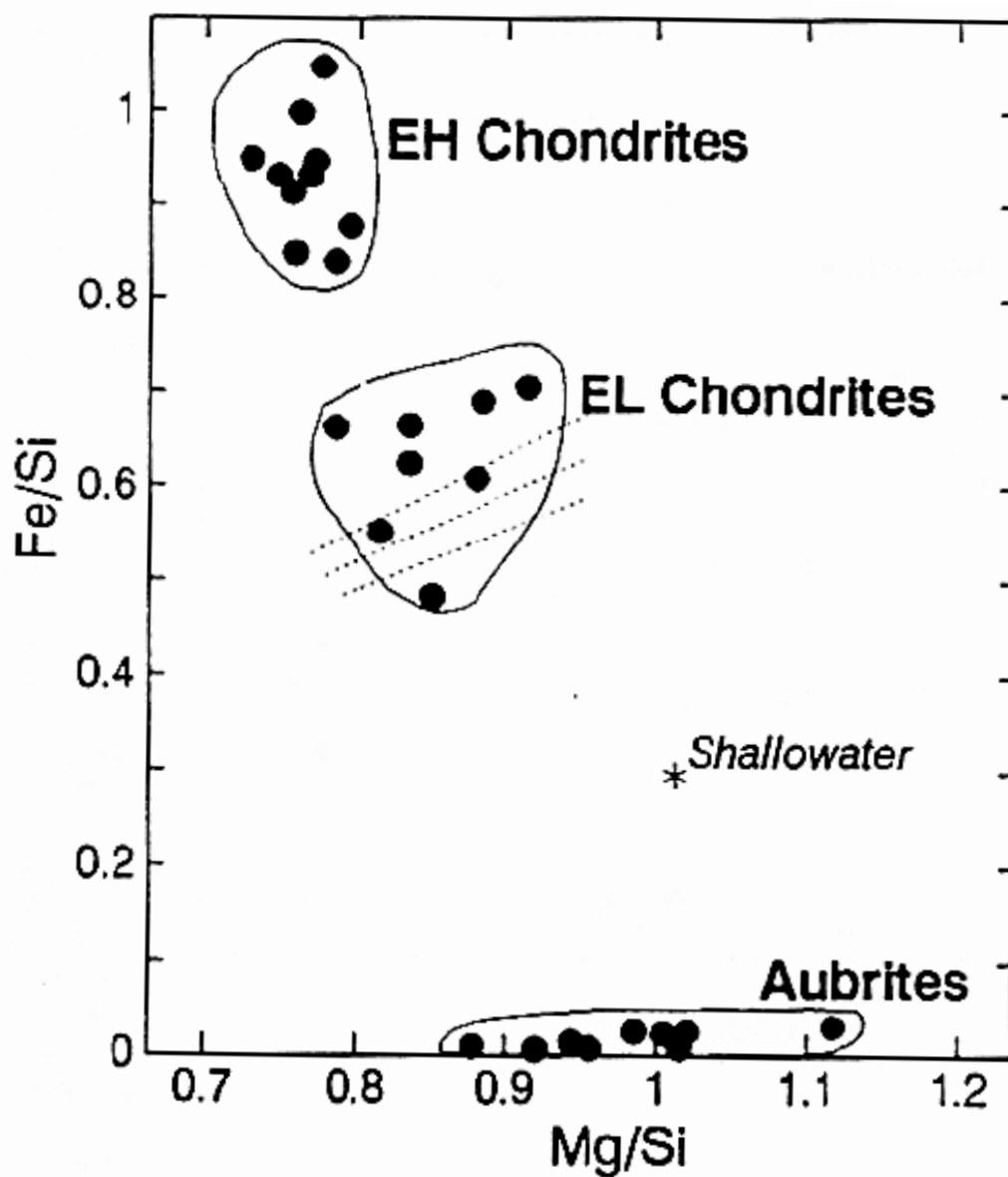


**Figure 1.3:** Bulk composition plot of  $Fe/Si$  vs  $Mg/Si$  for enstatite meteorites. Note that the low  $Fe/Si$  ratios in aubrites are explained by the depletion in siderophile and chalcophile elements in minerals which possibly separated by density-driven segregation after partial melting (Shirley and Fairbridge, 1997). Dashed lines represent meteorites whose Si content is unknown.

Although aubrites formed in similar reducing conditions and share similar mineralogy and oxygen isotopic compositions, it is believed aubrites originated from an E-like precursor different than the EH and EL chondrites (Keil, 1989). The main arguments for suggesting a separate parent body for the aubrites is the high-Ti (~6 wt%) in troilite and low ratios of metal to troilite compared to a low-Ti (~0.5 wt %) content and high ratios of metal to troilite in enstatite chondrites and that there are no EH or EL clasts present in the aubrites (Weiss et al., 2013). Therefore, aubrites were probably not derived from known enstatite chondrites of either an EL or EH parent body and possibly then represent a third enstatite meteorite parent body (Keil, 1989).

### *1.3.3 Anomalous enstatite-rich meteorites*

There is a subset of enstatite rich meteorites that have experienced substantial metamorphism and differ mineralogically and texturally from the aubrites. These have been defined as anomalous enstatite meteorites. The term anomalous implies that these meteorites have not been placed into a category of known enstatite meteorite types due to the unique mineral and textural features these exhibit and in many cases, are simply defined as ungrouped enstatite achondrites. These are igneous rocks that do not contain chondrules, and have been melted and recrystallized; despite being achondritic, these rocks do not belong to the aubrite achondrite group. For instance, one of the meteorite samples chosen in this thesis, NWA 8173, has been melted and recrystallized and although its texture suggests an achondritic nature, it contains higher Si content in metal, substantially more plagioclase, metal and sulfides than the aubrites (MetSoc Bulletin 103; Bouvier, 2017 *pending*; Uribe et al., 2016). Investigation of anomalous enstatite meteorites may provide information about early processes in the early solar system.

### *1.3.4 Primitive enstatite achondrites*

Some anomalous enstatite achondrites have been proposed as primitive enstatite achondrites (Pilsky et al., 2011; Izawa et al., 2011), which are a subtype of meteorites that have undergone some melting, have lost the textural signatures of a nebular origin, but still retain chondritic geochemical signatures. These likely represent the remaining residue after partial melting of the chondritic protolith. The study of these rocks might

therefore represent the early stages of planetary differentiation in the early solar system, when melting became significant but large-scale differentiation into a core-mantle-crust structure had not occurred.

#### **1.4 Processes of formation**

Many of the enstatite achondrites have been described as impact melt rocks of EH or EL chondrite parentage. That is, after the parent rock gets hit by an impactor, the rock is heated to high temperatures, allowing melting and subsequent recrystallization of the rock. There are various textural and mineralogical features that authors have identified as impact melt indicators (Keil, 2007; Rubin, 2015). The fact that these rocks still contain high proportions of metal, sulfide and plagioclase favors impact melt of an EH- or EL-like precursor, as one would expect density-driven segregation of high density phases during fractional crystallization of a partial melt.

Alternatively, melt induced by internal heating causing fractional crystallization has been discussed as a formation mechanism for some anomalous enstatite meteorites. Some authors describe that fractional crystallization can explain the mineral assemblages seen in some meteorites (i.e. Zakłodzie) (Przylibski et al., 2005) where density driven segregation of high density phases did not occur. Another possible formation mechanism for these meteorites is increasing thermal metamorphism (petrologic type E7) being able to cause nearly complete solid state recrystallization of the rock (Brearley and Jones, 1998). Lastly, the possibility for melting induced by internal heating, followed by impact melt may explain the mineral and textural assemblages some of these meteorites as well.

#### **1.5 Implications for planetary differentiation**

Enstatite chondrite groups, E-chondrites (EH/EL) and aubrites have similar oxygen isotopic compositions indicating they formed from a reservoir of similar composition and in the same region in the solar system (Keil, 1989). Moreover, their isotopic composition is also similar to that of the Earth-Moon system and they are the only type of meteorites to plot in the terrestrial oxygen isotopic fractionation line (Fig. 1.4; Clayton et al., 1984). This indicates that Earth and the enstatite meteorites may share a common precursor

material. Moreover, E-chondrites have been considered analogues for Earth prior to differentiating, where incorporation of silicon in metal in enstatite meteorites serves as a proxy for Earth's core as redox conditions were thought to be more reducing than presently (Ziegler et al., 2010). Silicon has been suggested (Birch, 1952; Sherman, 1997; Hillgren et al., 2000) as a main light element that accounts for the density deficit in Earth's core and its study in metal of enstatite meteorites might provide information about early stages of planetary differentiation. Some anomalous enstatite achondrites may represent objects that were melted, accumulated metal and incorporated silicon but their parent body was not able to differentiate into a core.

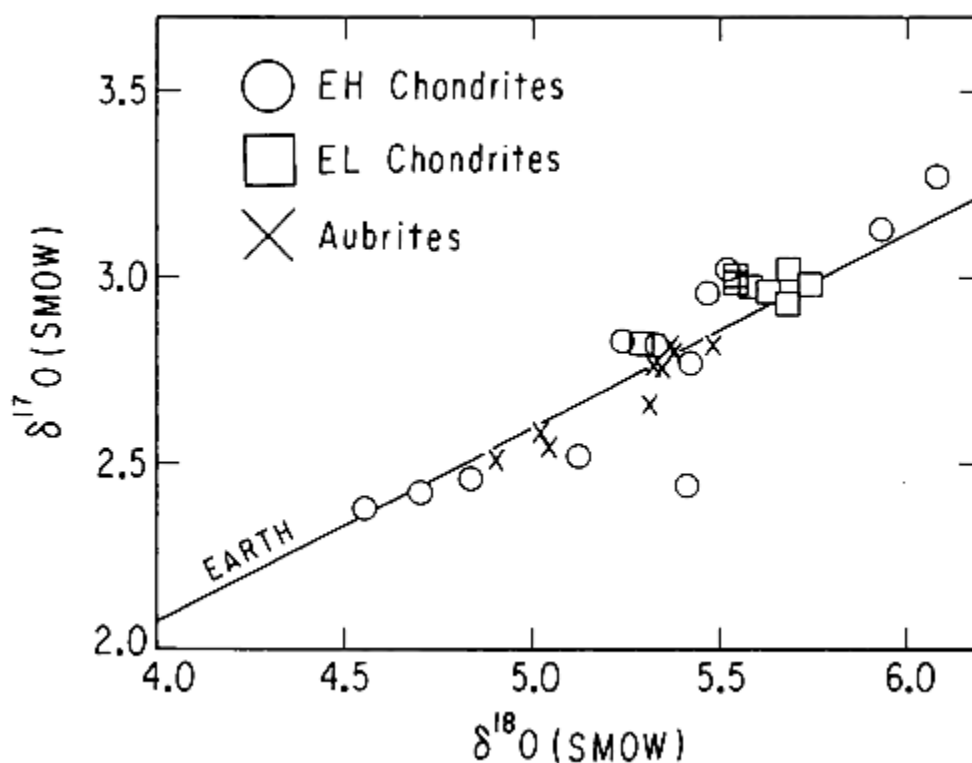


**Figure 1.4:** Oxygen isotopic composition of whole-rock enstatite chondrites and aubrites. The reference line represents the terrestrial fractionation line. Notice that most enstatite meteorites have a composition similar to Earth and therefore plot on or close to the terrestrial fractionation line (Clayton et al., 1984).

In summary, enstatite meteorites are the best available representatives of material accreted in same solar nebular region as Earth and the terrestrial planets. While they are not necessarily identical with the precursors of Earth (e.g., Righter and Drake, 1997), enstatite chondrites are isotopically and chemically analogous to Earth's precursors. Investigation of the metamorphic history of enstatite meteorites can provide insights into the mineral and chemical changes during the earliest stages of planetary differentiation in objects accreted in the (nearly) anhydrous inner solar system. Anomalous enstatite achondrites including NWA 8173, NWA 4301, and Zakłodzie record either substantial metamorphism and incipient partial melting of enstatite chondrites, or, protracted annealing of whole-rock impact melts of enstatite chondrites. In either case, the metamorphism or melting has not led to the density-driven separation of metal (and sulphide) from silicates. Such primitive enstatite achondrite material was likely common in the early stages of accretion in the inner solar system, and may have played an important role in the assembly of Earth and the other terrestrial planets.

## 1.6 References

- Birch, F. (1952). Elasticity and constitution of the Earth's interior. *Journal of Geophysical Research*, 57(2), 227-286.
- Bouvier, A. (Ed). (2017 *pending*). Meteoritical Bulletin 103. *Meteoritics & Planetary Science*.
- Clayton, R. N., Mayeda, T. K., & Rubin, A. E. (1984). Oxygen isotopic compositions of enstatite chondrites and aubrites. *Journal of Geophysical Research: Solid Earth*, 89(01).
- Hillgren, V. J., Gessmann, C. K., & Li, J. (2000). An experimental perspective on the light element in Earth's core. *Origin of the Earth and Moon*, 245-263.
- Hutchison, R. (2004). Meteorites: A petrologic, chemical and isotopic synthesis. Cambridge University Press, 506.
- Izawa, M. R., Flemming, R. L., Banerjee, N. R., & Matveev, S. (2011). QUE 94204: A primitive enstatite achondrite produced by the partial melting of an E chondrite-like protolith. *Meteoritics & Planetary Science*, 46(11), 1742-1753.
- Javoy, M., Kaminski, E., Guyot, F., Andrault, D., Sanloup, C., Moreira, M., & Jaupart, C. (2010). The chemical composition of the Earth: Enstatite chondrite models. *Earth and Planetary Science Letters*, 293(3), 259-268.
- Keil, K. (1965). Occurrences of Sinoite,  $\text{Si}_2\text{N}_2\text{O}$ , in Meteorites. *Nature*, 207, 745.
- Keil, K. (1989). Enstatite meteorites and their parent bodies. *Meteoritics*, 24(4), 195-208.
- Maneck, A., & Łodziński, M. (2001). Spherical pyroxene crystal aggregates found in Zakłodzie meteorite—are they chondrules. In *conference materials "Nauki o Ziemi w badaniach podstawowych, złożowych i ochronie środowiska na progu XXI wieku."* Wydział Geologii, Geofizyki i Ochrony Środowiska Akademii Górniczo-Hutniczej, Kraków, 28, 21-24).
- McBride K. and Mason B. 1996. Description of QUE 94204. *Antarctic Meteorite Newsletter* 19:15.
- McSween, H.Y. (1999). Meteorites and their parent planets. In introduction to meteorites. Cambridge University press, Cambridge, 115-119.
- Pilski, A. S., Przylibski, T. A., & Łuszczek, K. (2011). Primitive enstatite achondrites. *Meteorites: meteorites, tektites, impactites*, 9-21.

- Przylibski, T. A., Zagożdżon, P. P., Kryza, R., & Pilski, A. S. (2005). The Zakłodzie enstatite meteorite: Mineralogy, petrology, origin, and classification. *Meteoritics & Planetary Science*, 40(9).
- Righter, K., & Drake, M. J. (1997). A magma ocean on Vesta: Core formation and petrogenesis of eucrites and diogenites. *Meteoritics & Planetary Science*, 32(6), 929-944.
- Rubin, A. E. (1997). Mineralogy of meteorite groups. *Meteoritics & Planetary Science*, 32, 231-247.
- Rubin, A. E. (2015). Impact features of enstatite-rich meteorites. *Chemie der Erde-Geochemistry*, 75 (1), 1-28
- Schneider, D. M., Symes, S. J. K., Benoit, P. H., & Sears, D. W. G. (2002). Properties of chondrules in EL3 chondrites, comparison with EH3 chondrites, and the implications for the formation of enstatite chondrites. *Meteoritics & Planetary Science*, 37(10), 1401-1416.
- Sears, D. W., Kallemeyn, G. W., & Wasson, J. T. (1982). The compositional classification of chondrites: II The enstatite chondrite groups. *Geochimica et Cosmochimica Acta*, 46(4), 597-608.
- Sherman, D. M. (1997). The composition of the Earth's core: constraints on S and Si vs. temperature. *Earth and planetary science letters*, 153(3-4), 149-155.
- Shirley, J. H., & Fairbridge, R. W. (1997). Encyclopedia of Planetary Sciences. Encyclopedia of Planetary Sciences. Shirley, JH; Fairbridge, RW (Eds.), pp. 234-236. Springer-Verlag Berlin Heidelberg, 1997, 1020.
- Stepniewski, M., Borucki, J., Durakiewicz, T., Giro, L., & Sharp, Z. D. (2000). Preliminary study of a new enstatite meteorite from Zakłodzie (southeast Poland). *Meteoritics and Planetary Science Supplement*, 35, A152.
- Van Niekerk, D., Keil, K., & Humayun, M. (2014). Petrogenesis of anomalous Queen Alexandra Range enstatite meteorites and their relation to enstatite chondrites, primitive enstatite achondrites, and aubrites. *Meteoritics & Planetary Science*, 49(3), 295-312.
- Van Schmus, W. R., & Wood, J. A. (1967). A chemical-petrologic classification for the chondritic meteorites. *Geochimica et Cosmochimica Acta*, 31(5).
- Ziegler, K., Young, E. D., Schauble, E. A., & Wasson, J. T. (2010). Metal-silicate silicon isotope fractionation in enstatite meteorites and constraints on Earth's core formation. *Earth and Planetary Science Letters*, 295(3), 487-496.



## **Chapter 2: Methods**

### **2.1 Introduction of Methodology**

This study of the mineralogy, textures and context of anomalous enstatite achondrite meteorites requires the selection of appropriate samples and the application of a number of laboratory techniques. In this chapter, the sample selection for this thesis is outlined as well as their preparation for analysis. Each of the methods that were used to examine sample mineralogy and textures is fully introduced and described in this chapter, for reference in subsequent chapters that deal with research on specific samples.

### **2.2 Samples selected**

In this thesis, several slabs and epoxy mounts were used to represent the anomalous enstatite achondrites NWA 8173, NWA 4301 and Zakłodzie. The Zakłodzie sample was kindly loaned from meteorite collector Simon De Boer, two small fragment of the Zakłodzie meteorite were obtained from Western University meteorite collection, the NWA 4301 slabs were purchased from Nature's Vault meteorite dealers and the NWA 8173 samples were purchased from meteorite dealer Gary Fujihara in 2015. These meteorites were chosen because they represent objects in the early solar system that were molten and reprocessed by impact or internal heating during extremely reducing conditions in the inner solar system and their study might provide information about processes and environments that took place in planetary bodies in the early solar system.

#### *2.2.1 Sample preparation*

No sample preparation was required for X-ray methods ( $\mu$ CT and  $\mu$ XRD) but mounting in epoxy and surface polishing for electron microbeam methods (SEM, EPMA) and for Raman. Detail on sample preparation description is described accordingly with each method used.

## 2.3 Non-destructive X-ray techniques

Initial examination of the enstatite achondrites in this thesis was non-destructive, using X-rays to investigate the 3D structure of the samples via micro-computed tomography ( $\mu$ CT) and the identity of constituent minerals by *in situ* micro X-ray diffraction ( $\mu$ XRD). The following sections deal with each of these methods in turn.

### 2.3.1 Introduction to Micro-CT

Micro-computed tomography is commonly used as a medical tool to visualize tissue, bones and organs in humans and animals. However, in recent years, the use of biomedical  $\mu$ CT scanners has diversified substantially, opening a new range of applications, including the geosciences, (Baker et al., 2012). Micro-computed tomography serves as a useful tool for non-destructive analysis of meteorite samples. Meteorites are the only extraterrestrial rock samples which we can directly analyze without the need for spacecraft sample return missions.

Analyzing pristine meteorite samples is not always possible given that terrestrial weathering often forms alteration phases which alter the original mineralogy of the meteorite.  $\mu$ CT imaging can be used to non-destructively visualize the interior of meteorite samples. For instance, one can see the extent to which weathering has altered the meteorite. It provides fully digitized 2D and 3D data of the internal density structures of rare and valuable materials without the samples being damaged (Uesugi et al., 2010). This technique not only allows the user to identify the internal features of meteorite materials but it allows for 3D image reconstruction to identify spatial and textural relations in mineral phases of meteorites. It is also possible to determine volumetric proportions of some phases (Ketcham and Carlson, 2001), as different materials will have different attenuation values.  $\mu$ CT is used in this thesis to observe the textural relations and phase distribution in anomalous enstatite achondrites to understand the physical processes they experienced since their formation. This can be done because the density transitions often correspond to boundaries between materials or phases (Ketcham and Carlson, 2001) which can then be interpreted like a typical petrographic image. This work also demonstrates that by setting threshold intensity ranges of high vs. low

attenuation phases, modal abundances can be determined (e.g., Edey et al., 2014) and are similar to those reported in the literature (Przylibsky et al., 2005; Connolly et al., 2007).

### 2.3.2 Theoretical Overview of computed tomography (CT)

In X-ray tomography, X-rays are projected through an object at different image orientations which are then used to reconstruct 3D images of the object. Each X-ray radiograph image is composed of pixels that provide a 2D record of the integrated X-ray attenuation along each raypath. The images are used to make a 3D reconstruction consisting of voxels (volume elements) which record the reconstructed X-ray transmissibility of a location within the object (Griffin et al., 2012).

The term Micro-CT is applied to scanners that use a small field of view and higher reconstruction resolution than conventional CT scanners. Although biomedical CT scanners do not have the same power range as industrial scanners, they are useful for analyzing cm-sized meteorite samples. The CT scans obtained images have been calibrated to Hounsfield Units (HU). The Hounsfield unit represents a linear transformation of the original attenuation coefficient measurement of an object where the density of water is defined as zero and air is defined at -1000 HU.

X-ray attenuation is a function of atomic number density as well as sample thickness. The attenuation of X-rays is expressed by Beer's law [1]:

$$I=I_0 \exp(-\mu x) [1]$$

Where I is the transmitted X-ray intensity,  $I_0$  is the incident intensity and  $\mu$  is the linear attenuation coefficient of the material comprising the sample and x is the sample thickness (Knoll, 1999). Increasing grayscale values in a CT images are related to larger X-ray absorption, which relates to the amount of X-rays that are absorbed as they pass through a voxel. The above equation only applies to one type of material. If the object in question is made of different materials then the equation can be modelled by [2]:

$$I = I_0 \exp [ \sum_i (-u_i x_i) ] [2]$$

Where each  $i$  increment represents a single material with attenuation coefficient  $\mu_i$  over a linear extent of  $x_i$  (Hanna and Ketcham, 2017).

In medical scanners that use energies between 40 -140 keV, the photoelectric and Compton effects are the main means X-rays interact with an object to become attenuated (Fig. 2.1). In the photoelectric effect, a photon ejects a linked electron of the target atom by giving it energy, where the probability of interaction is proportional to a power of the X-ray photon energy. The Compton effect takes place when the wavelength of the light is in the order of magnitude of the space between electrons. Where these are free or weakly bonded, absorption of part of the X-ray photon energy occurs in kinetic form as a photon strikes an electron and causes it to re-emit a lower frequency photon in  $q$  direction.

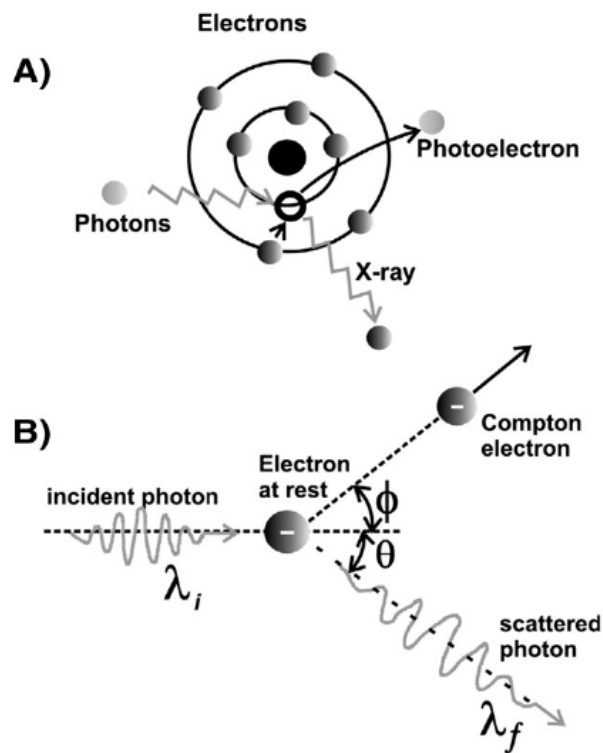


**Figure 2.1:** A) photoelectric and B) Compton effects in CT (Dushesne et al., 2009).

### 2.3.3 Operating conditions

Micro-CT scans of the meteorite samples were acquired using the GE eXplore Locus scanner at the Robarts Pre-clinical imaging center at Western University (Fig. 2.2). The main components of the scanner are: shutter, specimen bed, Gantry, X-ray source and detector. The gantry contains both the X-ray source and the detector which rotate around the specimen as it remains stationary (Fig. 2.3). This scanner, as well as most modern  $\mu$ CT scanners, uses a cone-beam X-ray source and a 2D X-ray detector which results in the simultaneous detection of multiple attenuation paths in each 2D image. The scan mode used has an in-plane field of view of view of 20 mm and an axial one of 3 mm. The scanner operated with an X-ray tube voltage of 80 kVp and a tube current of 0.45 mA. Nine hundred views of data were collected at angular increments of 0.4 degrees around the objects for 7 hours for each scan. The samples were run using a protocol which had longer exposure times than is usual for biomedical scans, to make sure that the X-rays were able to fully penetrate the meteorite samples effectively. The data were then reconstructed using an algorithm developed by Parallax innovations, into a 3D image volume with an isotropic voxel size of 20  $\mu$ m. Beam hardening was corrected using a custom calibration phantom by Edey (2014). Reconstructed 3D volumes were processed using the *MicroView* software developed by Parallax Innovations.



**Figure 2.2:** GE eXplore Locus  $\mu$ CT scanner used for meteorite scans at the Robarts pre-clinical imaging center (Healthcare GE, 2005).

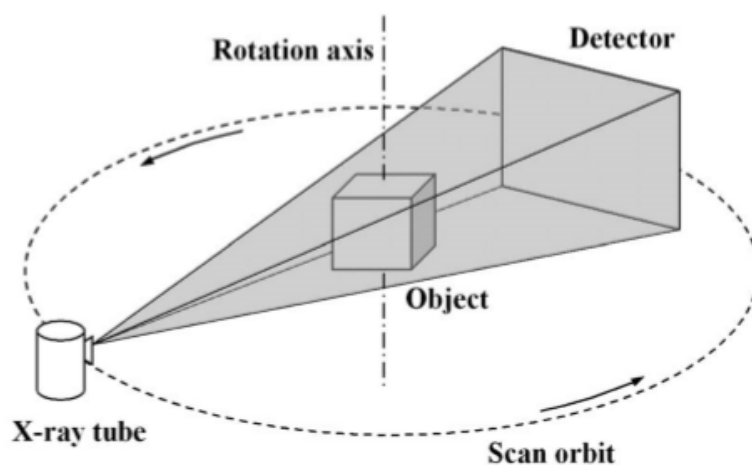


**Figure 2.3:** Cone beam configuration in CT scanning. As the object remains stationary, X-ray images are recorded as the source and detector move around an object (Cai and Ning, 2008).

#### *2.3.4 Modal abundance determination from threshold limit selection*

The MicroView software was not only used to visualize the scans taken but also to determine modal abundance by selecting threshold limits for high vs. low attenuation phases. Meteorite slabs of the Zakłodzie and NWA 4301 meteorite were used as these have documented modal abundances by some authors (Przylibsky et al., 2005; Connolly et al., 2007). Histograms of the voxel distribution of each scan were used to select the threshold limits for high and low density attenuation phases, respectively. 3D Isosurfaces of high density attenuation phases were produced and were overlaid on 2D virtual slice images. We then selected the lower limits of voxel background values as the starting point for selecting low density attenuation phases. As certain values are selected in the histograms, the CT images will highlight the areas that correspond to the specific attenuation values, therefore allowing an examination of the lower limits of low density attenuation phases (Fig. 2.4). Threshold limits for silicates were selected as the intensity values that delineate the isosurface that represents metal and sulfide phases. This means that any value that is highlighted inside the isosurface only belongs to the metal and sulfide phases. This value was then selected as the higher limit of the high-density attenuation phases and the upper limit was set at the highest intensity value seen in the

histogram. The histogram is plotted on a frequency vs intensity graph, where the peak at -1000 represents air (by HU definition) and the main peak at ~1000 HU intensity represents silicates with the end of the histogram represents higher density phases such as sulfide and metal as illustrated in Fig 2.4.

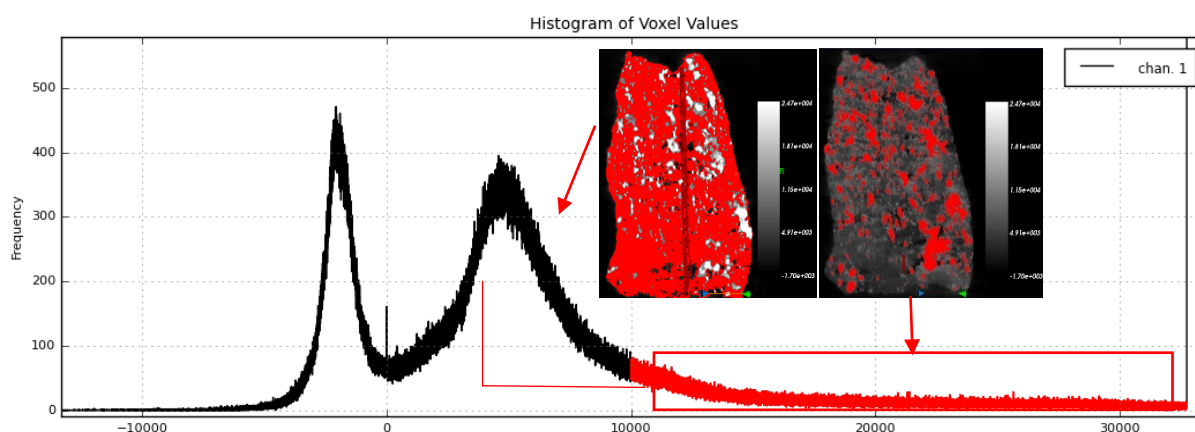


**Figure 2.4** : Micro-CT histogram of NWA 8173. Threshold selection limits for low attenuation (silicates) and high attenuation (metal, sulfide) from a frequency vs intensity histogram using NWA 8173 as an example. Note that the limit for low attenuation phases only encompasses the area outside the isosurface (white) for high attenuation phases representative of metal and sulfides. The first peak at -1000 HU represents air and after ~1000 HU lower limits of silicates begin with the tail of the graph representing high density phases.

Once threshold values are selected, a volume fraction of high vs low attenuation phases is calculated by the MicroView program. The volume fractions are then normalized and treated so that they are represented as modal percent for high and low attenuation phases. The values obtained are within ~5% difference from those reported in literature. The high intensity phases (metal and sulfide) and silicates can be calculated over the total volume of the sample. The method described above, takes less time and serves only as first attempt approximation of the composition of a meteorite in question in terms of low and high density attenuation phases. Although the method can only be quantified for high and low density attenuation phases, it is still a useful qualitative method that can be used to visualize the extent and distribution of the phases present in meteorite samples. However, this method cannot distinguish between silicate phases and cannot separate metal and

sulfide phases give that with low power, medical CT scanners, high density phases reach voxel saturation and cannot be distinguished.

### 2.3.5 An introduction into micro X-ray diffraction ( $\mu$ XRD)

Compared to conventional powder diffractometers, micro X-ray diffraction allows for non-destructive, in situ analysis of terrestrial and planetary materials. In  $\mu$ XRD, X-rays are diffracted at a  $2\theta$  angle, which is dependent on the interplanar lattice spacing of a crystal structure, resulting in characteristic angles of diffracted X-rays onto a detector (Fig. 2.5).

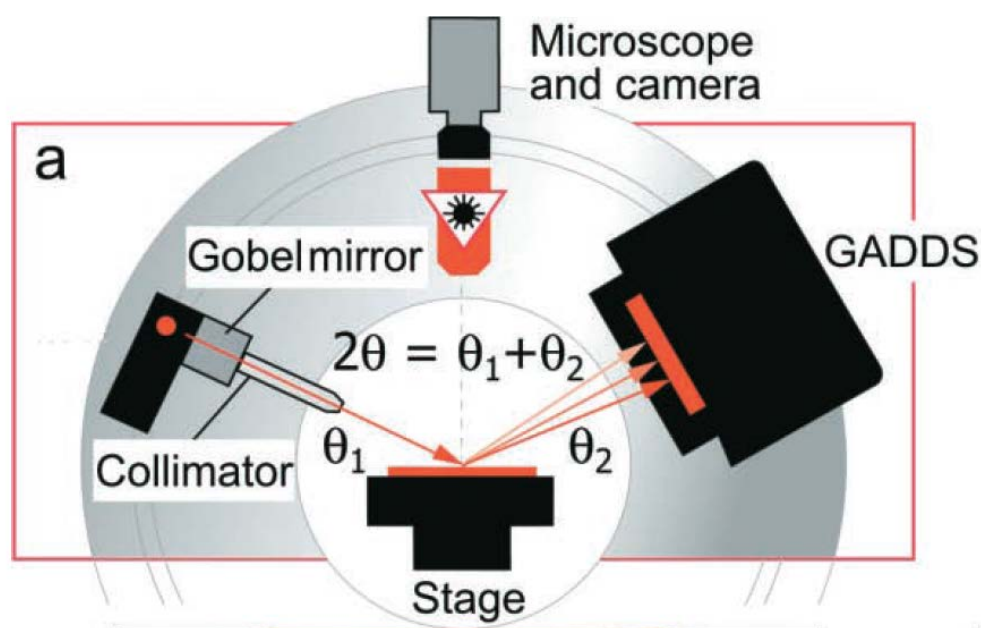


**Figure 2.5:** Schematic diagram of the Bruker D8 x-ray diffractometer (Flemming, 2007).  $\theta_1$  incident X-ray angle,  $\theta_2$  is diffraction angle, Diffracted X-rays are then collected on the GADDS 2D detector. In omega scan the source and detector move around the sample while still maintain  $2\theta$  geometry.

The advantage of  $\mu$ XRD over conventional powder X-ray diffraction is its ability to perform omega and coupled scans on in situ samples, without requiring sample powdering. In omega scans the source and detector are rotated through an omega angle ( $\omega$ ) at fixed  $2\theta$ . Omega scans enable more lattice planes in a single crystal to satisfy the Bragg's law diffraction conditions (Flemming, 2007). Omega scans also increases the



number of diffracted lattice planes, allowing for a broader range of peaks to be identified in  $2\theta$ . In coupled scans, the source and detector remain stationary at the same angle with respect to the sample surface, resulting in conventional Bragg geometry where  $\theta_1 + \theta_2 = 2\theta$ .

In X-ray diffraction, the atomic planes of a crystal cause an incident beam of X-rays to interfere with each other as they leave the crystal. X-rays interact with a crystal lattice planes at an incidence angle  $\theta_1$  and are then diffracted onto a 2D detector at an angle  $\theta_2$  (Fig. 2.5). The diffraction of X-rays will only occur if Bragg's law is satisfied. Here, diffracted X-rays must remain in phase to produce constructive interference. In constructive interference, the path length travelled by incoming X-rays plus diffracted X-rays must be equal to an integer multiple of the wavelength of the X-rays, so that the X-rays interacting with the crystal lattice remain in phase. In other words, the amplitude of wavelengths from X-rays diffracted in a crystal lattice planes must be the same for constructive interference to occur, according to Bragg's Law as described by eq. [3]:

$$n\lambda = 2d\sin\theta \quad [3]$$

where  $n$  is an integer,  $\lambda$  is the X-ray wavelength and  $d$  is the distance between lattice planes and  $\theta$  is the angle between the incident ray and the diffracted plane (Fig. 2.6) (Reed, 2005).

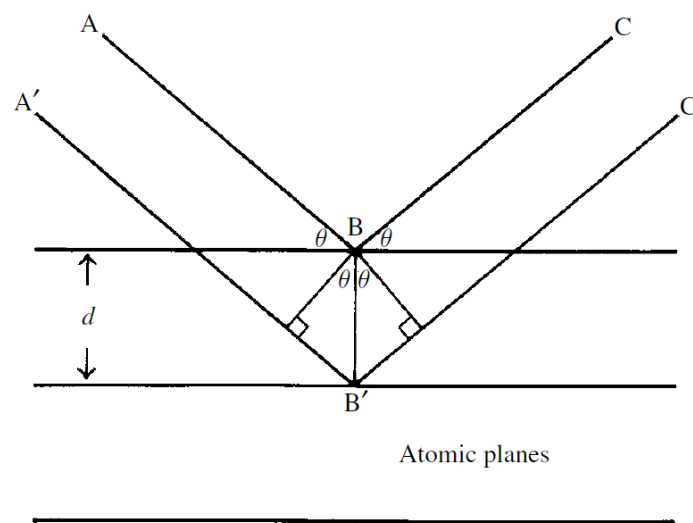


**Figure 2.6:** Bragg's law schematic. Diffracted X-rays are in phase when distance  $A'B'$  differs  $A'B$  by an integral number of wavelengths (Reed, 2005).

The equation  $2d\sin\theta$  refers to the extra distance that an X-ray beam must travel to remain in phase with the beam that is diffracted by the top lattice plane in a crystal. The X-rays that satisfy Bragg's law will be diffracted into the 2D detector and each unique set of lattice planes  $\{hkl\}$  in a crystal diffracts X-rays at an angle  $2\theta$  depending on its interplanar lattice spacing (Flemming, 2007).

### *2.3.5.1 Typical $\mu$ XRD operating parameters*

A Bruker D8 Discover Micro X-ray diffractometer ( $\mu$ XRD) at Western University was used for mineral identification of the enstatite achondrites samples used. The diffractometer uses a Co  $K\alpha$  radiation ( $\lambda = 1.78897 \text{ \AA}$ ) source and operates at 35 kV and 45 mA beam current. The X-ray beam is collimated with a 60-mm Göbel mirror and for all work in this thesis has a nominal incident beam diameter of 300  $\mu\text{m}$ . The instrument operates in theta-theta geometry, with diffracted X-rays falling onto a Vantec-500, 2D general area detector diffraction system (GADDS) where phase ID was then performed using the International Centre for Diffraction (ICCD) database. Textural analysis can be performed on the 2D diffraction images, and mineral structures can be identified by integrating the image to produce a standard intensity versus  $2\theta$  diffraction pattern which can be searched for matches with the International Centre for Diffraction Data (ICDD) (<http://www.icdd.com>; Flemming, 2007; Uribe et al., 2016).

The instrument used a Co $K\alpha$  radiation ( $\lambda = 1.78897 \text{ \AA}$ ) source and was operated at 35 kV and 45 mA current. Meteorite samples were scanned in Omega scan mode selecting  $\theta_1=14.5$ ,  $\theta_2=21$ ,  $w=11^\circ$  for frame 1 and  $\theta_1=34.5$ ,  $\theta_2=40$ ,  $w=19^\circ$  for frame 2, at 15 minutes per frame for silicate, sulfide and metal scans. For fluorophlogopite analysis, two frames were ran at  $\theta_1=14.5$ ,  $\theta_2=17.5$ ,  $w=7^\circ$  (Frame 1) and  $\theta_1=29$ ,  $\theta_2=43$ ,  $w=21$  (Frame 2) at 120 and 180 minutes for each frame, respectively. Omega scans were chosen in order to produce diffraction of more lattice planes than in coupled scan mode. In couple scan mode the source and detector remain fixed, and results in less diffraction lattices but higher intensity than omega scans.

## 2.4 Electron Microbeam methods

Contextual images, elemental mapping and quantitative analyses of specific minerals for their chemistry and structure were obtained using two electron microbeam instruments at Western University, a field-emission electron probe micro-analyzer (FEG-EPMA) and a field-emission scanning electron microscope (FEG-SEM). For both instruments, samples required preparation of a cut and polished surface with carbon coating, as described above in sample preparation. Electron microbeam operational theory, instrument parameters and procedures are outlined below for each instrument.

### 2.4.1 Mineral Chemistry via EPMA

Electron probe micro analyses (EPMA) were performed to obtain quantitative and qualitative chemical data at a microscopic scale. In electron probe micro analysis, an electron beam is focused toward the material in question which results in the emission of X-rays characteristic of a specific chemical element. Fig. 2.7 illustrates the internal setup of an electron micro probe with each of its components.

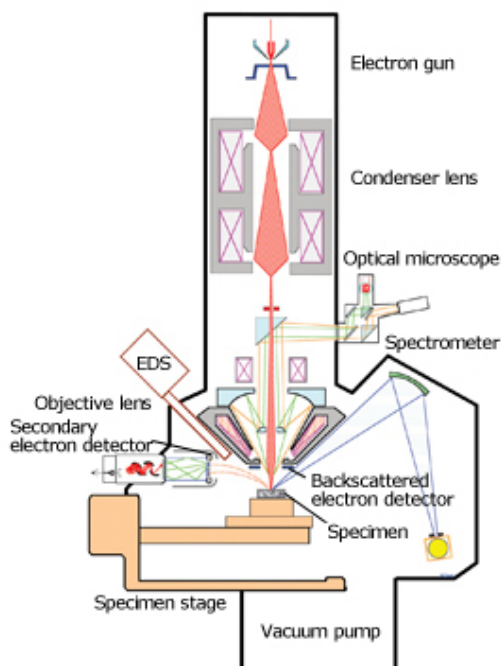


**Figure 2.7:** Internal structure of EPMA (adapted from JEOL website). Diagram shows an electron beam is focused into the sample where characteristic X-rays are detected onto spectrometers.

The X-rays produced result from the displacement of an atoms “inner shell electrons” as the energy of the incident electron beam targets an atom of the element in question. The difference in energy between the inner and outer electron shell produce X-rays whose wavelength represents the difference in energies between inner and outer electron shells respectively. X-ray emission will only occur if the energy of the electron source reaches the critical excitation energy needed to ionize the shell of the element in question (Reed 2005). The intensity of characteristic X-rays can be affected by absorption within the sample itself and can be modeled by the equation [4]:

$$I=I_0exp(-\mu px) [4]$$

Where  $I$  is X-ray intensity after absorption,  $I_0$  is the initial intensity,  $\mu$  is the mass absorption coefficient (<100 for low atomic number ( $Z$ ) and >1000 for high  $Z$ ),  $p$  is the material’s intensity and  $X$  is the path length of the incident beam into the sample (Reed, 2005). Characteristic X-rays are then analyzed by energy dispersive spectrometer (EDS) or wavelength dispersive spectrometer (WDS). EDS uses a solid-state semiconductor to collect X-rays of all wavelengths simultaneously and produces an intensity plot of intensity vs X-ray photon energy. The broad wavelength detection of EDS can be used to obtain semi-quantitative mineral chemistry by locating characteristic peaks in the X-ray spectrum. WDS targets only a specific wavelength, and it does so using Bragg diffraction. In WDS, X-rays of a specific wavelength are reflected by atomic layers with interplanar spacing  $d$ , at a certain angle of incidence and reflection, called, Bragg’s angle (Reed, 2005). Better spectral resolution is obtained by WDS as it focuses on the specific peak wavelength of the element in question and compares to the intensity of that of a standard sample of known composition. It however, leads to lower intensity peaks than EDS.

#### 2.4.2 EPMA operating conditions

Mineral compositions were measured using a JEOL JXA-8530F field emission electron microprobe at the Earth and Planetary materials analysis laboratory at Western University (Fig. 2.8).

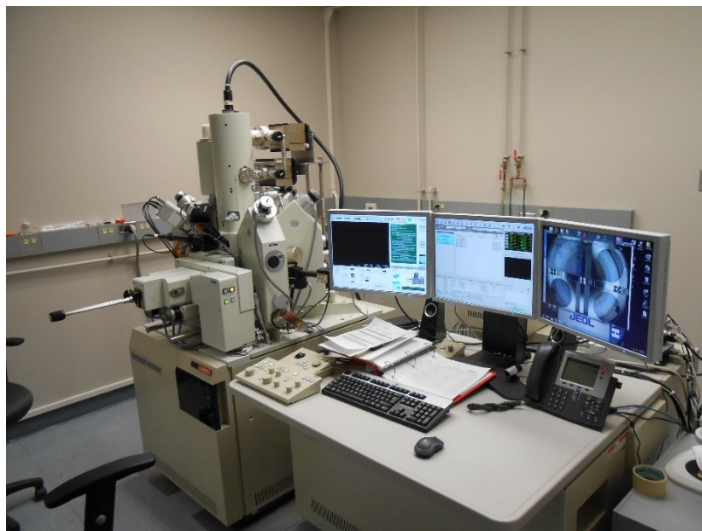


**Figure 2.8:** JEOL JXA-8530F field emission electron microprobe at the Earth and Planetary materials analysis laboratory at Western University.

Sample cut surfaces were initially polished using diamond paste of different grinds from 6  $\mu\text{m}$  down to 0.25  $\mu\text{m}$  and sonicated in isopropyl alcohol. The samples were then carbon coated to a thickness of 200-220  $\text{\AA}$  in addition to placing copper tape in the edges of the slabs and mounted epoxy mounts to minimize electron charging. The microprobe has a range of acceleration voltages of 1-30 kV and a probe current range of (10 pA- 500 nA). The microprobe was operated at an accelerating voltage of 15 kV, beam current of 20 nA and beam size of 5  $\mu\text{m}$  for silicate minerals and at 20 kV and 40 nA for sulfides, with a 1  $\mu\text{m}$  spot size, respectively. However, a spot size of 10  $\mu\text{m}$  was used for plagioclase to prevent elemental migration. Lower voltage and higher current were used for analysis of the exsolution lamellae which ranged in size from 1-4  $\mu\text{m}$  in size. The current was increased to ensure enough electrons penetrate the sample to produce characteristic X-rays for the sulfide grains to be analyzed. According to Reed (2005), for quantitative analysis the accelerating voltage should preferably be at least twice the highest relevant excitation potential, in order to obtain reasonable intensities. 15 kV is chosen as the minimum accelerating voltage used for elements with atomic number up to Fe. The use of a smaller beam spot was done to prevent contamination of the surrounding sulfide host.

A WDS raster of the sulfide minerals in the samples were performed to determine the elements present to be able to choose adequate standards and to ensure that any initial EDS sulfide spectra was not missing any element due to peak overlap (Appendix 2.1). Natural and synthetic standards were used for calibration and can be found in Appendix (1). Since there were not synthetic or natural standards for the sulfide mineral present in the samples, the peak position of the selected standards as well as the samples were compared to identify the best peak position for analysis. The peak positions of the elements in the standards were then compared to the peak positions in the samples to ensure that adequate totals were obtained (Appendix 2.2). BSE images and elemental maps were obtained using EDS spectrometers and quantitative data used WDS spectrometers of the electron microprobe. Scan times for quantitative analysis were set at 3 minutes per target. The operating conditions for EDS maps were 15 kV accelerating voltage and 5-10 nA beam current. Dwell times were 10 milliseconds and step size varied from 0.5 to 4  $\mu\text{m}$ , where the former was used for detailed maps containing a fluorine bearing phase and to identify other textural features such as zoning. For analysis of a fluorine bearing phase in NWA 8173, a WDS raster was run in an attempt to identify the presence of other halogen elements present in this mineral (Appendix 2.3).

## **2.5 Electron Backscatter Diffraction (EBSD)**

Electron backscatter diffraction (EBSD) is a scanning electron microscope (SEM) based technique which has become a versatile tool in the fields of geology and planetary science. Its discovery dates to 1928 when Shoji Nishikawa and Seishi Kikuchi directed a beam of electrons from a gas discharge on a calcite cleavage face at an incidence angle of  $6^\circ$  and the diffraction patterns were recorded on photographic plates placed behind and in front of the crystal (Zhou and Wang, 2007). EBSD allows for structural phase identification of various materials. It also enables the identification of individual grain orientations, local texture, phase identification and distribution of minerals at the microscopic scale (Schwartz et al., 2000). Compared to electron diffraction with transmission electron microscopy (TEM), EBSD has the advantage of having faster data acquisition and simpler specimen preparation (Reed, 2005).

The EBSD technique uses electron diffraction to create diffraction bands (Kikuchi bands) which are produced by the crystal structure of a mineral. As a complement to EBSD, it is also possible to do EDS and WDS analysis with the same instrument as most SEMs with an EBSD detector also have an EDS or WDS detector attached. It provides chemical confirmation on the structural phase identification in samples. The spatial resolution of EBSD is influenced by the microscope parameters, atomic number of the specimen in question, geometry, acceleration voltage and diffraction pattern quality (Randle, 2009). Moreover, accurate phase indexing is affected by system calibration, quality and magnification of a diffraction pattern. Angular resolution in EBSD is limited to  $0.5^\circ$  which is dictated by the resolution of the EBSD detector and its position with respect to the sample (Zhou and Wang, 2007).

In EBSD, an electron beam interacts with the polished surface of a sample, that is tilted 70 degrees on the SEM stage, creating a shallow angle to the incident electron beam. As the electron beam interacts with the crystal lattice of the sample, low energy loss backscatter electrons are diffracted through constructive and non-constructive interference. The diffracted electrons are then detected by a phosphor screen placed at a close distance from the sample (Fig. 2.9). Rather than diffraction spots as seen in XRD the diffracted electrons in EBSD produce two cones of diffraction that are intercepted by a phosphor screen forming Kikuchi patterns, seen as intersecting planes. The geometry of the diffraction pattern is related to the crystal structure of the sample. The width of the Kikuchi bands is related to the interplanar spacing,  $d_{hkl}$ , per Bragg's law (Zhou and Wang, 2007) and it is inversely related to the lattice spacing in a crystal structure. Moreover, the wider the bands appear, the smaller lattice plane distance in a crystal structure. Crystal orientation is determined by the angles between diffraction bands, specimen tilt and camera position in EBSD (Payton and Nolze, 2013).

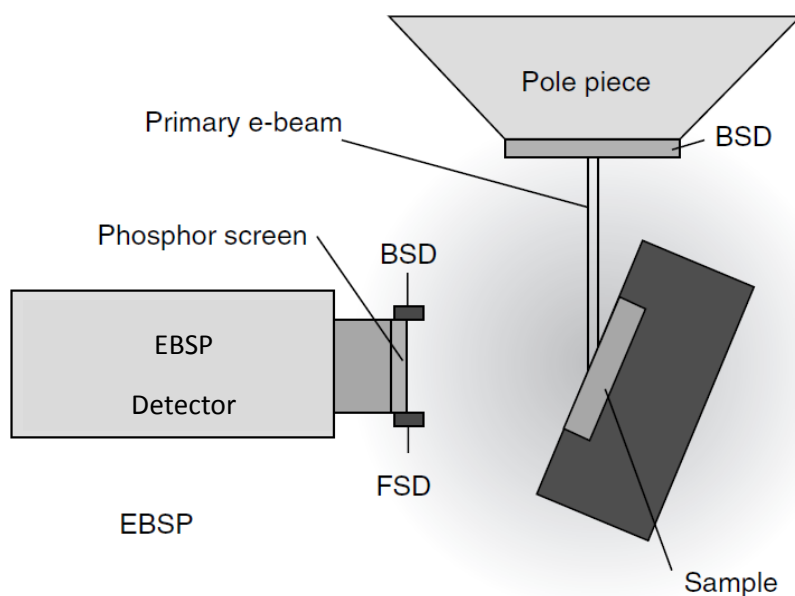


**Figure 2.9:** Schematic diagram illustrating EBSD setup in a SEM. Note: Tilting the stage at  $70^\circ$  creates a small angle ( $\sim 20^\circ$ ) between the incident electron beam and the sample (Zhou and Wang, 2007).

### 2.5.1 EBSD mineral phase index preparation

Unit cell cards for various sulfide minerals, fluorophlogopite and silica polymorphs were created as reference structures for matching with the EBSD data. All the phases indexed had a mean angle of deviation  $< 1.1$  degrees. Mean angle of deviation refers to how well the acquired EBSD pattern matches the reference structural cards used by the program to do phase indexing. The closer to 0, the better the diffraction pattern matches the structure of the reference mineral. In other words, the mean angular deviation describes the average angular misfit between detected and reference Kikuchi bands (Zhou and Wang, 2007). To properly select targets in the SEM, BSE montages with EDS elemental maps were obtained for each of the specimens studied here prior to EBSD.

### 2.5.2 EBSD Sample preparation

Six slabs and epoxy mounts were prepared from enstatite achondrite NWA 4301, Zakłodzie and NWA 8173 samples for EBSD analysis. Out of the 6 samples, 4 were



made into epoxy mounts for further chemical analysis, one for the small Zakłodzie fragments, one of NWA 4301 “c” and two for NWA 8173 “a” and “b”, respectively. Samples were initially polished using a vibratory polisher and alumina solution in oil for 3 hours each. After polishing, samples were sonicated and inspected with optical microscopy to ensure removal of contaminants. The samples were then carbon coated to a thickness similar to that used in EPMA analysis (200-220 Å) and placed in the SEM for EBSD analysis where the diffraction quality was found to be poor for all the samples.

The samples were polished again in the vibratory polisher for 3 hours but using colloidal silica solution instead. Subsequently, the samples were carbon coated again but with a decreased thickness of (150-180 Å), as carbon can drastically degrade the quality of EBSD patterns (Reed, 2005), as well as carbon painted around the specimens to minimize electron charging. Fig. 2.10 illustrates the diffraction quality of alumina vs. silica polishing solutions. The sample preparation stage is essential for EBSD as inadequate specimen preparation will result in degraded diffraction patterns which feed through to loss of data quality (Randle, 2009).

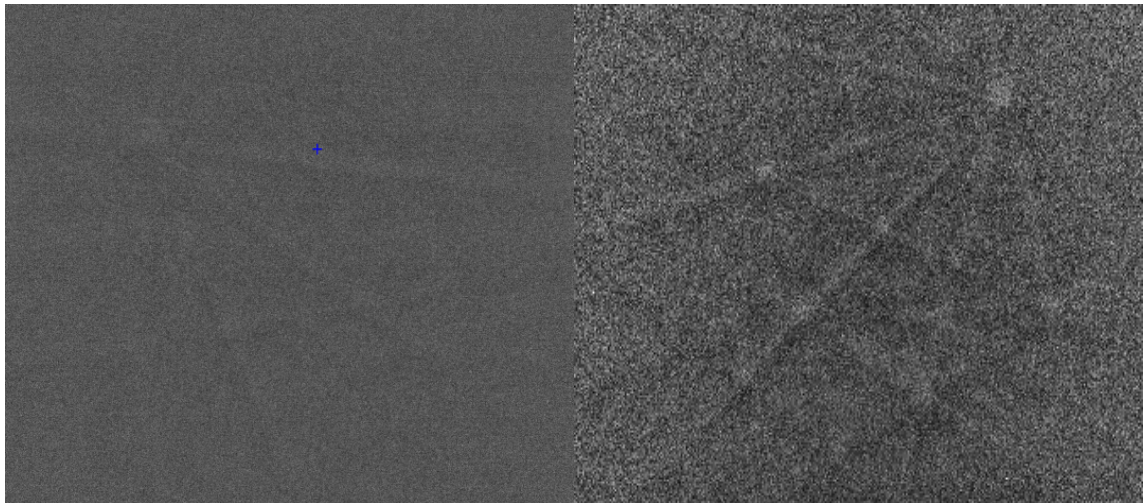


**Figure 2.10:** EBSD diffraction patterns of SiO<sub>2</sub> grain in NWA 8173 with a) Alumina oil based polish, b) colloidal silica polishing. Note: Quality of the diffraction pattern is considerably better in b than in a. Zone axis and band centers can be identified in b.

### 2.5.3 EBSD operating conditions

A Hitachi SU6600 FE-SEM at the Zircon and Accessory Phase Laboratory (ZAPLab) at Western University was used for EDS and EBSD analysis (Fig. 2.11). An Oxford Xmax 80 mm<sup>2</sup> silicon drift detector and an HKL, Nordlys EBSD detector were attached to the SEM. The instrument operated at 20 kV and ~2.5 nA beam current. For EBSD analysis a working distance of 19 mm and 70-degree sample tilt were used. EBSD phase indexing used band centers, minimum 5 and maximum 7 bands with 30 milliseconds per frame. For EBSD mapping, 30 ms dwell time, 4 x 4 binning, and step sizes ranged from 1-2.5  $\mu\text{m}$ . Wild spike correction and hole filling were applied to the EBSD maps respectively. Wild spiking omits any misindexed values within an area and hole filling matches the nearest non-indexed point to the closest indexed phase. EDS and EBSD data processing were done using the Oxford INCA and HKL Channel5 software suites, respectively. Software calibration was performed using an iterative pattern fitting routine which refines the calibration parameters and was done on a good quality sample from a known material (Randle, 2009), usually enstatite for the meteorites studied in this project.



**Figure 2.11:** Hitachi SU 6600 FEG-SEM at the ZAPLab at Western University.

## 2.6 Micro Raman spectroscopy

Raman spectroscopy requires little sample preparation and uses a monochromatic light source which causes the scattering of photons as they interact with a sample and cause molecules to vibrate. As the incident beam interacts with the sample it produces scattering of photons in all directions. A small fraction of scattered photons will have a different frequency to that of the incident beam and are therefore used in Raman spectroscopy. The shift in frequency from incident to scattered photons is referred to as inelastic scattering. In inelastic scattering, the energy of the photons scattered by interaction with a molecule is less than the incident beam energy and is used to construct a Raman spectrum (Fig. 2.12). When the frequency of incident radiation is higher than the scattered radiation, Stokes lines are produced and as the incident radiation frequency of the beam source is lower than the scattered radiation anti-Stokes are produced, conversely (Bumbrah and Sharma, 2016). Raman peak positions are related to the vibration mode between two atoms. The vibrational mode of a molecule will produce different Raman peaks at various wavelengths.

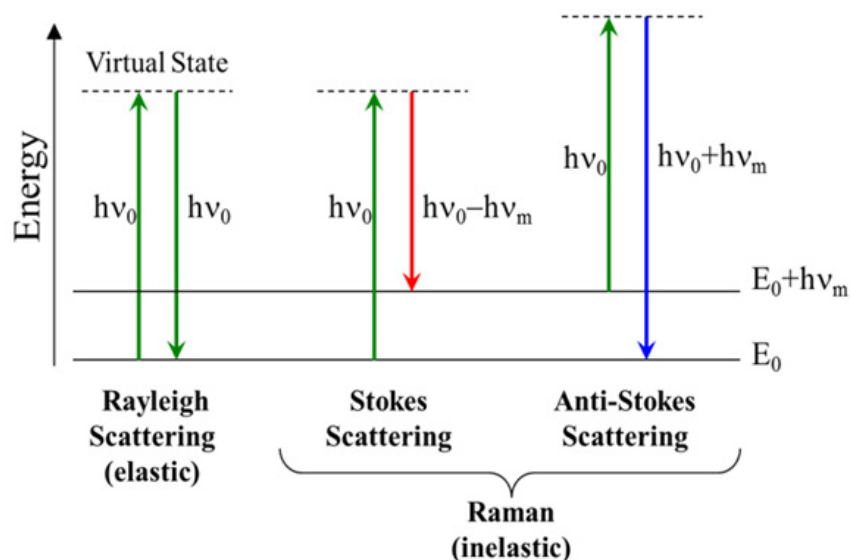


**Figure 2.12:** Schematic diagram of various types of photon scattering.  $h\nu_0$  refers to the energy of the incident beam and  $h\nu_m$  refers to the energy of photons after scattering (adapted from [www.bwtek.com](http://www.bwtek.com)).

### 2.6.1 Micro Raman Operating Parameters

Micro Raman analysis was performed on a Renishaw InVia Reflex Raman spectrometer at Surface Science Western at Western University (Fig. 2.13). It used a green laser beam of 514 nm and had a spectral range of 150-2000  $\text{cm}^{-1}$ , 4.5-7.5  $\text{cm}^{-1}$  spectral resolution and used a beam diameter of 2  $\mu\text{m}$ . Identification of Raman peaks was done via spectral curve fitting using the WIRE 4.2 software. The instrument was used to confirm the presence of fluorophlogopite in the meteorite NWA 8173 as well as to test for the presence of OH in this mineral. An initial 5% laser power, 30 second exposure time and spectral range of 100-2000  $\text{cm}^{-1}$  in static mode were used to acquire the Raman spectra of the F-bearing mineral which was then compared with the reference spectra of phlogopite and fluorophlogopite phases. An initial scan in static mode was done using 5 % laser power and 30 seconds' exposure, covering a spectral range from 3000-4000  $\text{cm}^{-1}$  to analyze for OH. Laser power was then increased to 10% in order to induce more scattering to obtain better signal at the same spectral range. Lastly, a continuous mode scan was performed using 45 second exposure, covering a spectral range from 100-4000 $\text{cm}^{-1}$  to verify the presence of other halogen elements in the F-bearing mica grain in the meteorite NWA 8173. Spectral ranges of 3600-3750  $\text{cm}^{-1}$  were carefully analyzed to confirm the presence of OH as the typical OH- stretching absorption bands appear in this range (Scordari et al., 2013). Detail on Raman operating conditions can be found in Appendix 2.4.



**Figure 2.13:** Renishaw InVia Reflex Raman Spectrometer (adapted from surfacesciencwestern.com).

## 2.7 References

- Baker, D. R., Mancini, L., Polacci, M., Higgins, M. D., Gualda, G. A. R., Hill, R. J., & Rivers, M. L. (2012). An introduction to the application of X-ray microtomography to the three-dimensional study of igneous rocks. *Lithos*, *148*, 262-276.
- Bumrah, G. S., & Sharma, R. M. (2016). Raman spectroscopy–Basic principle, instrumentation and selected applications for the characterization of drugs of abuse. *Egyptian Journal of Forensic Sciences*, *6*(3), 209-215.
- Cai, W., & Ning, R. (2008). Preliminary study of a phase-contrast cone-beam computed tomography system: the edge-enhancement effect in the tomographic reconstruction of in-line holographic images. *Optical Engineering*, *47*(3), 037004-037004.
- Cnudde, V., & Boone, M. N. (2013). High-resolution X-ray computed tomography in geosciences: A review of the current technology and applications. *Earth-Science Reviews*, *123*, 1-17.
- Connolly, H. C., Zipfel, J., Folco, L., Smith, C., Jones, R. H., Benedix, G., ... & Grossman, J. N. (2007). The Meteoritical Bulletin, No. 91, 2007 March. *Meteoritics & Planetary Science*, *42*(3), 413-466.
- Duchesne, M. J., Moore, F., Long, B. F., & Labrie, J. (2009). A rapid method for converting medical Computed Tomography scanner topogram attenuation scale to Hounsfield Unit scale and to obtain relative density values. *Engineering Geology*, *103*(3), 100-105.
- Edey, David R., "Micro-Computed Tomography Semi-Empirical Beam Hardening Correction: Method and Application To Meteorites" (2014). *Electronic Thesis and Dissertation Repository*. 2000.
- Griffin, L. D., Elangovan, P., Mundell, A., & Hezel, D. C. (2012). Improved segmentation of meteorite micro-CT images using local histograms. *Computers & Geosciences*, *39*, 129-134.

- Hanna, R. D., & Ketcham, R. A. (2017). X-ray computed tomography of planetary materials: A primer and review of recent studies. *Chemie der Erde-Geochemistry*.
- Healthcare, G. E. (2005). eXplore Locus user guide. *Technical Publication Direction*, 2394683, 1-73.
- Ketcham, R. A., & Carlson, W. D. (2001). Acquisition, optimization and interpretation of X-ray computed tomographic imagery: applications to the geosciences. *Computers & Geosciences*, 27(4), 381-400.
- Mees, F., Swennen, R., Van Geet, M., & Jacobs, P. (2003). Applications of X-ray computed tomography in the geosciences. *Geological Society*, London, Special Publications, 215(1), 1-6.
- Payton, E. J., & Nolze, G. (2013). The backscatter electron signal as an additional tool for phase segmentation in electron backscatter diffraction. *Microscopy and Microanalysis*, 19(04): 929-941.
- Przylibski, T. A., Zagożdżon, P. P., Kryza, R., & Pilski, A. S. (2005). The Zakłodzie enstatite meteorite: Mineralogy, petrology, origin, and classification. *Meteoritics & Planetary Science*, 40(S9).
- Randle, V. (2009). Electron backscatter diffraction: strategies for reliable data acquisition and processing. *Materials Characterization* .60(9): 913-922
- Reed, S. J. B. (2005). Electron microprobe analysis and scanning electron microscopy in geology. Cambridge University Press.
- Schwartz, A. J., Kumar, M., Adams, B. L., & Field, D. P. (Eds.). (2009). Electron backscatter diffraction in materials science (Vol. 2). New York: Springer.
- Scordari, F., Schingaro, E., Ventruti, G., Nicotra, E., Viccaro, M., & Tagliani, S. M. (2013). Fluorophlogopite from Piano delle Concazze (Mt. Etna, Italy): Crystal chemistry and implications for the crystallization conditions. *American Mineralogist*, 98(5-6), 1017-1025.

- Scordari, F., Schingaro, E., Ventruti, G., Nicotra, E., Viccaro, M., & Tagliani, S. M. (2013). Fluorophlogopite from Piano delle Concazze (Mt. Etna, Italy): Crystal chemistry and implications for the crystallization conditions. *American Mineralogist*, 98(5-6), 1017-1025.
- Sears, D. W., Sears, H., Ebel, D. S., Wallace, S., & Friedrich, J. M. (2016). X-ray computed tomography imaging: A not so nondestructive technique. *Meteoritics & Planetary Science*, 51(4), 833-838.
- Tsuchiyama, A., Nakamura, T., Nakano, T., & Nakamura, N. (2002). Three-dimensional description of the Kobe meteorite by micro X-ray CT method: Possibility of three-dimensional curation of meteorite samples. *Geochemical Journal*, 36(4), 369-390.
- Uesugi, M., Uesugi, K., & Oka, M. (2010). Non-destructive observation of meteorite chips using quantitative analysis of optimized X-ray micro-computed tomography. *Earth and Planetary Science Letters*, 299(3), 359-367.
- Zhou, W., & Wang, Z. L. (Eds.). (2007). Scanning microscopy for nanotechnology: techniques and applications. Springer science & business media. XIV, 522

## Chapter 3: Insights on early parent body processes through mineralogical and textural investigation of the anomalous enstatite achondrite NWA 8173

### 3.1 Introduction

Enstatite chondrites are undifferentiated meteorites which have similar isotopic compositions to that of Earth possibly having sampled the same region of the solar nebula as that of Earth's precursors (Javoy et al., 2010). Enstatite achondrites share a similar mineralogy and bulk compositions with the enstatite chondrites through their range of metamorphic petrologic grades 3-6, but the enstatite achondrites are a product of melting and/or recrystallization. Aubrites make up most of the enstatite achondrites, however, there are a subset of enstatite achondrites that differ texturally and mineralogically from the aubrites (Keil and Bishoff, 2008; Izawa et al., 2010; Izawa et al., 2011; Boesenberg et al., 2014), and have been denoted as anomalous enstatite achondrites.

Enstatite meteorites exhibit unusual mineralogy generally attributed to having been formed under extremely reducing conditions, with negligible hydrogen and at least in some cases elevated sulfur (Herndon and Sues, 1975). Some of the distinctive features of these meteorites include: near-end member enstatite  $\text{MgSiO}_3$ , Si-bearing metal, silica polymorphs, sinoite ( $\text{Si}_2\text{N}_2\text{O}$ ) and an array of unusual sulfides. Under the anhydrous, reducing, high-sulphur conditions experienced by enstatite meteorites, elements such as Ca, Mg, Mn that are normally lithophile become chalcophile and will tend to form the exotic sulfide minerals such as oldhamite  $(\text{Ca},\text{Mg})\text{S}$ , niningerite  $(\text{Mg},\text{Fe},\text{Mn})\text{S}$ , keilite  $(\text{Fe},\text{Mg},\text{Mn})\text{S}$ , alabandite  $(\text{Mn},\text{Mg},\text{Fe})\text{S}$ , djerfisherite  $\text{K}_6\text{Na}(\text{Fe}^{2+},\text{Cu},\text{Ni})_{25}\text{S}_{26}\text{Cl}$ , daubr elite  $(\text{FeCr}_2\text{S}_4)$ , and numerous others (e.g., Rubin, 1997). Hydrous phases and phases containing ferric iron are conspicuously absent from fresh enstatite meteorites, but rapidly form upon interaction with the terrestrial environment.

This chapter reports on the mineralogy, mineral chemistry and textures of the anomalous enstatite achondrite NWA 8173 (MetSoc Bulletin 103; Bouvier, 2017 *in press*) and discusses possible processes that this meteorite experienced during its history. Also, reported here are the crystal structure and chemistry of a fluorine-bearing mica mineral,



which has previously been identified in a few enstatite meteorites but has not been yet studied in detail. The mineral and textural assemblages record the petrogenesis of this meteorite and, more importantly, provide insight on key processes enstatite achondrites have undergone during their formation in the early solar system.

### 3.2 Methods

Two slice samples of the Northwest Africa 8173 (NWA 8173) meteorite were obtained for this study from meteorite dealer Gary Fujihara in 2015. The slices are designated “a” (0.98 g) and “b” (0.92 g). NWA 8173 is described in the MetSoc Meteorite bulletin (Bouvier, 2017 *in press*) as an anomalous enstatite achondrite. The meteorite hand sample is described as being covered by fusion crust with some rust stained white regions seen in fractured surfaces. NWA 8173 is composed of mostly untwinned enstatite with FeNi metal containing ~20% Si-bearing metal (with an average of 3.21 wt % Si in metal) and some accessory minerals. The reported purity of the enstatite and the high silicon content in metal make this meteorite unique from other enstatite meteorites (Bouvier, 2017 *in press*). NWA 8173 thus far has not been studied in significant detail and has been selected for this project due to its unique features amongst enstatite meteorites.

Sample NWA 8173a is darker and has more disseminated metal and sulfide grains whereas sample NWA 8173b is lighter in appearance and coarser grained than fragment a. Slabs and probe mounts of lighter and darker fragments of NWA 8173 were prepared for electron beam analysis using a vibratory polisher and 0.05  $\mu\text{m}$  colloidal silica for two hours and then carbon coated for electron probe micro-analysis (EPMA) and electron backscatter diffraction (EBSD). In order to obtain better diffraction in EBSD, a lighter carbon coat was used (150-200  $\text{\AA}$ ) than for EPMA analysis.

A detailed account of the methods employed in this thesis is given in Chapter 2. Below, a brief summary is given of the instruments, operating parameters and procedures used in the study of NWA 8173 samples. For EBSD, an Oxford Xmax 80mm<sup>2</sup> silicon drift EDS detector and HKL, Nordlyis EBSD detector was used. These detectors are attached to a Hitachi SU6600 FE-SEM at the Zircon and Accessory Phase Laboratory (ZAPLab) at

Western University. The instrument operated at 20 kV, and ~2.5 nA. Samples were tilted 70° and a working distance of 19 mm was used during EBSD analysis. EBSD phase indexing used band centers, using a minimum of 5 and maximum of 7 bands with 30 milliseconds per frame respectively. Oxford INCA and HKL Channel5 software suites were used to process EDS and EBSD data.

Quantitative mineral compositions were measured using a JEOL JXA-8530F field emission electron microprobe at the Earth and Planetary Materials Analysis laboratory at Western University. The probe was operated with an accelerating voltage of 15 kV, beam current of 20 nA and a beam spot size of 5 µm. Natural and synthetic standards were used for calibration (Appendix 1). Micro X-ray diffraction (µXRD) analysis was performed using a Bruker D8 Discover µXRD at Western University (Flemming, 2007). The µXRD has a 60 mm cobalt Göbel mirror and was operated with a 300 µm pinhole collimator snout and a 2D Vantec-500 detector with (GADDS) software and phase ID was done using the ICCD database. Omega scans (see Chapter 2) were obtained for silicates, sulfide and fluorine-bearing mica minerals. Micro-CT (µCT) data were obtained using a Locus and eXplore speCZT scanners and operated with an X-ray tube voltage of 80 kVp, 110 kVp and a tube current of 0.45 mA. Nine hundred 2D radiograph views were collected at an angular increment of 0.4 degrees for 360 degrees around the object. Images were then reconstructed into a 3D image volume with an isotropic voxel size of 20 µm. Beam hardening correction was done with Edey's (2013) calibration method for the speCZT scanner. *MicroView* software was used to interact with the 3D reconstructions to create 3D volumes and threshold voxel intensity isosurfaces. Micro Raman spectroscopy was done on a Renishaw 2000 Raman spectrometer at Surface Science Western and used a green laser beam of 514 nm. Raman peak identification was done by spectral curve fitting using the WIRE 4.2 software. Detailed operating parameters of the Raman instrument can be found in Appendix 2.4.

### **3.3 Results**

The results reported in this section will be discussed in terms of petrography, mineral chemistry and structural analysis on the NWA 8173 slab samples. Petrographic results

will be based on EPMA (SEI, BSE, CL and EDS mapping) of mineral phases, and the spatial distribution of 3D isosurfaces of silicates versus metal-sulfides, as obtained from  $\mu$ CT computed tomography scans. Quantitative mineral chemistry from EPMA is reported on silicates, sulfides, silica, metal, and F-bearing mica minerals identified in NWA 8173. Lastly, crystal structural analysis will be based on  $\mu$ XRD and EBSD findings of mineral phase identified in conjunction with co-located mineral chemistry.

### 3.3.1 Petrography (EPMA and $\mu$ CT)

The two slice samples of NWA 8173 studied here (Fig. 3.1) are contrasting in that fragment “a” has a darker visual appearance than fragment “b”. Fragment “b” has a white interior with minor, orange- iron oxide staining. Both slice fragments were examined with micro computed tomography ( $\mu$ CT) to non-destructively identify internal features of the meteorites as well as to see the overall mineral distribution and texture in the samples. Lithology “a”, exhibited smaller and more disseminated metal and sulfide grains throughout the sample as well as having slightly higher density attenuation values than fragment “b” (Fig. 3.2). Isosurface rendering of high density attenuation phases revealed fragment “b” to be coarser-grained with some locally enriched clumps of sulfide and metal which are larger than similar sulfide and metal volumes in fragment “a”.



**Figure 3.1:** NWA 8173 samples "a" (Top 0.98g slice) and "b" (Bottom 0.92g slice). Note the two apparent lithologies, a light lithology represented by slice b wraps around the darker lithology in slab "a". The white regions show rusty iron oxide due to weathering. Images are from Big Kahuna meteorites, operated by Gary Fujihara.

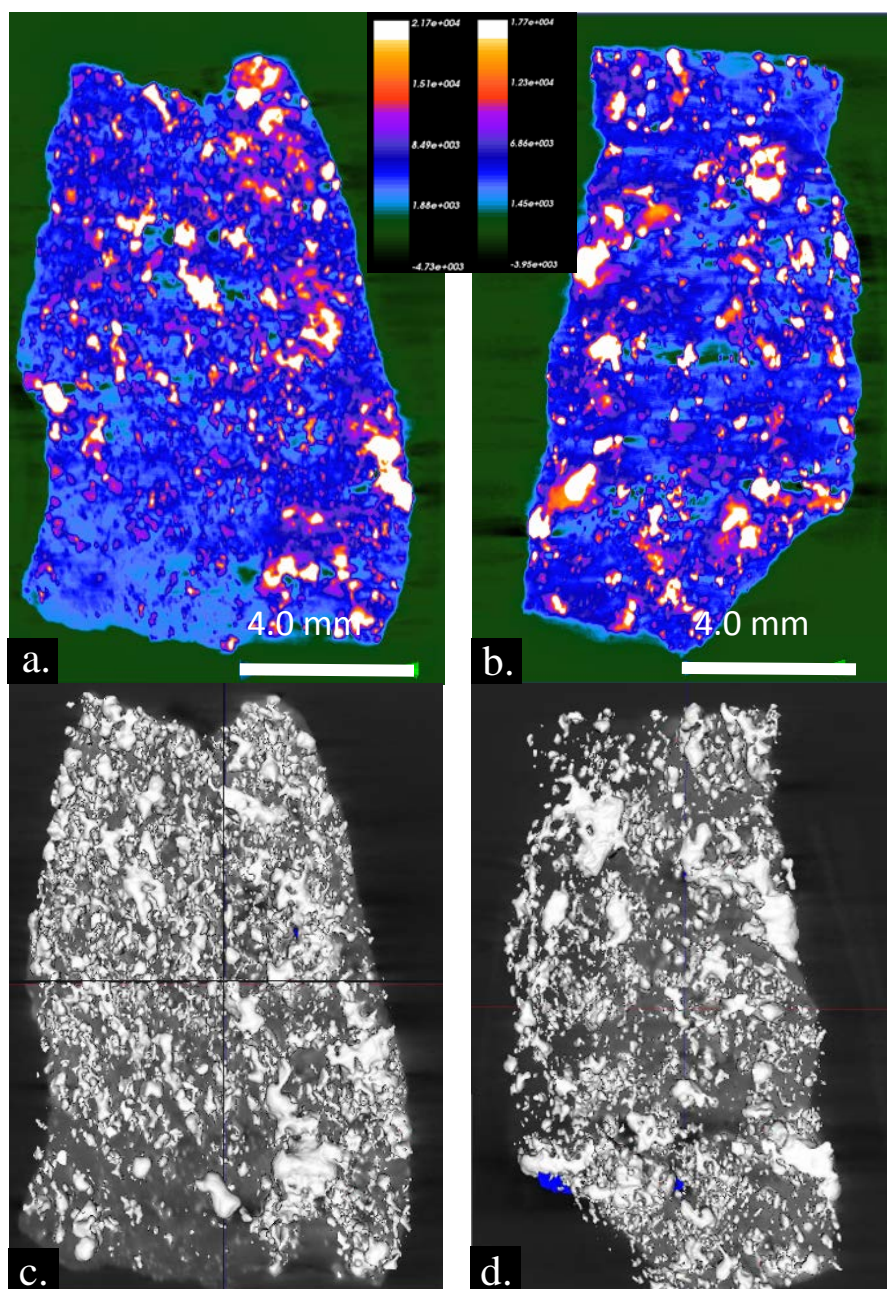


**Fig 3.2:** Micro-CT virtual slice views of (a) NWA8173a and (b) NWA 8173b. Color scheme is used to better illustrate contrast difference between samples. Blue represents low attenuation regions corresponding with low density phases and orange/white represents high attenuation regions that mark higher density phases. As seen on (c) fragment a, appears to have more disseminated metal and sulfide grains than fragment b (d). The metal and sulfide grains in fragment b (d), appear to be coarser grained. c) and d) are isosurface rendering of high-density phases overlaid on grayscale virtual slice view images.



BSE, EDS and X-ray maps of NWA 8173a-b revealed that both fragments consist of 100-400  $\mu\text{m}$ , anhedral to subhedral, untwinned, enstatite grains with smaller (5-80  $\mu\text{m}$ ), anhedral enstatite surrounded by interstitial plagioclase (Fig 3.3.a, d). The larger enstatite grains are prismatic in form, consistent with the initial description (MetSoc Bulletin 103; Bouvier, 2017 *in press*). The plagioclase that surrounds the smaller enstatite grains occurs as intergrowth with silica grains, resembling micrographic or myrmekitic texture (Fig. 3.4) and it is not present in association with larger enstatites in this sample. Irregular plagioclase grains were also seen in both fragments as inclusions in larger metal and sulfide grains. The larger enstatite grains show evidence of minor recrystallization, with some grains being semi rounded with simplified grain boundaries, including triple-junction contacts typical of metamorphic terrestrial rocks.

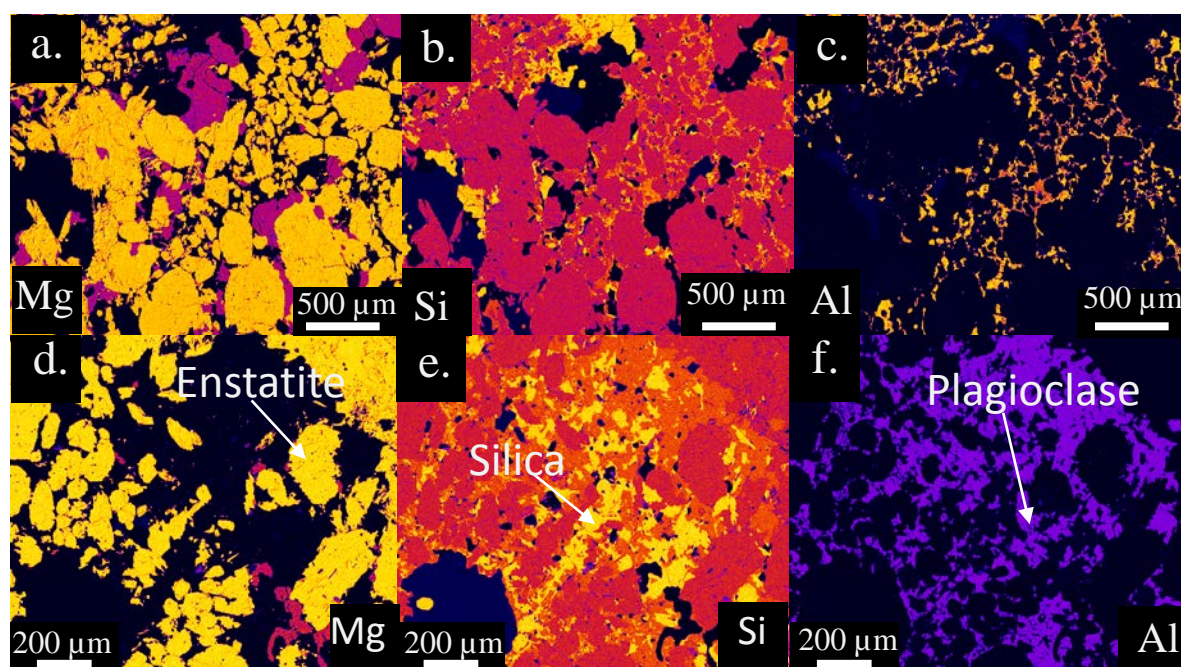


**Figure 3.3:** Elemental X-ray maps of Mg, Si and Al of NWA 8173 "a" a-c) and NWA 8173 "b" d-f). This figure shows the distribution and relative associations of main silicate phases in NWA 8173. Note: large and smaller enstatite grains surrounded by interstitial plagioclase and irregular silica grains.

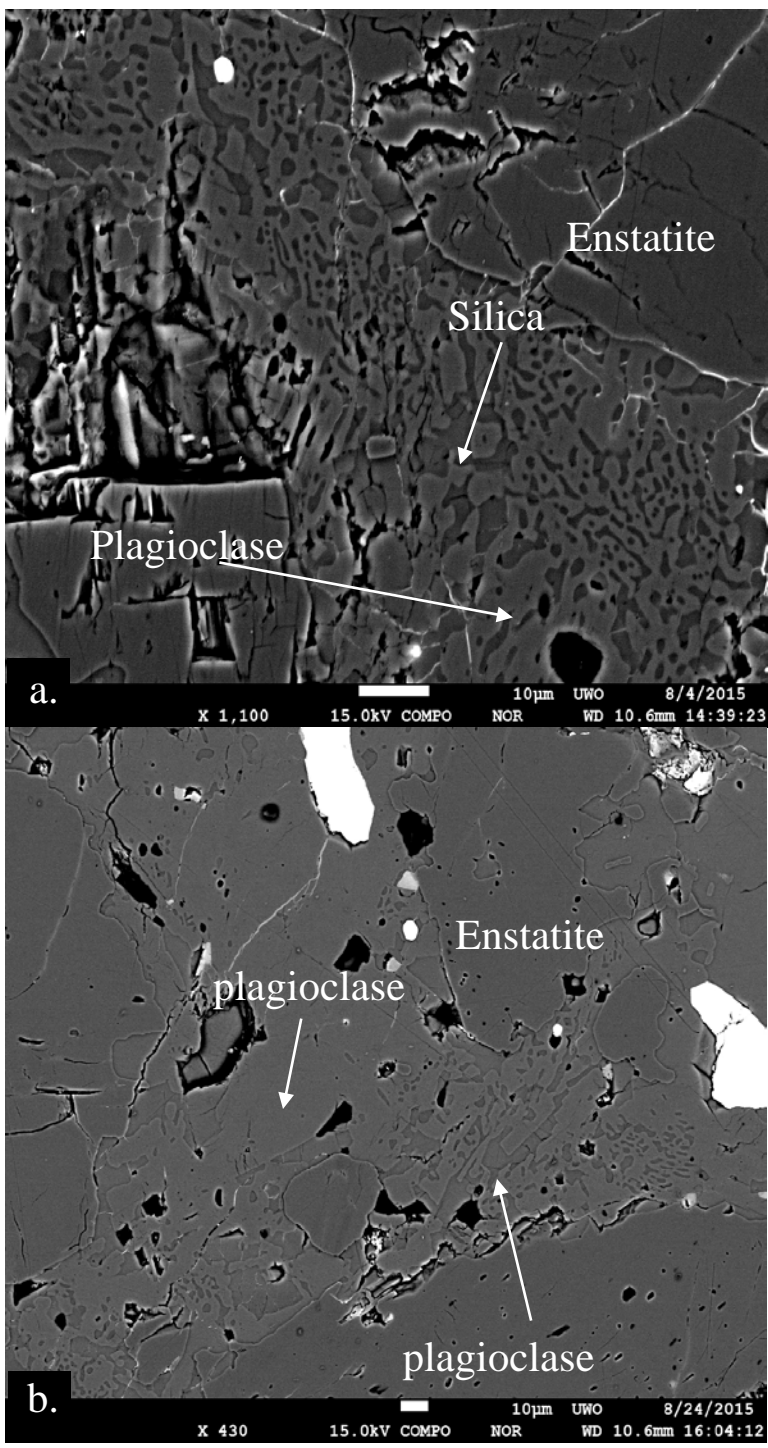


**Figure 3.4:** BSE images of NWA 8173 fragments "a" in a) and "b" in b) exhibiting myrmekitic intergrowth texture of plagioclase and silica surrounded by enstatite. Silica appears as the darker and low relief grains in BSE images.

Free silica occurs as small, irregular grains in proximity with plagioclase, around metal and sulfide grains, and sometimes as round inclusions in sulfides only. Silica grains are larger and more abundant around metal and sulfide grains. The silicon X- ray maps of fragment “a” and “b” show the spatial relation of silicon with respect to silicates, sulfides and metal (Fig. 3.3). In fragment “b”, there are some areas where silica and plagioclase appear to lie interstitially along linear trends between surrounding enstatite grains and occur locally. Moreover, the silica grains appear to partially surround some large metal grains in the sample (Fig. 3.3e).

Metal grains in both fragments occur as irregular shaped, sometimes holly leaf- shaped (MetSoc Bulletin 103; Bouvier, 2017 *in press*), 10  $\mu\text{m}$  up to 200  $\mu\text{m}$  sized grains of kamacite with smaller, grains of shreibersite contained in some kamacite grains. Metal grains are in close association with sulfide grains with thin reaction bands which are observed to cut through sulfide grains along fractures offsetting the lamellae as well as occurring along sulfide-metal grain boundaries (Fig. 3.5). These bands contain mostly calcium, sulfur, and minor amounts of iron and magnesium. The reaction bands can be interpreted either as a result of the breakdown of oldhamite (CaS) from weathering or as weathering of the host sulfide along the bands that delineate grain boundaries in the samples (Fig. 3.5 c,d). However, we support the former as weathering veins appear different chemically and texturally (Fig. 3.5 c, d) than in Fig. 3.5 (a,b). The weathered rims and veins seen in Fig. 3.5 c, d are composed of mostly iron oxide.

Tens of microns sized, dendritic graphite grains are seen in metal grains on both fragments. These are generally present as inclusions and in the rims of large metal grains (Fig. 3.6). In fragment “a”, some of the graphite occurs as irregular grains that can be as large as 100  $\mu\text{m}$  in longest dimension.

Both fragments of NWA 8173 contain sulfide grains which range from tens of micrometers to hundred micrometer-sized grains showing exsolution lamellae that appear to be oriented in the  $\{111\}$  planes of the sulfide host. The exsolution sulfide phases also occurs as small, irregular blebs at grain boundaries, along fractures and around metal, when metal is in contact with sulfide grains (Fig. 3.7).

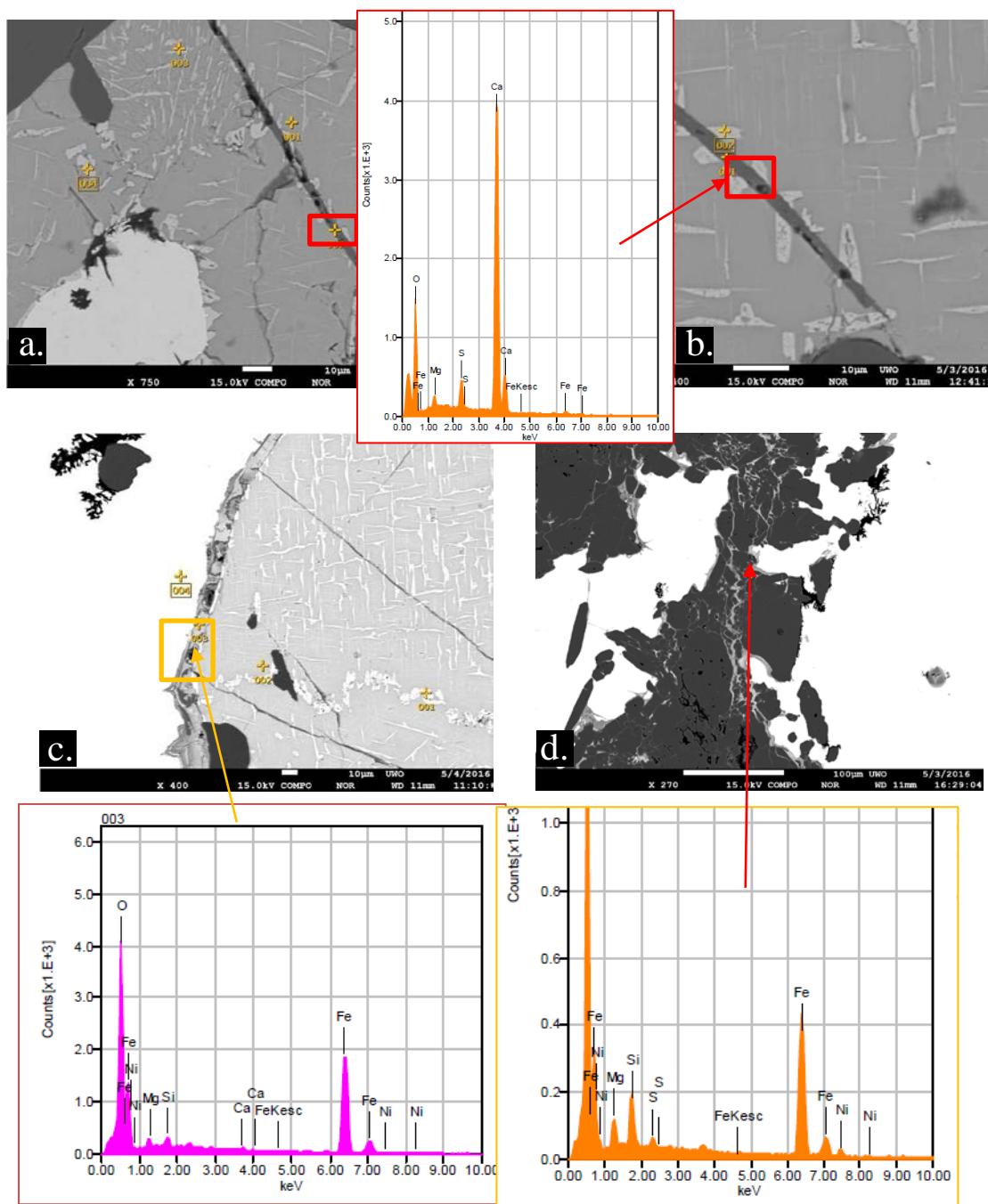


**Figure 3.5:** BSE images of reaction bands in sulfides with EDS spectra. a) and b) contain S and Ca with some O. c) and d) represent weathering product mostly composed of Fe and O with minor Fe, Ca and Mg. Note that the chemical composition and BSE contrast of reaction bands in a) and b) differ from c) and d).



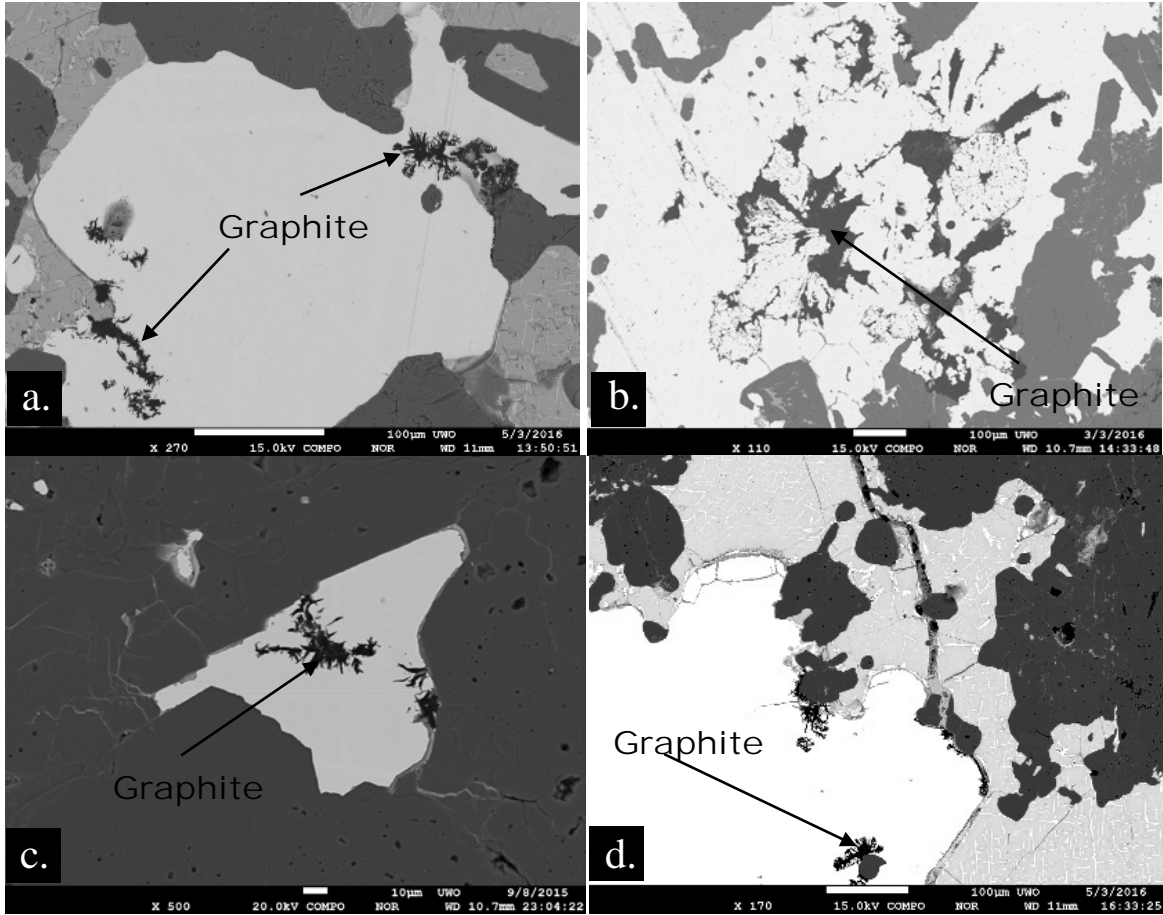


**Figure 3.6:** Graphite inclusions in metal. a) dendritic graphite inclusion in NWA 8173 "a", b) shows large, irregular graphite inclusions in fragment "a". c) and d) shows dendritic graphite inclusions in NWA 8173 "b". Note graphite is dendritic for most past and large graphite inclusion seen in b) was only present in NWA 8173 "a".

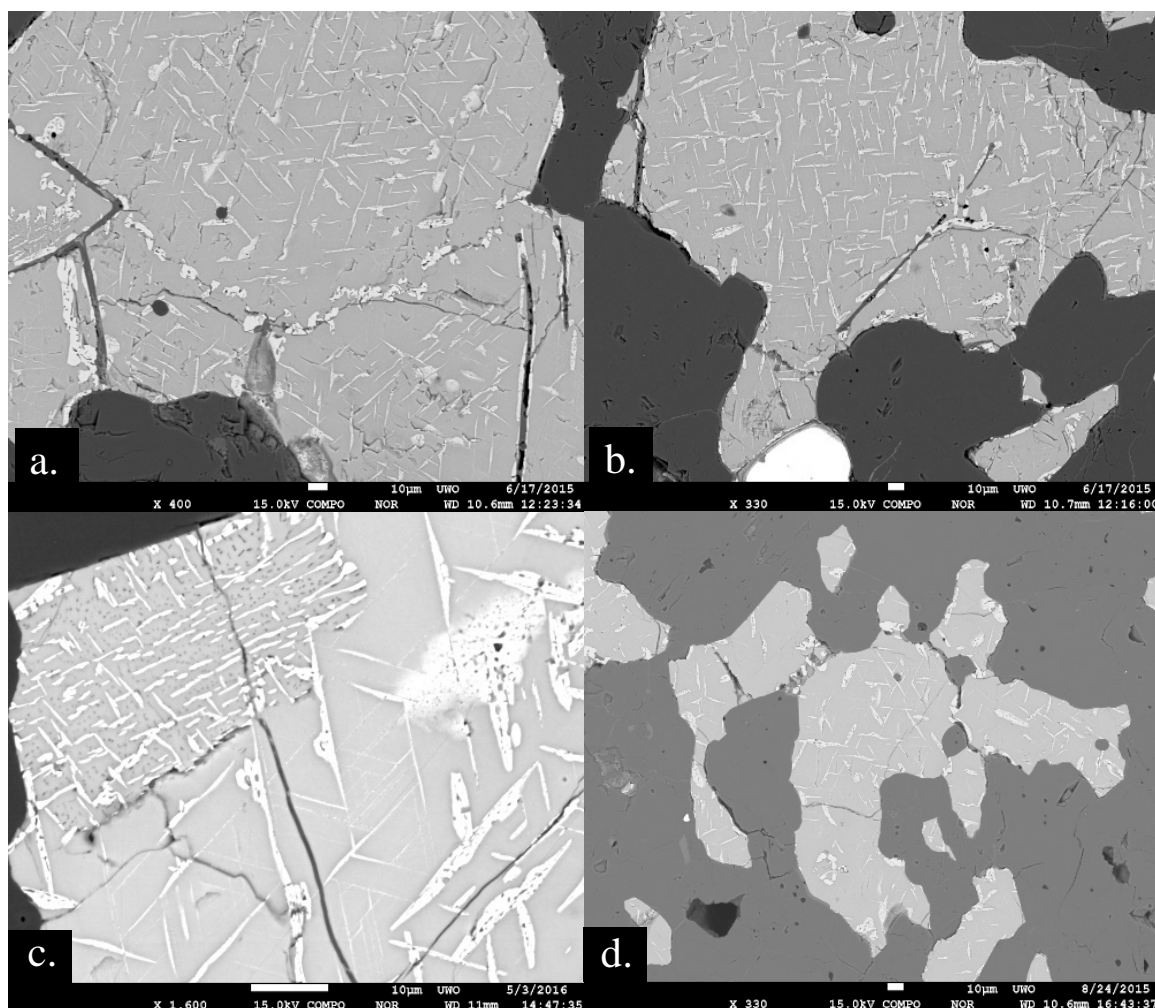


**Figure 3.7:** Exsolution of FeS from niningerite in NWA 8173 "a" in a), b) and NWA 8173 "b" in c) and d). a) illustrates the relation of irregular versus aligned exsolved FeS lamellae. The irregular grains are located along grain boundaries and cracks. c) illustrates the variability of FeS lamellae in sulfide host. In some areas (see top left of c)) the lamellae are aligned at nearly right angles in the plane of section whereas in the rest of the grain these are aligned in the  $\{1\ 1\ 1\}$  direction.

The lamellae range from 5-8  $\mu\text{m}$  in length and can be as thick as 5  $\mu\text{m}$  in some instances. Most of the exsolved lamellae contain rounded submicron inclusions of what appears to be breakdown of oldhamite (Fig. 3.8). The largest of the inclusions contained mostly calcium, sulfide with some oxygen due to weathering, along with small amounts of iron and magnesium, which are likely derived from the host sulfide. The inclusion also contained small amounts of iron and magnesium, which could have been derived from the host sulfide. Compositions of the smallest inclusions were not possible to obtain due to their small size. All of the sulfides in both fragments exhibit this exsolution texture and often contain irregular silicate grain inclusions of plagioclase, enstatite and round silica blebs.

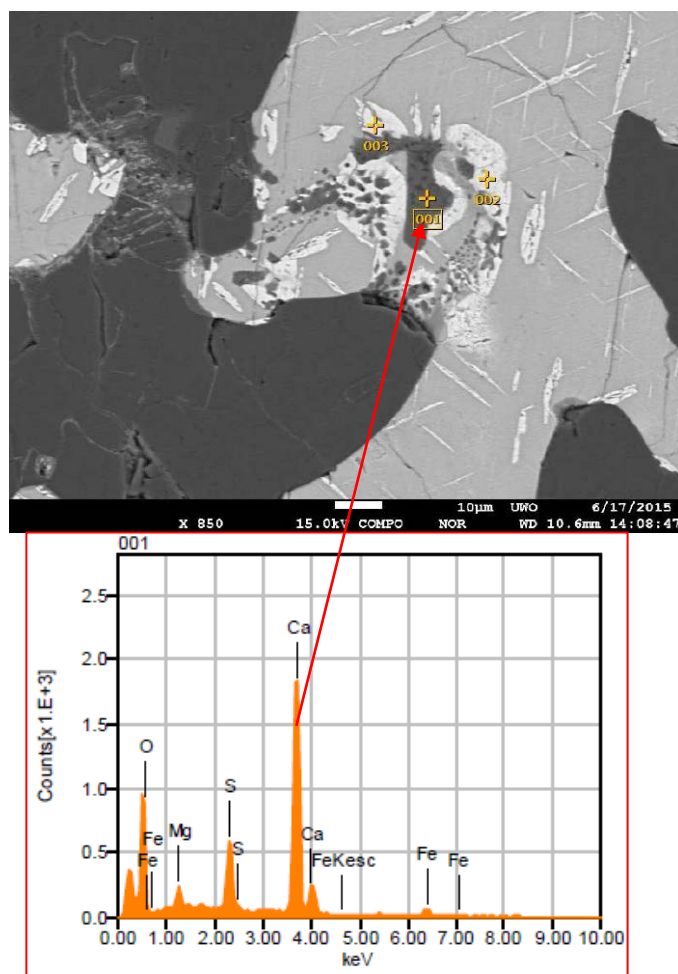


**Figure 3.8:** BSE image and EDS spectra of partially broken down oldhamite associated with FeS exsolved phase in host niningerite. The small inclusions in this figure are seen at the submicron scale in many of the FeS exsolved lamellae.

Fluorine-bearing phyllosilicate grains were identified in BSE and EDS (Fig. 3.9). The largest grains were found on fragment “a” in association with sulfide and silica. Both NWA8173 “a” and “b” fragments had smaller (3-10  $\mu\text{m}$ ) sized grains of the phyllosilicate located within enstatite and plagioclase. EDS spectra of the larger and the smaller grains confirmed the compositional uniformity of both grain populations. A SEI image one of the largest F-bearing grains shows a basal or sheet like texture, characteristic of micas (Fig. 3.9a). EDS spectra of this grain were compared with the EDS spectra glossary of Reed (2005), to confirm the presence of a phyllosilicate and not an amphibole (richterite), which has been previously recognized in other enstatite meteorites (e.g., Rubin, 2008; Rubin and Choi, 2009). All the X-ray elemental maps for NWA 8173 “a” and “b” can be found in Appendix 3.1.

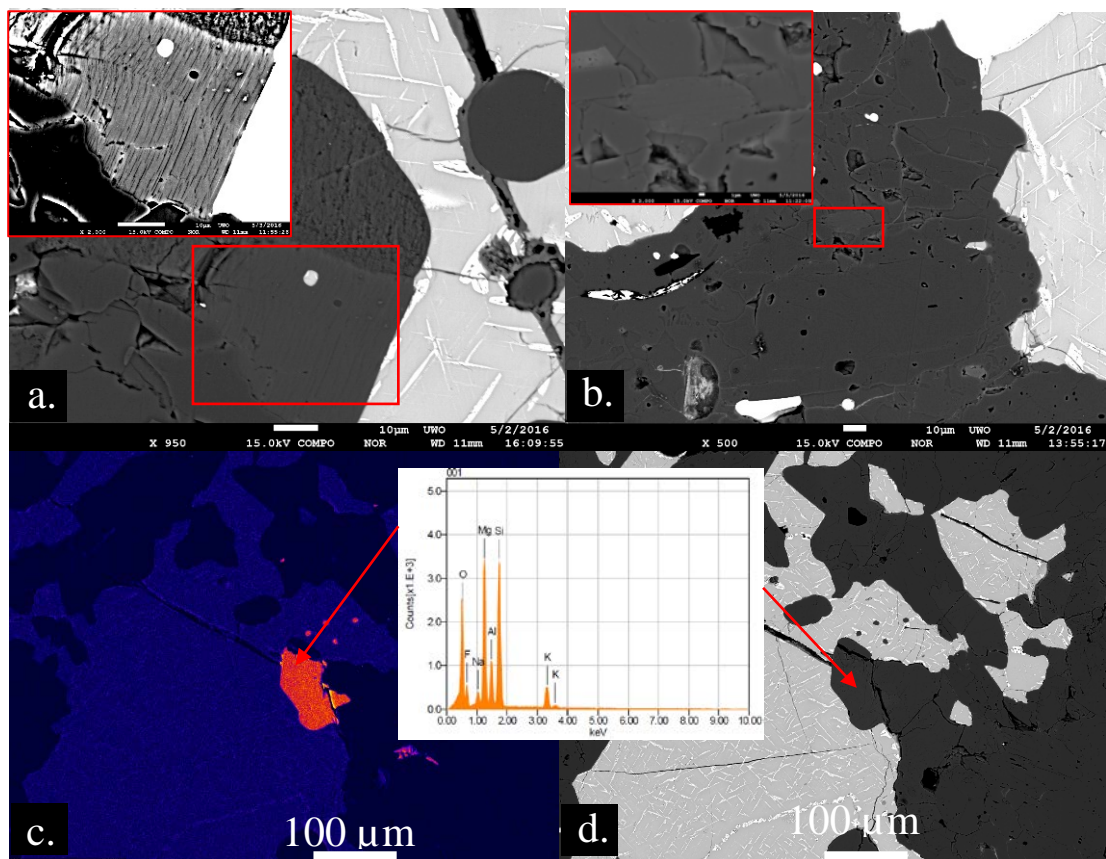


**Figure 3.9:** F-bearing mica association in NWA 8173. a) BSE and SEI (inset) image of F-mica illustrating the sheet-like texture typical of micas. b) BSE image of F-mica grain associated with silicates. c) and d) show fluorine X-ray map and BSE context image of F-mica associated with sulfides. An EDS spectrum describes the composition of the F-mica grain. The spectra are similar to that reported in Reed (2005) for micas.

### 3.3.2 Mineral Chemistry

Compositionally, both textural types of enstatite in NWA 8173 do not vary and are near-end member  $\text{MgSiO}_3$ . One of the unique features of this meteorite is the purity of the enstatite, compared to other enstatite achondrites (Metsoc Bulletin 103: Bouvier, 2017 *in press*). Both large and small enstatite grains have similar compositions in both lithologies. Plagioclase in both lithologies is predominantly albitic ( $\sim\text{Ab}_{90}\text{An}_4\text{Or}_6$ ) with some more potassic compositions up to  $\sim\text{Ab}_{86}\text{An}_1\text{Or}_{13}$  in interstitial plagioclase grains (Fig. 3.10). Interstitial plagioclase appears to be slightly more calcic (0.67-1 Ca wt %) than the irregular grains included in sulfide.

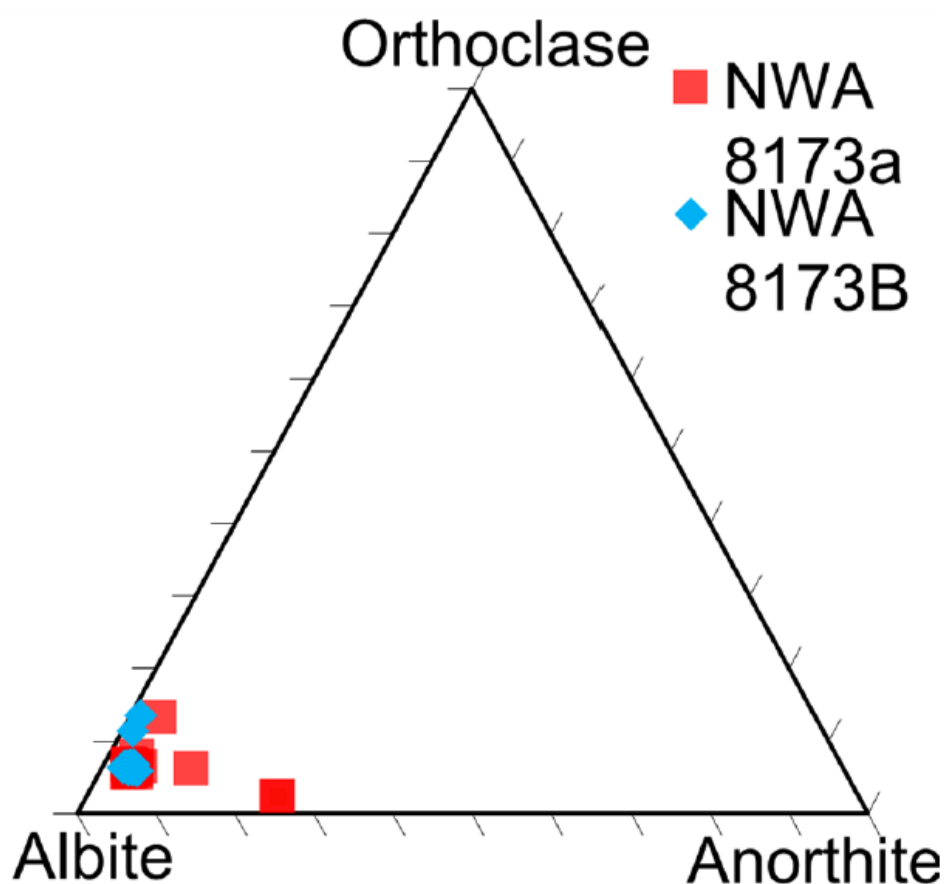


**Figure 3.10:** Plagioclase ternary compositional diagram for NWA 8173. Composition is predominantly albitic in both lithologies with minor orthoclase component.

The compositions of the metal in lithology “a” consists of ~3.15 wt% Si, ~6.36 wt % Ni and ~0.42 wt % Co and in lithology “b” of ~3.30 wt % Si, 6.41 wt % Ni and 0.42 wt % Co. Both lithologies contain similar compositions in the metal except that lithology “a” has slightly higher Si content in the metal (~0.3 wt %). Schreibersite in lithology “a” contains 0.4 wt % Si, ~15 wt % P, 5 wt % Ni and 0.35 wt % Co similar to the schreibersite in lithology “b”. Mineral chemistry data can be found in Appendix 3.2. Silica grains are mostly SiO<sub>2</sub> (~98.5 wt %) with minor NaO (~0.3 wt%) and ~0.7 wt % Al<sub>2</sub>O<sub>3</sub> in both lithologies. The silica content in the metal of NWA 8173 is higher than any other enstatite achondrite, therefore it has been classified as an anomalous enstatite achondrite (MetSoc Bulletin 103; Bouvier, *in press*). The atomic Si content in kamacite may indicate linkage with a EH parent body precursor as Si content in metal is known to be higher in EH than EL chondrites (Hutchison, 2004). The rounded silica droplets embedded in sulfide grains on NWA 8173 “a”, contain ~2 wt% NaO, ~5 wt% Al<sub>2</sub>O<sub>3</sub>, ~0.4 wt% S and ~2 wt% K<sub>2</sub>O and are the only silica grains that have substantial impurities.

The host sulfides in both lithologies contain average compositions of (all wt % n=30) 29 % Fe, 14% Mg, 5% Mn, 4% Ca, 2.6% Cr, 0.6% Na and 0.3 % Ti respectively. The exsolved lamellae and irregular grains contain 0.7-0.9% Mg, 0.5-0.7% Ca, ~0.5% Ti, 0.5% Mn and 5-6% Cr. Compared to the host sulfide, the exsolved sulfide is devoid of Mg, Ca and Mn and contains higher amounts of Cr and Ti. A ternary diagram (Fig. 3.11) of sulfide endmembers (FeS-MgS-MnS) illustrates the dichotomy in sulfide compositions in both lithologies of NWA8173, with the host sulfide identified as niningerite whereas the exsolved phase is essentially an FeS end member.

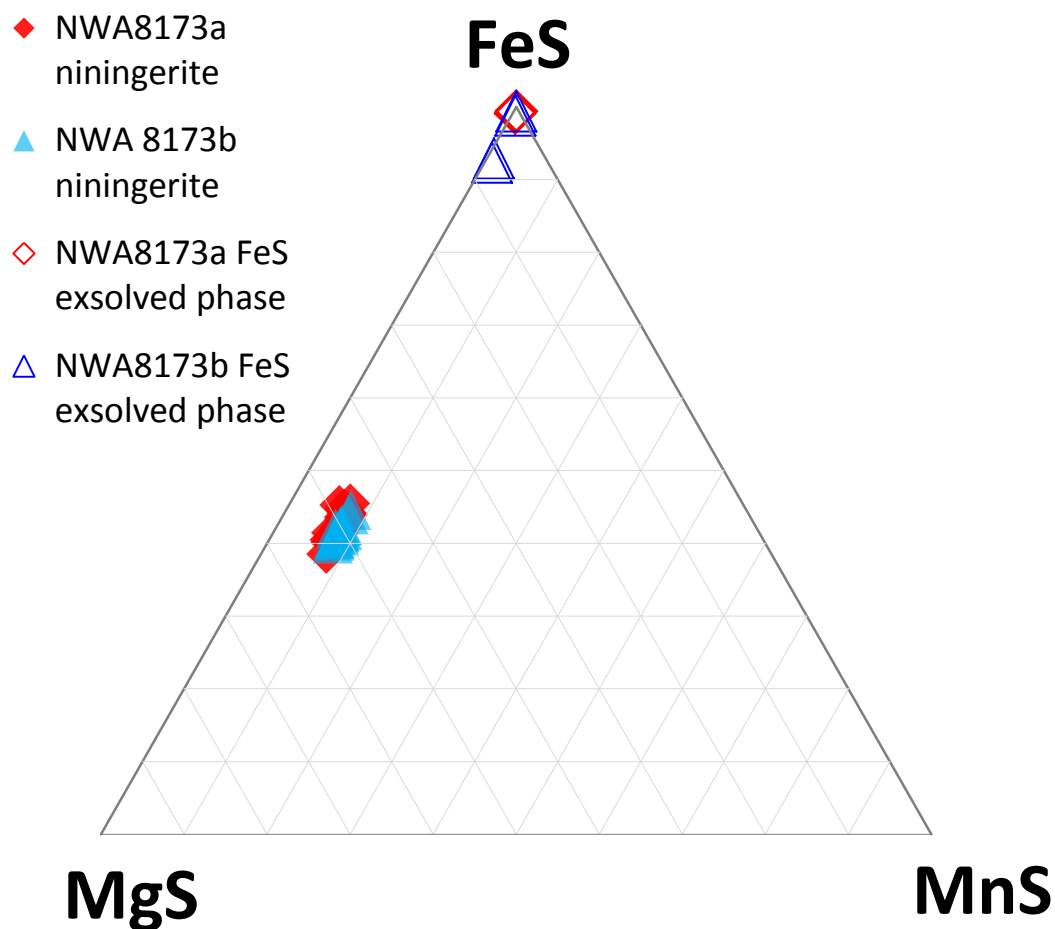


**Figure 3.11:** Ternary diagram of (MgS-FeS-MnS) system for NWA 8173 "a" (in red) and "b" (in blue). Note: Identification of sulfide minerals is based on mineral composition only.

The fluorine-bearing phyllosilicate in NWA 8173 contains ~44.5 wt % SiO<sub>2</sub>, ~12 wt % Al<sub>2</sub>O<sub>3</sub>, ~28.5 wt % MgO, ~2 wt % NaO, ~0.3 wt % FeO, ~7 wt % K<sub>2</sub>O, ~0.15 wt % SO<sub>3</sub> and ~ 8 wt % F, with an average chemical formula of:



Mineral formula stoichiometric calculation shows that the F-site is not fully filled. The shortfall may have been due to the presence of cracks in the phyllosilicate under the beam spot, or analytical error as analyzing light elements, particularly fluorine might be difficult. Some of the individual analysis did yield 1.95-1.98 for the fluorine site indicating the F site is filled completely, indicating that the mica mineral in NWA 8173 likely contains mostly or entirely fluorine in that site. The chemical composition of this



mineral is similar to that reported by Lin and Kimura (1998), for the EH chondrite Y-82189, one of the few meteorites where fluorophlogopite is documented and a mineral chemistry is reported. Raman spectra of the fluorine-bearing mica were compared with spectra of phlogopite (ID R070330) and fluorophlogopite (ID R040042) reported in the RRUFF database (LaFuente et al., 2015). The Raman peaks at 199, 280 and 683  $\text{cm}^{-1}$  are consistent with those in the phlogopite spectra (R070330). However, the Raman peaks are more akin to the peaks on the fluorophlogopite sample (R040042) from the RRUFF database (Fig. 3.12). Neither OH nor Cl were identified, specifically, no Raman peak was identified at  $\sim 3600\text{--}3800 \text{ cm}^{-1}$  (Fig. 3.13), which corresponds to the OH peak, and WDS analysis for Cl showed that Cl concentrations were below limit ( $<0.03 \text{ wt}\%$ ). Absence of an OH Raman peak and Cl from WDS analysis confirm that the mica in fact anhydrous fluorophlogopite.

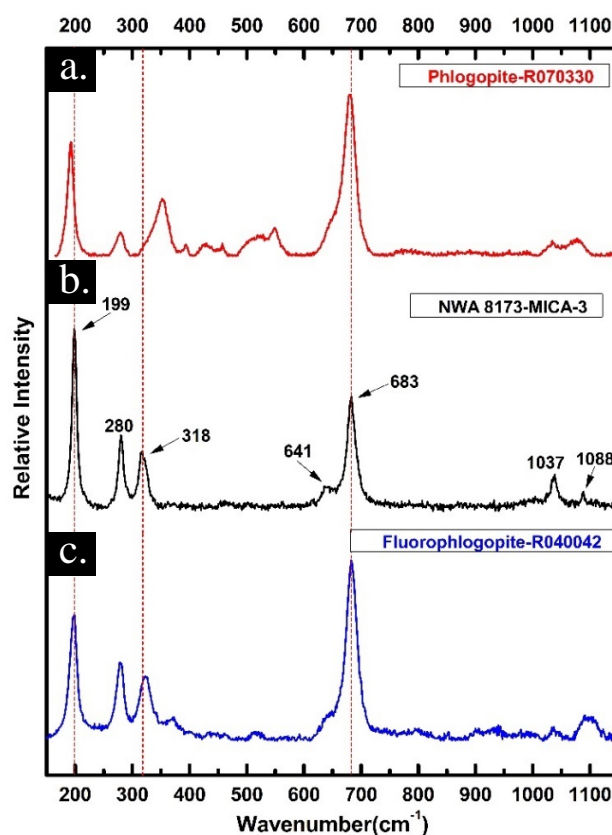


**Figure 3.12:** Raman spectra of F-bearing mica grain in NWA 8173 in b). Reference phlogopite in a) and fluorophlogopite in c) obtained from RRUFF database (La Fuente et al., 2015) are used to verify presence of fluorophlogopite.



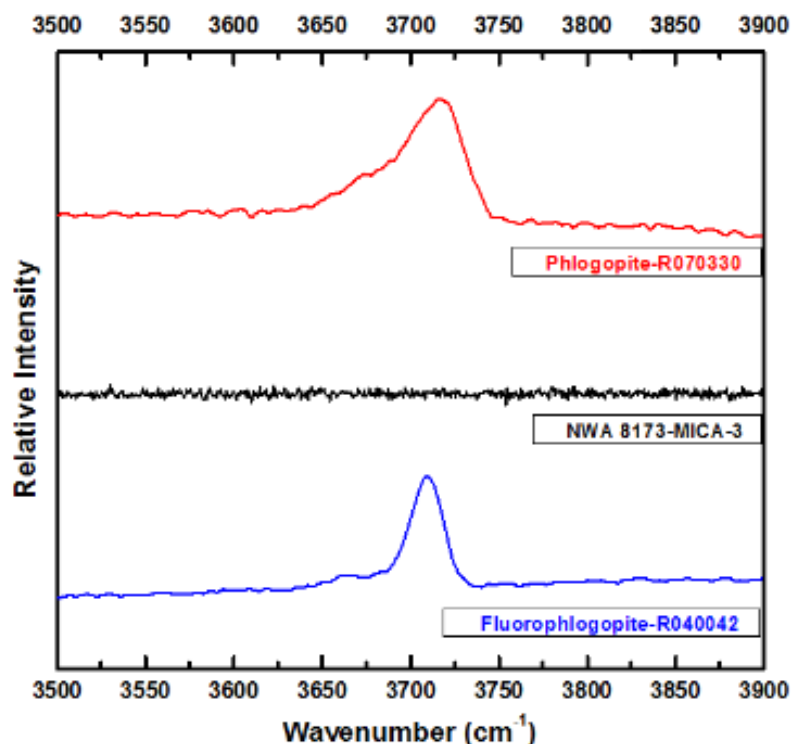


**Figure 3.13:** Raman spectra test for OH peak in NWA 8173 fluorophlogopite by comparison with Raman spectra for phlogopite and fluorophlogopite references from RRUFF database (La Fuente et al., 2015). No corresponding OH peak is detected in NWA 8173 fluorophlogopite.

### 3.3.3 Crystal structure ( $\mu$ XRD and EBSD)

Based on mineral chemistry, it was tentatively determined that the sulfide minerals in NWA 8173 were niningerite, with FeS occurring as an exsolved phase. Micro-XRD spot analysis of the sulfides in NWA 8173 revealed the presence of troilite, and isostructural keilite/niningerite/alabandite. The latter minerals were also indexed by EBSD. However, since these minerals are isostructural, both chemistry and structural data were used to determine the types of sulfide in NWA 8173. Although troilite was identified via  $\mu$ XRD, it was necessary to narrow down exactly what grains were being identified as troilite, given that the  $\mu$ XRD target area is of 300  $\mu\text{m}$  width. EBSD of the exsolved lamellae in the host sulfide of NWA 8173 were indexed as hexagonal troilite (Fig 3.14).

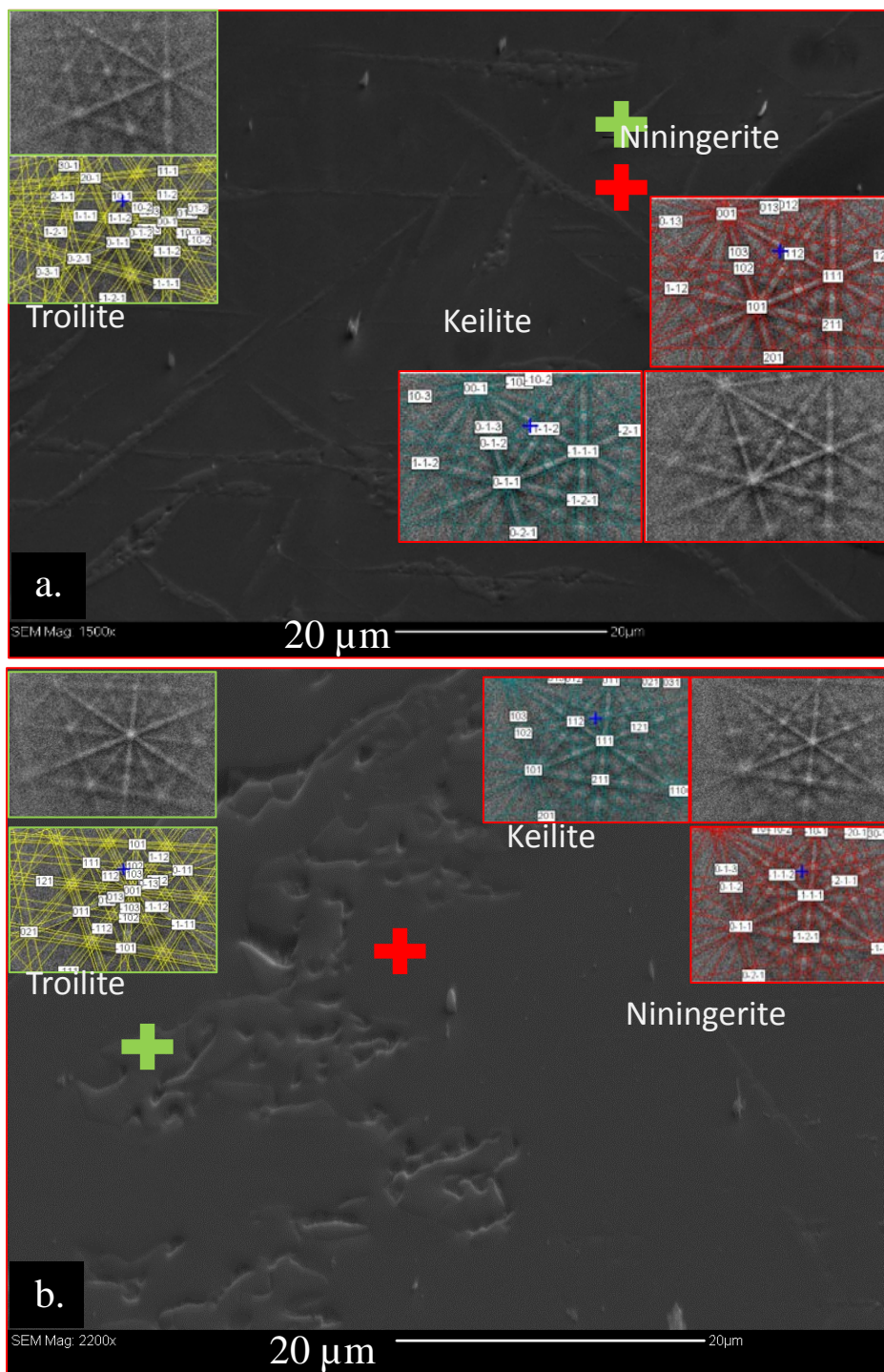


**Figure 3.14:** EBSD of host and exsolved lamellae NWA 8173 "a" in a) and NWA 8173 "b" in b).

EBS maps of sulfide grains were done to identify the orientation of the exsolved lamellae in sulfide host. This was not achieved as the lamellae were too small to produce a coherent diffraction pattern. Moreover, an EBSD map of the host sulfide indexed all the cubic monosulfides, preventing proper indexing of the single sulfide host since these are isostructural and therefore indistinguishable with EBSD (Appendix 3.3). Overall, sulfides in both NWA 8173 lithologies consist typically of a cubic monosulfide host (niningerite) of intermediate composition between FeS and MgS, with exsolved lamellae of hexagonal, chromium bearing troilite.

Tridymite was identified as the silica polymorph present in NWA 8173 via *in situ*  $\mu$ XRD and EBSD. The peaks at low  $2\theta$  (23-20°) were consistently matched by the tridymite ICDD card in most of the grains analyzed by  $\mu$ XRD (Fig 3.15). EBSD was used to confirm this finding but to also try to identify any other silica polymorphs present in this meteorite. Most silica grains in both lithologies were indexed as tridymite via EBSD, confirming the original finding of tridymite through  $\mu$ XRD. Moreover, quartz was indexed in lithology “a”, in an irregular grain surrounded by silicates. No quartz was indexed in lithology “b”. Irregular silica grains in sulfide and interstitially found with plagioclase were both indexed as tridymite. However, the rounded silica droplets embedded in sulfide examined by EBSD did not diffract and are, therefore, identified as amorphous silica (Fig 3.16). The lack of a diffraction pattern for the rounded silica grains appears to be legitimate and not an artifact of poor polishing quality or grain damage, given that no visible damage was seen optically and smaller grains elsewhere did produce diffraction patterns.

Micro-XRD and EBSD were also utilized to determine the presence of graphite vs. amorphous carbon in NWA 8173a. Initial  $\mu$ XRD scans revealed small peaks that were matched by graphite (Fig 3.15). Dendritic graphite grains in metal were then examined with EBSD to confirm this finding. The carbon rich inclusions did not produce enough diffraction to be adequately indexed but did produce partial diffraction nonetheless. This minor diffraction was compared with a typical graphite pattern (Oxford instruments EBSD glossary) and the main nodes seem to correlate with graphite.

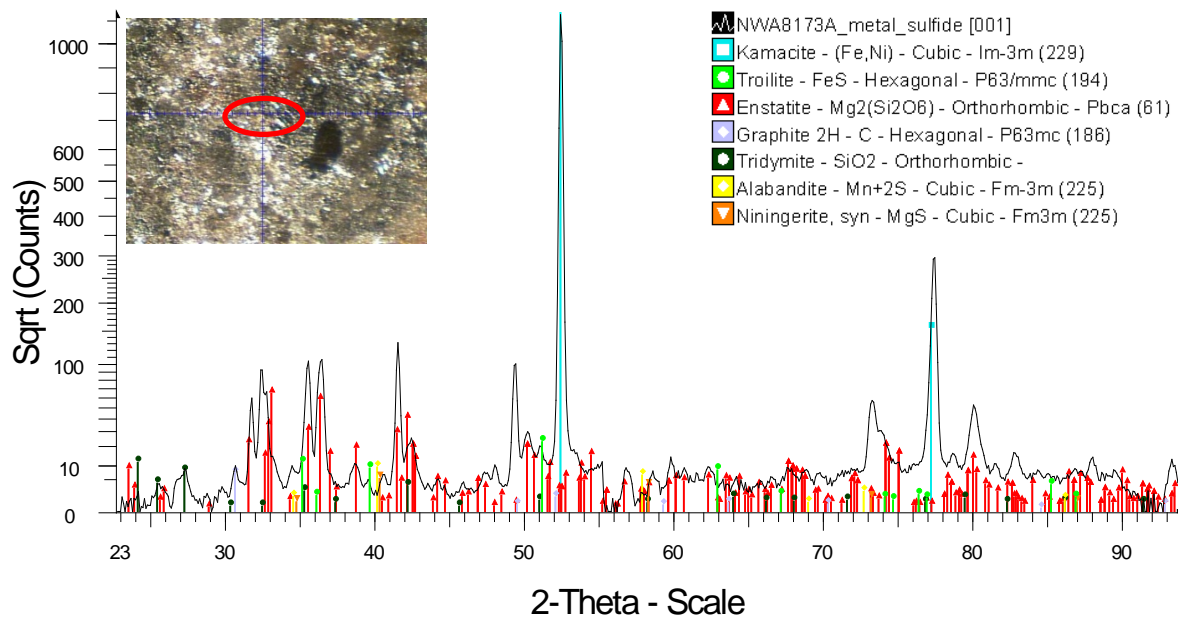


**Figure 3.15:** X-ray diffractogram of NWA8173 "a" sulfide target. Red ellipse minor axis in target image denotes the 300  $\mu\text{m}$  nominal beam width.

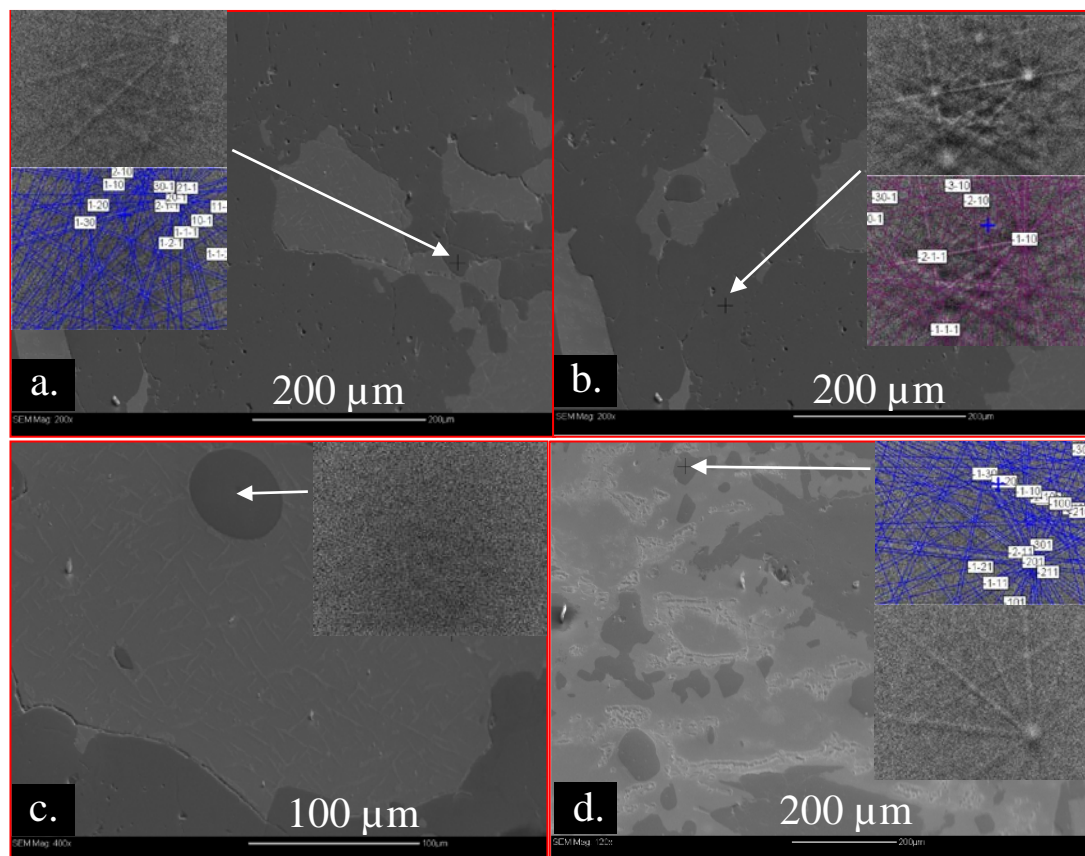


**Figure 3.16:** EBSD of silica polymorphs in NWA 8173 "a". a) shows tridymite, b) identifies quartz around ferromagnesian silicates and c) shows amorphous silica where no diffraction was produced, sitting as a round inclusion within sulfide. d) shows the association of tridymite with metal in NWA 8173 "b".

The fluorine-bearing mica previously described chemically, was also studied with  $\mu$ XRD and EBSD. Fluorophlogopite was matched by X-ray diffraction peaks in one of the sulfide target areas in NWA 8173a. Later  $\mu$ XRD and EBSD scans of the largest mica grain found in NWA 8173a were acquired to reproduce the initial structural and chemical results. An initial  $\mu$ XRD analysis of the area revealed fluorophlogopite as the best match for some of the peaks in the diffraction pattern. This initial analysis had a nominal beam width of 300  $\mu$ m, so a second run was done using an X-ray absorbing mask (sticky notes) around the target fluorophlogopite grain to limit X-ray diffraction to the mica grain only. Some peaks in the second scans were also matched by fluorophlogopite (Fig. 3.17).

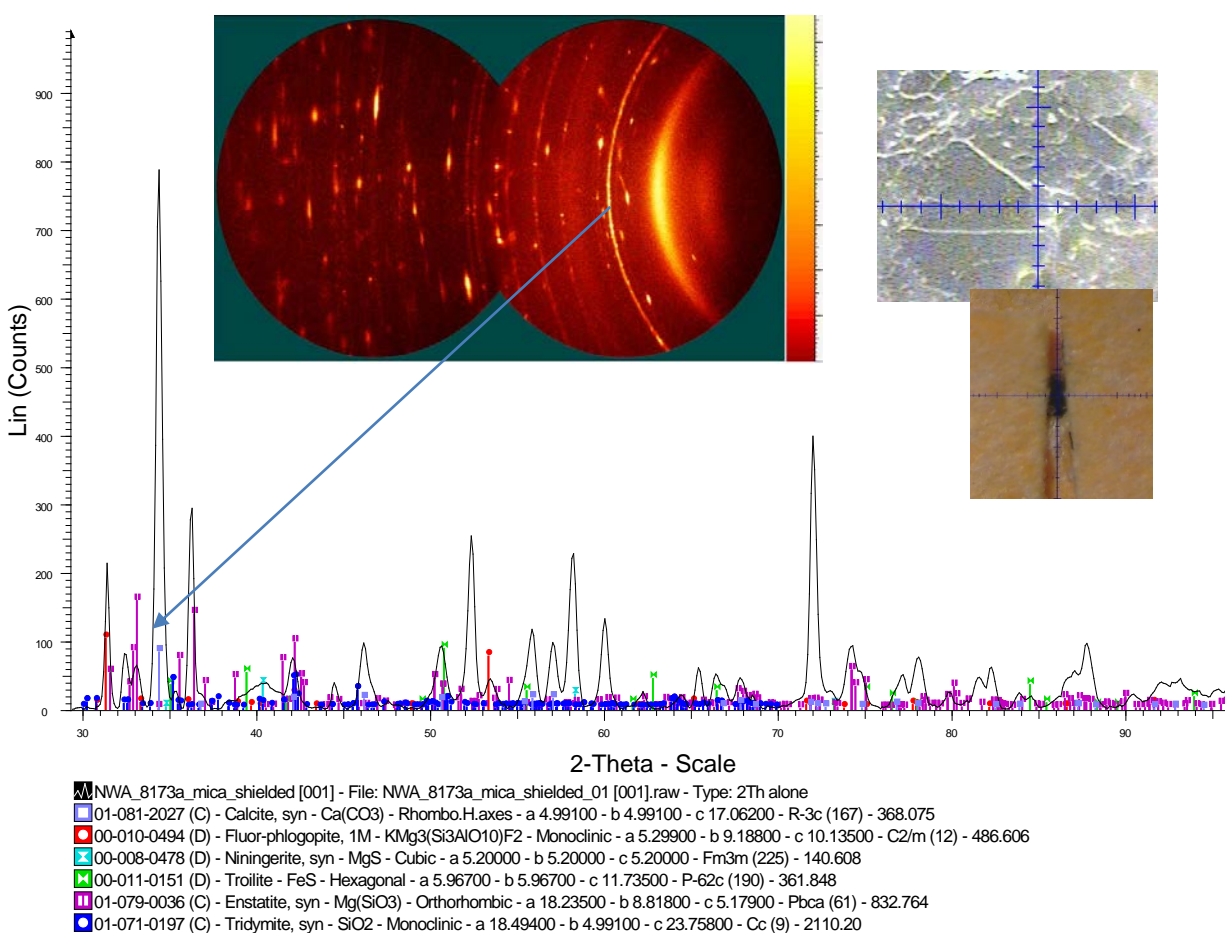


**Figure 3.17:** X-ray diffractogram of F-bearing mica grain in NWA 8173a. Note that calcite is from the sticky note and small spots for fluorophlogopite and appears as rings in the GADDS image.



In both cases, the same ICCD card matched the fluorophlogopite peaks effectively. EBSD of this mica grain was also done to corroborate the  $\mu$ XRD findings, to obtain higher resolution, structural data on the fluorine bearing mica. Unit cell data of a terrestrial fluorophlogopite was used as reference, and showed that the crystal structure of the mica effectively matched that of the reference structure (Fig. 3.18). All the indexed locations had a mean angle deviation of less than 1, indicating that the mica analyzed here matches well structurally with the reference material.

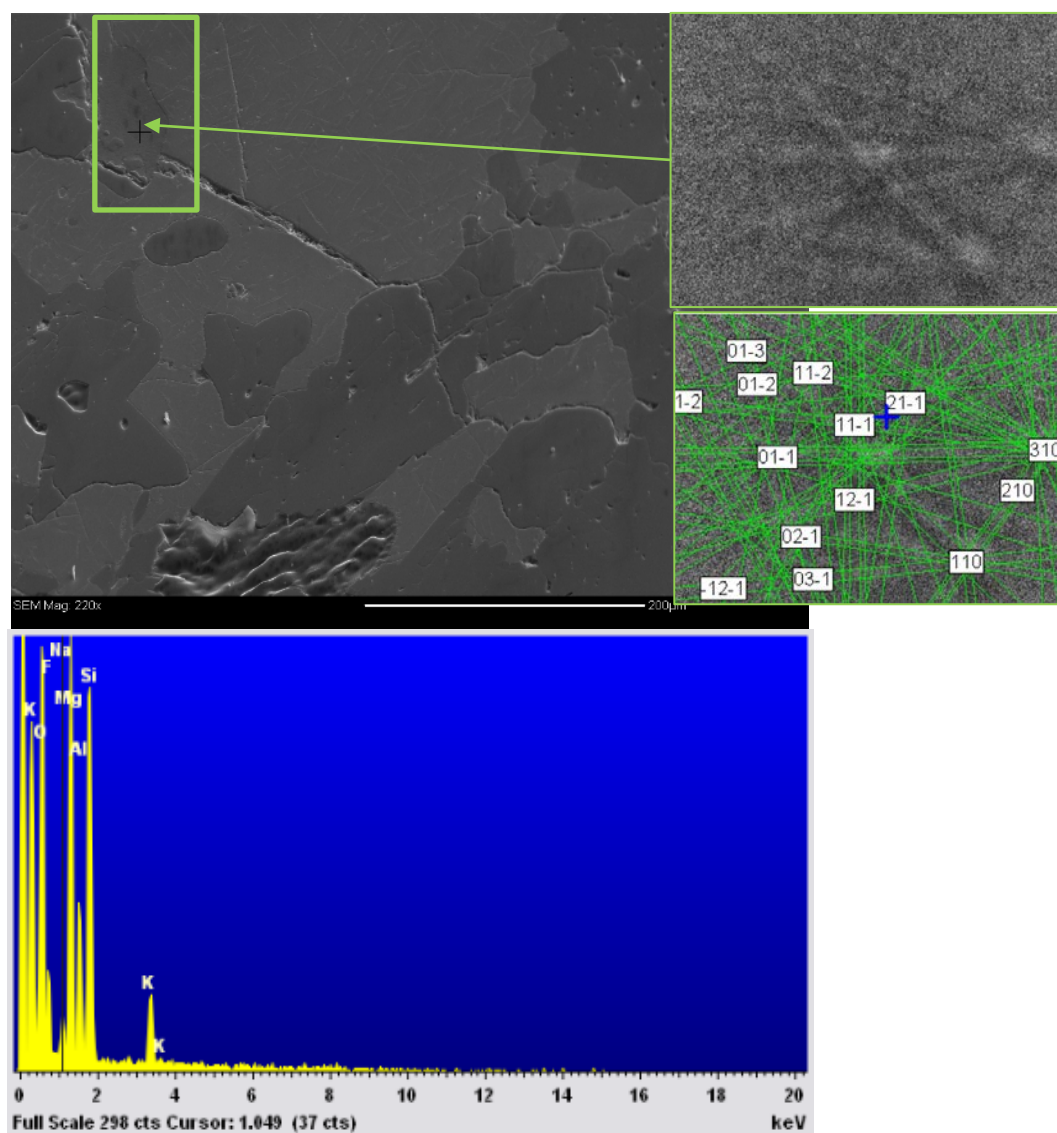


**Figure 3.18:** SEI image of F-bearing mica grain in NWA 8173 indexed as fluorophlogopite by EBSD. EDS spectrum is inserted for chemical reference.

### 3.4 Discussion

The observed mineralogy and textures in NWA 8173 are the result of starting materials (likely enstatite chondritic) that have been modified by thermal, chemical and, potentially, shock metamorphic processes that acted in a parent body during the early history of the solar system. Possible formation mechanisms include: 1) impact melting of, E-precursor material; 2) local melting associated with high levels of thermal metamorphism; and, 3) onset of differentiation of the parent body where an internally derived melt fractionates, with high density components later differentiating into a core. What can be inferred about these processes based on the observations from this meteorite? What information do these observations provide about formation environments and halogen role during the formation of the anomalous enstatite achondrites?

The most striking features of NWA 8173 are the apparent uniformity of enstatite compositions throughout, being nearly pure  $\text{MgSiO}_3$  (orthoenstatite, by  $\mu\text{XRD}$  and EBSD), and the presence of silica polymorphs, abundant Si in the FeNi metal, troilite lamellae in MgS, and of fluorophlogopite grains. These minerals, compositions and the textural relations provide some constraint upon the formation conditions of the rock.

Discussion here is limited to observations made in NWA 8173 with comparison to analogues but will be expanded upon in the thesis discussion chapter 5 to consider observations from other anomalous enstatite achondrites and their overall context and the implications for their formation and evolution.

#### 3.4.1 Enstatite

Orthoenstatite is the only type of enstatite present in NWA 8173 as seen by  $\mu\text{XRD}$  and EBSD, and is typically found to be euhedral. The enstatite in EPMA analyses (Appendix 3.2) are unusually low in Mn, compared with enstatite in other meteorites (Hutchinson, 2004). Low Mn content in enstatite and Mn enrichment in troilite has been described as impact melt indicator in enstatite meteorites as MnO is thought to be removed from enstatite during impact shock metamorphism and incorporated into the sulfide melt

(Rubin, 2015). For meteorites that contain euhedral enstatite grains, the MnO contents are very low, consistent with what is found in NWA 8173. Some of the enstatite grains in NWA 8173 show an embayment texture, with laths of enstatite surrounded by metal, another possible feature of impact melting (Rubin, 2015), in which the mobilized FeNi metal surrounds existing enstatite grains. But do these features uniquely indicate an origin from a shock melt?

Enstatite grains in both NWA 8173 lithologies do not show clinoenstatite lamellae in EBSD or  $\mu$ XRD analyses, which therefore limits the meteorite to a shock stage less than S3 (Rubin et al., 1997). As part of a review paper, Rubin (2015) reports petrographic observations that the enstatite grains in NWA 8173 show slight undulose extinction, characteristic of shock stage S2, with some grains showing weak mosaic extinction, characteristic of an S4 shock stage. From these observations and the high modal metal content (20%) he deduces that NWA 8173 represents an impact shock melt, and that the S2 enstatite grains represent a post-melting shock overprint, with the S4 enstatite grains possibly representing unmelted relicts.

The smaller enstatite grains with interstitial plagioclase and silica intergrowth may have formed by localized melting in a late stage heating event, followed by annealing as reflected by the uniformity in enstatite compositions. The smaller enstatites crystallized relatively quickly at high temperatures whereas plagioclase stayed as a melt with subsequent cooling until it formed the micrographic growth.

More broadly, Van Niekirk (2012) states that because silica, feldspars, metal and troilite solidify at lower temperatures, they remained in a liquid state longer and filled the spaces between the enstatite, which starts crystallizing at higher temperature. After melting, NWA 8173 experienced rapid cooling, possibly by assimilation of clastic material or it was initially located near the surface of its parent body and was subsequently buried deeper leading to slow cooling. The initial rapid cooling allowed the preservation of tridymite and was then followed by annealing as the meteorite was buried deeper in its parent body. From the melt, enstatite formed first then the remaining phases crystallized around them as cooling progressed. The euhedral enstatites surrounded by metal grains



are similar to those in the Yamato 82189 and Abee meteorites. This texture is not as prevalent in NWA 8173 that in Yamato 82189 (Fig. 3.19) nor in the Abee meteorite, possible reflecting greater subsolidus annealing in NWA 8173.

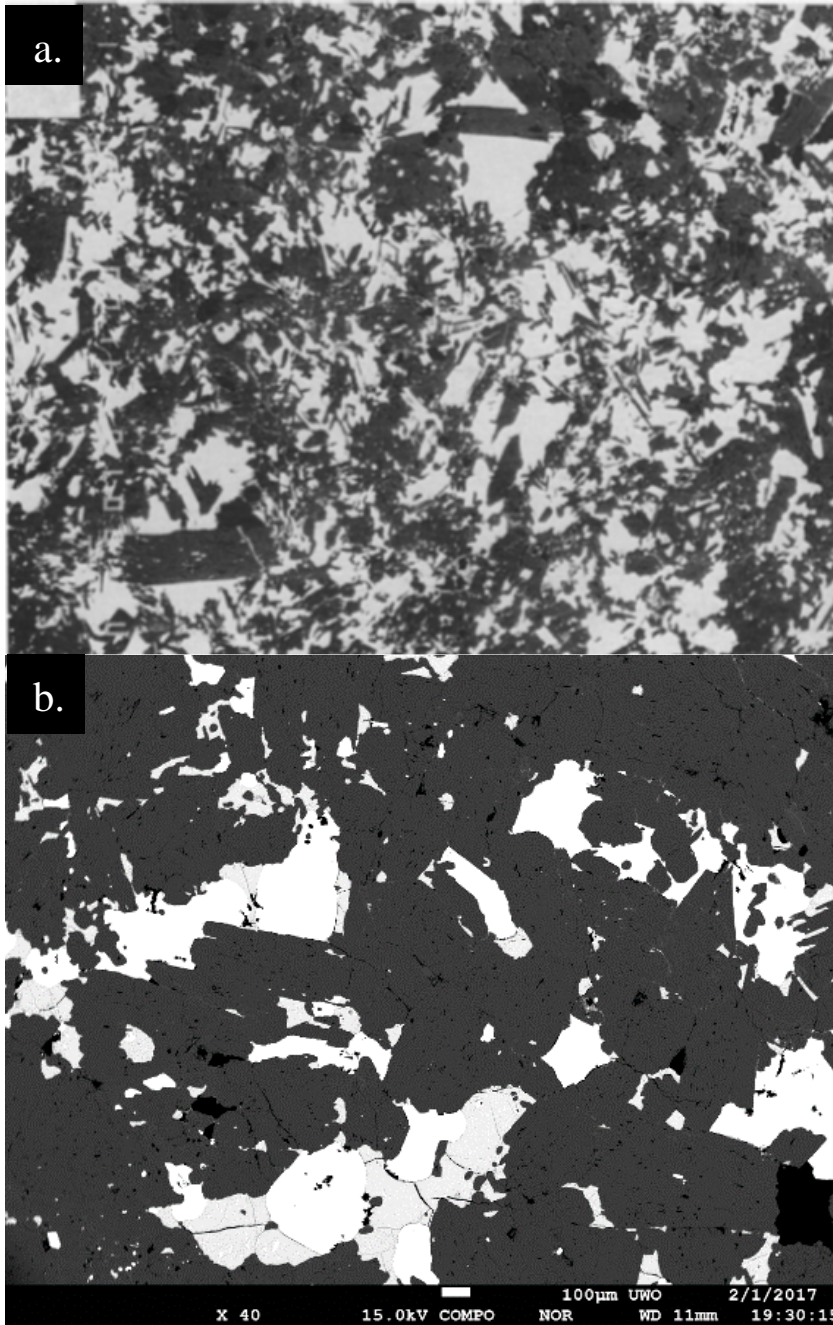


**Figure 3.19:** Euhedral enstatite grains in a) Y-82189 (Lin and Kimura, 1998) and b) NWA 8173 "a" surrounded by metal. Texture is described by Rubin (2015), as characteristic of impact melting.

### 3.4.2 *What do the silica polymorphs tell us about the thermal history of NWA 8173?*

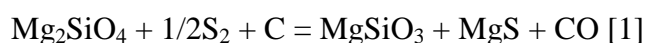
Abundance of silica has long been recognized as one of the unique features characteristic of enstatite meteorites. In terrestrial rocks, silica polymorphs have been used to constrain pressure- temperature conditions experienced during their formation. Kimura et al. (2005), state that the study of silica polymorphs may provide constraints on the thermal histories of enstatite meteorites as the stability of silica polymorphs are dependent on pressure-temperature conditions. Furthermore, Putnis (1992) noted that, silica polymorphs should preserve the primary temperature and pressure conditions under which they formed given that the transition rate between silica polymorphs is relatively sluggish.

Rubin (2015), argued for a reaction where reduced silicon from metal reacted with FeO from melted enstatite to produce silica and metallic Fe during crystallization following impact melting. Silica could have also been produced by sulfidation of silicates during crystallization from an impact melt (Lehner et al., 2013). In this study, tridymite is identified as the main silica polymorph in NWA 8173, suggesting that high temperatures in the stability range of tridymite (860-1470 °C) were experienced during the silica formation (Kimura et al., 2005). Quartz is normally stable above 867 °C at high pressures but may persist metastably. Since these meteorites formed under low pressure, quartz in NWA 8173a could have formed by the transition of tridymite during slow cooling or long, low temperature metamorphism, under conditions where quartz is stable (Kimura et al., 2005). This is also supported by the sulfide textures seen in this meteorite. Preservation of tridymite in NWA 8173 may be explained by rapid cooling to a temperature in the tridymite stability field, followed by annealing, allowing formation of quartz. Additionally, Dapiaggi et al. (2015) discuss that during cooling, tridymite changes its structure from hexagonal to monoclinic. Only monoclinic tridymite was found in NWA 8173, suggesting that all the initially formed tridymite at ~860 °C cooled slowly enough to allow a transition from hexagonal to monoclinic structure. The rounded, amorphous silica droplets included in sulfide grains probably represent the last stage of crystallization from a melt, where upon cooling, the silica formed a glass. The silica inclusions reported here contain significant impurities which may also have

inhibited crystallization; such amorphous silica has also been reported in other meteorites (Kimura et al., 2005).

### 3.4.3 *Chemical reactions and geothermometry from sulfides*

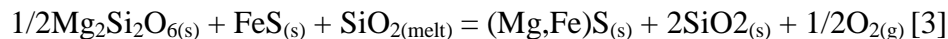
The high abundances of Ca in NWA 8173 niningerite (3.5-4 wt %) may support formation by quenching of a high temperature sulfide melt followed by subsolidus annealing, exsolution and local remobilization with the sulfide phase. The sulfide minerals present in NWA 8173 may represent high temperature sulfidation of ferromagnesian silicates, a reaction discussed by Fleet and MacRae (1987) for enstatite chondrites. They discuss the possibility that the carbon required for sulfidation of enstatite existed as organic carbon or graphite, and was present in the primitive enstatite chondrite material as a low temperature condensate. The proposed reaction by Fleet and MacRae (1987) is as follows [1]:



This sulfidation reaction (Fleet and MacRae, 1987) requires the presence of carbon along with sulfur gas to produce niningerite. This requirement for carbon may be met in the observed presence of graphite in NWA 8173. Sulfidation reaction of silicates has also been reported in EH3 chondrites by Lehner et al. (2013). They argue that as silicates react with S gas, Fe, Ca and Mg are incorporated into sulfides, free silica is produced by the breakdown of olivine to form enstatite, or the breakdown of enstatite to form silica, liberating oxygen. The sulfides in NWA 8173 would have been formed from the sulfidation of ferromagnesian silicates (here pyroxene) as seen in [2] (Lehner et al., 2013):



Piani et al. (2016) discuss that sulfidation of a silicate melt may not be enough to produce the amount of free silica found in EH3 chondrules. They instead propose the following reaction [3]:



Piani et al. (2016) propose that protracted gas-melt interactions under high partial pressures of Si and SiO lead to the formation of niningerite-silica associations in EH3 chondrules by destabilization of formed FeS and low-Ca pyroxene. The euhedral enstatite textures and phase relations in NWA 8173, however, favor a role for sulfidation of a silicate melt to produce MgFe sulfides and SiO<sub>2</sub>.

Furthermore, Malavergne et al. (2012) discuss that the formation of sulfides does not require extremely reducing conditions (at 1 GPa), but that high temperatures might be enough to keep large amounts of sulfide in a silicate melt and as the melt reaches sulfide saturation it begins to precipitate sulfides by reacting with enstatite. However, this interpretation might only be applicable to high pressure environments. Additionally, experimental work by Berthet et al. (2009) argues that at temperatures higher than 1500 °C the sulfur content of the silicate melt decreases due to the changing composition of the metallic liquid at higher temperatures, therefore affecting the ability for sulfidation of ferromagnesian silicates to occur at higher temperatures.

The sulfide exsolution lamellae seen in NWA 8173 are similar to those reported by Kimura and Lin (1998) for the meteorite Y82189; these indicate that the meteorite cooled slowly or was re-equilibrated at low temperatures to exsolve troilite from niningerite (Fig. 3.20). Upon cooling, initially formed keilite exsolved troilite to form niningerite (Keil, 2007) resulting in the decrease of Fe from the host sulfide. Additionally, the experimental study (albeit under 1 GPa conditions more relevant to planetary mantles) by Malavergne et al. (2012) showed that the exsolution of troilite from keilite can be seen in slow quenched samples which were heated from 1200 to 600 °C below the melting point.

The irregularly shaped troilite blebs seen in niningerite may have formed by further segregation of exsolved material upon cooling. Sulfidation of ferromagnesian silicates is thought to be more efficient at high temperatures (1400-1600 K) Lehner et al. (2013). Lehner et al. (2013) and supports the idea of Malavergne et al. (2012) where high temperatures may be enough to keep a large amount of sulfide in the melt. Following FeS exsolution of a homogeneous monosulfide to a niningerite host with troilite lamellae, niningerite and silica were stabilized at about 800 °C which agrees with the equilibration

temperature of niningerite determined by Skineer and Luce (1971). However, the average chemical composition of the host sulfides (slightly towards niningerite field) in NWA 8173 indicates that the host sulfide (ninningerite) cooled slowly or re-equilibrated at temperatures of 650-700 °C (Fig. 3.21). If cooling was very slow, Lehner et al. (2013) state that niningerite compositions are sensitive to temperature where it becomes more Mg-rich as temperatures decrease. Since the composition of niningerites in NWA 8173 are slightly Mg-rich, it indicates that slow cooling was not prolonged as more FeS would have been removed from the sulfide host, exhibiting compositions increasingly more towards niningerite than are observed here. Another constraint on cooling not being prolonged comes from the observation of the silica polymorph tridymite in NWA 8173, which is metastable below 860 °C, reverting to quartz if cooling is slow enough to allow the phase change. Because the reconstructive transformation from tridymite to quartz is sluggish, and because tridymite may form metastably at significantly lower temperatures than 860 °C, the presence of tridymite is not consistent with substantial thermal annealing.

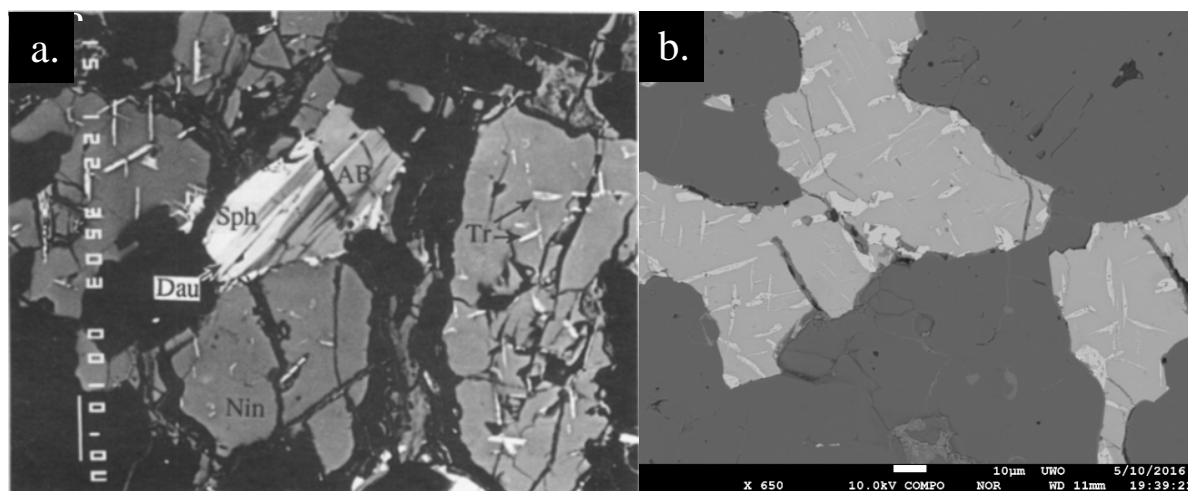


**Figure 3.20:** Troilite exsolution in niningerite in Y-82189 in a) (Lin and Kimura., 1998) and NWA 8173 b) this study.

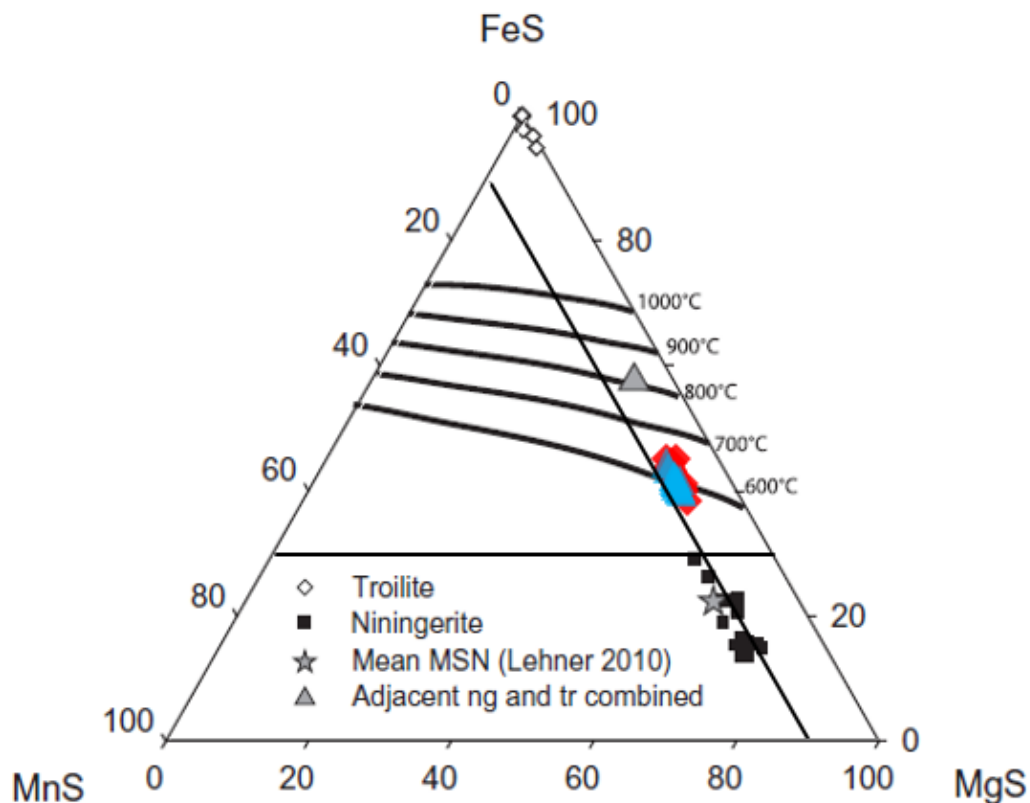


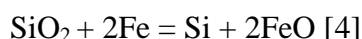
**Figure 3.21:** Compositional diagram for the (FeS-MnS-MgS) sulfide system with temperature stability isotherms. The diagram includes data for NWA 8173 sulfides (Red for fragment “a” in blue for fragment “b”) and data by Lehner et al., (2013). Diagram modified from (Lehner et al., 2013).

#### 3.4.4 Metal

One of the unique features NWA 8173 exhibits is the high abundance of metal compared to other enstatite achondrites. The abundance of metal in NWA 8173 may indicate that this meteorite represents metal concentration prior to differentiation but that the process was never completed. Additionally,  $\mu$ CT images show that distribution of metal in fragments “a” and “b” is heterogeneous which may indicate that metal distribution varied locally and that the larger, coarser grains might represent areas where metal was preferentially congregating. Alternatively, the local variation in metal concentration, and the generally high modal abundance of metal in NWA 8173 may instead represent the transport of metal from elsewhere in the parent body via impact-related mobilization of the metal and sulfide

### 3.4.5 Silicon content in the metal

NWA 8173 is notable for having an unusually high Si content (~3.15 wt%) in its FeNi metal compared with most meteorites (Hutchison, 2004) and other enstatite achondrites such as QUE 94204 (2.09-2.5 wt% Si; Izawa et al., 2011). The high silicon content in metal for NWA 8173 supports kinship with an EH-like precursor (2.7 -3.7 wt% for EH; Dickinson et al., 1992) and is similar to that in the Y-82189 enstatite achondrite meteorite (3.10 wt%). The higher silicon content in the metal may suggest a role for the disproportionation of SiO (as a silicate component) into Si and SiO<sub>2</sub> at high temperature and reducing conditions (Javoy, 1995). More specifically the reaction to incorporate silicon in metal is as follows (Javoy, 1995; Javoy, 2010; Ziegler et al., 2010):



where the SiO component from silicates will react with Fe metal resulting in incorporating of Si as metal component and FeO in silicate melt as seen in eq. [4]. This disproportionation reaction is recognized as an important mechanism for core differentiation and can explain the increase in mantle FeO and  $f_{\text{O}_2}$  without the need for accreting oxidized material during late stage planetary accretion. Consequently, Dickinson et al. (1992) propose a reaction where enstatite and graphite react to form olivine, silicon in metal and CO. However, no olivine was observed in the NWA 8173 meteorite. It is also possible that the reaction proceeded to completion where olivine was consumed to produce enstatite, graphite as well as to make sulfides and enstatite.

The importance of Si content in the metal of enstatite meteorites is that the Si content increases with increasing temperature (Dickinson et al., 1992) and it provides information about temperatures experienced during their formation. For the case of NWA 8173 and similar meteorites i.e. Y-82189, these rocks possibly experienced high temperatures to allow incorporation of sufficient silicon in FeNi metal under reduced conditions.

Interestingly, silicon in the metal of enstatite meteorites may explain planetary differentiation conditions of planetary bodies such as the Earth. Specifically, Si may account for the anomalously low density of Earth's core (10% light elements (Javoy,

2010)) which may be explained by the incorporation of silicon into the core (Ringwood, 1979; Javoy, 1995) during reducing conditions as Earth was differentiating.

#### *3.4.6 Fluorophlogopite and the importance of halogens in NWA 8173*

In terrestrial rocks fluorophlogopite has been identified in volcanic rocks from the Mt. Etna volcano (Scordari et al., 2013). Various studies ( Giordani et al., 2004; Tagliani et al., 2012) have investigated the role and importance of halogens in magma behavior and the role of gas-rock interactions, particularly, fluorine. Fluorine is an important proxy for magmatic differentiation processes in the shallow parts of volcanic plumbing systems (Scordari et al., 2013). It is also known that fluorine can increase the rates of crystal-melt and melt-vapor interactions in magmatic system (Giordani et al., 2004).

The volatile concentration governs the solidus temperature, thermodynamic properties, the viscosity and eruptive style of magmas in terrestrial rocks (Giordani et al., 2004). In terrestrial volcanic rocks, formation of fluorophlogopite is attributed to the high solubility and high fluorine content in some benmoreitic melts (Tagliani et al., 2012). In these volcanic rocks, flushing of metal-halogen complexes into a volatile-unsaturated magma may lead to the halogen enrichment in these magmas. Moreover, melts enriched in fluorine decrease the viscosity of Si-rich magmas and the crystallization of fluorophlogopite occurs during late stage crystallization (Nicotra et al., 2010). The decrease in melt viscosity due to F content in anhydrous melts (Giordani et al., 2004) could help enable continued melt mobility and mixing in partially a partially crystallized setting.

Although the felsic environment of formation of terrestrial fluorophlogopite is different than that in enstatite meteorites, its study may provide information about importance and role of halogens during the formation of enstatite meteorites. For the case of NWA 8173, halogen enrichment, specifically, fluorine may have occurred via a metal-halogen complex or by a gas carrier phase that interacted with a halogen-unsaturated silica melt. The source of halogens in enstatite achondrites is posited to be chondrule mesostasis of an EH precursor (Rubin and Choi, 2009). Once mobile, halogens may have been



complexed with metal or sulfur and have become enriched in some regions of the enstatite meteorite (EH chondrite) parent body.

The observed association of fluorophlogopite with sulfide and silica in NWA 8173 may support the role of metal or sulfur gas as a halogen carrier, as similarly discussed by Nicotra et al. (2012) where  $\text{SiF}_4$  gas can sublime into Si-rich amorphous concretions in terrestrial systems. For the case of NWA 8173 a sulfur gas phase may have served as the fluorine carrier which, upon reacting with the silicate melt, resulted in sulfidation of ferromagnesian minerals and ultimately formation of fluorophlogopite. Similarly, halogen melt saturation could have occurred after melting of an EH like precursor, leading to the liberation of fluorine as a gas phase and then its interaction with the melt under changing conditions to form fluorophlogopite. The textural association of fluorophlogopite with sulfide and silica may support the idea of an F-carrier that gets incorporated in the melt, lowering the crystallization temperature of the melt and leading to late-stage crystallization of fluorophlogopite, sulfide and silica.

Alternatively, Agangi et al. (2010) investigated the role of fluorine in felsic magmas and argue that fluorine dissolved in magma can lower the crystallization temperature of accessory minerals which causes trace elements to behave as incompatible elements. Then for the case of NWA 8173, fluorine may have played an important role during melt-volatile interactions by lowering the crystallization temperature of mineral phases and finally crystallizing as fluorophlogopite. Melzer and Foley (1986), discuss that in the presence of large amounts of fluorine, melting relations between mineralogical phases are characterized by a large liquidus field for fluorophlogopite even if enstatite is added to the system. More importantly, the fluorine content in the fluorophlogopite in NWA 8173 is high was absent of OH. It is the complete substitution of OH by F that can lead to the stability of fluorophlogopite up to 1150 °C at 1 bar of pressure (Tagliani et al., 2012). This provides P-T conditions for the formation of fluorophlogopite in NWA 8173 where it could have formed at temperatures of 1150 °C. The crystallization of fluorophlogopite in NWA 8173 may have occurred relatively early during crystallization and need not be a product of slow cooling.

The fluorophlogopite mineral identified in NWA 8173a is similar in composition to the meteorite Yamato 82189 (Lin and Kimura., 1998). Until recently, only a couple of meteorites have a reported presence of this mineral, with Yamato 82189 being the only one characterized chemically and is the only one previously reported in enstatite meteorites. This mineral could indicate a local source of halogens during the formation of these enstatite meteorites. Per Lin and Kimura (1998), the fluorophlogopite is expected to have crystallized from a fluorine enriched melt. However, they discuss that it is not known if the fluorine source was present in source rock prior to melting or if it subsequently became enriched in the melt. Rubin (2015), interpreted the occurrence of fluorophlogopite as the result of impact melting. This also provides an idea of the timing of impact since if impact occurred during slightly more oxidizing conditions, then fluorine would have formed apatite instead of fluorophlogopite.

Rubin and Choi (2009), argue that halogens such as fluorine may have condensed in sufficiently reducing conditions from the solar nebula as simple halides and nitrides that would have been subsequently destroyed and redistributed during parent-body processing involving oxidation. Absence of minerals like fluorophlogopite in other chondrite groups in this view is probably due to the more oxidizing conditions present during their formation and evolution, as halogens would have remained in a gas phase under more oxidizing nebular conditions. High C/O ratios and increased sulfur fugacity could have caused an increase in halogen affinity to form halogen compounds. Under reducing conditions the most reactive halogens, such as fluorine, were the most efficient at forming compounds that were incorporated into enstatite-chondrites precursor materials. Rubin (2015), also states that halogen abundance in enstatite chondrites did not form from chondrite accretion prior to the complete condensation of halogens for gas with canonical solar composition or preferential loss of the most volatile halogens due to heating. After impact melting it is possible that not all fluorine was driven off during a heating event and the remaining fluorine crystallized grains of fluorophlogopite (Rubin, 2015). However, it is possible that impact melting would have devolatilized an EH precursor completely and F-rich phases would not be expected in NWA 8173 if it was impact melted. The presence and abundance of fluorophlogopite in NWA 8173 may point towards an internal heating mechanism where fluorine acts as fluxing agent in the melt,

lowering melting temperatures and ultimately crystallizing fluorophlogopite. Lorenz et al. (2003) also identified fluorophlogopite in the enstatite meteorite NWA 1235 and describe that phlogopite could have crystallized from a residual melt.

#### 3.4.7 Petrogenetic sequence of NWA 8173

Based on the petrography, mineral chemistry and structural mineral analysis, the petrogenetic sequence, formation temperatures and cooling history of NWA 8173 can be determined and are summarized below.

- Enstatite crystallizes first after melting and its followed by plagioclase
- Fluorophlogopite was complexed as SF<sub>6</sub> (or other carrier) where S sulfidized the melt and formed sulfides and SiO<sub>2</sub> and F served as the source for fluorophlogopite (based on the textural association), and formed shortly after (1150 °C)
- Tridymite forms as a product of Sulfidation of the silicate melt (forming keilite and oldhamite)
- Metal and sulfide crystallize and wrap or engulf silicates (enstatite plagioclase and silica)
- Annealing then causes exsolution of FeS (troilite) and CaS from keilite giving niningerite and troilite as host sulfide and exsolved lamellae
- Myrmekite intergrowth represents the last stage of the crystallization sequence where it surrounds smaller enstatite grains, which were not able to grow as they were surrounded by the residual silica/plagioclase carrying melt.
- Quartz forms as rock cools at low temperature for a while from the transition of tridymite
- Cooling rate must have been slow enough to cause exsolution of sulfide but not too slow to cause all tridymite to revert to quartz.
- If tridymite is stable at 860 °C and the niningerite equilibrated at ~700 °C, then 700 °C represent the lower limits of cooling temperatures for NWA 8173 since lower temperatures would have resulted in the increase in Mg for niningerite and therefore would be reflected by having a composition more MgS rich. At this temperature, most of the tridymite was stable where occasional grains reverted to quartz due to annealing.

### 3.5 References

- Berthet, S., Malavergne, V., & Richter, K. (2009). Melting of the Indarch meteorite (EH4 chondrite) at 1GPa and variable oxygen fugacity: Implications for early planetary differentiation processes. *Geochimica et Cosmochimica Acta*, 73(20), 6402-6420.
- Boesenberg, J. S., Weisberg, M. K., Greenwood, R. C., Gibson, J. M., & Franchi, I. A. (2014, March). The Anomalous Enstatite Meteorites---Part 2: The Recrystallized EL Meteorites. *In Lunar and Planetary Science Conference*, 45, 1486).
- Bouvier, A. (Ed). (2017 *in press*). Meteoritical Bulletin 103. *MAPS*
- Dapiaggi, M., Pagliari, L., Pavese, A., Sciascia, L., Merli, M., & Francescon, F. (2015). The formation of silica high temperature polymorphs from quartz: Influence of grain size and mineralising agents. *Journal of the European Ceramic Society*, 35(16), 4547-4555.
- Dickinson, T. L., Lofgren, G. E., & Casanova, I. (1992, March). High Temperature Reduction of Silicon in Enstatite Meteorites: Evidence from the Experimental Studies of Indarch. *In Lunar and Planetary Science Conference*, 23.
- Edey, D. R., Holdsworth, D., McCausland, P. J. A., and Flemming, R. L. 2013. Extended range micro-computed tomography of meteorites using a biomedical scanner. 44<sup>th</sup> *Lunar and Planetary Science Conference*, # 2693
- Fleet, M. E., and MacRae, N. D. 1987. Sulfidation of Mg-rich olivine and the stability of niningerite in enstatite chondrites. *Geochimica et Cosmochimica Acta*. 51, 1511-1521
- Flemming, R.L. 2007. Micro X-ray diffraction (XRD): A versatile technique for characterization of Earth and planetary materials. *Canadian Journal of Earth Sciences*, 44(9): 1333–1346.
- Foley, S. F., Taylor, W. R., & Green, D. H. (1986). The effect of fluorine on phase relationships in the system  $\text{KAlSiO}_4\text{-Mg}_2\text{SiO}_4\text{-SiO}_2$  at 28 kbar and the solution

mechanism of fluorine in silicate melts. *Contributions to Mineralogy and Petrology*, 93(1), 46-55.

Giordano, D., Romano, C., Dingwell, D. B., Poe, B. T., & Behrens, H. (2004). The combined effects of water and fluorine on the viscosity of silicic magmas. *Geochimica et Cosmochimica Acta*, 68(24), 5159-5168.

Hutchison, R. (2004). *Meteorites: A petrologic, chemical and isotopic synthesis*. Cambridge University Press.

Izawa, M. R. M., King, P. L., Flemming, R. L., Peterson, R. C., & McCausland, P. J. A. (2010). Mineralogical and spectroscopic investigation of enstatite chondrites by X-ray diffraction and infrared reflectance spectroscopy. *Journal of Geophysical Research: Planets*, 115(E7).

Izawa, M. R., Flemming, R. L., Banerjee, N. R., & Matveev, S. (2011). QUE 94204: A primitive enstatite achondrite produced by the partial melting of an E chondrite-like protolith. *Meteoritics & Planetary Science*, 46(11), 1742-1753.

Izawa, M. R., Flemming, R. L., Banerjee, N. R., & Matveev, S. (2011). QUE 94204: A primitive enstatite achondrite produced by the partial melting of an E chondrite-like protolith. *Meteoritics & Planetary Science*, 46(11), 1742-1753.

Javoy, M. (1995). The integral enstatite chondrite model of the Earth. *Geophysical Research Letters*, 22(16), 2219-2222.

Javoy, M., Kaminski, E., Guyot, D. A., Sanloup, C., Moreira, M., Labrosse, S., Jambon, A., Agrinier, P., Davaille, A., and Jaupart, C. 2010. The chemical composition of the Earth: Enstatite chondrite models. *Earth and Planetary Science letters*. 293, 259-268

Keil, K. (1989). Enstatite meteorites and their parent bodies. *Meteoritics*, 24(4), 195-208.

Keil, K., & Bischoff, A. (2008). Northwest Africa 2526: A partial melt residue of enstatite chondrite parentage. *Meteoritics & Planetary Science*, 43(7), 1233.

- Kimura, M., Weisberg, M. K., Lin, Y., Susuki, A., Ohtani, E., and Okazaki, R. 2005. Thermal history of the enstatite chondrites from silica polymorphs: *Meteoritics & Planetary Science* 40-6, 855-868
- Lafuente, B., Downs, R. T., Yang, H., & Stone, N. (2015). The power of databases: the RRUFF project. *Highlights in mineralogical crystallography*, 1-30.
- Lehner, S. W., Petaev, M. I., & Buseck, P. R. (2012, March). Sulfidation of Enstatite in the Fine-Grained Matrix of EH3 Sahara 97072. *In Lunar and Planetary Science Conference*, 43.
- Lehner, S. W., Petaev, M. I., Zolotov, M. Yu., and Buseck, P. R. (2013). Formation of niningerite by silicate sulfidation in EH3 enstatite chondrites. *Geochimica et Cosmochimica Acta*. 101, 34-56.
- Lin, Y., and Kimura, M. 1998. Petrographic and mineralogical study of new EH melt rocks and a new enstatite chondrite grouplet: *Meteoritics & Planetary Science*. 33, 501-211
- Lorenz, C., Kurat, G., Brandstater, F., and Nazarov, M. A. NWA 1235: A phlogopite-bearing enstatite meteorite. 2003. *Lunar and Planetary Science XXXIV*. # 1211
- Malavergne, V., Brunet, F., Richter, K., Zanda, B., Avril, C., Borensztajn, and Berther, S. 2012. Experimental behavior of sulfur under primitive planetary differentiation processes, the sulfide formations in enstatite meteorites and implications for Mercury. *Lunar and Planetary Science Conference XXXIII*. Houston, Abstract #1860
- McCoy, T. J., Keil, K., Bogard, D. D., Garrison, D. H., Casanova, I., Lindstrom, M. M., Brearley, A. J., Kehm, K., Nichols Jr. R. H., and Honenberg, C. M. 1995. Origin and history of impact-melt rocks of enstatite chondrites parentage. *Geochimica et Cosmochimica Acta*. 59, 161-175.

- Melzer, S., & Foley, S. F. (1996). Phase relationships in the system  $\text{KAlSiO}_4\text{-Mg}_2\text{SiO}_4\text{-SiO}_2\text{-F}_2\text{O}$ -1 and the stability of F-phlogopite at atmospheric pressure, 10 and 18 kbar. *Neues Jahrbuch für Mineralogie-Abhandlungen*, 171(1), 1-31.
- Nicotra, E., Viccaro, M., Ferlito, C., & Cristofolini, R. (2009). F-enriched magmas at Mt. Etna (Italy) and related Volcanological implications. *EGU General Assembly*, Abstract # 4258
- Nicotra, E., Viccaro, M., Ferlito, C., & Cristofolini, R. (2010). Influx of volatiles into shallow reservoirs at Mt. Etna volcano (Italy) responsible for halogen-rich magmas. *European Journal of Mineralogy*, 22(1), 121-138.
- Piani, L., Marrocchi, Y., Libourel, G., & Tissandier, L. (2016). Magmatic sulfides in the porphyritic chondrules of EH enstatite chondrites. *Geochimica et Cosmochimica Acta*, 195, 84-99.
- Putnis, A. (1992). Introduction to mineral sciences. Cambridge: Cambridge University Press. 457.
- Reed, S. J. B. (2005). Electron Microprobe Analysis and Scanning Electron Microscopy in geology. Cambridge University Press.
- Rubin, A. E. (1997) Mineralogy of Meteorite Groups, *Meteoritics*, 32, 231-247
- Rubin, A. E. (1997). Igneous graphite in enstatite chondrites. *Mineralogical Magazine*, 61(5), 699-703.
- Rubin, A. E. (2008). Explicating the behavior of Mn bearing phases during shock melting and crystallization of the Abee EH chondrite impact melt breccia. *Meteoritics & Planetary Science*, 43(9), 1481-1485.
- Rubin, A. E. (2015). Impact features of enstatite-rich meteorites. *Chemie der Erde-Geochemistry*. 75 (1), 1-28

- Rubin. A. E., and Choi. B. (2009). Origins of Halogens and Nitrogen in Enstatite Chondrites. *Earth Moon Planet.* 105, 41-53
- Scordari, F., Schingaro, E., Ventruti, G., Nicotra, E., Viccaro, M., & Tagliani, S. M. (2013). Fluorophlogopite from Piano delle Concazze (Mt. Etna, Italy): Crystal chemistry and implications for the crystallization conditions. *American Mineralogist*, 98(5-6), 1017-1025.
- Skinner. B. J., and Luce. F. D. 1971. Solid solutions of the type (Ca, Mg, Mn, Fe)S and their use as geothermometers for the enstatite chondrites. *American Mineralogist*, 56, 1269-1296
- Tagliani, S. M., Nicotra, E., Viccaro, M., & Gianfagna, A. (2012). Halogen-dominant mineralization at Mt. Calvario dome (Mt. Etna) as a response of volatile flushing into the magma plumbing system. *Mineralogy and Petrology*, 106(1-2), 89-105.
- Van Niekerk, D. (2012). Petrology of enstatite chondrites and anomalous enstatite achondrites. Ph.D. Thesis, University of Hawai'i, 124.
- Ziegler, K., Young, E. D., Schauble, E. A., & Wasson, J. T. (2010). Metal–silicate silicon isotope fractionation in enstatite meteorites and constraints on Earth's core formation. *Earth and Planetary Science Letters*, 295(3), 487-496.



## Chapter 4: Extensively metamorphosed anomalous enstatite achondrites Zakłodzie and NWA 4301 and insights on early solar system processes

### 4.1 Introduction

This chapter provides detailed descriptions of the petrography, mineral chemistry and mineralogy of the highly-metamorphosed enstatite achondrites Zakłodzie and NWA 4301 to determine their petrogenetic history as well as processes of formation for these meteorites early in the solar system. This chapter will provide a detailed description of NWA 4301, a meteorite that has not yet been studied in detail, along with Zakłodzie, a meteorite that has been the subject of previous studies (e.g., Patzer et al., 2002; Przylibski et al., 2005). The findings in this chapter will be compared with those for NWA 8173 in Chapter 3 and will be further discussed in Chapter 5. Additionally, a comparison between the meteorites is made to determine if Zakłodzie and NWA 4301 are in fact paired as has been suggested by some authors (Boesenberg et al., 2014., Irving et al., 2006) based on similar textures and chemical compositions, leading to a discussion of the potential for the two meteorites to have originated from the same parent body.

Zakłodzie is an enstatite rich meteorite that was found in the near the Polish village of Zakłodzie in 1998 and was defined as a recent fall (Patzer et al., 2002). The Meteoritical Bulletin 84 (Grossman et al., 2000) describes it as an ungrouped enstatite rich meteorite containing mainly orthoenstatite rich pyroxene (~60 vol %), ~20 vol % metal, ~10 vol% troilite, ~10 vol % feldspar with accessory minerals such as schreibersite, silica, oldhamite, alabandite and amphibole. The enstatite in Zakłodzie is subhedral to rounded and the plagioclase is reported to have a bimodal composition ranging from  $\text{Ab}_{59-64}\text{An}_{36-41}\text{Or}_{0-0.5}$  to K-enriched  $\text{Al}_{86-89}\text{An}_{0-5}\text{Or}_{9-12}$ . The metal contains 6-16 wt% Ni and 1.6 wt% Si whereas troilite contains 4.7 wt % Cr, 1.4 wt% Mn and 0.9 wt % Ti (Grossman et al., 2000).

Connolly et al. 2007, described NWA 4301 as a rock that contains sub-equigranular cumulate texture with coarse grained silica, metal and sulfide grains. The meteorite is composed of polysynthetically twinned pure enstatite (70 vol %), kamacite (15 vol %), subordinate interstitial plagioclase, with composition  $\text{An}_{30.7-37.6}\text{Or}_{1.8-1.3}$  (10 vol %) and

troilite (5 vol %). NWA 4301 is suggested to be similar in texture and composition to Zakłodzie.

These two enstatite achondrites are a useful addition to this work because, unlike NWA 8173, they appear to have been extensively metamorphosed. Zakłodzie and NWA 4301 are texturally and chemically different from the igneous-textured NWA 8173 (Chapter 3) and may represent complementary (metamorphic versus igneous) formation processes from similar enstatite chondrite starting material. Ultimately, these meteorites and NWA 8173 may represent stages in incipient planetary differentiation, or possibly each may represent a unique process and environment of formation.

## 4.2 Methods

Slab samples of the Zakłodzie (4.04 g) and NWA 4301 (1 - 1.4 g) enstatite meteorites were obtained for this study. The Zakłodzie slab was obtained from meteorite collector Simon De Boer. Physically, the large Zakłodzie slab exterior is covered by an oxide stained fusion crust and has a weathering profile where metal is progressively weathered out from one end of the slab into the most pristine area in the interior. Two smaller slabs of the Zakłodzie meteorite (0.4 g) were obtained from the meteorite collection of Western University and were made into epoxy mounts for further analysis. The NWA 4301 slab was obtained from the Nature's Vault meteorite dealer website in 2015. More detailed sample descriptions can be obtained in Chapter 2.

Below is a summary of the instruments used in in these meteorites. For detailed description on instrumentation and procedures see Chapter 2.

Micro-CT ( $\mu$ CT) scans were obtained using the GE eXplore Locus scanner at the Robarts Pre-Clinical imaging center at Western University where the scanner operated with an X-ray tube voltage of 80 kVp and a tube current of 0.45 mA. For EBSD analysis, an Oxford Xmax 80mm<sup>2</sup> silicon drift EDS detector and HKL, Nordlyis EBSD detector was used. These detectors are attached to a Hitachi SU6600 FE-SEM at the Zircon and Accessory Phase Laboratory (ZAPLab) at Western University and operated at 20 kV, and ~2.5 nA using a 70° stage tilt and a working distance 19 mm for EBSD analysis. Phase indexing

in EBSD used band centers with 30 milliseconds per frame. INCA and HKL Channel 5 programs were used to process EBSD and EDS data. Quantitative mineral compositions were obtained using a JEOL JXA-8530F field emission electron microprobe in Western University. A variety of BSE, SEI, EDS and CL images were also used for EPMA and the probe was operated at 15 kV, beam current of 20 nA and a beam spot size of 5  $\mu\text{m}$  (for silicates) and 1  $\mu\text{m}$  (for sulfides). X-ray diffraction was done using the Bruker D8 Discover  $\mu\text{XRD}$  at Western University where it operated at 35 kV voltage, 45 mA current with a 60 mm Göbel mirror and a nominal incident beam diameter of 300  $\mu\text{m}$  using  $\text{Co K}\alpha$  radiation.

### 4.3 Results

This section will provide a detailed description of the textures, chemical compositions and mineral assemblages of the Zakłodzie and NWA 4301. Petrographic observations are based on  $\mu\text{CT}$  and electron microbeam imaging (BSE, SEI, CL, EDS), mineral chemistry is obtained from EPMA and mineral structural determination will use  $\mu\text{XRD}$  and EBSD. These findings will be discussed in a further section of the chapter.

#### 4.3.1 *Micro computed tomography ( $\mu\text{CT}$ )*

##### 4.3.1.1 *Zakłodzie*

Micro-CT ( $\mu\text{CT}$ ) scans reveals the presence of a metal content gradient from surface to interior in Zakłodzie (Fig. 4.1a). A 3D isosurface of high density phases in Zakłodzie (Fig. 1e) illustrates this weathering profile better. The interior of the meteorite can be identified as the left section of the isosurface where most of the metal and sulfides appear to be pristine compared to the more weathered regions in the right where metal is scarce.

Micro-CT scans also show that the meteorite has slightly higher density attenuation values of silicates and are likely due to iron oxyhydroxides produced by terrestrial weathering present throughout the rock (Fig. 4.1c). Additionally,  $\mu\text{XRD}$  identified goethite as a weathering phase in both meteorites and EDS spectra revealed that the

weathered material is predominantly oxyhydroxides containing various amounts of Ca, Fe, Mg, Al and other elements that have been oxidized due to weathering.

#### 4.3.1.2 NWA 4301

The metal and sulfide grains in NWA 4301 appear to be coarser and more interconnected than those in Zakłodzie (Fig 4.1f). Although most metal and sulfides are unevenly distributed through the sample, there are some areas where these are not seen and can be observed in both the CT scan and 3D isosurface. The weathering in NWA 4301 occurs as iron oxide veins which can be readily identified in the CT scan images (Fig. 4.1b, d). The weathering veins appear to surround the metal and sulfide grains and seem to be oriented preferentially in one direction subparallel to the exterior weathered surfaces of the original stone, along the right and left sides of the slab in Fig 4.1d.

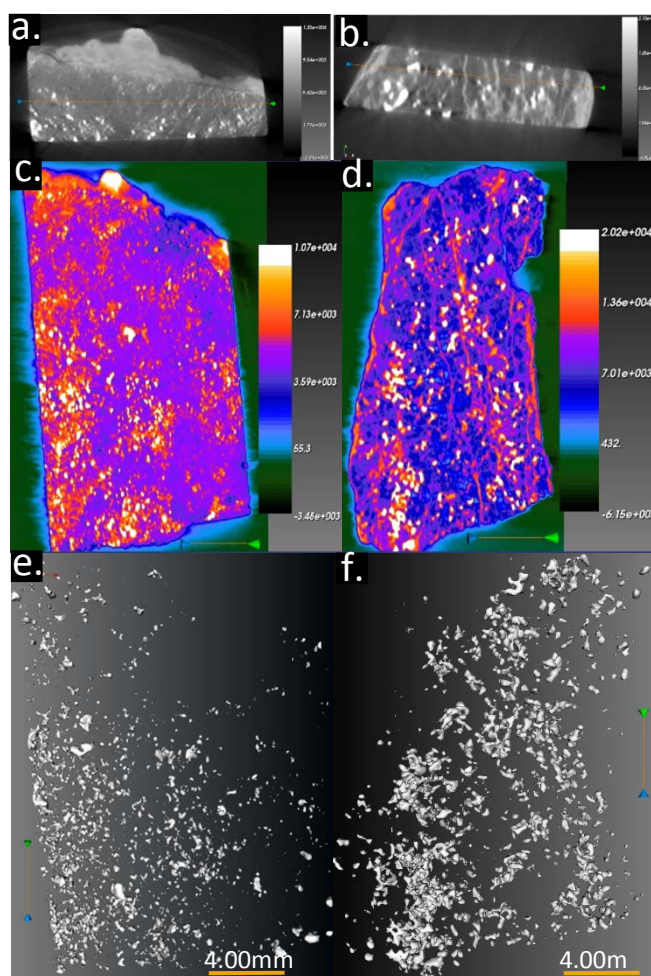


**Figure 4.1:** Micro-CT virtual slices a-d) and high density phase isosurface representing metal/sulfide e-f) in Zakłodzie and NWA 4301.

### *4.3.2 Petrography (BSE imaging)*

#### *4.3.2.1 Zakłodzie*

Enstatite grains are sub rounded to anhedral ranging in size from 20- 300  $\mu\text{m}$ , with some round enstatite resembling relict chondrules (Fig. 4.2), based on enstatite shape only exhibiting granoblastic texture with some grains associated across triple junction textures. Most of the enstatites are surrounded by interstitial plagioclase and contain very small metal inclusions. Grain boundaries are filled by iron oxide veining and the enstatites show some banding in CL and BSE images (Fig. 4.3). Plagioclase grains in Zakłodzie are zoned and some grains exhibit micrographic intergrowth with silica in the edges where compositions are more potassic (Fig. 4.3). The zoning in plagioclase appears to transition from a Ca, Al rich zone in one half of each grain to a more sodic one in the other (Fig. 4.4). In addition, the potassic areas do not contain Ca. Silica grains are predominantly present as micrographic intergrowth (Fig 4.5 a,b) with plagioclase and are also seen as irregular grains ( $\sim 10\text{-}40 \mu\text{m}$ ) in close association with sulfide and in proximity to plagioclase, with occasional grains included and surrounded by metal. Metal grains are irregular and can be a couple several hundred micrometers in size. Most metal grains are surrounded by plagioclase and silica intergrowth (Fig. 4.5 c, d) and sometimes contain inclusions of enstatite.

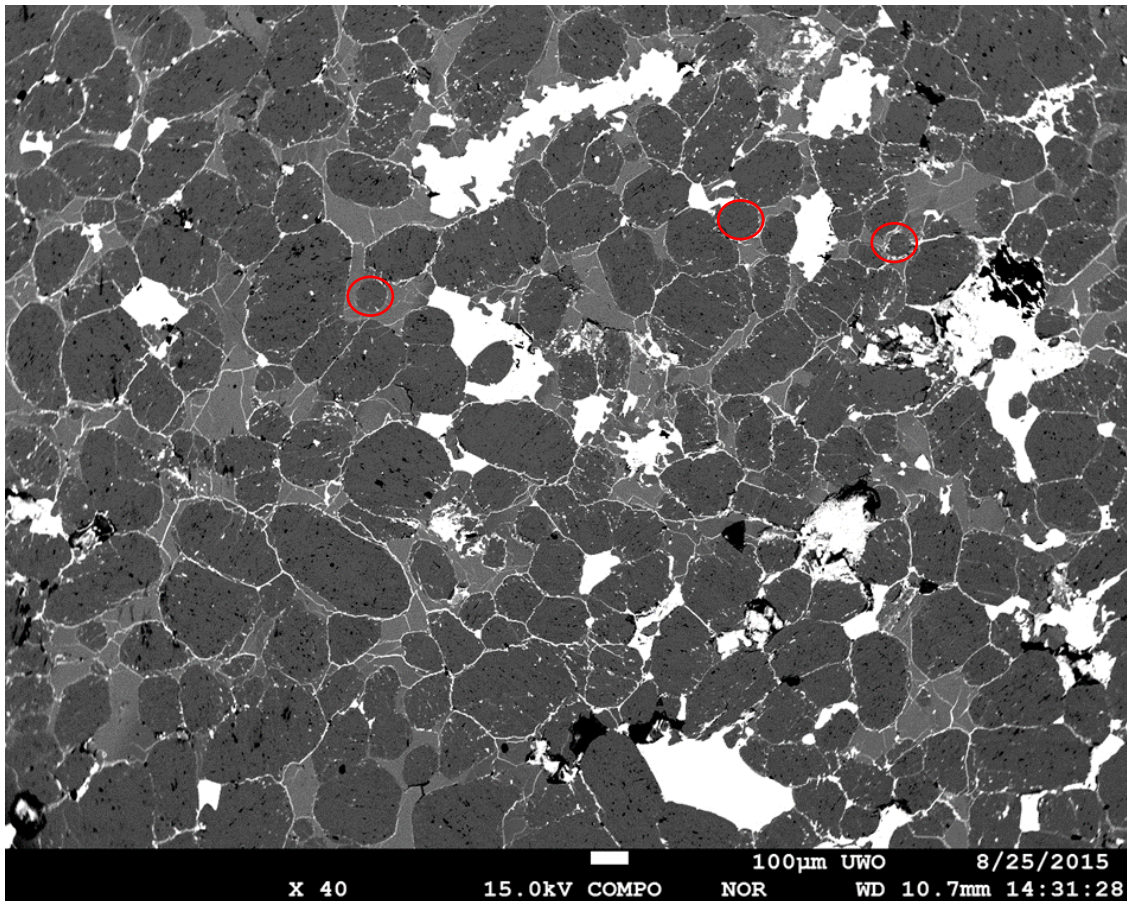


**Figure 4.2:** High Contrast BSE context image of Zakłodzie. Note the equigranular texture of the enstatites with triple junction textures and the smaller rounded crystals that resemble relict chondrules (marked by red circles); interstitial lighter greyscale phase is plagioclase and highest intensity phases are FeNi metal and sulfide. Grain boundaries and cracks tend to be lined by an Fe-oxide terrestrial weathering phase.)



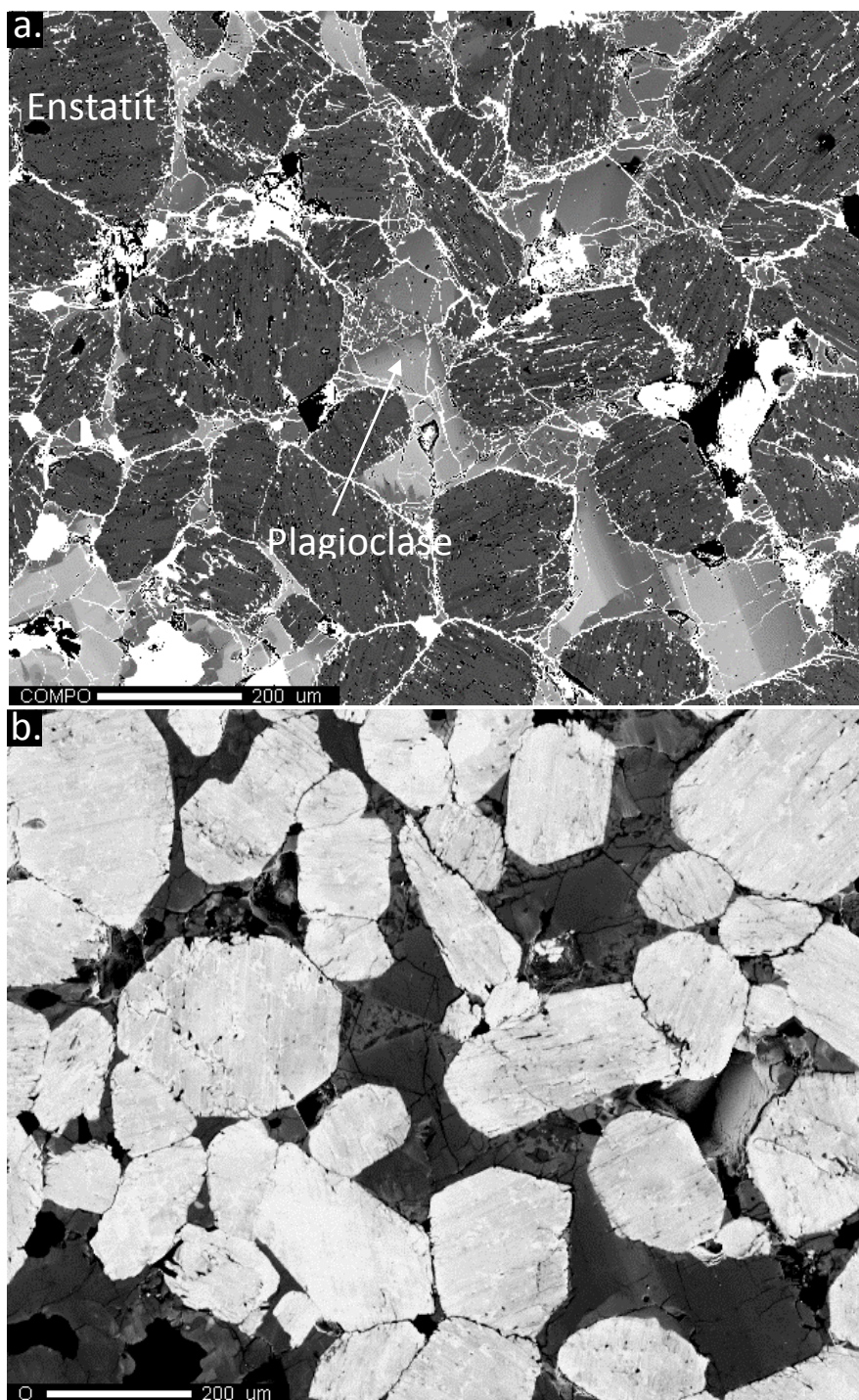


**Figure 4.3:** a) BSE image and b) CL map of Zakłodzie showing striation in enstatite and zoning is apparent in plagioclase.



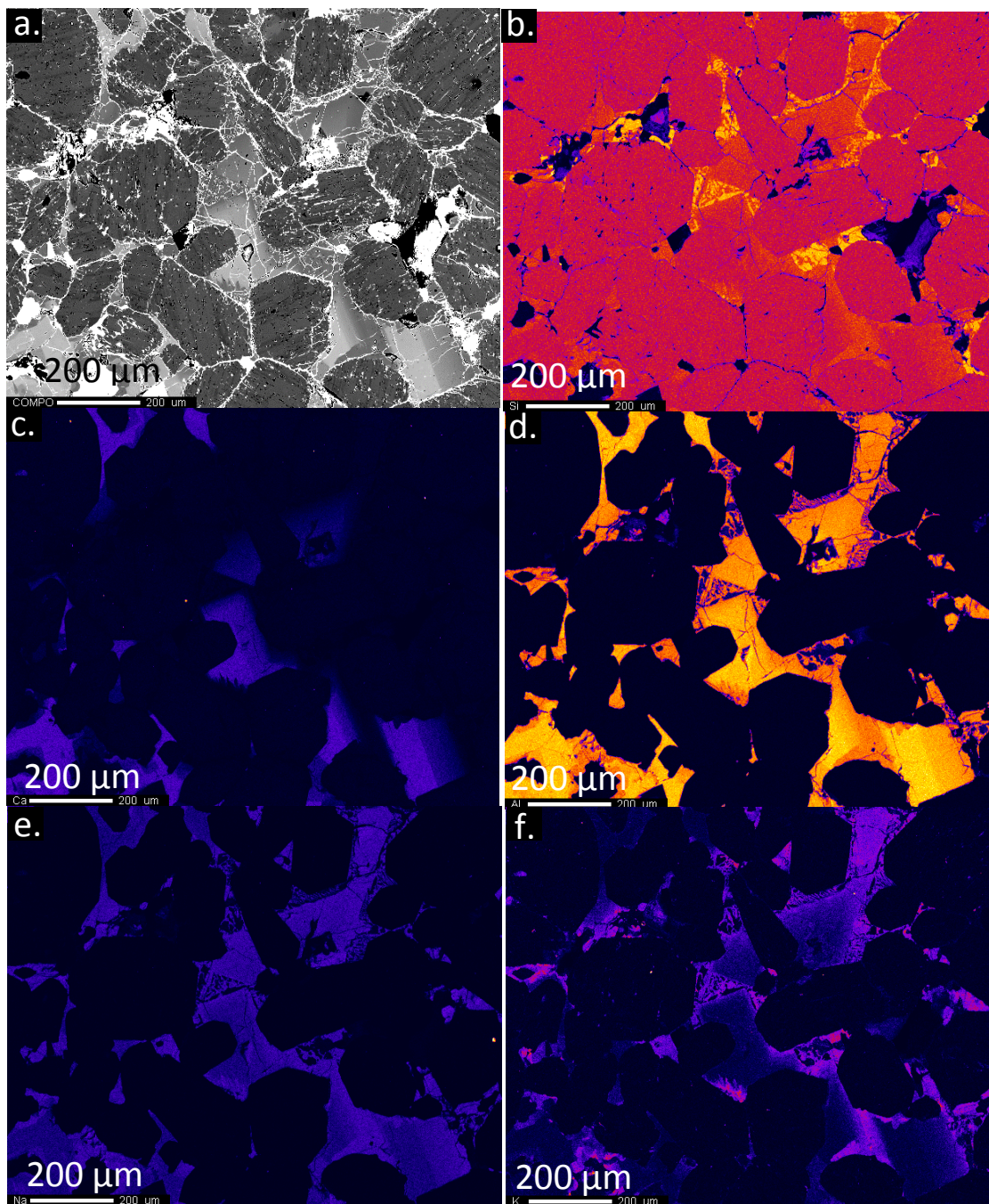


**Figure 4.4:** BSE context image a) and X-ray elemental maps for silicon b), Calcium c), Al d), Na e) and K e) for Zakłodzie. Note the silica micrographic intergrowth with silica b) is associated with K rich areas in e)



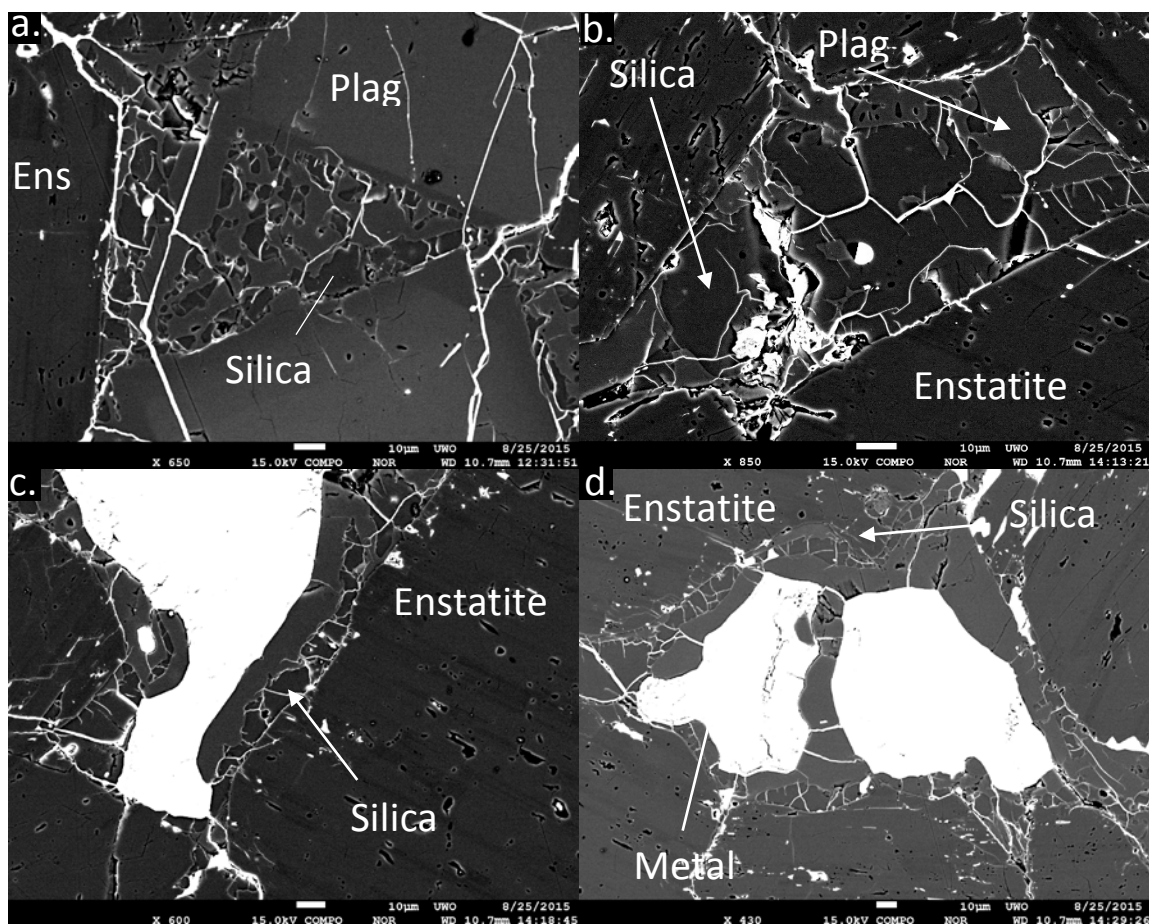


**Figure. 4.5:** silica grains and associations in Zakłodzie. in a) and b) silica is associated with plagioclase. In c) and d) silica and feldspar surround metal grains.

Metal grains also contain anhedral, irregular grains of graphite which can sometimes be as large as 100 micrometers and are frequently surrounded by iron oxide weathering (Fig. 4.6 a, b). Additionally, schreibersite grains are accompanied by metal and can be as large as 100 µm in size. Sulfides occur as subhedral/anhedral grains that can be as large as 200 µm and are often in proximity with metal and are surrounded by irregular, small silica grains. Two types of sulfides can be discerned from BSE images and both occur in close association with each other and frequently surround enstatite grains (Fig. 4.7). Included in some sulfide grains, acicular grains of sinoite, identified by EDS, are identified and resemble a radiating texture (Fig. 4.8).

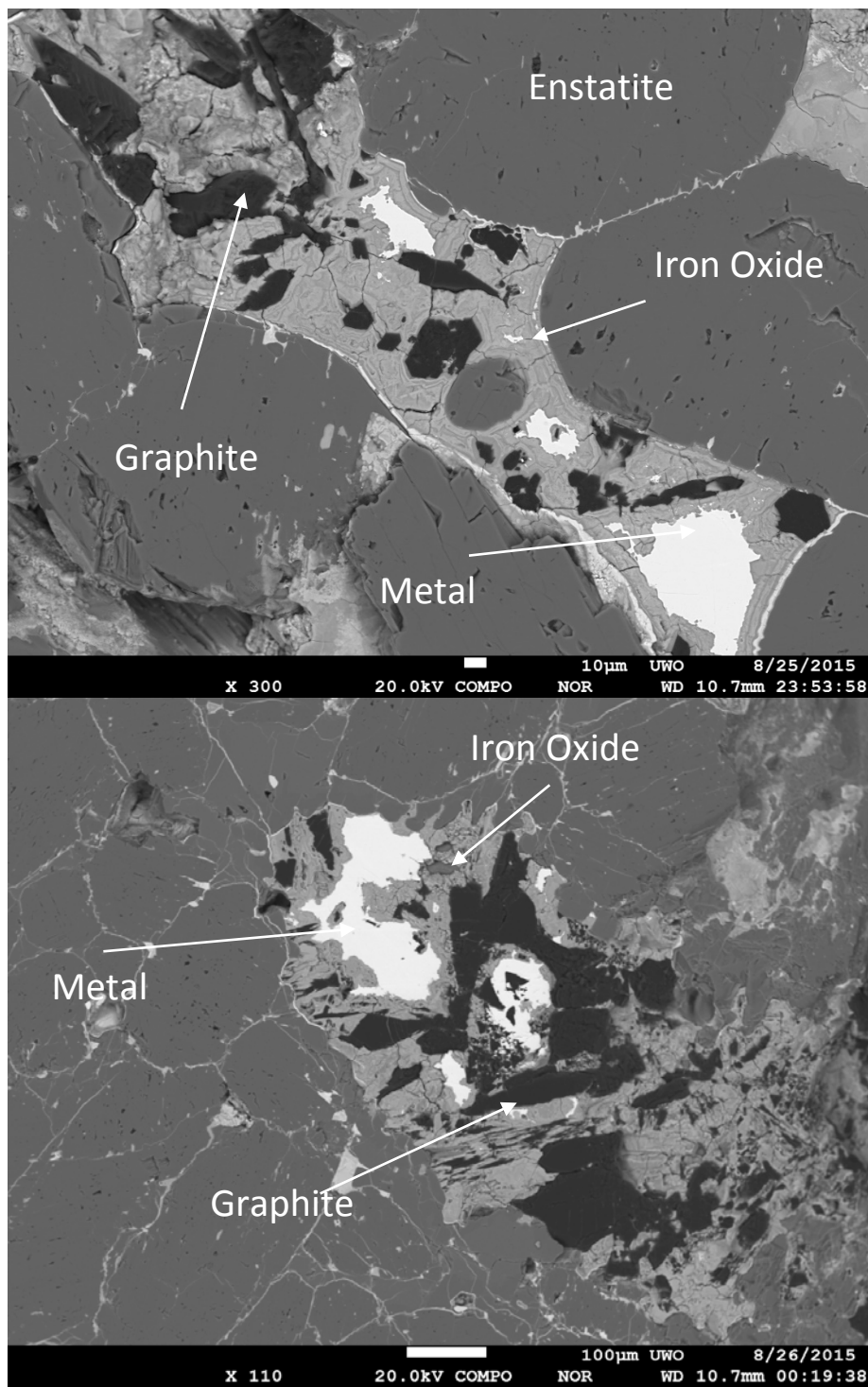


**Figure 4.6:** Graphite laths associated with metal and iron oxide in Zakłodzie.

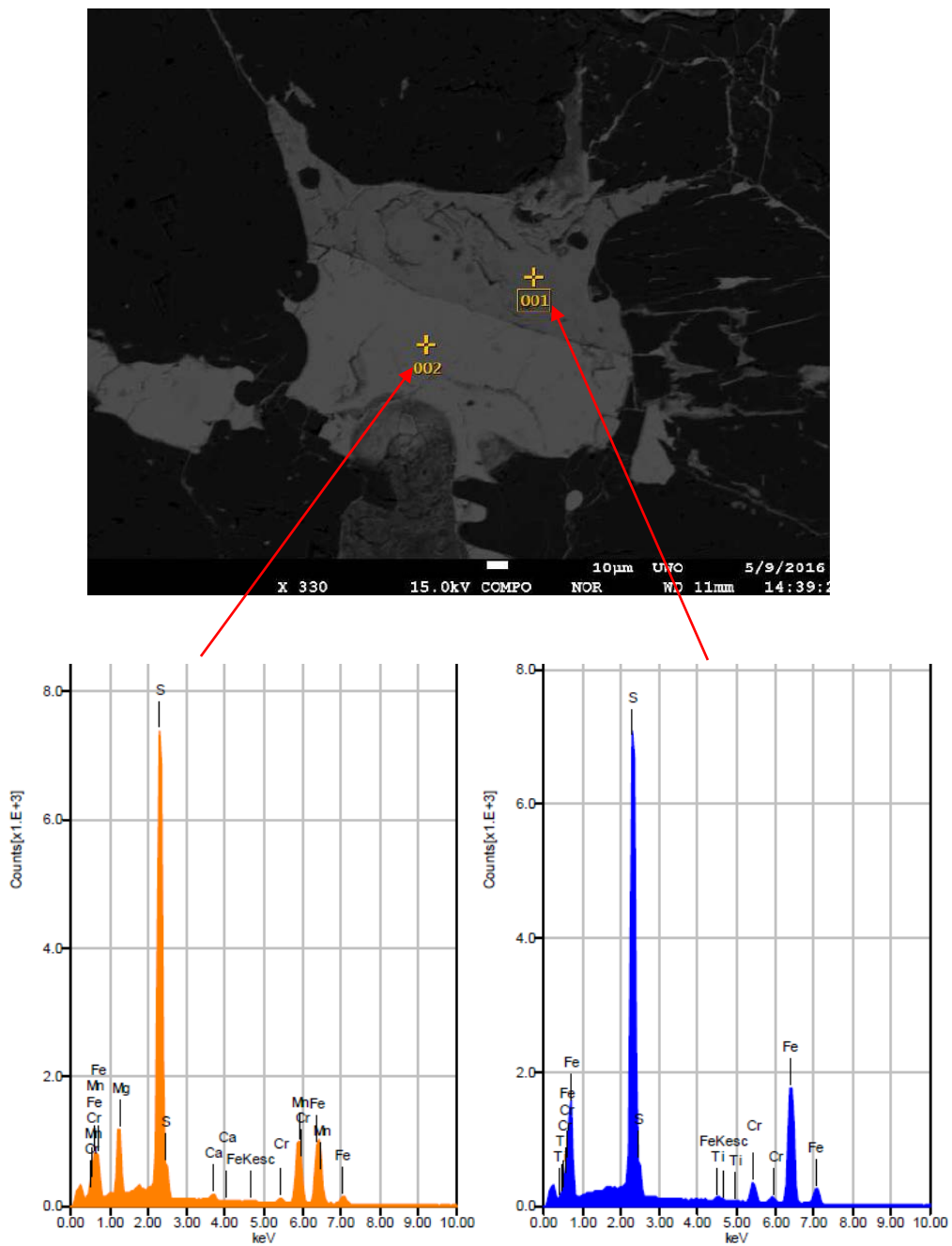


**Figure 4.7:** BSE image of sulfides types in Zaklodzie with EDS spectra.

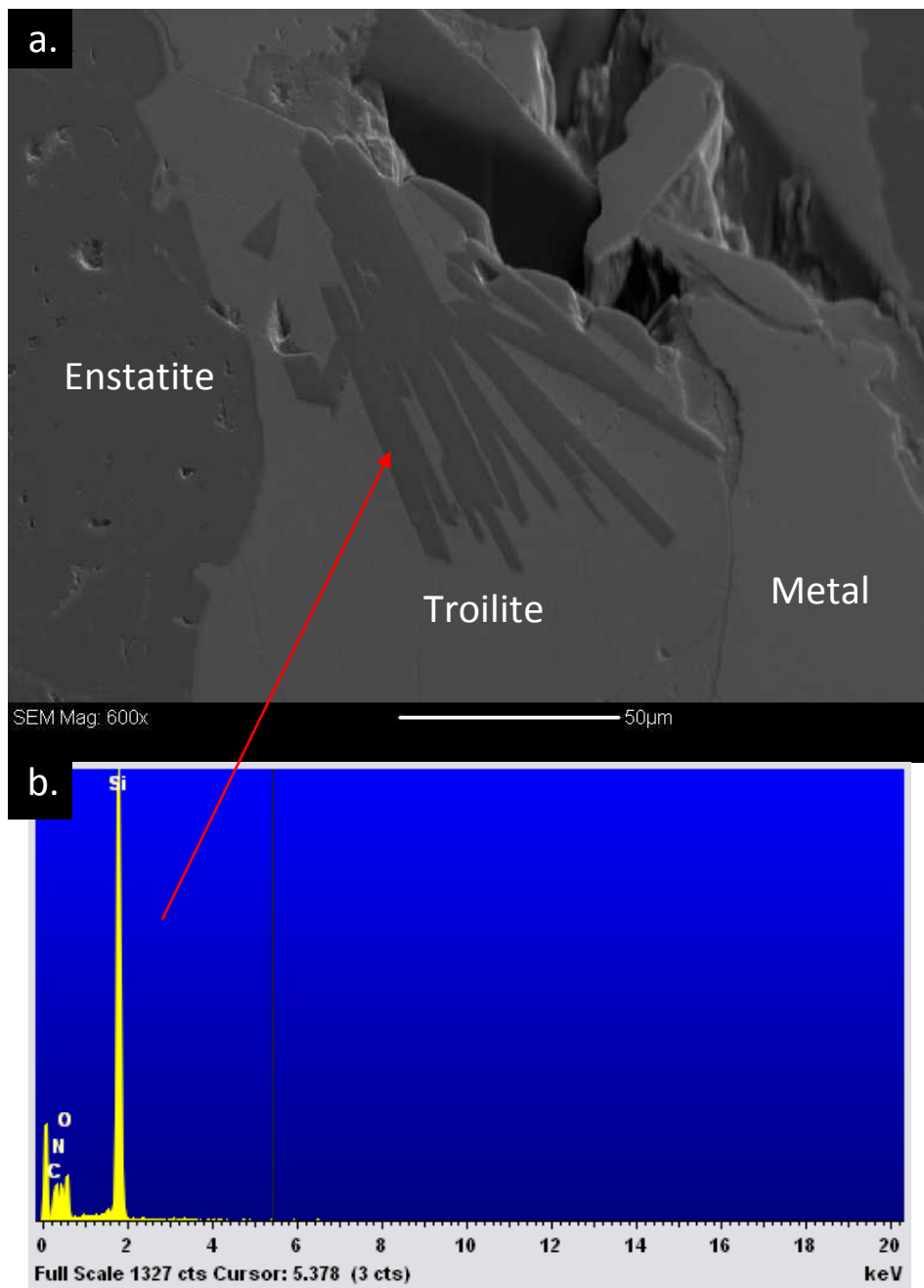


**Figure 4.8:** a) SEI image of Zakłodzie showing acicular sinoite grains contained in sulfide (troilite), b) EDS spectra confirming the presence of sinoite in Zakłodzie.

#### 4.3.2.2 NWA 4301

Enstatite grains in NWA 4301 also exhibit granoblastic texture, ranging in size from tens to hundreds of micrometers and containing small metal inclusions. Triple junction

textures are seen between some grains, and most of the enstatites are crosscut and enveloped by Fe oxide veining (Fig. 4.9a). The smaller enstatite grains tend to be rounder than the larger ones and may resemble relict chondrules. Enstatite grains are readily identified by their activity in the catholuminescence image (Fig. 4.9b). The enstatites also show small, alternating bands on darker contrast BSE images similar to those in Zakłodzie. Plagioclase occurs interstitially and some grains show reverse zoning (Fig. 4.10) where a more sodic composition is seen in the core transitioning towards higher temperature, Al, Ca rich composition in the rims. Additionally, some of the plagioclase grains exhibit a more uniform composition, predominantly more Ca and Al rich with slightly more potassic and sodic compositions in the rims of some grains (Fig. 4.10).

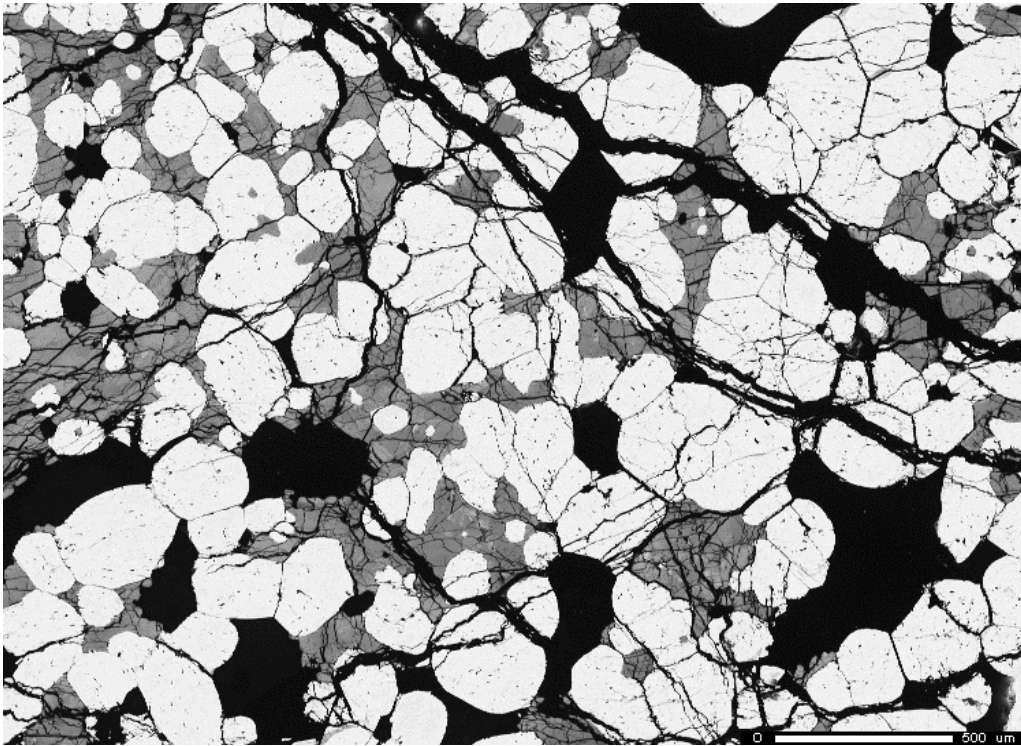


**Figure. 4.9:** Catholuminescence map showing interstitial plagioclase in grey and enstatite grains in white in NWA 4301.



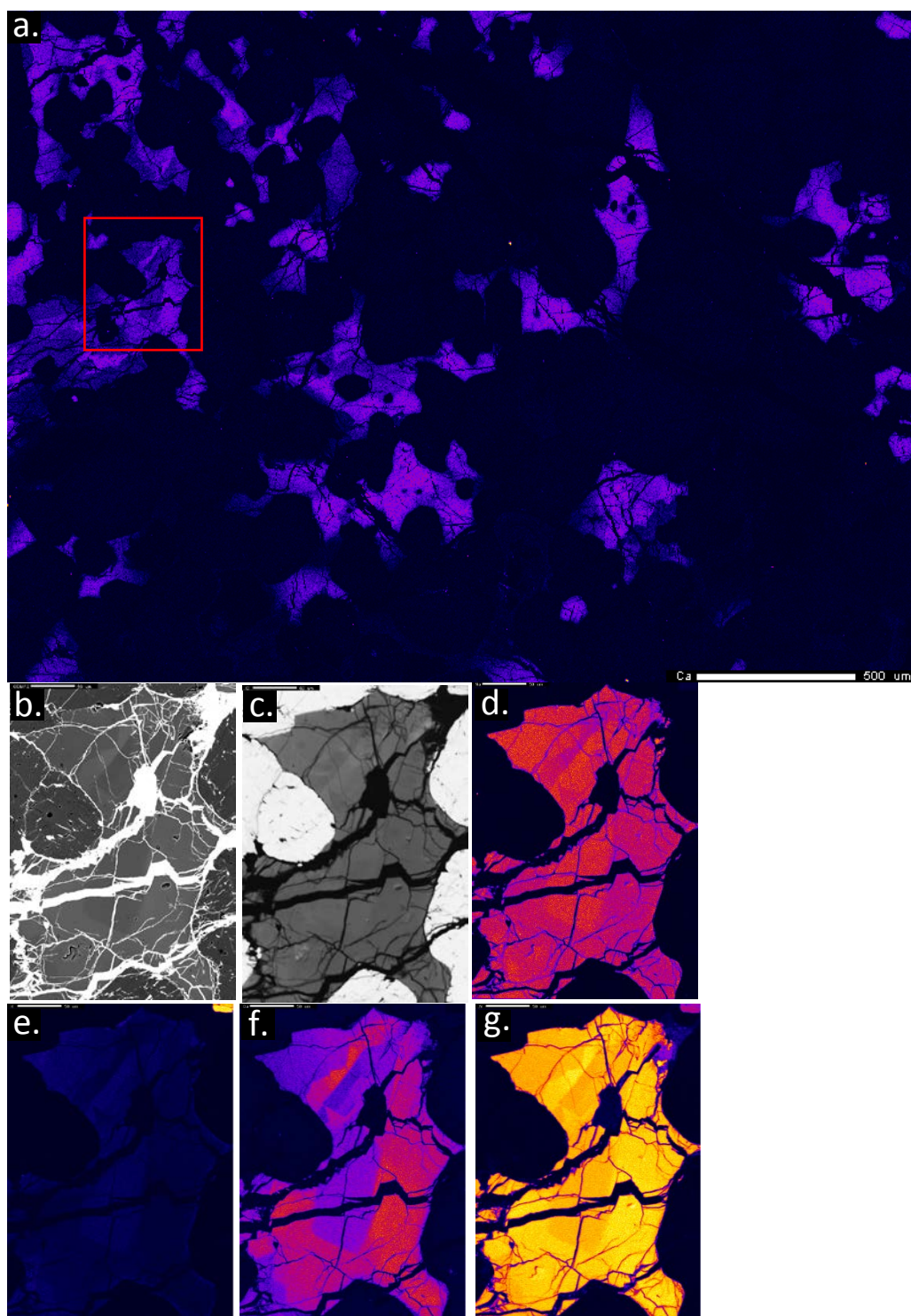


**Figure 4.10:** X-ray elemental map for Ca in NWA 4301 at 4 μm step size in a). BSE image b), CL map c), X-ray elemental mapping at 0.5 μm resolution for Na c), d) K, e) Ca, f) Al. Note: images b-f) contain detailed elemental mapping of area delineated in red in image a).

Silica in NWA 4301 occurs as small (3-5  $\mu\text{m}$ ), irregular grains and are only contained within and around metal/iron oxide veining (Fig. 4.11). Metal grains can be several hundred micrometers in size and are surrounded by iron oxide due to weathering. Some small (10-30  $\mu\text{m}$ ) graphite inclusions are included in occasional metal grains. Graphite is also seen as subhedral laths (100-350  $\mu\text{m}$ ), and were observed within iron oxide veins in and proximity to sulfide and metal. (Fig. 4.12). Schreibersite grains (10-100  $\mu\text{m}$ ) have also been identified in association with metal. Sulfide grains are anhedral, range in size from 15  $\mu\text{m}$  to 150  $\mu\text{m}$  and are surrounded by iron oxide and occasionally in proximity to metal. Based on EDS spectra, the sulfides contained are, Cr-bearing FeS, and a Fe-Mn rich sulfide. Lastly, tabular sinoite grains were identified in NWA 4301 and are found in the edges of some metal grains (Fig .4.13).

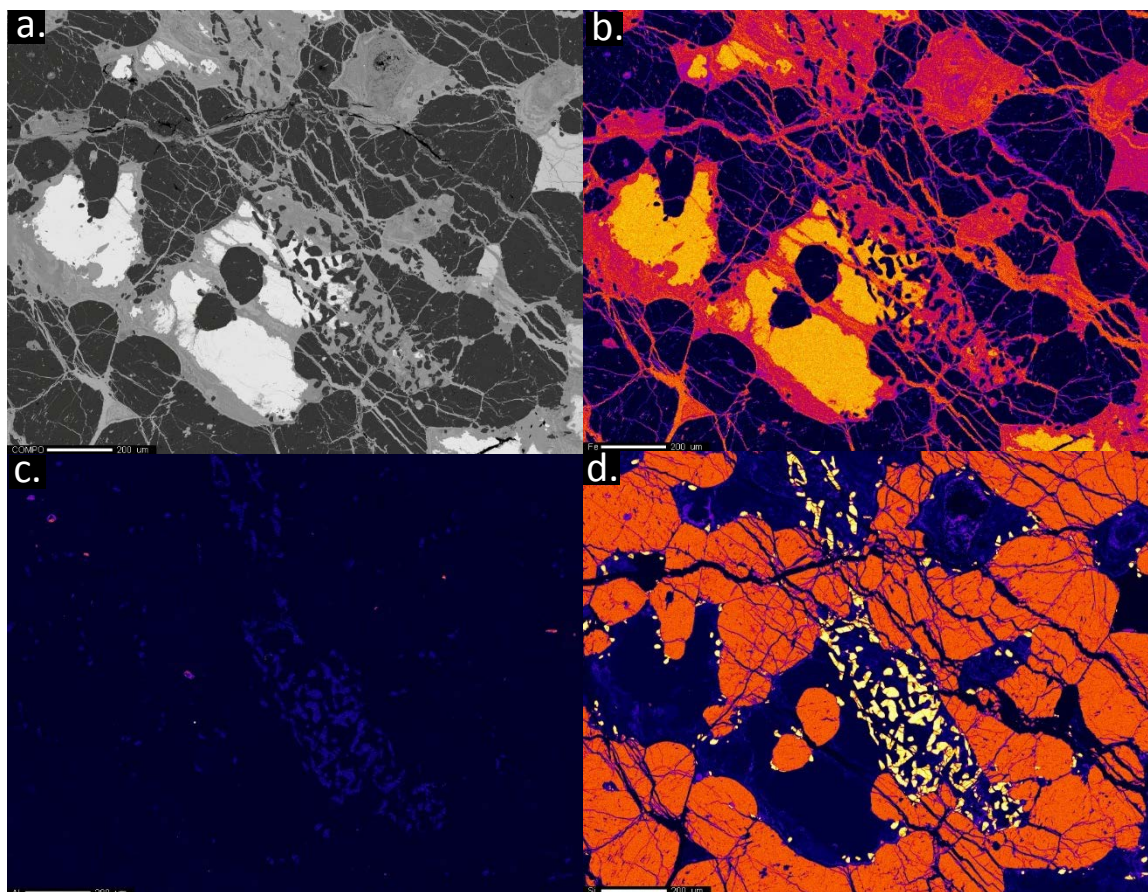


**Figure 4.11:** a) BSE context image of silica grains contained in metal and iron oxide veining. X-ray elemental maps at 2  $\mu\text{m}$  resolution for b) Fe, c) K and d) Si.



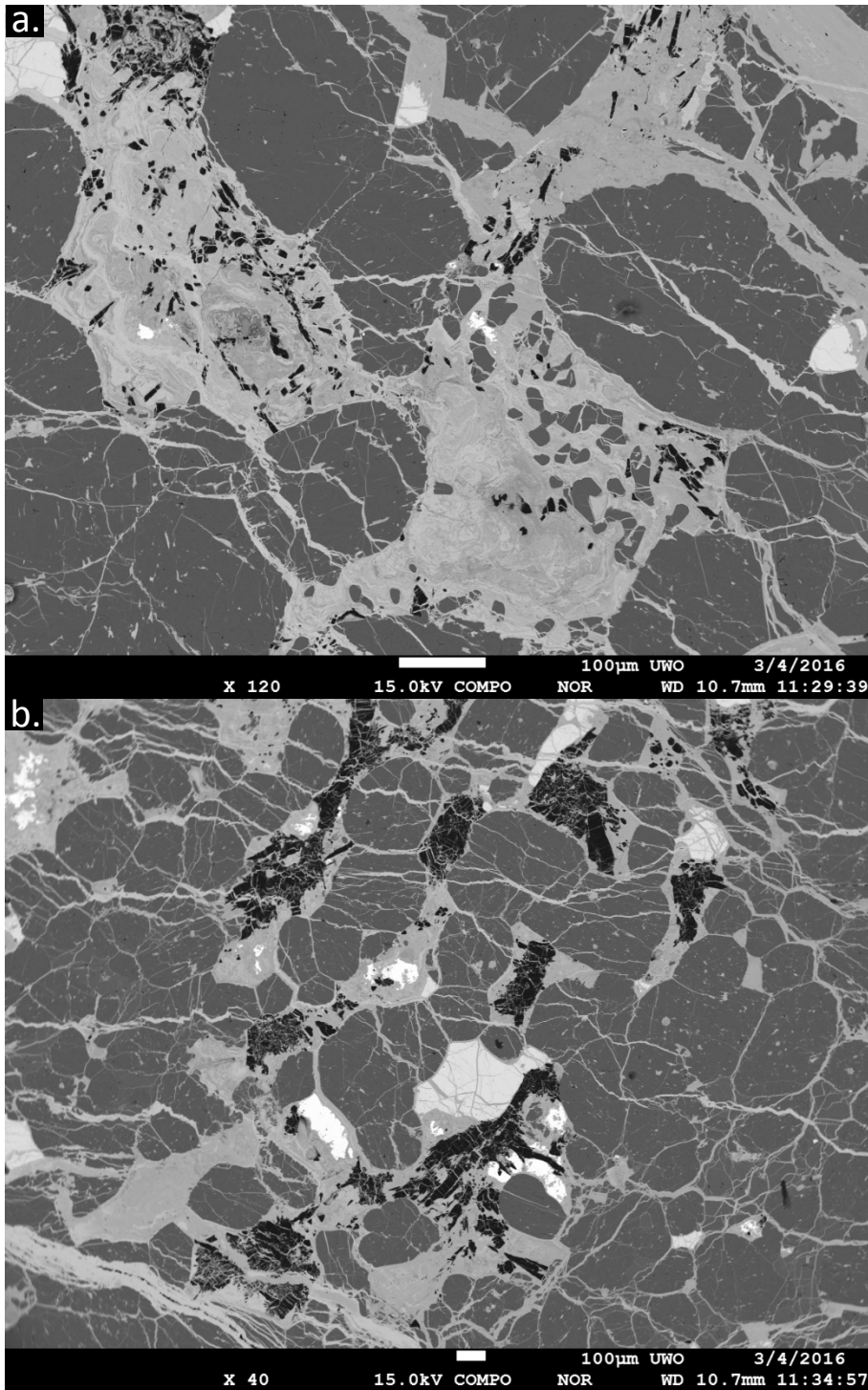


**Figure 4.12:** BSE context images of NWA 4301 illustrating graphite and its mineral associations. a) small graphite inclusions in iron oxide veining and in proximity with irregular, silica grains. b) large, euhedral graphite laths associated with iron oxide veining, sulfide and metal.



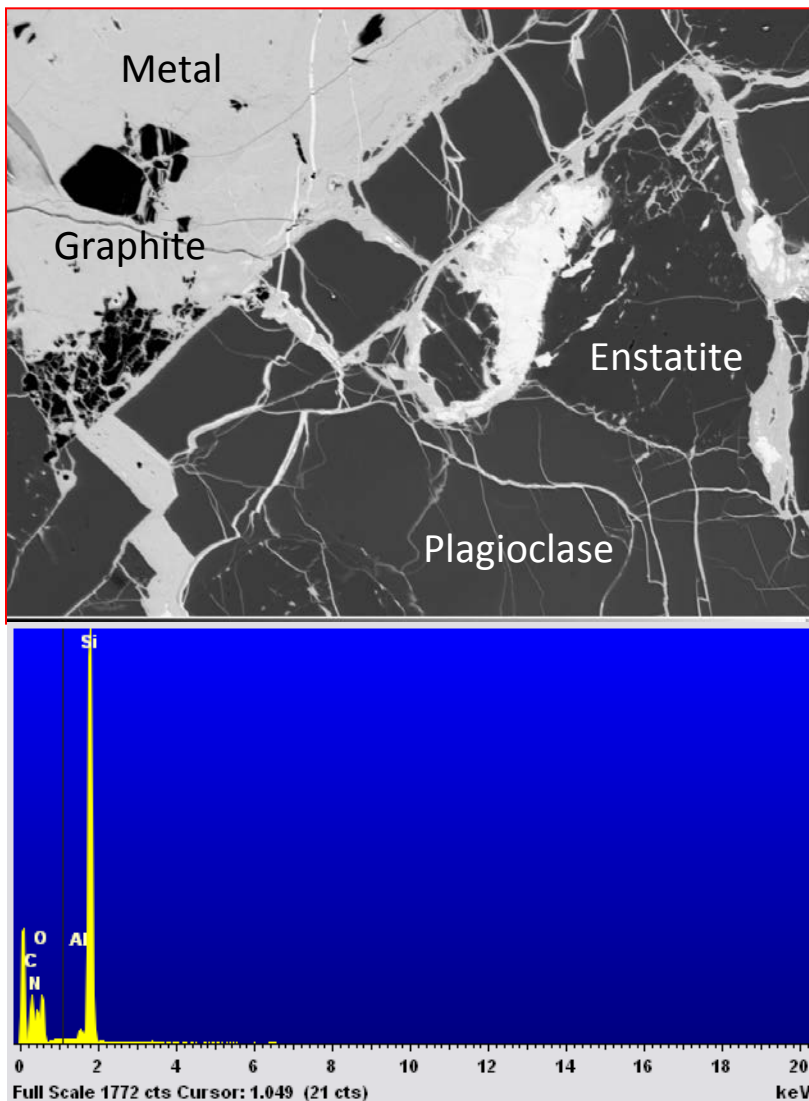


**Figure 4.13:** BSE context image of tabular sinoite grain in NWA 4301 associated with metal. Silicates surrounding the crystal are plagioclase and enstatite. EDS spectra map shows the chemical composition confirming the presence of sinoite.

In one of the NWA 4301 slabs (Fig. 4.14a), there is a region of about 8 mm which contains most of the sulfide, silica and graphite in the sample while being devoid of plagioclase (Fig. 14b). There is another area in the slab that contains mostly plagioclase but is absent of sulfide, silica and graphite (Fig. 4.14c). It is worth noting that while the plagioclase rich area contains small amounts of sulfide, there are no silica nor graphite grains present. Any additional information on elemental X-ray maps of Zaklodzie and NWA 4301 can be found in Appendix 4.1-4.2.

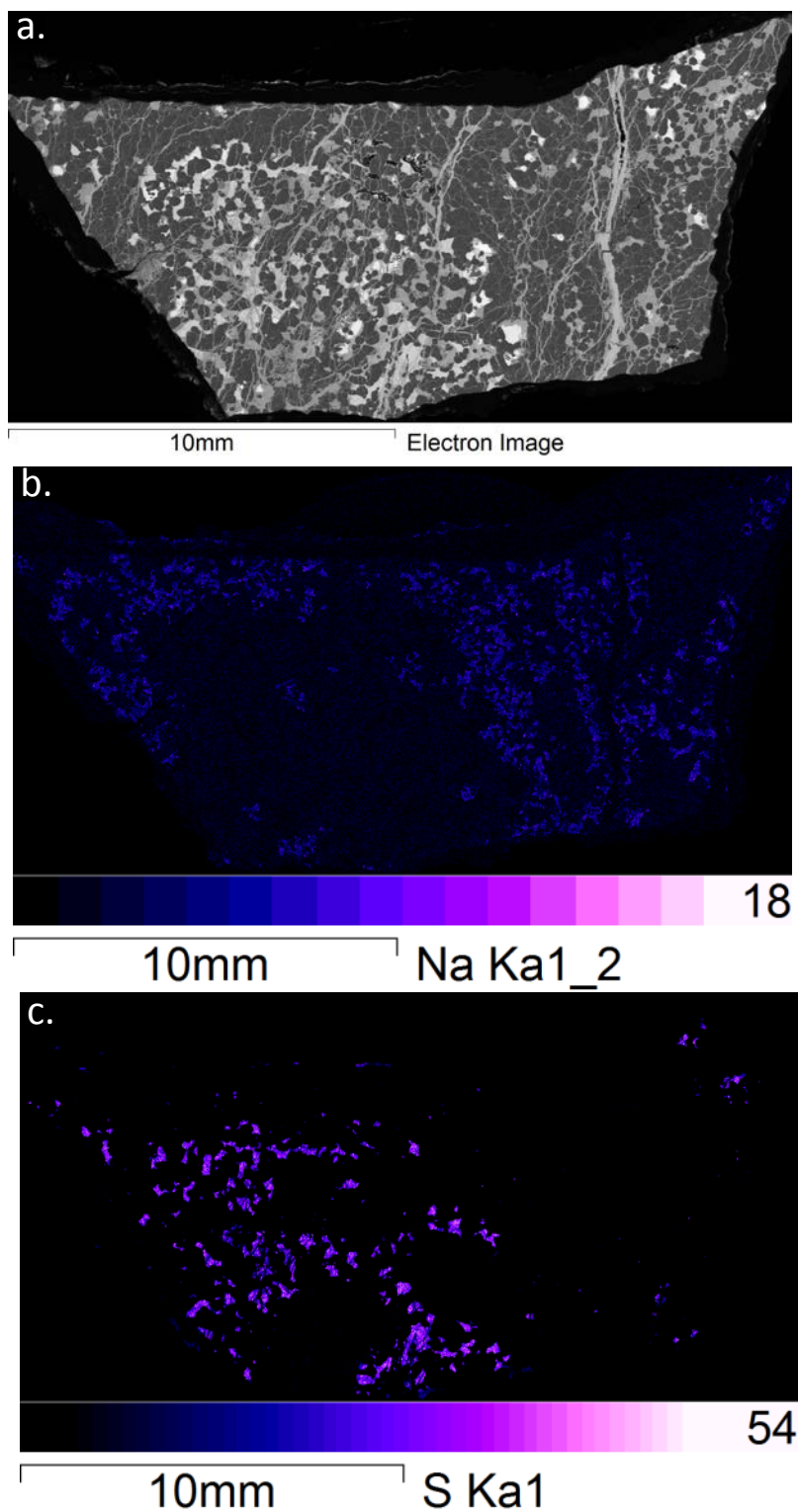


**Figure 4.14:** BSE context image and Ka EDS elemental maps of Na in NWA 4301 b) and S in c). Note the dichotomy in elemental distribution in the sample. The sulfur rich area in c) contains silica and graphite while these are absent in the plagioclase area, represented by the Na K $\alpha$  X-ray map.

### 4.3.3 Mineral Chemistry

#### 4.3.3.1 Zakłodzie

Enstatite has an average composition of  $\text{En}_{98.94}\text{Fs}_{0.24}\text{Wo}_{0.83}$ , similar to that reported by Przylibski et al. (2005), and does not vary compositionally within the thin, alternating bands seen in BSE images. The plagioclase compositions range from  $\text{Ab}_{59.2-88.4}\text{An}_{3-39.8}\text{Or}_{1-8.6}$  (Fig. 4.15); this broad compositional range is due to zoning in plagioclase as previously seen in Fig. 4 and Fig. 10. The silica grains are about 96 wt% SiO with minor impurities that include ~1.16 wt%  $\text{Na}_2\text{O}$ , ~2 wt%  $\text{Al}_2\text{O}_3$  and ~0.56 wt % FeO. The silicon content in the metal is ~1.25 wt% and is composed of ~5.8 wt % Ni and 0.45 wt% Co. The silicon content in metal is within range of EL chondrites. The schreibersite associated with metal contains approximately 15.11 wt % P, 12.9 wt % Ni and 0.23 wt % Co.

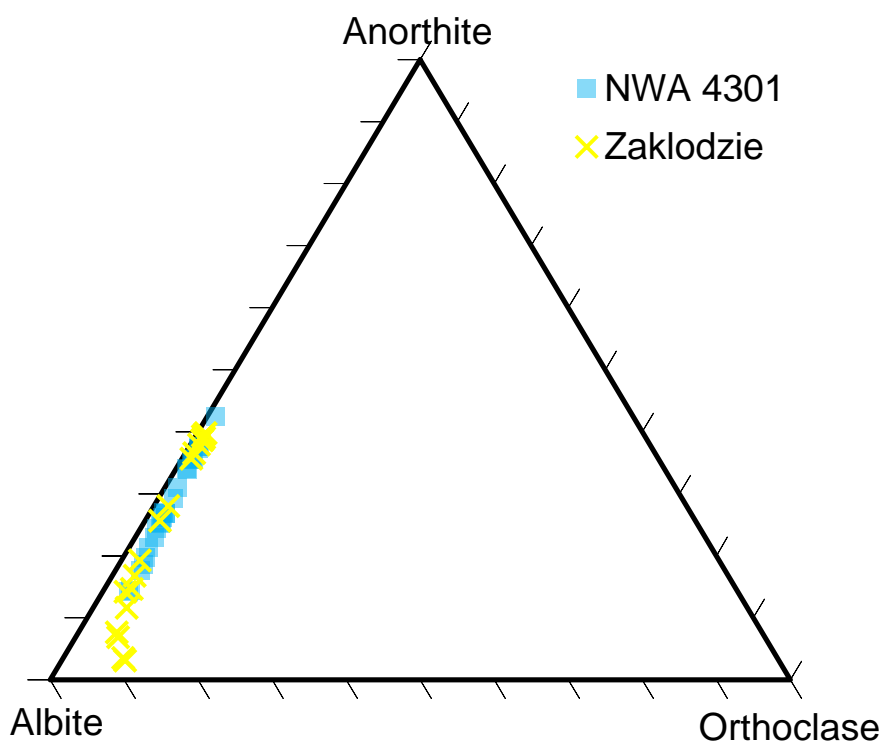


**Figure 4.15:** Ternary compositional diagram of plagioclase (Ab-An-Or) solid solution in Zakłodzie (yellow) and NWA 4301 (blue). The range of compositions reflect zoning nature of the feldspars in both meteorites

There are two types of sulfide present in Zakłodzie; one that is mostly FeS with 4.7 wt % Cr, 1.23 wt % Mn and 0.8 wt % Ti and a Fe-Mn rich sulfide that is composed of ~14 wt % Mn, 29.6 wt % Fe, 4.14 wt % Mg, 1.4 wt % Cr, 0.85 wt % Ca, 0.18 wt % Na and 0.16 wt % Zn respectively. The Fe and Mn rich sulfide appears to contain micro exsolution lamellae. The composition of the exsolved phase could not be measured accurately using EPMA because the lamellae are much smaller than the excitation volume. Overall, the FeS rich sulfide appears to be more abundant throughout the Zakłodzie samples studied. One possible grain of oldhamite was found surrounded by iron oxide and EDS composition showed it had been partially oxidized (Fig. 4.16). The grain contained ~39 wt % Ca, 29 wt% S, 30 wt% O and 1.97 wt % Fe. Sinoite grains associated with troilite contain 34 wt % N, 41 wt% Si, 24 wt% O and ~0.3 wt % Fe. Mineral chemistry data can also be found in Appendix 4.3.

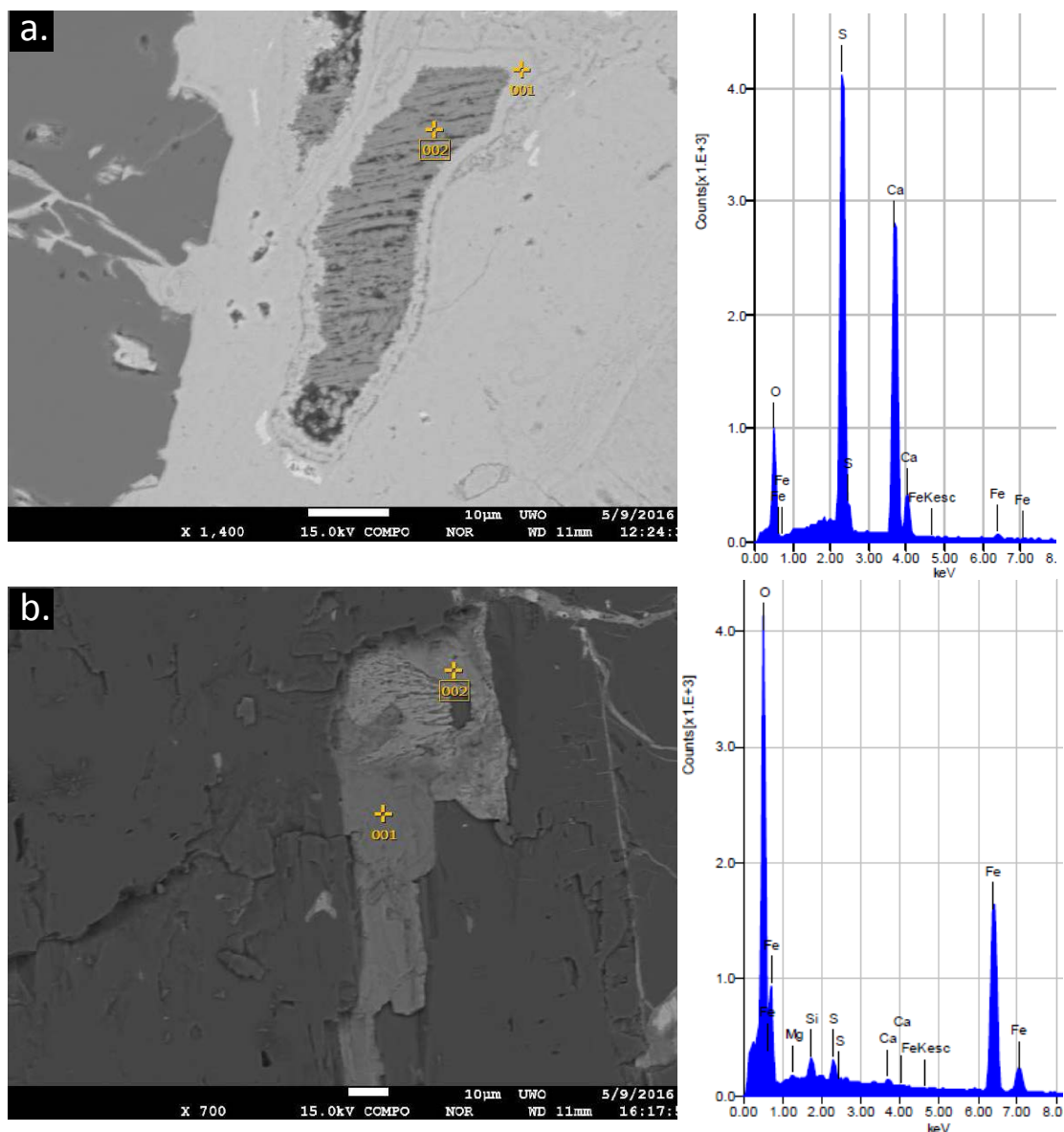


**Figure 4.16:** BSE images and EDS spectra of partially degraded oldhamite remnants in NWA 4301 a) and Zakłodzie b). Note the grain in Zakłodzie has almost been completely weathered out while the one in NWA 4301 appears more pristine. The remnant grain is included in iron oxide weathering while the one in Zakłodzie is surrounded by silicates with the higher part of the grain being completely weathered out.

### 4.3.3.2 NWA 4301

In NWA 4301 enstatite compositions range from  $Fs_{0.31-1.38}$ ,  $Ws_{0.35-0.76}$  and the slightly higher  $Fs$  values may be attributed to the small metal inclusions present throughout the sample. The plagioclase in NWA 4301 has a compositional range of  $Ab_{56.4-86.91}An_{7.4-42.37}Or_{1.20-5.7}$  (Fig. 4.15), the compositional variations are due to zoning texture of the plagioclase in this meteorite. Boesenberg et al. (2004) also mention that the feldspars in NWA 4301 are slightly more calcic than in Zakłodzie and that feldspars are occasionally found as inclusions in enstatite. The chemical maps of NWA 4301 in this work do not, however, show any included feldspars in enstatite. The metal in NWA 4301 contains 1.23 wt % Si, 5.7 wt % Ni and 0.46 wt % Co and the sinoite occasionally associated with it has a composition of ~ 36.6 wt % N, 40 wt % Si and ~23 wt % O with some containing minor impurities of Al (~0.7 wt %) and Br (~0.4 wt %), respectively. Additionally, the irregular silica grains entrained in metal/iron oxide have an average composition of ~95.6 wt% SiO with minor impurities that include ~ 1.44 wt % FeO, ~1.17 wt %  $Al_2O_3$ . And minor amounts of Na (~0.45 wt %  $Na_2O$ ) and K (~0.23 wt %  $K_2O$ ).

Only one type of sulfide was found in NWA 4301 and is predominantly FeS (troilite) which contains ~ 3.4 wt % Cr, ~1.35 wt% Mn, ~0.4 wt % Ti and in some cases ~0.2 wt % Ni. One grain of possible oldhamite was also identified and was surrounded by iron oxide weathering where the oldhamite remnant had broken down but retained compositions of ~29 wt % S and ~39 wt % Ca with minor ~1.97 wt % Fe (Fig. 16a). For additional information on mineral chemistry, see Appendix 4.4.

### 4.3.4 Mineralogy and crystal structure based on $\mu$ XRD and EBSD

#### 4.3.4.1 Enstatite and Plagioclase

During  $\mu$ XRD spot analysis of pyroxene grains in Zakłodzie and NWA 4301, diffraction patterns of both samples were matched by the ICDD cards of both ortho- ( $Pbca$ ) and clino- ( $P2_1/c$ ) structured enstatite (Fig. 4.17) which are also reported by (Przylibski et al., 2005) for Zakłodzie. Additionally, to complement the initial  $\mu$ XRD findings, EBSD was used to confirm the presence of both enstatite structures at the microscopic level since the

target area in XRD is about 300  $\mu\text{m}$ . Initial EBSD indexing confirmed the presence of both orthorhombic and monoclinic enstatite structures in both Zakłodzie and NWA 4301.

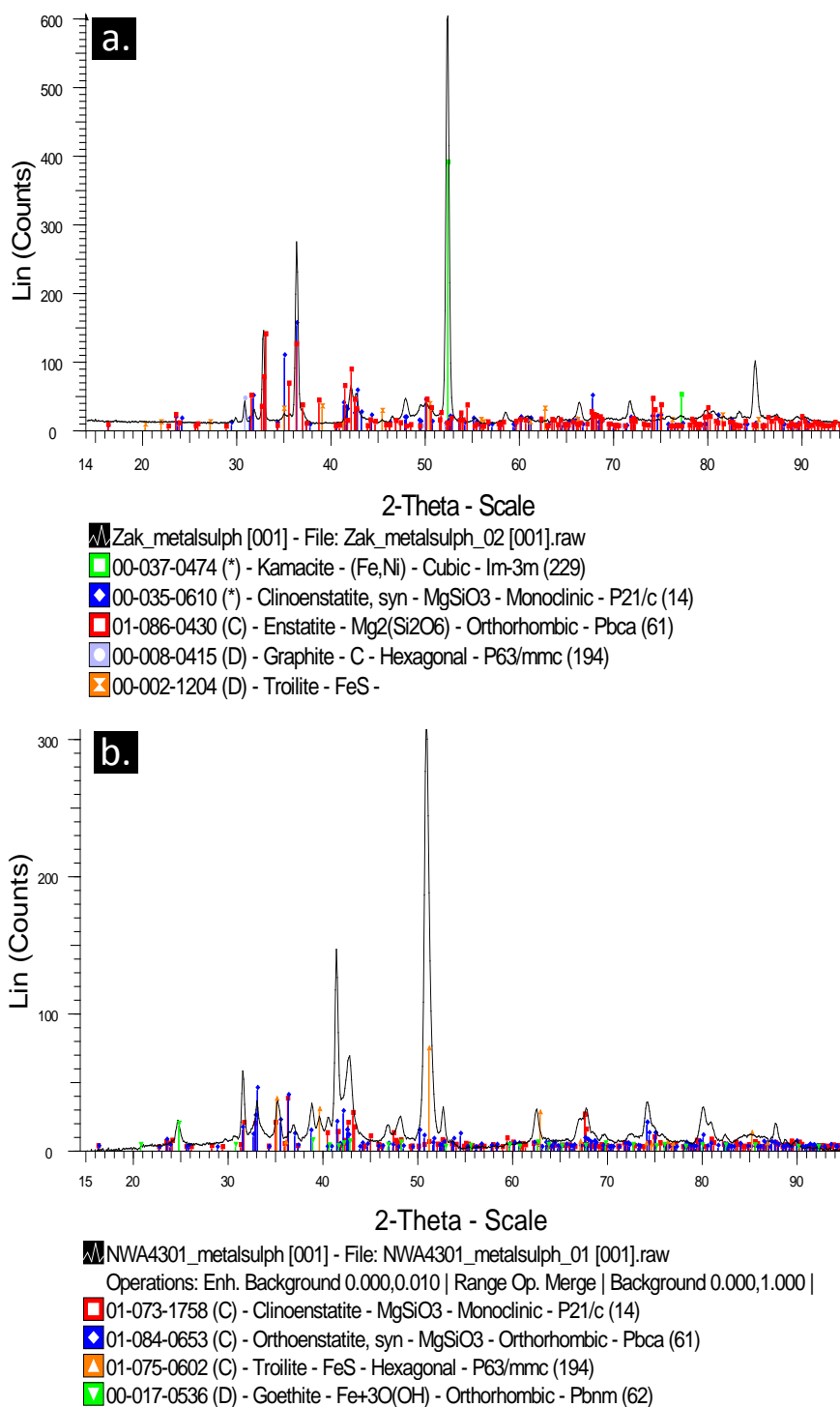
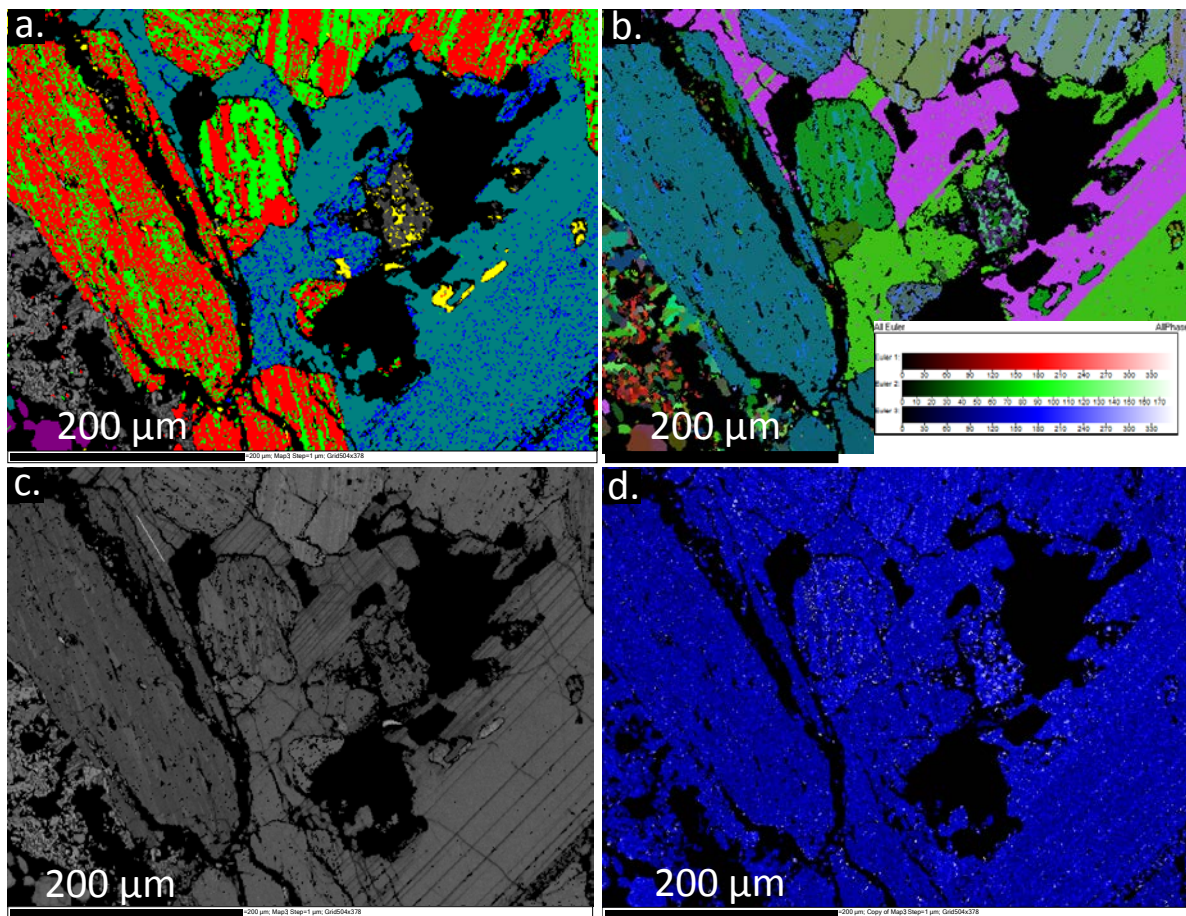


**Figure 4.17:** X-ray diffractograms of Zakłodzie a) and NWA 4301 b) showing matches for ortho and clino pyroxene and the matches are similar to those reported by (Przylibski et al., 2005).

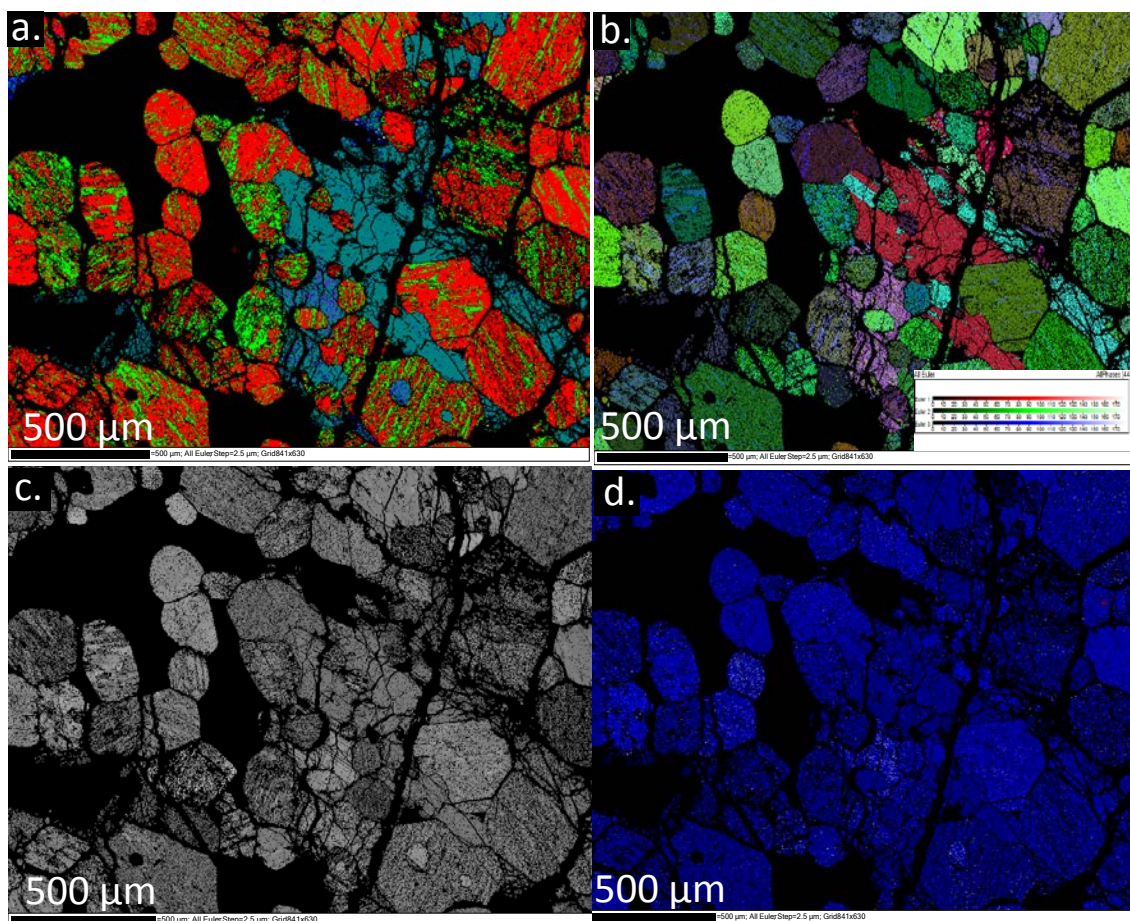
Furthermore, EBSD enstatite maps showed that clinoenstatite occurs as alternating bands of varying thickness (1-30  $\mu\text{m}$ ) and amount which are distributed throughout the enstatites in both meteorites (Fig. 4.18a-4.19a). The EBSD maps include a phase map, Euler map, contrast maps and pattern misfit map (Fig 4.18-19) to check the validity of the EBSD findings. For instance, the Euler map for both meteorites (Fig. 4.18b- 4.19 b) show the orientational variations of the orthoenstatite with respect with the clinoenstatite bands. The band contrast measures the quality of the diffraction pattern with respect to the background (Fig 4.18c- 4.19c). For example, areas with low band contrast are usually found in grain boundaries, unpolished and damaged areas where little to no diffraction is produced. The pattern misfit map shows the mean angle of deviation values for the mapped area which indicates the misfit between measured and calculated angles between bands and is therefore a measure of index confidence (Fig. 4.18d- 4.19d). For both meteorites, the pattern misfit bands show that the mean angle deviation for most of the mapped areas is less than one (appearing as blue in map), representing mean angle of deviation angles  $<1^\circ$ ; those with higher angles represent either misindexing or the lack of indexing due to poor diffraction and appear white as seen in Fig. 4.18d-4.19d).

EBSD of plagioclase indexed albite and anorthite as the main feldspar mineral present in both samples. However, EPMA analysis revealed that feldspars in both meteorites have compositional variations, mostly albitic and some anorthitic compositions (Fig. 15), which therefore explains the ambiguity in EBSD indexing of feldspars in Zakłodzie and NWA 4301. Additionally, the Euler and band contrast map also show that the feldspar grains are twinned (Fig. 14.8b-4.19b), a finding that has also been reported by (Przylibski et al., 2005; Ma et al., 2012).



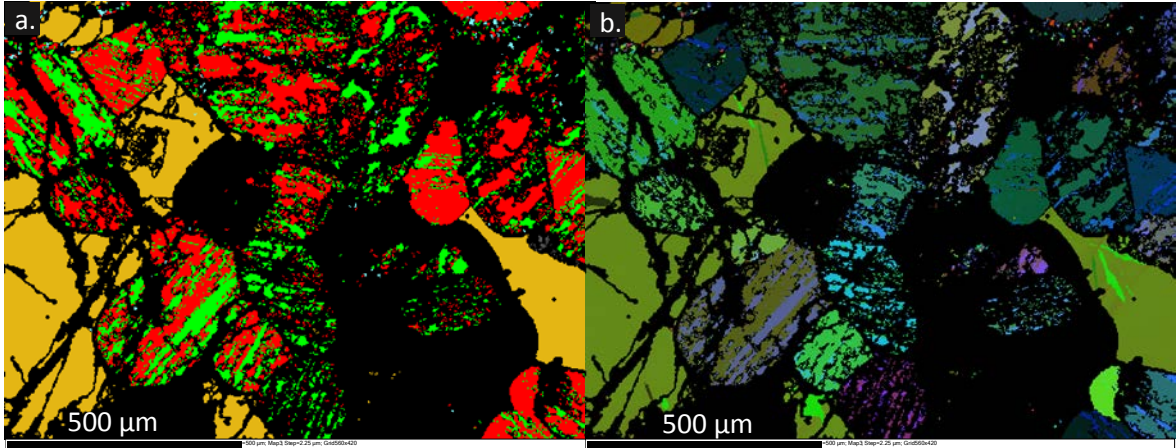


**Figure 18:** EBSD phase maps of Zakłodzie. Phase Map in a) shows ortho enstatite in red and clinoenstatite bands in green. Euler map in b) shows orientation of enstatite and plagioclase in Zakłodzie, c-d) illustrate pattern misfit and band contrast maps reflect confidence in indexed EBSD data.



**Figure 4.19:** EBSD phase maps of NWA 4301. Phase Map in a) shows ortho enstatite in red and clinoenstatite bands in green. Euler map in b) shows orientation of enstatite and plagioclase in Zakłodzie, c-d) illustrate pattern misfit and band contrast maps which reflect confidence in indexed EBSD data. White values in the pattern misfit map in c) represent areas of phase misindexing and the black values in the band contrast map in d) are areas of poor diffraction due to the presence of surface defects or grain boundaries.

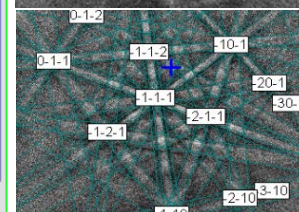
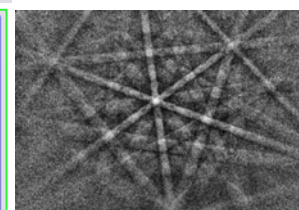
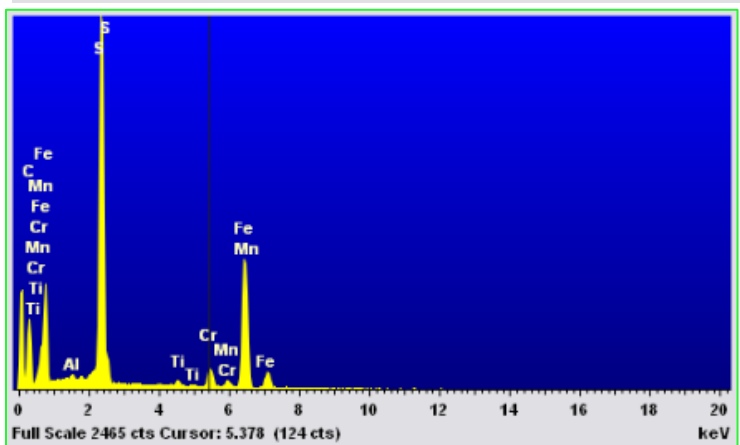
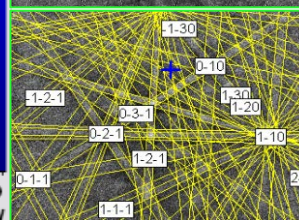
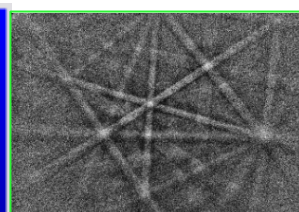
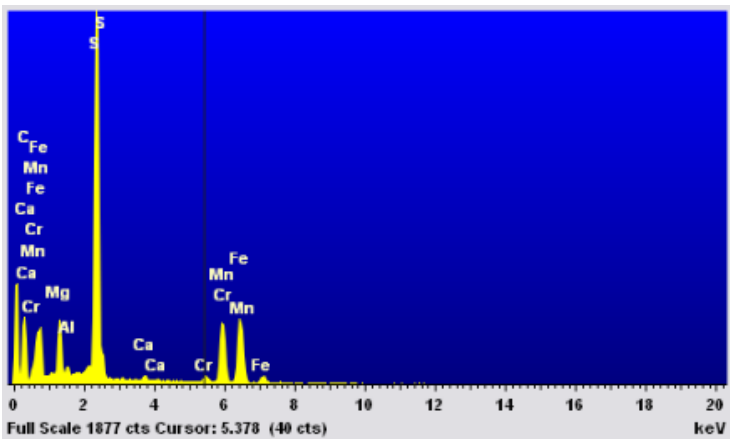
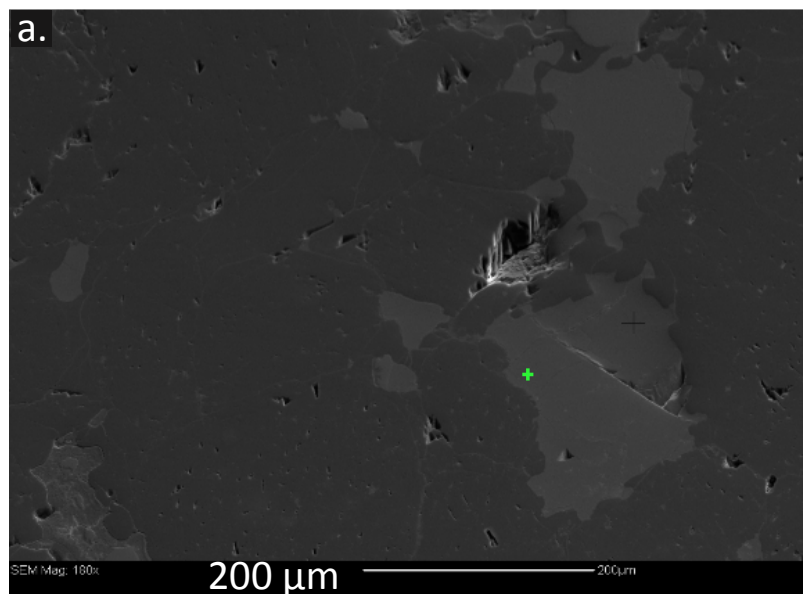


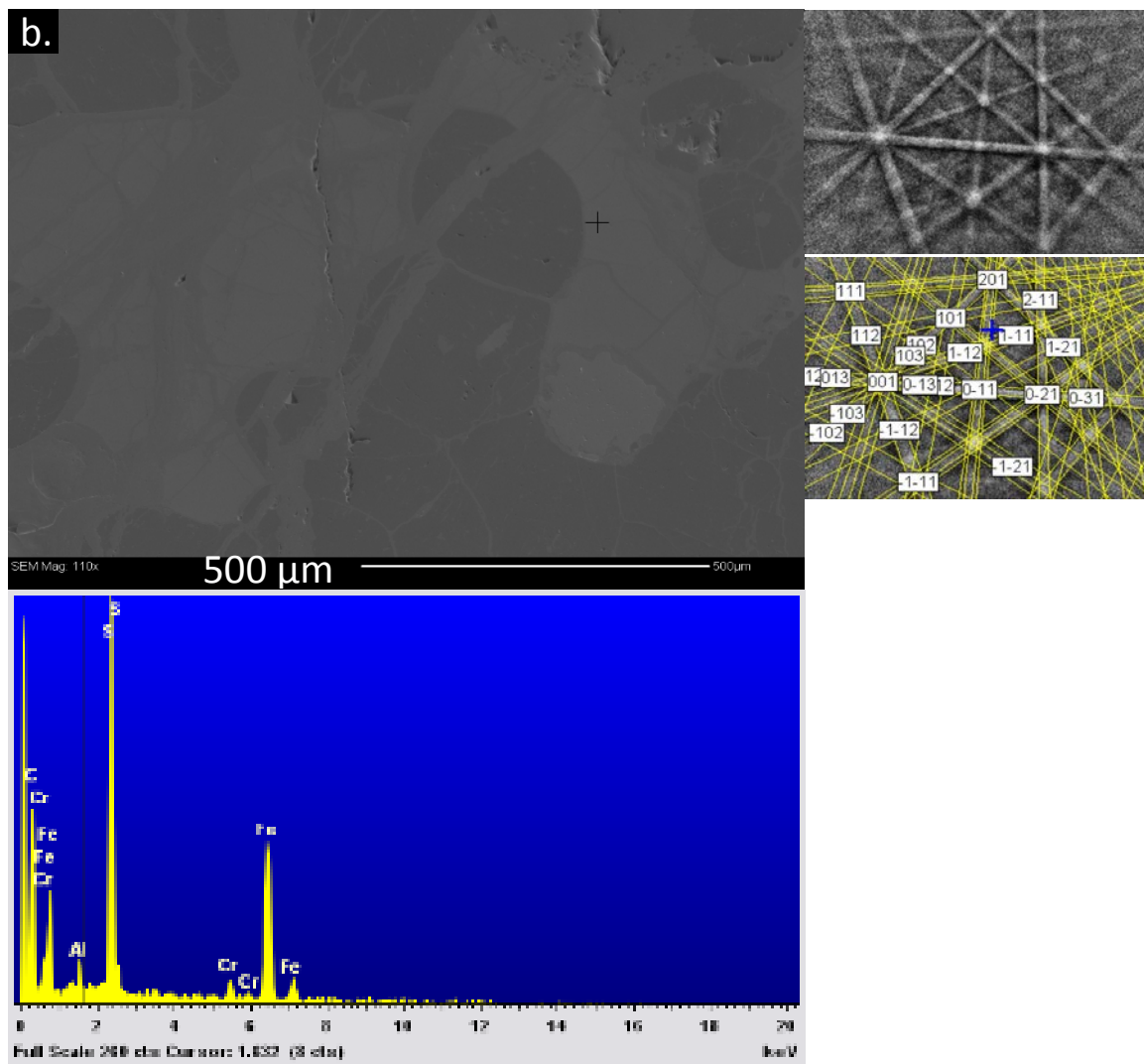


**Figure 20:** EBSD Phase map a) and Euler map b) of NWA 4301 showing needle like orientation variation in b) within troilite (in yellow) in a).

#### 4.3.4.2 Sulfides

Troilite was identified by  $\mu$ XRD in both meteorites. However, EBSD revealed the presence of keilite/alabandite and troilite in the Zakłodzie meteorite (Fig. 19a) whereas only troilite and pyrrhotite were identified in NWA 4301 (Fig. 19b, c). Moreover, EPMA data was used to verify the presence of keilite vs alabandite in Zakłodzie given that many of the cubic monosulfides present in enstatite meteorites are isostructural and chemical data is further required to verify the sulfide present in the meteorite. Mineral chemistry in this work indicates a keilite composition, although Karwoski et al. (2007) argue that the keilite composition is closer to alabandite; this might therefore explain the EBSD indexing of both keilite and alabandite for the sulfide in the Zakłodzie meteorite. Additionally, the troilite grains in the Euler map of Fig. 4.20b show needle-like inclusions in the larger troilite grains that are not seen in the EBSD phase map on Fig. 4.20a.

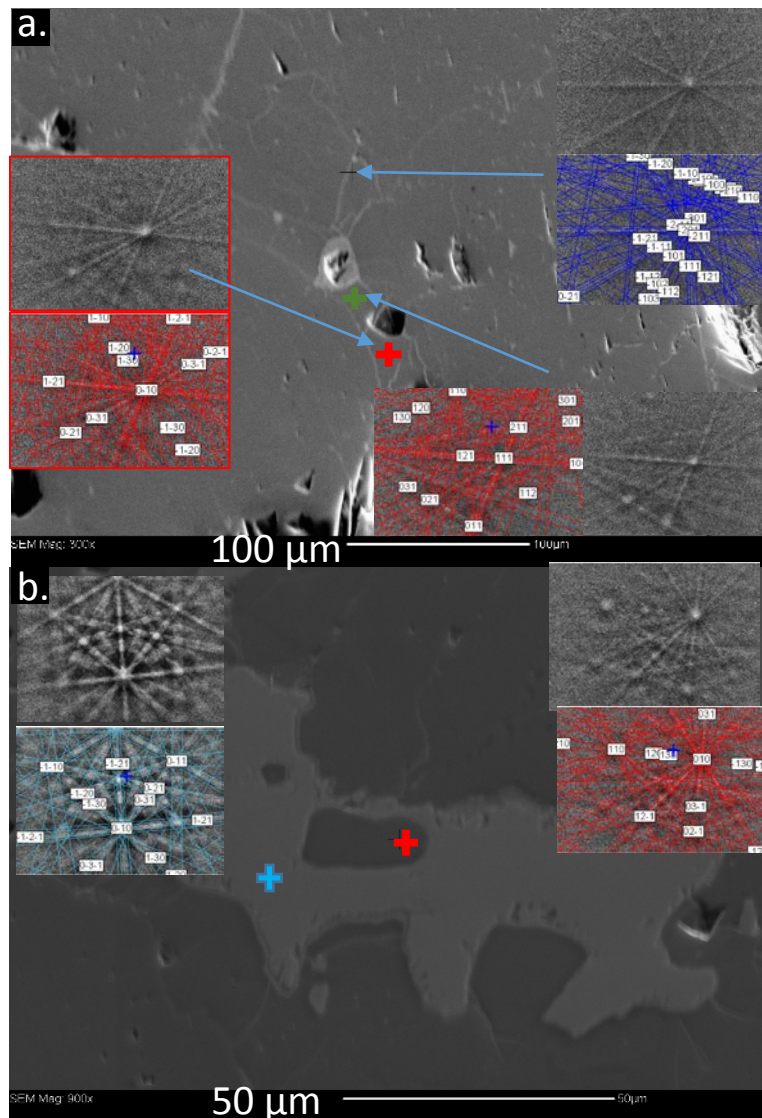




**Figure 4.21:** SEI context images of EBSD target areas for sulfides in Zakłodzie a) and NWA 4301 in b). Each image contains EBSD raw pattern, indexed pattern and EDS spectra confirming EBSD structure.

#### 4.3.4.3 Silica

The silica polymorphs identified by EBSD in the Zakłodzie meteorite were tridymite and cristobalite and, as reported by Uribe et al., (2017), tridymite occurs as small irregular grains that are associated with metal, troilite, and interstitial plagioclase whereas cristobalite, although similar to that of tridymite in most associations, was not seen in proximity or associated with sulfides. That is, only tridymite included or surrounded sulfide while cristobalite was seen with interstitial plagioclase and metal only (Fig. 4.22). All the silica grains indexed by EBSD had a mean angle deviation less than  $1^\circ$ , reflecting the confidence of the identification of the silica polymorphs recognized in both samples.





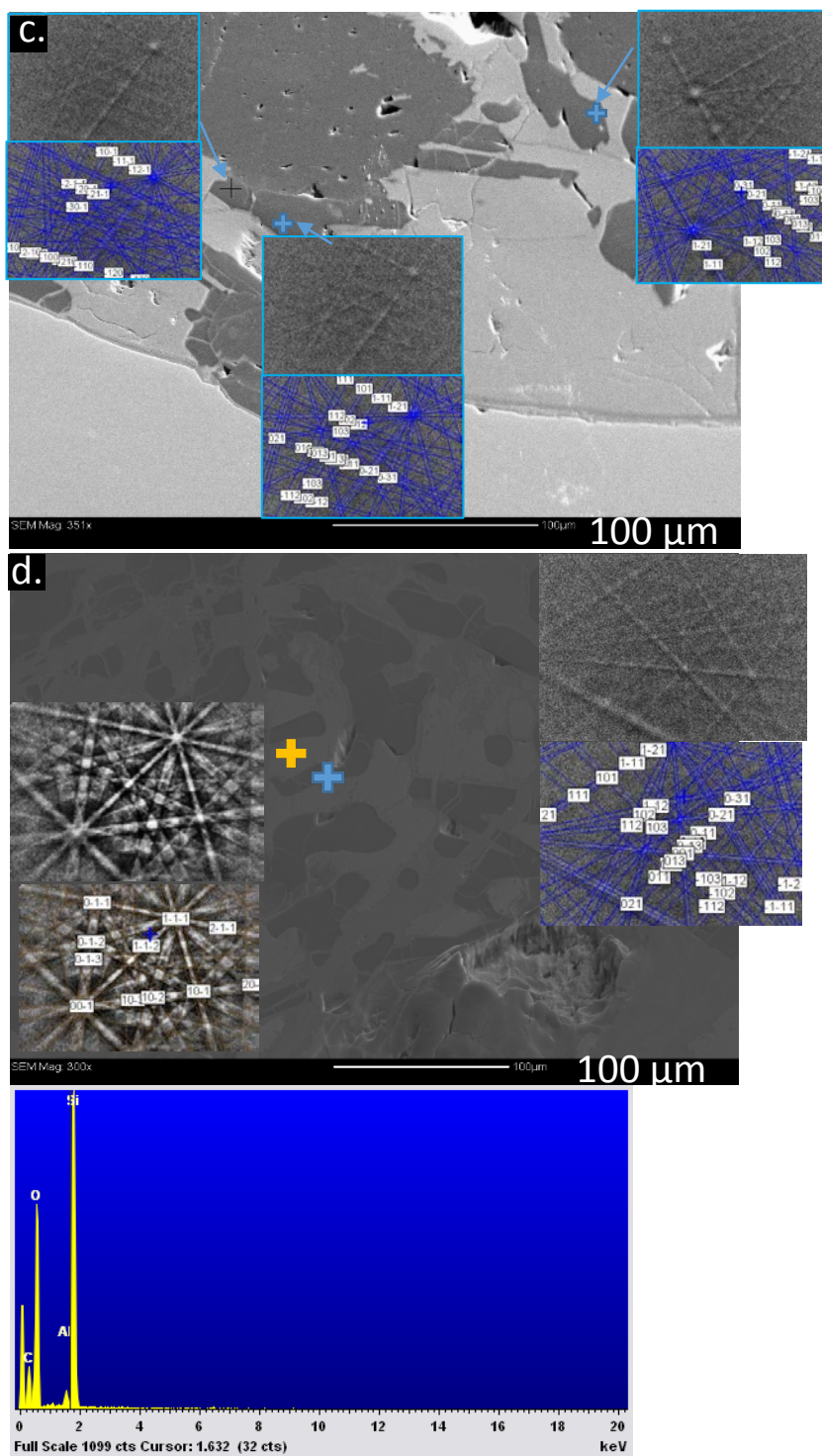
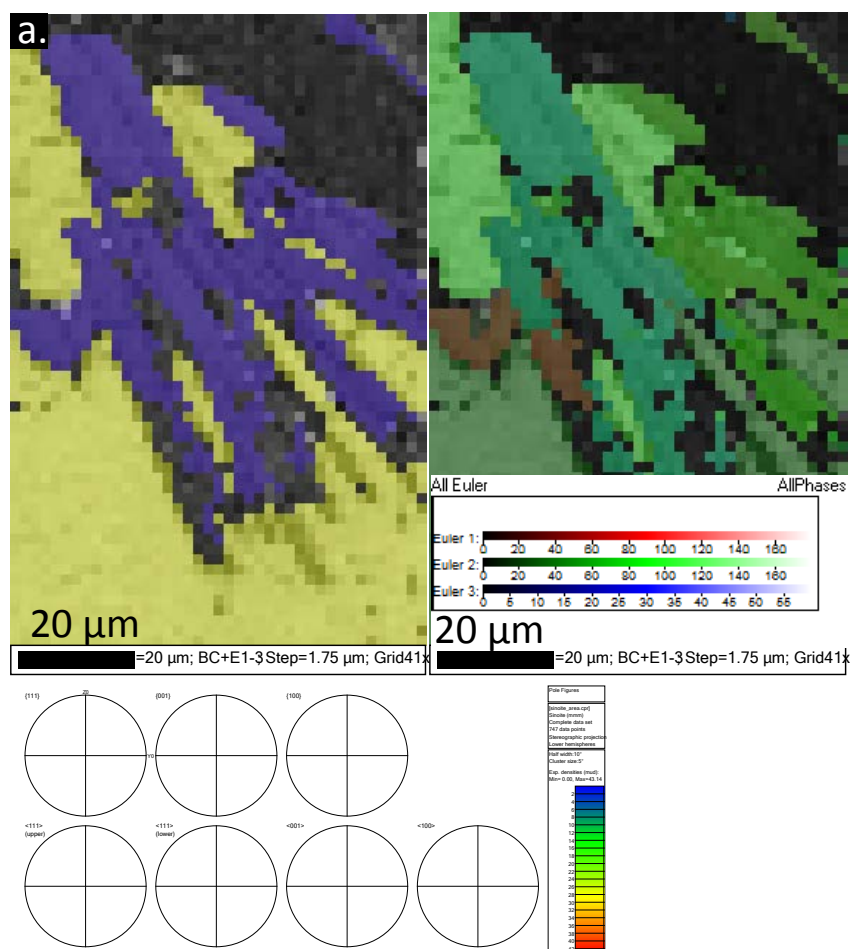


**Figure 4.22:** SEI context images and EBSD patterns of silica polymorphs and their different association in Zakłodzie a), b) c) and NWA 4301 in d). a) reflect the coexistence of cristobalite and tridymite in plagioclase/silica micrographic intergrowth area. b) shows cristobalite association with metal, in this case as an inclusion within metal and c) reveals only the presence of tridymite in and around sulfide. d) shows tridymite present in irregular silica grains contained in metal and iron oxide veining.

#### 4.3.4.4 Sinoite

Sinoite was identified in both Zakłodzie and NWA 4301 but with different textural associations. The sinoite grains in Zakłodzie were acicular, appeared to have a fan-out or radiating texture and were predominantly located inside a large troilite grain (Fig. 4.23a). Additionally, each of the acicular grains appeared near the same orientation with only slight rotation as seen in the Euler map and EBSD patterns on Fig. 4.23a. The tabular, large grains of sinoite in NWA 4301 had the same orientation throughout the grain and only showed variation in the areas nearer to the metal grain (Fig. 4.23b). EBSD patterns reveal a uniform orientation for the entire grain, with orientation changes occurring only in the nearer edges of the grains in proximity to metal. This indicates that the sinoite identified in NWA 4301 (Fig. 4.23b) may represent one large grain rather than a succession of smaller grains that are separated by iron oxide weathering.







#### 4.3.4.5 Graphite

Graphite was initially identified by  $\mu$ XRD (Fig. 4.17) for the Zakłodzie meteorite and further EBSD was invoked to confirm the XRD findings and to also investigate the presence of graphite in NWA 4301 as well. Carbon rich grains in both meteorites provided partial diffraction, confirming that the carbon source was likely graphite and not amorphous carbon in NWA 4301. This partial diffraction, however, was not enough to index the patterns by EBSD. To confirm that the partial diffraction was indeed indicative of graphite, the partial diffraction patterns obtained were compared to a standard graphite pattern from the Oxford instrument (JEOL) website and the symmetry of the partially diffracted graphite did correlate with that of the standard (Fig. 4.24). No EBSD data were obtained for graphite in Zakłodzie but was confirmed with EDS analysis as seen in Fig. 4.6.

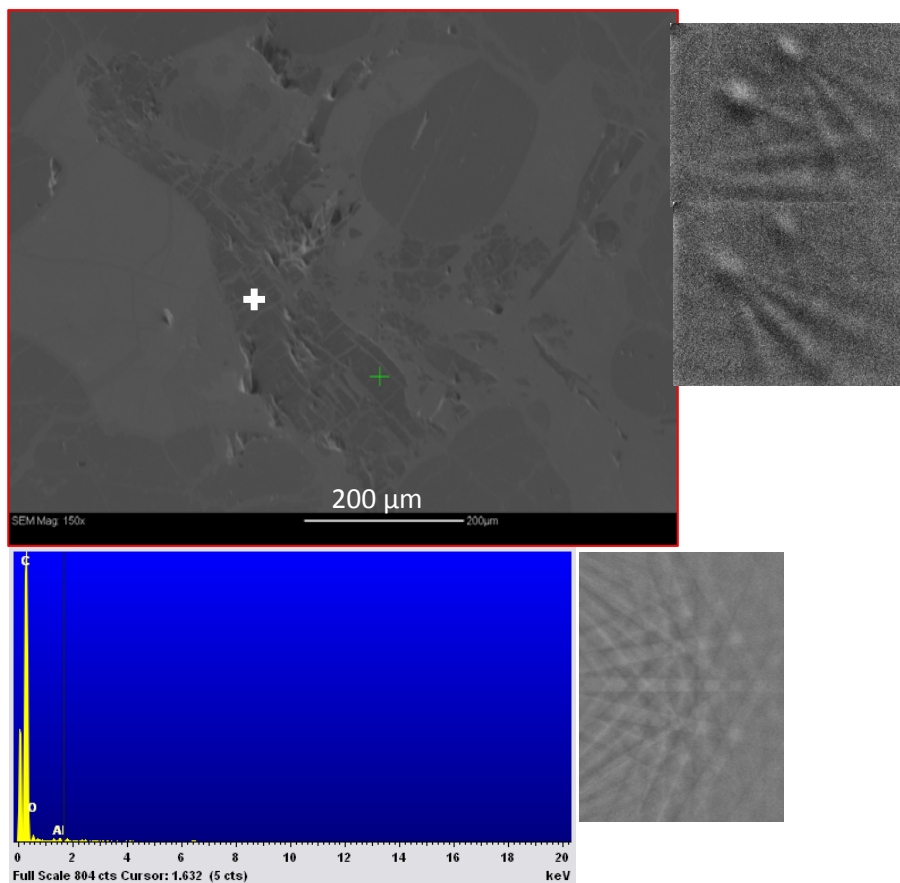


**Figure 4.24:** SEI context image of large, euhedral, graphite laths in NWA 4301 showing partial diffraction. Figure includes EDS spectra and reference diffraction pattern of graphite besides EDS spectrum (JEOL EBSD glossary).

## 4.4 Discussion

This section will compare the findings for Zakłodzie and NWA 4301 to determine if they are paired as well as to determine the petrogenetic sequence and ultimately provide insight about their mechanisms of formation. Environments of formation will also be discussed based on the mineral assemblages of both meteorites.

### 4.4.1 Petrographical interpretation from silicates

The granoblastic texture of the enstatites in Zakłodzie and NWA 4301 suggest formation due to cumulate crystallization similar to that of terrestrial pyroxenites. Przylibski et al. (2005) interpret this texture as a result of indigenous melting process and initially slow fractional crystallization followed by rapid cooling as an ascending magma. Other authors (Stepniewski et al., 2000) have classified this rock as an EL7 (highly metamorphosed) enstatite chondrite or as an impact melt rock (Keil, 2007). Ortho- and clinoenstatite identified by  $\mu$ XRD and EBSD in this work have also been reported by Przylibski et al. (2005) using XRD and CL; these authors interpret the change in symmetry from orthorhombic to monoclinic enstatite to be due either to rapid cooling of an ascending magma or a result of impact induced melt, with the authors favouring the former explanation as the enstatite twinning forming mechanism after slow fractional crystallization of the rock took place. Additionally, Przylibski et al. (2005) also suggest that some small clusters of enstatite grains are preferentially oriented, suggestive of an oriented texture, typical of cumulates.

TEM analysis of enstatites in Zakłodzie by Krezesinska et al. (2015), however, showed that pyroxene grains are striated and are composed of a disordered mixture of orthorhombic and monoclinic polymorphs, where the thickness of the bands varies throughout the grains. This was also observed in EBSD mapping of pyroxene grains for both Zakłodzie and NWA 4301 meteorites in this work (Fig. 4.18-4.20). Furthermore, Krezensinka et al. (2015) attribute the clinoenstatite band heterogeneity to kinking and further show that in cracks, traces of recrystallization and annealing were identified, therefore leading the authors to conclude that the change in pyroxene structure is due to shearing and shock. Their findings further support a role for impact melting and shock in the formation of clinopyroxene bands; they discuss that annealing features identified by

TEM can be explained by the burial of Zakłodzie in a deep part of warm ejecta blanket, where temperatures were high enough to cause partial melting of plagioclase as discussed by (Przylibski et al., 2005).

Despite the similarities in texture, chemical composition and structure of enstatite grains in Zakłodzie and NWA 4301, it is necessary to look at the rest of the mineral phases to determine if these meteorites are paired and to determine the petrogenetic sequence they experienced.

Although both meteorites have similar chemical composition and variability due to zoning, the zoning textures are significantly different in each meteorite. Feldspars in Zakłodzie show potassic rich areas interstitially intergrown with silica and do not exhibit the typical normal zonation where a calcic rich core transitions into a lesser Ca rim. Instead, feldspar in Zakłodzie shows a zonation of Ca-rich areas in some cases on half of a given crystal with the other half containing less calcium. The variety of feldspar compositions in Zakłodzie and NWA 4301 can be attributed to zoning. However, zoning in both meteorites is different it is possible that both meteorites experienced different metamorphic conditions. The feldspars in NWA 4301 exhibit reverse zoning where a calcium poor core transitions into a calcium rich rim possibly indicative of a rapid transition from low to high temperatures. Some of the feldspar grains do not show reverse zoning but are predominantly Ca-rich throughout.

Overall, the textural association, mineral chemistry and structure of pyroxene are consistent with Zakłodzie and NWA 4301 being paired and suggests that they experienced similar metamorphic conditions.

#### *4.4.2 Thermal history from silica polymorphs*

The presence of cristobalite in Zakłodzie indicates the meteorite nominally experienced peak temperatures above 1470 °C, since that is the minimum temperature where cristobalite is stable (Kimura, 2005). Przylibski et al. (2005) describe that crystallization of silicates began at ~ 1600 °C where at 1557 °C olivine reacted with the melt to form enstatite, leaving some residual SiO<sub>2</sub> in the melt and as fractional crystallization progressed (1543 °C) cristobalite crystallized along with feldspars (Fig. 4.25). At

temperatures lower than 1470 °C tridymite crystallized and the final stages of crystallization were reached with the crystallization of metal, sulfides and schreibersite; the sulfides would have crystallized at ~580-600 °C (minimum temperature of crystallization). According to the diagram in Fig. 4.25, with continuous fractional crystallization the dominant silica polymorph to form should be tridymite and not cristobalite since SiO<sub>2</sub> is a late phase based on the phase assemblages in Zakłodzie (Ma et al., 2012). Additionally, the silica grains identified by Przylibsky et al. (2005) and Ma et al. (2012) were rounded rare inclusions in sulfide whereas in this study all the silica grains identified occurred as irregular grains with various associations depending on the silica polymorph. Although both cristobalite and tridymite were associated with interstitial plagioclase, sulfides and metal, it was noted that only tridymite was associated with sulfide. Cristobalite was mostly found in micrographic intergrowth zones and in association with metal (as inclusions and grains surrounding the metal).

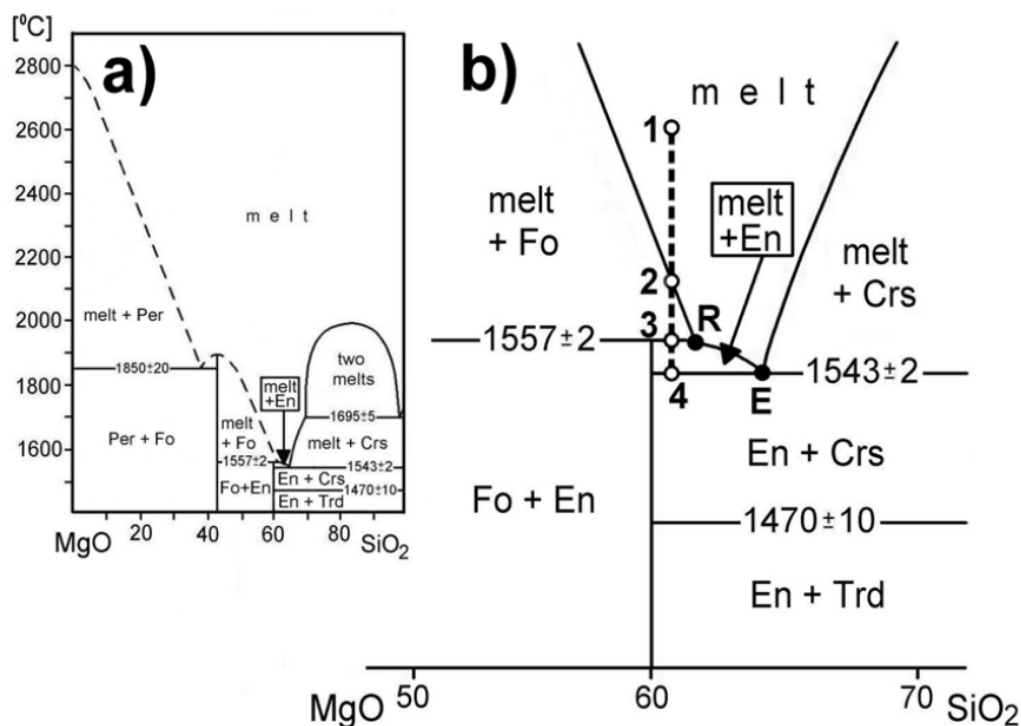


**Figure 4.25:** Phase diagram of the MgO-SiO<sub>2</sub> system showing evolution of silicate melt in Zakłodzie as a result of fractional crystallization due to internal heating (Extracted from Przylibski et al., 2005).

Ma et al. (2012) argue that since silica is a late stage phase, any pre-existing silica prior to melting would have been dissolved into the melt at temperatures above 1200 °C. They argue that albite coexisting with cristobalite is inconsistent for producing cristobalite at 1470 °C since albite is a low temperature igneous phase and would have melted at the formation temperatures of cristobalite. One way to explain the presence of cristobalite is that silica can sometimes crystallize as cristobalite and then transform to tridymite if a flux or mineralizer is present (Stevens et al., 1997). Additionally, experiments by Holmquist (1961), showed that with the addition of an impurity, cristobalite can occur as an intermediate phase above 893°C. This scenario is supported by the co-occurrence of both tridymite and cristobalite identified by EBSD in interstitial plagioclase with micrographic intergrowth.

Additionally, it is possible that the cristobalite found in metal formed due to the disproportionation reaction where SiO as a silicate component reacted with Fe metal and produced SiO<sub>2</sub> and Si in the metal (Javoy, 2010). Cristobalite associated with metal was also observed in the proposed “primitive enstatite achondrite” QUE 92404 by Izawa et al. (2011). Tridymite would therefore represent the main silica polymorph present during fractional crystallization of Zakłodzie and not cristobalite.

Overall, the presence of both cristobalite and tridymite in Zakłodzie indicate the meteorite experienced temperatures of 1470 °C (to form cristobalite) and tridymite (below 1470 °C) followed by fast cooling to allow preservation of these minerals. The cristobalite identified in Zakłodzie by EBSD was of tetragonal form, identified as  $\alpha$ -cristobalite by (Withers et al., 1989; Hatch and Ghose, 1991; Duffrene and Kieffer, 1997). High temperature cristobalite has a cubic structure and undergoes a (metastable) first order phase transition to a tetragonal structure at around 220 °C (Hatch and Ghose, 1991).

It is also possible that if Zakłodzie was formed due to impact melting, temperatures above 1470 °C could have crystallized cristobalite, followed by rapid cooling leading to preservation of some cristobalite with most of it converting to tridymite at temperatures lower than 1470 °C while the few cristobalite relicts transformed to the low temperature,  $\alpha$ -cristobalite.

In contrast, the only silica polymorph present in NWA 4301 is tridymite and it is texturally different than any of the silica grains found in Zakłodzie. As stated previously in the results section, silica grains in NWA 4301 occur as irregular grains contained within metal and iron oxide (due to weathering). Since silica is only restricted to metal, a silicon disproportionation reaction by Javoy (2010), is favoured rather than fractional crystallization mechanism for the formation of metal.

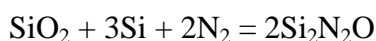
Some authors identified quartz in Zakłodzie (Przylibski et al., 2005; Ma et al., 2012) in association with sinoite, and propose that this quartz formed by the oxidation of sinoite through the reaction ( $\text{Si}_2\text{N}_2\text{O} + 3/2\text{O}_2 = 2\text{SiO}_2 + \text{N}$ ) and that the origin of N is derived from exsolution of N and Si from opaque phases (metal) as per Rubin, (1997).

#### 4.4.3 Sinoite

As stated earlier, the sinoite in Zakłodzie and NWA 4301 have different textural associations, with most sinoite being acicular and associated with sulfide in Zakłodzie and as tabular, large grains in metal for NWA 4301. Sinoite has been identified in enstatite meteorites since 1960 and its presence in enstatite achondrites might have implications regarding the role of halogens and environments of formation in the early solar system. Since sinoite is absent in the entire EH meteorite class (Fogel et al., 1989) and is restricted to EL chondrites of higher petrologic type (Bischoff et al., 2005), it is likely that Zakłodzie and NWA 4301 originated from an EL-like precursor.

Muenow et al., (1992) suggest that the N source in enstatite meteorites occurs mainly within lattice defects of sulfide phases and it is released at temperatures between 950 and 1080 °C. The source of N could have also been derived from the silicate melt from impact-related melt-filled cavities in otherwise unmelted EL material where local nitrogen fugacity may have been higher (Rubin, 1997). One notable aspect is that the average chemical composition of the sinoite for various enstatite meteorites reported by Keil (1965), is significantly different than that of NWA 4301. The average composition of the sinoites described by Keil (1965), for various meteorites is about 57 wt% Si, 31.5 wt% N and 13 wt % O whereas EDS analysis of the sinoite in NWA 4301 revealed it contains 41 wt% N, 10 wt% more than those reported by Keil (1965).

Some workers have described the formation of sinoite as a condensation product at high temperature from a solar nebula (Herndon and Suess, 1976). Others argue that formation of sinoite can be explained by an increase in oxygen fugacity during formation of chondrites which prevented Si from being incorporated into the metal phase and combined with nitrogen through the reaction:



During reheating (internal or impact) lower oxygen fugacity conditions prevailed again which resulted in nitrogen being fixed as sinoite (Moore and Gibson, 1969). It is possible that Zakłodzie and NWA 4301 may have experienced a short lived, slight change in redox conditions allowing for the formation of sinoite as most of the silicon would not then be able to be included in metal; this is consistent with the lower observed Si content in metal compared with NWA 8173. Additionally, Rubin (1997) describes that through the above reaction, N<sub>2</sub> reacted with reduced Si dissolved in the metallic Fe-Ni melt and with silica derived from the silicate fraction of EL chondrite assemblage at 1400-1500°C or at lower temperatures, with the help of a catalyst such as Si-bearing, metallic Fe-Ni (Muenow et al., 1992).

It is also possible that sinoite formed by crystallization from an EL chondrite impact melt prior to metamorphism (Rubin, 1997). Thermodynamic calculations by (Alexander et al., 1993) show that sinoite is the stable nitride phase if SiO<sub>2</sub> was present during metamorphism of an EL chondrite. Since both NWA 4301 and Zakłodzie contain abundant free silica, it then makes sense that sinoite was the nitrogenous phase formed rather than Si<sub>3</sub>N<sub>4</sub>. An oxygen fugacity study by Fogel et al. (1989), states that the enstatite chondrites that contain sinoite equilibrated under high nitrogen fugacity and that formed in a nebula of high pressure or likely as a result of planetary metamorphism, favouring the latter as it is found in EL6 meteorites. If nitrogen fugacity controls the formation of sinoite, it is possible that the meteorites where sinoite is absent represent locally low nitrogen fugacity conditions. Additionally, experimental work by Sekine et al. (2006) showed that sinoite may not be a crystallization product from impact melts and that it may be a metamorphic product of high temperatures and relatively low pressure. In their study, Sekine et al. (2006) showed that sinoite is only stable at pressure of up to 28



GPa, and that if a meteorite experiences higher pressures due to shock, sinoite will become amorphous. The observation of sinoite thus implies that the meteorite has not subsequently been exposed to peak shock pressure >28 GPa, but places no constraint on an impact melt origin for the mineral. It is possible that sinoite formed from a superheated impact melt at low pressures after passage of shockwaves. At least for the case of Zakłodzie and NWA 4301, if these formed by impact melting, they experienced at least shock stage 3, indicated by pyroxene twinning, and sinoite should be amorphous if pressures were higher than 28 GPa. Moreover, Rubin (1997) discusses that the sinoite grains within impact melted areas of the meteorite QUE 94368 are twinned and zoned and support crystallization of sinoite from a melt. However, the sinoite identified in Zakłodzie and NWA 4301 did not exhibit zoning or twinning which may indicate that sinoite formed at low pressures, consistent with crystallization and subsequent annealing of a high temperature melt.

#### *4.4.4 Are these meteorites paired?*

Based on chemical analysis and some textural similarities (i.e. cumulate texture, modal abundances) the Zakłodzie and NWA 4301 meteorites could be paired and may have originated from the same parent body. However, there is substantial petrographic and structural evidence to indicate that even though both meteorites shared a common parent body, they experienced different metamorphic histories. The reverse zoning in the feldspar of NWA 4301 indicate the meteorite may have experienced a rapid episode of heating some time after the enstatite crystals were forming (whether by fractional crystallization or impact melting). Some of the grains do not appear to be zoned in NWA 4301 and indicate that after an initially rapid heating event, temperatures remained high long enough to equilibrate some of the enstatite, and therefore the rock must have cooled slowly (Uribe et al., 2016).

The feldspars in Zakłodzie have been interpreted as having been formed in two generations (Przylibski et al., 2005), with the more potassic feldspars having been formed during a secondary thermal event which could only have caused a small degree of melting of the rock. The compositions of Zakłodzie plagioclase analyzed in this study, however, do not reflect two distinct generations of feldspar but instead, reflect the typical

compositional variation characteristic of zoning. That is, feldspars transition from albitic to anorthitic compositions and at the rims of the grains, the more potassic compositions occur as micrographic intergrowth with silica. Moreover, the two feldspar populations mentioned by Przylibski et al., (2005) are texturally associated, do not seem to reflect two distinct feldspar formation episodes. It is possible that the more potassic rims are a result of localized melting where only the rims of the feldspar grains are re-melted and, during cooling, resulted in micrographic intergrowth of potassic feldspar and silica.

The textural relation of silica with respect to other phases is different in both meteorites. If both meteorites experienced the same thermal events, it should be reflected in their chemistry and mineralogy. However, the silica grains in both meteorites are different. For instance, in NWA 4301 silica grains identified were tridymite only, and were present as irregular grains only found in metal/metal oxide and in an 8-mm area depleted in plagioclase. In Zakłodzie however, tridymite and cristobalite were both identified in association with plagioclase as micrographic intergrowth, around and occasionally included in sulfide and metal, where only tridymite was associated with sulfide. The silica grains in Zakłodzie could have formed either as a late stage product of slow fractional crystallization or through sulfidation of a silicate melt (Lehner et al., 2012) On the contrary, the tridymite grains in NWA 4301 were likely formed by the silicon disproportionation reaction mentioned previously. It is also possible that the melted metal reached silica saturation and crystallized tridymite instead.

Another feature that indicates both meteorites experienced different metamorphic conditions is seen in the sulfide assemblages. In Zakłodzie, although troilite is the predominant sulfide, Mn-rich keilite is often present in close association with sulfide whereas troilite is the only sulfide found in NWA 4301. This might indicate that Zakłodzie experienced higher temperatures during heating where keilite was formed by the reaction of niningerite or alabandite with troilite at temperatures well above 500 °C, maybe up to 1500 °C if the rocks formed by impact melting (Keil, 2007). The presence of Cr-rich troilite suggests that the meteorite experienced higher temperatures than 500 °C since below 600-700 °C daubréelite would have exsolved from Cr-bearing troilite (Kimura and Lin, 1999). For the case of Zakłodzie, keilite formed at temperatures higher

than 700 °C to retain chromium in troilite and was quenched to allow preservation of keilite. It is possible that the micro exsolution bands of keilite in Zakłodzie may indicate that temperatures could have been slightly lower than 700 °C where small amounts of FeS were able to exsolve from keilite and that cooling was not fast enough to preserve all of the keilite. These bands were too small to be analyzed by EPMA and the original statement that this rock was rapidly cooled remains.

Alternatively, the dominance of Cr-bearing troilite in NWA 4301 indicates the rock was initially heated to high temperatures, allowing incorporation of Cr, but not high enough to produce keilite by its reaction with troilite. Therefore, troilite remained as the only sulfide phase present in NWA 4301 and probably formed at temperatures below 600 °C to prevent daubréelite exsolution out of troilite (Keil, 2007). Based on the sulfide assemblages in both meteorites, it can then be concluded that the sulfides in Zakłodzie formed at higher temperatures and cooled faster than NWA 4301 and/or Zakłodzie experienced overall higher metamorphic temperatures during impact melting.

#### *4.4.5 Formation mechanism (Impact vs internal heating)*

##### *4.4.5.1 Impact melt*

One interpretation is that these meteorites originally formed in different parts on an EL-like parent body and therefore experienced different metamorphic conditions. The secondary, potassic feldspars in Zakłodzie as per Przylibski et al. (2005) formed from a secondary, short lived, thermal event of which no evidence is yet seen for NWA 4301. It is also possible that the more potassic feldspars in Zakłodzie simply represent the last stage of cooling after impact where it formed with silica as micrographic intergrowth.

Impact melting of Zakłodzie and NWA 4301 is supported by the presence of keilite (only in Zakłodzie), twining of pyroxenes (S3 stage; Rubin, 2015), zonation in the feldspars, large euhedral sinoite and graphite grains (Rubin, 2015), metal surrounding euhedral enstatite as well as nucleation of these enstatite grains on relict chondrules (Keil, 2007). Keil (2007), further adds that if Zakłodzie would have formed through internally derived

melting, the high -density opaques would have separated from the melt through density separation.

#### *4.4.5.2 Internal Heating*

Evidence for internal heating as a mechanism is based on the cumulate texture of the enstatites, with some of them showing preferred orientation, the lack of shock effect in relict chondrules, and enstatite twinning attributed to rapid cooling by ascending magma (Przylibsky et al., 2005). In addition, Sugiura and Fujiya (2008), performed Al-Mg dating on Zakłodzie and showed that it formed 5.4 million years after the formation of CAIs (the earliest condensates in the solar system), implying that the absolute age of formation of Zakłodzie is 4561.7 Ma. They suggest that that heat source for melting of Zakłodzie was through  $^{26}\text{Al}$  decay instead of impact melting. They also suggest that many of these meteorites may represent small, molten planetesimals in the early solar nebula.

### **4.5 Summary**

#### *4.5.1 Arguments for pairing*

- Similar enstatite composition and texture
- Both meteorites contain rounded enstatites, resembling relict chondrules on the basis of the enstatite shape alone.
- Similar metal compositions
- Similar Si content in metal

#### *4.5.2 Evidence for different metamorphic histories*

##### *4.5.2.1 Zakłodzie*

- Feldspar zoning indicative of fast cooling
- Two generations of feldspars (or potassic rich rims with silica) which may have resulted from a secondary thermal event

- Experienced high temperatures during melting to make keilite (close association of troilite and keilite) and then it was quenched to preserve keilite (high temperatures also support formation of SiO<sub>2</sub> by sulfidation of silicate melt)
- Fast cooling is also supported by lack of daubréelite exsolution in troilite
- Tridymite and cristobalite probably formed by sulfidation of silicate melt or during fractional crystallization

#### 4.5.2.1 NWA 4301

- Feldspars show reverse zoning which may indicate a relatively quick reheating event
- No confirmed secondary thermal event (no dating done nor second feldspar generation or clear indication of partial melting of feldspars)
- Homogeneous composition of some feldspars indicates slower cooling rate
- Main sulfide is troilite indicating the sulfides formed at lower temperatures and that the rock may have experienced lower metamorphic temperatures than Zakłodzie
- Although cooling was slow, it wasn't slow enough to cause daubréelite exsolution from troilite
- Tridymite only found in metal, and probably formed by disproportionation reaction discussed above instead of sulfidation of a silicate melt

## 4.6 Concluding Remarks

The Zakłodzie and NWA 4301 likely originated from an EL-like parent body but appear to have experienced different metamorphic histories. Impact melting (Keil, 2007; Ma et al., 2012) and internal heating (Przylibsky et al., 2005) have both been suggested as possible formation processes for Zakłodzie, with the former being favoured by multiple authors. Based on the findings reported in this chapter, it is not possible to definitively indicate which process primarily formed Zakłodzie and NWA 4301. These meteorites may have formed and metamorphosed by one or both processes in the EL parent body.

Further discussion of these findings for Zakłodzie and NWA 4301 and their implications in the context of NWA 8173 and other enstatite meteorites will be pursued in Chapter 5.

#### 4.7 References

- Alexander, C. M., Swan, P., & Prombo, C. A. (1994). Occurrence and implications of silicon nitride in enstatite chondrites. *Meteoritics & Planetary Science*, 29(1), 79-85.
- Anders, E., & Zinner, E. (1993). Interstellar grains in primitive meteorites: Diamond, silicon carbide, and graphite. *Meteoritics & Planetary Science*, 28(4), 490-514.
- Bischoff, A., Grund, T., Jording, T., Heying, B., Hoffmann, R. D., Rodewald, U. C., & Pöttgen, R. (2005). Occurrence, structure, and formation of sinoite in enstatite chondrites. *Meteoritics and Planetary Science Supplement*, 40, 5043.
- Boesenberg, J. S., Weisberg, M. K., Greenwood, R. C., Gibson, J. M., & Franchi, I. A. (2013, March). The Anomalous Enstatite Meteorites---Part 1: Anomalous Aubrites and Oxygen Isotopes. In *Lunar and Planetary Science Conference* (Vol. 44, p. 2320).
- Boesenberg, J. S., Weisberg, M. K., Greenwood, R. C., Gibson, J. M., & Franchi, I. A. (2014, March). The Anomalous Enstatite Meteorites---Part 2: The Recrystallized EL Meteorites. In *Lunar and Planetary Science Conference* (Vol. 45, p. 1486).
- Connolly, H. C., Zipfel, J., Folco, L., Smith, C., Jones, R. H., Benedix, G., ... & Grossman, J. N. (2007). The Meteoritical Bulletin, No. 91, 2007 March. *Meteoritics & Planetary Science*, 42(3), 413-466.
- Fogel, R. A., Hess, P. C., & Rutherford, M. J. (1989). Intensive parameters of enstatite chondrite metamorphism. *Geochimica et Cosmochimica Acta*, 53(10), 2735-2746.
- Grossman, J. N. (2000). The meteoritical bulletin, No. 84. *Meteoritics and Planetary Science Supplement*, 35, A199-A225.
- Hatch, D. M., & Ghose, S. (1991). The  $\alpha$ - $\beta$  phase transition in cristobalite, SiO<sub>2</sub>. *Physics and Chemistry of Minerals*, 17(6), 554-562.
- Herndon, J. M., & Suess, H. E. (1976). Can enstatite meteorites form from a nebula of solar composition? *Geochimica et Cosmochimica Acta*, 40(4), 395-399.

- Holmquist, S. B. (1961). Conversion of quartz to tridymite. *Journal of the American Ceramic Society*, 44(2), 82-86.
- Irving, A. J., Kuehner, S. M., Bunch, T. E., Wittke, J. H., Rumble III, D., & Hupe, G. M. (2006). More African Enstatite-rich Meteorites: Aubrite NWA 2828, Zakłodzie-like NWA 4301, NWA 1840 and EL6 Chondrites. *Meteoritics and Planetary Science Supplement*, 41, 5264.
- Javoy, M., Kaminski, E., Guyot, F., Andrault, D., Sanloup, C., Moreira, M., ... & Jaupart, C. (2010). The chemical composition of the Earth: Enstatite chondrite models. *Earth and Planetary Science Letters*, 293(3), 259-268.
- Karwowski, Ł., Kryza, R., & Przylibski, T. A. (2007). New chemical and physical data on keilite from the Zakłodzie enstatite achondrite. *American Mineralogist*, 92(1), 204-209.
- Keil, K. (2007). Occurrence and origin of keilite, (Fe > 0.5, Mg < 0.5) S, in enstatite chondrite impact-melt rocks and impact-melt breccias. *Chemie der Erde-Geochemistry*, 67(1), 37-54.
- Keil, K., and Andersen, C. A. (1965). Occurrences of sinoite, Si<sub>2</sub>N<sub>2</sub>O, in meteorites. *Nature*, 207(4998), 745-745.
- Kimura, M., & Lin, Y. (1999). Petrological and mineralogical study of enstatite chondrites with reference to their thermal histories. *Antarctic meteorite research*, 12, 1.
- Kimura, M., Weisberg, M. K., Lin, Y., Suzuki, A., Ohtani, E., & Okazaki, R. (2005). Thermal history of the enstatite chondrites from silica polymorphs. *Meteoritics & Planetary Science*, 40(6), 855-868.
- Krzesinska, A., Wirth, R., & Kusiak, M. A. (2015, October). Evolution of Zakłodzie enstatite meteorite-insight from TEM analyses. In European Planetary Science Congress 2015, held 27 September-2 October, 2015 in Nantes, France, Online at <http://meetingorganizer.copernicus.org/EPSC2015>, id. EPSC2015-651 (Vol. 10, p. 651).



- Lehner, S. W., Petaev, M. I., & Buseck, P. R. (2012, March). Sulfidation of Enstatite in the Fine-Grained Matrix of EH3 Sahara 97072. In Lunar and Planetary Science Conference, 43.
- Ma, C., Beckett, J. R., & Rossman, G. R. (2012). Buseckite, (Fe, Zn, Mn) S, a new mineral from the Zakłodzie meteorite. *American Mineralogist*, 97(7), 1226-1233.
- Moore, C. B., Gibson, E. K., & Keil, K. (1969). Nitrogen abundances in enstatite chondrites. *Earth and Planetary Science Letters*, 6(6), 457-460.
- Muenow, D. W., & Wilson, L. (1992). High-temperature mass spectrometric degassing of enstatite chondrites: Implications for pyroclastic volcanism on the aubrite parent body. *Geochimica et Cosmochimica Acta*, 56(12), 4267-4280.
- Patzer, A., Franke, L., & Schultz, L. (2001). New noble gas data of four enstatite chondrites and Zakłodzie. *Meteoritics and Planetary Science Supplement*, 36, A157.
- Przylibski, T. A., Zagożdżon, P. P., Kryza, R., & Pilski, A. S. (2005). The Zakłodzie enstatite meteorite: Mineralogy, petrology, origin, and classification. *Meteoritics & Planetary Science*, 40(S9).
- Rubin, A. E. (1997). Sinoite (Si<sub>2</sub>N<sub>2</sub>O): Crystallization from EL chondrite impact melts. *American Mineralogist*, 82(9-10), 1001-1006.
- Rubin, A. E., & Choi, B. G. (2009). Origin of halogens and nitrogen in enstatite chondrites. *Earth, Moon, and Planets*, 105(1), 41-53.
- Rubin, A. E. 2015. Impact features of enstatite-rich meteorites. *Chemie der Erde-Geochemistry*. 75 (1), 1-28
- Sears, D. W. (1980). Formation of E chondrites and aubrites—A thermodynamic model. *Icarus*, 43(2), 184-202.
- Sekine, T., He, H., Kobayashi, T., & Shibata, K. (2006). Sinoite (Si<sub>2</sub>N<sub>2</sub>O) shocked at pressures of 28 to 64 GPa. *American Mineralogist*, 91(2-3), 463-466.

- Stepniewski, M., Borucki, J., Durakiewicz, T., Giro, L., & Sharp, Z. D. (2000). Preliminary study of a new enstatite meteorite from Zakłodzie (southeast Poland). *Meteoritics and Planetary Science Supplement*, 35, A152.
- Stevens, S. J., Hand, R. J., & Sharp, J. H. (1997). Polymorphism of silica. *Journal of Materials Science*, 32(11), 2929-2935.
- Sugiura, N., & Fujiya, W. (2008, March). Al-Mg Age of the Zakłodzie Enstatite Meteorite. In *Lunar and Planetary Science Conference*, 39, 1503).
- Uribe, D. D., McCausland, P. J. A., & Izawa, M. R. M. (2016, March). A Comparative Study of the Zakłodzie and Northwest Africa 4301 Anomalous Enstatite Achondrites. In *Lunar and Planetary Science Conference*, 47, 3071).
- Uribe, D. D., McCausland, P. J. A., Izawa, M. R. M., Flemming, R. L., Moser, D., & Barker, I. (2017, March). Structural and Chemical Microanalysis of Anomalous Enstatite Achondrites via Electron Backscatter Diffraction (EBSD). In *Lunar and Planetary Science Conference*, 48.
- Withers, R. L., Thompson, J. G., & Welberry, T. R. (1989). The structure and microstructure of  $\alpha$ -cristobalite and its relationship to  $\beta$ -cristobalite. *Physics and Chemistry of Minerals*, 16(6), 517-523.

## **Chapter 5: Synthesis, General Conclusions and Future Research**

This concluding chapter will summarize and discuss the major observations and interpretations made in Chapter 3 and Chapter 4 to assess the validity of the hypothesis set out in Chapter 1, that the anomalous enstatite achondrites NWA 8173, Zakłodzie and NWA 4301 are linked with and represent a continuum with enstatite chondrites along the process towards planetary differentiation. After a brief review of the findings presented in Chapters 3 and 4, this chapter will discuss the impact of these findings on the relations of NWA 4301, NWA 8173, and Zakłodzie to other enstatite meteorites. This chapter also addresses the merits and shortcomings of the two major models for the heating required to create the primitive enstatite achondrites, namely internal heating likely driven by short-lived  $^{26}\text{Al}$  and heating by impacts. Finally, this chapter offers some potential future directions notably the potential importance and role of halogens such as fluorine in the petrogenesis of enstatite meteorites.

These findings have important implications for explaining the formation processes and environments present in the early solar system, including the early differentiation processes of planetary bodies. The anomalous enstatite achondrites may represent a continuum of common processes between enstatite chondrites (petrographic types 3-6), partial melting and differentiated aubrites. Before discussing the implications the meteorites investigated in this project provide about overall processes and environments of formation in the early solar system, a description of main observations and summary of the petrogenetic sequence each meteorite is in order.

### **5.1 Summary of findings in NWA 8173**

Chapter 3 involved investigation of an anomalous enstatite achondrite of unusual igneous textured characteristics that differ from those of typical aubrites. Petrographic, chemical and structural analysis showed that NWA 8173 contains large euhedral/subhedral enstatites, predominantly orthoenstatite, with interstitial myrmekitic plagioclase. Myrmekitic plagioclase was only associated with smaller, rounded to sub-rounded

enstatite grains whose composition is similar to the larger enstatite grains that dominate the samples. Niningerite sulfide host and exsolved troilite were the main sulfides present and metal contained inclusions of dendritic graphite as well as an average content 3.2 wt % Si in the metal. Tridymite was the main silica polymorph identified along with a round, amorphous inclusion in sulfide, which contained substantial impurities. Large grains of fluorophlogopite were identified and characterized through EPMA, EBSD, XRD and Raman.

From the findings summarized above, it is notable that NWA 8173 contains features unique from other enstatite achondrites. NWA 8173 contains higher silicon content in the metal (~3.2 wt% Si), higher than most enstatite achondrites such as QUE 94204 and NWA 1235 (Izawa et al. 2011; Lorenz et al., 2003) and aubrites. The enstatites in NWA 8173 are very pure with little to no FeO in silicates even compared to other enstatite achondrites, high metal content (~20 vol %) as per MetSoc Bulletin 103 (Bouvier, 2017 *pending*) and contain the largest amount of fluorophlogopite compared with other fluorophlogopite-bearing meteorite such as Y-82189 and NWA 1235 (Lin and Kimura, 1998; Lorenz et al., 2003). The silicon content of the metal, presence of albitic plagioclase, and niningerite-rich sulfide compositions that are characteristic of EH chondrites (Shirley and Fairbridge, 1997) support linkage of NWA 8173 with an EH-like parent body.

## **5.2 Formation mechanisms for NWA 8173**

Overall, present findings cannot uniquely identify the formation mechanism (internal heating or impact heating) for the anomalous enstatite achondrites studied in this thesis. An argument can be made to explain each process but no definitive answer can be placed at this moment and it is subject of contention in the study of enstatite meteorites (Przylibski et al., 2005; Keil, 2007; Rubin, 2015). The anomalous enstatite meteorite samples investigated here show evidence that may support both formational models, with impact melting being the more broadly accepted one (Keil, 2007; Rubin, 2015).

### *5.2.1 Impact melting*

Some of the minerals and textures resemble some of the characteristic indicative of melting (McCoy, 1995; Rubin and Scott, 1997; Rubin, 2015; Keil, 2007), and may therefore support an impact melt origin for NWA 8173. The euhedral enstatite crystals surrounded by metal, abundance of silica, and presence of fluorophlogopite have been interpreted to support a role for impact melting. It is possible that the NWA 8173 fluorophlogopite formed similarly as fluor-richterite (both as F-containing phases) in the enstatite impact melt breccia Abee where Rubin (2008), has interpreted the fluorine to have been widely distributed throughout the rock prior to impact, possibly in part adsorbed on grain surfaces. Following impact, not all the volatilized fluorine escaped, with some remaining to form the F-bearing phyllosilicates (Rubin, 2008).

The minerals, textures and chemistry of NWA 8173 may indicate it formed as the result of impact melting, based on the features defined by (Keil, 2007; Rubin, 2015) on an EH like precursor, which caused quenching of a high temperature sulfide melt that was then followed by sub-solidus annealing, exsolution and local remobilization of the sulfide phase. The abundance of metal, silicon content of the metal make this meteorite an anomalous enstatite meteorite whose parent body could have formed in a locally halogen enriched area, reflected by the presence of fluorophlogopite. Since halogen bearing minerals are not common in all enstatite meteorites, their presence may reflect local heterogeneity in the parent body accretion area. If the NWA 8173 parent body formed in a halogen enriched area, even with volatile loss due to impact, some fluorine remained to form fluorophlogopite. Alternatively, it is possible that fluorine was incorporated and retained in the melt while other halogens such as chlorine were lost from the melt (e.g. Nicotra et al., 2010).

Thus far the link of fluorophlogopite to impact melting is based on the fact that meteorites that contain this mineral also have other petrographic properties typical of impact melting. Rubin (2015), deems it enough to consider F-rich phases as independent indicators of impact processing. Besides impact melting, no other process has been suggested in forming F-rich phases in enstatite meteorites. Moreover, F-rich phases alone have not been used as an indicator of a geologic process nor have been investigated in

detail in meteorites. In Chapter 3 the behaviour of fluorine in terrestrial melts was discussed, perhaps providing a parallel mechanism in enstatite meteorites in highly reducing environments.

### *5.2.2 Internal Heating*

The textures in NWA 8173 result from partial melting of protolith material followed by crystallization of phases. It is possible that melting of NWA 8173 resulted from internal heating rather than impact melting. One possibility is that fluorine was complexed with metal or sulfur as a gas phase which then interacted with the silicate melt and incorporated fluorine and sulfidated the silicate melt, which ultimately formed sulfides, and fluorophlogopite at the expense of silicates (Chapter 3). Fluorine served as a fluxing agent in the silicate melt, lowering the melting temperature and therefore allowing for complete melting and recrystallization of the rock without the need of impact as a heat source.

### **5.3 Zakłodzie and NWA 4301**

Both Zakłodzie and NWA 4301 contain large euhedral/subhedral enstatite grains that exhibit granoblastic texture with many grains appearing to have triple junction contacts. Both meteorites contain large grains of the N-bearing phase sinoite included in sulfide (Zakłodzie) and in metal (NWA 4301). Feldspars in both meteorites exhibit zoning, with NWA 4301 showing reverse zoning and some grains with more uniform composition, whereas zoning of feldspar in Zakłodzie transitions from Ca rich tabular zones to a Ca poor zones within individual grains. Silica polymorph grains in Zakłodzie are found as micrographic intergrowths in the edges of large plagioclase grains, around sulfides and metal, with only tridymite being associated with sulfide. The silica grains in NWA 4301 were identified as tridymite and only occurred as irregular grains associated with metal and iron oxide veining.

### 5.3.1 *Impact heating source*

If impact is invoked as a heating mechanism, it is possible that NWA 4301 was located further away from the point of impact in the Zakłodzie and NWA 4301 EL like parent body, or that it was covered by an ejecta blanket where it cooled more slowly than Zakłodzie to equilibrate some of the feldspars in NWA 4301. Some of the mineral assemblages and textures may support an impact origin for Zakłodzie and NWA 4301 (e.g., Rubin, 1997; Keil, 2007; Rubin, 2015). The presence of sinoite, keilite in Zakłodzie, clinopyroxene lamellae in enstatite, zoning in plagioclase, euhedral graphite, abundance of silica may be indicative of impact melting. Both meteorites experienced high temperatures during melting, crystallized enstatite first, but remained at high temperatures long enough to form the observed granoblastic texture, the clinoenstatite lamellae formed as a result of shock from impact (S3; Rubin, 2015). During the high temperature phase, keilite formed via sulfidation of the silicate melt (Lehner et al., 2013) where SiO<sub>2</sub> formed as a product, with sinoite and graphite forming shortly after. After initial heating the rocks were quenched and cooled rapidly, preventing keilite exsolution, and forming the zoning in plagioclase. Some authors also add that the rocks then experienced a second impact event that creates a second generation of feldspars in Zakłodzie (Przylibski et al., 2005). However, Chapter 4 showed that feldspar composition shows a continuum rather than two generations of feldspar.

### 5.3.2 *Internal heating source*

Przylibski et al. (2005), proposed that Zakłodzie formed as result of partial melting induced by internal heating from <sup>26</sup>Al decay. Crystallization of the silicate portion of the melt started at 1600°C with segregation of Mg-rich olivine from the melt where magmatic fractional crystallization took place. After crystallization, rapid cooling resulted from upward migration of magma which explains the clinopyroxene lamellae and plagioclase zoning in Zakłodzie. The cumulate texture seen in Zakłodzie and NWA 4301 is similar to that of terrestrial pyroxenites that fractionally crystallized in a magma chamber which may support fractional crystallization of an internally heated magma for the formation of Zakłodzie and NWA 4301.

### 5.3.3 Do Zakłodzie and NWA 4301 share a common parent body?

The similarity in mineral composition and texture of enstatites and troilite in Zakłodzie and NWA 4301 may indicate these meteorites originated from the same parent body. However, after detailed study in Chapter 4, some textures and mineral assemblages may indicate that they experienced different metamorphic histories during their formation. The differences in plagioclase zoning indicate the meteorites experienced different cooling histories, with NWA 4301 having cooled more slowly than Zakłodzie. The silica polymorph and silicon assemblage in Zakłodzie point to higher temperatures compared with NWA 4301, where cristobalite and keilite were identified in Zakłodzie and tridymite and troilite for NWA 4301.

## 5.4 Linkages with enstatite meteorites

This thesis has investigated three anomalous enstatite achondrites that have chondritic geochemical signatures, and that contain different textural mineral assemblages which can provide insight about formation mechanisms of enstatite meteorites in the early solar system. The findings in Chapter 3 and 4 showed that both impact and internal heating can explain the formation of these meteorites and there is no definitive answer at the present time. However, based on the findings in this thesis, and excluding impact melt as a formation mechanism, it is possible to describe a model that can explain the gap between the undifferentiated enstatite chondrites and the differentiated aubrites.

Higher metamorphic grades in some E chondrites, with textures similar to Zakłodzie and NWA 4301 may have formed deep in the parent body where solid state recrystallization can occur. As the rock is metamorphosed, fluorine derived from the mesostasis of the protolith material is liberated and forms simple halide compounds which can then be complexed by metal or sulfide and incorporated into the melt. As the fluorine interacts with the melt, it lowers the melting temperatures of the mineral assemblages, and ultimately drives melting (e.g., Niconda et al., 2010). That is, NWA 8173 may represent a chondritic rock that was being thermally heated deep in the enstatite parent body, melted as fluorine served as a fluxing agent in the silicate melt and lower melting temperatures,



causing melting of the rock, hence driving fractionation forward. The rock then concentrated more metal and incorporated Si in metal but was never able to differentiate. If differentiation would have proceeded, the rock would have undergone metal-silicate segregation (possibly leading to core formation) and resulted in a rock similar to an aubrite.

Fig. 5.1 represents a schematic diagram of the proposed model of formation of Zakłodzie/NWA 4301 and NWA 8173 and the link between enstatite chondrites and aubrites. Fig 5.1 illustrates how meteorites originated from multiple asteroid-sized bodies where individual bodies were differentiated, undifferentiated or partially differentiated. The mineral chemical compositions indicate that Zakłodzie and NWA 4301 represent EL-like body and that NWA 8173 represents an EH like body. However, this schematic illustrates overall parent body process relationships between these meteorites and other enstatite meteorites. The outermost layers depend on petrologic type of enstatite chondrites, with increasing petrologic grade by depth. Zakłodzie/NWA 4301 represent highly metamorphosed rock in which the chondritic texture has essentially been lost, and NWA 8173 represents a high grade metamorphosed rock deep in the parent body that has melted, possibly due to fluorine lowering melting temperature. NWA 8173 may have accumulated some metal but is not significantly differentiated. The above model requires further investigation on the behavior of fluorine in highly reduced magmas as well as finding other meteorites that can better exhibit characteristics of this model. For instance, following the process outlined above, the existence of Si-rich metal-dominated meteorites is predicted. Possible further linkages may also exist with some type IIE iron meteorites that have been proposed to be linked with more highly reduced chondrites, representing either partially differentiated bodies or impact melt pools (Scott and Goldstein, 2016; Fischer-Gödde et al., 2016).

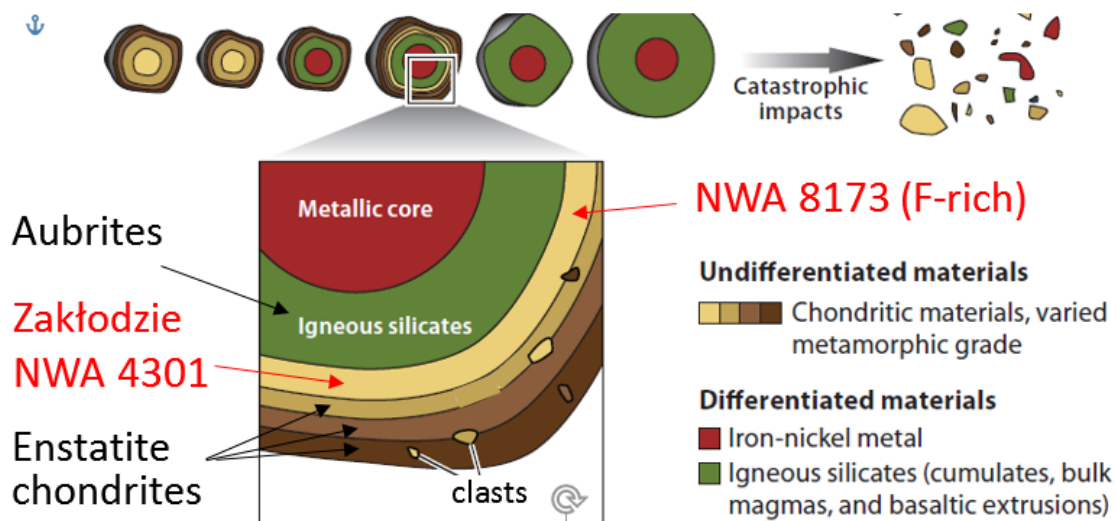


**Figure 5.1.** Meteorite parent body schematic model for context of anomalous enstatite achondrites, modified from Weiss et al. (2013).

### 5.5 Concluding statement

The current study does not allow for a definitive determination of impact melt or internal heating as the formation processes of anomalous enstatite achondrites. Many of the textural features seen in anomalous enstatite meteorites have been interpreted as impact melt indicators (McCoy, 1995; Keil, 2007; Rubin & Scott, 2007; Rubin, 2008; Rubin, 2015). However, an internal heat source cannot be excluded on the basis that many of these anomalous enstatite chondrites contain high amounts of metal and sulfide and that if these were truly the result of partial melting, density driven segregation of metal and sulfide into the core should be expected. It is possible that these rocks were partially melted, accumulated high amounts of metal incorporated Si in the metal but were never able to differentiate. Although this thesis cannot currently define a single formation mechanism for these meteorites, it provides an alternative that can explain the evolution of enstatite chondrites, primitive achondrites and aubrites without invoking impact melt as a heat source.

This thesis also provides a detailed petrological, chemical and structural description of enstatite achondrites NWA 8173 and NWA 4301 that had previously been studied in little detail. The discovery of large fluorophlogopite grains in NWA 8173 suggests a critical

role for halogens, fluorine in particular, in the formation of these enstatite achondrites, whereby fluorine may have served as a fluxing agent during igneous melting of enstatite chondrites in early solar system bodies.

### **5.6 Ideas for future work**

The following section will provide a brief description of possible ideas for further research that will help constrain the formation mechanism of the enstatite meteorites in order to determine if these might represent primitive rocks that experienced melting and were never able to differentiate. Some of the suggested ideas may also provide insight about the role of halogens in magmatic systems under reducing conditions.

- Current use of  $\mu$ CT scans cannot distinguish between individual mineral phases. Using higher power CT scanners might provide better resolution scans as well as discern individual mineral phases to provide quantitative modal percentages.
- Based on Sugiura and Fuyija, (2008), Al-Mg dating of anomalous meteorites is possible given the abundance of plagioclase in these rocks. Al-Mg isotope dating on NWA 8173 will help determine if heating mechanism was internal or impact, assuming that it formed within the first 5 million years after initial  $^{26}\text{Al}$  heating.
- Mn-Cr dating of NWA 4301 and NWA 8173 may provide additional means to determine timing of their formation.
- Study the behavior of fluorine in highly reducing systems as a fluxing component in silicate melts to test the idea that as fluorine enters the melt, it lowers the crystallization temperature and allows for melting of a EH6 rock that recrystallizes without the need of impact as a heat source.
- Analyze Rare Earth Element (REE) patterns of fluorophlogopite and other phases in NWA 8173 may determine the source of fluorine and if it fractionated from a melt as well as REE of plagioclase in NWA 4301 and Zakłodzie to determine if

multiple generations of feldspar are in fact present as suggested by Przylibski et al., (2005).

- Crystal size distribution analysis on enstatite grains in the anomalous enstatite meteorites may help to more quantitatively distinguish between igneous, cumulate, metamorphic and primitive source (chondritic) textures (e.g., Higgins, 2006).

## 5.7 References

- Burbine, T. H., McCoy, T. J., & Dickinson, T. L. (2000). Origin of Plagioclase-  
"Enriched", Igneous, Enstatite Meteorites. *Meteoritics and Planetary Science  
Supplement*, 35, A36.
- Fischer-Gödde, M., Kruijer, T. S., Kleine, T. and Wasson, J. T. (2016). W, Pt, Mo and Ru  
isotope systematics of IIE iron meteorites. *Lunar and Planetary Science  
Conference*, 47, 2704.
- Higgins, M. D. (2006). Quantitative textural measurements in igneous and metamorphic  
petrology. Cambridge University Press, 265 pp.
- Izawa, M. R., Flemming, R. L., Banerjee, N. R., & Matveev, S. (2011). QUE 94204: A  
primitive enstatite achondrite produced by the partial melting of an E chondrite-  
like protolith. *Meteoritics & Planetary Science*, 46(11), 1742-1753.
- Keil, K. (2007). Occurrence and origin of keilite, (Fe > 0.5, Mg < 0.5) S, in enstatite  
chondrite impact-melt rocks and impact-melt breccias. *Chemie der Erde-  
Geochemistry*, 67(1), 37-54.
- Keil, K., & Bischoff, A. (2008). Northwest Africa 2526: A partial melt residue of  
enstatite chondrite parentage. *Meteoritics & planetary science*, 43(7), 1233.
- Lin, Y., & Kimura, M. (1998). Petrographic and mineralogical study of new EH melt  
rocks and a new enstatite chondrite grouplet. *Meteoritics & Planetary  
Science*, 33(3), 501-511.
- Lorenz, C., Kurat, G., Brandstätter, F., & Nazarov, M. A. (2003, March). NWA 1235: A  
phlogopite-bearing enstatite meteorite. In *Lunar and Planetary Science  
Conference*, (34).
- McCoy, T. J., Keil, K., Bogard, D. D., Garrison, D. H., Casanova, I., Lindstrom, M. M.,  
& Hohenberg, C. M. (1995). Origin and history of impact-melt rocks of enstatite  
chondrite parentage. *Geochimica et Cosmochimica Acta*, 59(1), 161-175.
- Rubin, A. E. (1997). Igneous graphite in enstatite chondrites. *Mineralogical  
Magazine*, 61(5), 699-703.
- Rubin, A. E. (1997). Sinoite (Si<sub>2</sub>N<sub>2</sub>O): Crystallization from EL chondrite impact  
melts. *American Mineralogist*, 82(9-10), 1001-1006.
- Rubin, A. E., & Scott, W. R. (1997). Abee and related EH chondrite impact-melt  
breccias. *Geochimica et Cosmochimica Acta*, 61(2), 425-435.
- Rubin, A. E. (2015). Impact features of enstatite-rich meteorites. *Chemie der Erde-  
Geochemistry*. 75 (1), 1-28

- Scott, E. R. D. and Goldstein, J. I. (2016) Thermal histories and origins of Group IIE and IAB iron meteorites and their parent asteroids. *Lunar and Planetary Science Conference*, 47, 2685.
- Sugiura, N., & Fujiya, W. (2008, March). Al-Mg Age of the Zakłodzie Enstatite Meteorite. In *Lunar and Planetary Science Conference*, 39, 1503.
- Weiss, B. P., & Elkins-Tanton, L. T. (2013). Differentiated planetesimals and the parent bodies of chondrites. *Annual Review of Earth and Planetary Sciences*, 41, 529-560.

### **Appendix 1: EPMA results and standards used in this thesis**

All electron probe microanalysis (EPMA) results from NWA 8173 (Chapter 3) and Zakłodzie and NWA 4301 (Chapter 4) are provided in the associated Appendix 3.2-4.3 Excel spreadsheets, which comprise the bulk of Appendix 3.2 and 4.3. An example set of the standards used for each meteorite mineral phase analysis is given in Table form below, showing the analyzed phase, the EPMA operating conditions, the elements analyzed for, chosen standards, spectrometers and the peak positions. Note that peak positions were found to vary slightly from probe session to probe session and so each session required tweaking of the peak positions. These serve as an example.

<b>Phase:</b> Silica / Plagioclase / Enstatite									
<b>Operating Conditions:</b> 5 kV, 20 nA, 10 $\mu$ m spot - Plagioclase, 5 $\mu$ m spot - Silica, Enstatite									
		<b>Spectrometers</b>							
		<b>1</b>	<b>2</b>	<b>3</b>	<b>4</b>	<b>5</b>			
<b>Element</b>	<b>Std</b>	<b>TAP/LDE1</b>	<b>TAP/LDE2</b>	<b>PETJ/LIF</b>	<b>PETH/LIFH</b>	<b>PETL/LIFL</b>	<b>L-Value</b>	<b>Counts</b>	<b>Back + / Back -</b>
Si	Quartz		TAP				77.284	21747	3/6.5
Ti	Rutile			PETJ			88.281	11061	3.5/4
Cr	Chromite					LIFL	159.284	3908	4/4
Al	Albite		TAP				90.589	4121	3.5/6
Mg	Enstatite	TAP					107.538	6321	3.5/3.5
Mn	Rhodonite				LIFH		146.369	4431	4/4
Fe	Hematite				LIFH		134.833	10580	4/5
Cu	Dioside			PETJ			107.794	3674	2/3
Nu	Albite	TAP					124.551	1066	3.5/4
K	Orthoclase					PETL	119.944	6420	2.5/2.5
Si	Enstatite		TAP				77.284	10956	3/6.5
Si	Albite		TAP				77.284	13126	3/6.5

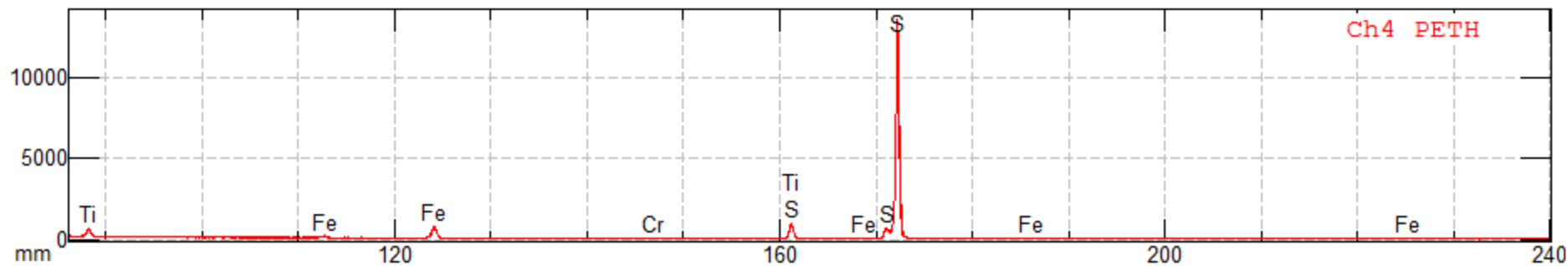
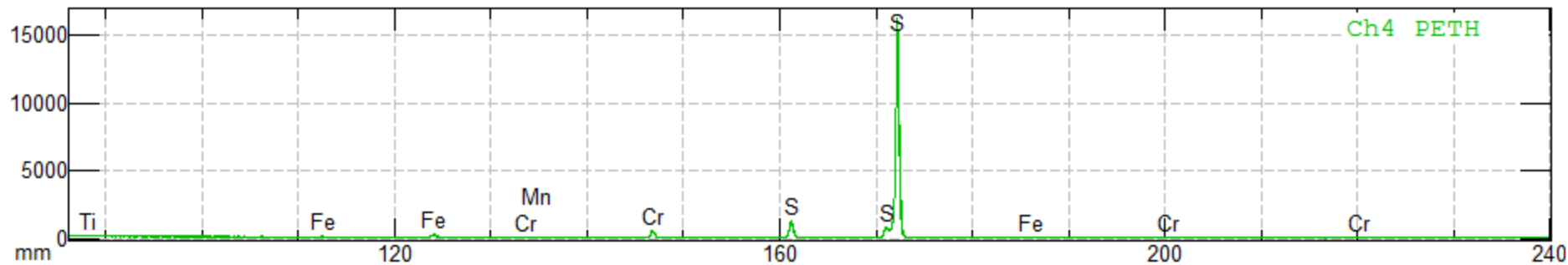
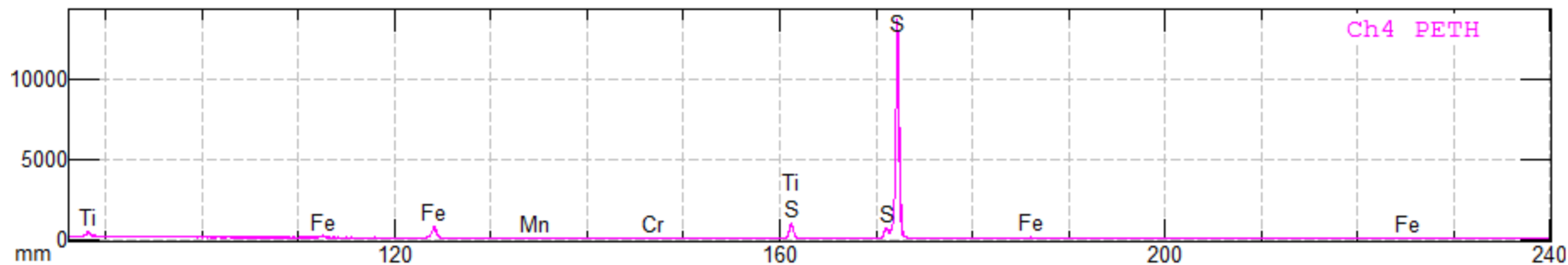
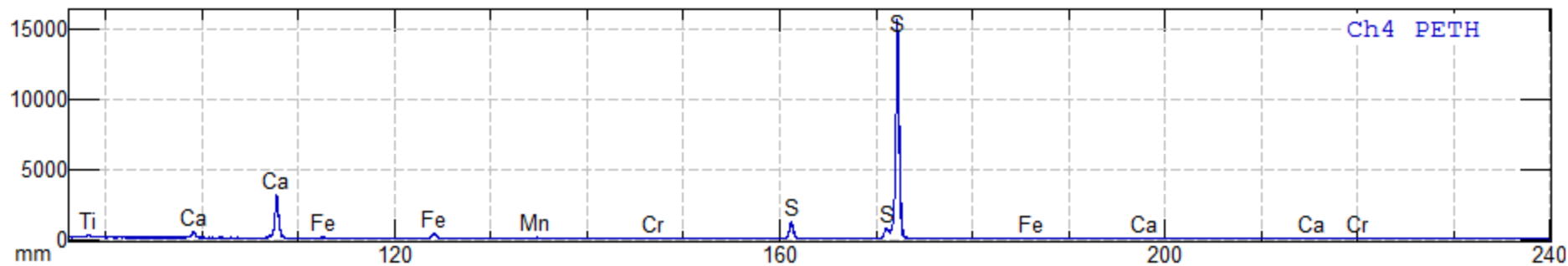
<b>Phase:</b> Mapping (Fluorophlogopite)									
<b>Operating Conditions:</b> 5 kV, 100 nA , 1 $\mu$ m spot									
		<b>Spectrometers</b>							
		<b>1</b>	<b>2</b>	<b>3</b>	<b>4</b>	<b>5</b>			
<b>Element</b>	<b>Std</b>	<b>TAP/LDE1</b>	<b>TAP/LDE2</b>	<b>PETJ/LIF</b>	<b>PETH/LIFH</b>	<b>PETL/LIFL</b>	<b>L-Value</b>	<b>Counts</b>	<b>Back + / Back -</b>
F	Fluorite	LDE1					86.14		
Si	Orthoclase		TAP				77.252		
Fe	Pyrite			LIF			134.812		
S	Pyrite				PETH		172.141		
K	Orthoclase					PETL	120.004		

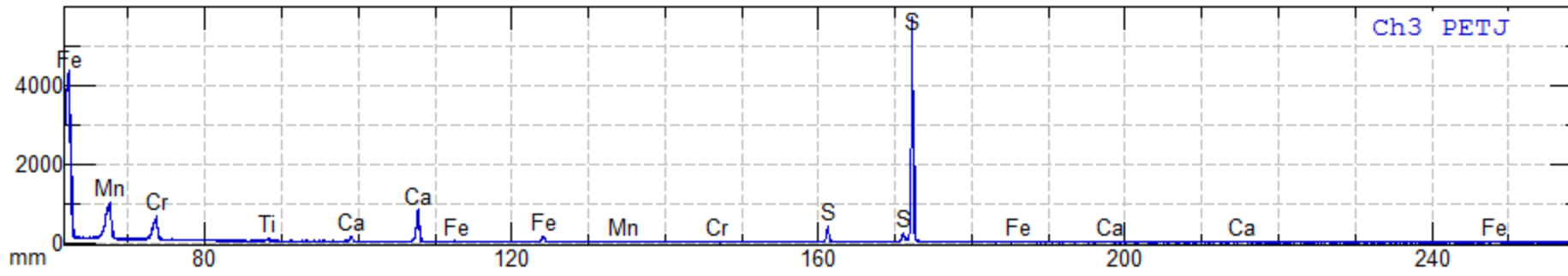


<b>Phase:</b> Sulfides									
<b>Operating Conditions:</b> 20 kV, 40 nA, 1 $\mu$ m spot									
<b>Spectrometers</b>									
		<b>1</b>	<b>2</b>	<b>3</b>	<b>4</b>	<b>5</b>			
<b>Element</b>	<b>Std</b>	<b>TAP/LDE1</b>	<b>TAP/LDE2</b>	<b>PETJ/LIF</b>	<b>PETH/LIFH</b>	<b>PETL/LIFL</b>	<b>L-Value</b>	<b>Counts</b>	<b>Back + / Back -</b>
Fe	Pyrite					LIFL	134.701	13333	4/5
	Pyrrhotite						134.702	1900	
S	Pyrite			PETJ			172.246	10114	2.5/6
	Pyrrhotite				172.241	7265			
Mg	Magnesium		TAP				107.548	55540	3.5/5.5
	Periclase			107.543	7265				
Mn	Rhodonite					LIFL	146.217	28749	3.5/4.5
	Manganese						146.232		
Ca	Diopside			PETJ			107.794	6269	2/3
Zn	Sphalerite				LIFH		100.033	21530	2/2
Ti	Titanium			PETJ			88.271	36805	3.5/4
Cu	Chalcopyrite				LIFH		107.362	10767	2.5/4.6
Cr	Cr-Oxide					LIFL	159.265	24565	3/4
	Chromium						159.284		
Ni	Millerite				LIFH		115.523	23866	3/4.5
Co	Cobalt					LIFL	124.477	36608	3/5
Na	Albite		TAP				129.584	1273	3.5/4
Si	Albite	TAP					77.384	15669	3/6.5
P	Indium Phosphide			PETJ			197.356	2802	2.5/2.5
O	Hematite	LDE1					111.246	2555	1.5/1.5
C	Carbon		LDE2				124.16	33959	1.5/1.5
Fe	Pyrrhotite						134.698	19542	4/5
S	Pyrrhotite						172.241	7052	2.5/6
Fe	Iron Metal					LIFL	134.698		4/5

# Appendix 2.1

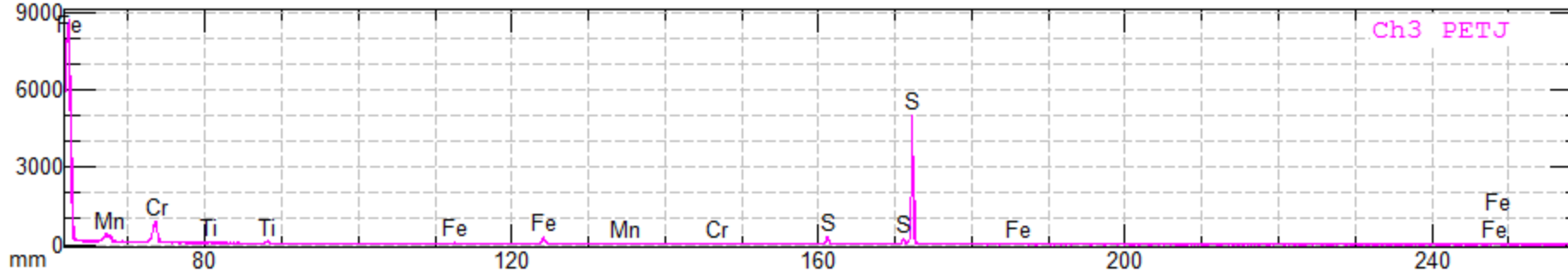
WDS raster of sulfides in meteorite samples to analyze for any possible element that could be present in sulfides.



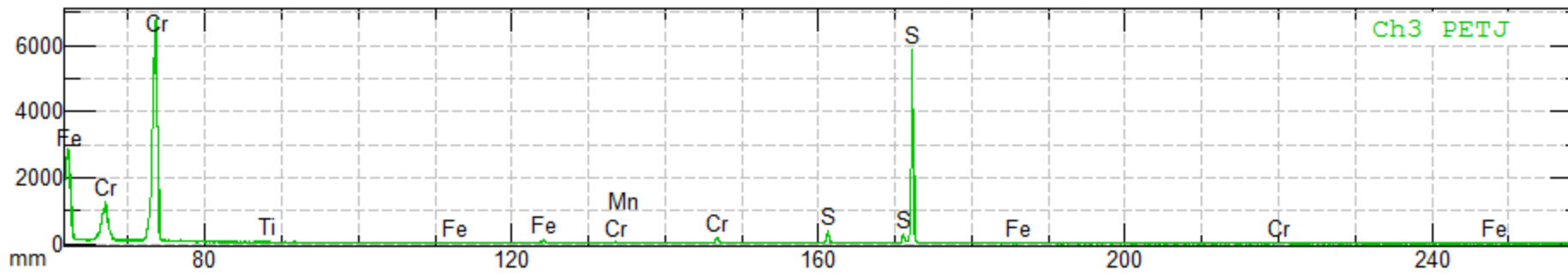


Path : D:\EPMA\_Data\Diego  
Project: August\_4\_2015\_0014

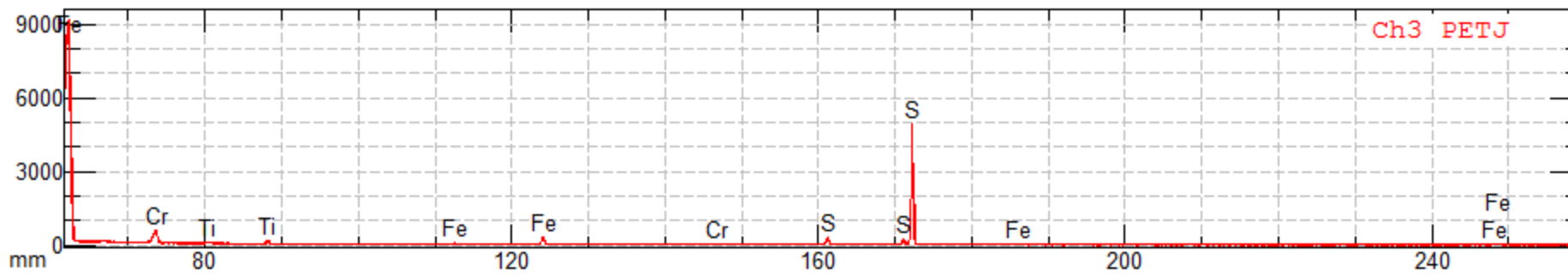
NWA8173\_sulfide\_scan  
\*ID-Doctor\*  
A-rank  
S Ca Ti Cr Mn  
Fe  
B-rank



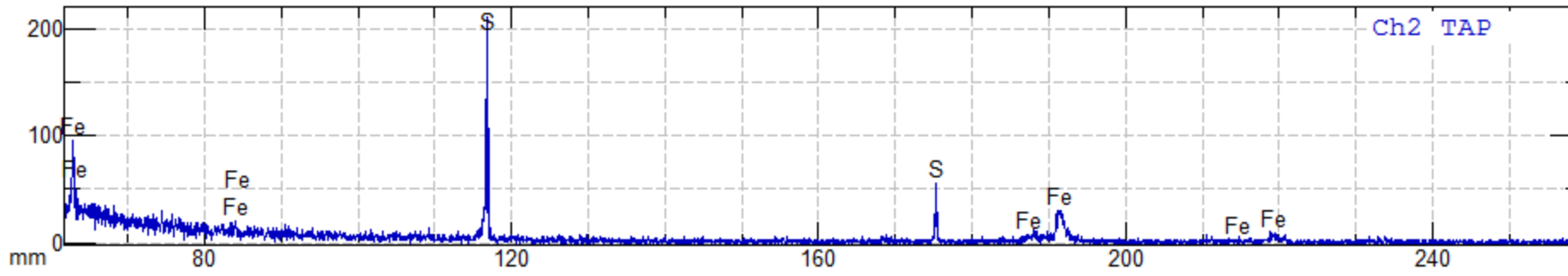
NWA4301\_sulfide\_scan  
\*ID-Doctor\*  
A-rank  
S Ti Cr Mn Fe  
B-rank



Hvittis\_sulfide1\_scan  
\*ID-Doctor\*  
A-rank  
S Ti Cr Mn Fe  
B-rank

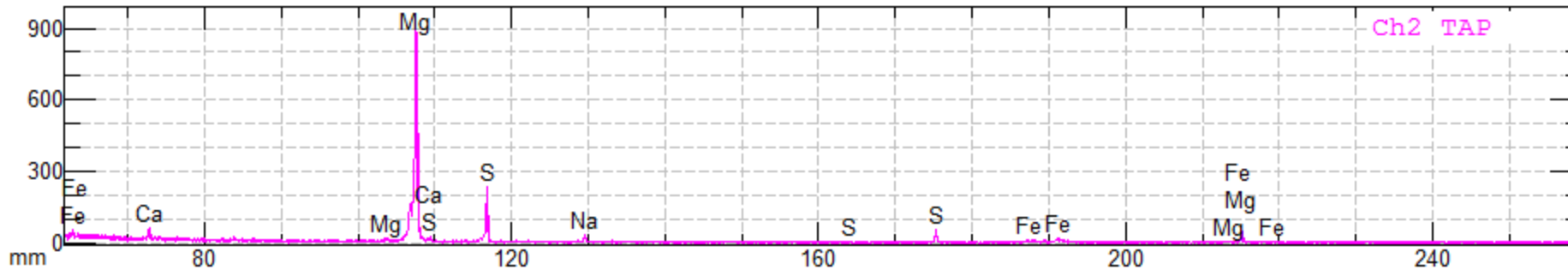


Hvittis\_sulfide2\_scan  
\*ID-Doctor\*  
A-rank  
S Ti Cr Fe  
B-rank

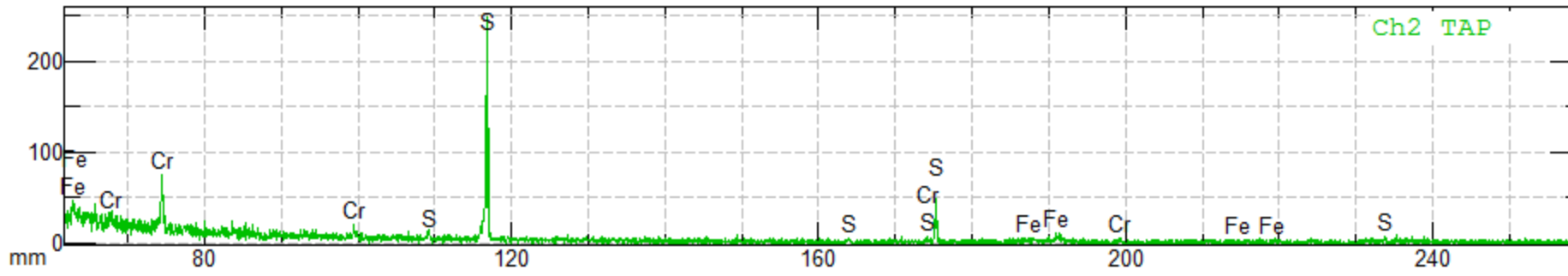


Path : D:\EPMA\_Data\Diego  
Project: August\_4\_2015\_0014

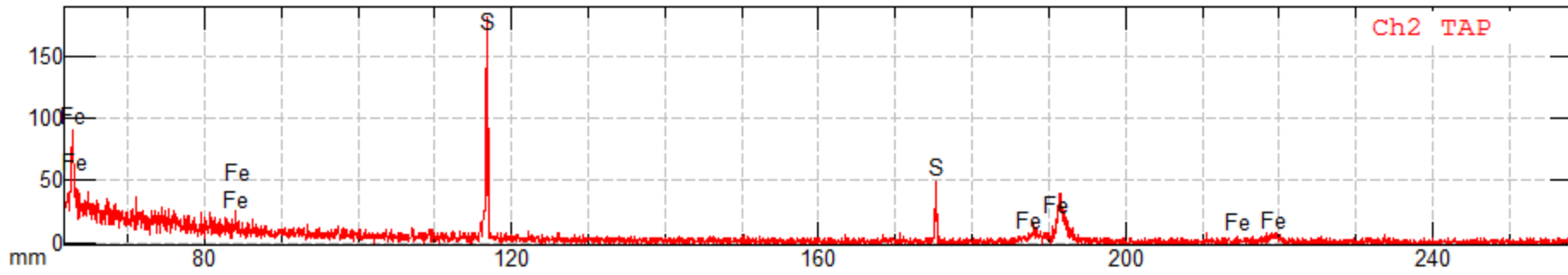
NWA4301\_sulfide\_scan  
Beam Shape SPOT Probe Dia. 0  
\*ID-Doctor\*  
A-rank  
S Fe  
B-rank



NWA8173\_sulfide\_scan  
Beam Shape Circle Probe Dia. 1  
\*ID-Doctor\*  
A-rank  
Na Mg S Ca Fe  
B-rank



Hvittis\_sulfide1\_scan  
Beam Shape SPOT Probe Dia. 0  
\*ID-Doctor\*  
A-rank  
S Cr Fe  
B-rank

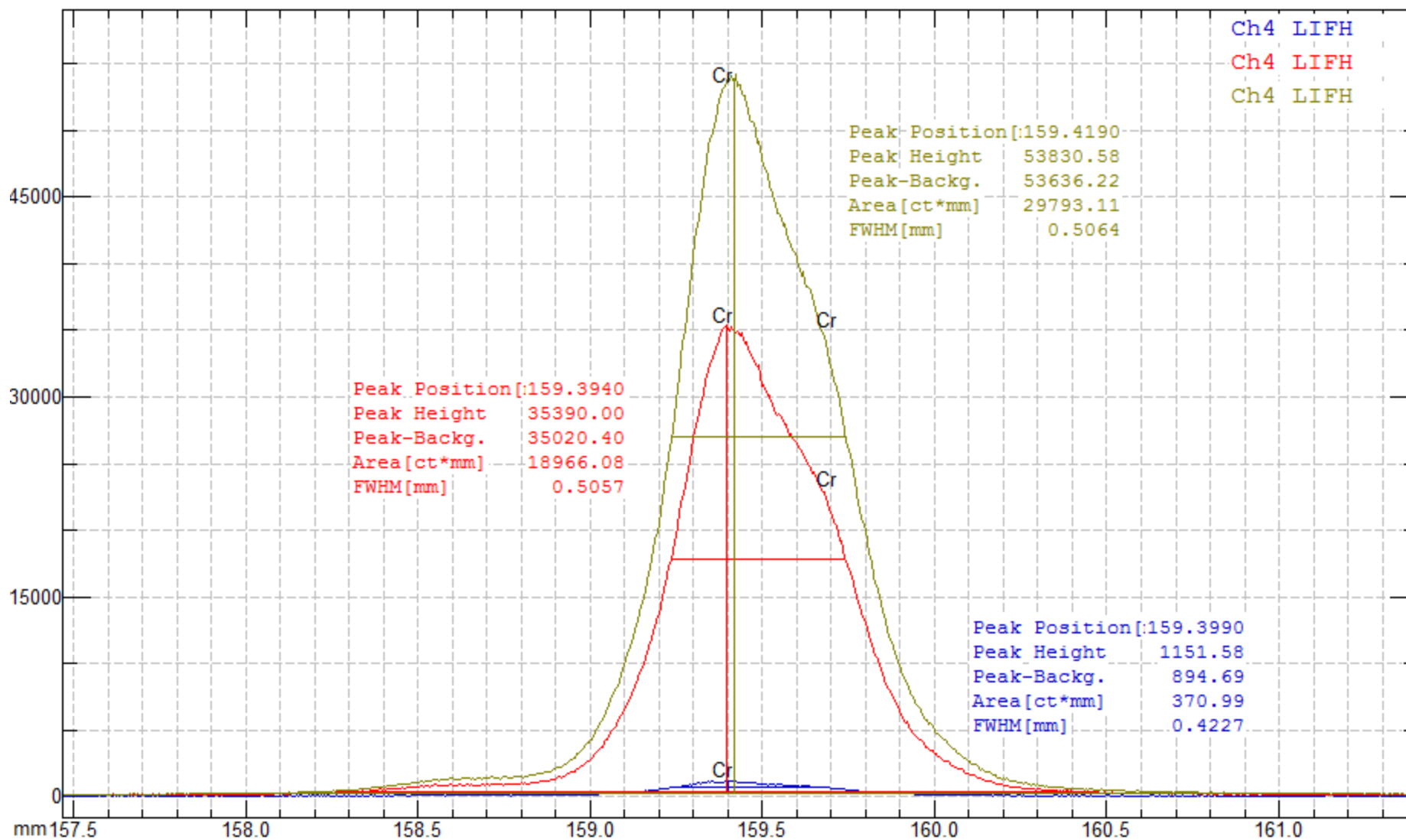


Hvittis\_sulfide2\_scan  
Beam Shape SPOT Probe Dia. 0  
\*ID-Doctor\*  
A-rank  
S Fe  
B-rank

# Appendix 2.2

WDS peak position of standards vs samples

Spectra images are of meteorite Abee as calibration and reference



Path : D:\EPMA\_Data\Diego

Project: September\_17\_2015\_003

Abee\_sulfide\_1

CH-4 LIFH

Dwell (ms) 1000

\*ID-Doctor\*

A-rank

Cr

B-rank

Project: September\_17\_2015\_003

MinM\_Cr-Oxide

CH-4 LIFH

Dwell (ms) 1000

\*ID-Doctor\*

A-rank

Cr

B-rank

Project: September\_17\_2015\_003

MetM\_Chromium

CH-4 LIFH

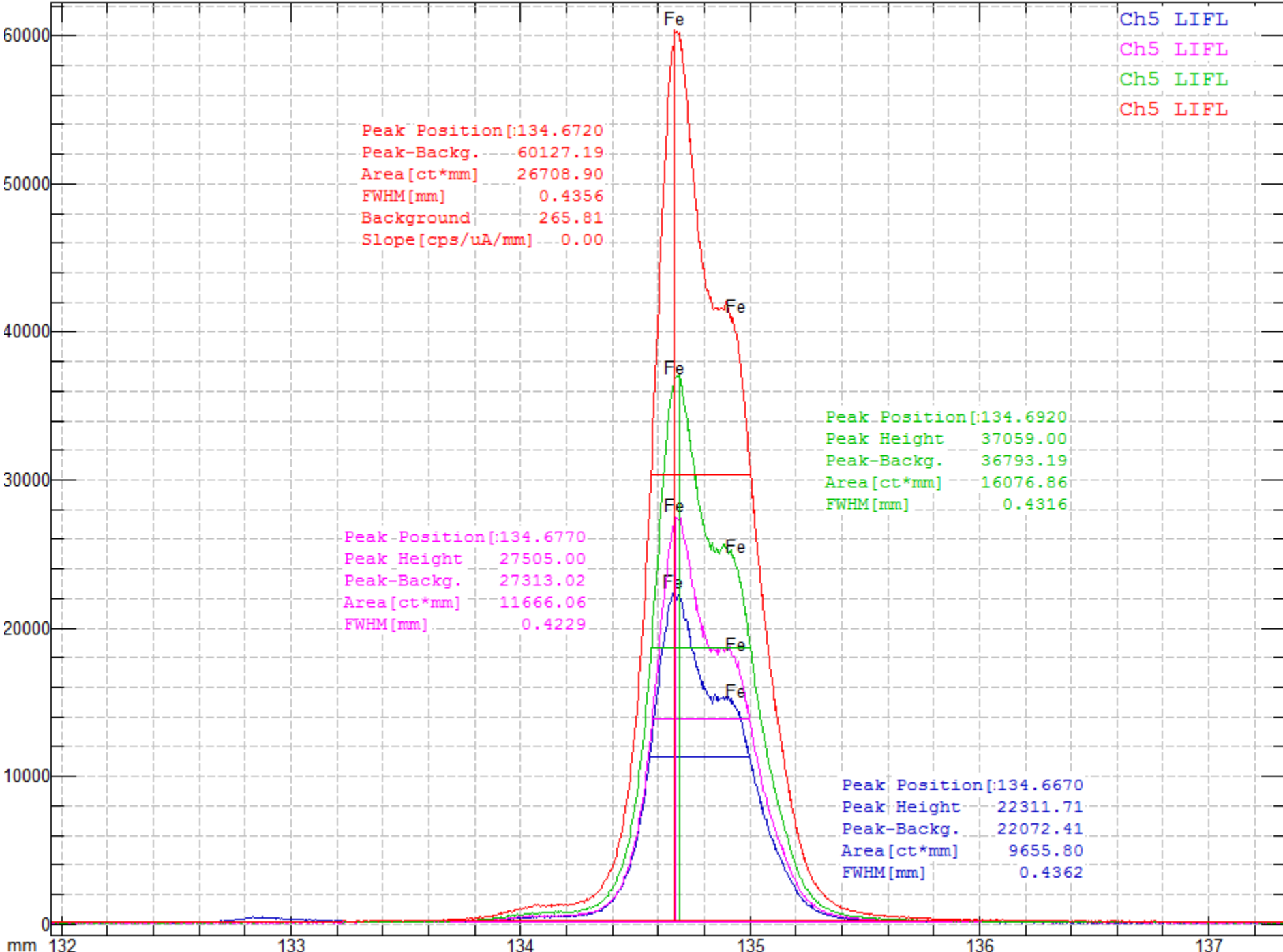
Dwell (ms) 1000

\*ID-Doctor\*

A-rank

Cr

B-rank



Ch5 LIFL  
 Ch5 LIFL  
 Ch5 LIFL  
 Ch5 LIFL

Path : D:\EPMA\_Data\Diego

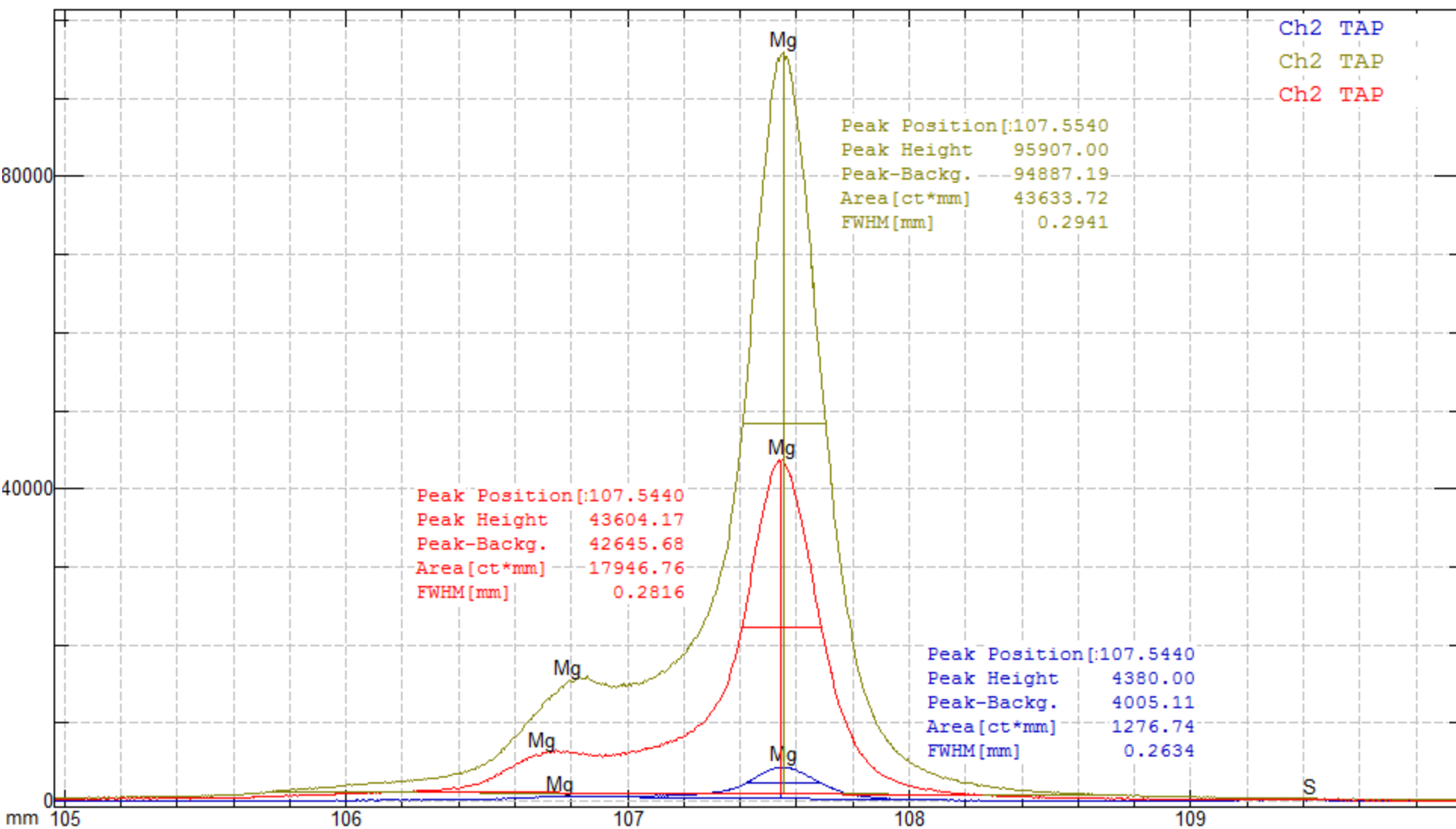
Project: September\_17\_2015\_003  
 Abee\_sulfide\_1  
 CH-5 LIFL  
 Dwell(ms) 1000  
 \*ID-Doctor\*  
 A-rank  
 Fe  
 B-rank

Project: September\_17\_2015\_003  
 MinM\_Pyrite  
 CH-5 LIFL  
 Dwell(ms) 1000  
 \*ID-Doctor\*  
 A-rank  
 Fe  
 B-rank

Project: September\_17\_2015\_003  
 A\_Pyrrhotite  
 CH-5 LIFL  
 Dwell(ms) 1000  
 \*ID-Doctor\*  
 A-rank  
 Fe  
 B-rank

Project: September\_17\_2015\_003  
 MetM\_Iron  
 CH-5 LIFL  
 Dwell(ms) 1000  
 \*ID-Doctor\*  
 A-rank  
 Fe  
 B-rank





Path : D:\EPMA\_Data\Diego

Project: September\_17\_2015\_003

Abee\_sulfide\_1

CH-2 TAP

Dwell(ms) 1000

\*ID-Doctor\*

A-rank

Mg S

B-rank

Project: September\_17\_2015\_003

MetM\_Magnesium

CH-2 TAP

Dwell(ms) 1000

\*ID-Doctor\*

A-rank

Mg

B-rank

Project: September\_17\_2015\_003

MinM\_Periclase

CH-2 TAP

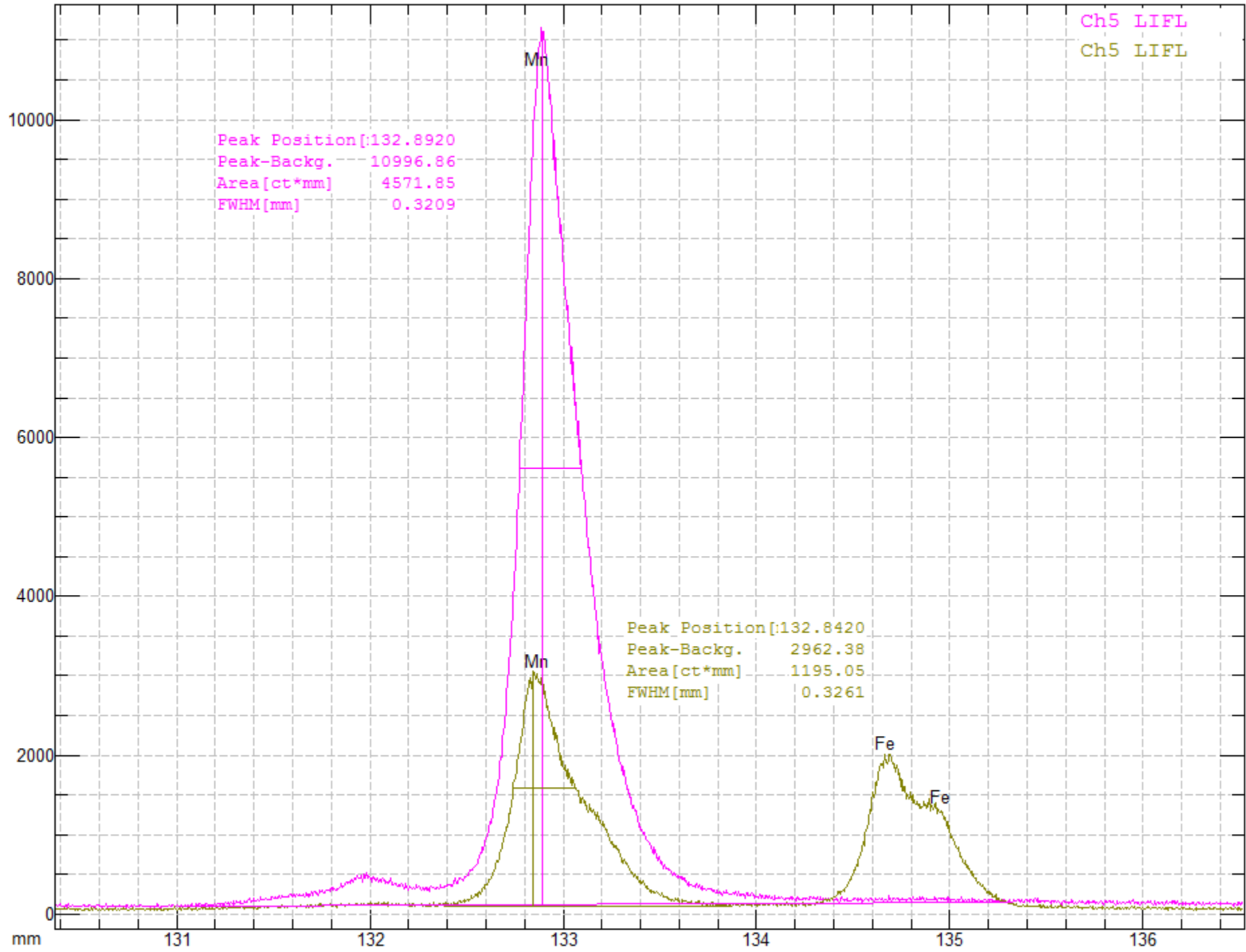
Dwell(ms) 1000

\*ID-Doctor\*

A-rank

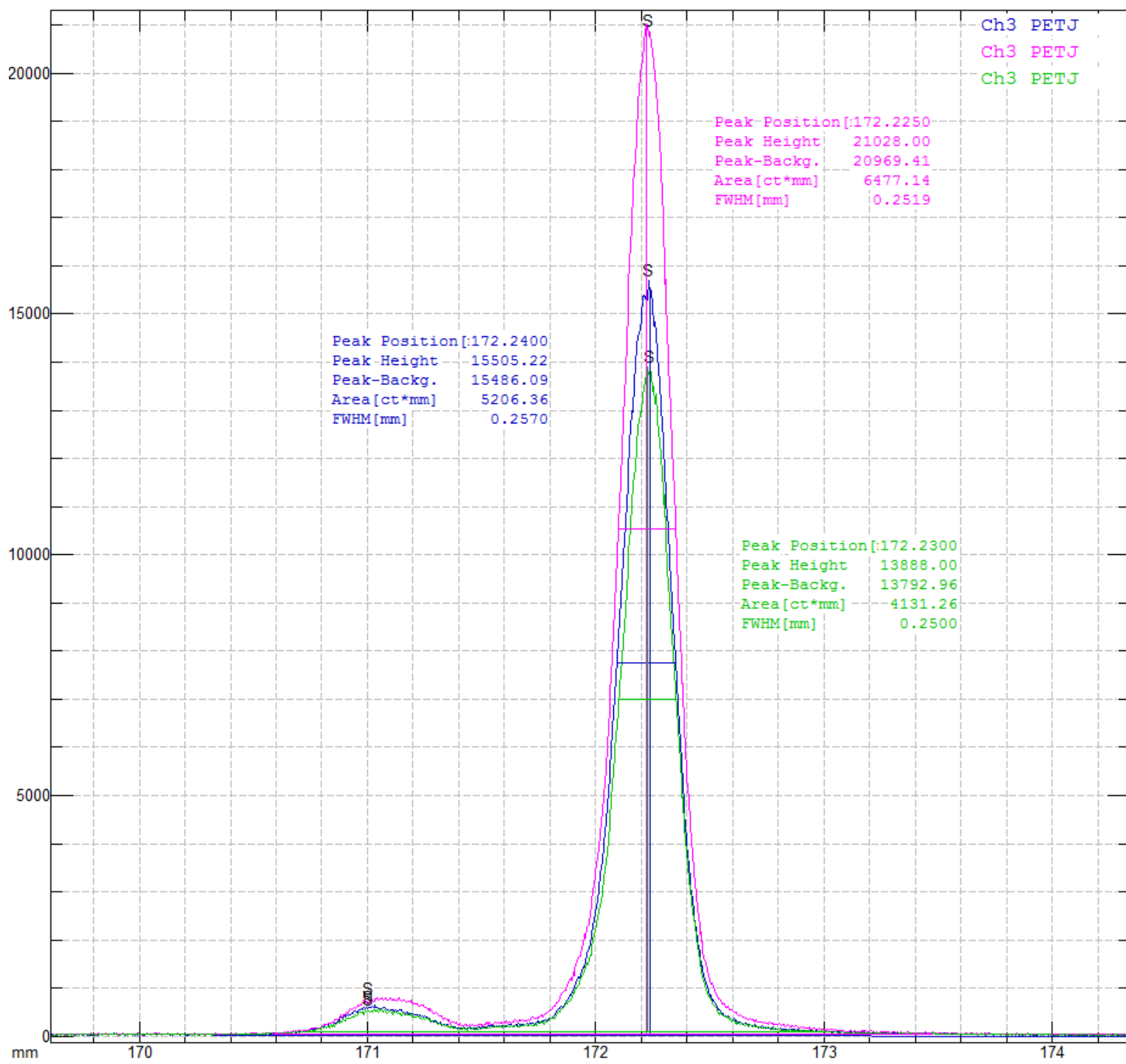
Mg

B-rank



MetM\_Manganese  
CH-5 LIFL  
Dwell(ms) 1000  
\*ID-Doctor\*  
A-rank  
B-rank  
Dy

MinM\_Rhodonite  
CH-5 LIFL  
Dwell(ms) 1000  
\*ID-Doctor\*  
A-rank  
Fe  
B-rank  
Dy



Ch3 PETJ  
 Ch3 PETJ  
 Ch3 PETJ

Path : D:\EPMA\_Data\Diego

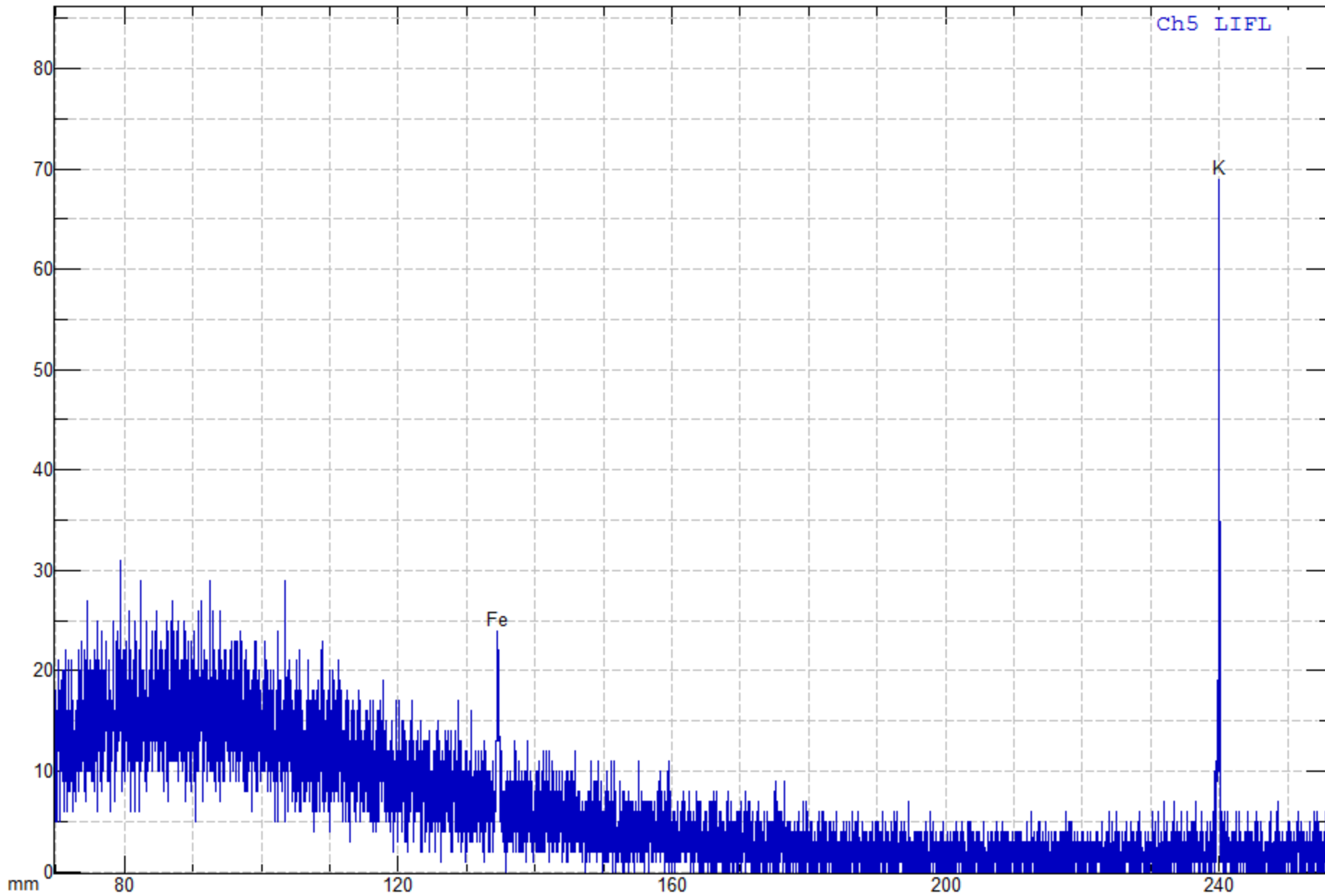
Project: September\_17\_2015\_003  
 Abee\_sulfide\_1  
 CH-3 PETJ  
 Dwell (ms) 1000  
 \*ID-Doctor\*  
 A-rank  
 S  
 B-rank

Project: September\_17\_2015\_003  
 MinM\_Pyrite  
 CH-3 PETJ  
 Dwell (ms) 1000  
 \*ID-Doctor\*  
 A-rank  
 S  
 B-rank

Project: September\_17\_2015\_003  
 A\_Pyrrhotite  
 CH-3 PETJ  
 Dwell (ms) 1000  
 \*ID-Doctor\*  
 A-rank  
 S  
 B-rank

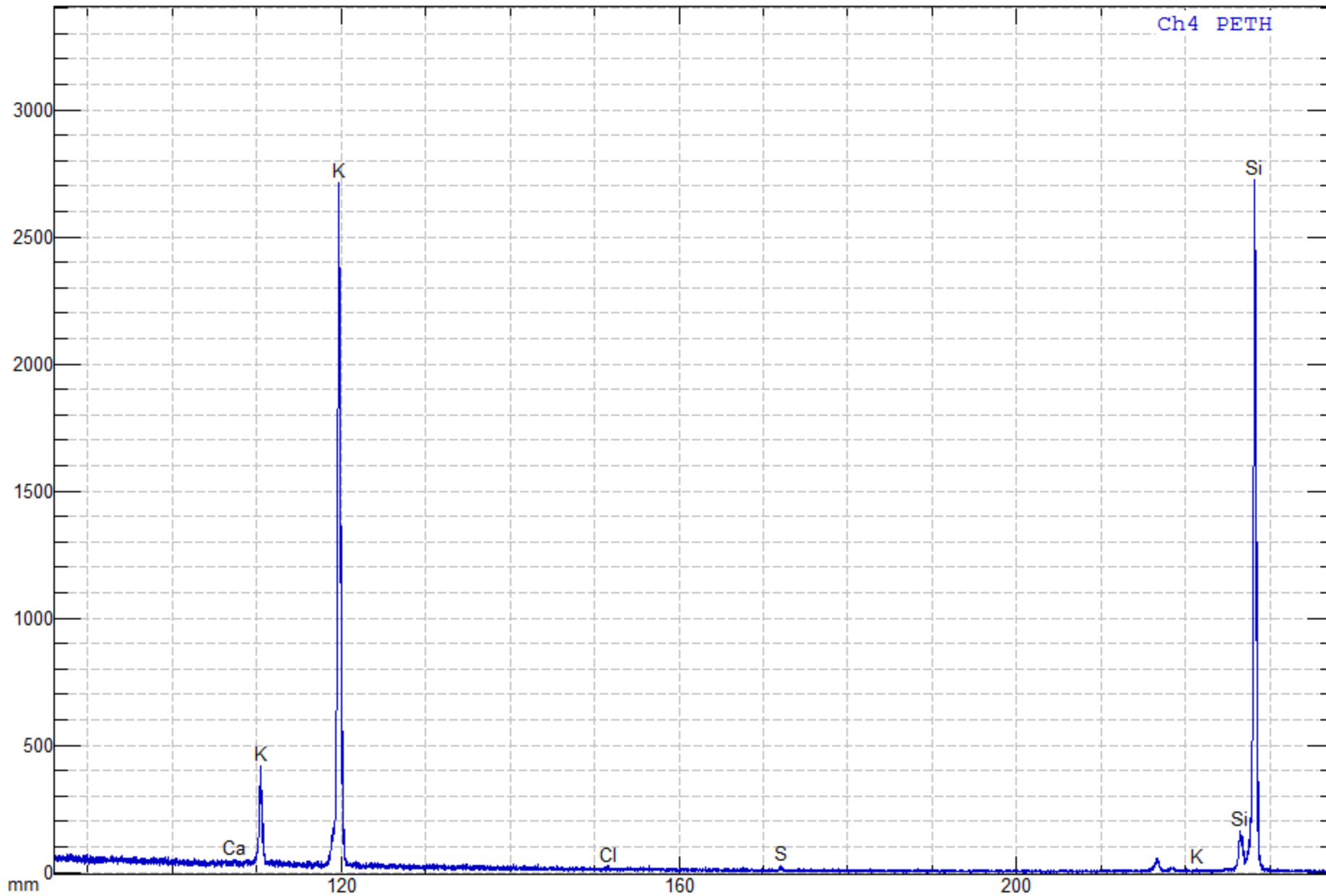
# Appendix 2.3

WDS Raster of F-mica grain in NWA 8173 showing the spectrum of each spectrometer to analyze for halogens in F-mica grain



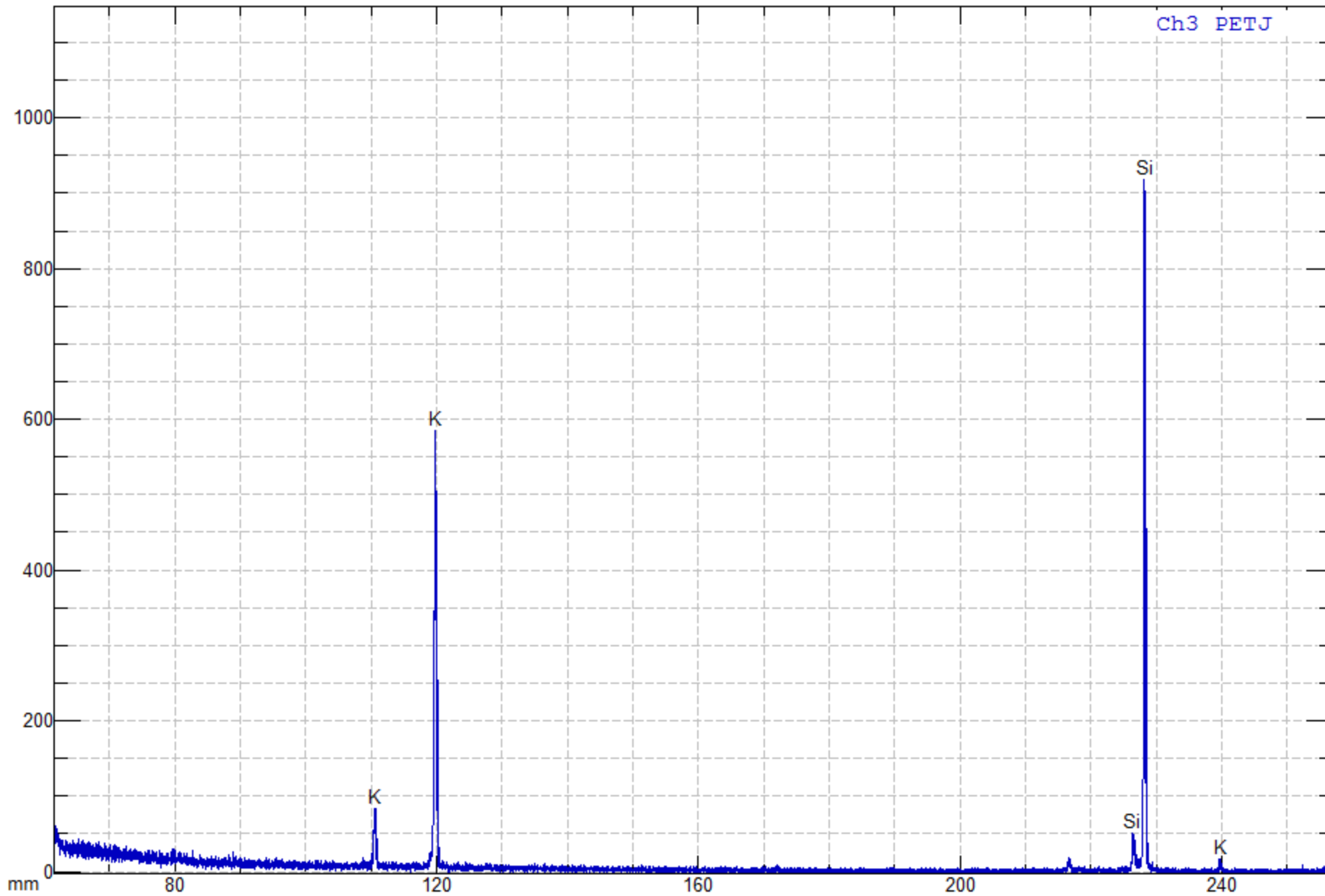
Path : D:\EPMA\_Data\Diego  
NWA8173a\_mica\_Feb1\_2017  
Feb 01 11:29 2017  
Acc. V 15.0 kV  
Prob C 5.005e-008 A

CH-5 LIFL  
Dwell (ms) 200  
Max 69



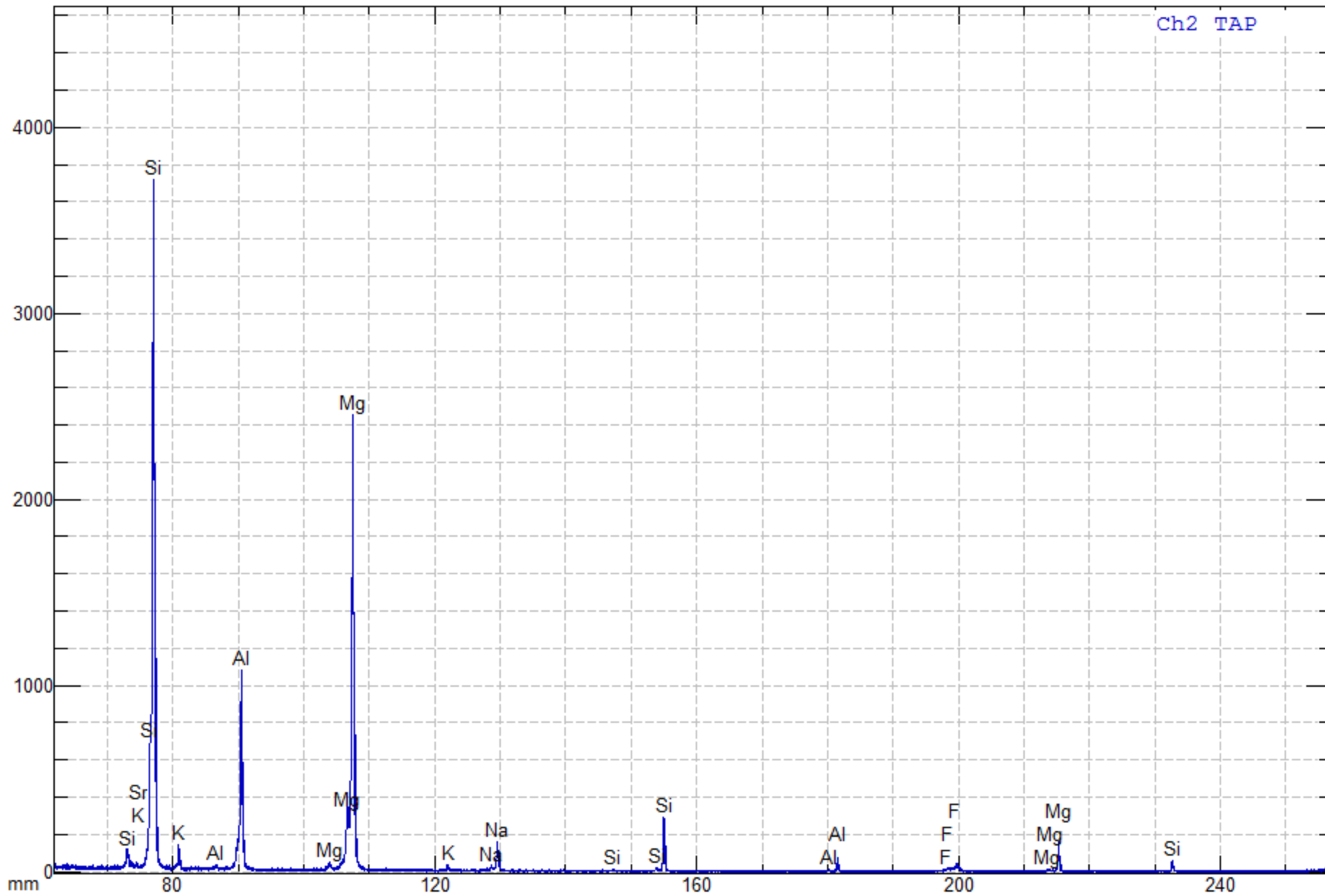
Path : D:\EPMA\_Data\Diego  
 NWA8173a\_mica\_Feb1\_2017  
 Feb 01 11:29 2017  
 Acc. V 15.0 kV  
 Prob C 5.005e-008 A

CH-4 PETH  
 Dwell (ms) 260  
 Max 2728



Path : D:\EPMA\_Data\Diego  
NWA8173a\_mica\_Feb1\_2017  
Feb 01 11:29 2017  
Acc. V 15.0 kV  
Prob C 5.005e-008 A

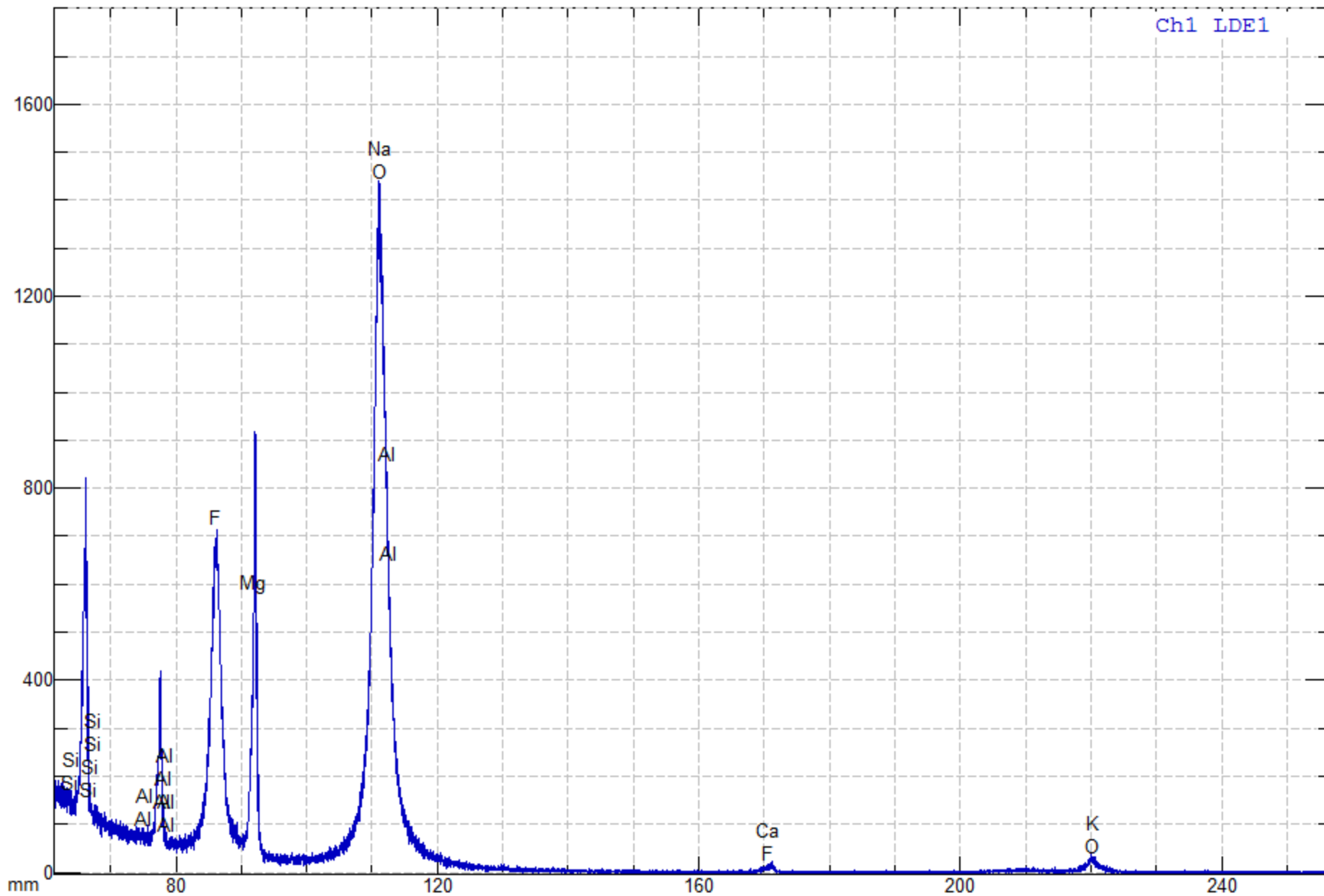
CH-3 PETJ  
Dwell (ms) 200  
Max 919



Path : D:\EPMA\_Data\Diego  
 NWA8173a\_mica\_Feb1\_2017  
 Feb 01 11:29 2017  
 Acc. V 15.0 kV  
 Prob C 5.005e-008 A

CH-2 TAP  
 Dwell (ms) 200  
 Max 3723





Path : D:\EPMA\_Data\Diego  
 NWA8173a\_mica\_Feb1\_2017  
 Feb 01 11:29 2017  
 Acc. V 15.0 kV  
 Prob C 5.005e-008 A

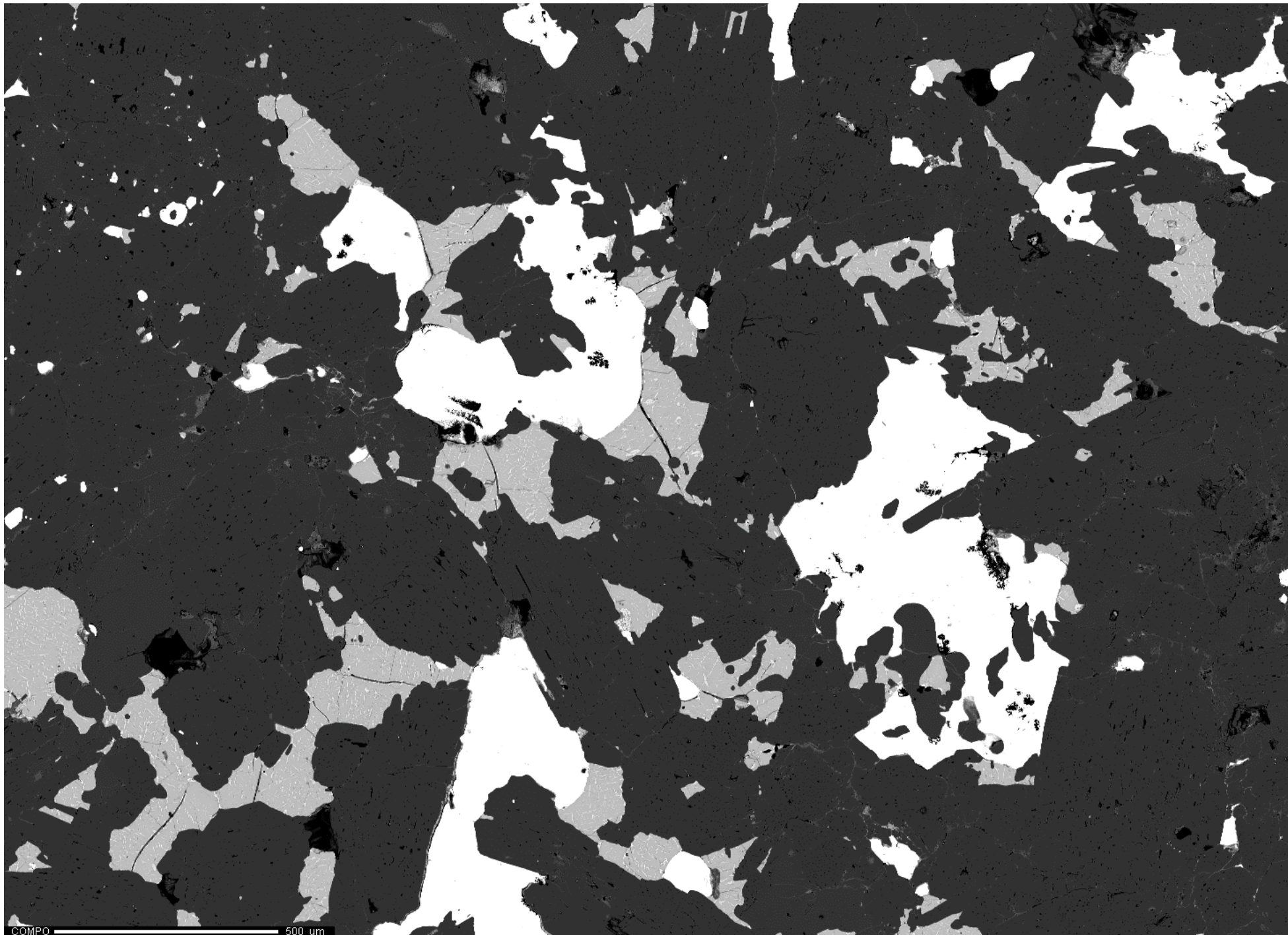
CH-1 LDE1  
 Dwell (ms) 200  
 Max 1442

# Appendix 2.4: Raman operating conditions

target	Expose time (s)	Laser power (%)	Spectral range	Total times (s)	mode
MICA-2	30	5	3000-4000	90	Static mode
MICA-3	45	10	100-4000	333	Continuous mode
MICA-4	30	10	3000-4000	30	Static mode

# Appendix 3.1

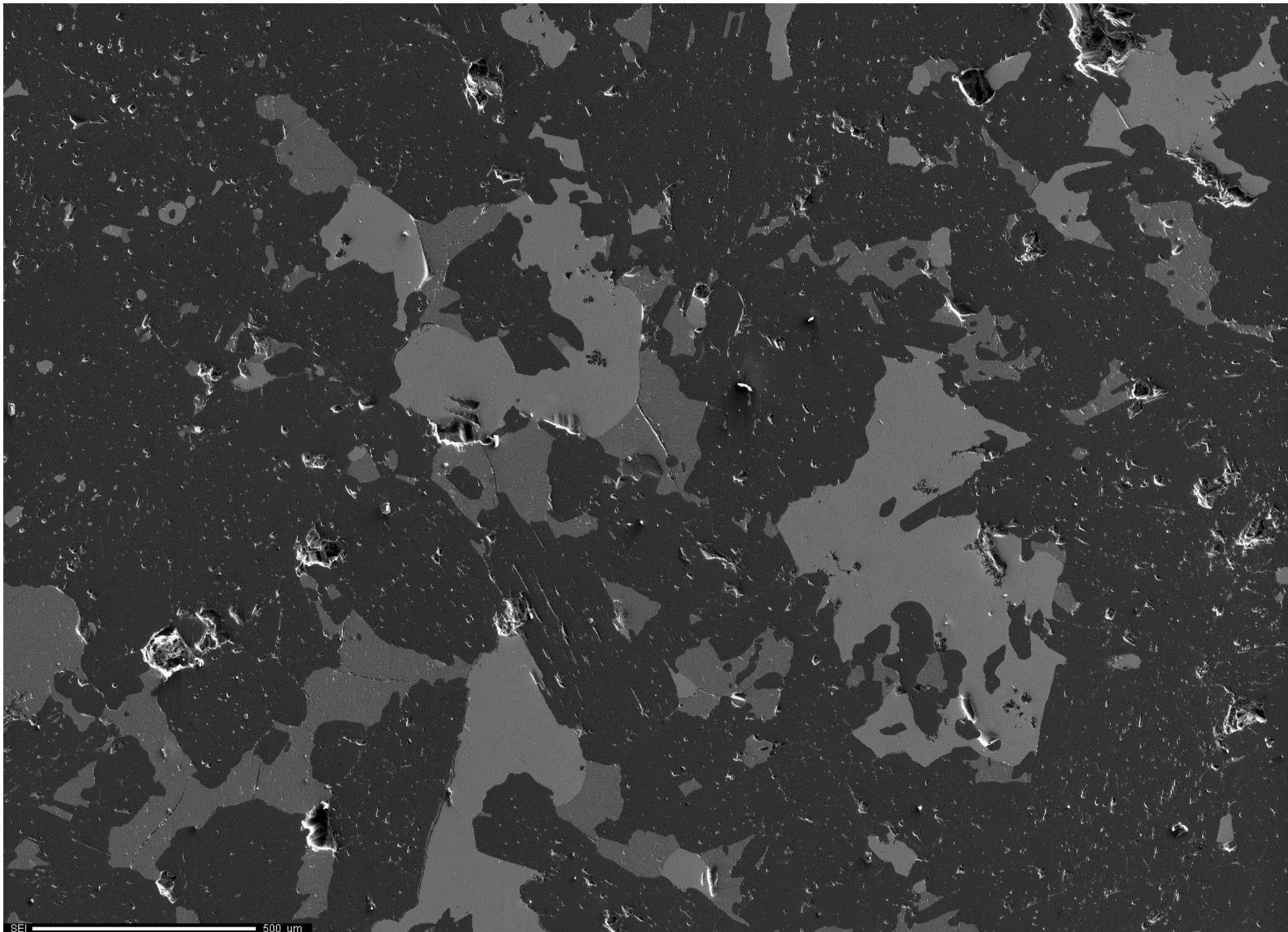
X-Ray Elemental Maps of NWA8173 a and b



Project: May\_2\_2016  
Comment: 8173a\_Fluorphlogopite\_map1\_2um  
Date: 2016/05/02  
Accel Voltage: 15.0 kV  
Beam Current: 9.958e-008 A  
Dwell Time: 10.0  
Image Size: 1469 x 1058

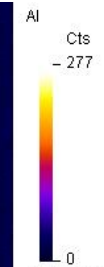
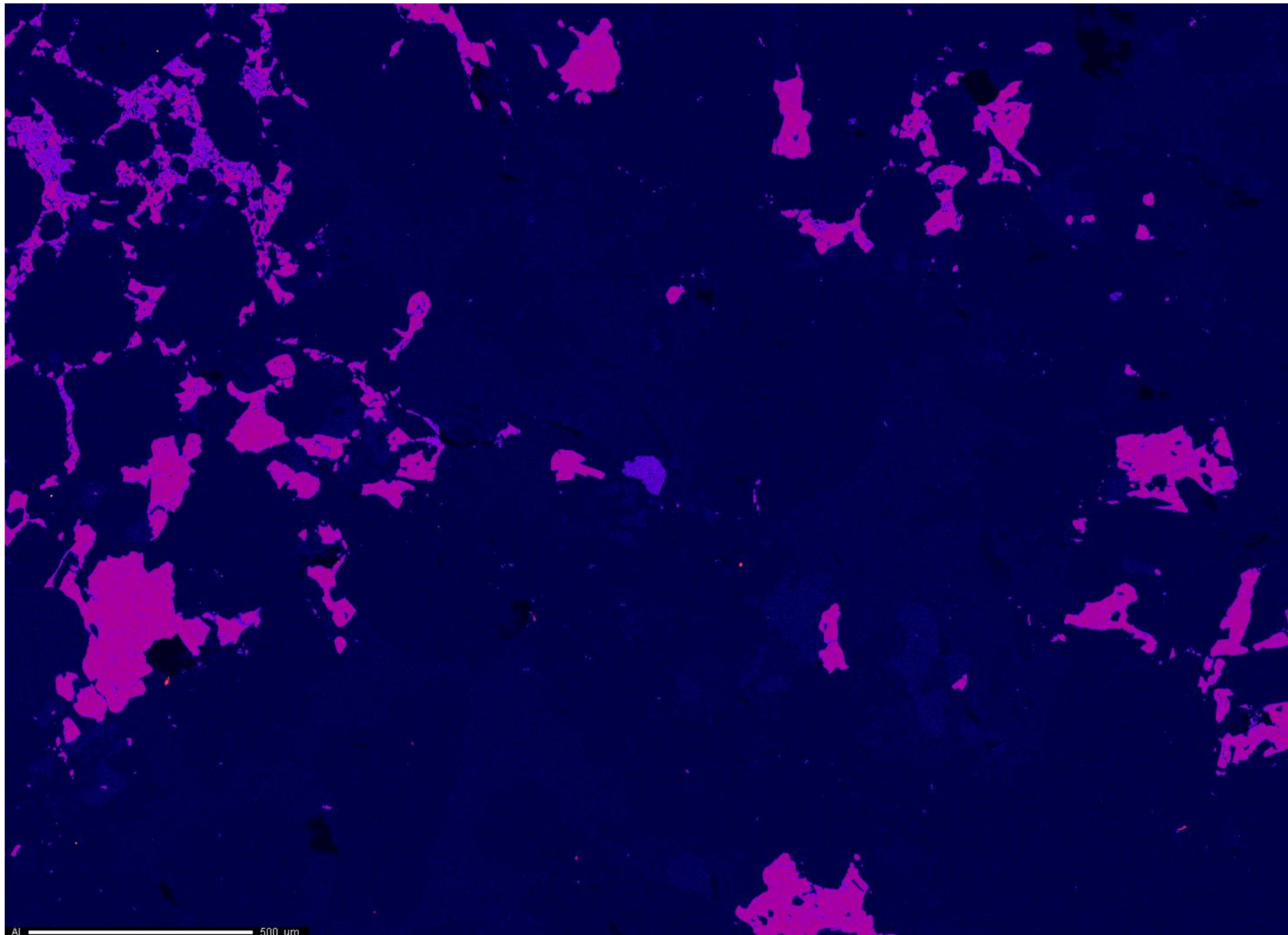
COMPO 500 um





SEI  
Cts  
- 4,095  
0  
Project: May\_2\_2016  
Comment: 8173a\_Fluorphlogopite\_map1\_2um  
Date: 2016/05/02  
Accel Voltage: 15.0 kV  
Beam Current: 9.958e-008 A  
Dwell Time: 10.0  
Image Size: 1469 x 1058

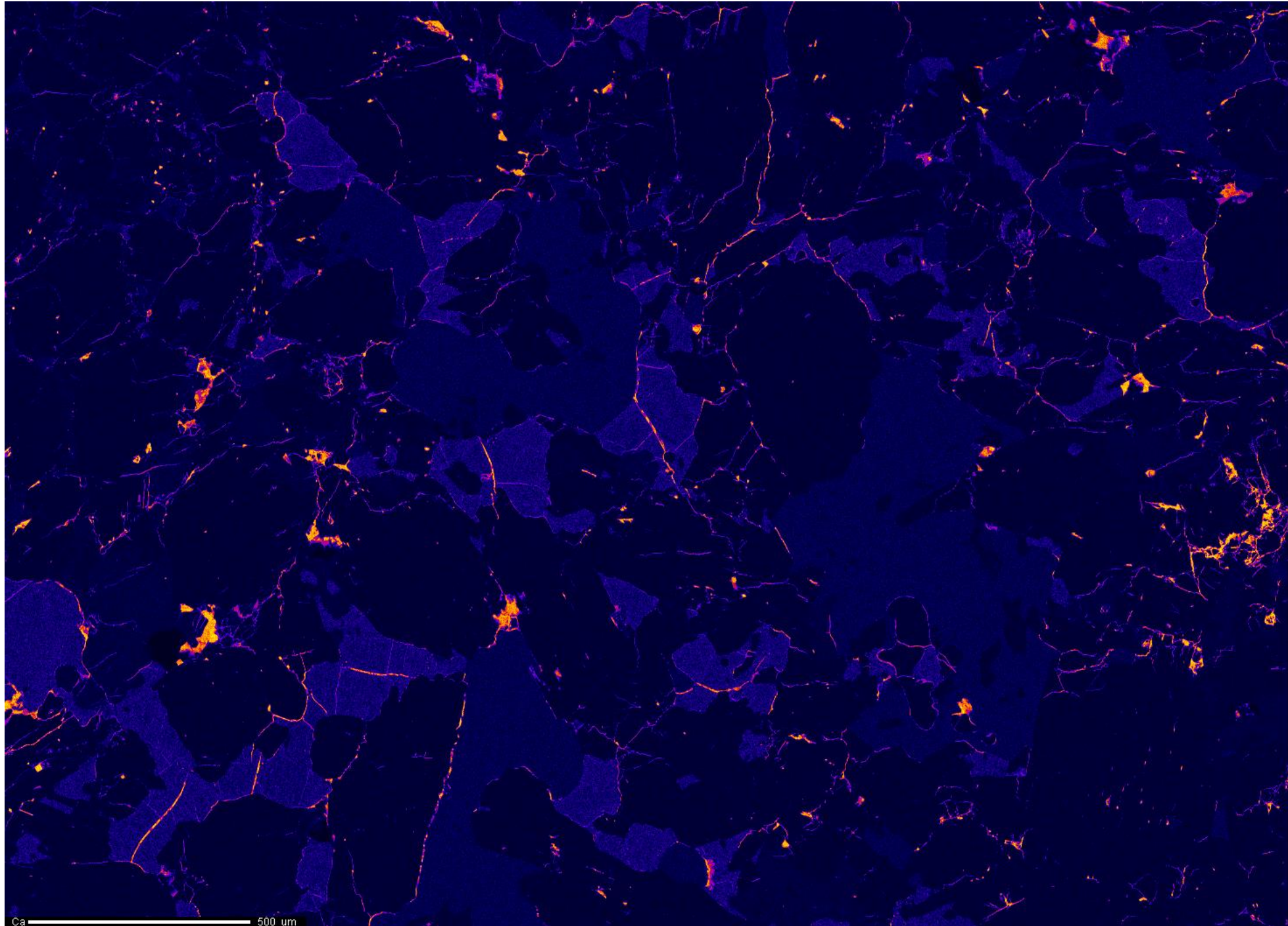




Project: May\_2\_2016  
Comment: 8173a\_Fluorhlogopite\_map1\_2um  
Date: 2016/05/02  
Accel Voltage: 15.0 kV  
Beam Current: 4.995e-008 A  
Dwell Time: 10.0  
Image Size: 1469 x 1058

Al 500 um



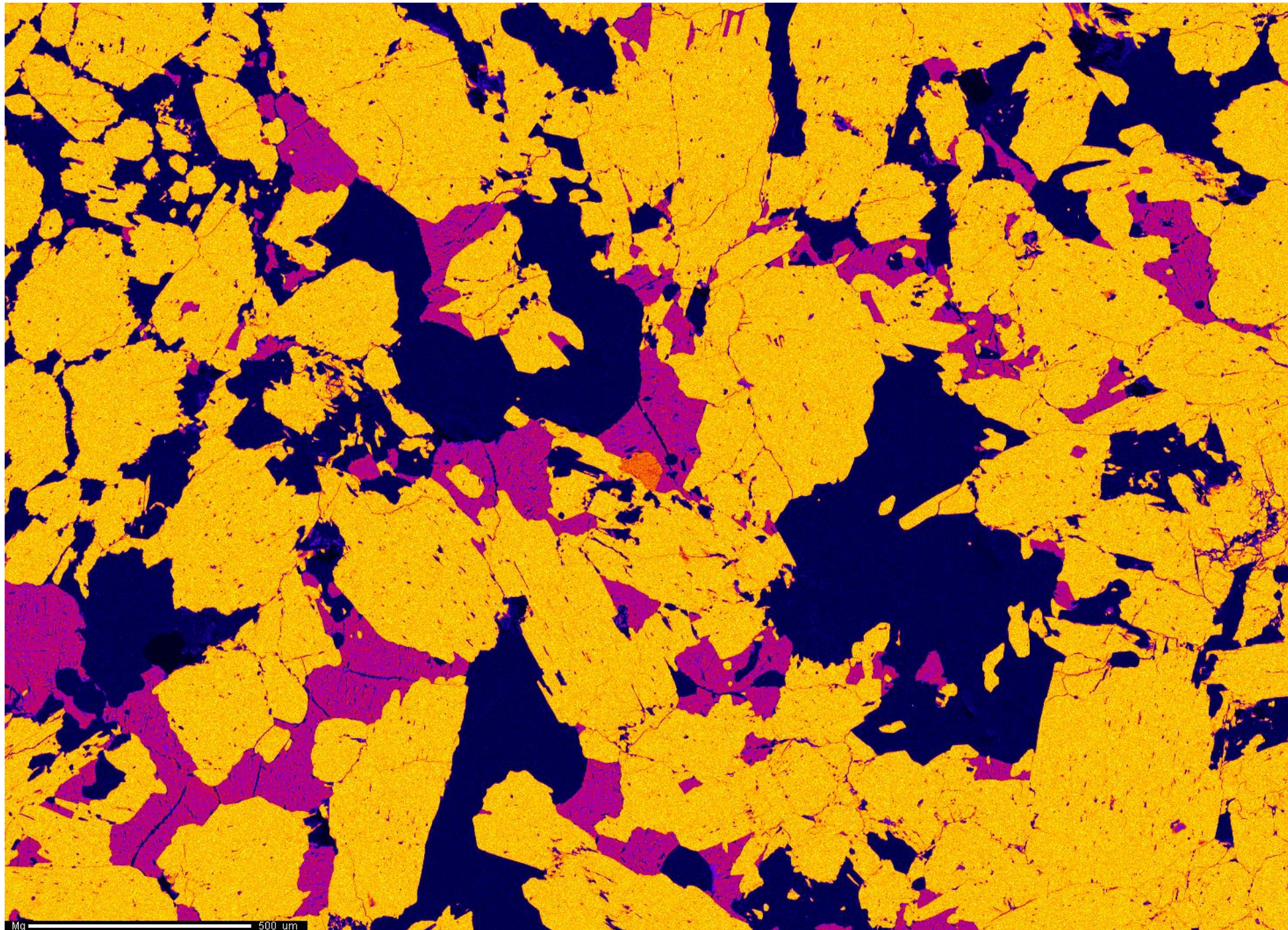


Ca  
Cts  
- 224  
0

Project: May\_2\_2016  
Comment: 8173a\_Fluorphlogopite\_map1\_2um  
Date: 2016/05/02  
Accel Voltage: 15.0 kV  
Beam Current: 4.995e-008 A  
Dwell Time: 10.0  
Image Size: 1469 x 1058

Ca 500 um

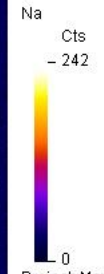
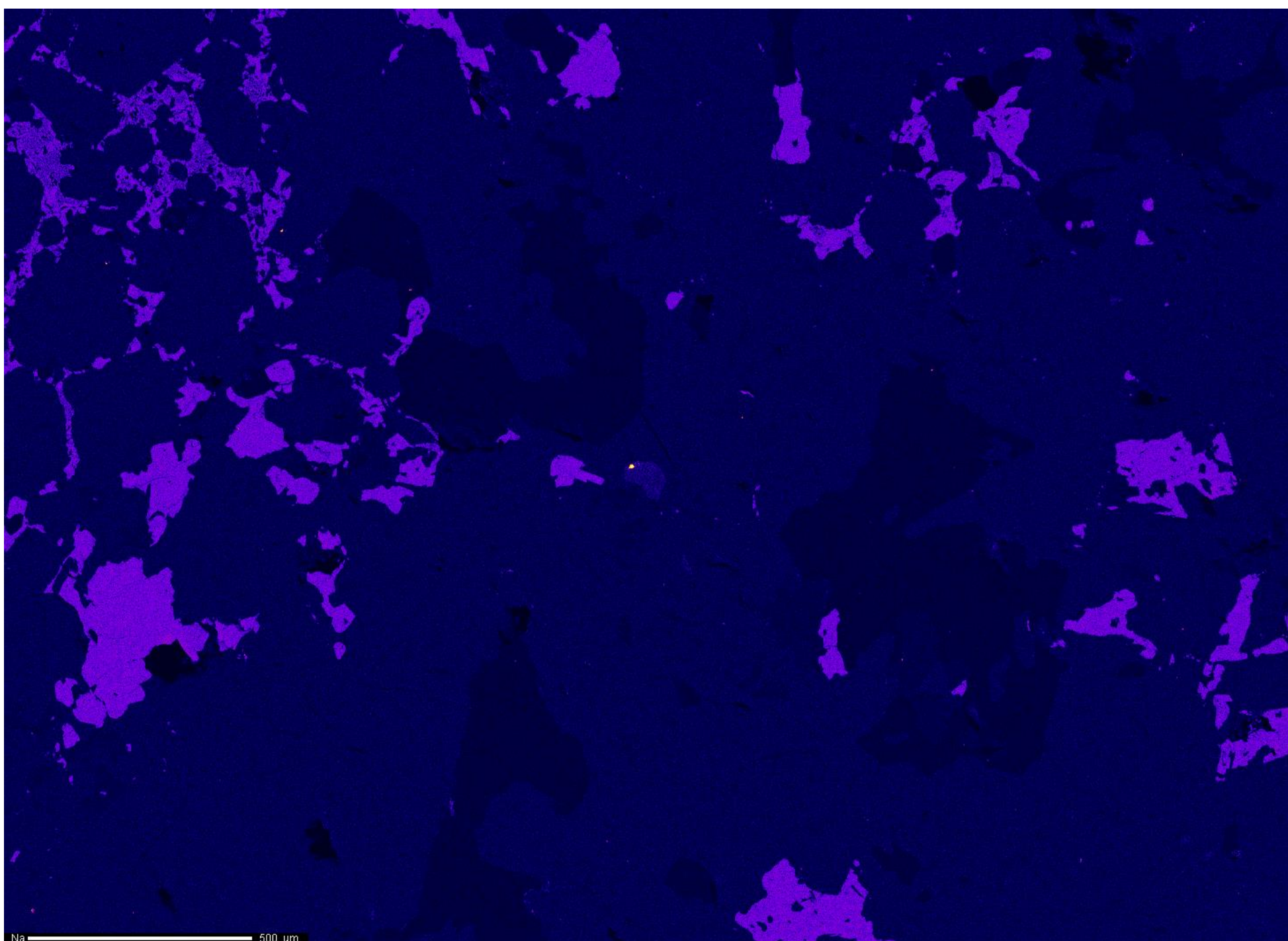




Mg  
Cts  
- 237  
0  
Project: May\_2\_2016  
Comment: 8173a\_Fluorphlogopite\_map1\_2um  
Date: 2016/05/02  
Accel Voltage: 15.0 kV  
Beam Current: 4.995e-008 A  
Dwell Time: 10.0  
Image Size: 1469 x 1058

Mg 500 um

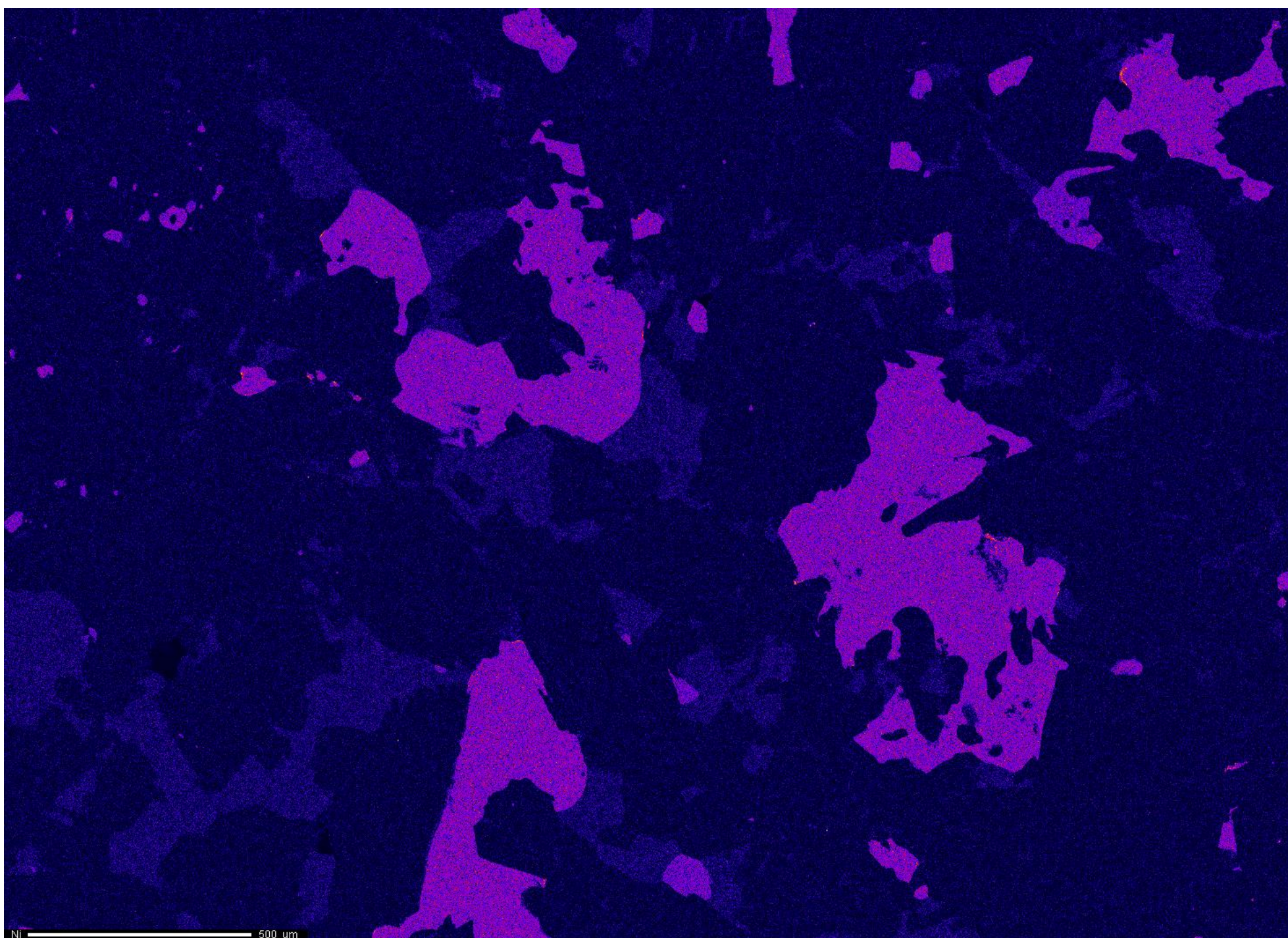




Project: May\_2\_2016  
Comment: 8173a\_Fluorphlogopite\_map1\_2um  
Date: 2016/05/02  
Accel Voltage: 15.0 kV  
Beam Current: 4.995e-008 A  
Dwell Time: 10.0  
Image Size: 1469 x 1058

Na  500 um

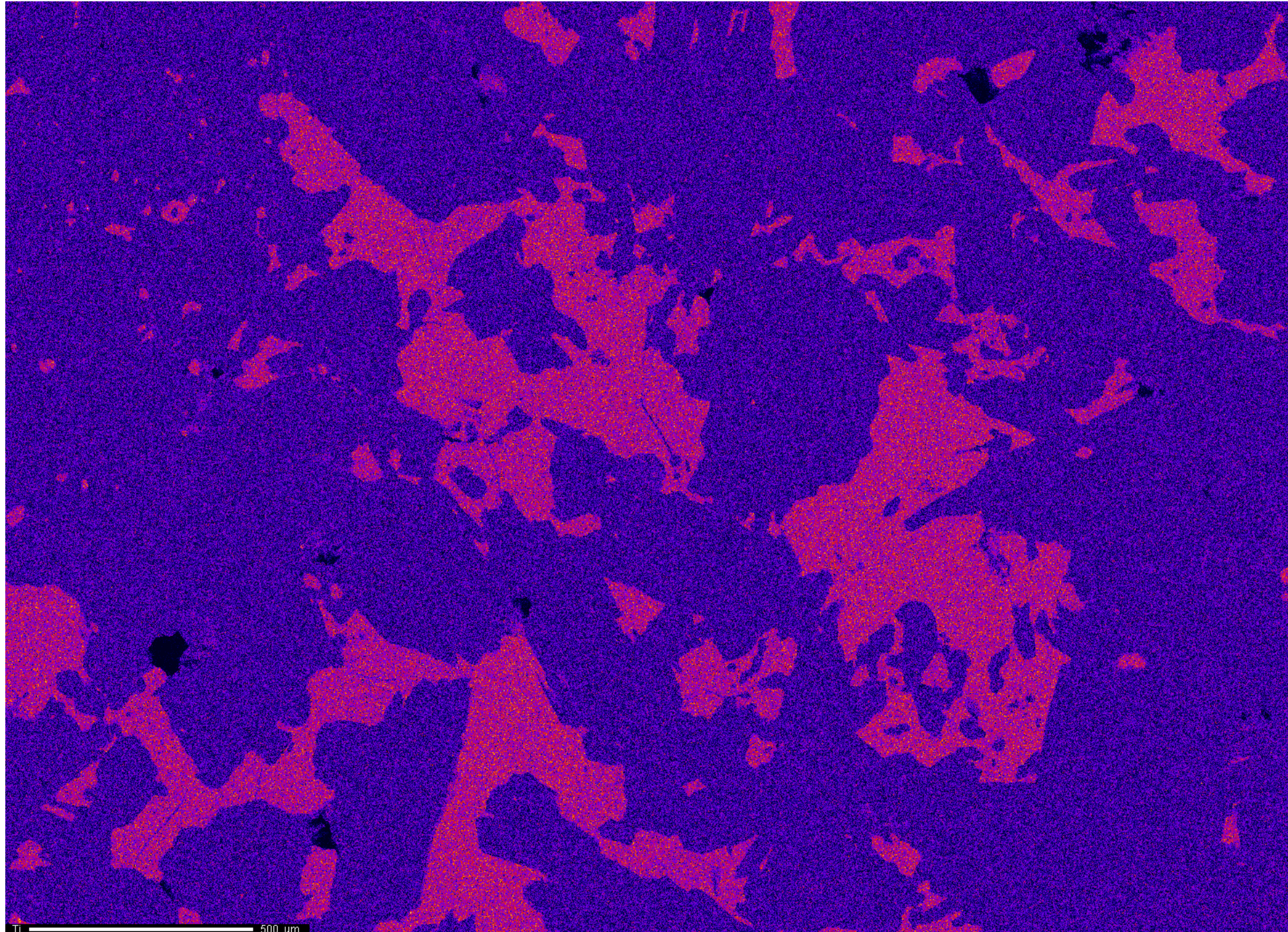




Ni  
Cts  
- 43  
0  
Project: May\_2\_2016  
Comment: 8173a\_Fluorophlogopite\_map1\_2um  
Date: 2016/05/02  
Accel Voltage: 15.0 kV  
Beam Current: 4.995e-008 A  
Dwell Time: 10.0  
Image Size: 1469 x 1058

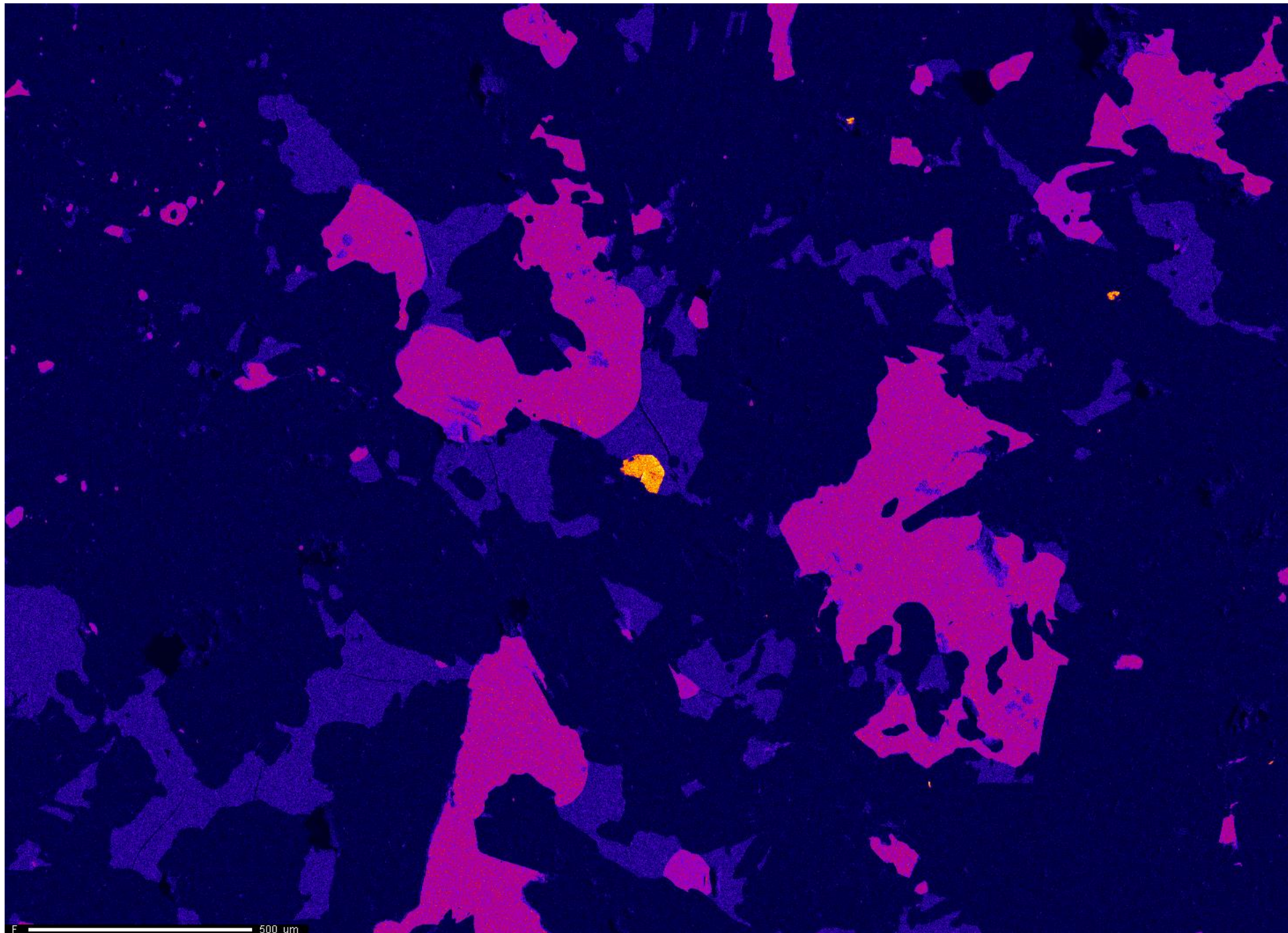
Ni 500 um





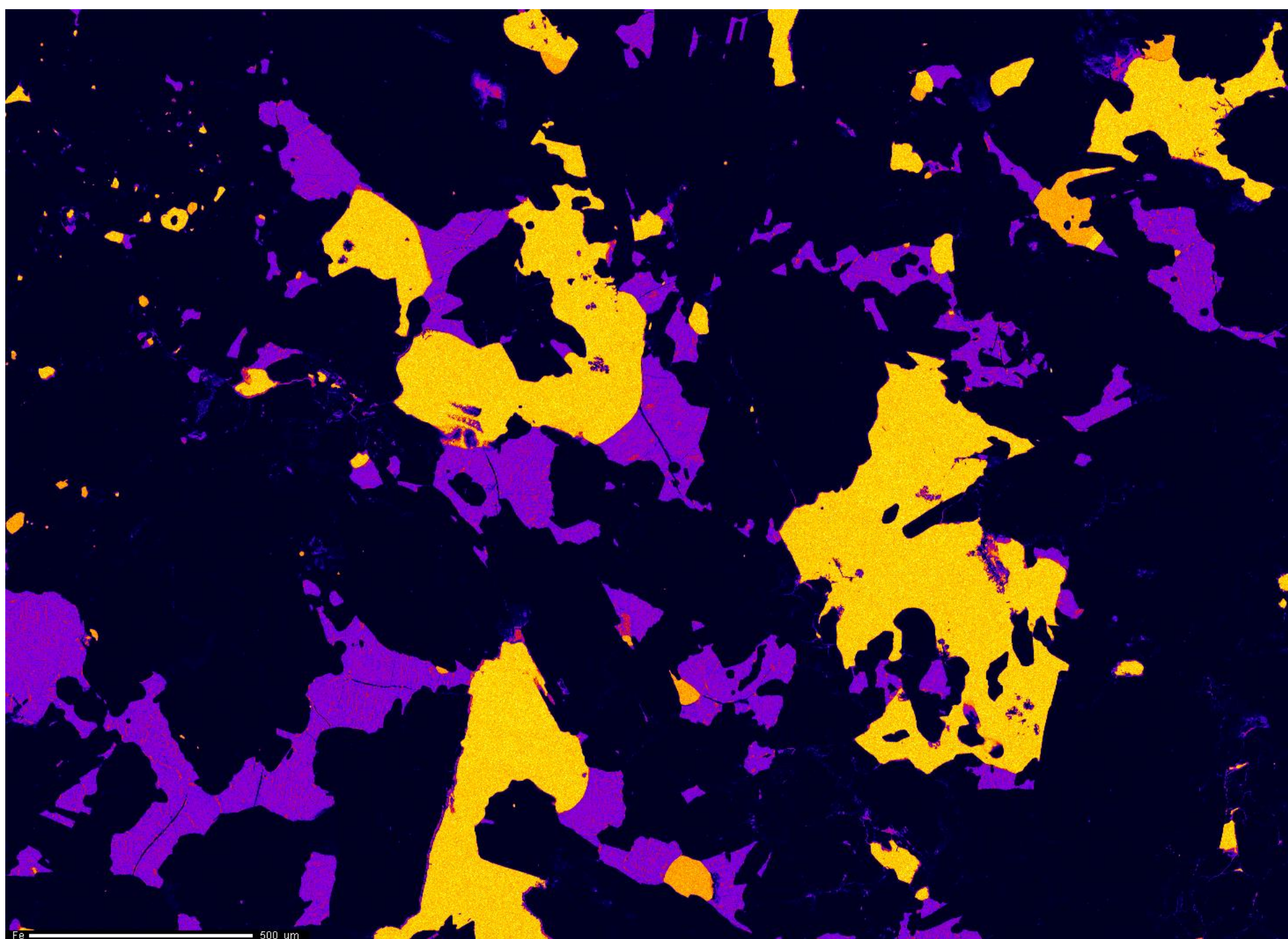
Ti  
Cts  
- 28  
0  
Project: May\_2\_2016  
Comment: 8173a\_Fluorphlogopite\_map1\_2um  
Date: 2016/05/02  
Accel Voltage: 15.0 kV  
Beam Current: 4.995e-008 A  
Dwell Time: 10.0  
Image Size: 1469 x 1058





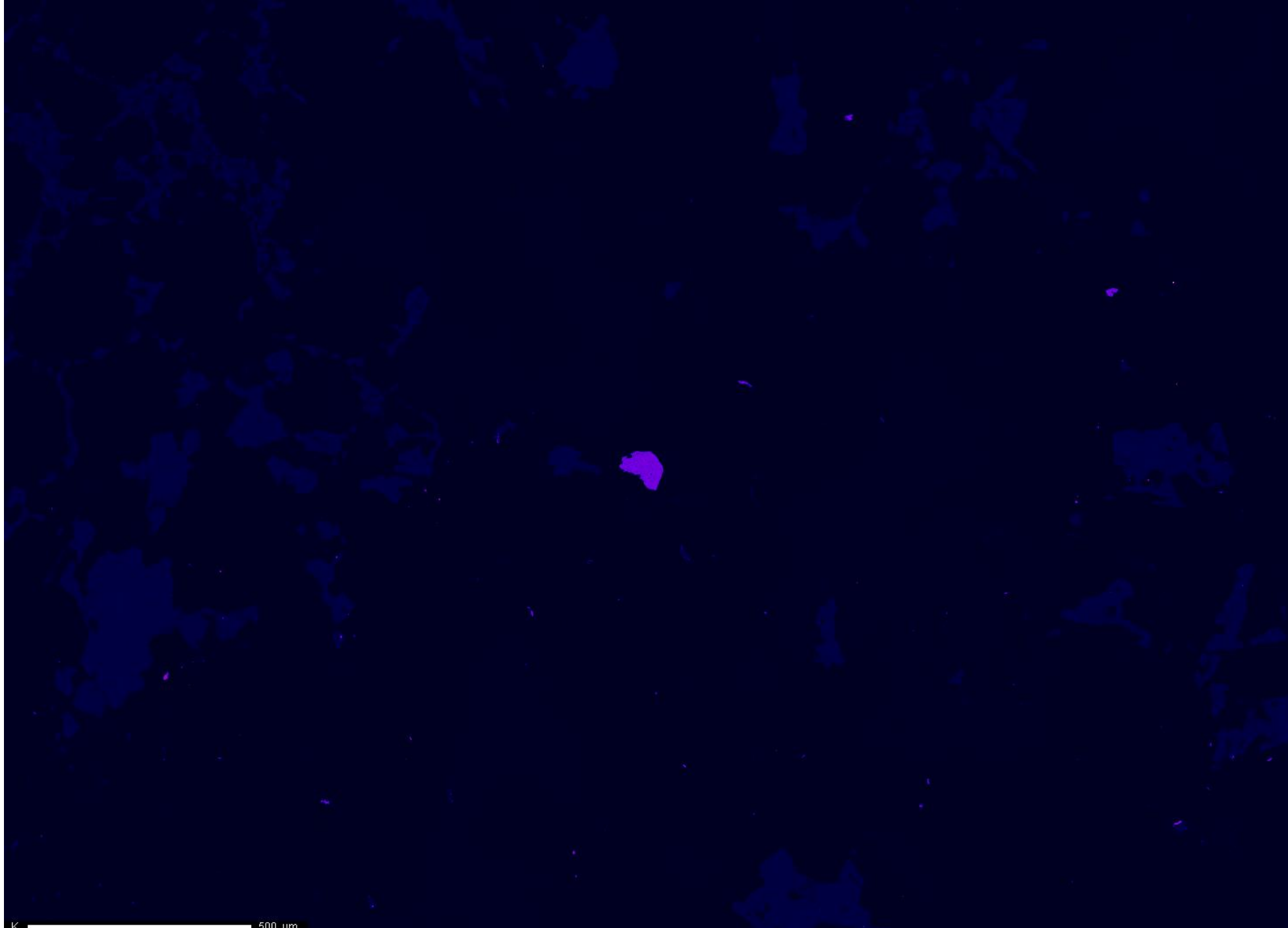
Project: May\_2\_2016  
Comment: 8173a\_Fluorophlogopite\_map1\_2um  
Date: 2016/05/02  
Accel Voltage: 15.0 kV  
Beam Current: 9.958e-008 A  
Dwell Time: 10.0  
Image Size: 1469 x 1058





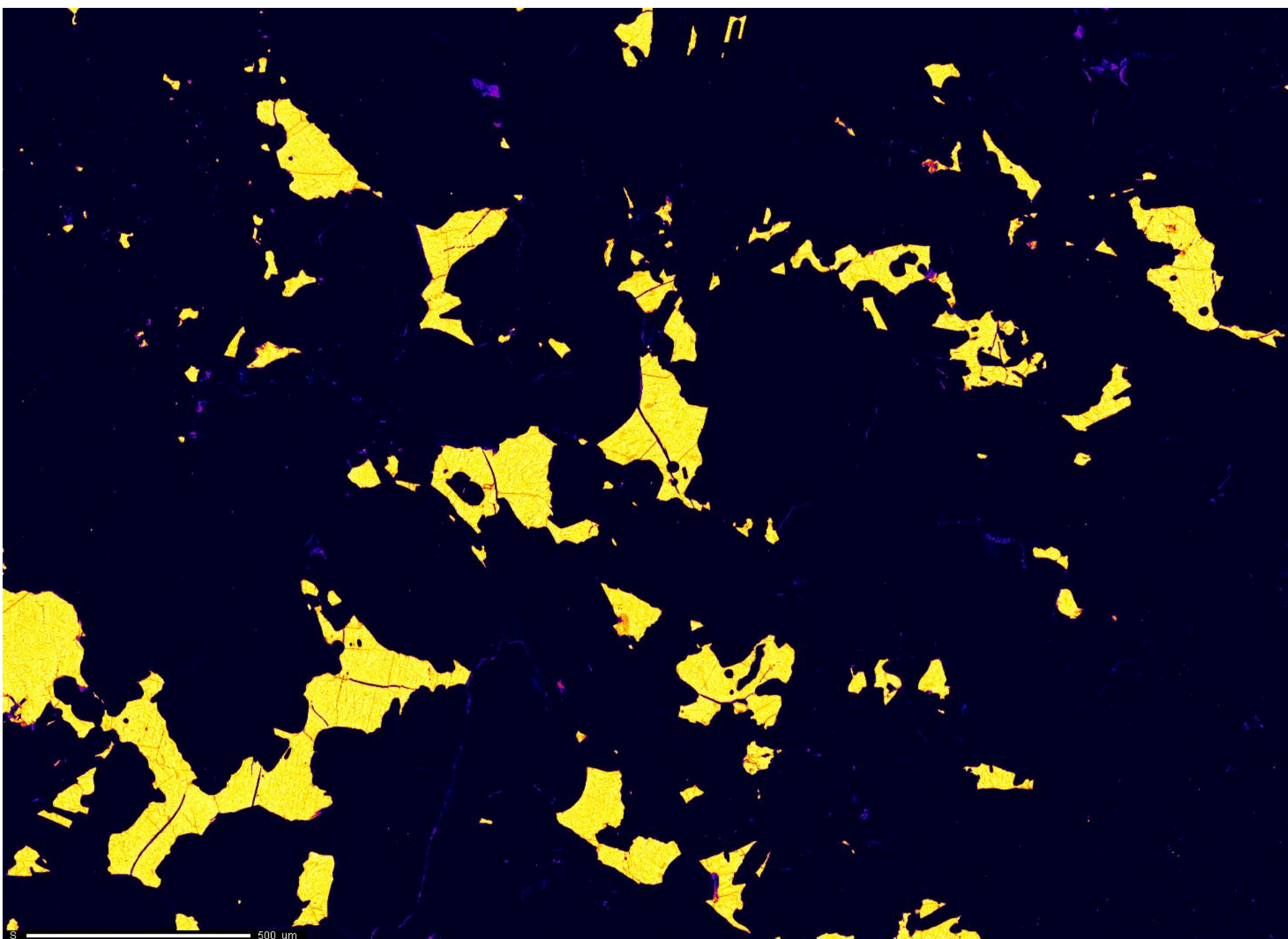
Project: May\_2\_2016  
Comment: 8173a\_Fluorphlogopite\_map1\_2um  
Date: 2016/05/02  
Accel Voltage: 15.0 kV  
Beam Current: 9.958e-008 A  
Dwell Time: 10.0  
Image Size: 1469 x 1058

Fe 500 um



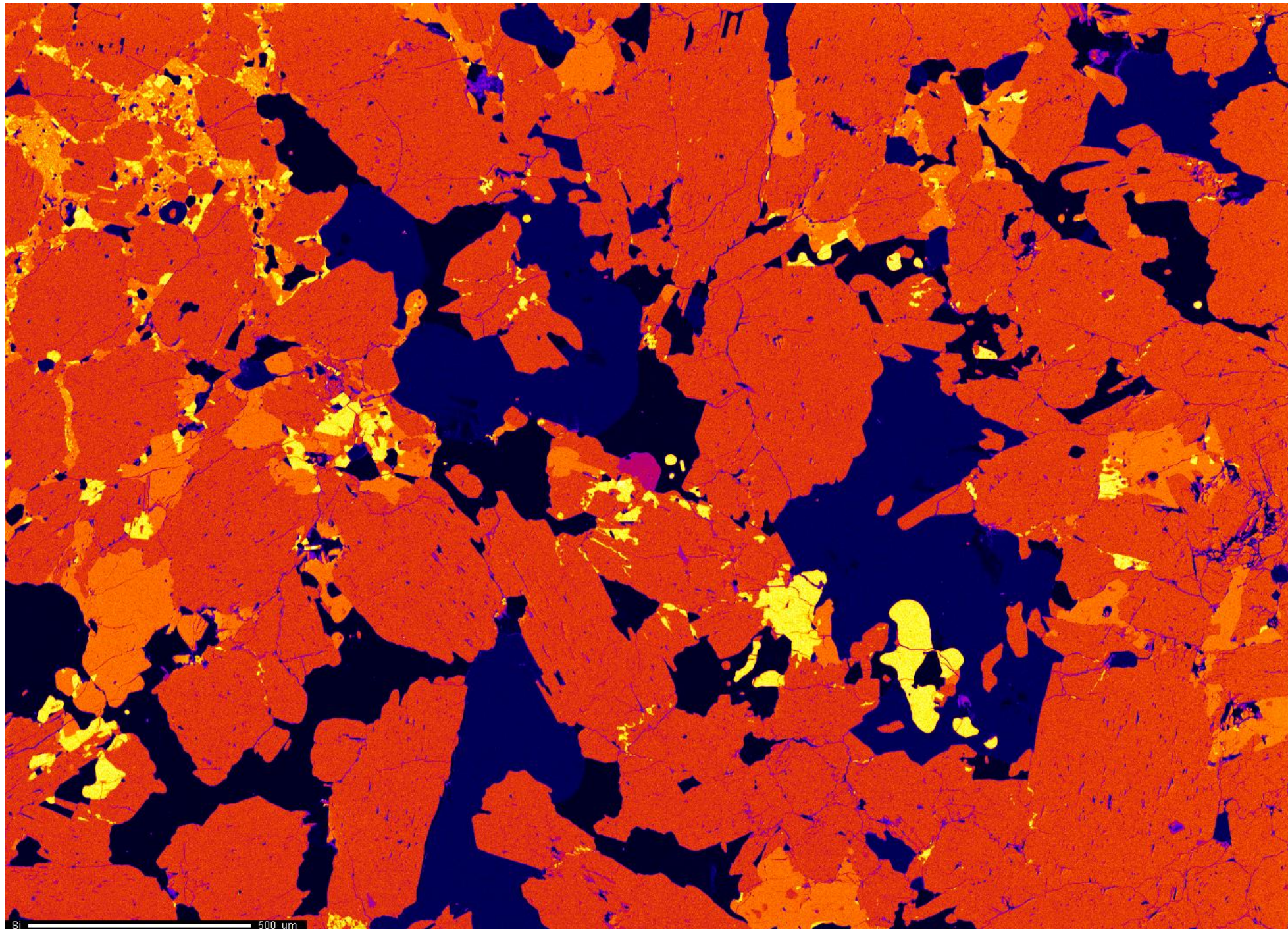
K  
Cts  
- 712  
0  
Project: May\_2\_2016  
Comment: 8173a\_Fluorphlogopite\_map1\_2um  
Date: 2016/05/02  
Accel Voltage: 15.0 kV  
Beam Current: 9.958e-008 A  
Dwell Time: 10.0  
Image Size: 1469 x 1058

K 500 um



S  
Cts  
- 888  
0  
Project: May\_2\_2016  
Comment: 8173a\_Fluorophlogopite\_map1\_2um  
Date: 2016/05/02  
Accel Voltage: 15.0 kV  
Beam Current: 9.958e-008 A  
Dwell Time: 10.0  
Image Size: 1469 x 1058

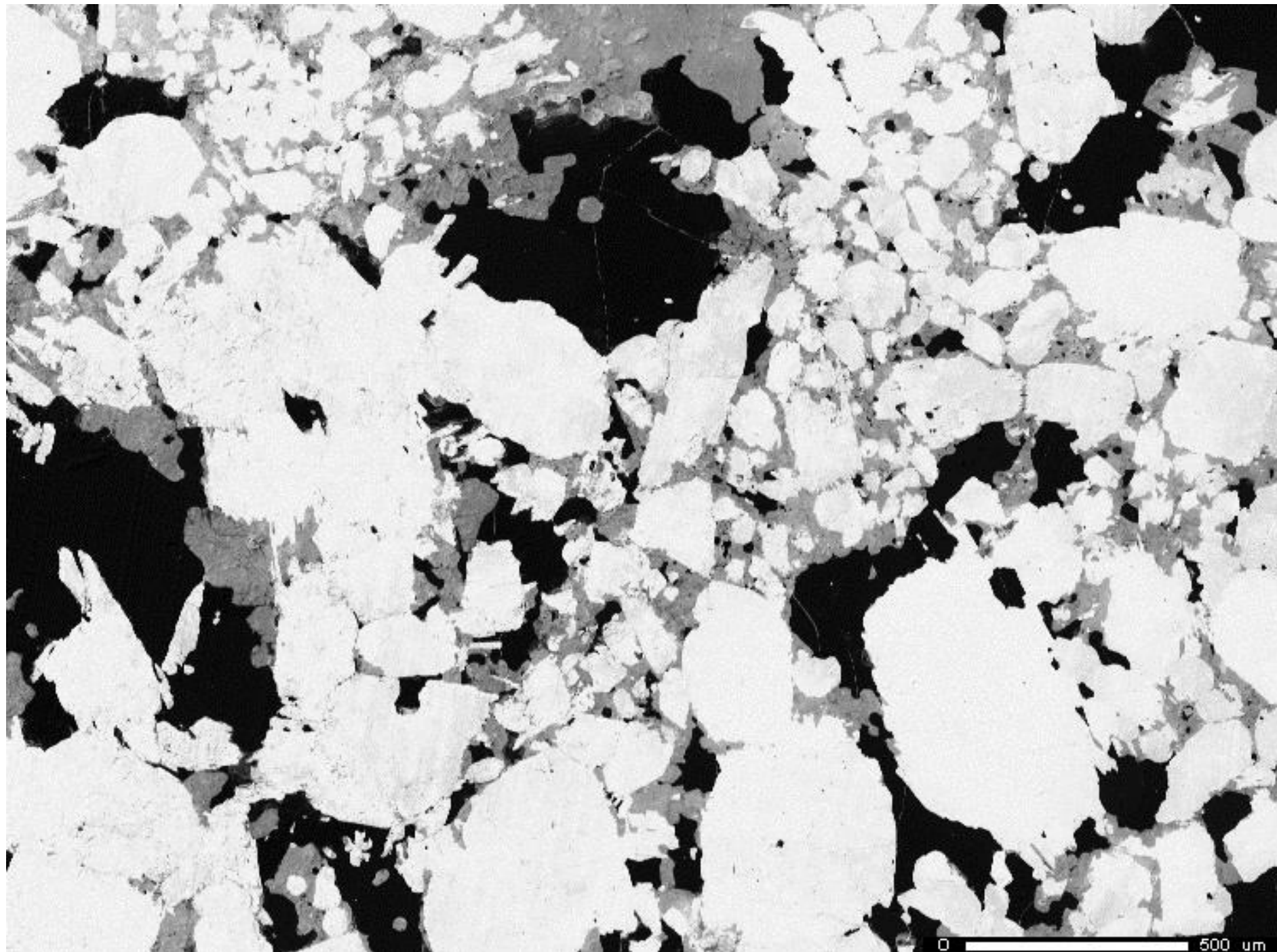




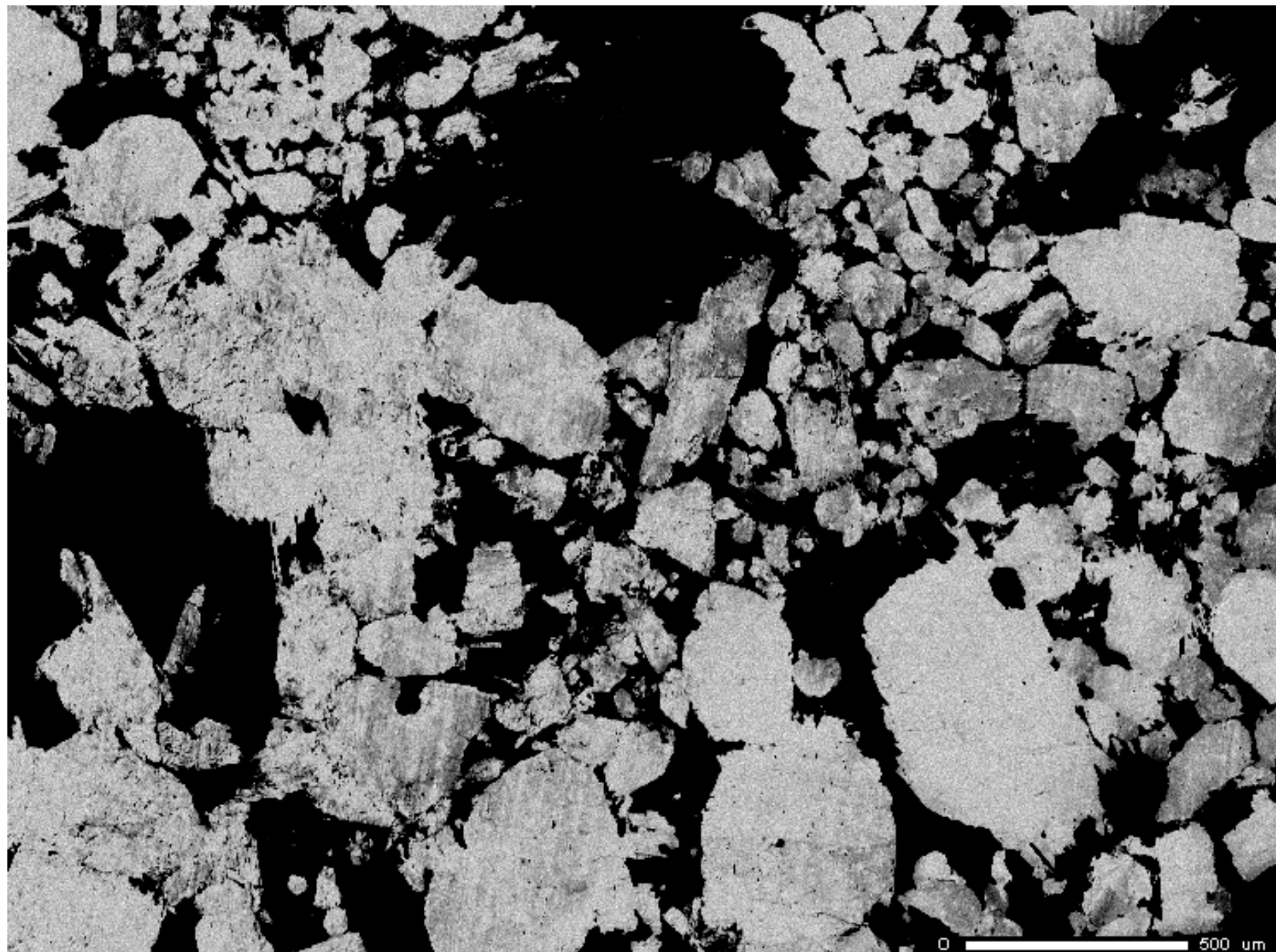
Si  
Cts  
- 932  
0

Project: May\_2\_2016  
Comment: 8173a\_Fluorphlogopite\_map1\_2um  
Date: 2016/05/02  
Accel Voltage: 15.0 kV  
Beam Current: 9.958e-008 A  
Dwell Time: 10.0  
Image Size: 1469 x 1058



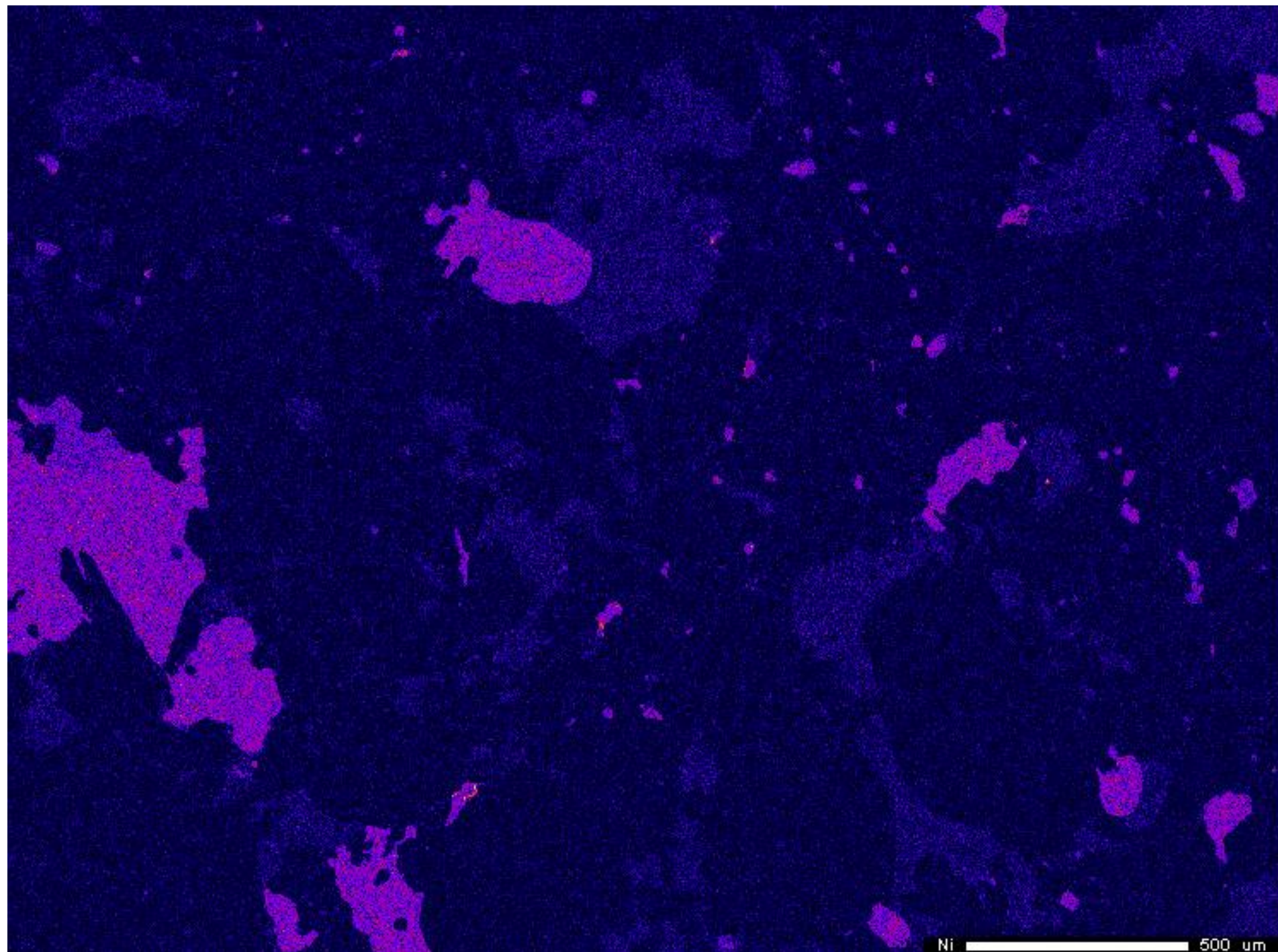


Project: June\_16\_2015  
Comment: NWA8173\_map01\_4um  
Date: 2015/06/17  
Accel Voltage: 15.0 kV  
Beam Current: 9.967e-008 A  
Dwell Time: 10.0  
Image Size: 746 x 555



Project: June\_16\_2015  
Comment: NWA8173\_map01\_4um  
Date: 2015/06/17  
Accel Voltage: 15.0 kV  
Beam Current: 9.967e-008 A  
Dwell Time: 10.0  
Image Size: 746 x 555

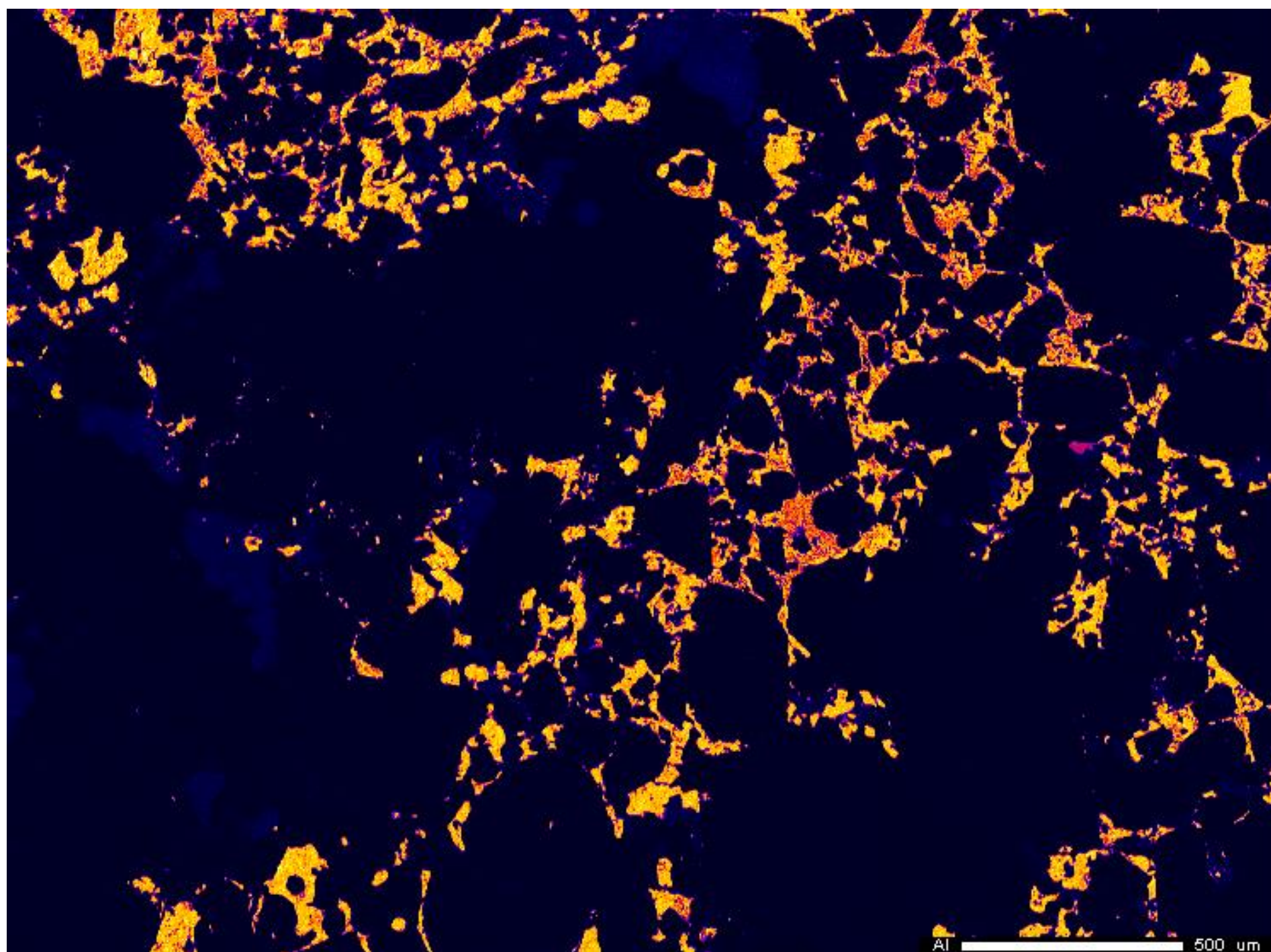




Project: June\_16\_2015  
Comment: NWA8173\_map01\_4um  
Date: 2015/06/17  
Accel Voltage: 15.0 kV  
Beam Current: 5.003e-008 A  
Dwell Time: 10.0  
Image Size: 746 x 555

Ni 500 um

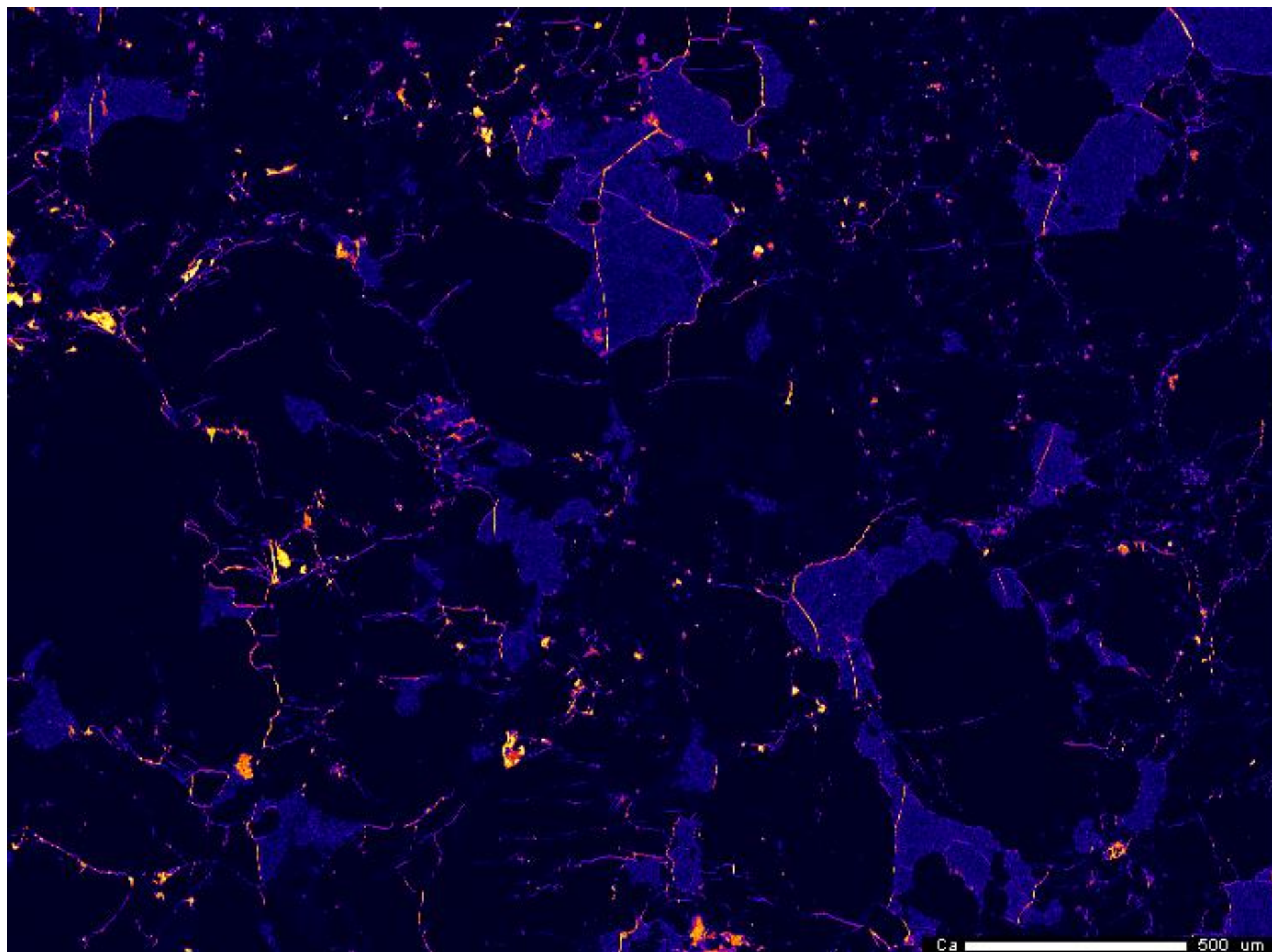




Project: June\_16\_2015  
Comment: NWA8173\_map01\_4um  
Date: 2015/06/17  
Accel Voltage: 15.0 kV  
Beam Current: 9.967e-008 A  
Dwell Time: 10.0  
Image Size: 746 x 555

Al 500 um

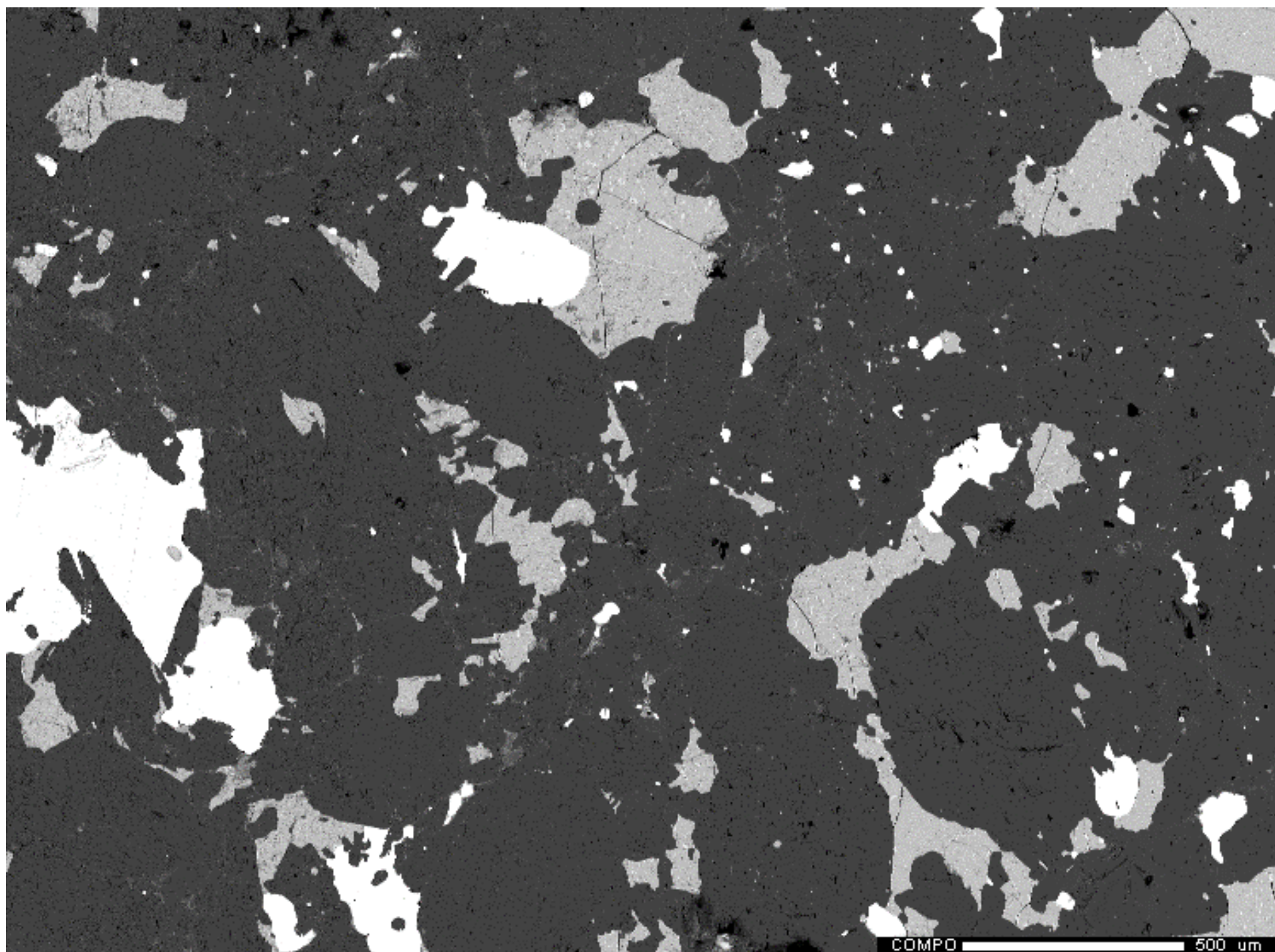




Project: June\_16\_2015  
Comment: NWA8173\_map01\_4um  
Date: 2015/06/17  
Accel Voltage: 15.0 kV  
Beam Current: 9.967e-008 A  
Dwell Time: 10.0  
Image Size: 746 x 555

Ca 500 um

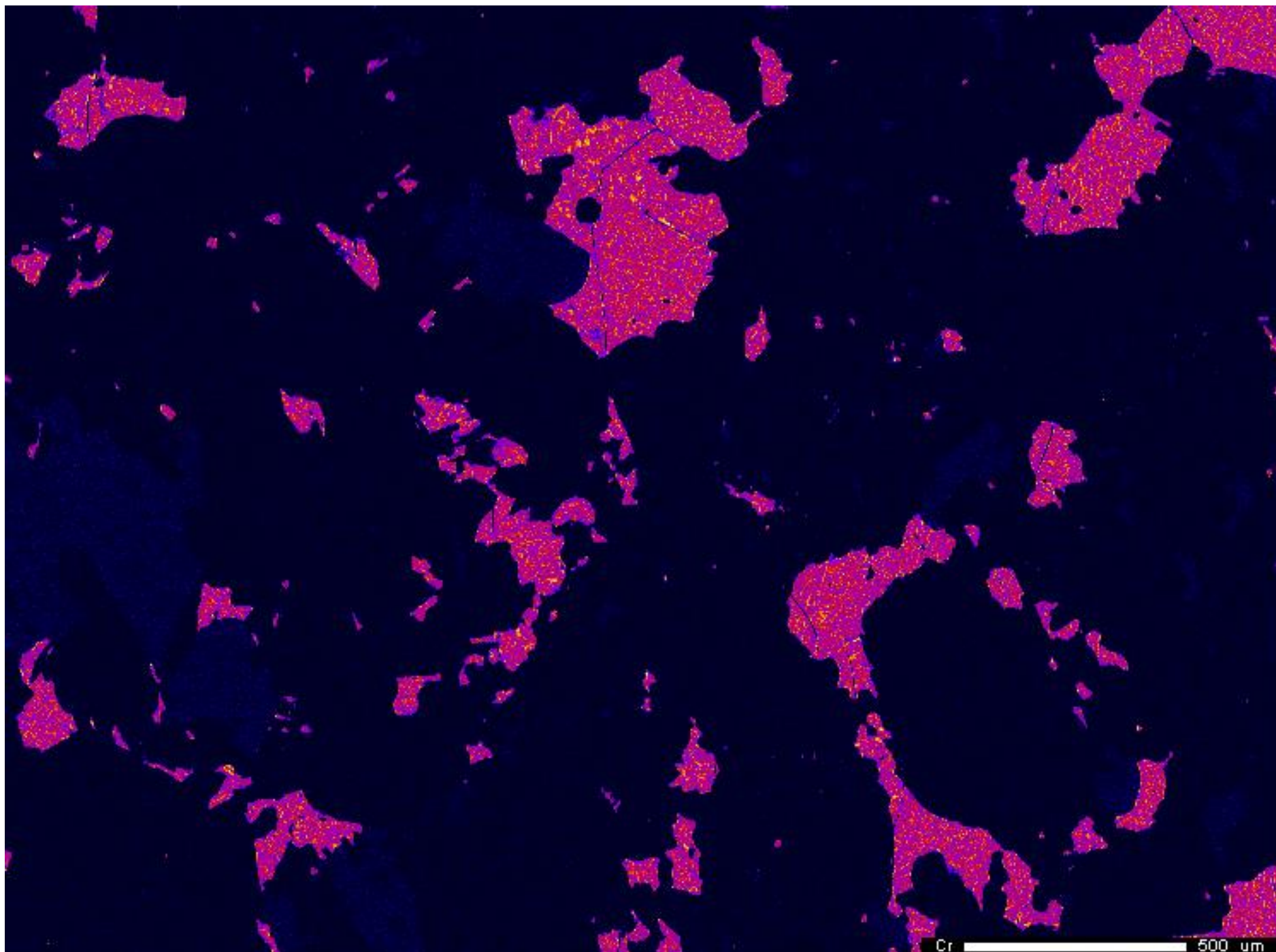




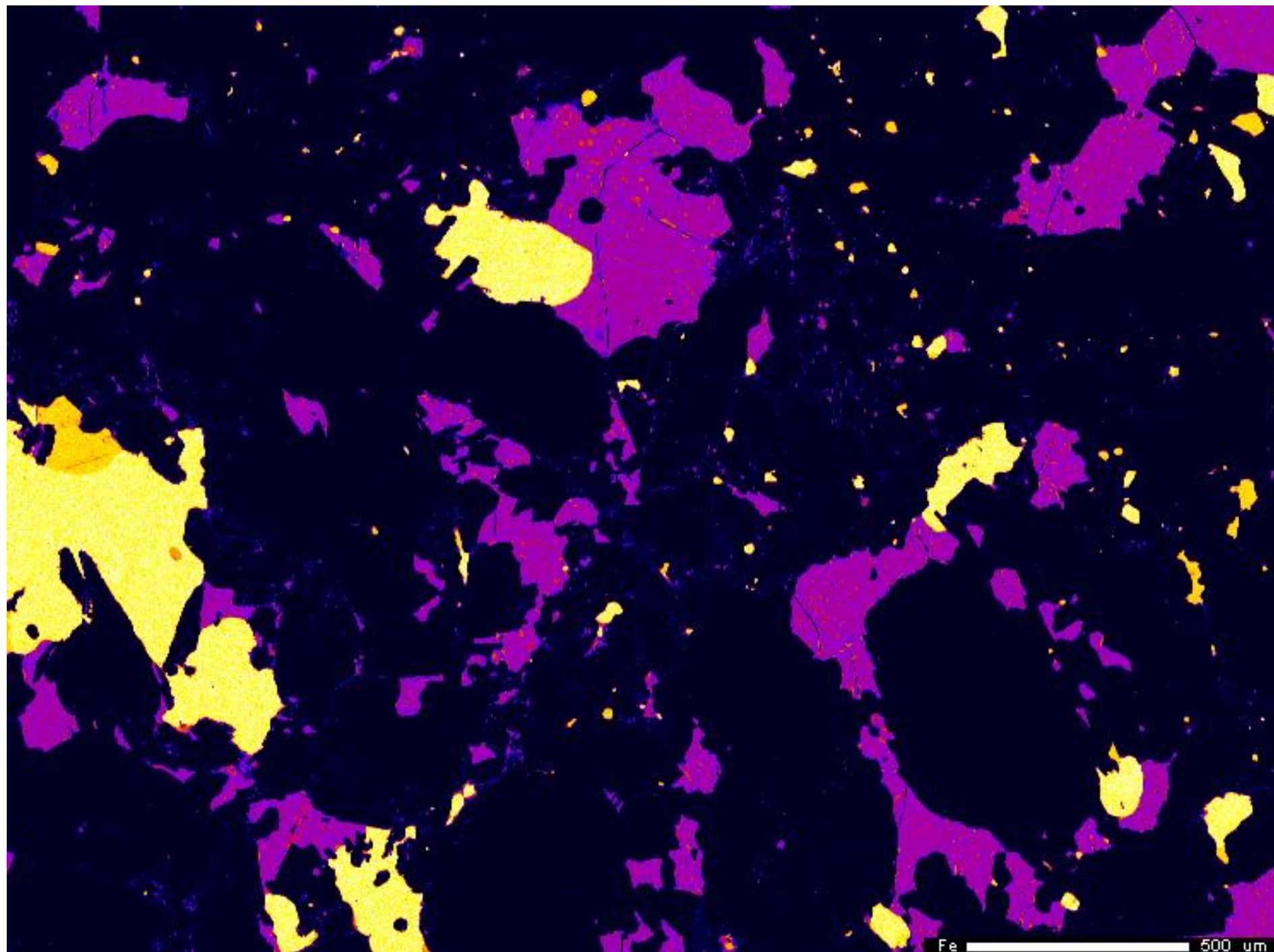
Project: June\_16\_2015  
Comment: NWA8173\_map01\_4um  
Date: 2015/06/17  
Accel Voltage: 15.0 kV  
Beam Current: 9.967 e-008 A  
Dwell Time: 10.0  
Image Size: 746 x 555

COMPO 500 um





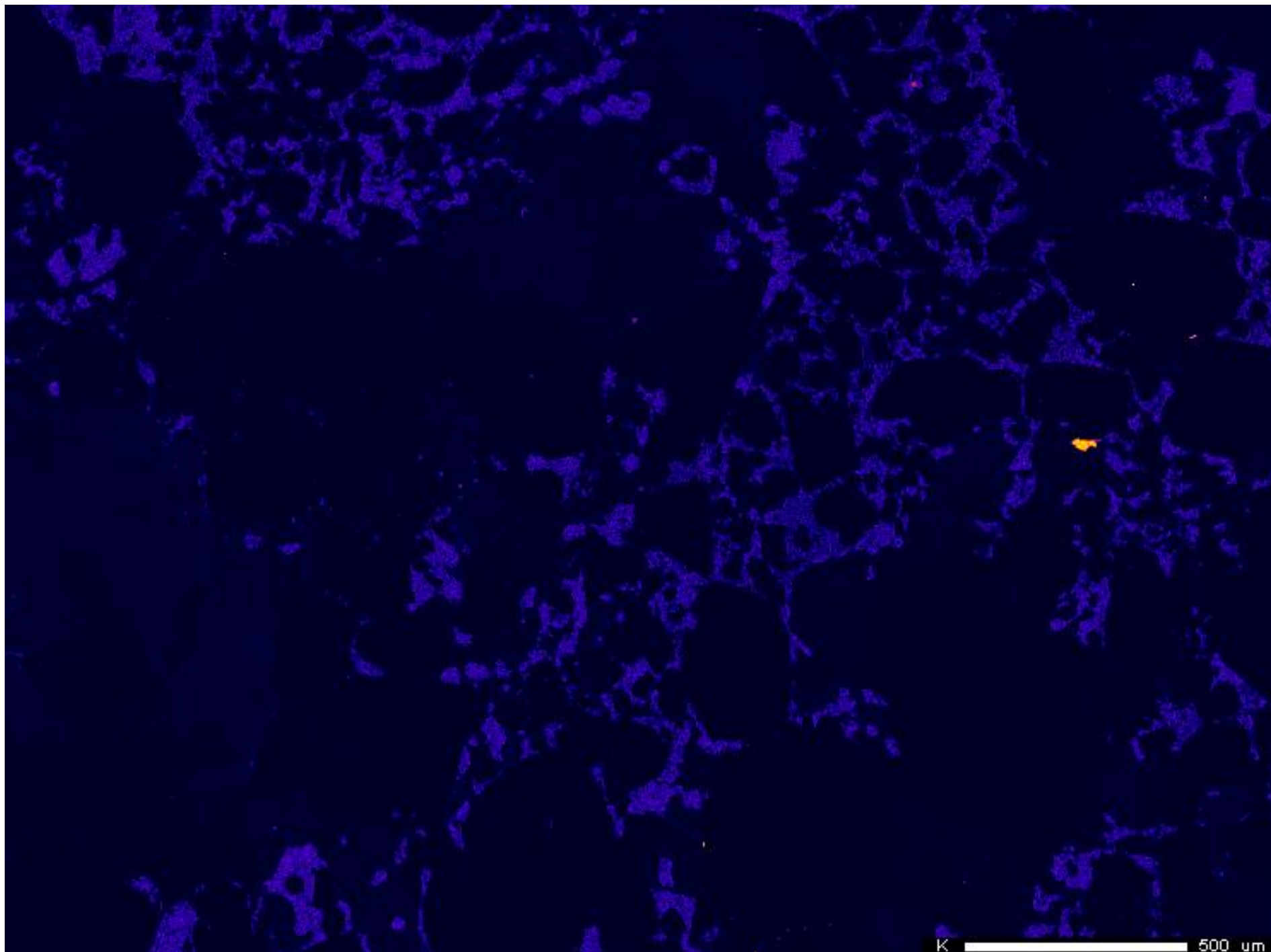
Project: June\_16\_2015  
Comment: NWA8173\_map01\_4um  
Date: 2015/06/17  
Accel Voltage: 15.0 kV  
Beam Current: 9.967e-008 A  
Dwell Time: 10.0  
Image Size: 746 x 555



Project: June\_16\_2015  
Comment: NWA8173\_map01\_4um  
Date: 2015/06/17  
Accel Voltage: 15.0 kV  
Beam Current: 9.967e-008 A  
Dwell Time: 10.0  
Image Size: 746 x 555

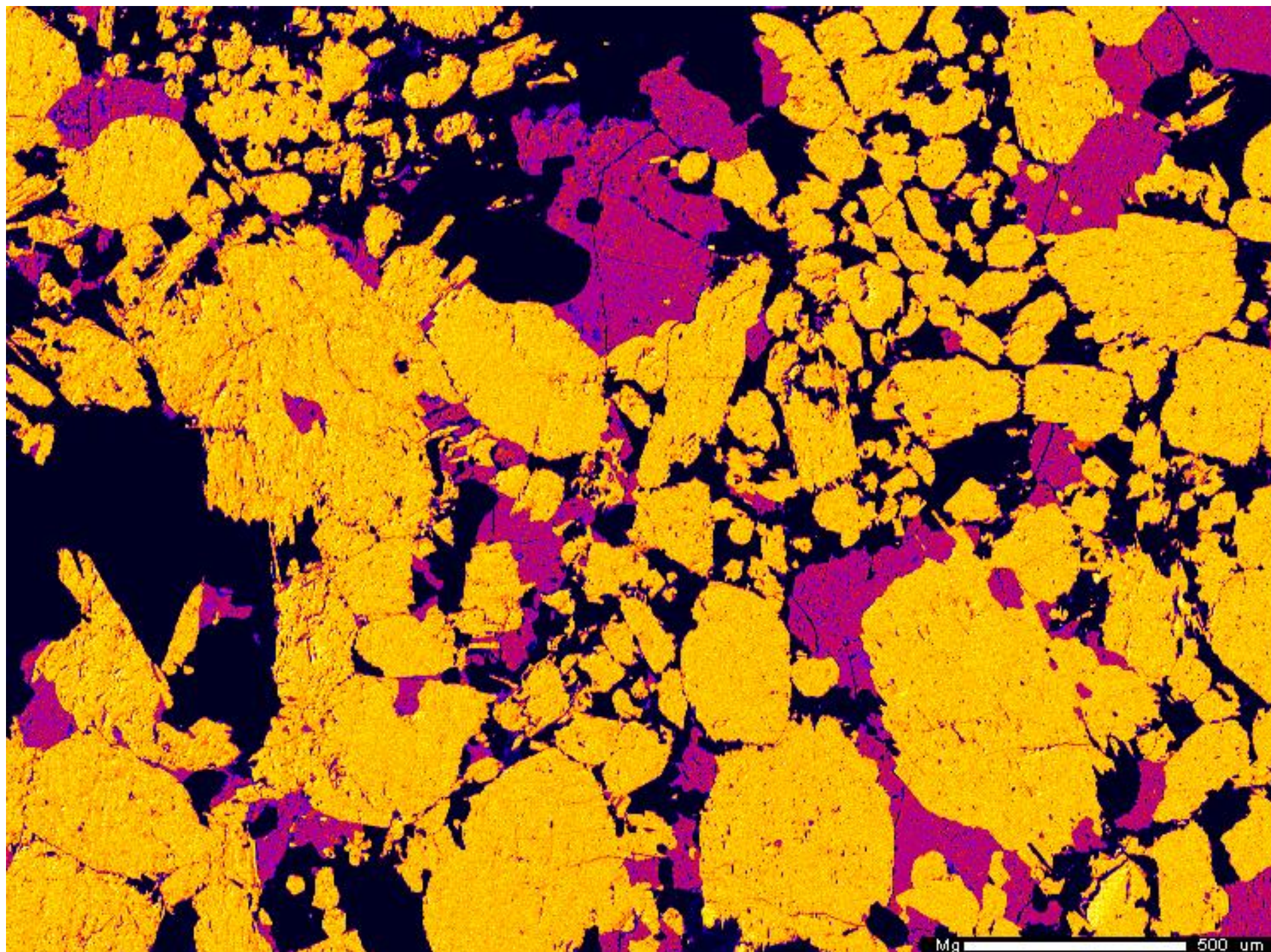
Fe 500 um





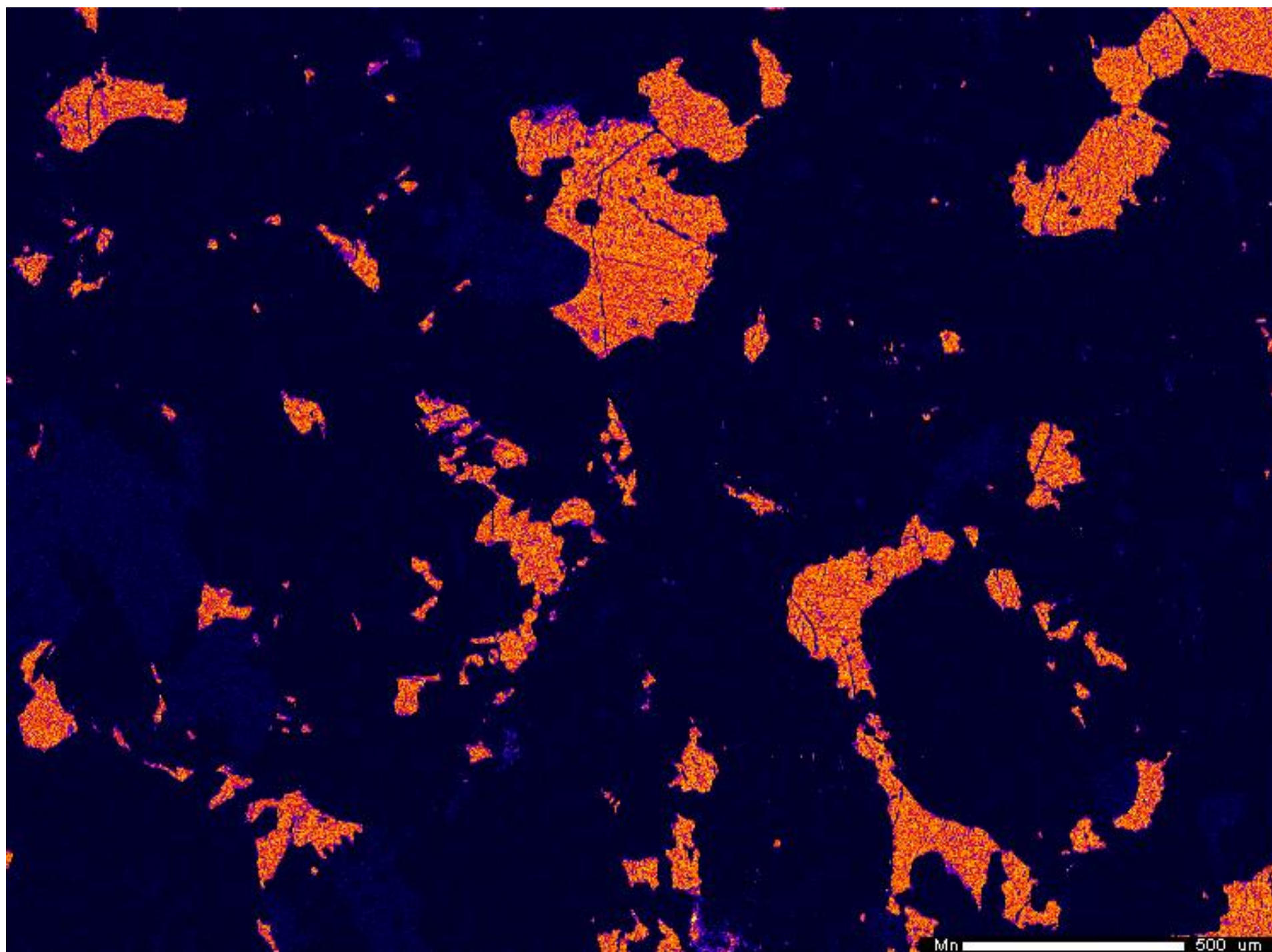
K  
Cts  
- 196  
0  
Project: June\_16\_2015  
Comment: NWA8173\_map01\_4um  
Date: 2015/06/17  
Accel Voltage: 15.0 kV  
Beam Current: 9.967e-008 A  
Dwell Time: 10.0  
Image Size: 746 x 555





Project: June\_16\_2015  
Comment: NWA8173\_map01\_4um  
Date: 2015/06/17  
Accel Voltage: 15.0 kV  
Beam Current: 9.967e-008 A  
Dwell Time: 10.0  
Image Size: 746 x 555

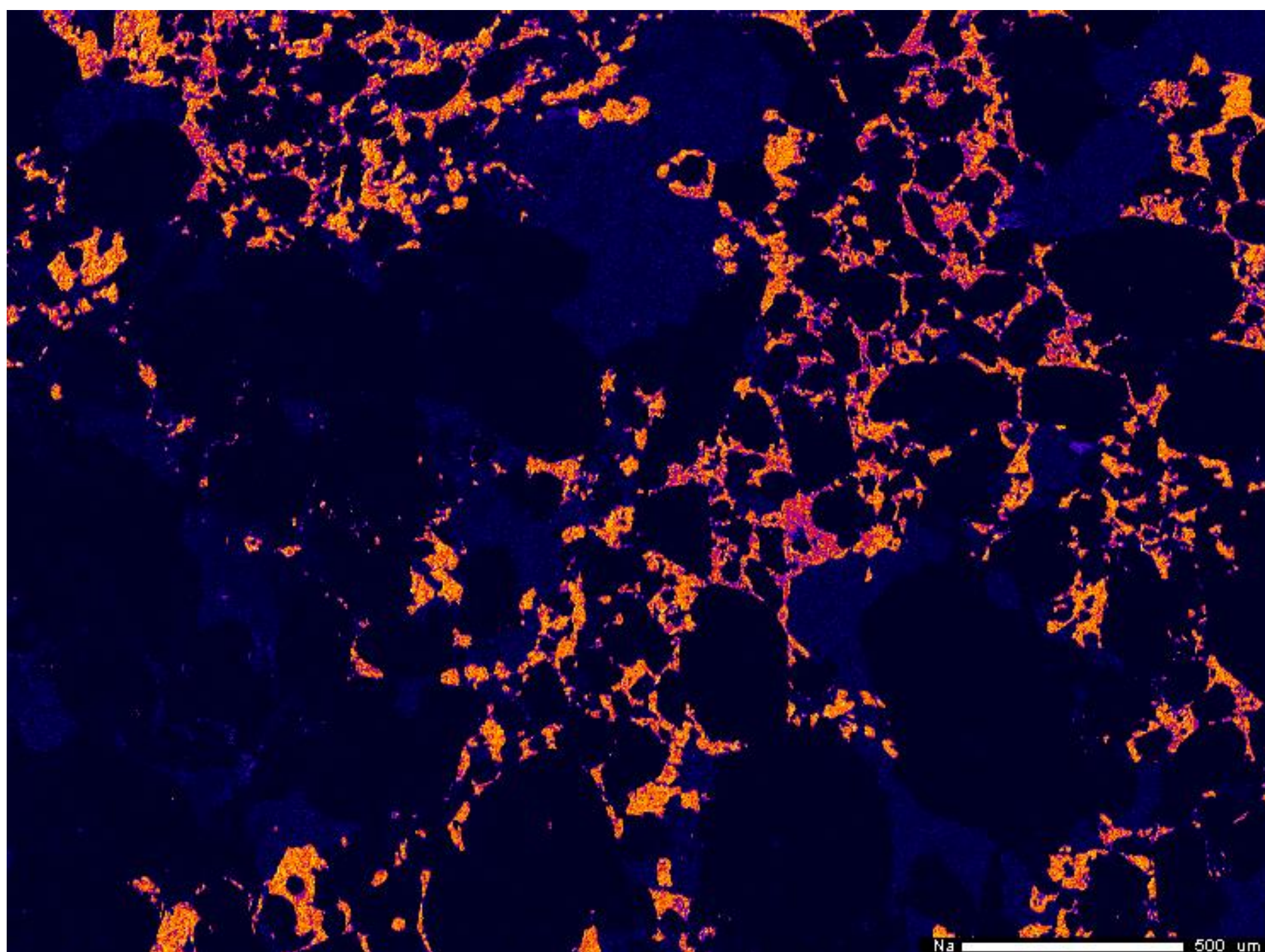




Project: June\_16\_2015  
Comment: NWA8173\_map01\_4um  
Date: 2015/06/17  
Accel Voltage: 15.0 kV  
Beam Current: 9.967e-008 A  
Dwell Time: 10.0  
Image Size: 746 x 555

Mn 500 um

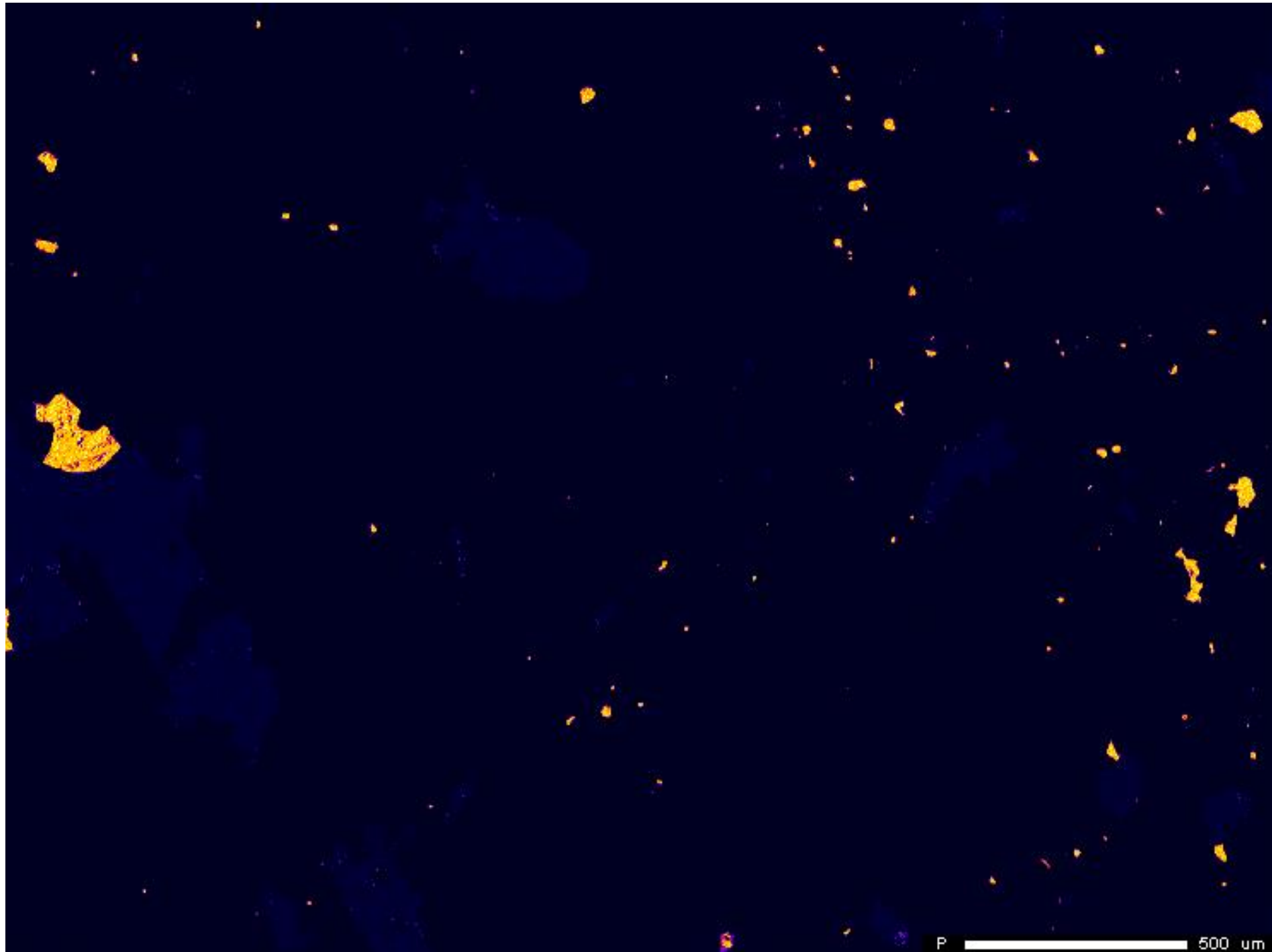




Project: June\_16\_2015  
Comment: NWA8173\_map01\_4um  
Date: 2015/06/17  
Accel Voltage: 15.0 kV  
Beam Current: 9.967e-008 A  
Dwell Time: 10.0  
Image Size: 746 x 555

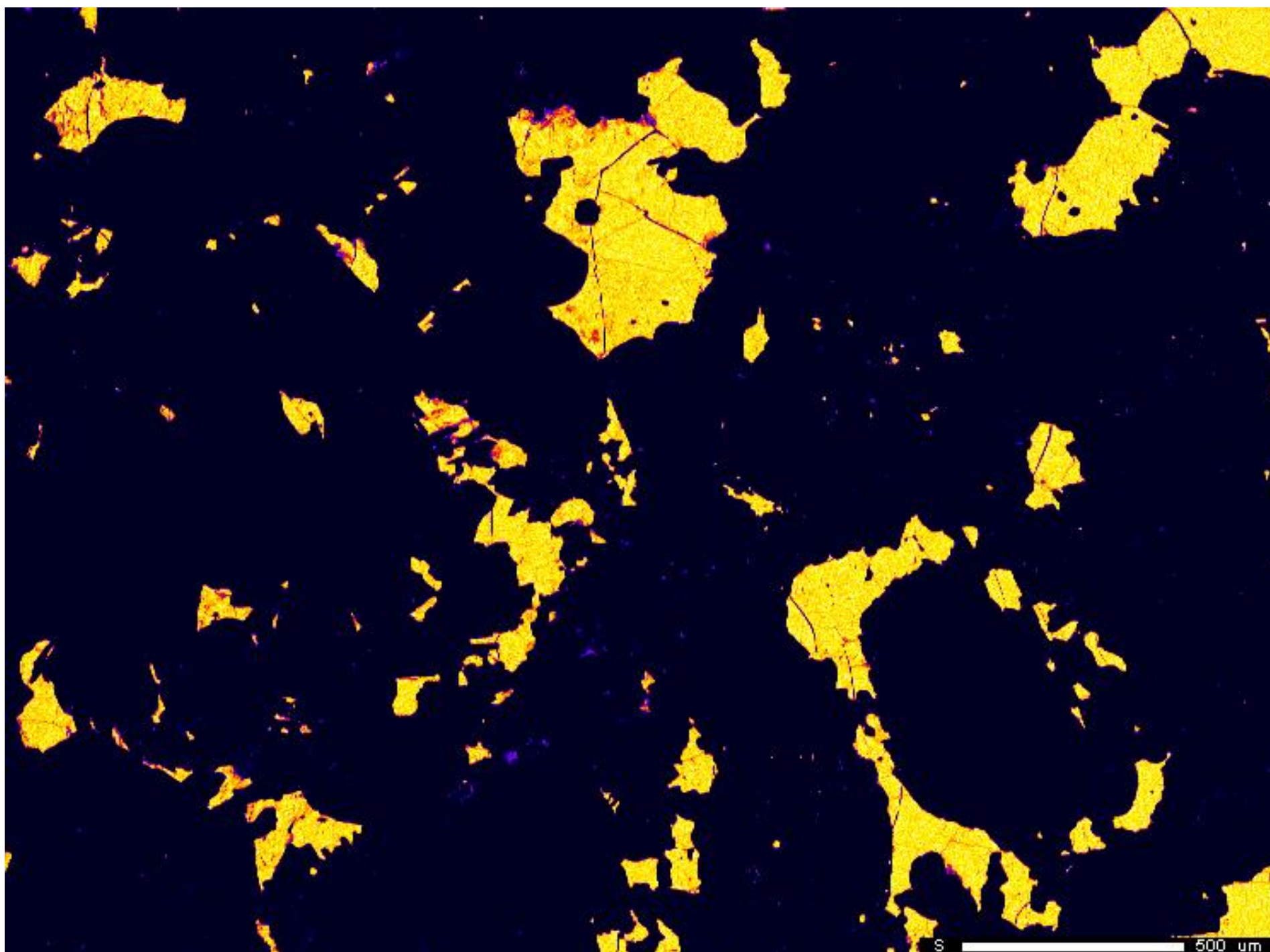
Na 500 um



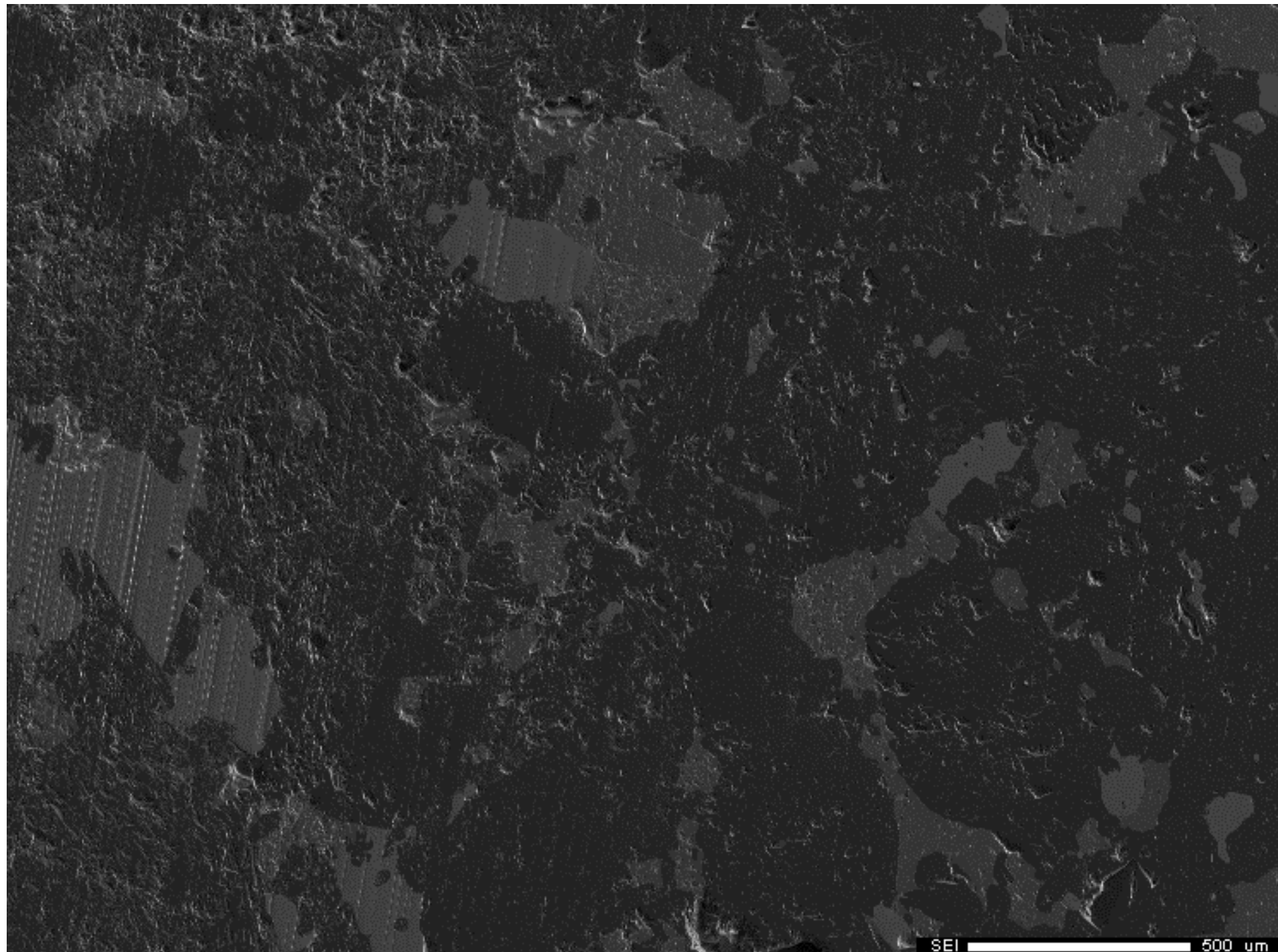


Project: June\_16\_2015  
Comment: NWA8173\_map01\_4um  
Date: 2015/06/17  
Accel Voltage: 15.0 kV  
Beam Current: 9.967e-008 A  
Dwell Time: 10.0  
Image Size: 746 x 555

P 500 um



S  
Cts  
- 646  
0  
Project: June\_16\_2015  
Comment: NWA8173\_map01\_4um  
Date: 2015/06/17  
Accel Voltage: 15.0 kV  
Beam Current: 9.967e-008 A  
Dwell Time: 10.0  
Image Size: 746 x 555



SEI

Cts

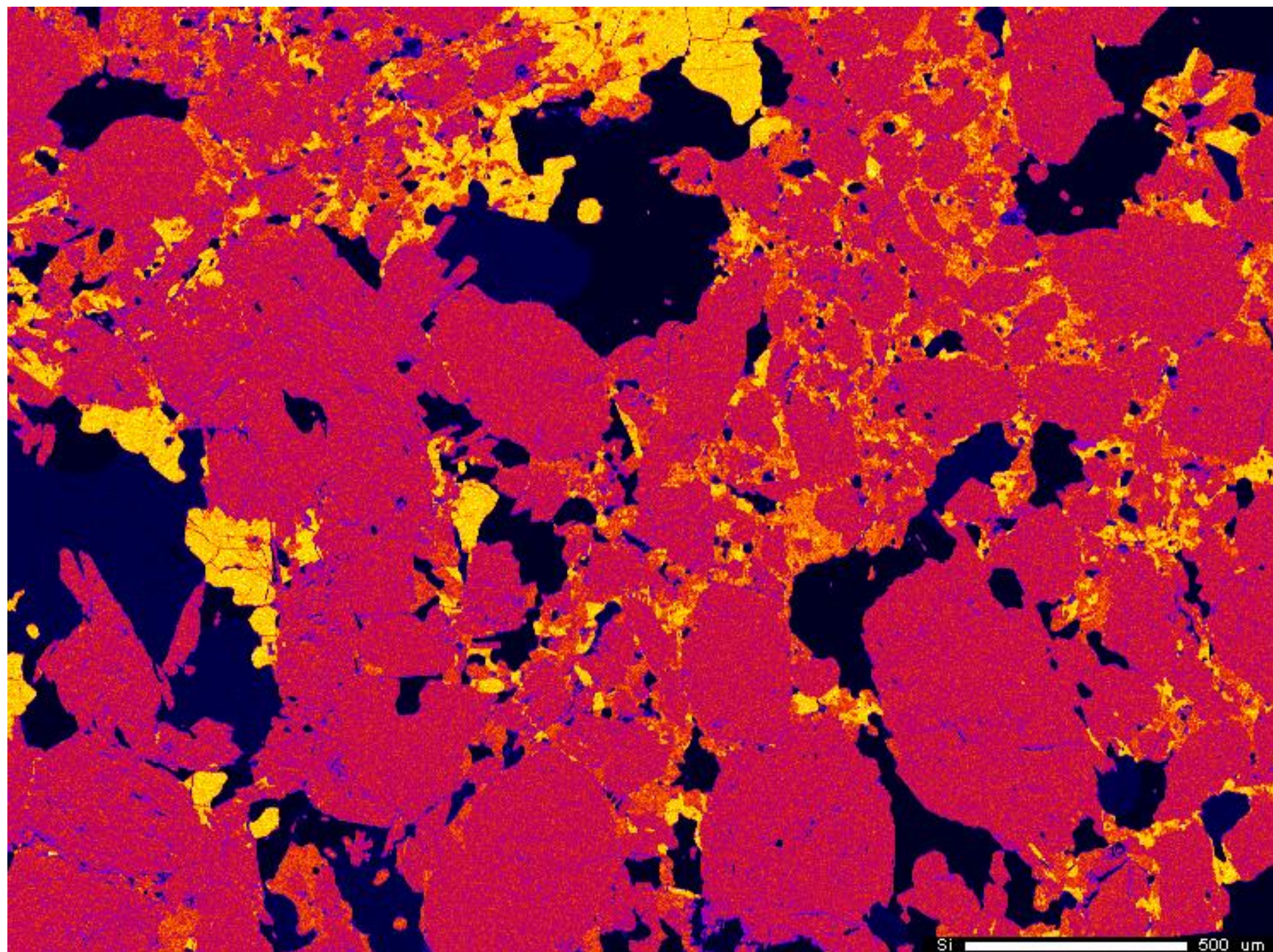
- 3,968

672

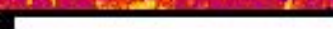
Project: June\_16\_2015  
Comment: NWA8173\_map01\_4um  
Date: 2015/06/17  
Accel Voltage: 15.0 kV  
Beam Current: 9.967e-008 A  
Dwell Time: 10.0  
Image Size: 746 x 555

SEI 500 um

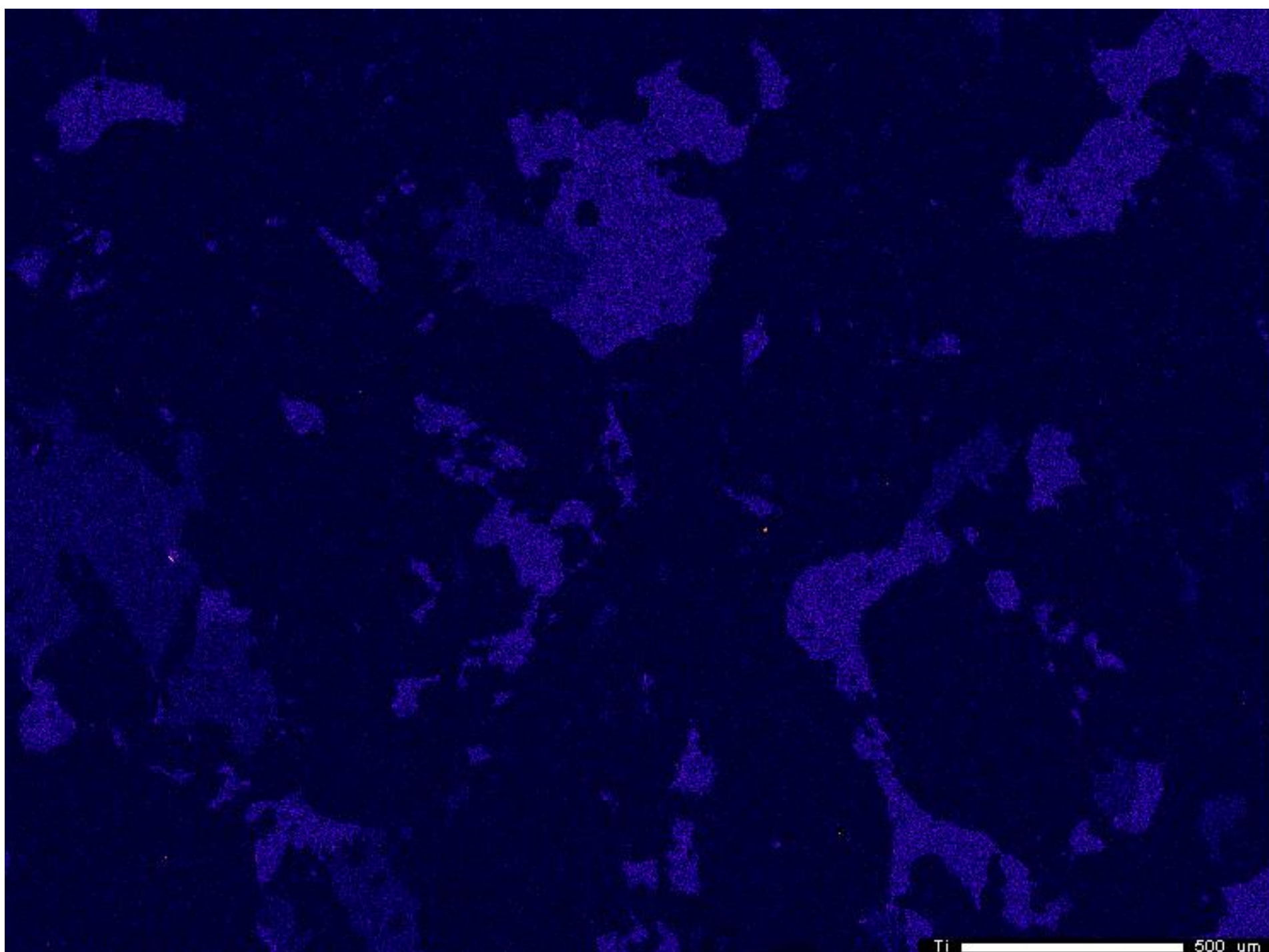




Project: June\_16\_2015  
Comment: NWA8173\_map01\_4um  
Date: 2015/06/17  
Accel Voltage: 15.0 kV  
Beam Current: 9.967e-008 A  
Dwell Time: 10.0  
Image Size: 746 x 555

Si  500 um



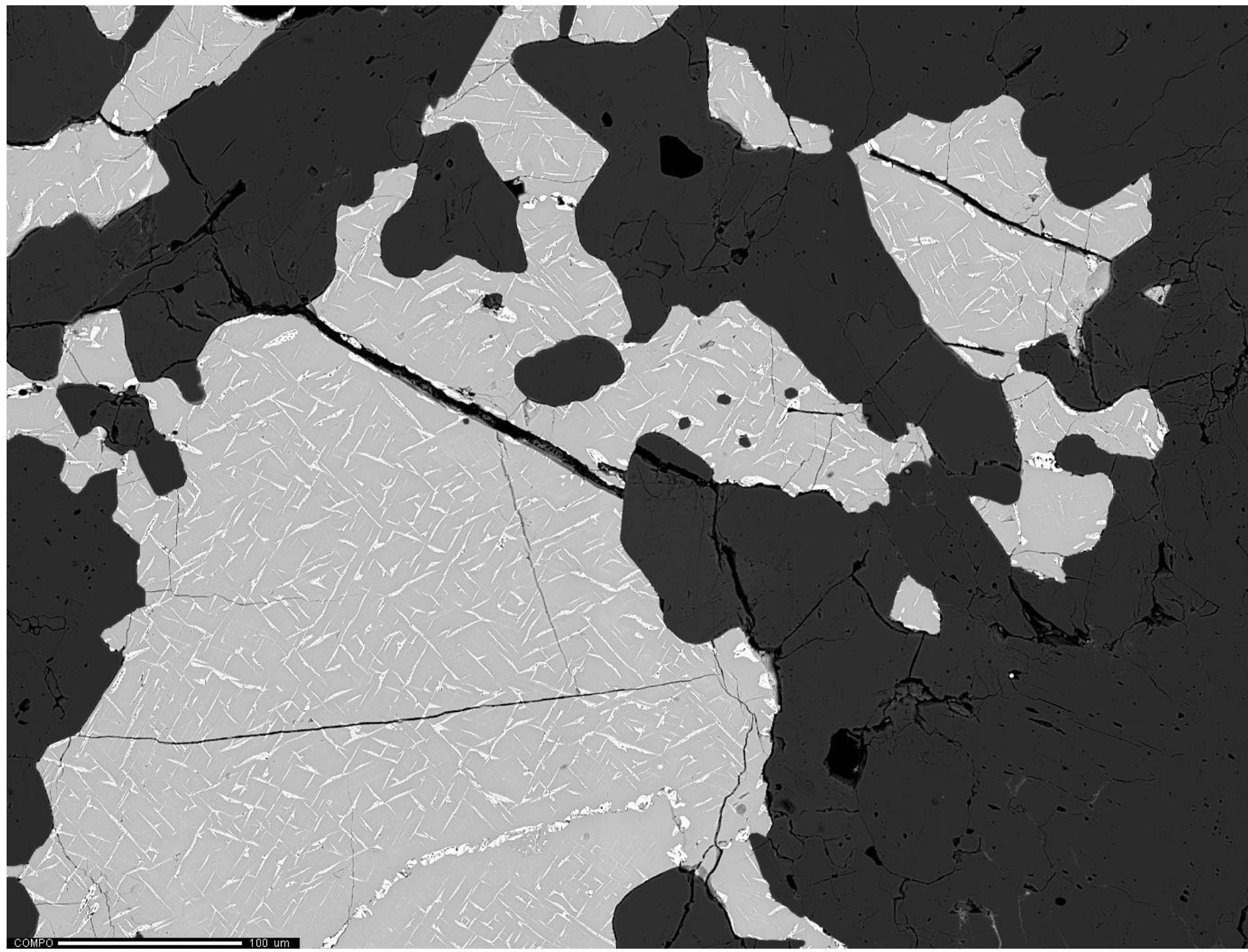


Project: June\_16\_2015  
Comment: NWA8173\_map01\_4um  
Date: 2015/06/17  
Accel Voltage: 15.0 kV  
Beam Current: 9.967e-008 A  
Dwell Time: 10.0  
Image Size: 746 x 555

Ti 500 um

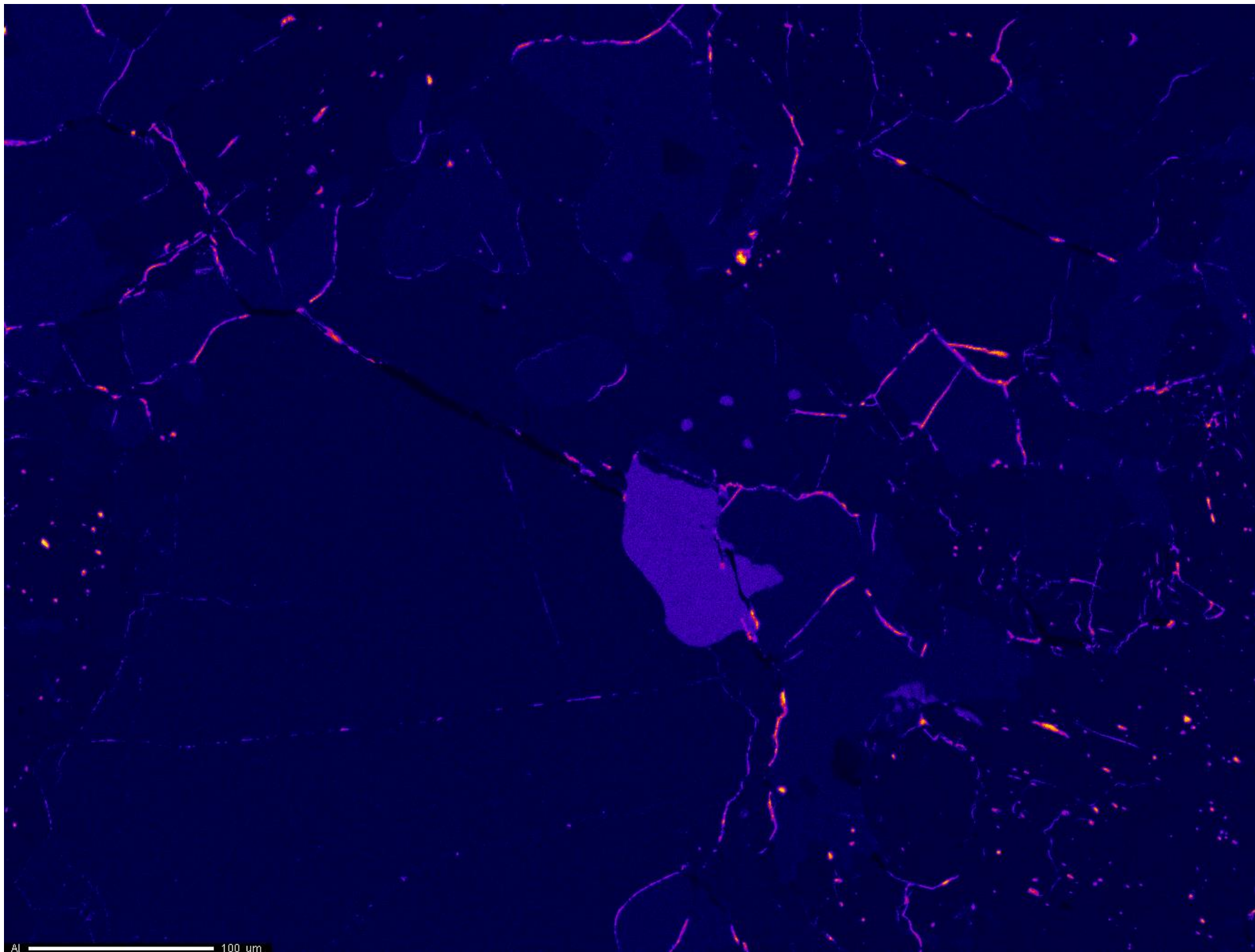


NWA 8173a Fluorophlogopite  
X-ray elemental maps



Project: February\_1\_2017  
Comment: 8173a\_Fluorphlogopite\_map2\_0p5um  
Date: 2017/02/01  
Accel Voltage: 15.0 kV  
Beam Current: 1.002e-007 A  
Dwell Time: 10.0  
Image Size: 1384 x 1045

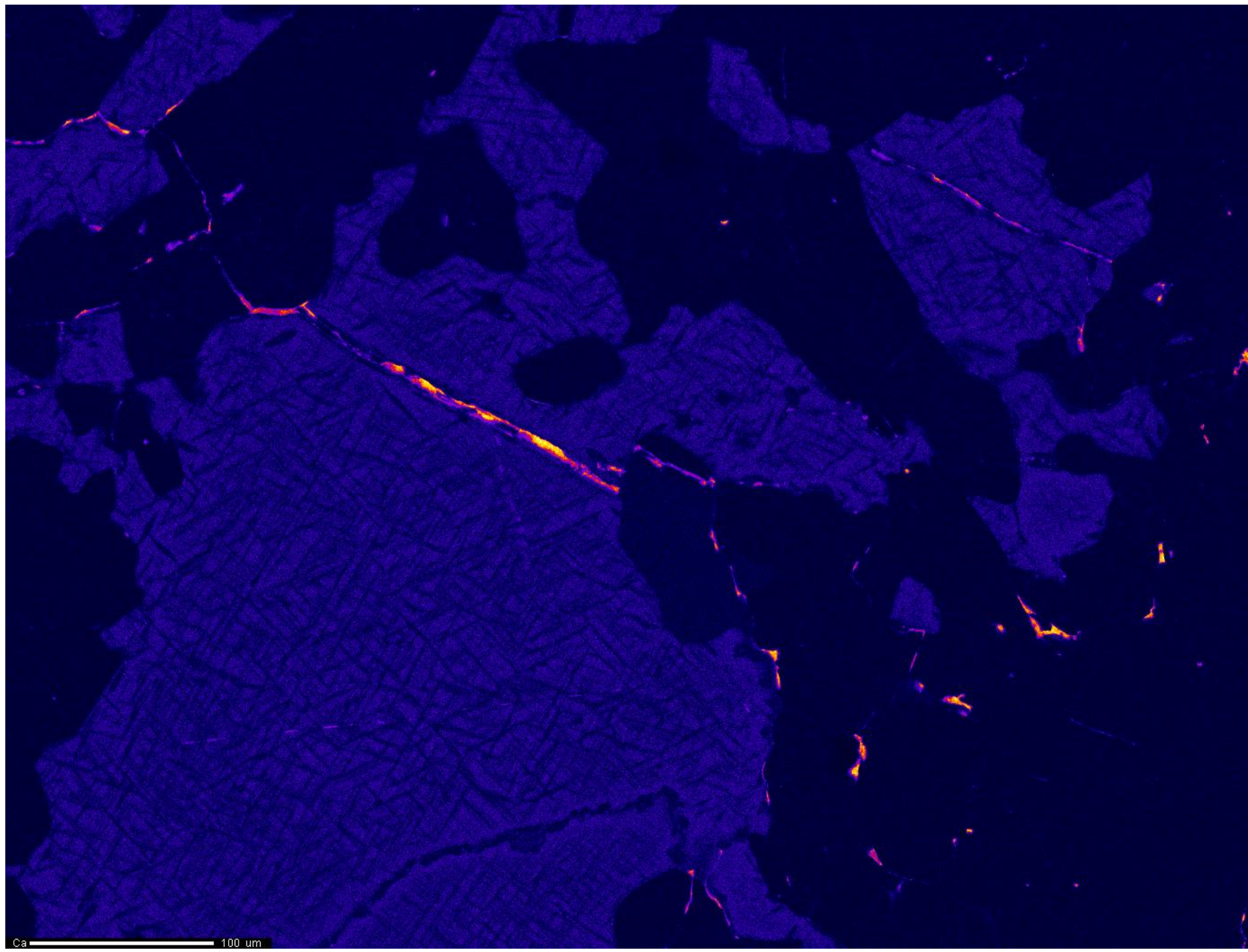
COMPO 100 um



AI  
Cts  
- 364  
0  
Project: February\_1\_2017  
Comment: 8173a\_Fluorphlogopite\_map2\_0p5um  
Date: 2017/02/01  
Accel Voltage: 15.0 kV  
Beam Current: 5.022e-008 A  
Dwell Time: 10.0  
Image Size: 1384 x 1045

AI 100 um



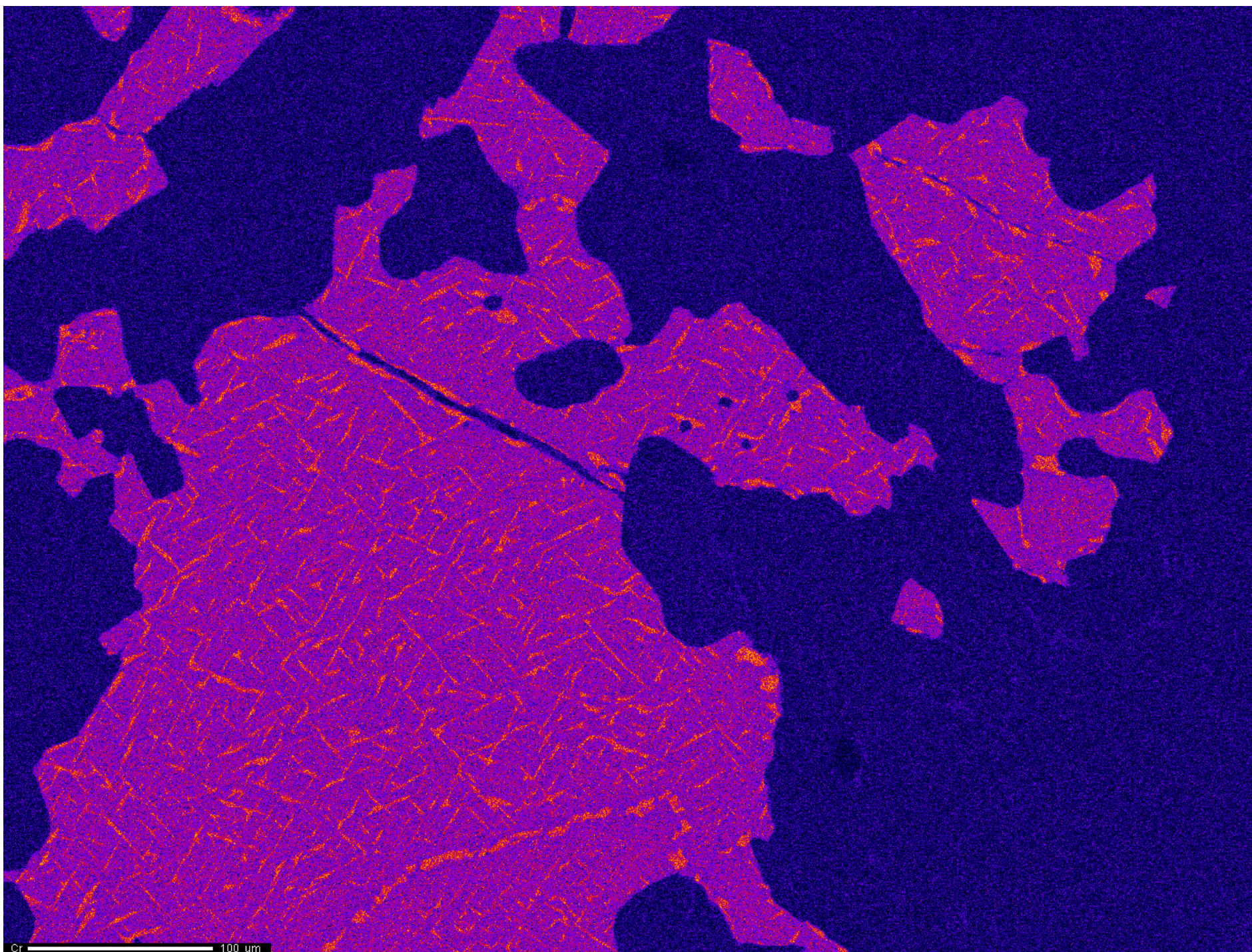


Ca  
Cts  
- 199  
0

Project: February\_1\_2017  
Comment: 8173a\_Fluorphlogopite\_map2\_0p5um  
Date: 2017/02/01  
Accel Voltage: 15.0 kV  
Beam Current: 5.022e-008 A  
Dwell Time: 10.0  
Image Size: 1384 x 1045

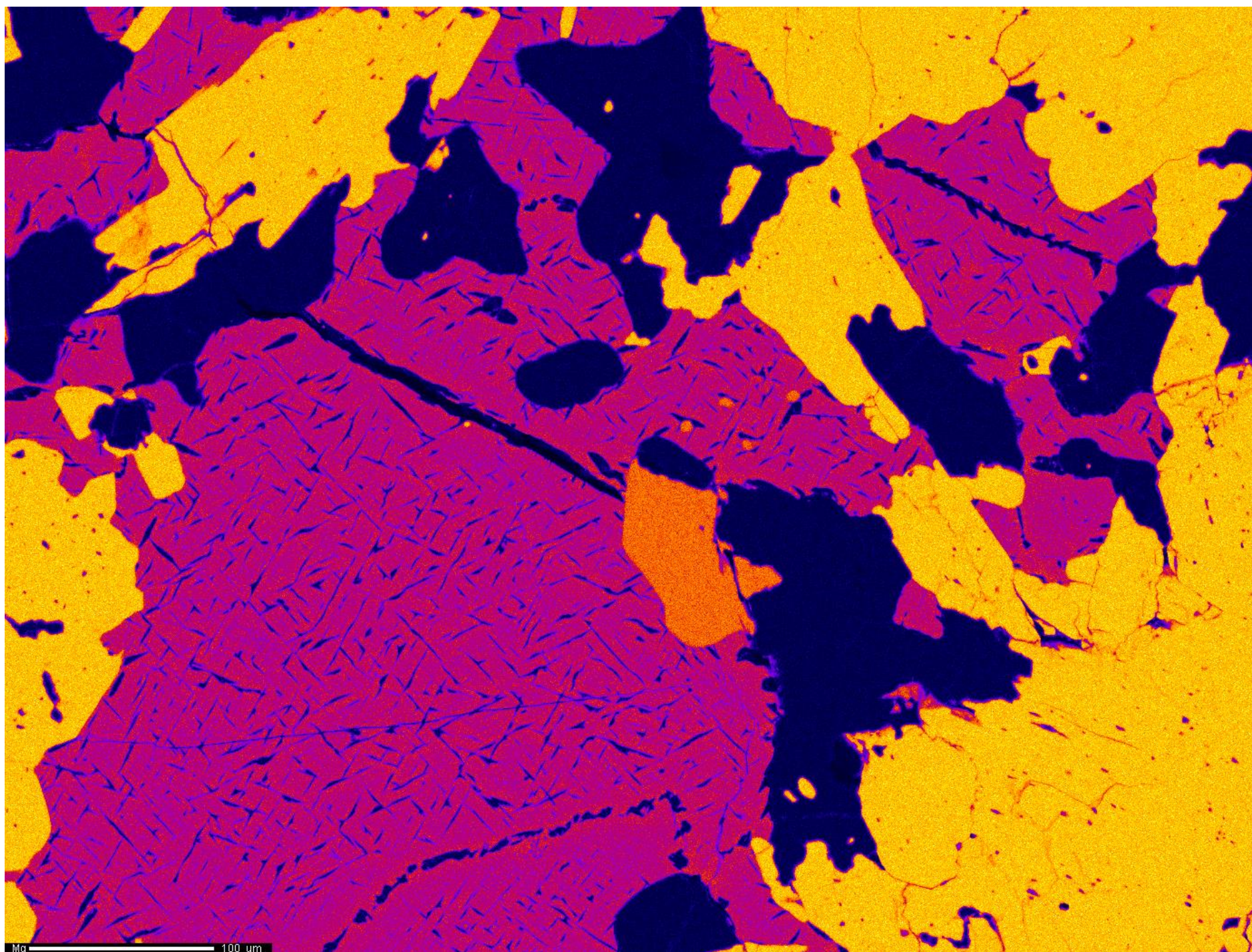
Ca 100 µm





Cr  
Cts  
- 37  
0  
Project: February\_1\_2017  
Comment: 8173a\_Fluorphlogopite\_map2\_0p5um  
Date: 2017/02/01  
Accel Voltage: 15.0 kV  
Beam Current: 5.022e-008 A  
Dwell Time: 10.0  
Image Size: 1384 x 1045



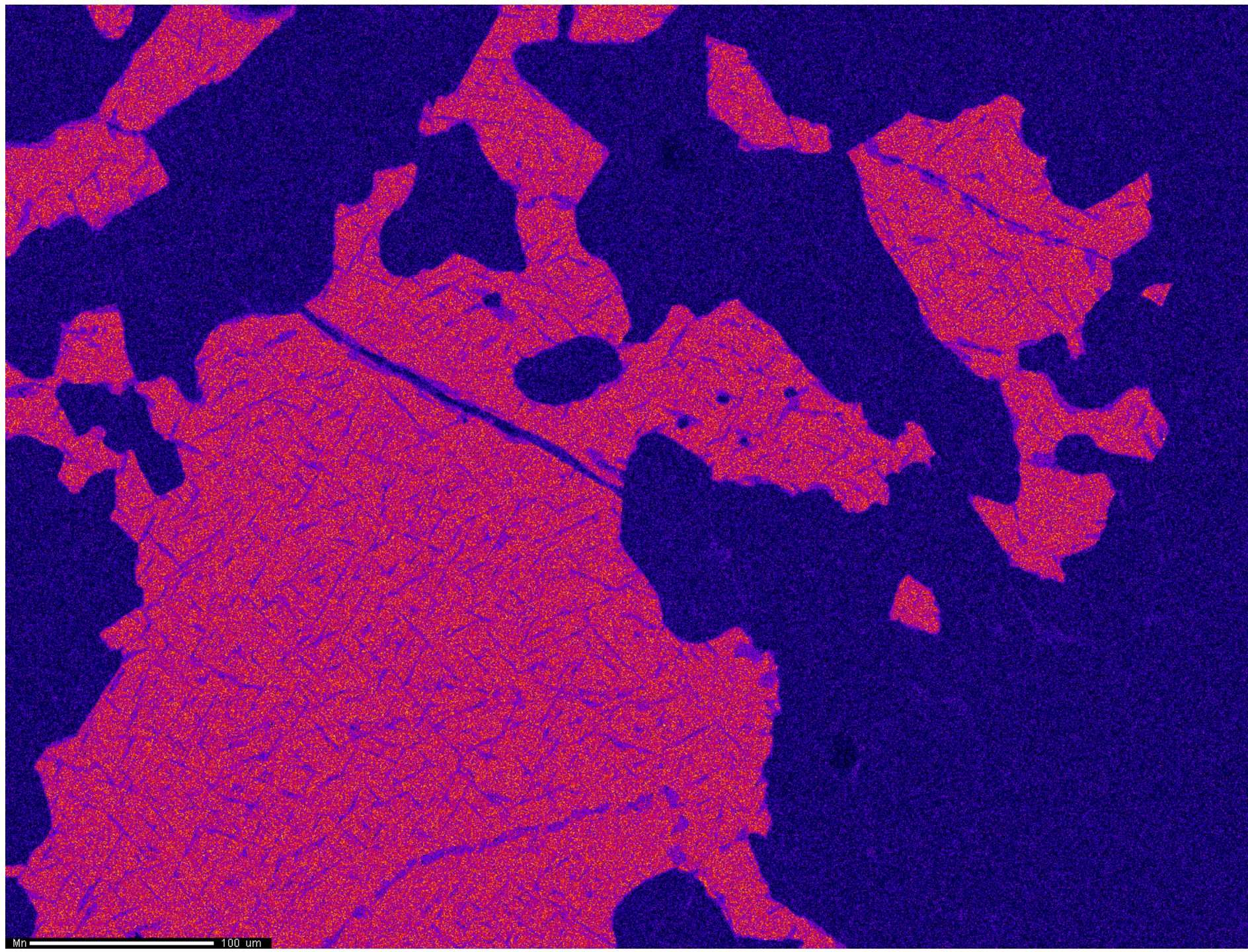


Mg  
Cts  
- 239  
0

Project: February\_1\_2017  
Comment: 8173a\_Fluorophlogopite\_map2\_0p5um  
Date: 2017/02/01  
Accel Voltage: 15.0 kV  
Beam Current: 5.022e-008 A  
Dwell Time: 10.0  
Image Size: 1384 x 1045

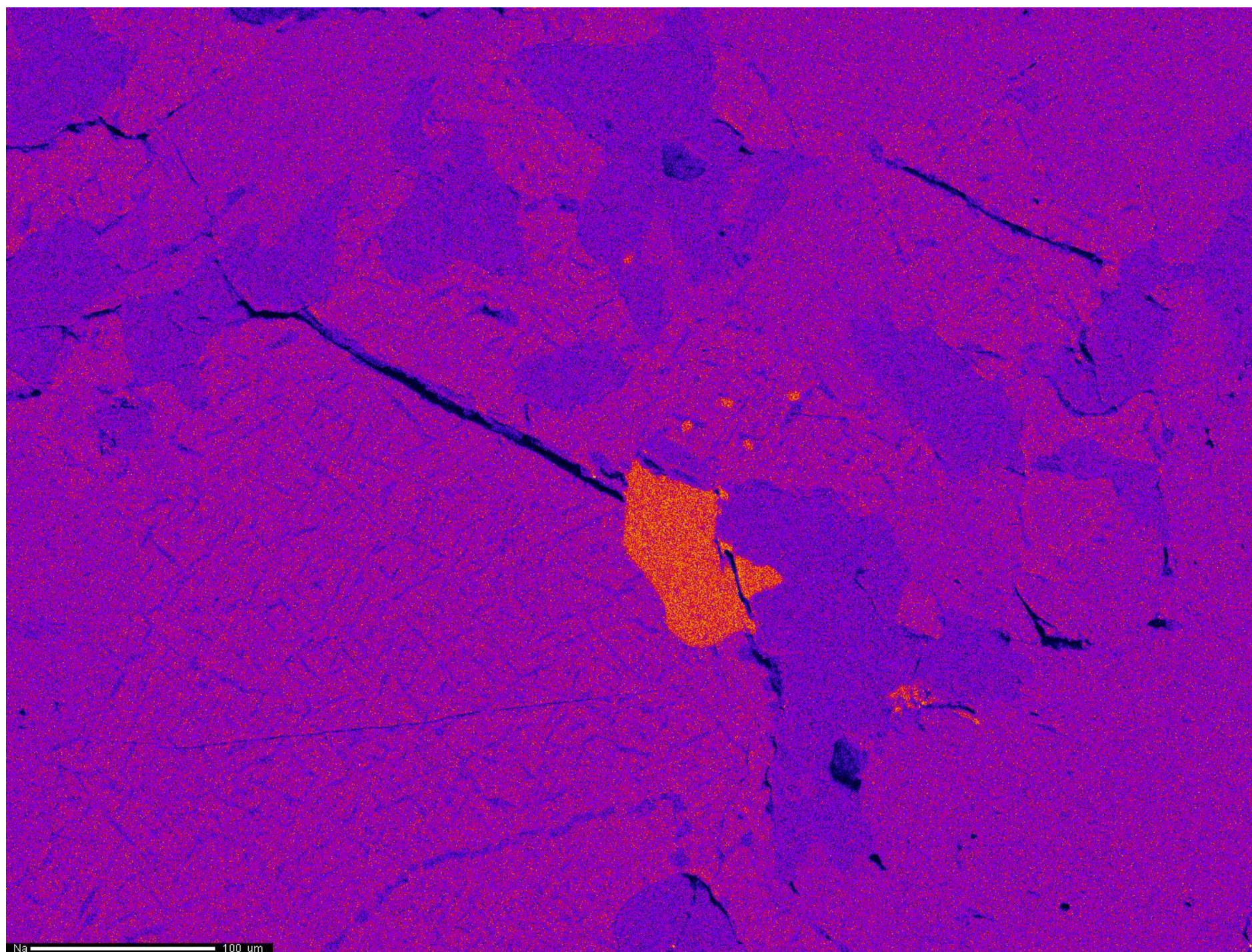
Mg 100 um





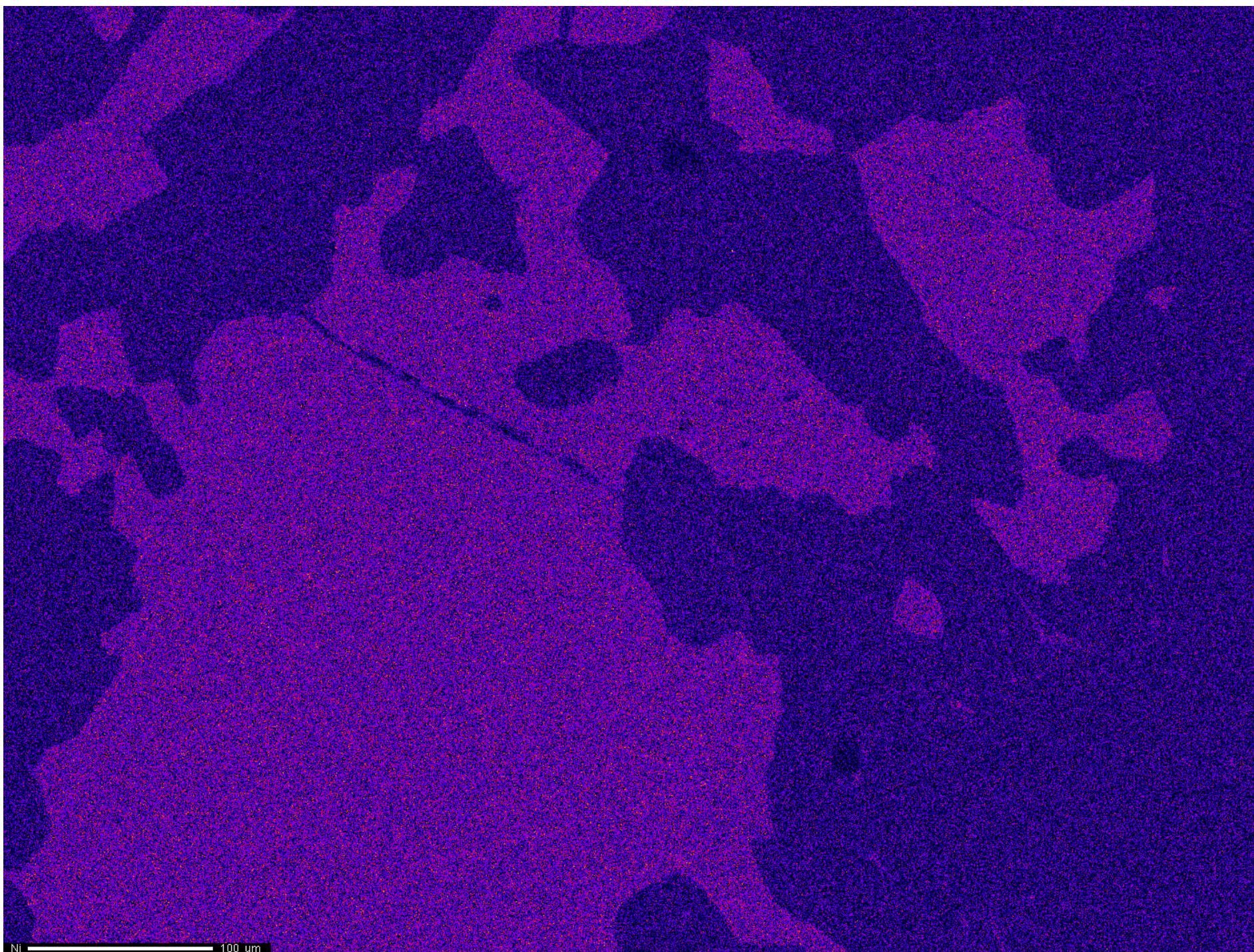
Mn  
Cts  
- 32  
0  
Project: February\_1\_2017  
Comment: 8173a\_Fluorphlogopite\_map2\_0p5um  
Date: 2017/02/01  
Accel Voltage: 15.0 kV  
Beam Current: 5.022e-008 A  
Dwell Time: 10.0  
Image Size: 1384 x 1045





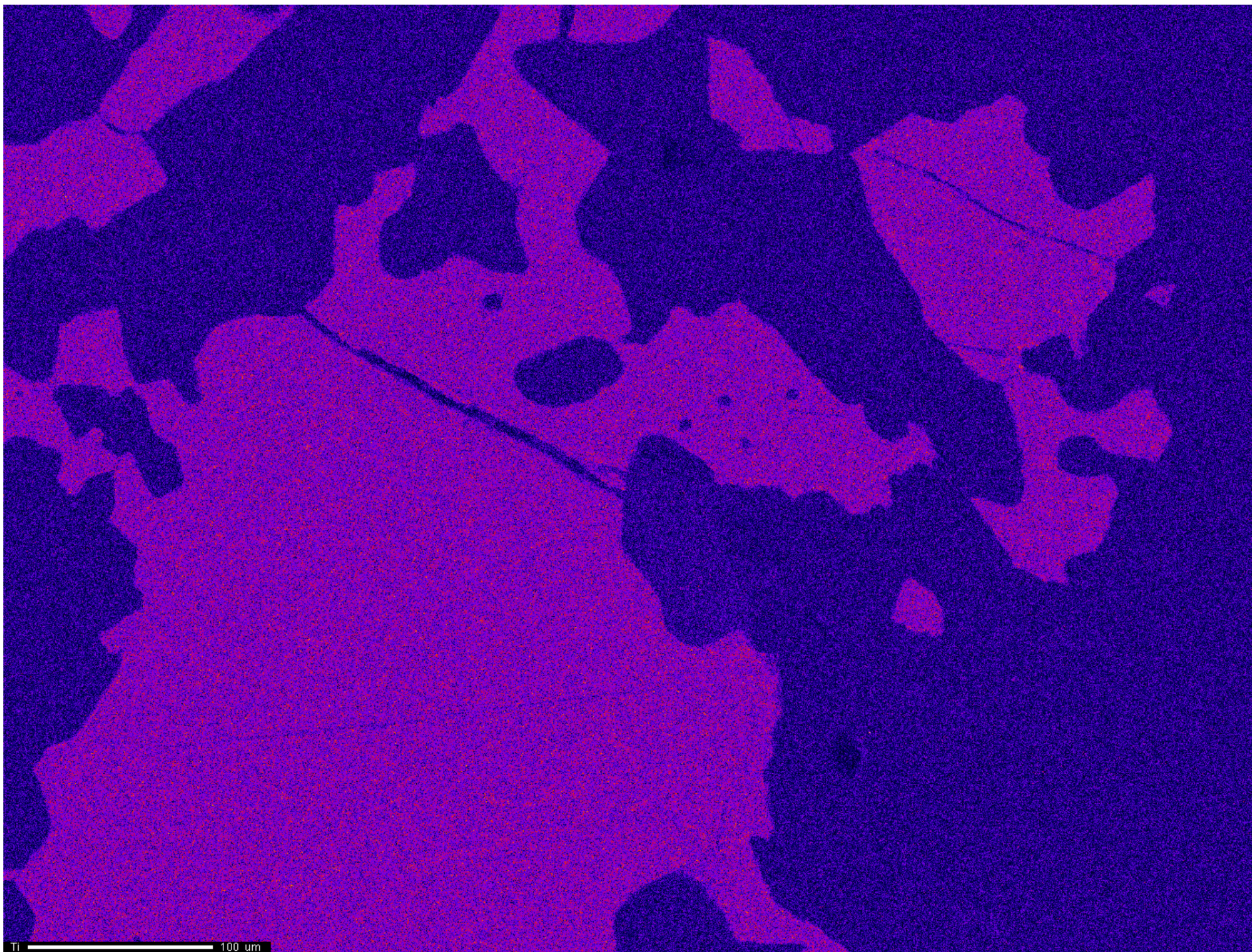
Na  
Cts  
- 42  
0  
Project: February\_1\_2017  
Comment: 8173a\_Fluorphlogopite\_map2\_0p5um  
Date: 2017/02/01  
Accel Voltage: 15.0 kV  
Beam Current: 5.022e-008 A  
Dwell Time: 10.0  
Image Size: 1384 x 1045





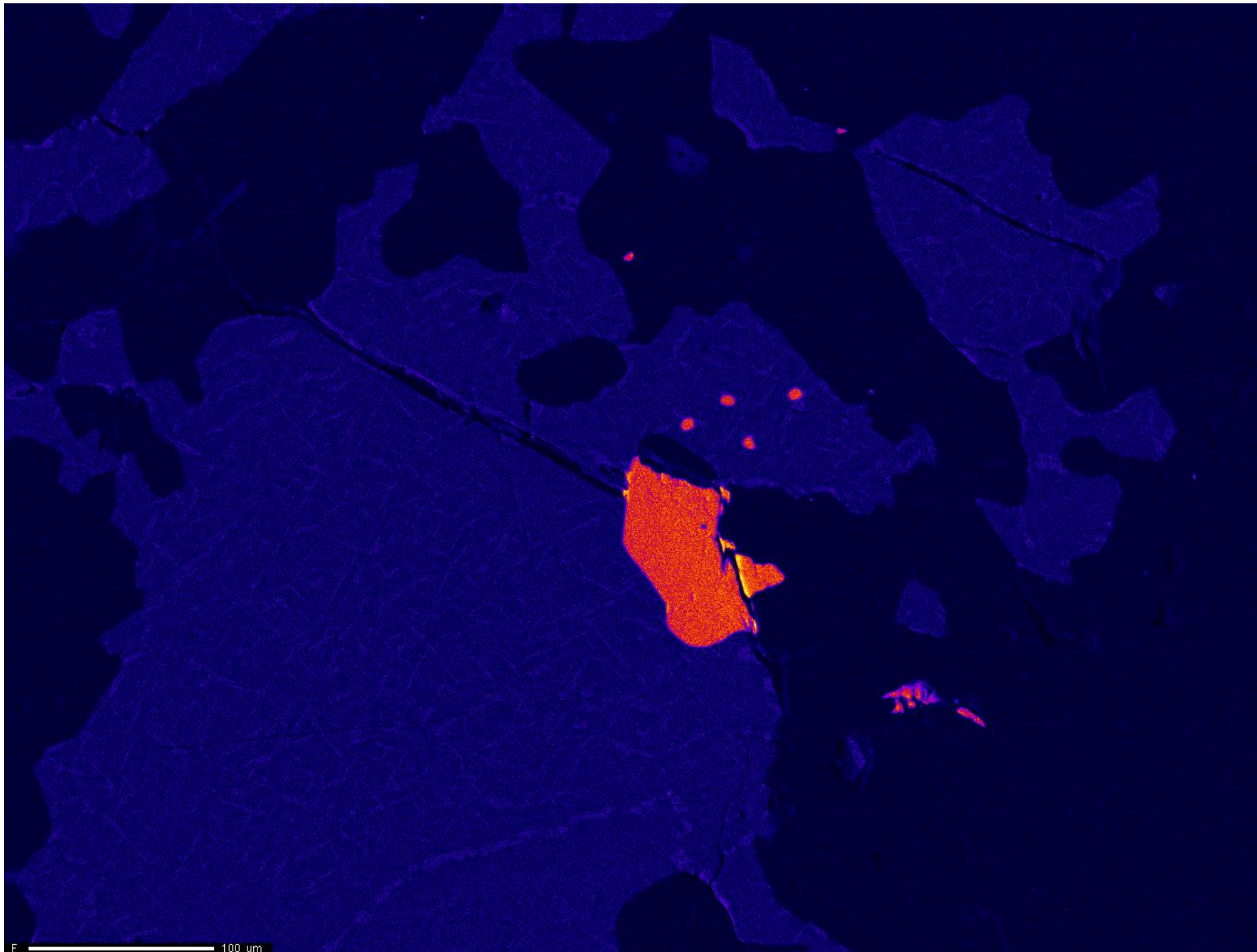
Ni  
Cts  
- 17  
0  
Project: February\_1\_2017  
Comment: 8173a\_Fluorphlogopite\_map2\_0p5um  
Date: 2017/02/01  
Accel Voltage: 15.0 kV  
Beam Current: 5.022e-008 A  
Dwell Time: 10.0  
Image Size: 1384 x 1045





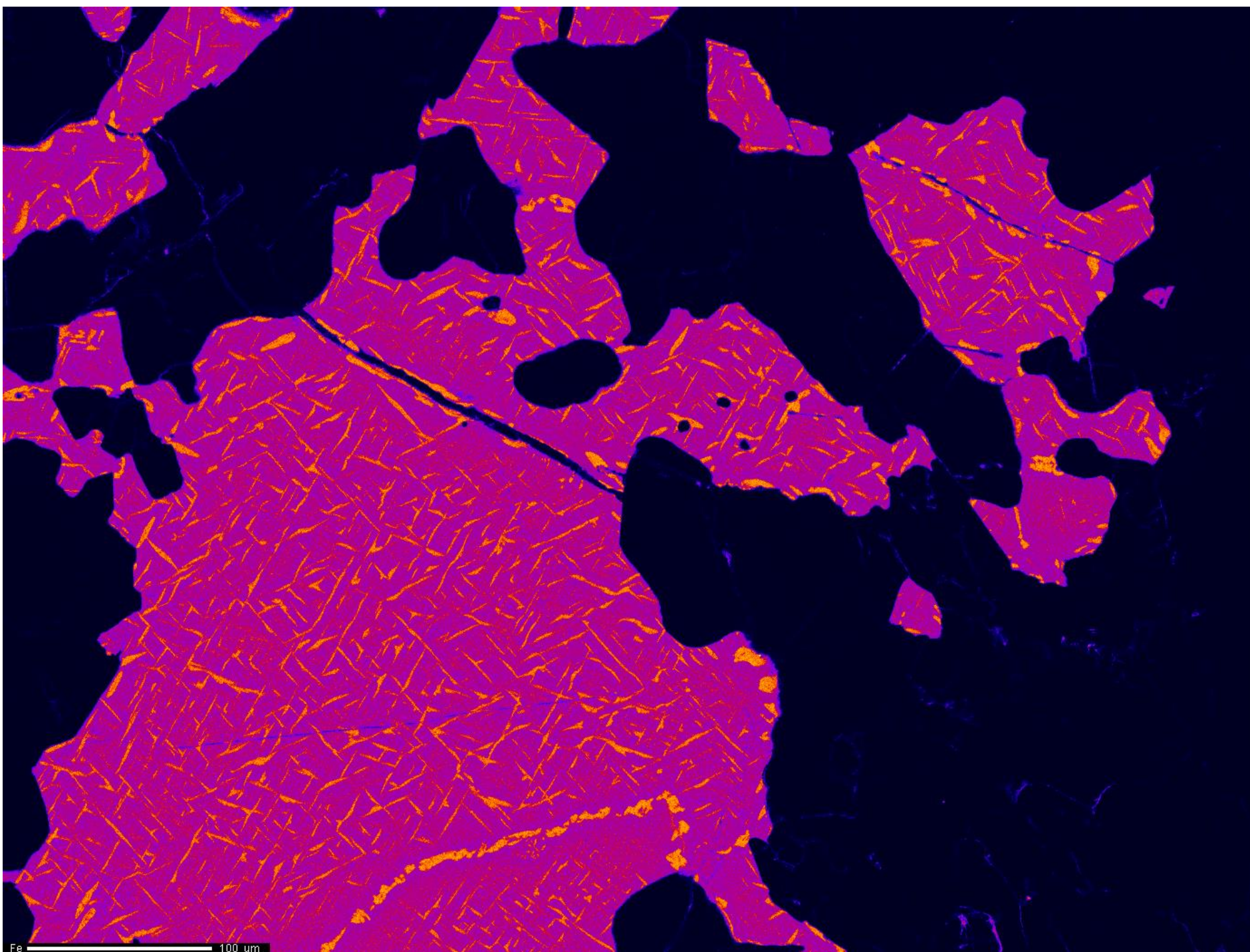
Ti  
Cts  
- 37  
0  
Project: February\_1\_2017  
Comment: 8173a\_Fluorphlogopite\_map2\_0p5un  
Date: 2017/02/01  
Accel Voltage: 15.0 kV  
Beam Current: 5.022e-008 A  
Dwell Time: 10.0  
Image Size: 1384 x 1045





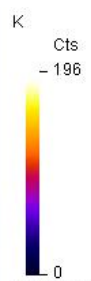
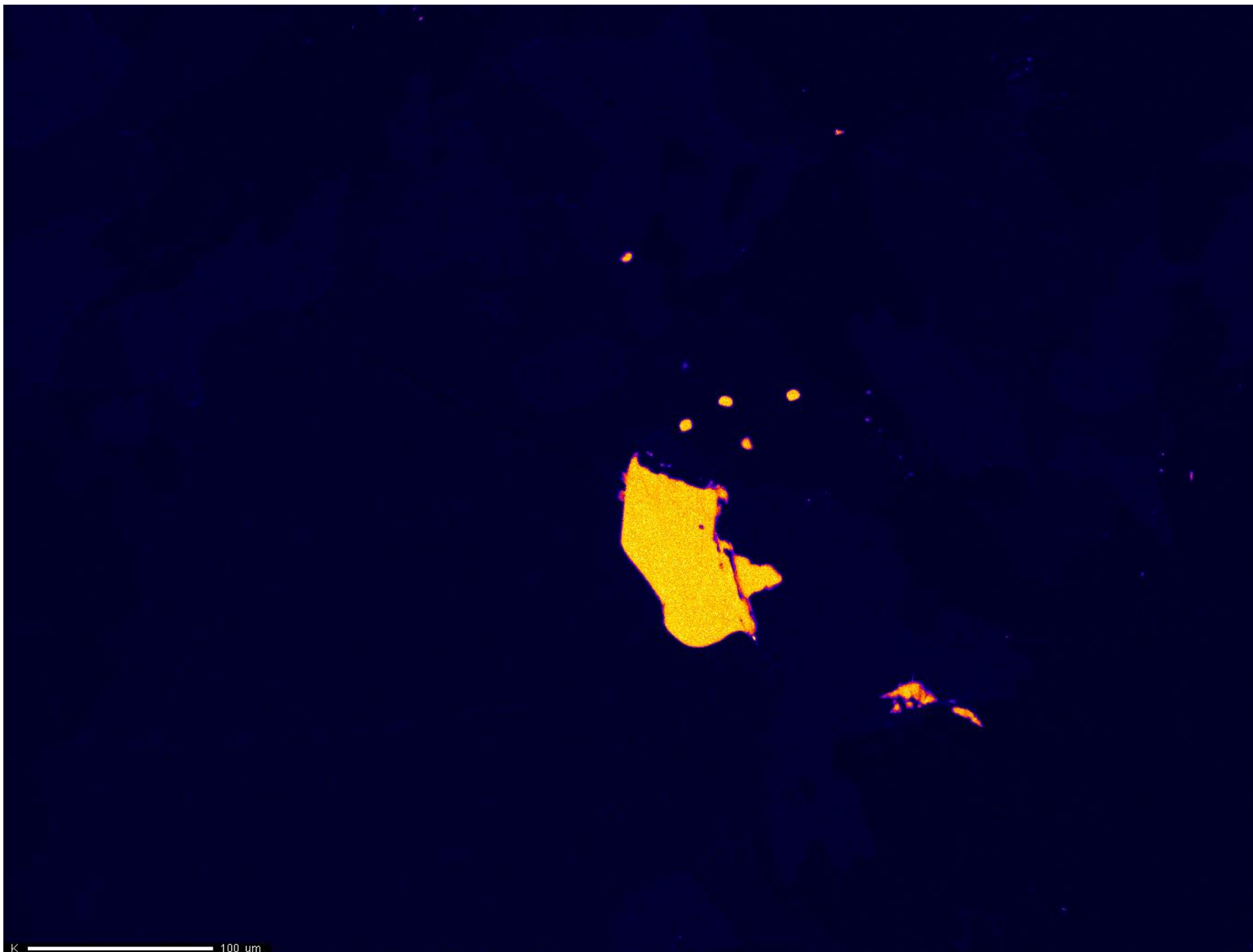
F  
Cts  
- 151  
0  
Project: February\_1\_2017  
Comment: 8173a\_Fluorophlogopite\_map2\_0p5um  
Date: 2017/02/01  
Accel Voltage: 15.0 kV  
Beam Current: 1.002e-007 A  
Dwell Time: 10.0  
Image Size: 1384 x 1045





Fe  
Cts  
- 201  
0

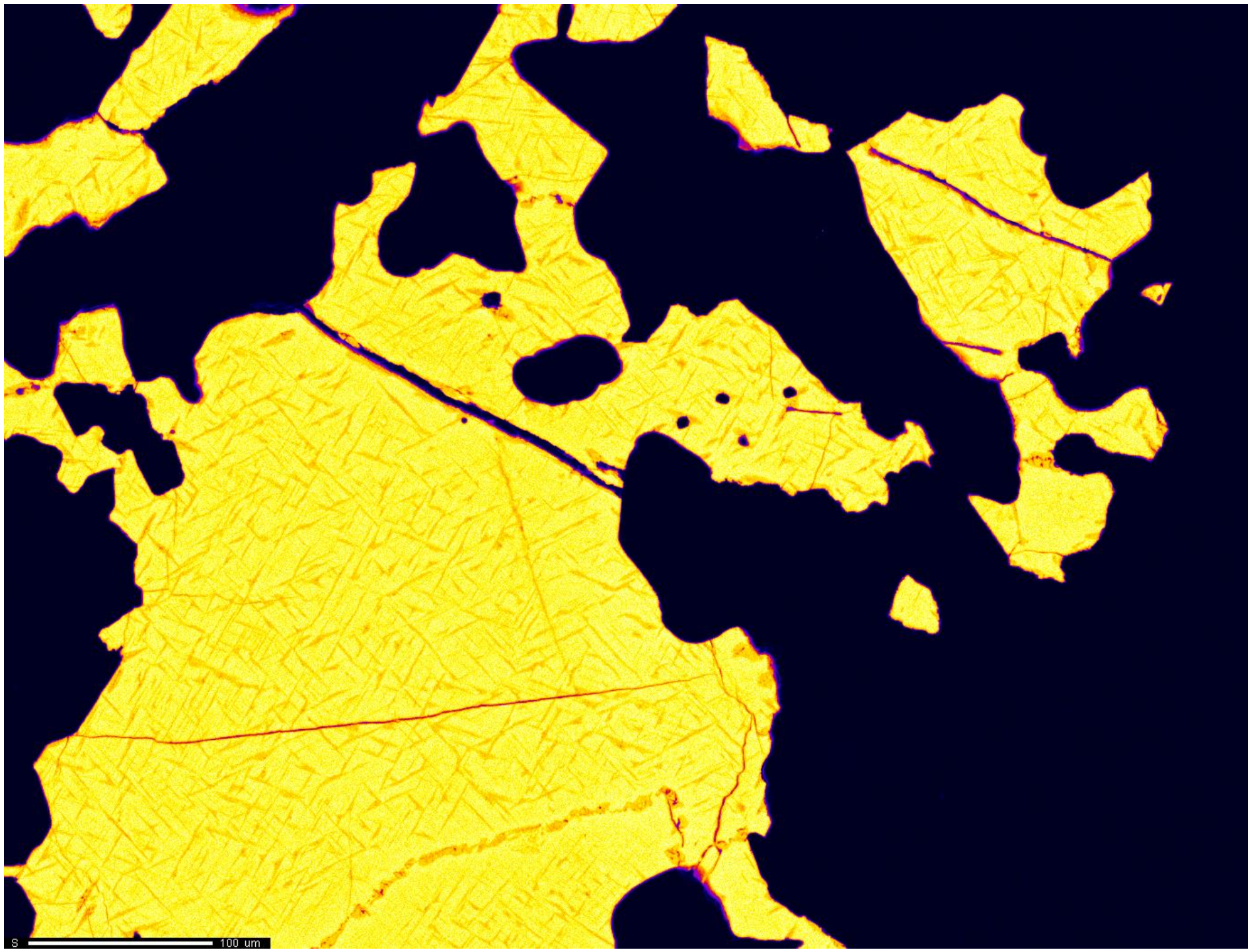
Project: February\_1\_2017  
Comment: 8173a\_Fluorphlogopite\_map2\_0p5um  
Date: 2017/02/01  
Accel Voltage: 15.0 kV  
Beam Current: 1.002e-007 A  
Dwell Time: 10.0  
Image Size: 1384 x 1045



Project: February\_1\_2017  
Comment: 8173a\_Fluorphlogopite\_map2\_0p5um  
Date: 2017/02/01  
Accel Voltage: 15.0 kV  
Beam Current: 1.002e-007 A  
Dwell Time: 10.0  
Image Size: 1384 x 1045

K 100 um

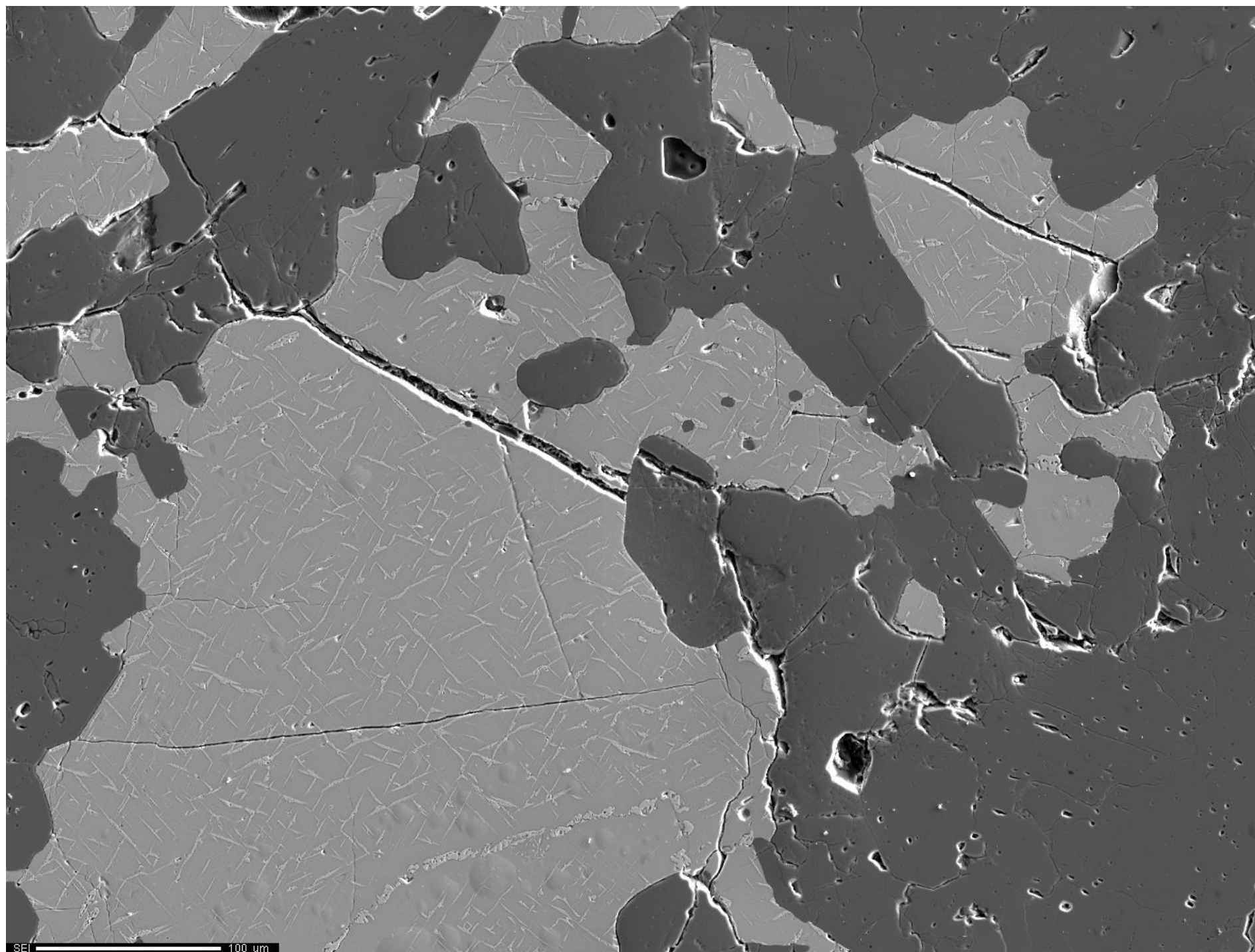




S  
Cts  
- 914  
0  
Project: February\_1\_2017  
Comment: 8173a\_Fluorphlogopite\_map2\_0p5um  
Date: 2017/02/01  
Accel Voltage: 15.0 kV  
Beam Current: 1.002e-007 A  
Dwell Time: 10.0  
Image Size: 1384 x 1045

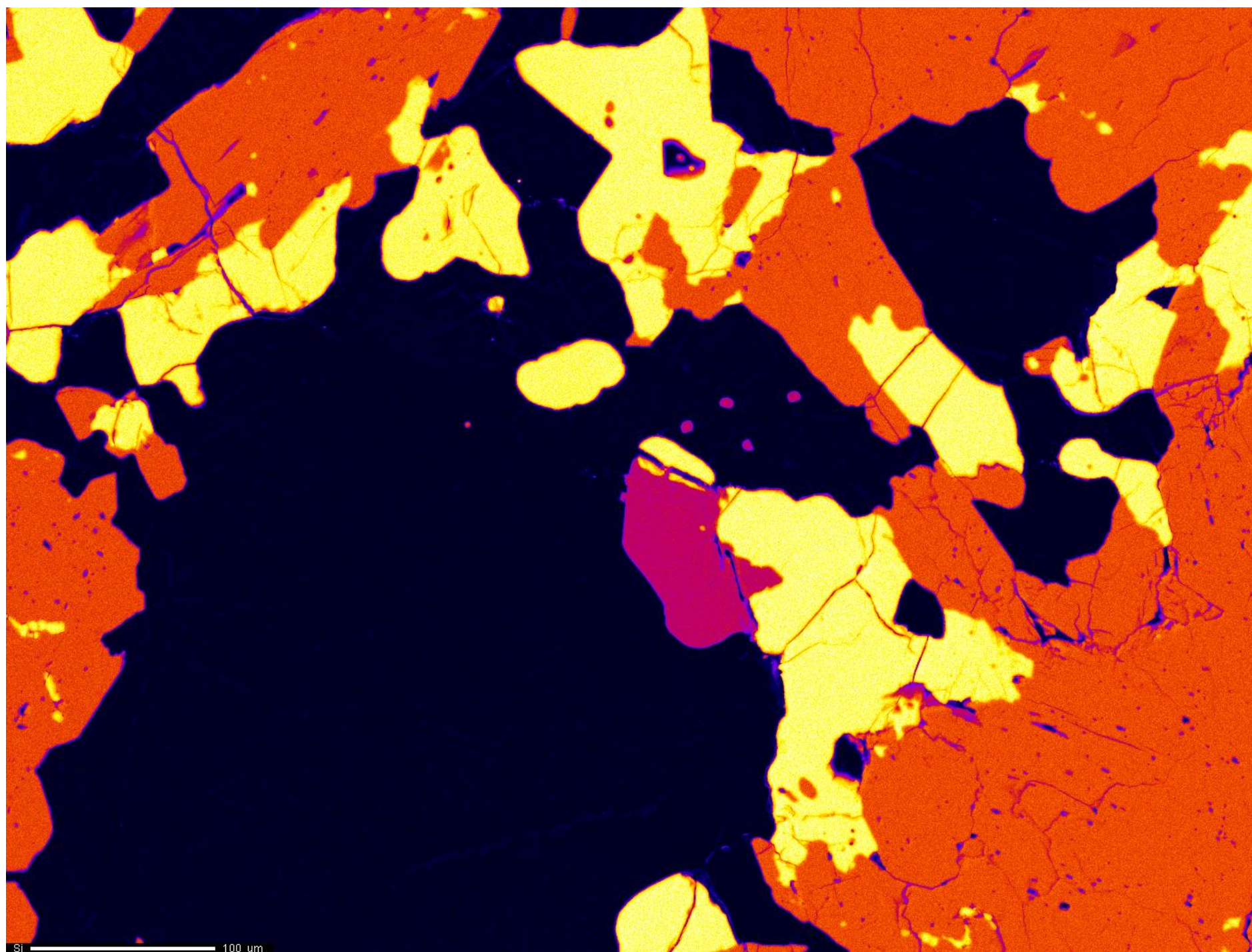
S 100 um





Project: February\_1\_2017  
Comment: 8173a\_Fluorphlogopite\_map2\_0p5um  
Date: 2017/02/01  
Accel Voltage: 15.0 kV  
Beam Current: 1.002e-007 A  
Dwell Time: 10.0  
Image Size: 1384 x 1045

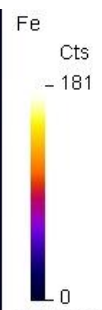
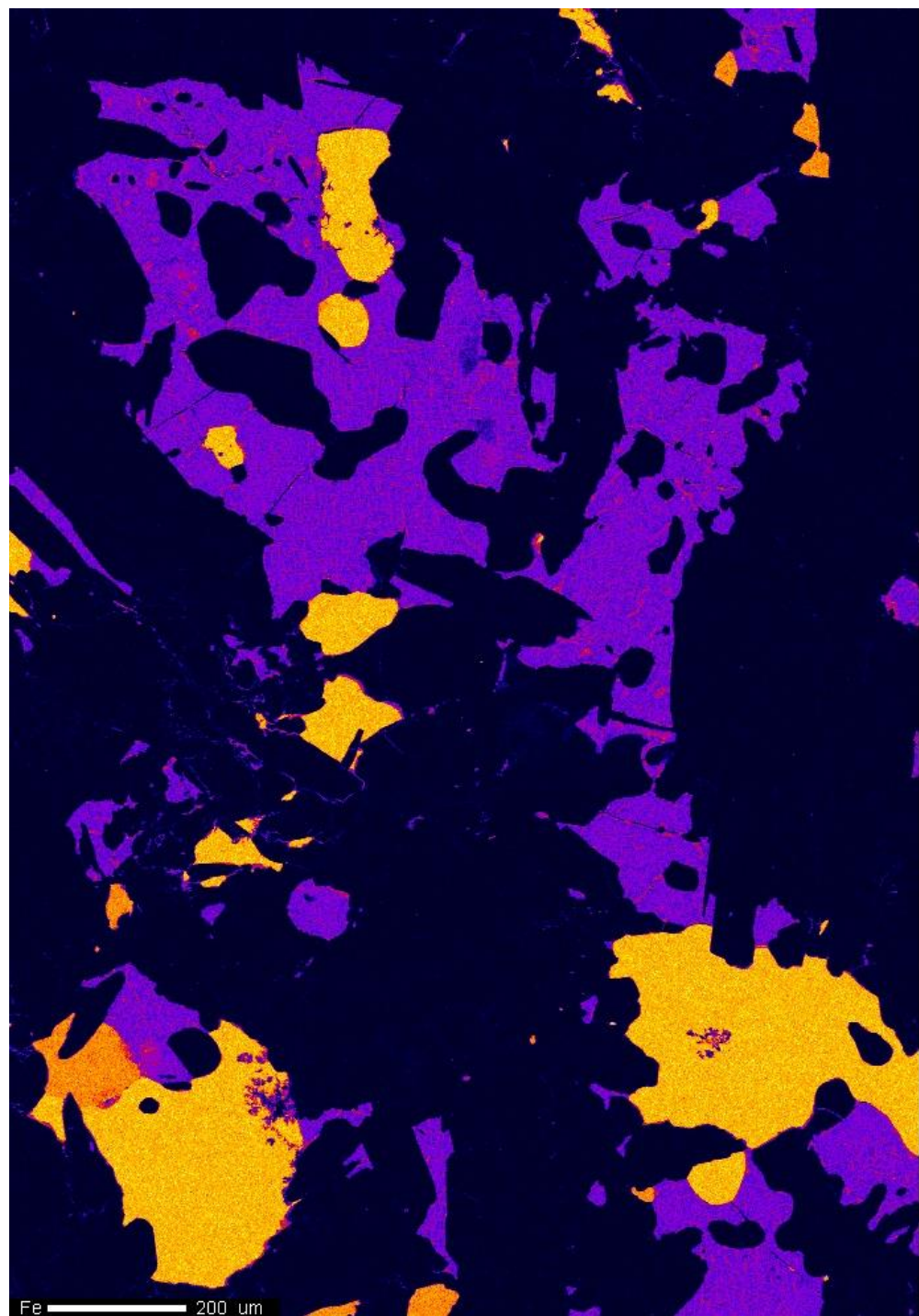
SEI 100 um



Si  
Cts  
- 988  
0  
Project: February\_1\_2017  
Comment: 8173a\_Fluorphlogopite\_map2\_0p5um  
Date: 2017/02/01  
Accel Voltage: 15.0 kV  
Beam Current: 1.002e-007 A  
Dwell Time: 10.0  
Image Size: 1384 x 1045

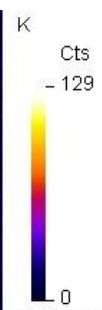
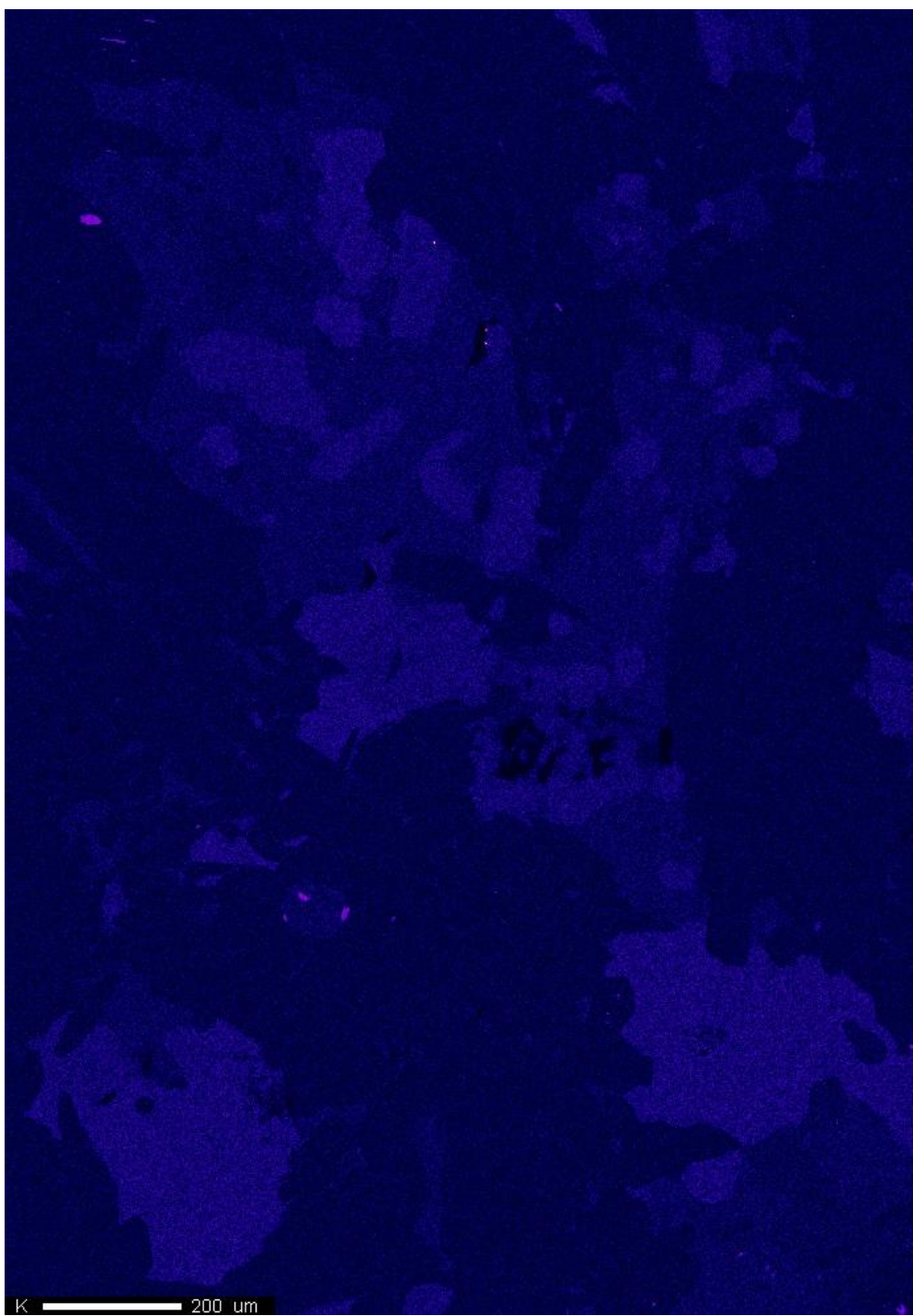
Si 100 um





Project: March\_2\_2016  
Comment: NWA8173A\_map02\_2um  
Date: 2016/03/02  
Accel Voltage: 15.0 kV  
Beam Current: 4.989e-008 A  
Dwell Time: 10.0  
Image Size: 689 x 990

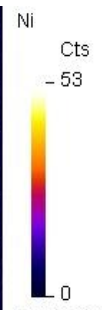
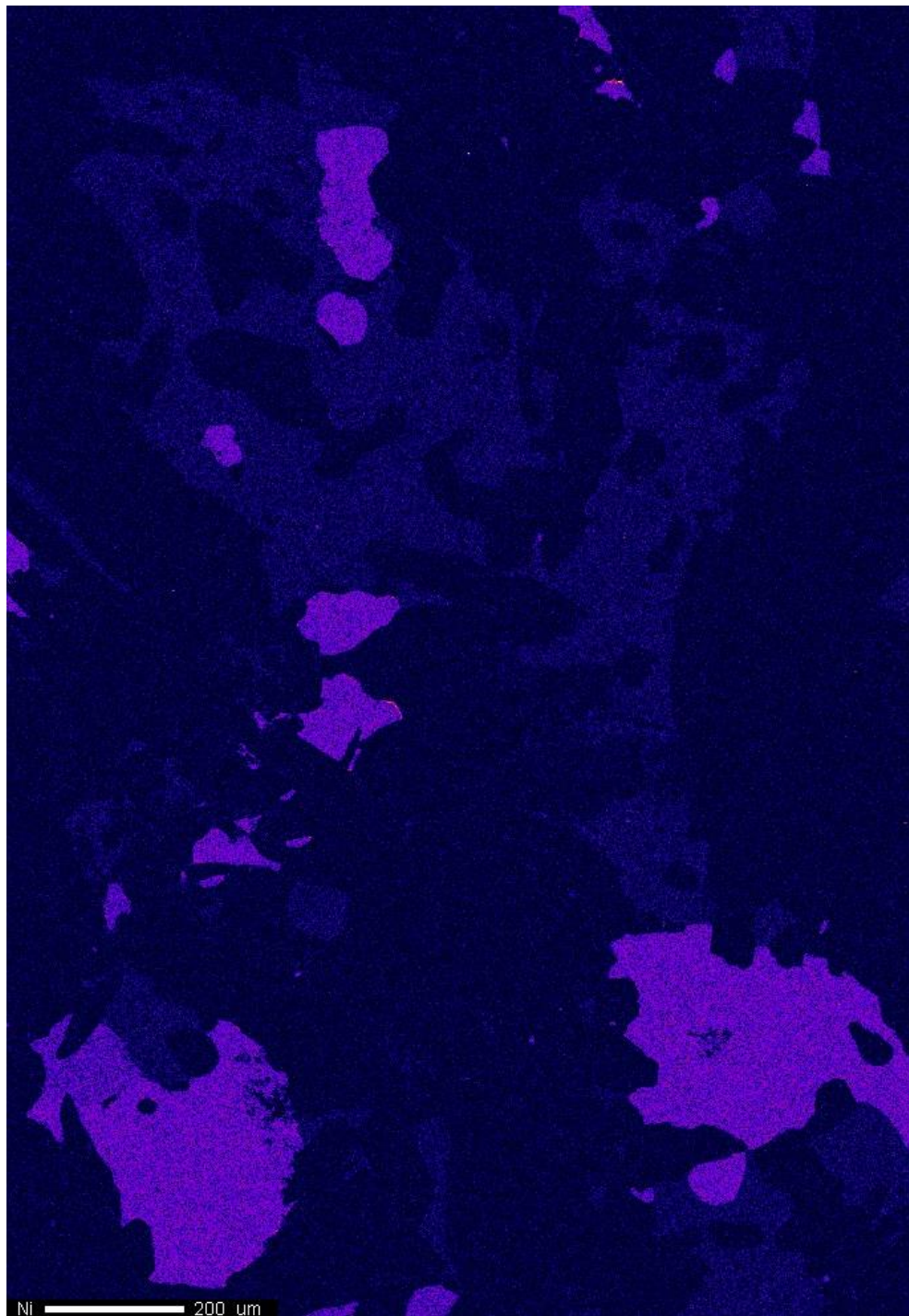
Fe 200 um



Project: March\_2\_2016  
Comment: NWA8173A\_map02\_2um  
Date: 2016/03/02  
Accel Voltage: 15.0 kV  
Beam Current: 4.989e-008 A  
Dwell Time: 10.0  
Image Size: 689 x 990

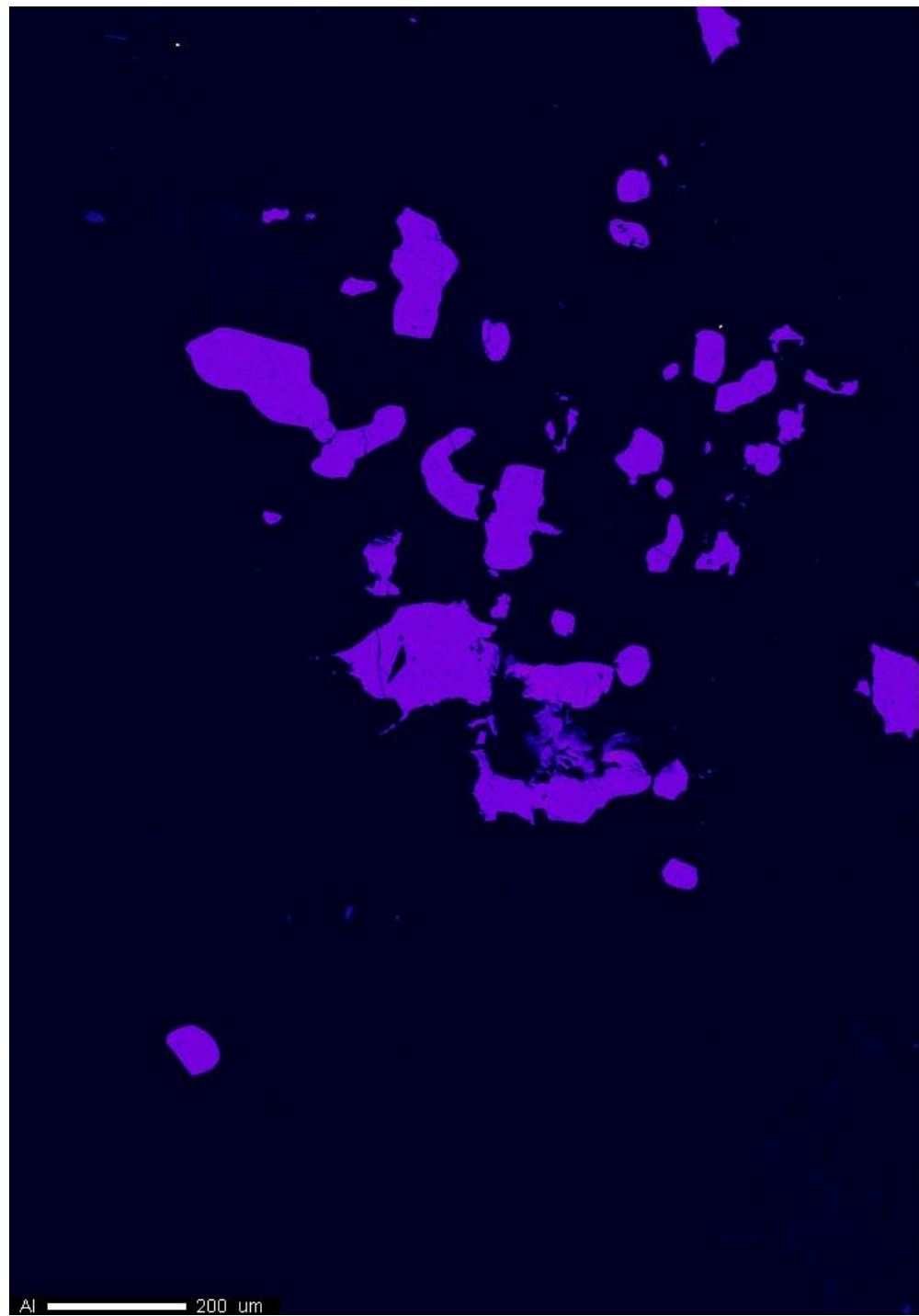
K 200 um





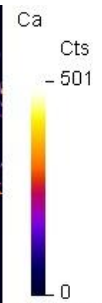
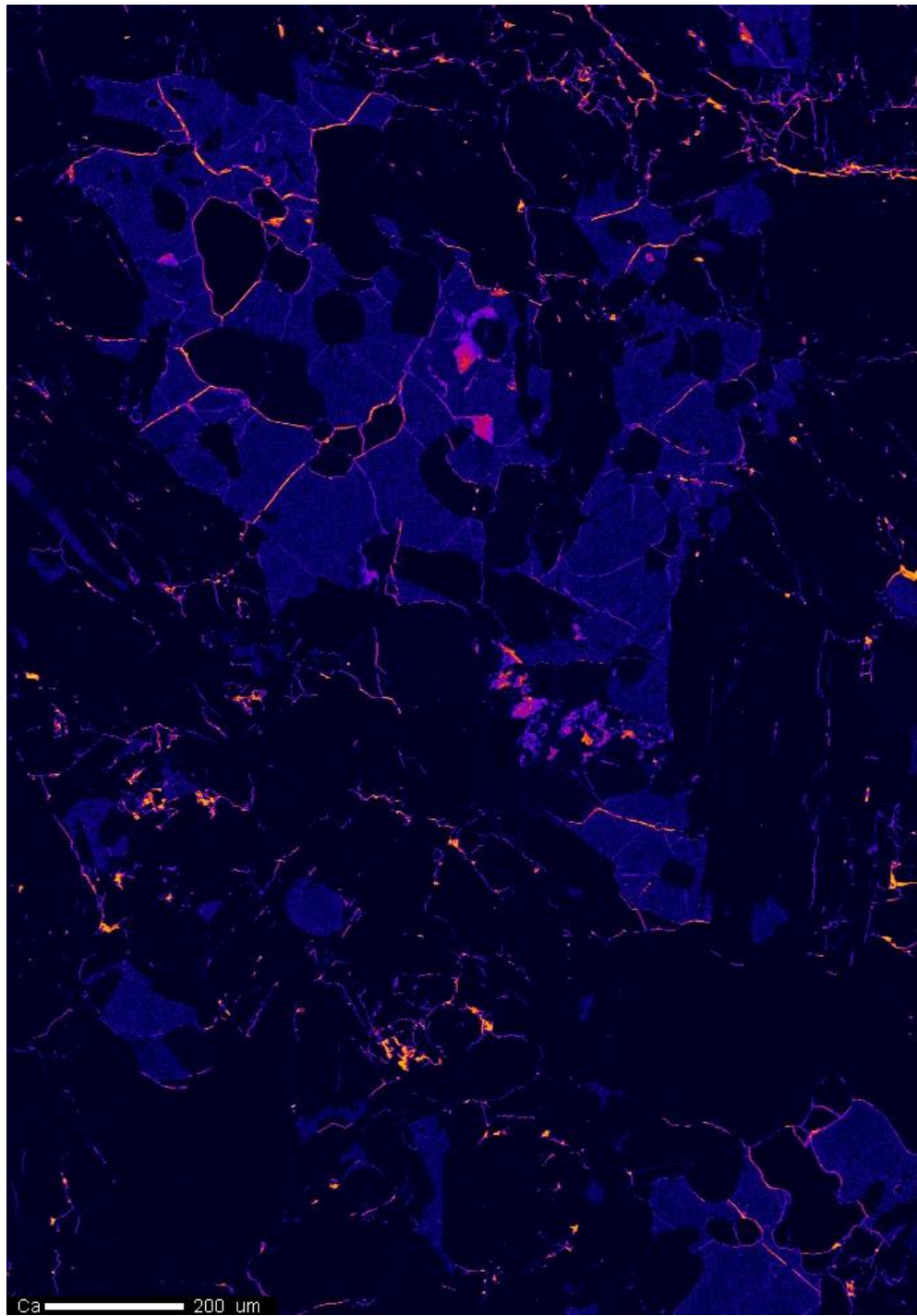
Project: March\_2\_2016  
Comment: NWA8173A\_map02\_2um  
Date: 2016/03/02  
Accel Voltage: 15.0 kV  
Beam Current: 4.989e-008 A  
Dwell Time: 10.0  
Image Size: 689 x 990

Ni 200 um



Al  
Cts  
- 893  
0

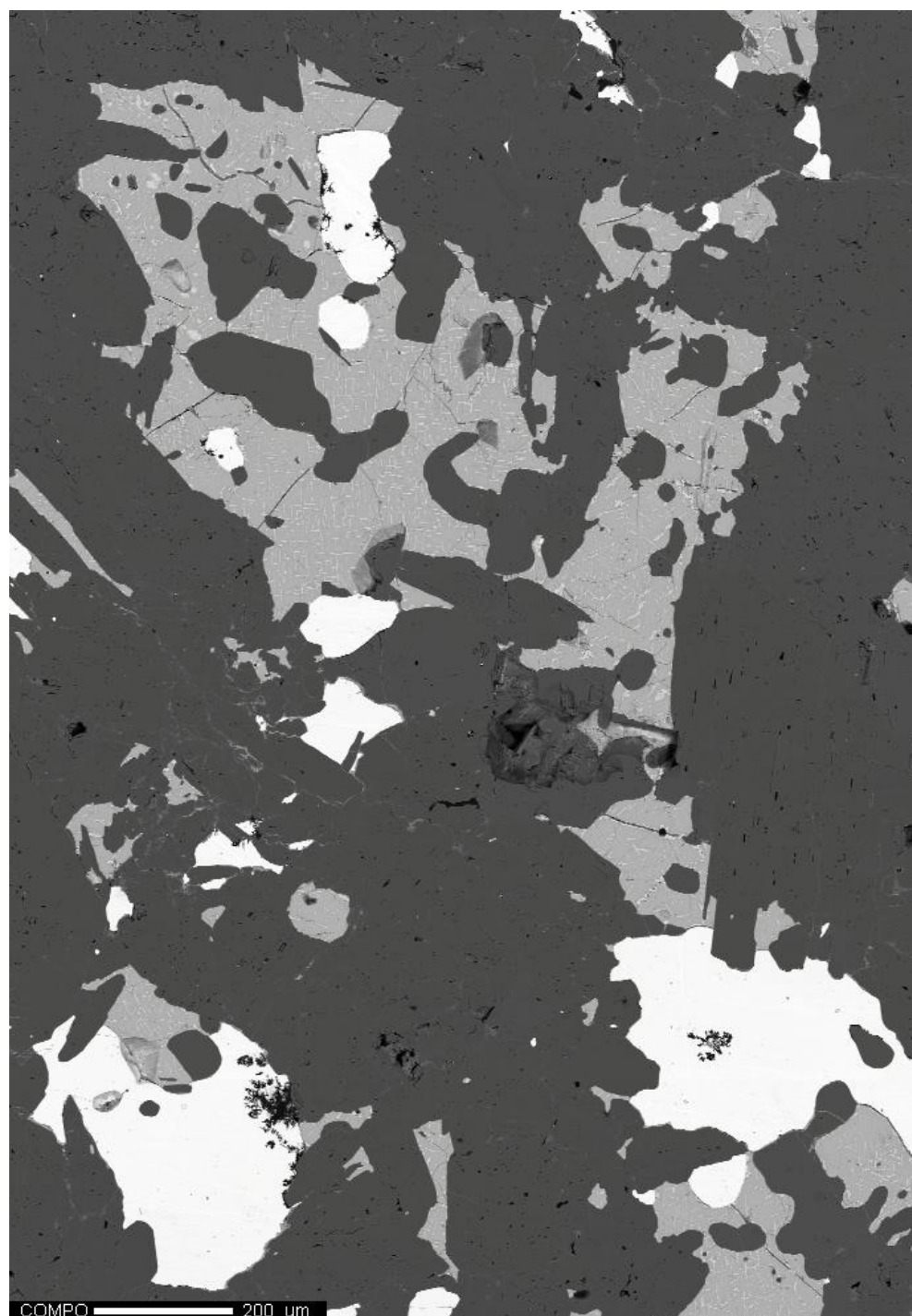
Project: March\_2\_2016  
Comment: NWA8173A\_map02\_2um  
Date: 2016/03/02  
Accel Voltage: 15.0 kV  
Beam Current: 9.883e-008 A  
Dwell Time: 10.0  
Image Size: 689 x 990



Project: March\_2\_2016  
Comment: NWA8173A\_map02\_2um  
Date: 2016/03/02  
Accel Voltage: 15.0 kV  
Beam Current: 9.883e-008 A  
Dwell Time: 10.0  
Image Size: 689 x 990

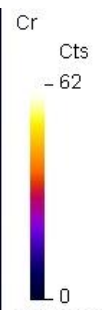
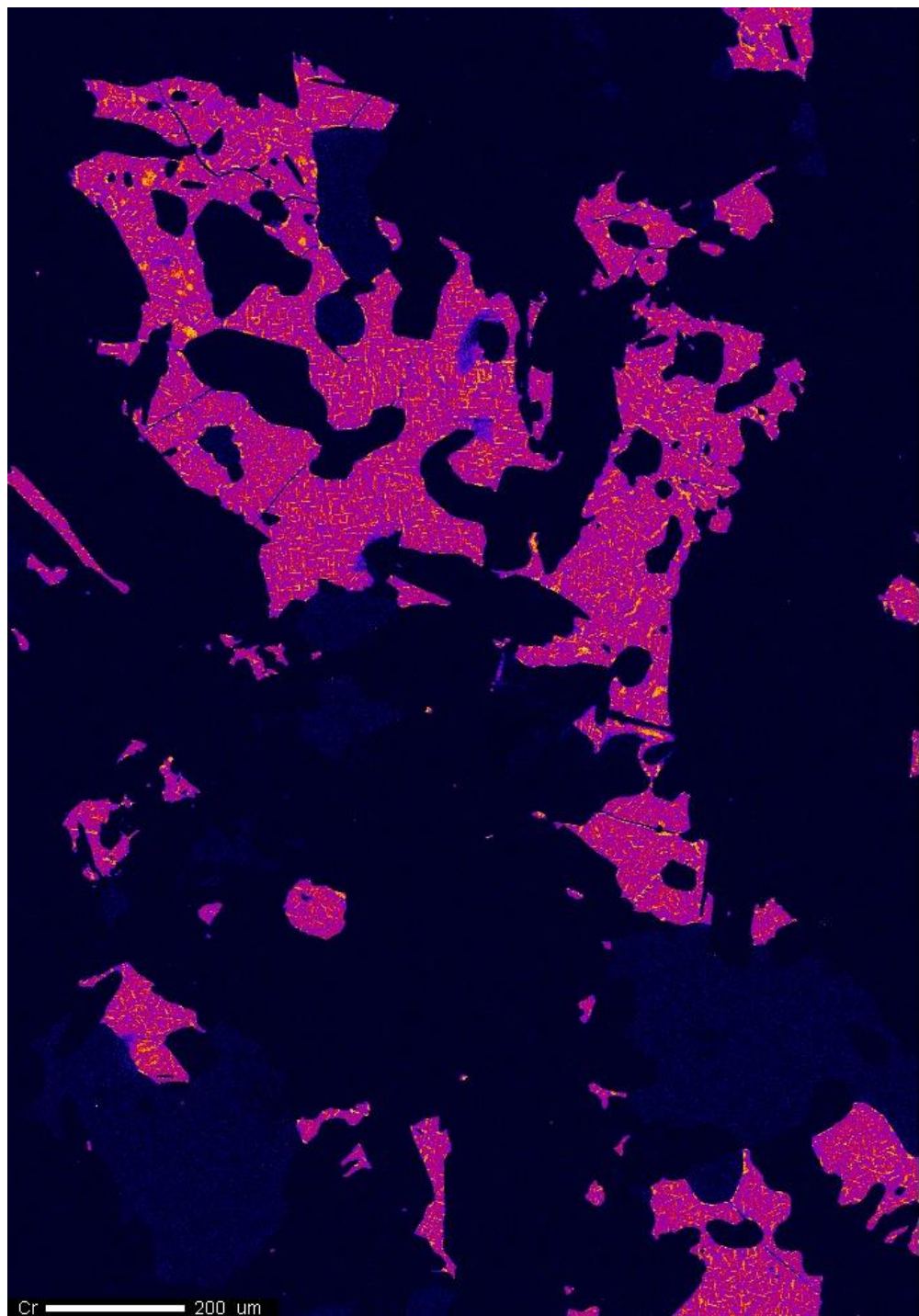
Ca 200 um





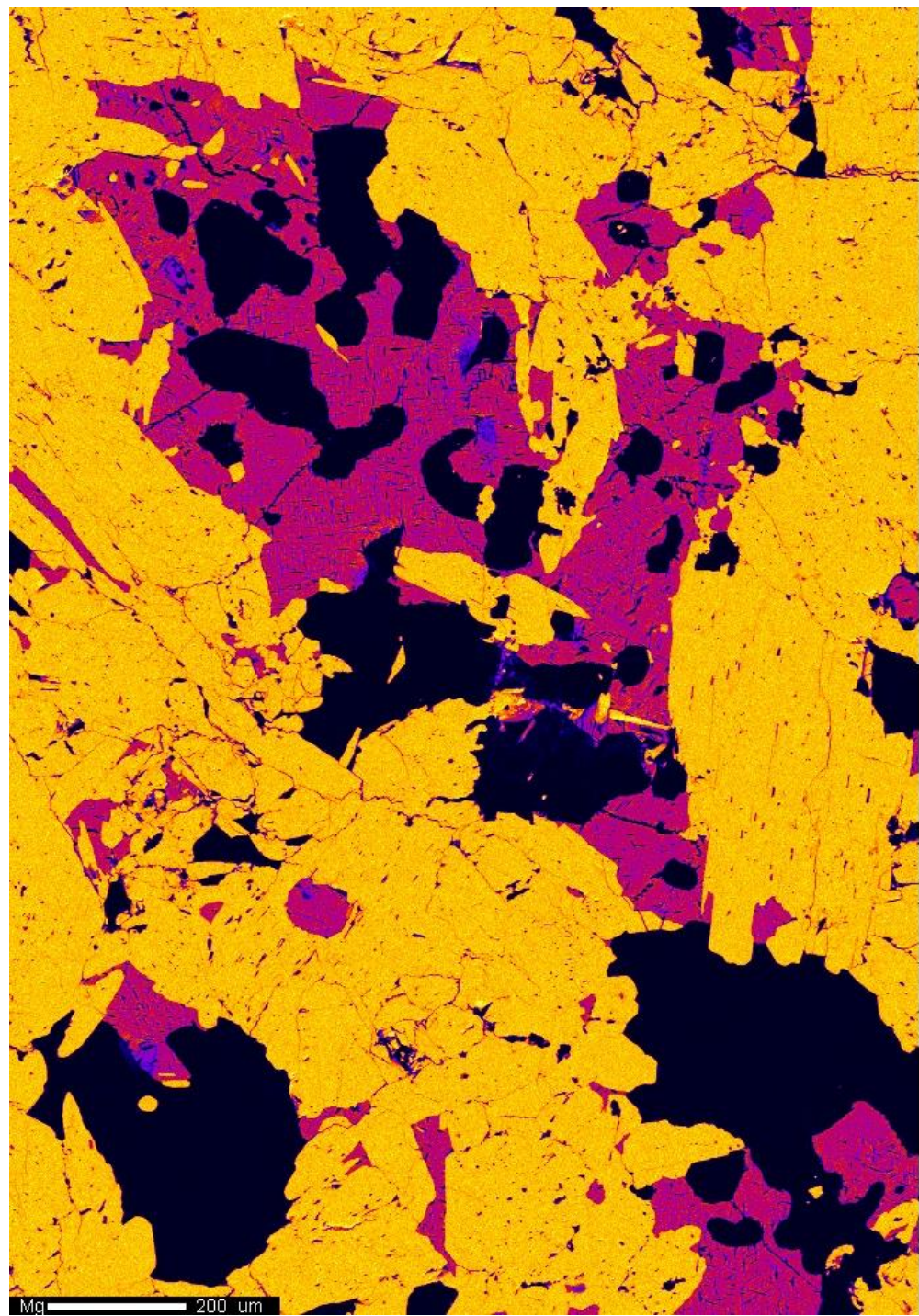
Project: March\_2\_2016  
Comment: NWA8173A\_map02\_2um  
Date: 2016/03/02  
Accel Voltage: 15.0 kV  
Beam Current: 9.883e-008 A  
Dwell Time: 10.0  
Image Size: 689 x 990





Project: March\_2\_2016  
Comment: NWA8173A\_map02\_2um  
Date: 2016/03/02  
Accel Voltage: 15.0 kV  
Beam Current: 9.883e-008 A  
Dwell Time: 10.0  
Image Size: 689 x 990

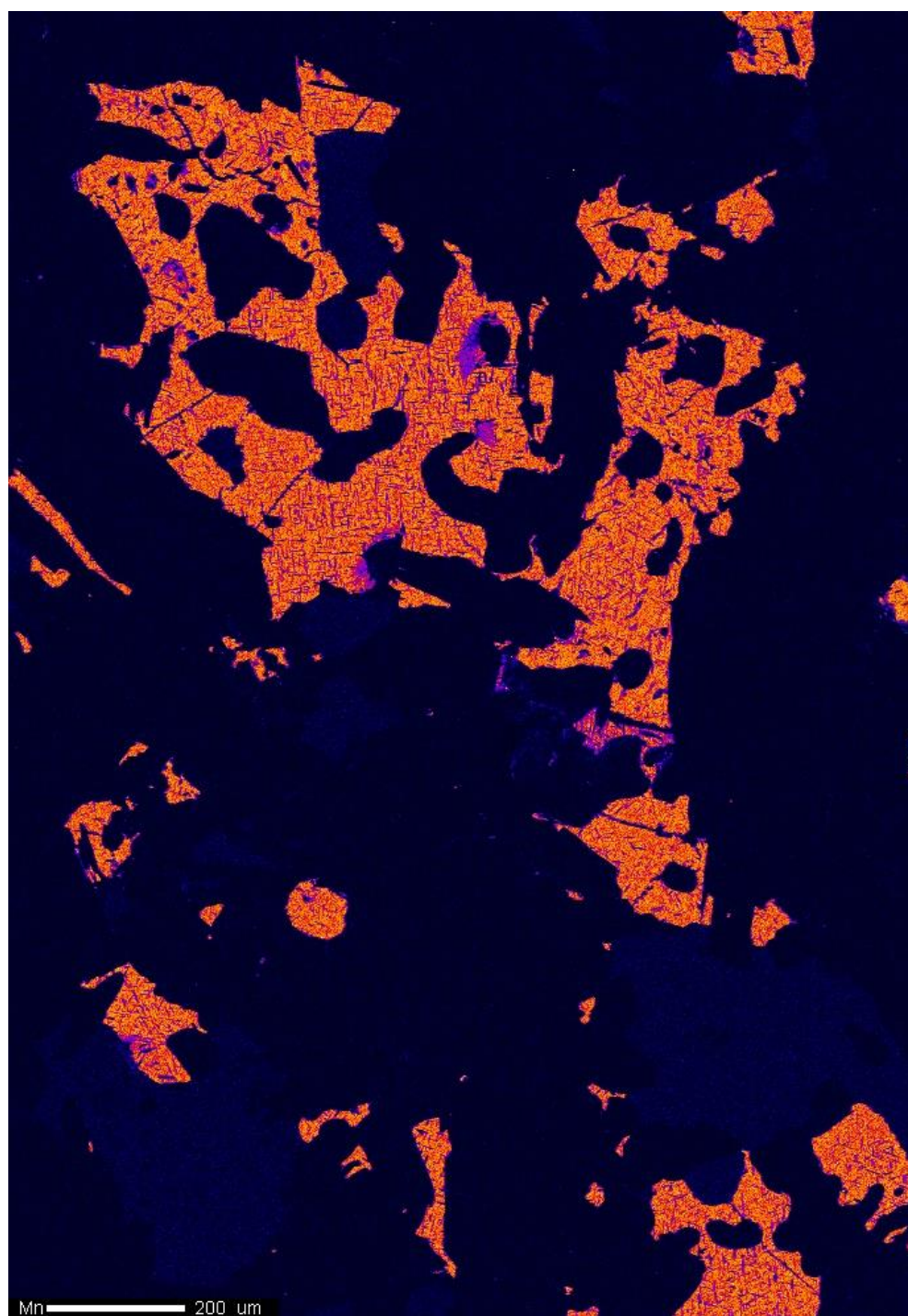
Cr 200 um



Mg  
Cts  
- 405  
0

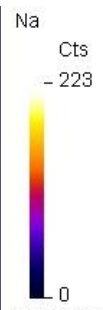
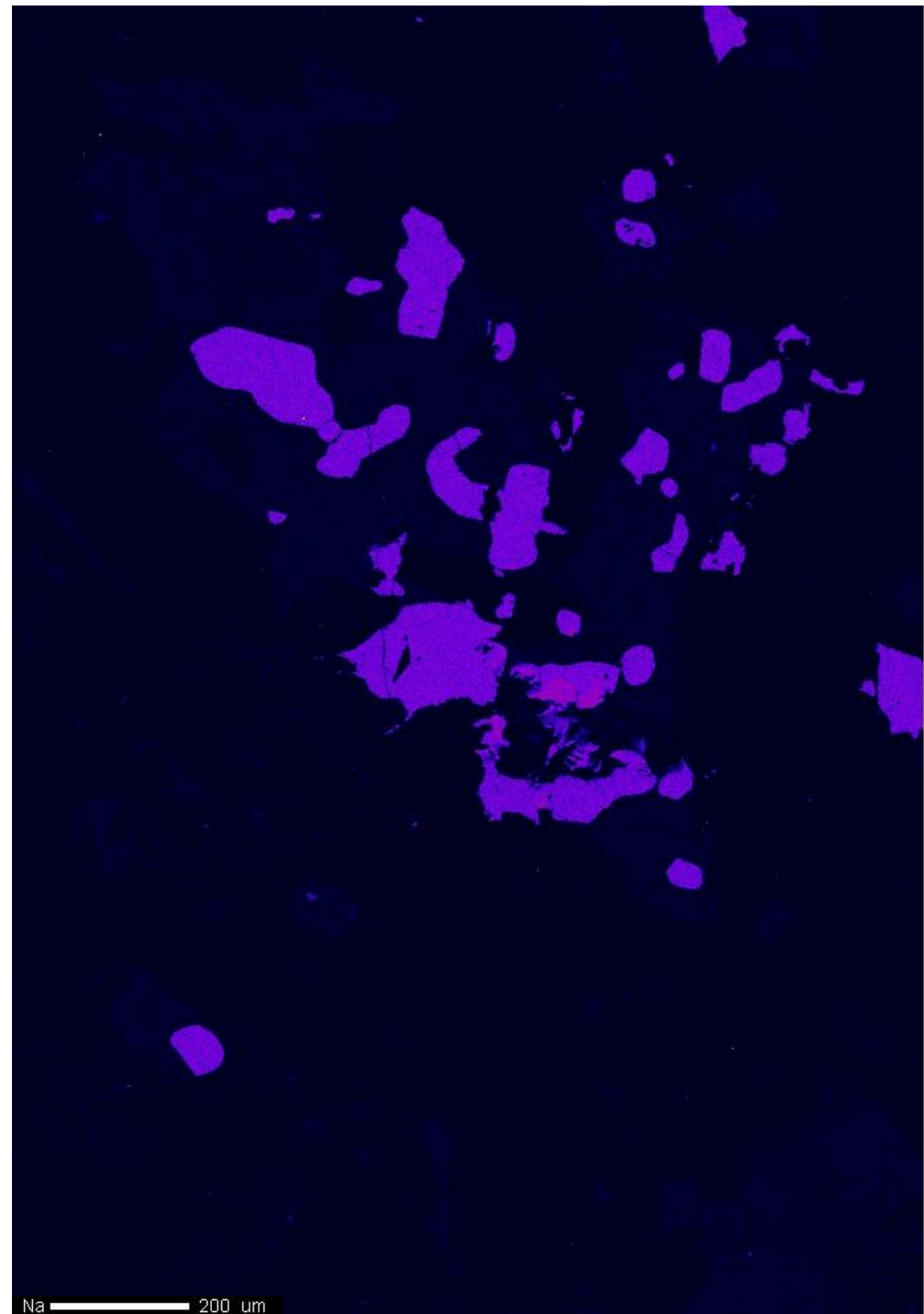
Project: March\_2\_2016  
Comment: NWA8173A\_map02\_2um  
Date: 2016/03/02  
Accel Voltage: 15.0 kV  
Beam Current: 9.883e-008 A  
Dwell Time: 10.0  
Image Size: 689 x 990





Project: March\_2\_2016  
Comment: NWA8173A\_map02\_2um  
Date: 2016/03/02  
Accel Voltage: 15.0 kV  
Beam Current: 9.883e-008 A  
Dwell Time: 10.0  
Image Size: 689 x 990

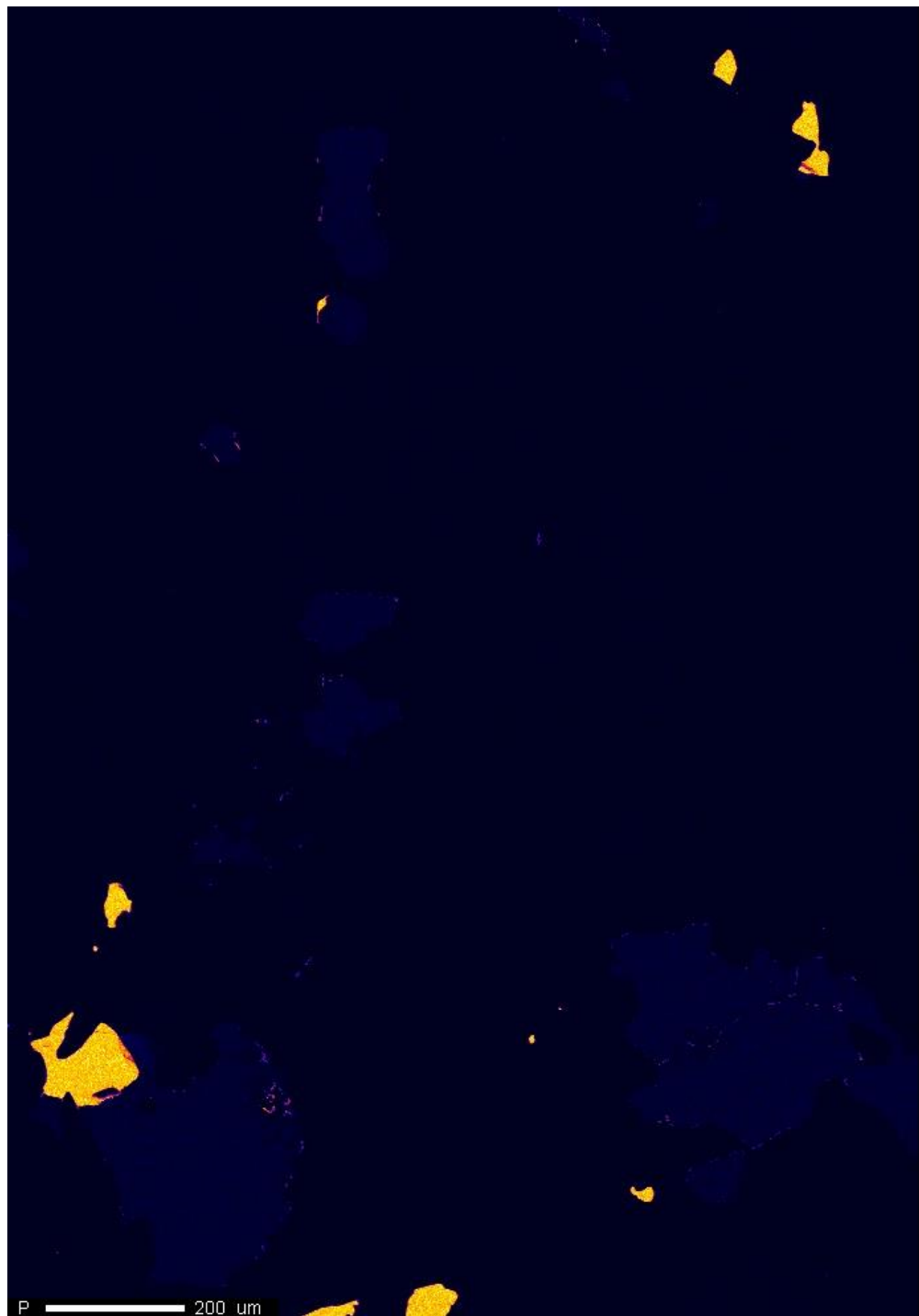
Mn 200 um



Project: March\_2\_2016  
Comment: NWA8173A\_map02\_2um  
Date: 2016/03/02  
Accel Voltage: 15.0 kV  
Beam Current: 9.883e-008 A  
Dwell Time: 10.0  
Image Size: 689 x 990

Na  200 um

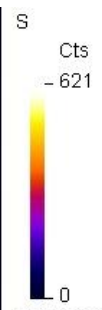
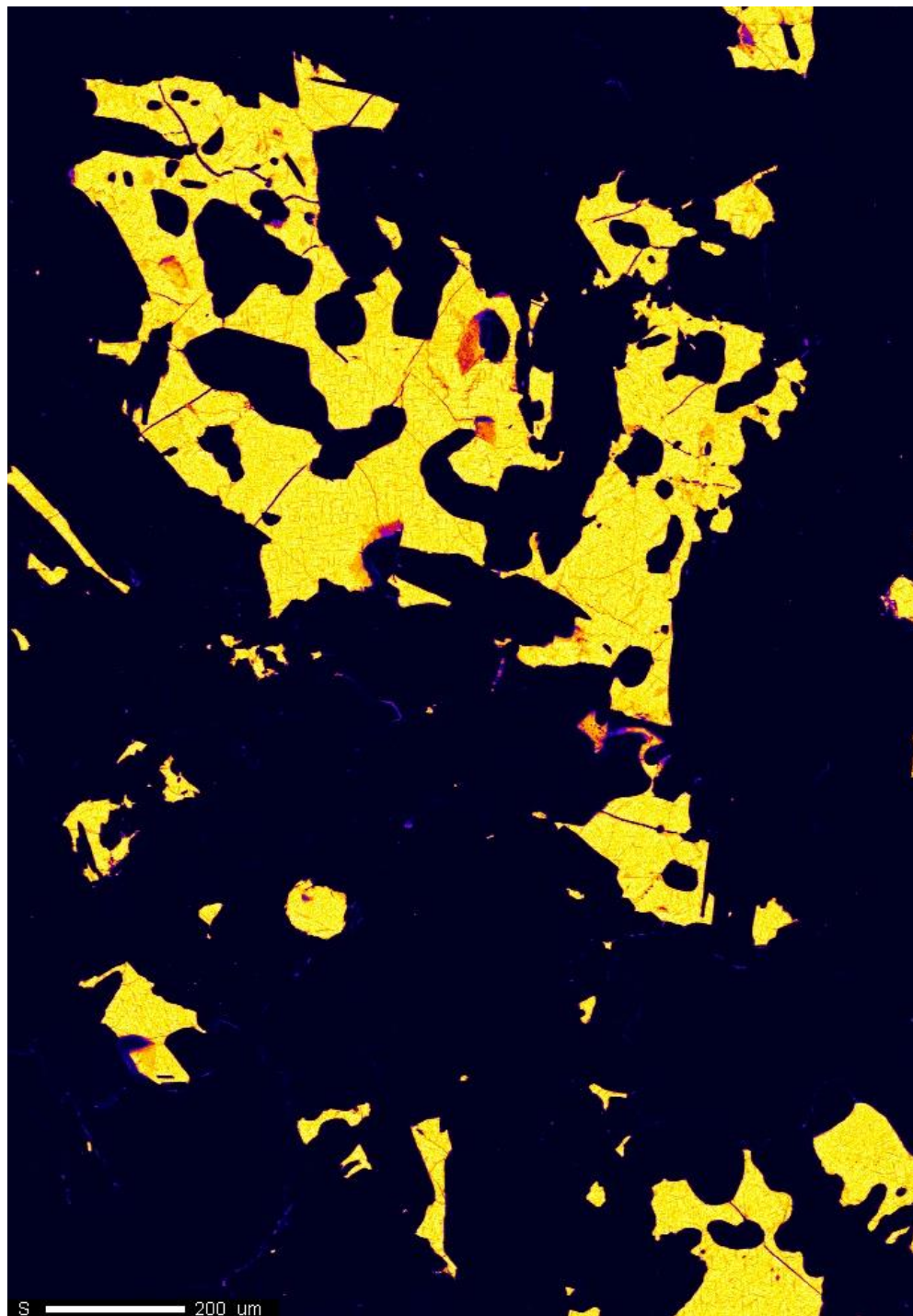




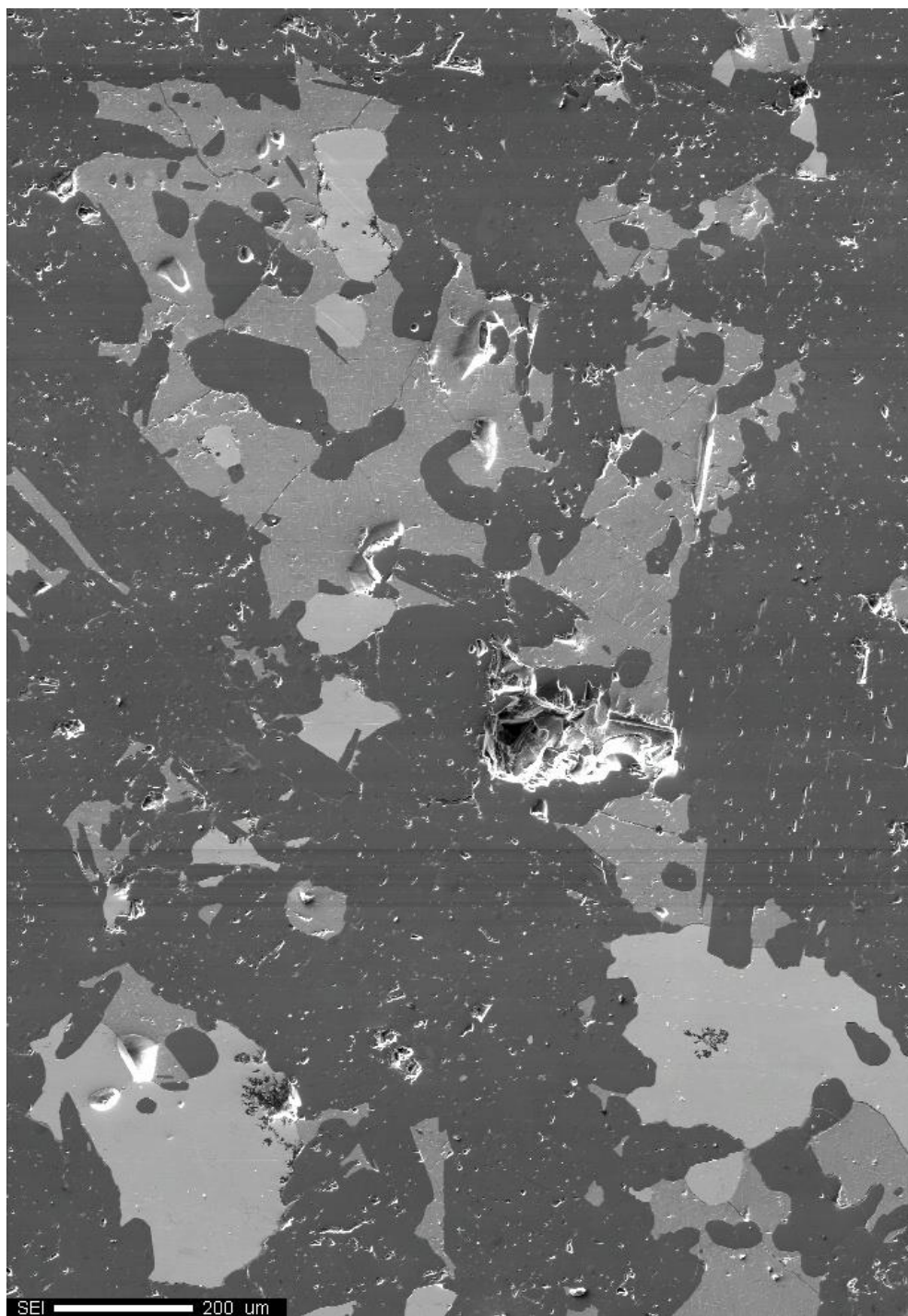
P  
Cts  
- 147  
0

Project: March\_2\_2016  
Comment: NWA8173A\_map02\_2um  
Date: 2016/03/02  
Accel Voltage: 15.0 kV  
Beam Current: 9.883e-008 A  
Dwell Time: 10.0  
Image Size: 689 x 990

P 200 um



Project: March\_2\_2016  
Comment: NWA8173A\_map02\_2um  
Date: 2016/03/02  
Accel Voltage: 15.0 kV  
Beam Current: 9.883e-008 A  
Dwell Time: 10.0  
Image Size: 689 x 990

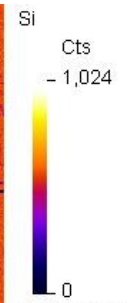
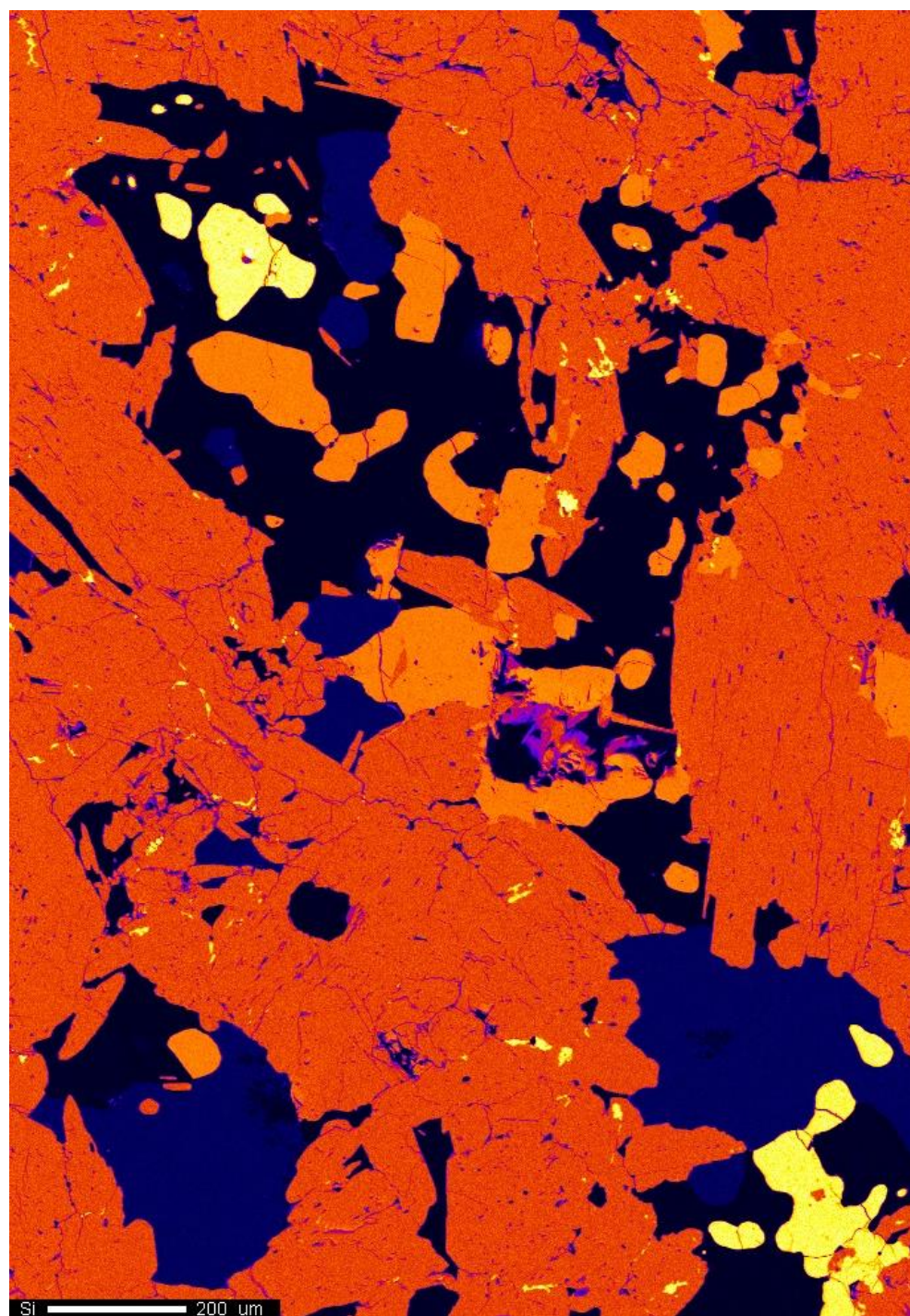


SEI  
Cts  
- 4,095  
0

Project: March\_2\_2016  
Comment: NWA8173A\_map02\_2um  
Date: 2016/03/02  
Accel Voltage: 15.0 kV  
Beam Current: 9.883e-008 A  
Dwell Time: 10.0  
Image Size: 689 x 990

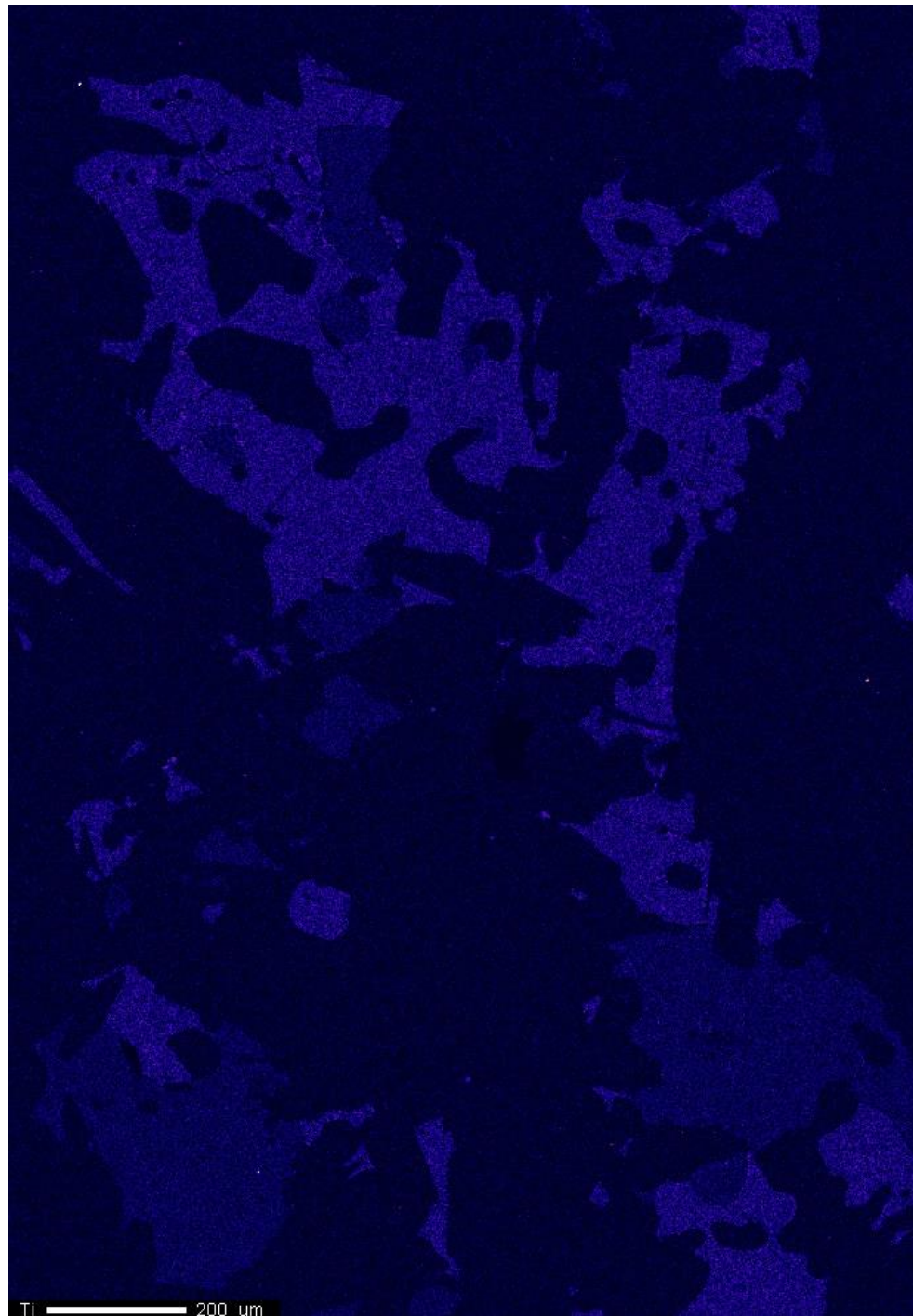
SEI 200 um





Project: March\_2\_2016  
Comment: NWA8173A\_map02\_2um  
Date: 2016/03/02  
Accel Voltage: 15.0 kV  
Beam Current: 9.883e-008 A  
Dwell Time: 10.0  
Image Size: 689 x 990



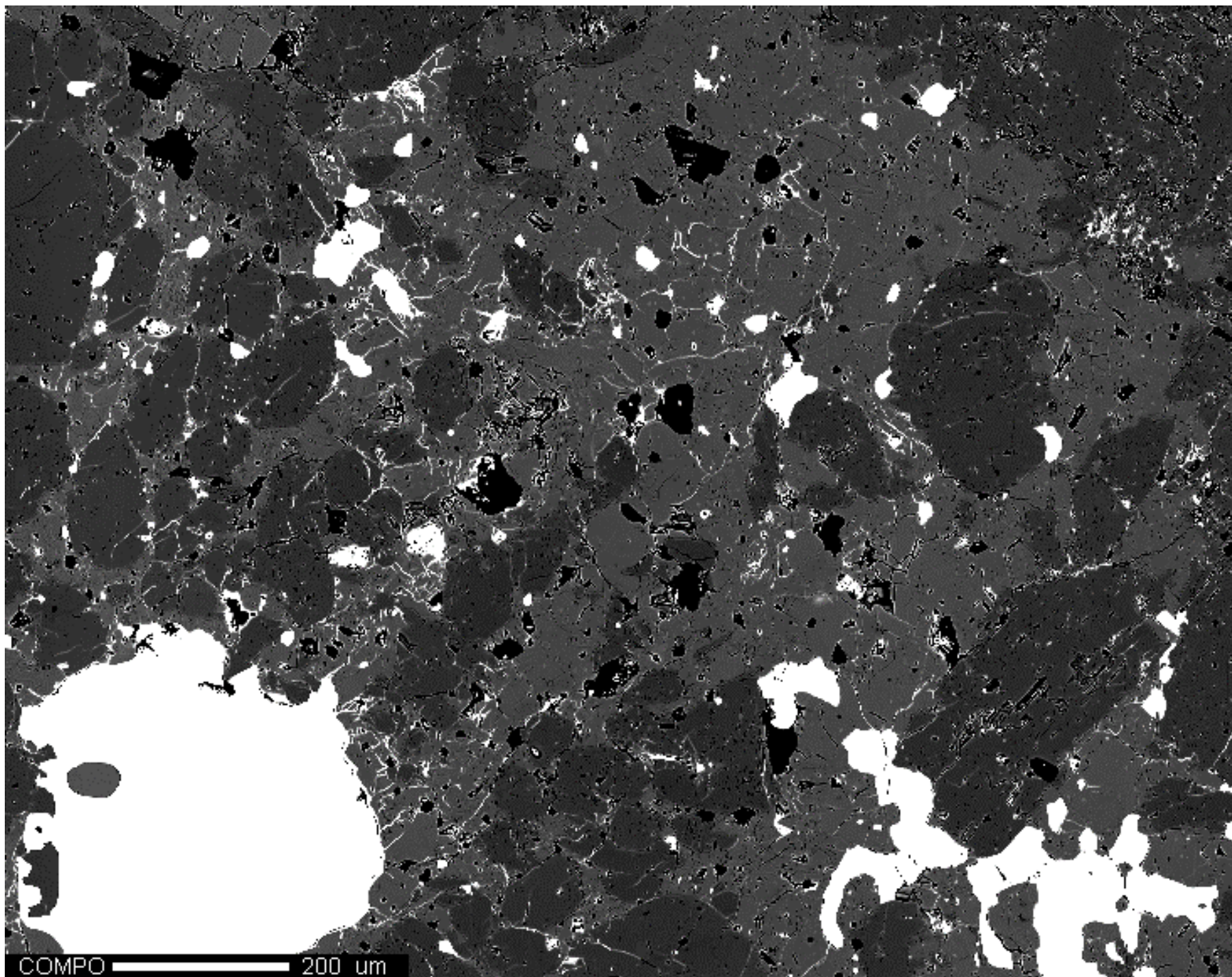


Project: March\_2\_2016  
Comment: NWA8173A\_map02\_2um  
Date: 2016/03/02  
Accel Voltage: 15.0 kV  
Beam Current: 9.883e-008 A  
Dwell Time: 10.0  
Image Size: 689 x 990

Ti 200 um

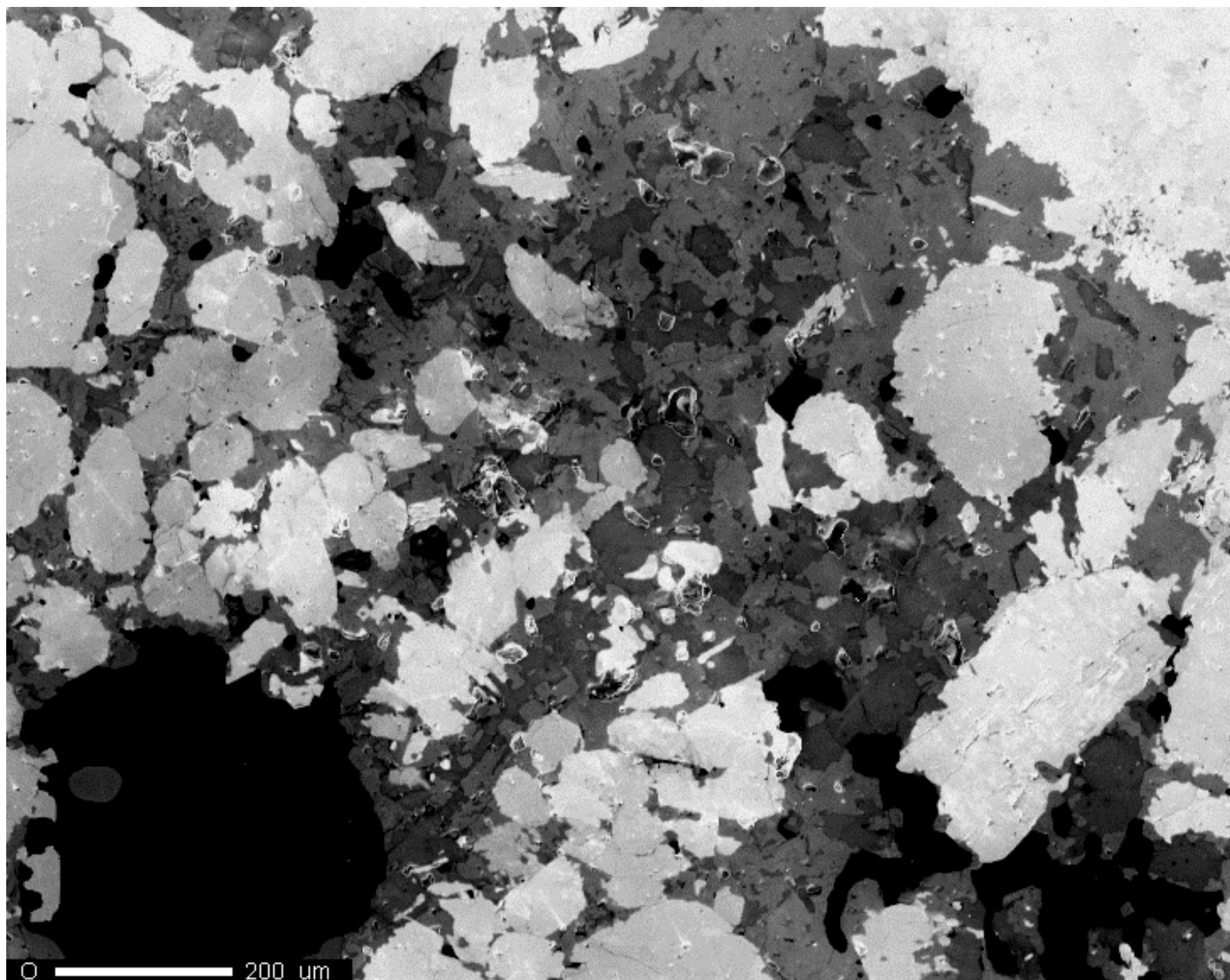
# NWA 8173b X-ray elemental maps





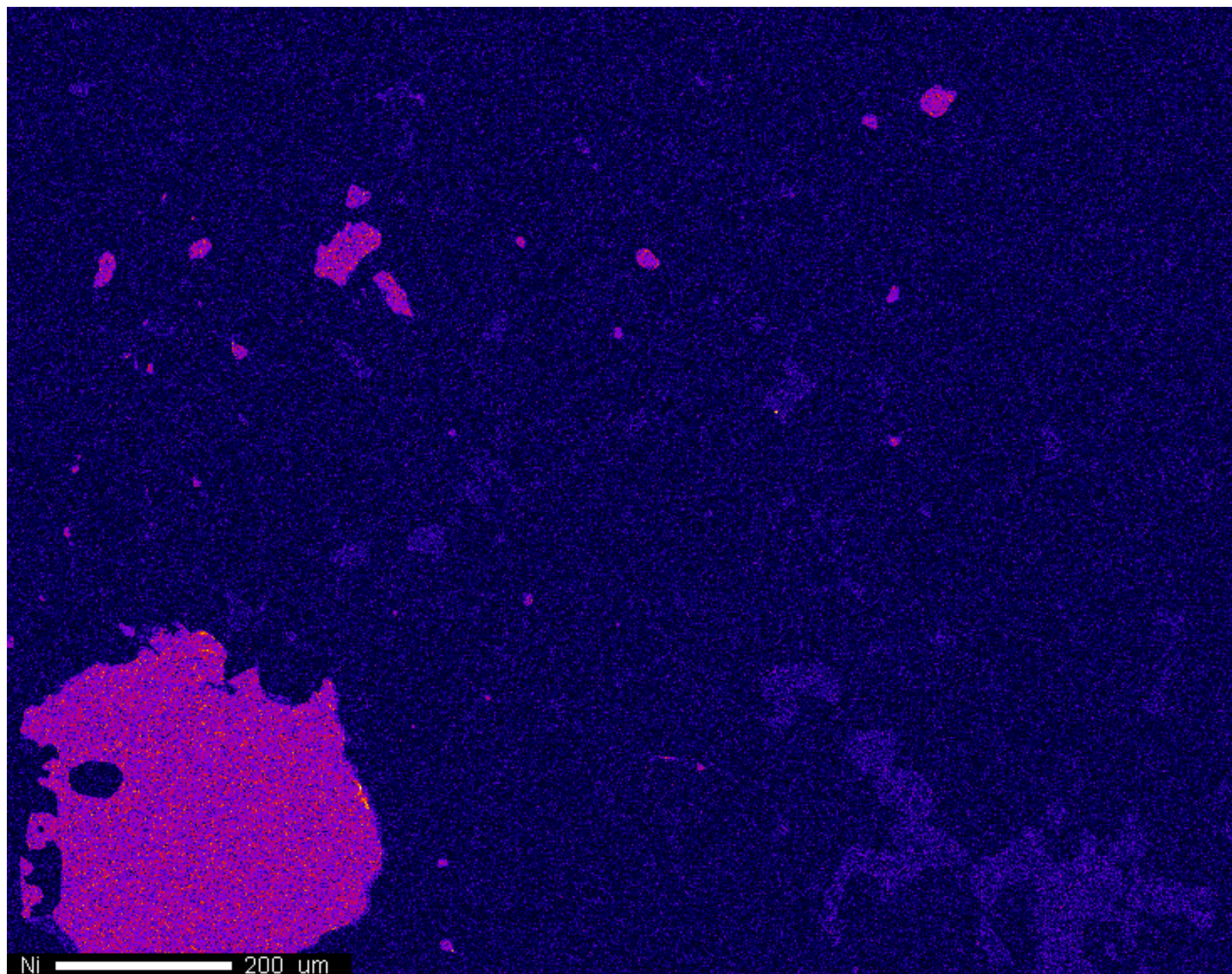
Project: September\_17\_2015  
Comment: NWA8173b\_map01\_2um  
Date: 2015/09/17  
Accel Voltage: 15.0 kV  
Beam Current: 9.928e-008 A  
Dwell Time: 10.0  
Image Size: 732 x 578





Project: September\_17\_2015  
Comment: NWA8173b\_map01\_2um  
Date: 2015/09/17  
Accel Voltage: 15.0 kV  
Beam Current: 9.928e-008 A  
Dwell Time: 10.0  
Image Size: 732 x 578





Ni

Cts

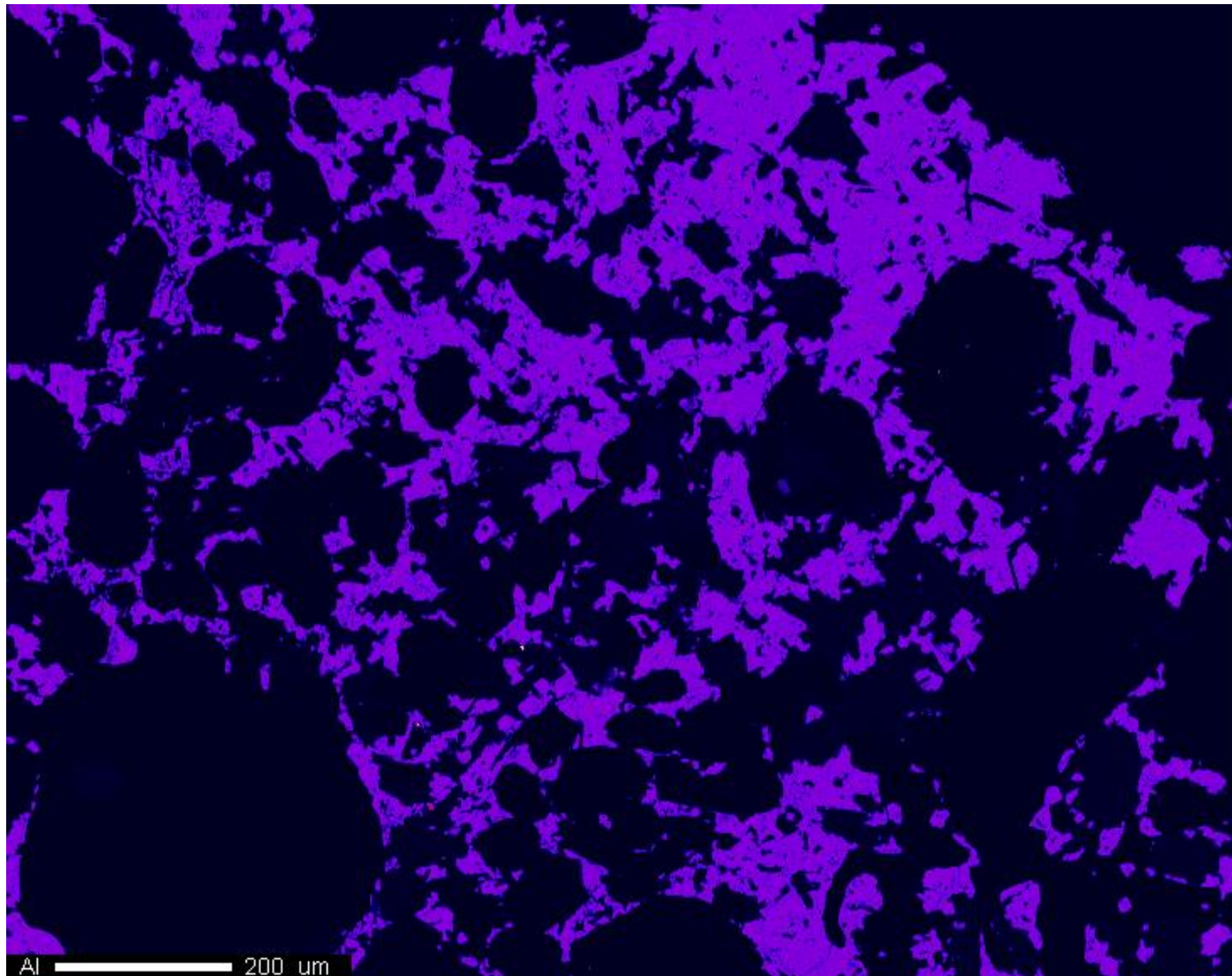
- 36



Project: September\_17\_2015  
Comment: NWA8173b\_map01\_2um  
Date: 2015/09/17  
Accel Voltage: 15.0 kV  
Beam Current: 5.001e-008 A  
Dwell Time: 10.0  
Image Size: 732 x 578

Ni 200 um





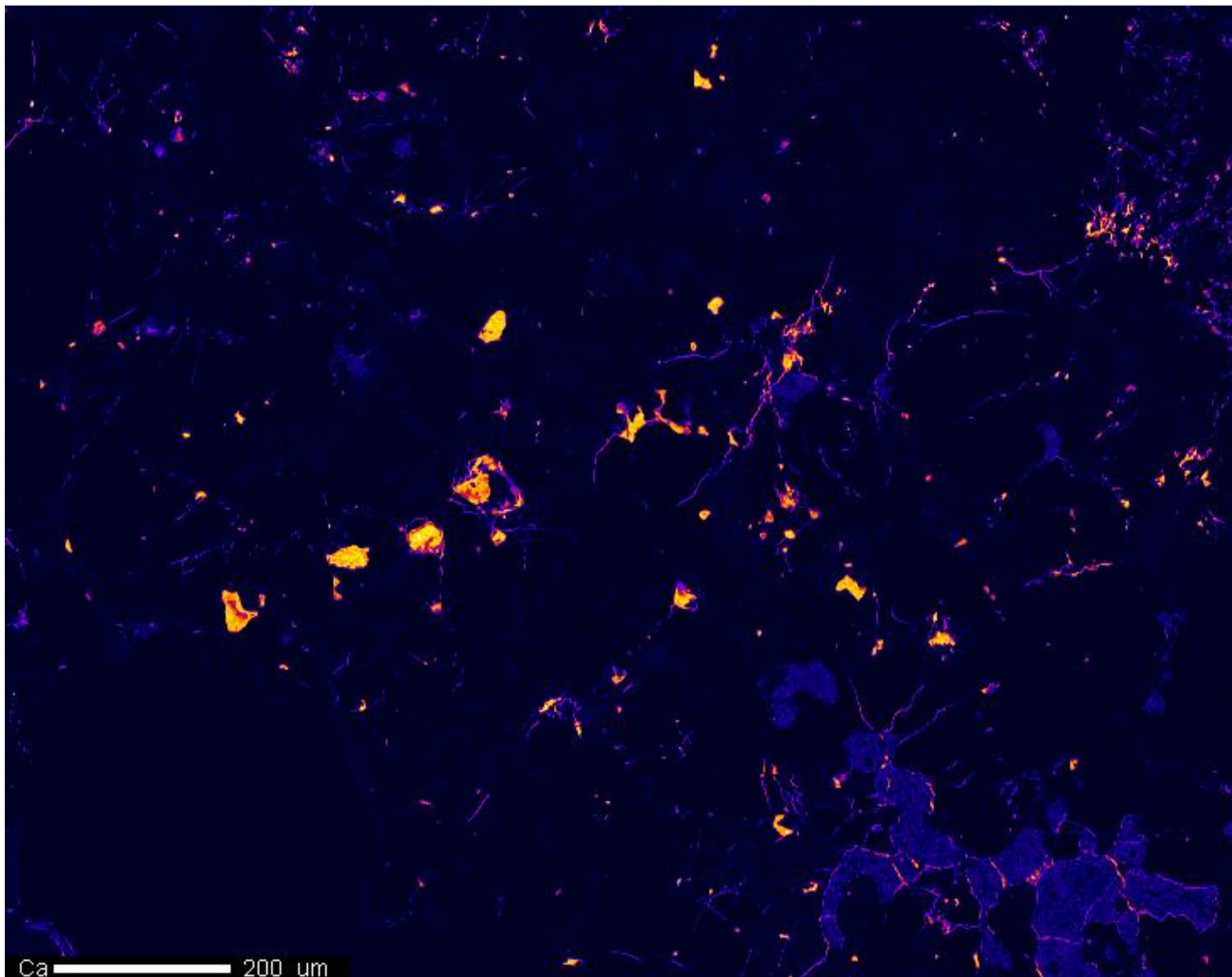
Al

Cts  
- 862

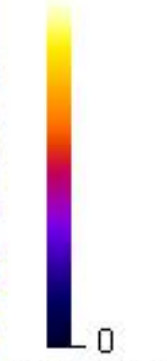


Project: September\_17\_2015  
Comment: NWA8173b\_map01\_2um  
Date: 2015/09/17  
Accel Voltage: 15.0 kV  
Beam Current: 9.928e-008 A  
Dwell Time: 10.0  
Image Size: 732 x 578

Al 200 um

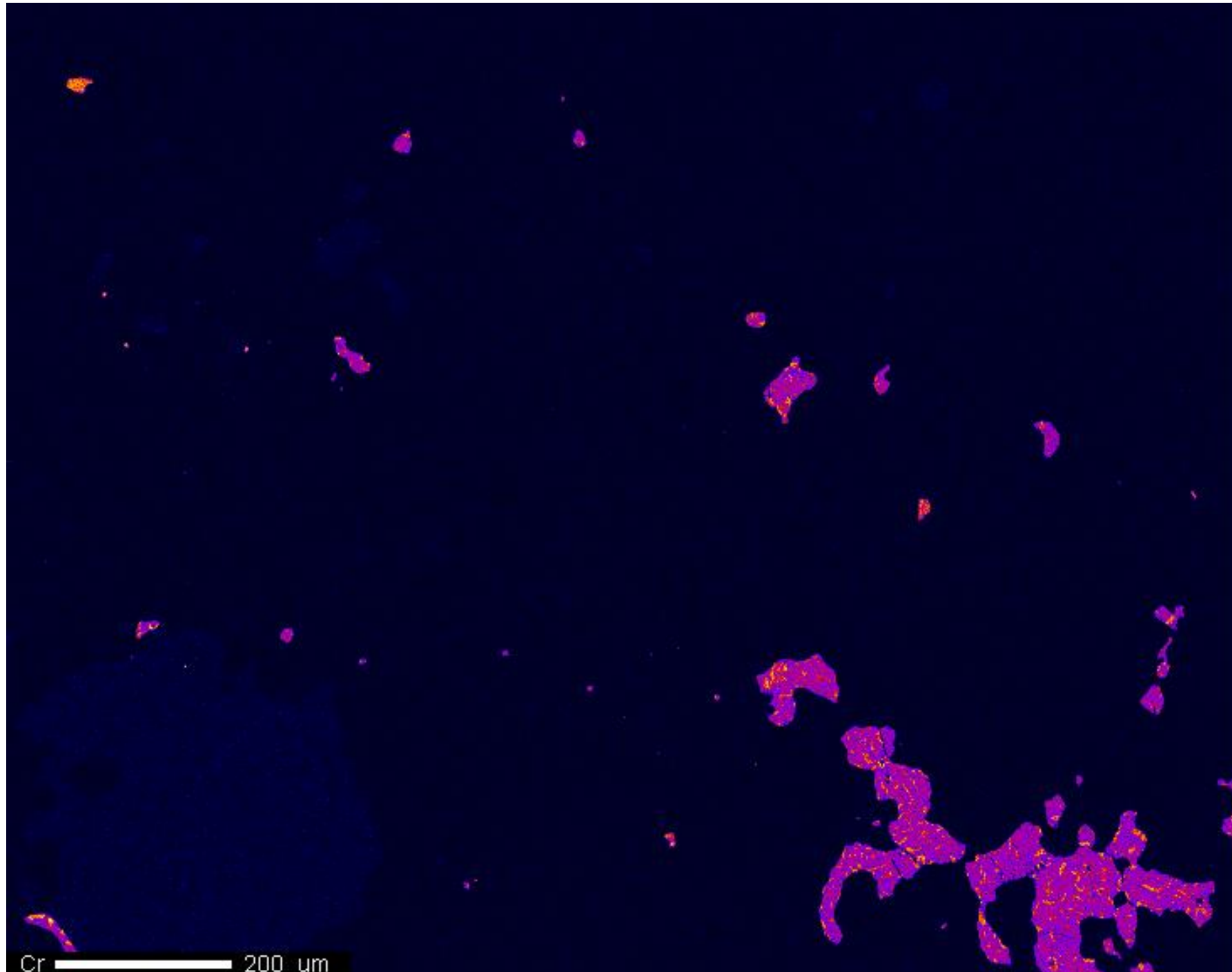


Ca  
Cts  
- 456



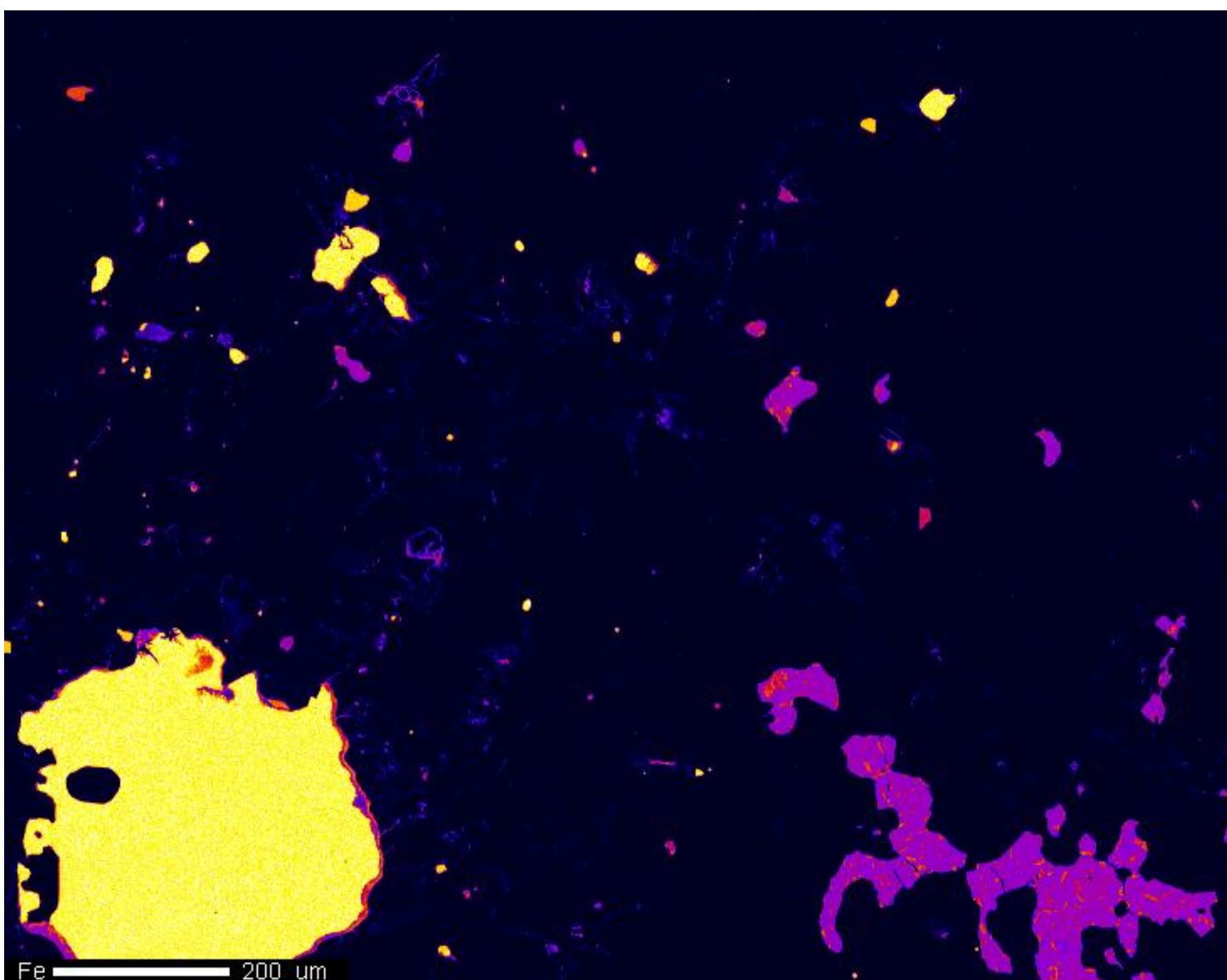
Project: September\_17\_2015  
Comment: NWA8173b\_map01\_2um  
Date: 2015/09/17  
Accel Voltage: 15.0 kV  
Beam Current: 9.928e-008 A  
Dwell Time: 10.0  
Image Size: 732 x 578





Project: September\_17\_2015  
Comment: NWA8173b\_map01\_2um  
Date: 2015/09/17  
Accel Voltage: 15.0 kV  
Beam Current: 9.928e-008 A  
Dwell Time: 10.0  
Image Size: 732 x 578





Fe

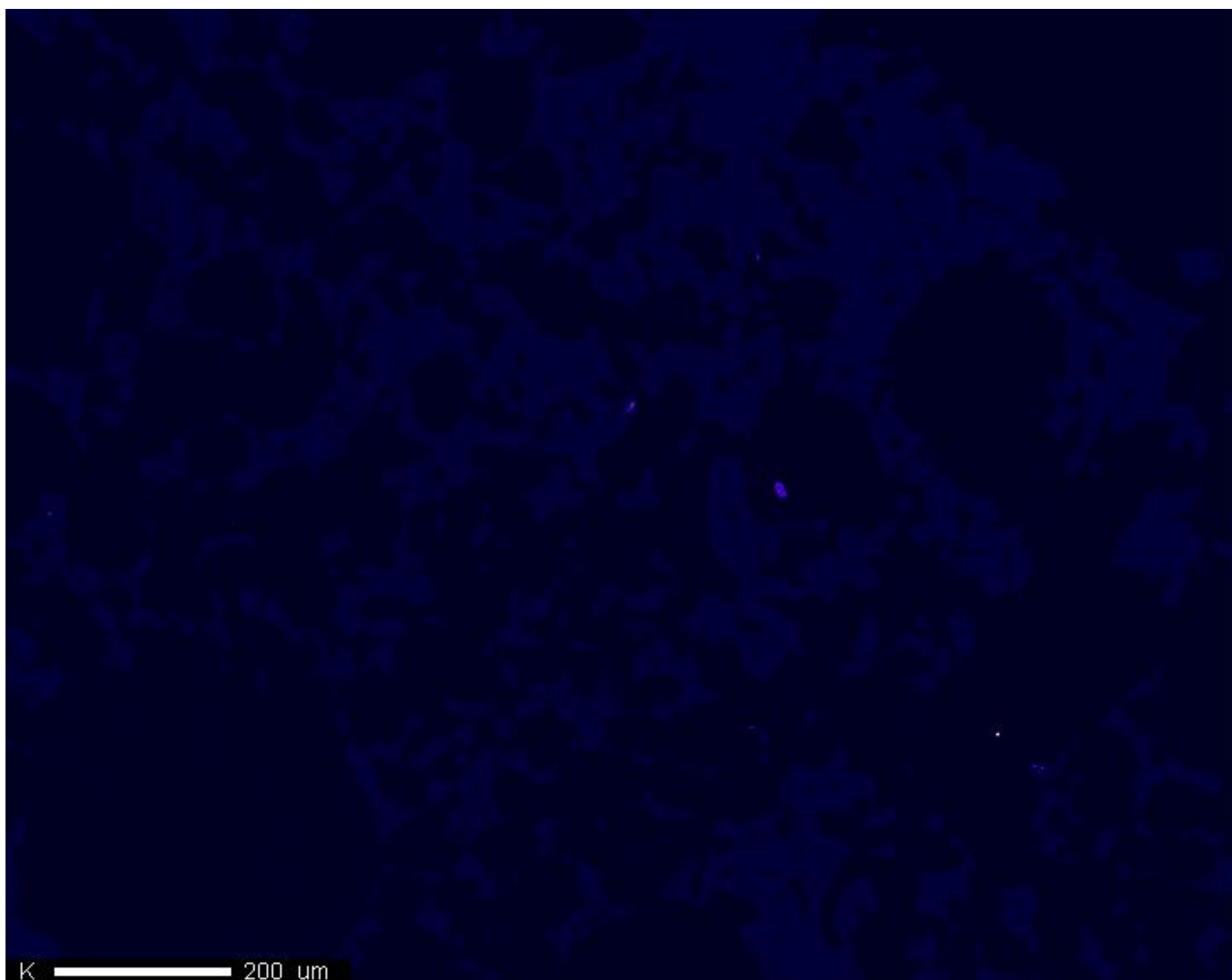
Cts

- 774



Project: September\_17\_2015  
Comment: NWA8173b\_map01\_2um  
Date: 2015/09/17  
Accel Voltage: 15.0 kV  
Beam Current: 9.928e-008 A  
Dwell Time: 10.0  
Image Size: 732 x 578

Fe 200 um



K

Cts

- 888



0

Project: September\_17\_2015

Comment: NWA8173b\_map01\_2um

Date: 2015/09/17

Accel Voltage: 15.0 kV

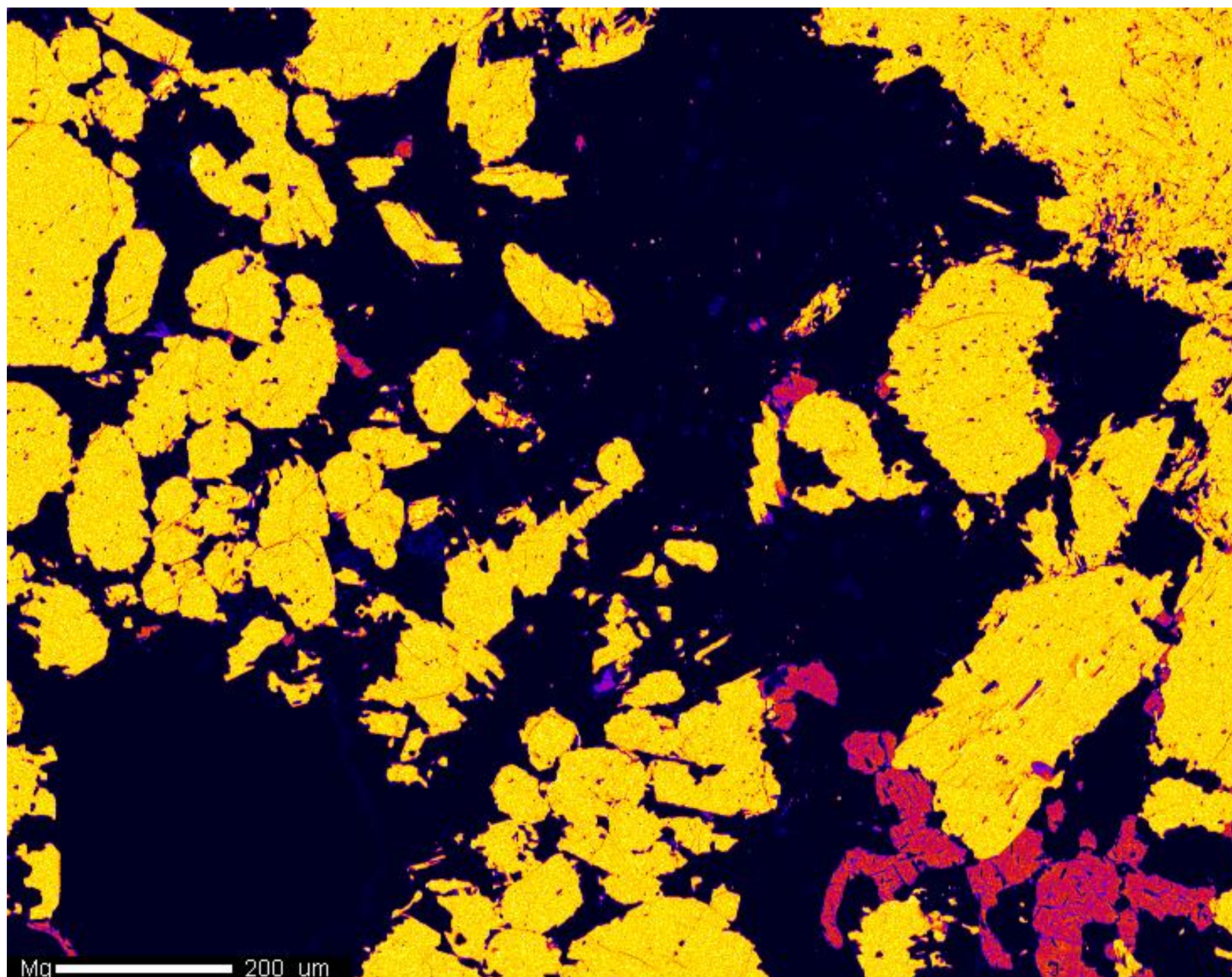
Beam Current: 9.928e-008 A

Dwell Time: 10.0

Image Size: 732 x 578

K  200 um

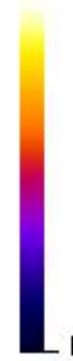




Mg

Cts

- 448



Project: September\_17\_2015

Comment: NWA8173b\_map01\_2um

Date: 2015/09/17

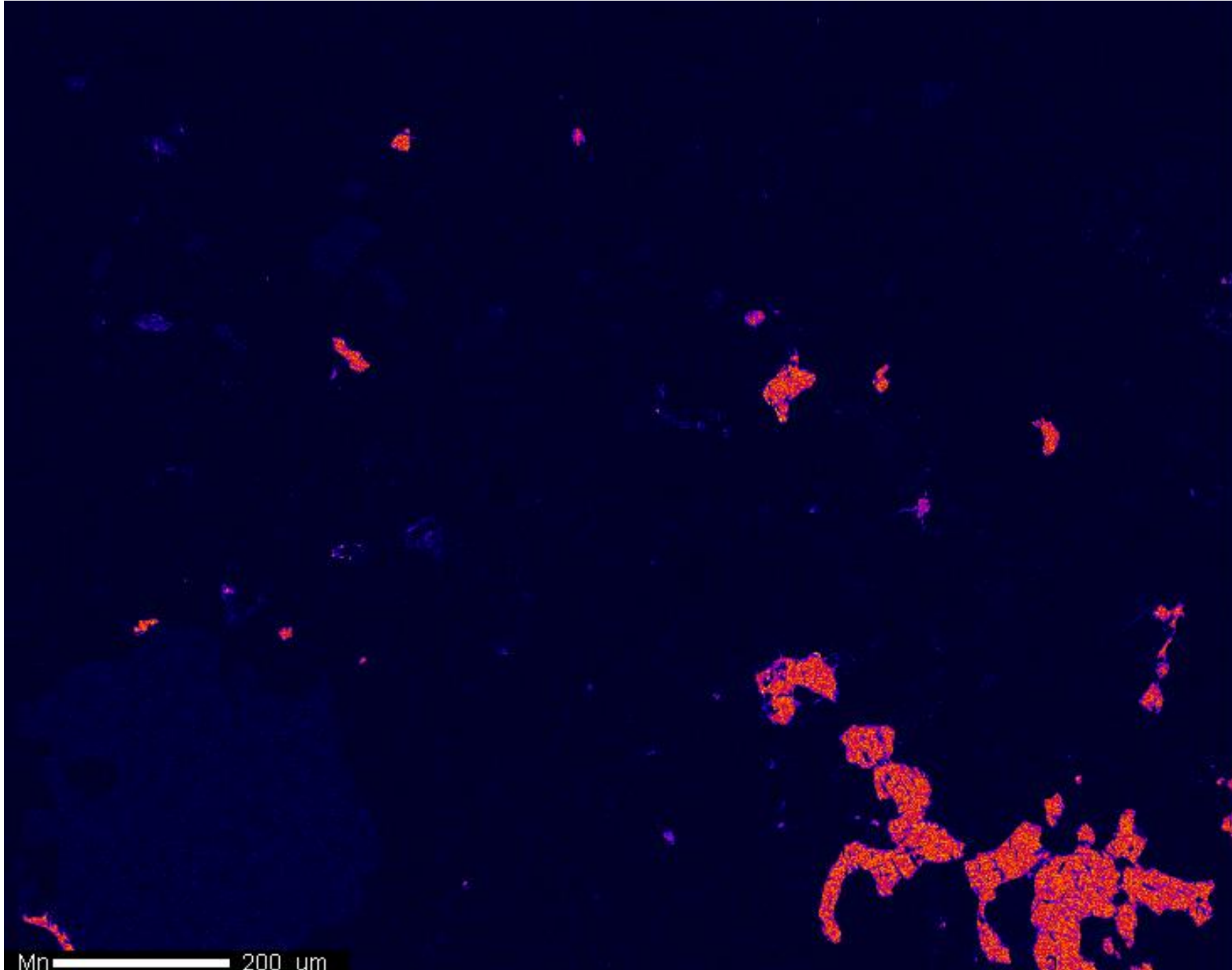
Accel Voltage: 15.0 kV

Beam Current: 9.928e-008 A

Dwell Time: 10.0

Image Size: 732 x 578

Mg 200 um



Mn

Cts

- 81

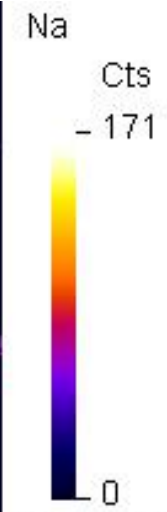
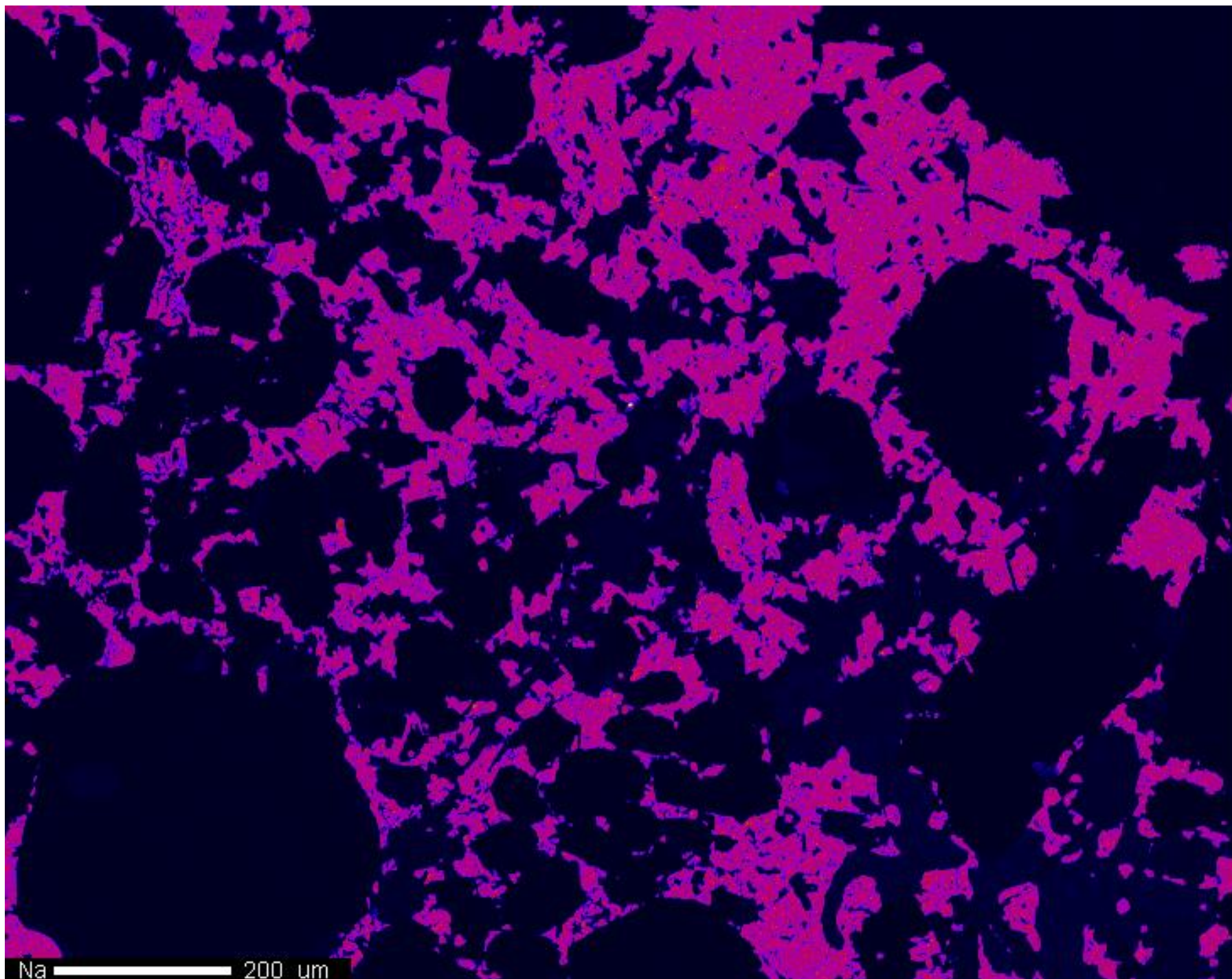


0

Project: September\_17\_2015  
Comment: NWA8173b\_map01\_2um  
Date: 2015/09/17  
Accel Voltage: 15.0 kV  
Beam Current: 9.928e-008 A  
Dwell Time: 10.0  
Image Size: 732 x 578

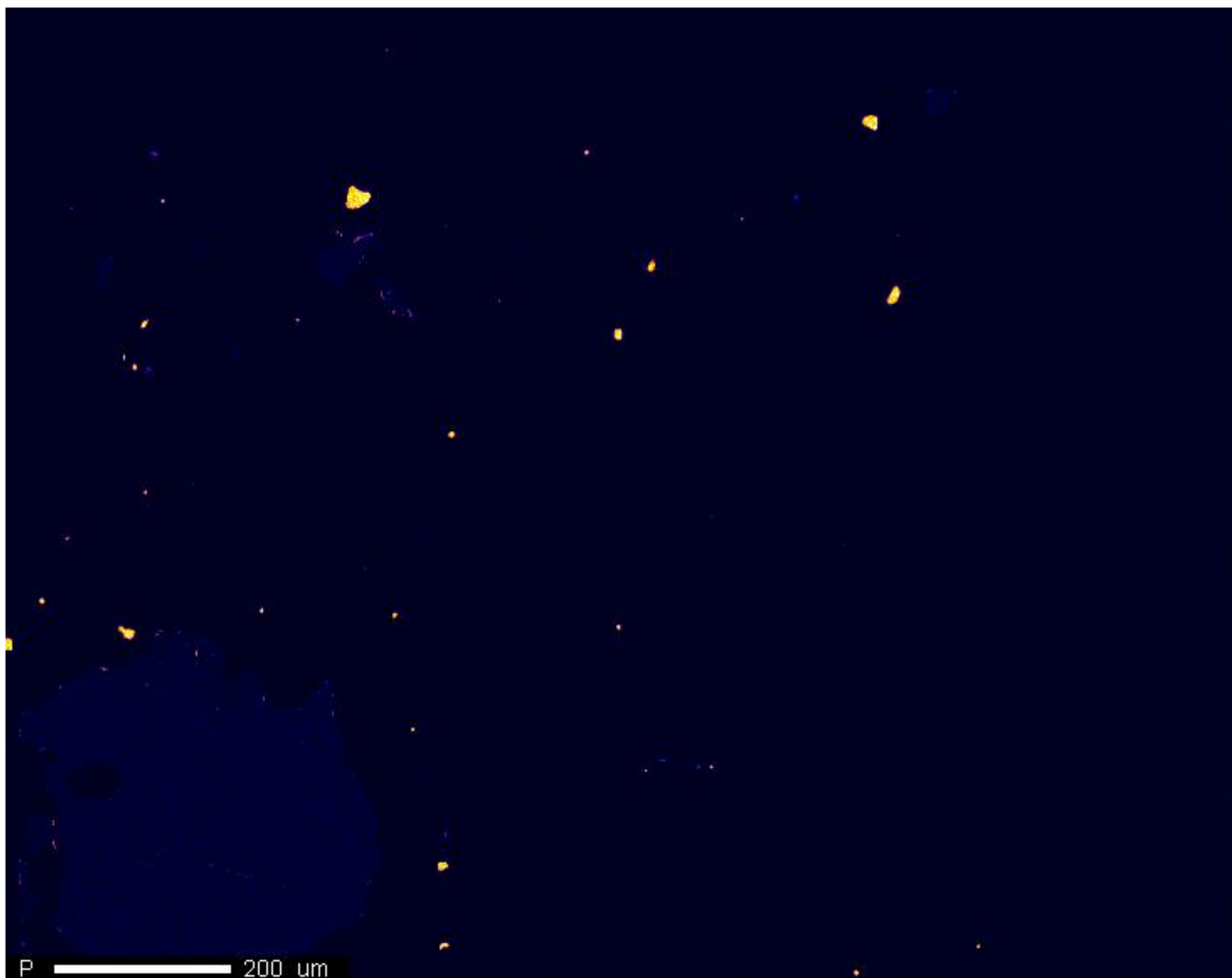
Mn 200 um





Project: September\_17\_2015  
Comment: NWA8173b\_map01\_2um  
Date: 2015/09/17  
Accel Voltage: 15.0 kV  
Beam Current: 9.928e-008 A  
Dwell Time: 10.0  
Image Size: 732 x 578

Na 200 um



P

Cts

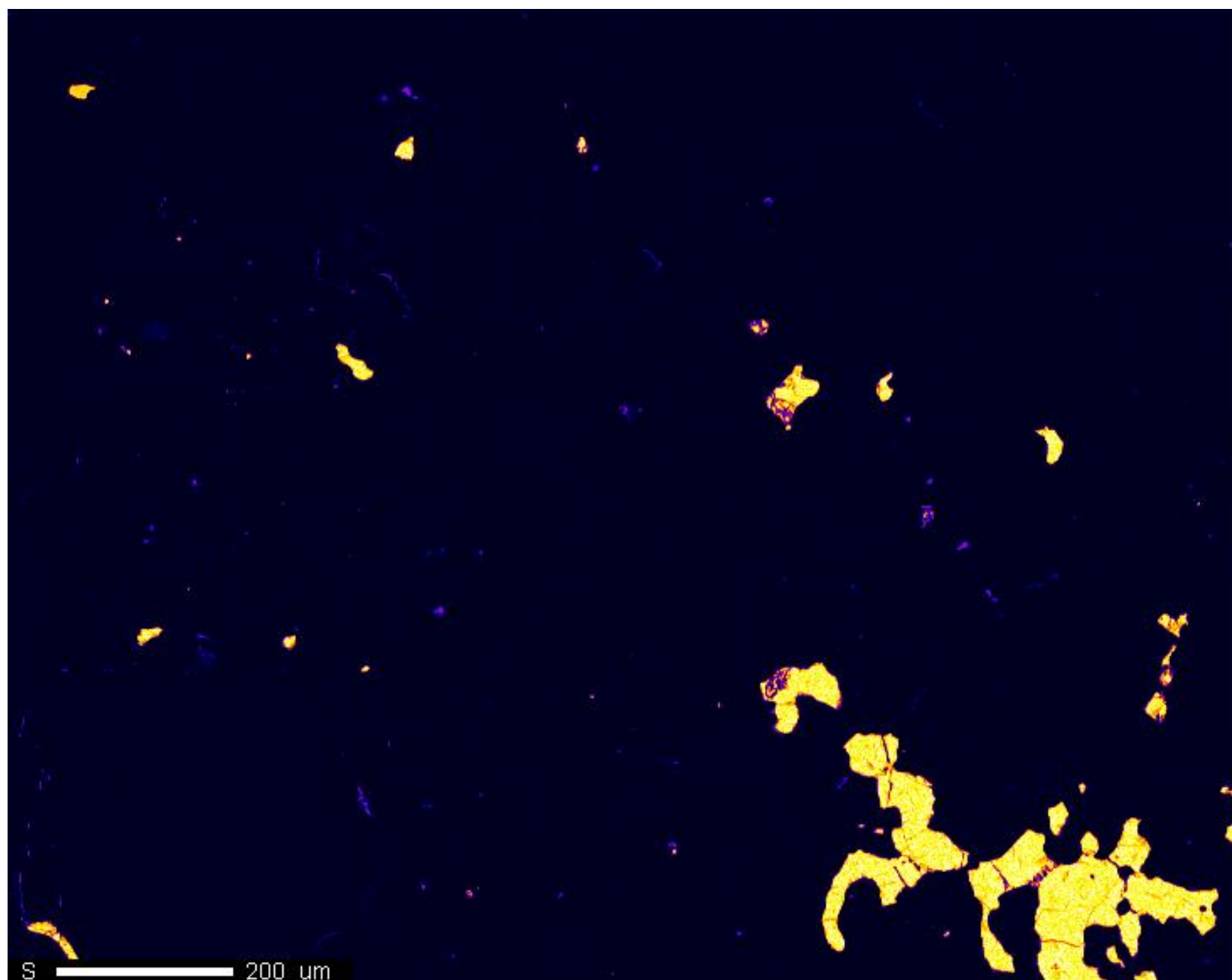
- 135



0

Project: September\_17\_2015  
Comment: NWA8173b\_map01\_2um  
Date: 2015/09/17  
Accel Voltage: 15.0 kV  
Beam Current: 9.928e-008 A  
Dwell Time: 10.0  
Image Size: 732 x 578

P  200 um



S

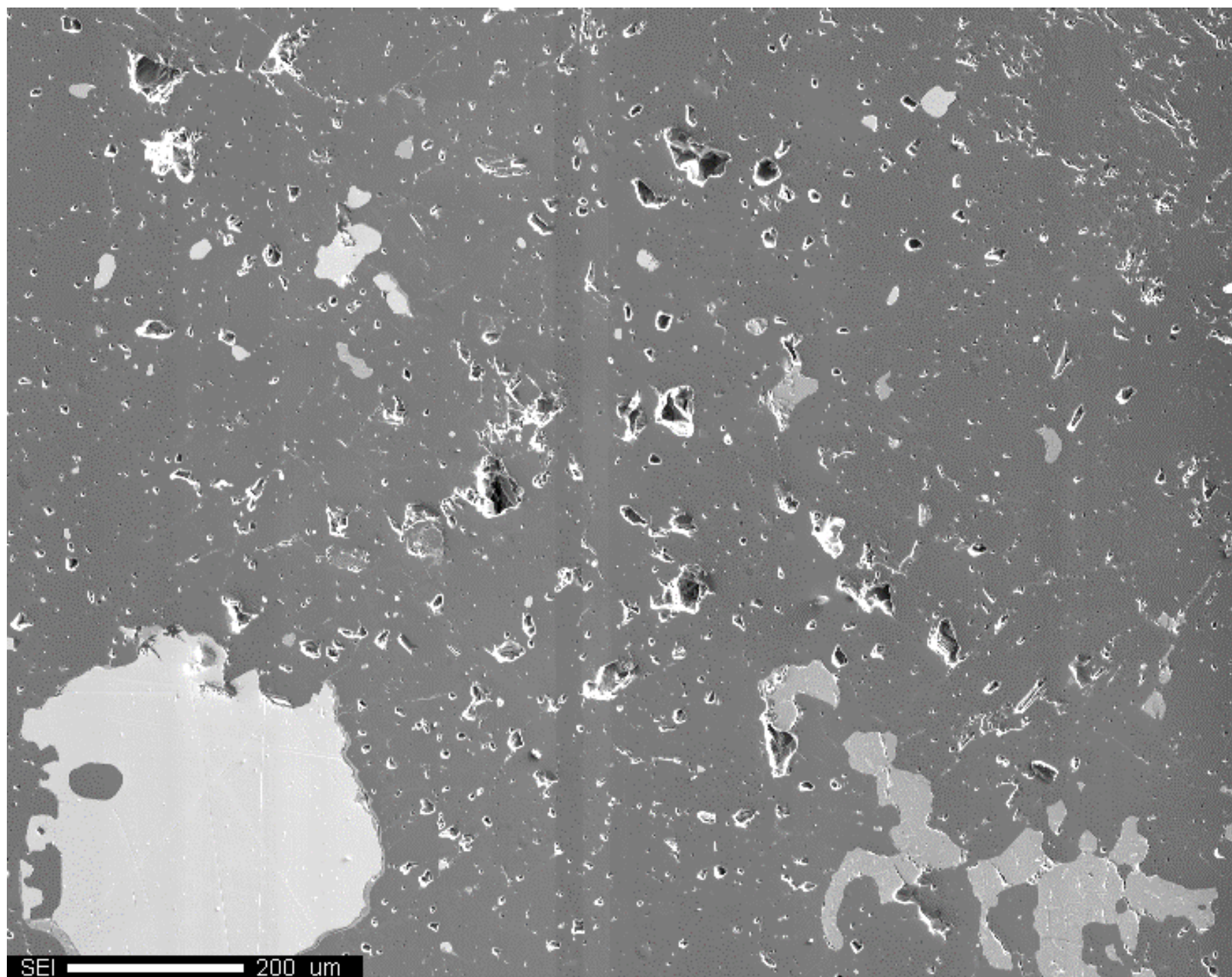
Cts  
- 608



Project: September\_17\_2015  
Comment: NWA8173b\_map01\_2um  
Date: 2015/09/17  
Accel Voltage: 15.0 kV  
Beam Current: 9.928e-008 A  
Dwell Time: 10.0  
Image Size: 732 x 578

S 200 um





SEI

Cts

- 4,095

0

Project: September\_17\_2015

Comment: NWA8173b\_map01\_2um

Date: 2015/09/17

Accel Voltage: 15.0 kV

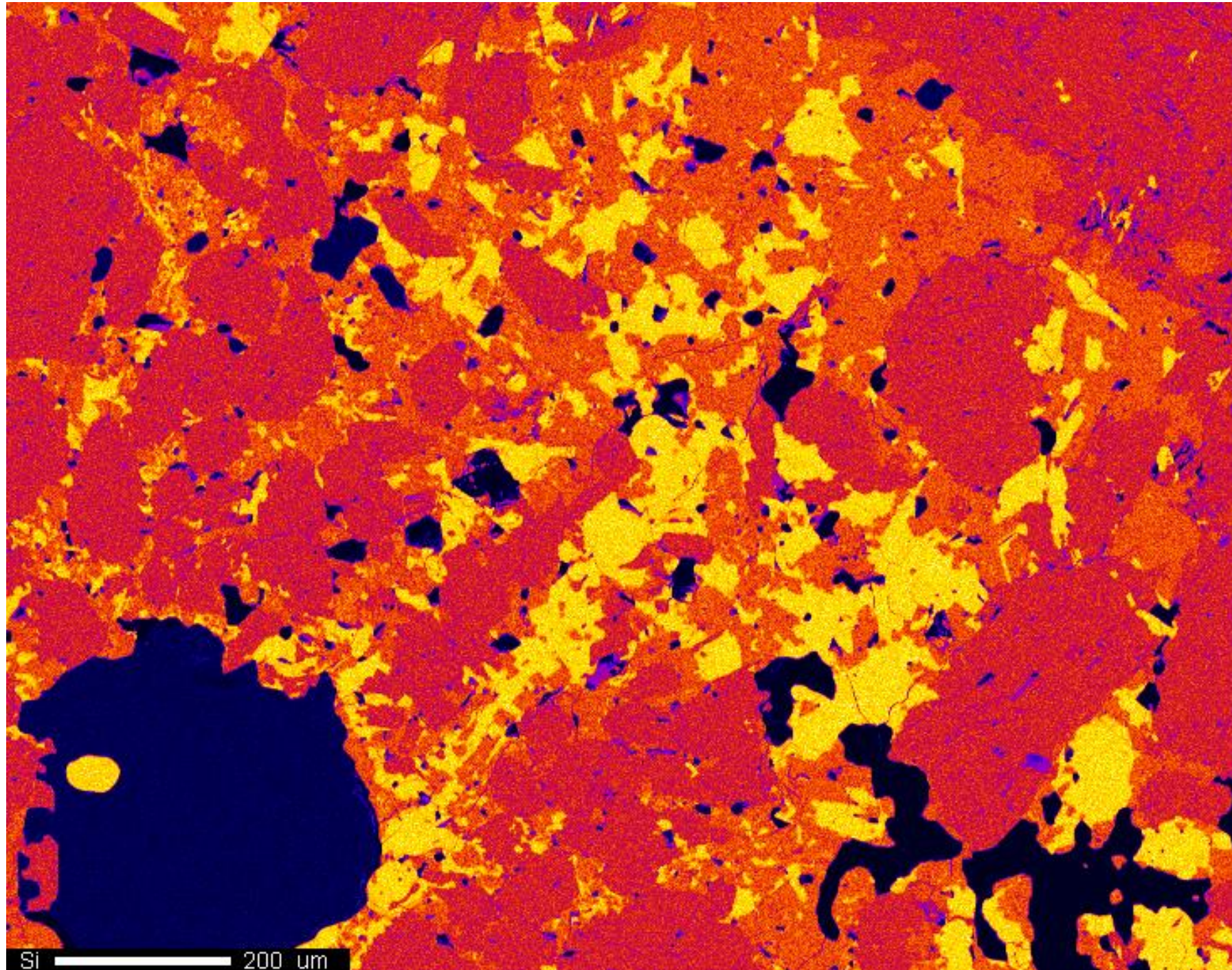
Beam Current: 9.928e-008 A

Dwell Time: 10.0

Image Size: 732 x 578

SEI 200 um





Si

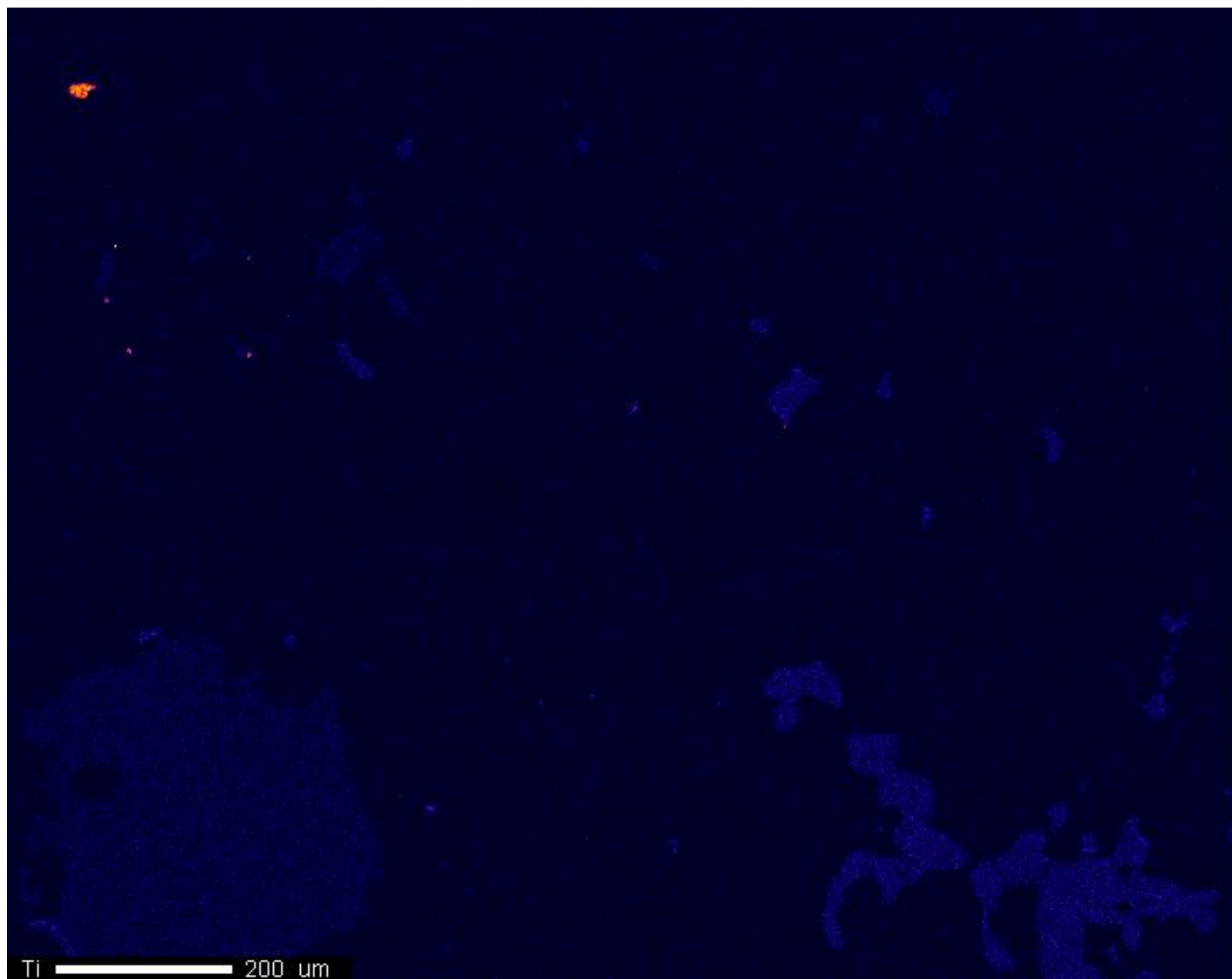
Cts  
- 281



Project: September\_17\_2015  
Comment: NWA8173b\_map01\_2um  
Date: 2015/09/17  
Accel Voltage: 15.0 kV  
Beam Current: 9.928e-008 A  
Dwell Time: 10.0  
Image Size: 732 x 578

Si 200 um





Ti

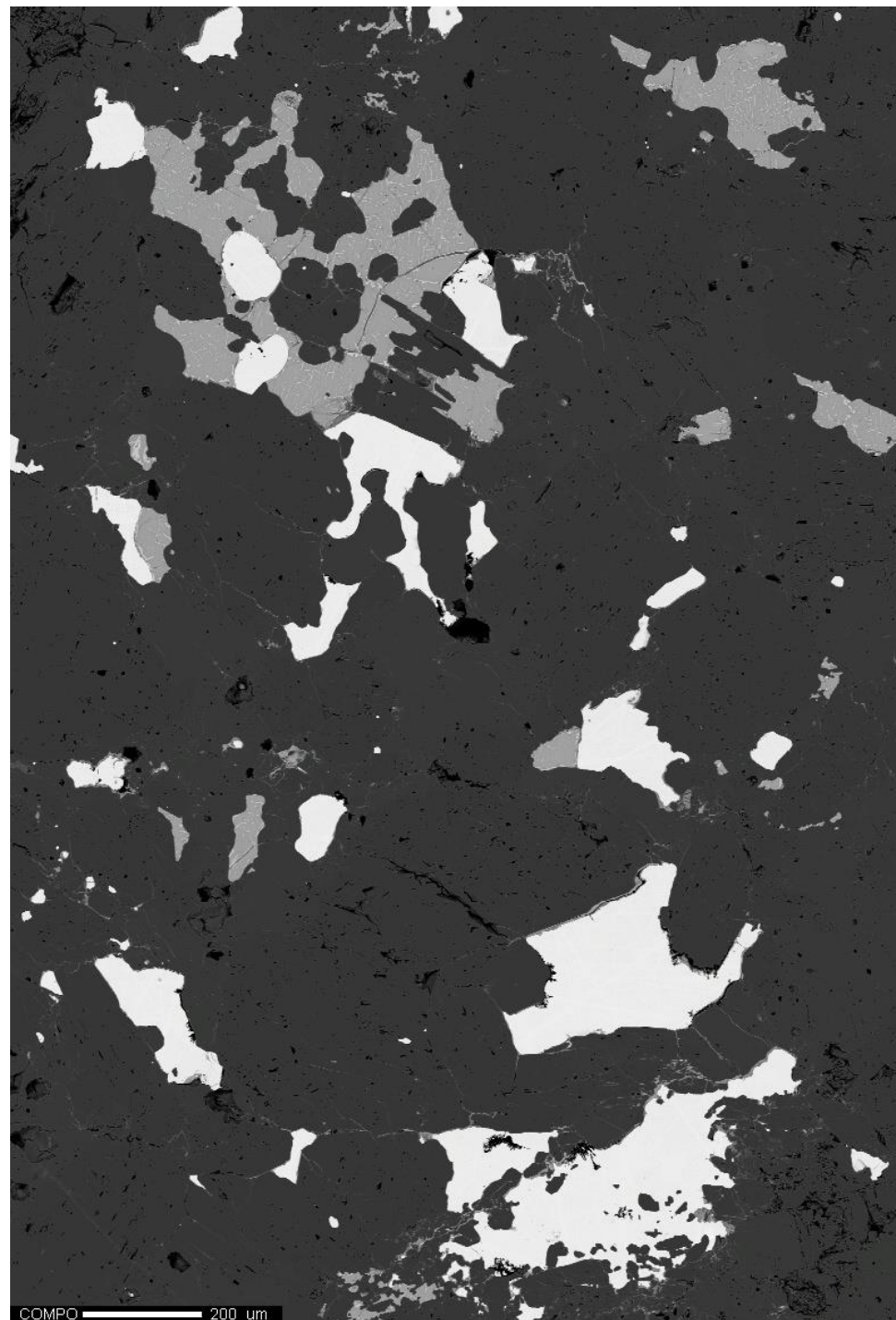
Cts

- 83



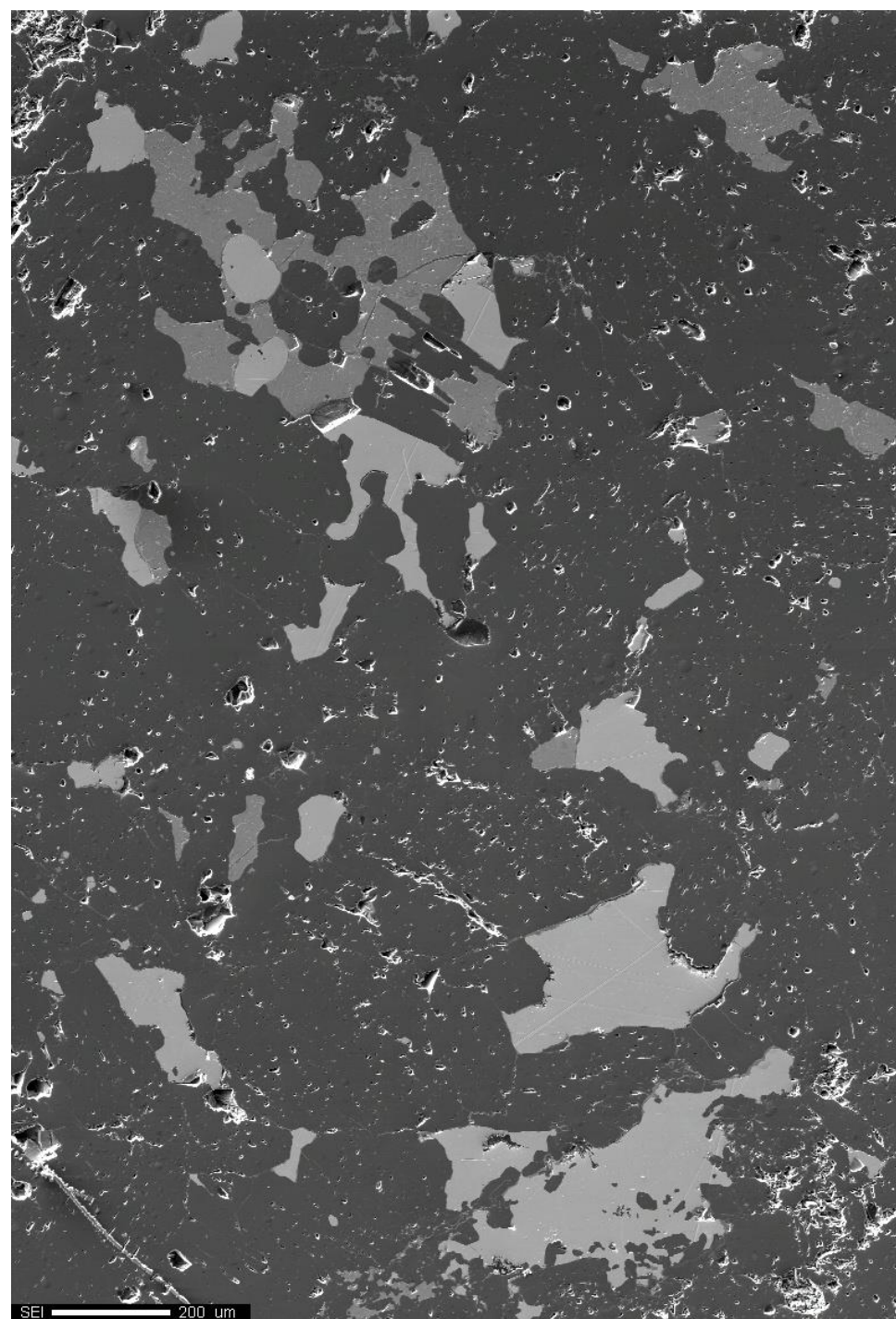
Project: September\_17\_2015  
Comment: NWA8173b\_map01\_2um  
Date: 2015/09/17  
Accel Voltage: 15.0 kV  
Beam Current: 9.928e-008 A  
Dwell Time: 10.0  
Image Size: 732 x 578

Ti 200 um



Project: March\_2\_2016  
Comment: NWA8173B\_map02\_2um  
Date: 2016/03/03  
Accel Voltage: 15.0 kV  
Beam Current: 1.002e-007 A  
Dwell Time: 10.0  
Image Size: 792 x 1159

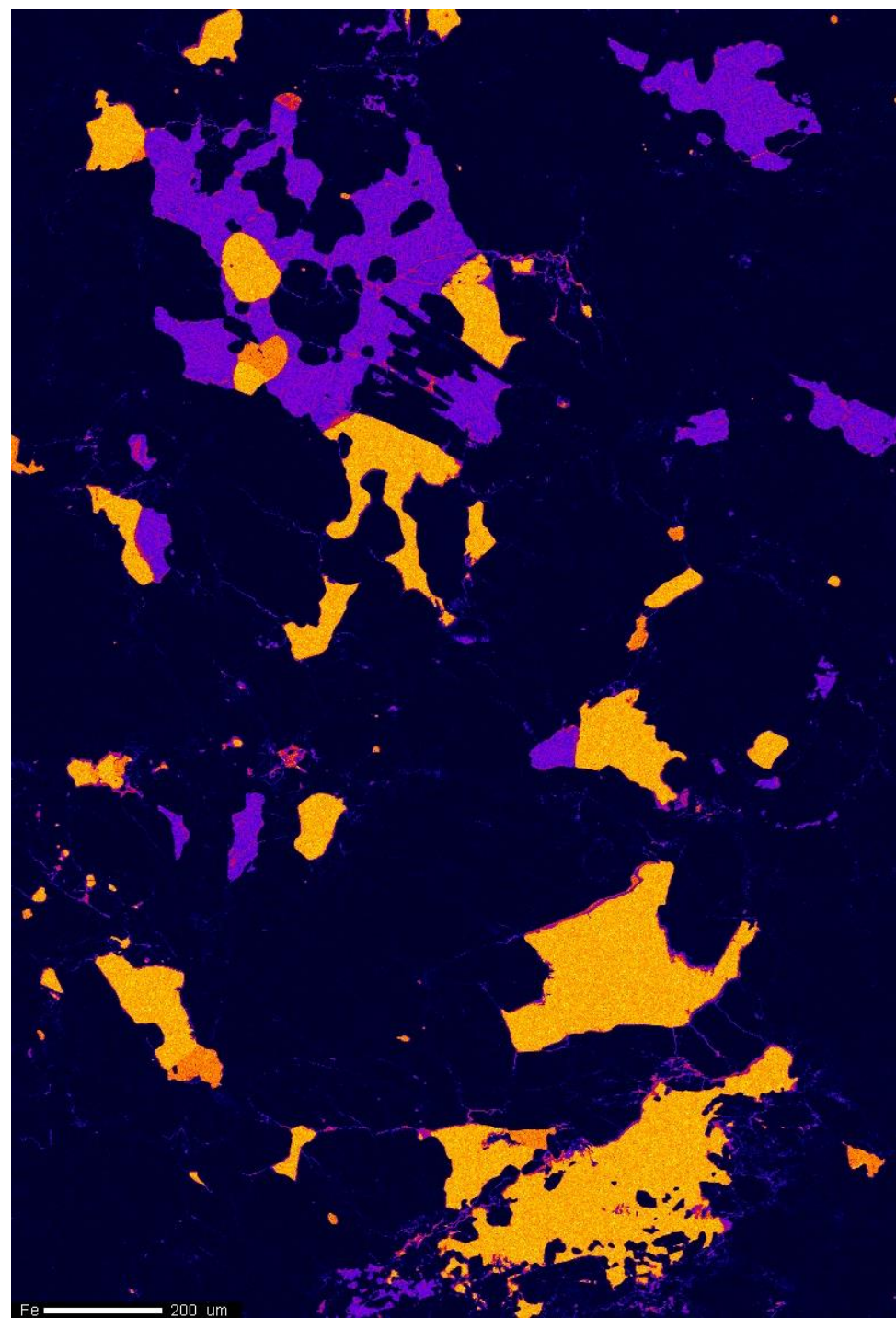
COMPO 200 um



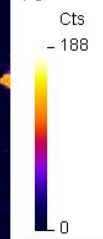
Project: March\_2\_2016  
Comment: NWA8173B\_map02\_2um  
Date: 2016/03/03  
Accel Voltage: 15.0 kV  
Beam Current: 1.002e-007 A  
Dwell Time: 10.0  
Image Size: 792 x 1159

SEI 200 um



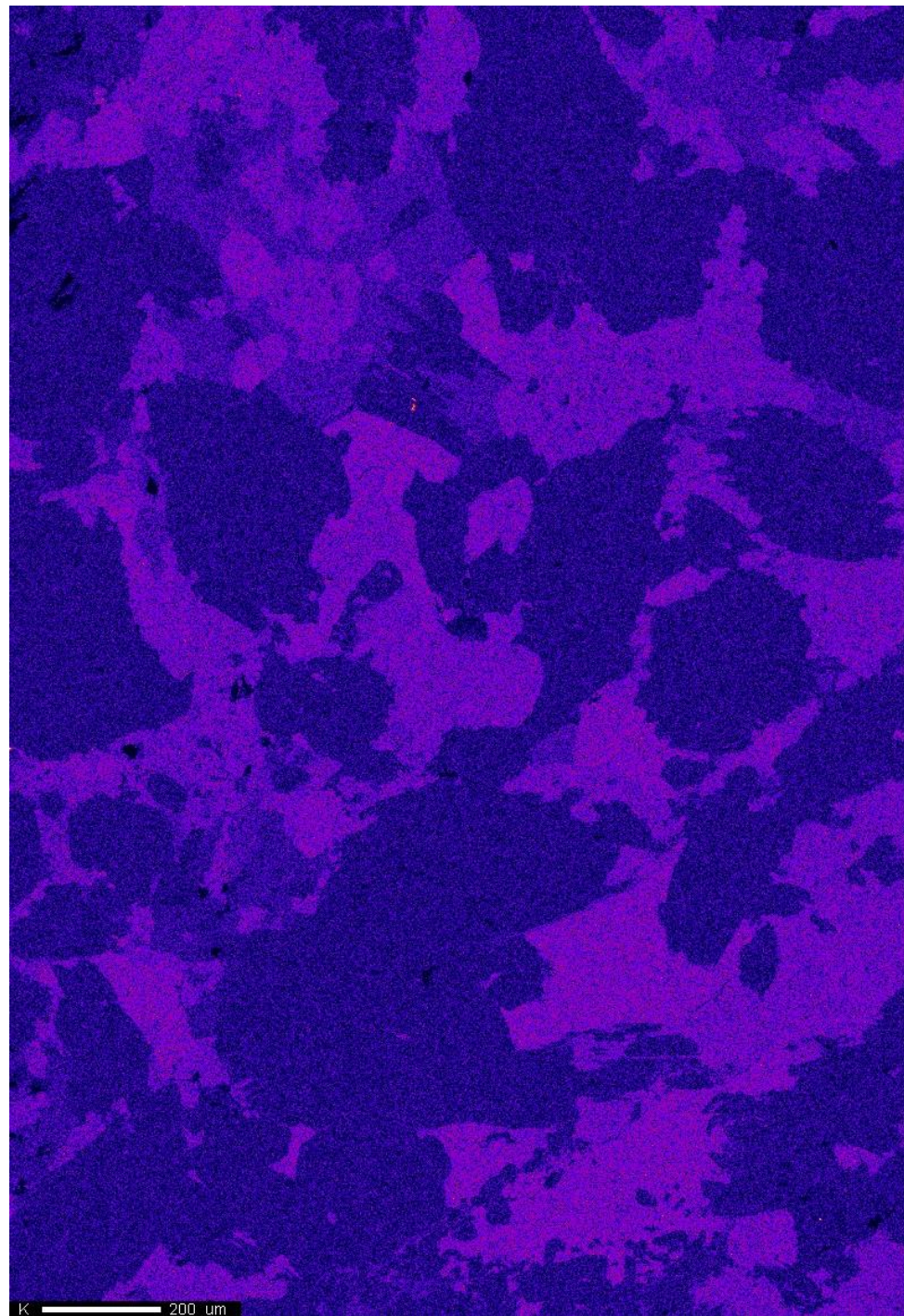


Fe



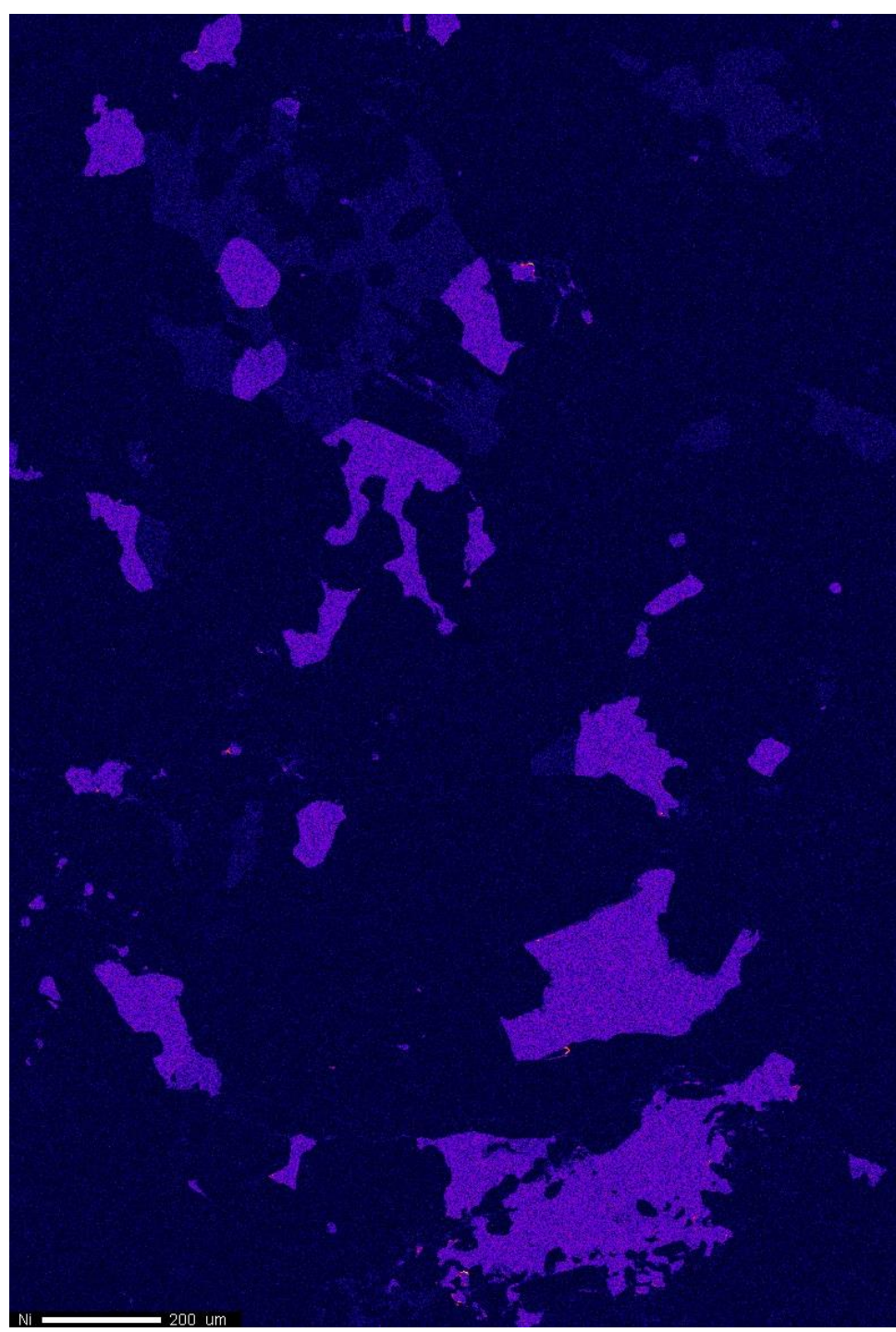
Cts  
- 188  
0  
Project: March\_2\_2016  
Comment: NWA8173B\_map02\_2um  
Date: 2016/03/03  
Accel Voltage: 15.0 kV  
Beam Current: 5.014e-008 A  
Dwell Time: 10.0  
Image Size: 792 x 1159

Fe 200 um



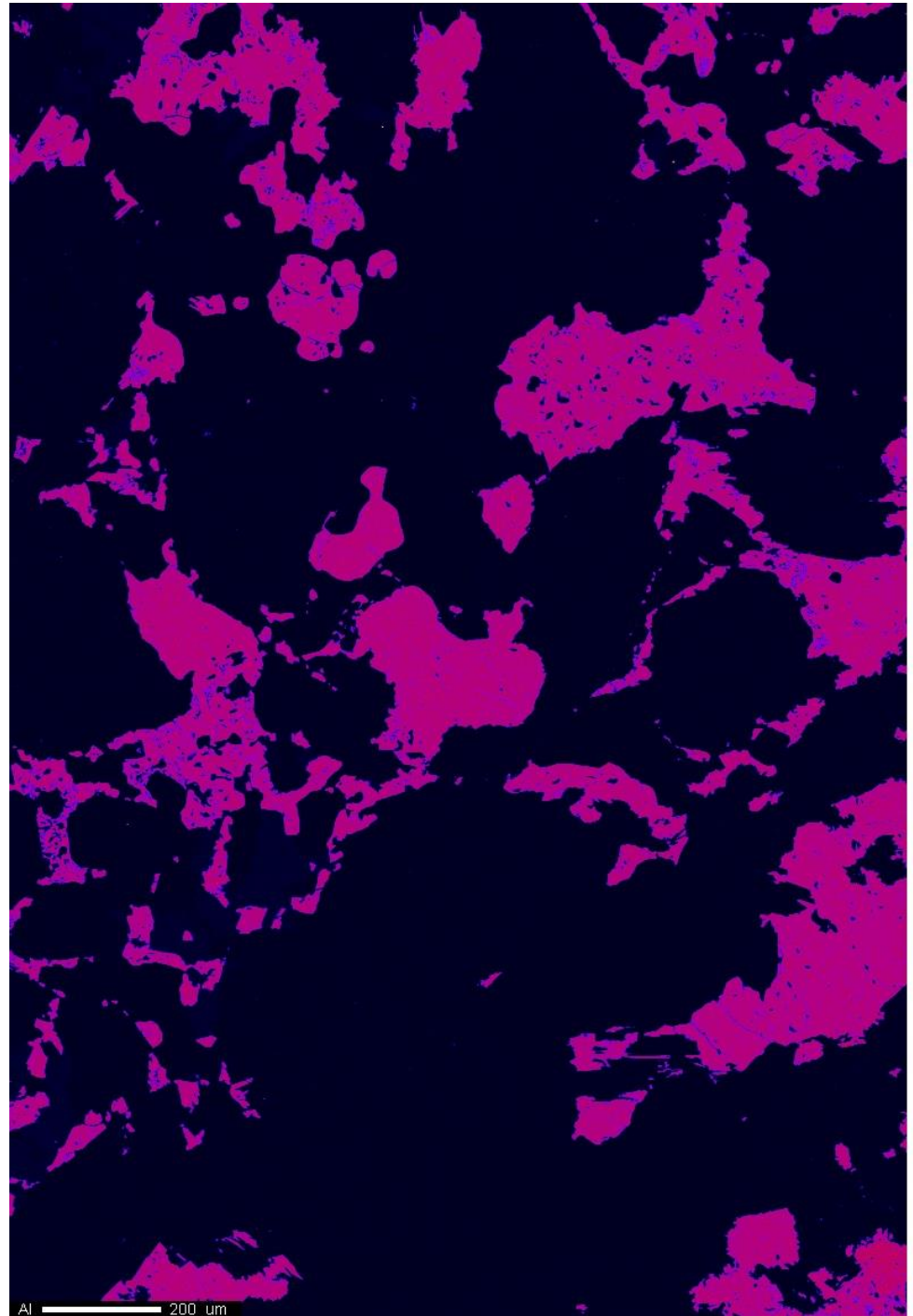
Project: March\_2\_2016  
Comment: NWA8173B\_map02\_2um  
Date: 2016/03/03  
Accel Voltage: 15.0 kV  
Beam Current: 5.014e-008 A  
Dwell Time: 10.0  
Image Size: 792 x 1159





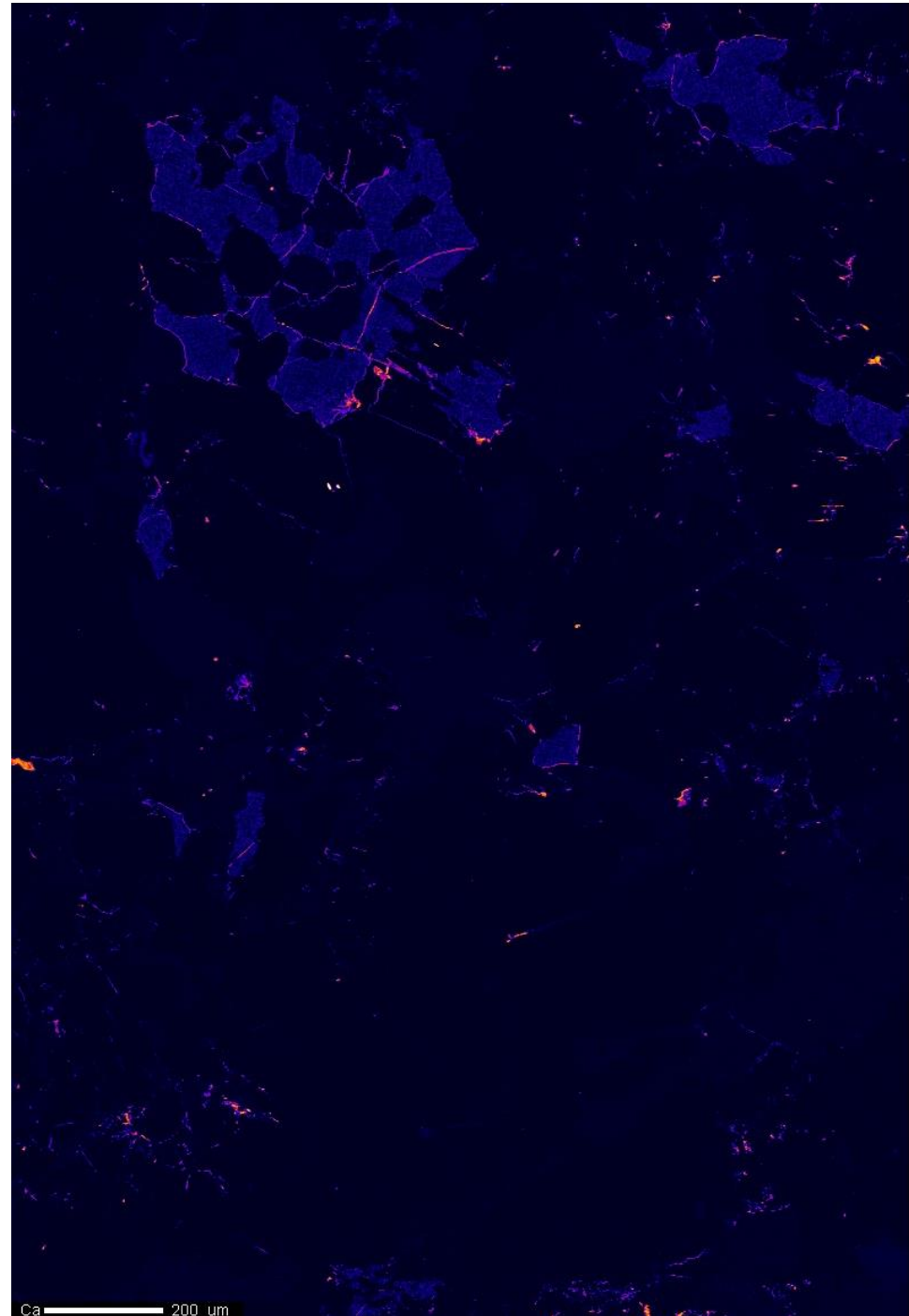
Ni  
Cts  
- 57  
0  
Project: March\_2\_2016  
Comment: NWA8173B\_map02\_2um  
Date: 2016/03/03  
Accel Voltage: 15.0 kV  
Beam Current: 5.014e-008 A  
Dwell Time: 10.0  
Image Size: 792 x 1159

Ni 200 um

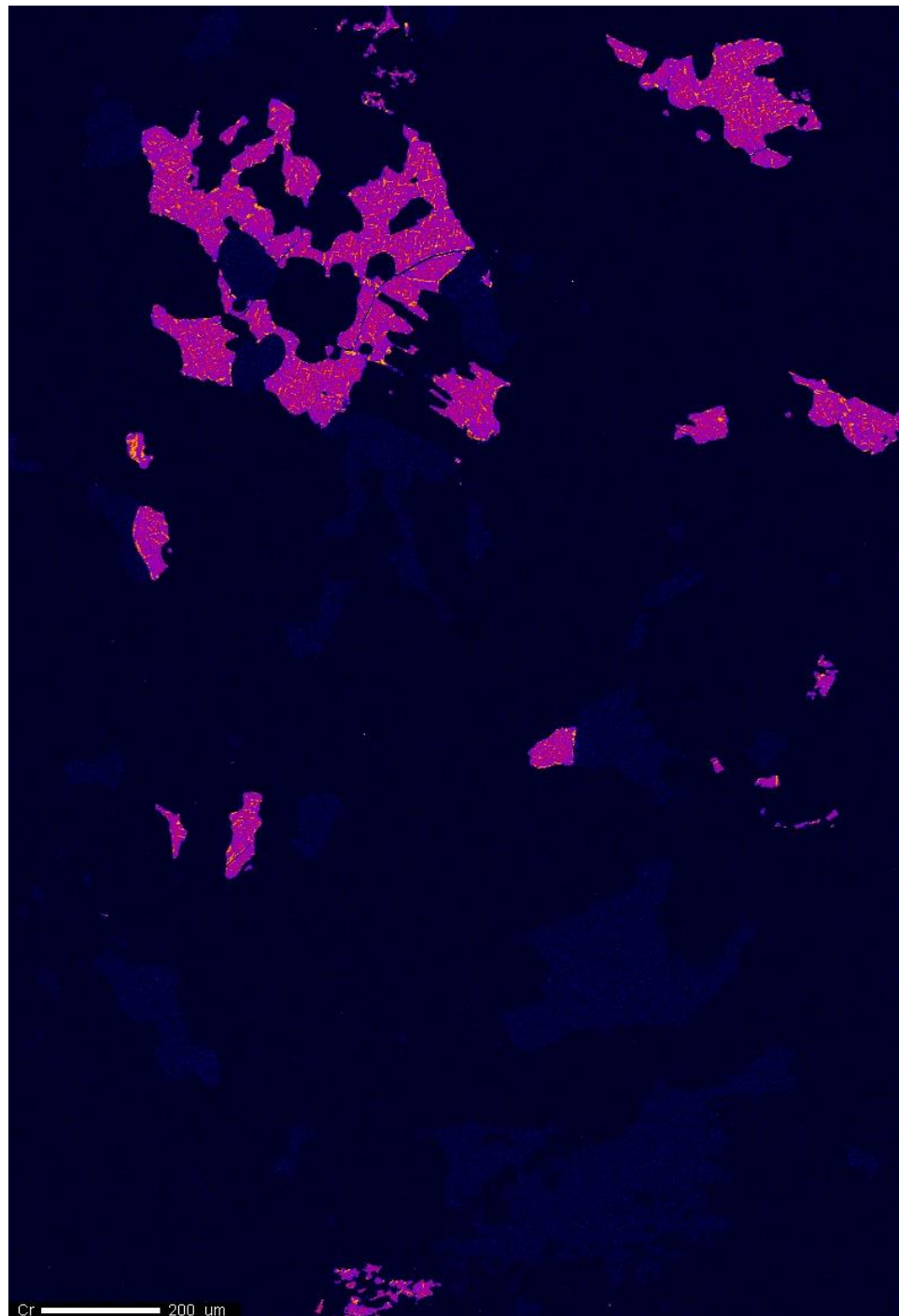


Project: March\_2\_2016  
Comment: NWA8173B\_map02\_2um  
Date: 2016/03/03  
Accel Voltage: 15.0 kV  
Beam Current: 1.002e-007 A  
Dwell Time: 10.0  
Image Size: 792 x 1159

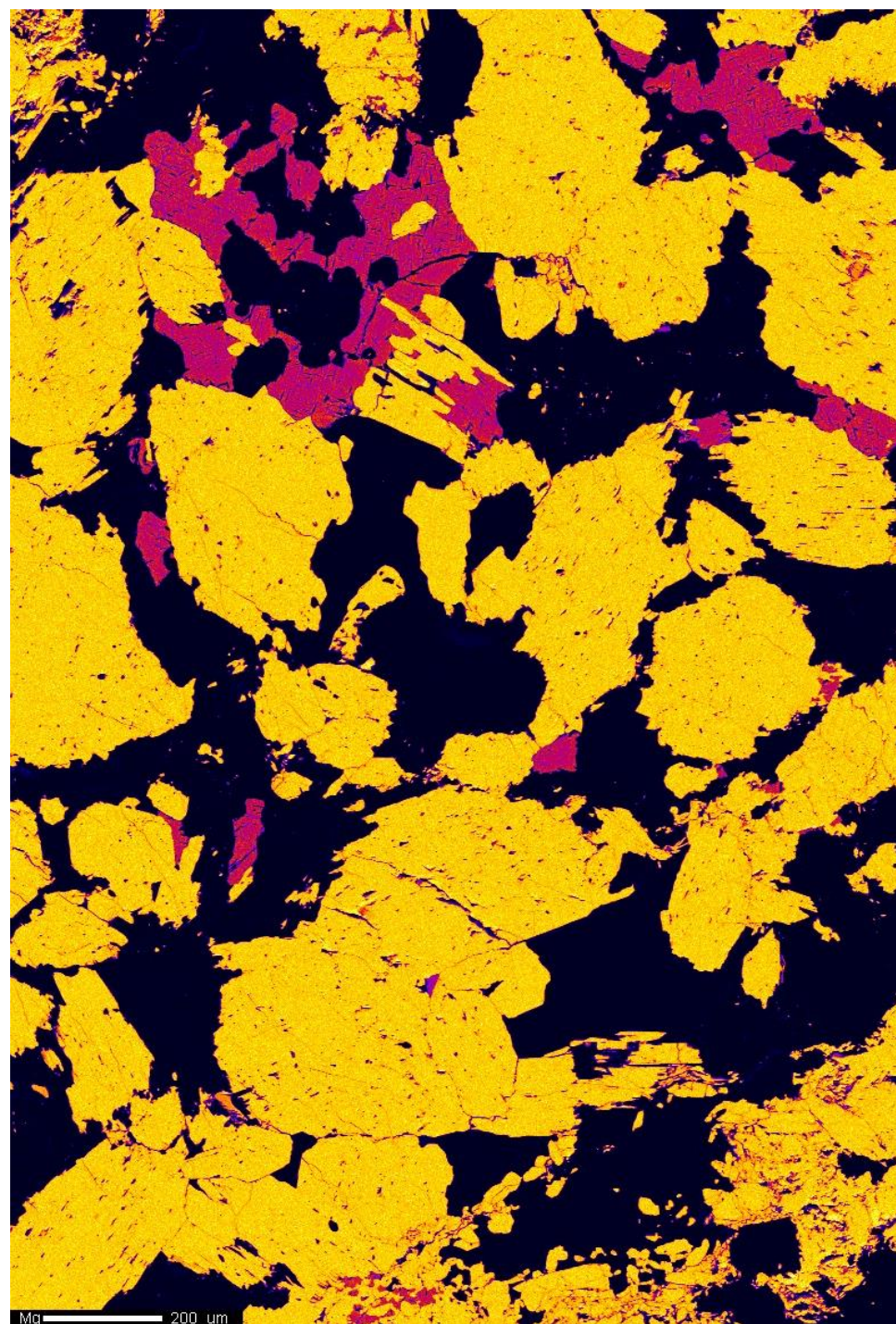




Project: March\_2\_2016  
Comment: NWA8173B\_map02\_2um  
Date: 2016/03/03  
Accel Voltage: 15.0 kV  
Beam Current: 1.002e-007 A  
Dwell Time: 10.0  
Image Size: 792 x 1159

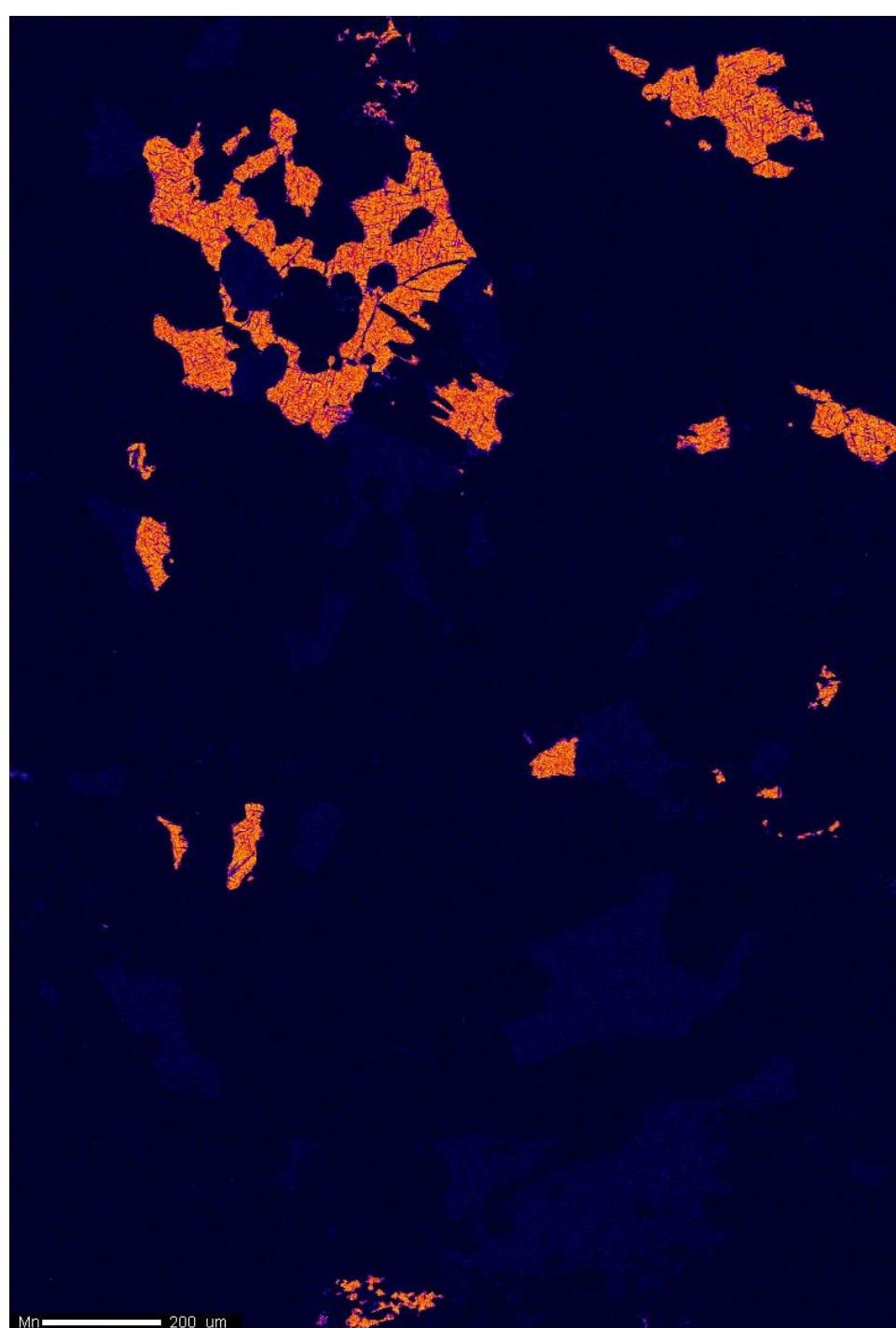


Cr  
Cts  
- 68  
0  
Project: March\_2\_2016  
Comment: NWA8173B\_map02\_2um  
Date: 2016/03/03  
Accel Voltage: 15.0 kV  
Beam Current: 1.002e-007 A  
Dwell Time: 10.0  
Image Size: 792 x 1159



Mg  
Cts  
- 404  
0  
Project: March\_2\_2016  
Comment: NWA8173B\_map02\_2um  
Date: 2016/03/03  
Accel Voltage: 15.0 kV  
Beam Current: 1.002e-007 A  
Dwell Time: 10.0  
Image Size: 792 x 1159

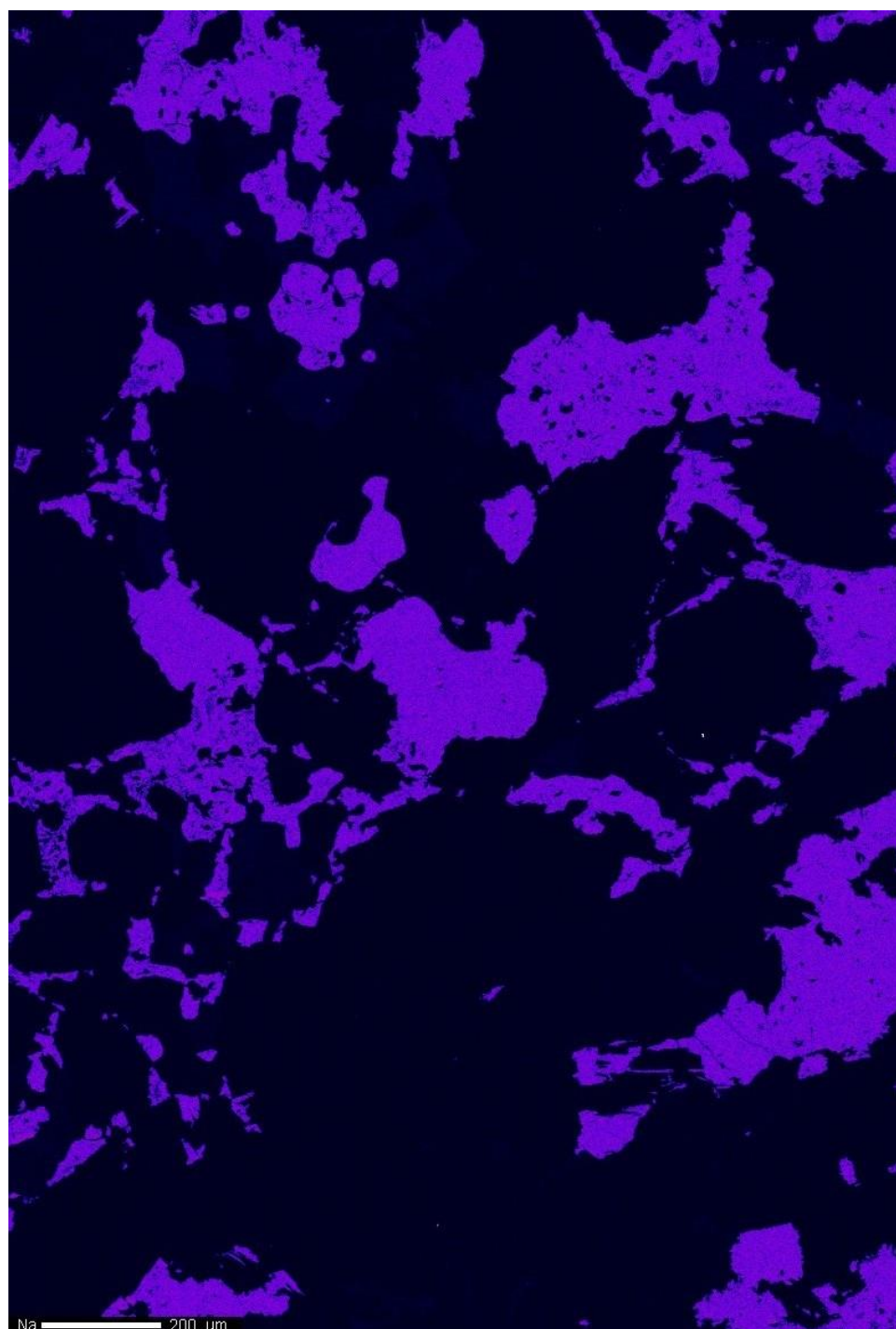




Project: March\_2\_2016  
Comment: NWA8173B\_map02\_2um  
Date: 2016/03/03  
Accel Voltage: 15.0 kV  
Beam Current: 1.002e-007 A  
Dwell Time: 10.0  
Image Size: 792 x 1159

Mn 200 um



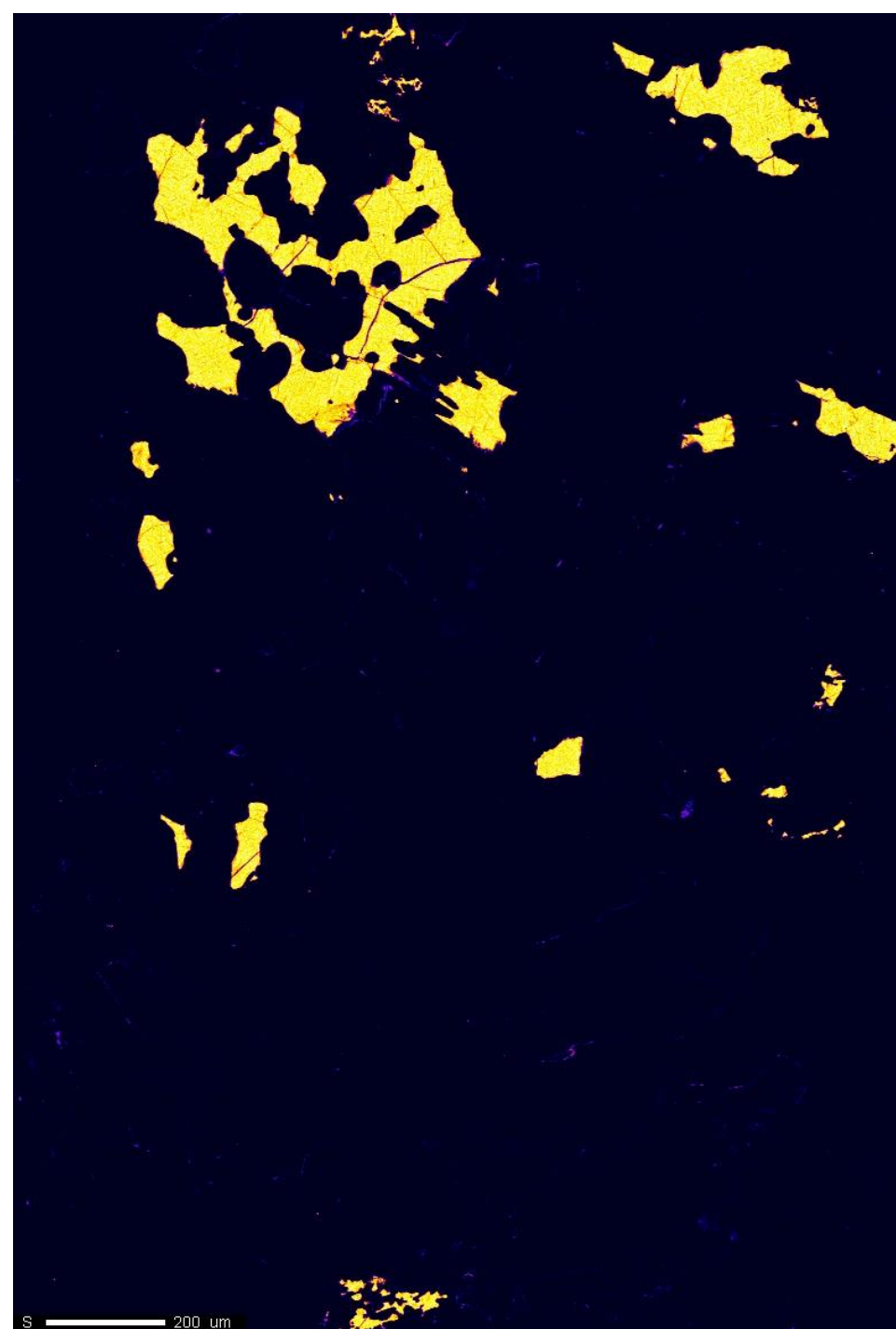


Na  
Cts  
- 230  
0  
Project: March\_2\_2016  
Comment: NWA8173B\_map02\_2um  
Date: 2016/03/03  
Accel Voltage: 15.0 kV  
Beam Current: 1.002e-007 A  
Dwell Time: 10.0  
Image Size: 792 x 1159

Na 200 um

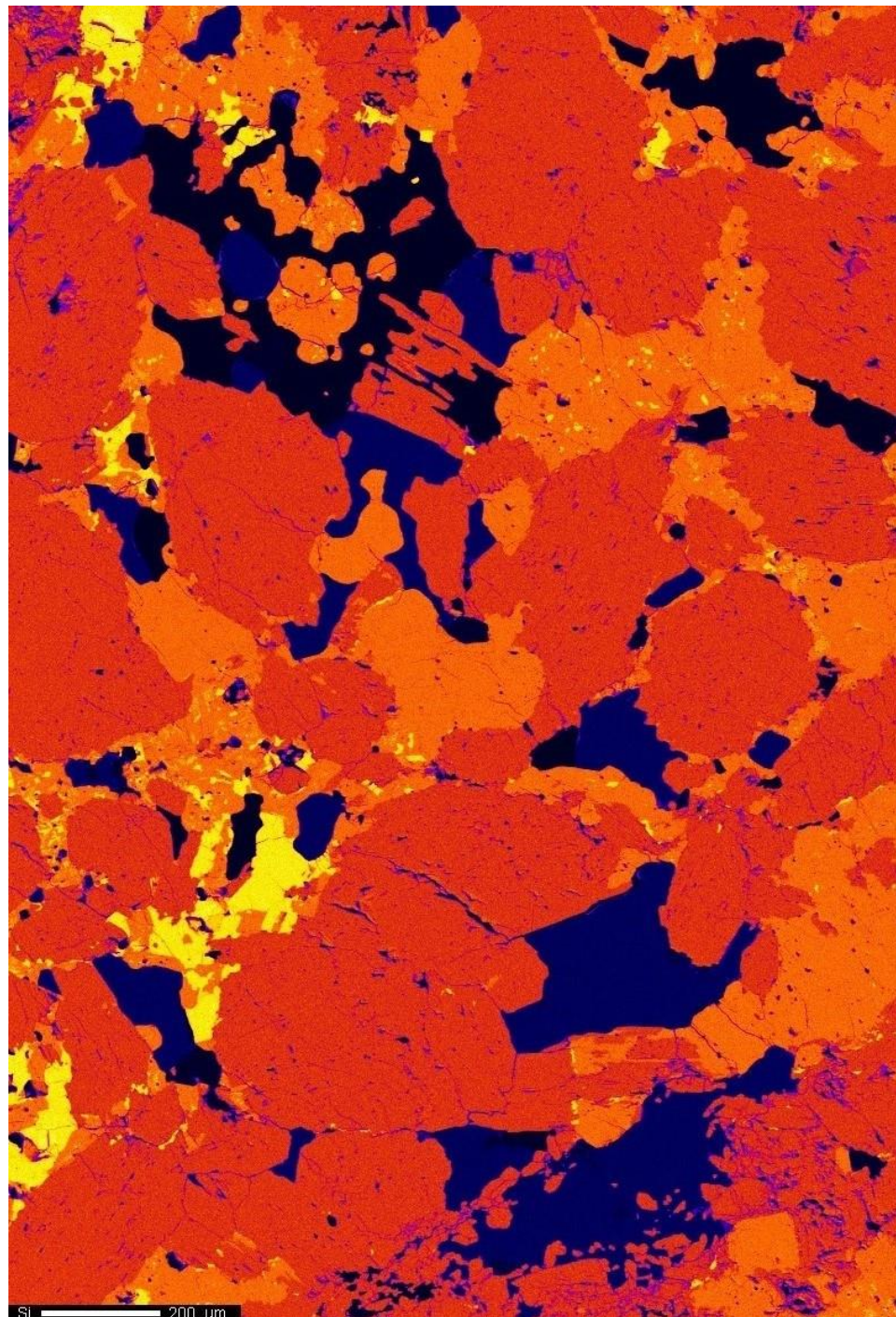


P  
Cts  
- 152  
0  
Project: March\_2\_2016  
Comment: NWA8173B\_map02\_2um  
Date: 2016/03/03  
Accel Voltage: 15.0 kV  
Beam Current: 1.002e-007 A  
Dwell Time: 10.0  
Image Size: 792 x 1159



S  
Cts  
- 620  
0  
Project: March\_2\_2016  
Comment: NWA8173B\_map02\_2um  
Date: 2016/03/03  
Accel Voltage: 15.0 kV  
Beam Current: 1.002e-007 A  
Dwell Time: 10.0  
Image Size: 792 x 1159



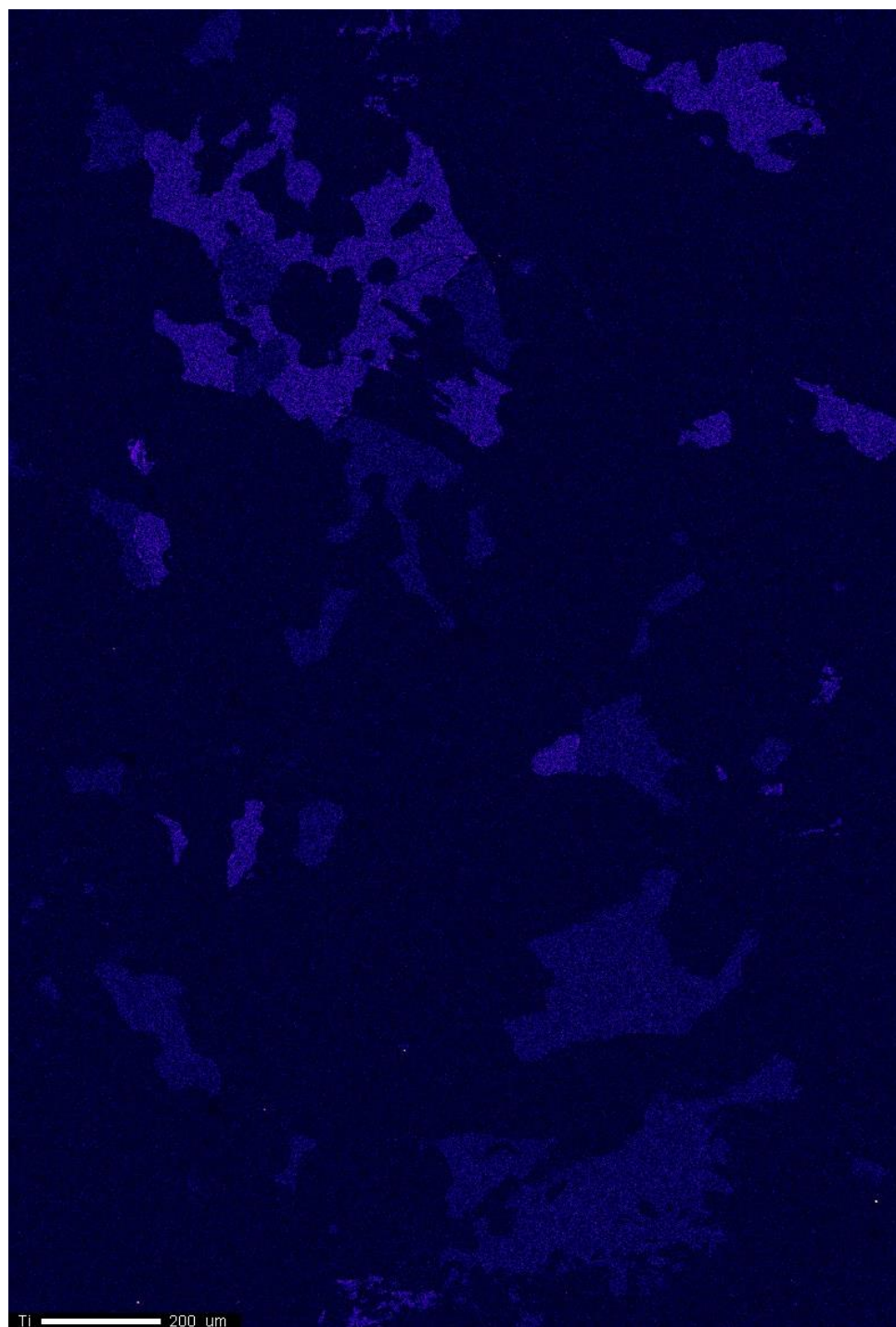


Si  
Cts  
- 1,120  
0

Project: March\_2\_2016  
Comment: NWA8173B\_map02\_2um  
Date: 2016/03/03  
Accel Voltage: 15.0 kV  
Beam Current: 1.002e-007 A  
Dwell Time: 10.0  
Image Size: 792 x 1159

Si 200 um





Project: March\_2\_2016  
Comment: NWA8173B\_map02\_2um  
Date: 2016/03/03  
Accel Voltage: 15.0 kV  
Beam Current: 1.002e-007 A  
Dwell Time: 10.0  
Image Size: 792 x 1159

## Appendix 3.3: EBSD map of sulfides in NWA 8173

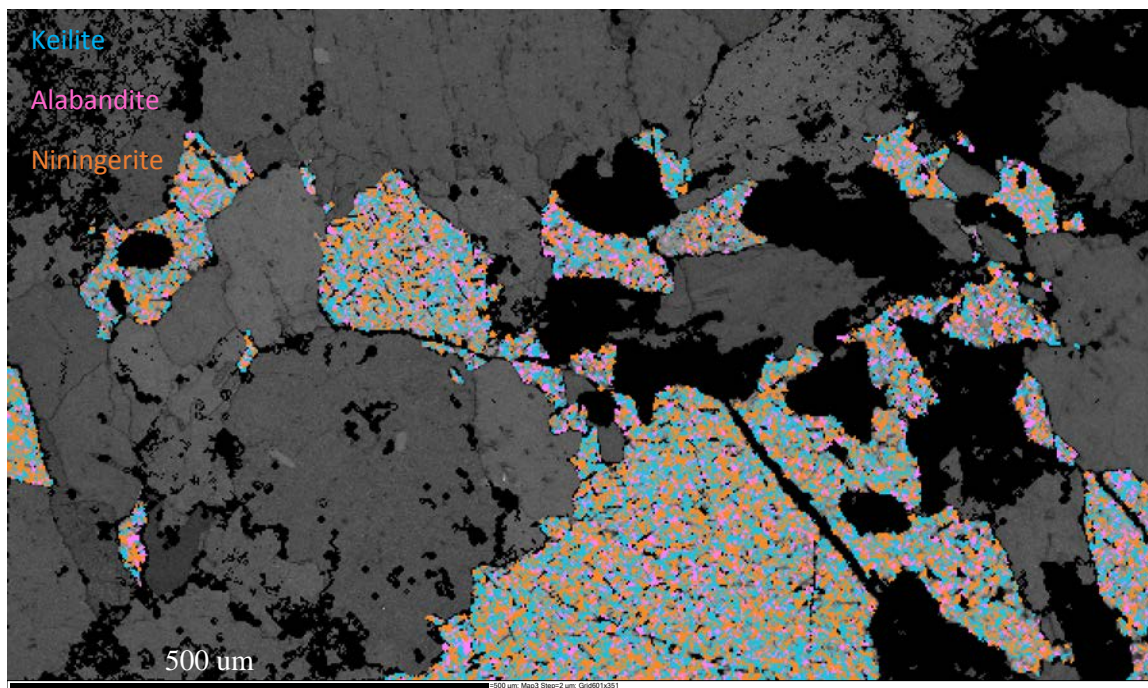
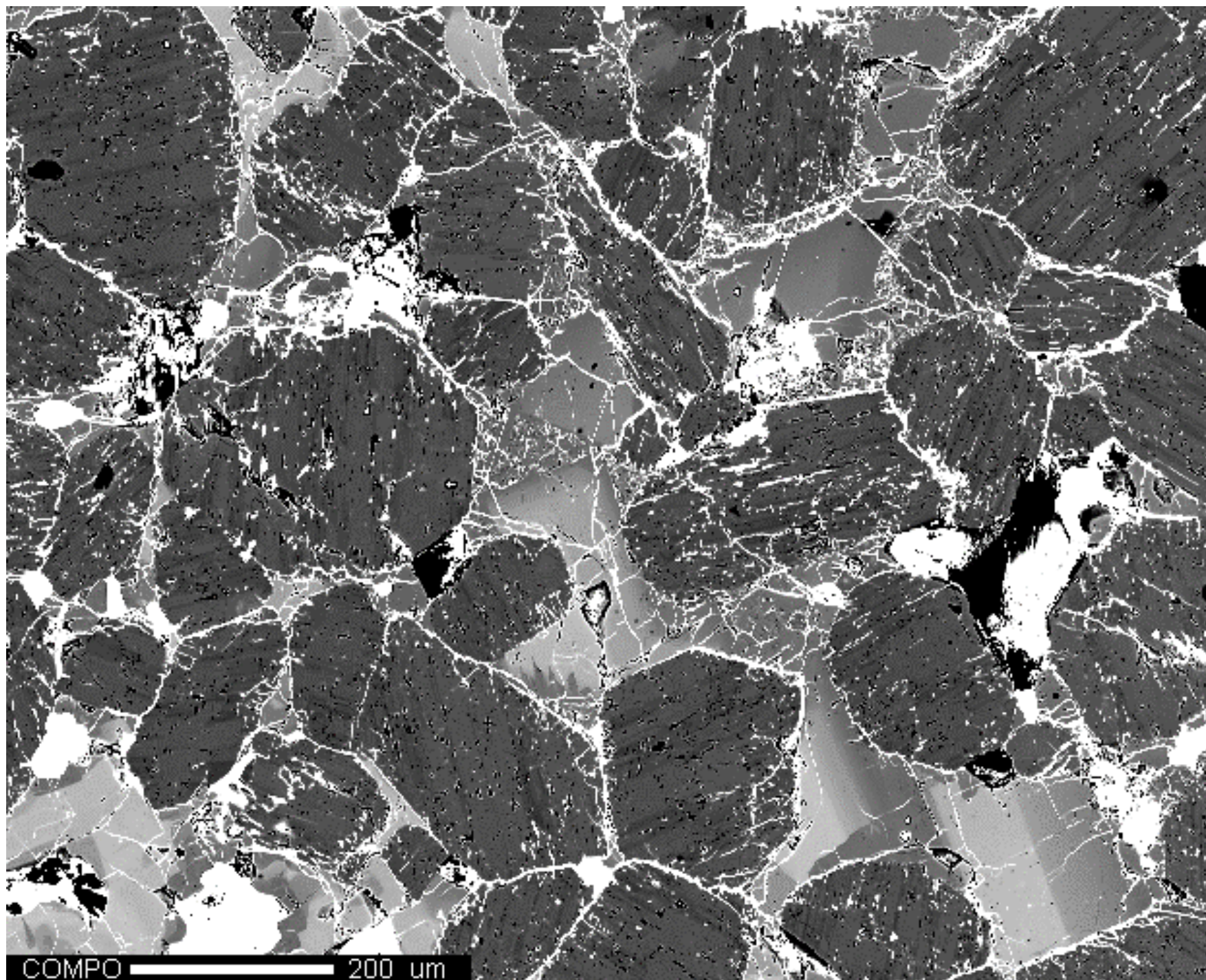


Figure 1. EBSD map of sulfide in NWA 8173 showing indexing of isostructural sulfides preventing determination of sulfide phase based on EBSD.

# Appendix 4.1

X-Ray Elemental maps of Zakłotzie





COMPO

Cts

- 4,095



0

Project: September\_17\_2015

Comment: Zak\_map01\_2um

Date: 2015/09/17

Accel Voltage: 15.0 kV

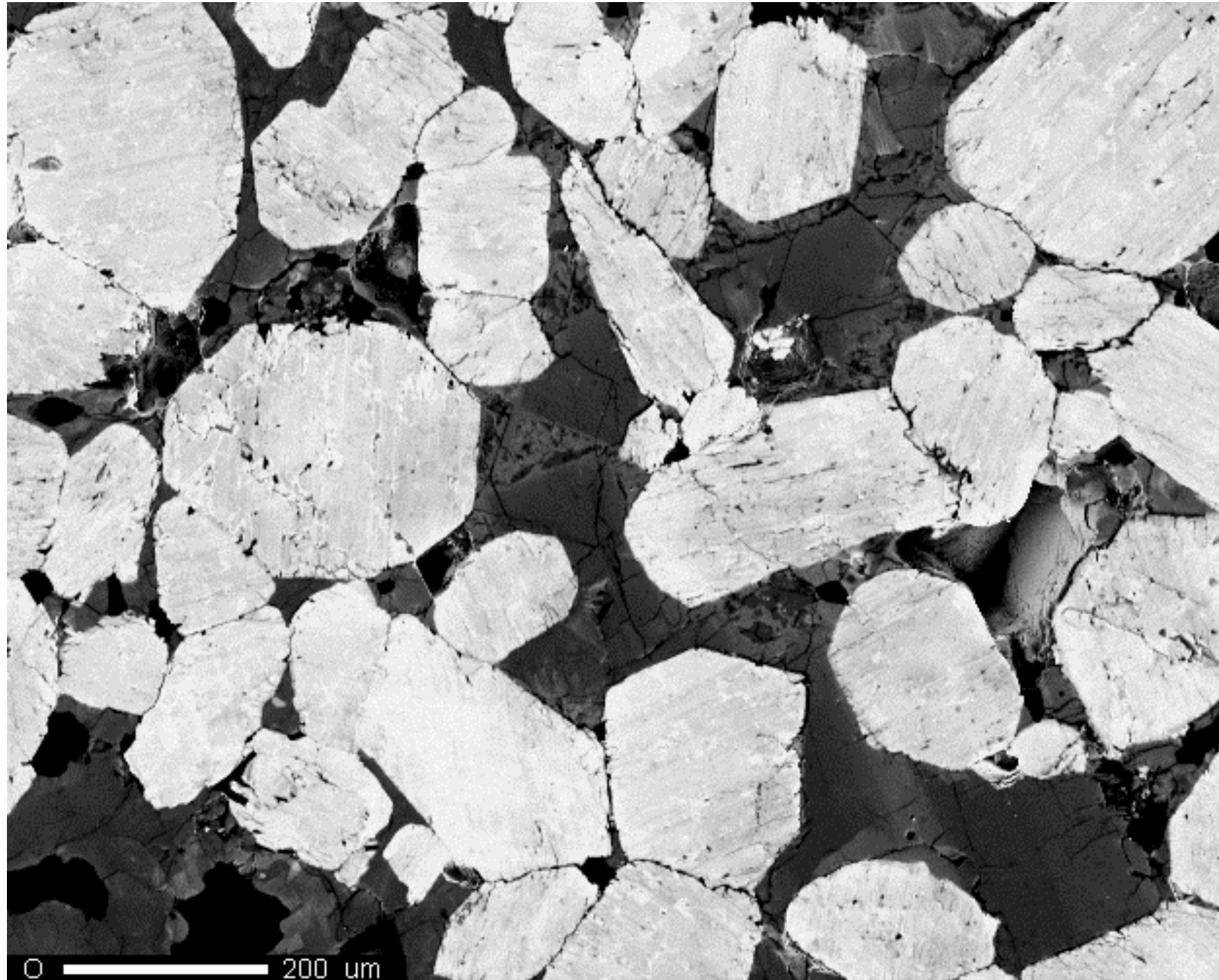
Beam Current: 9.976e-008 A

Dwell Time: 10.0

Image Size: 623 x 503

COMPO 200 um





O

Cts

- 2,764



434

Project: September\_17\_2015

Comment: Zak\_map01\_2um

Date: 2015/09/17

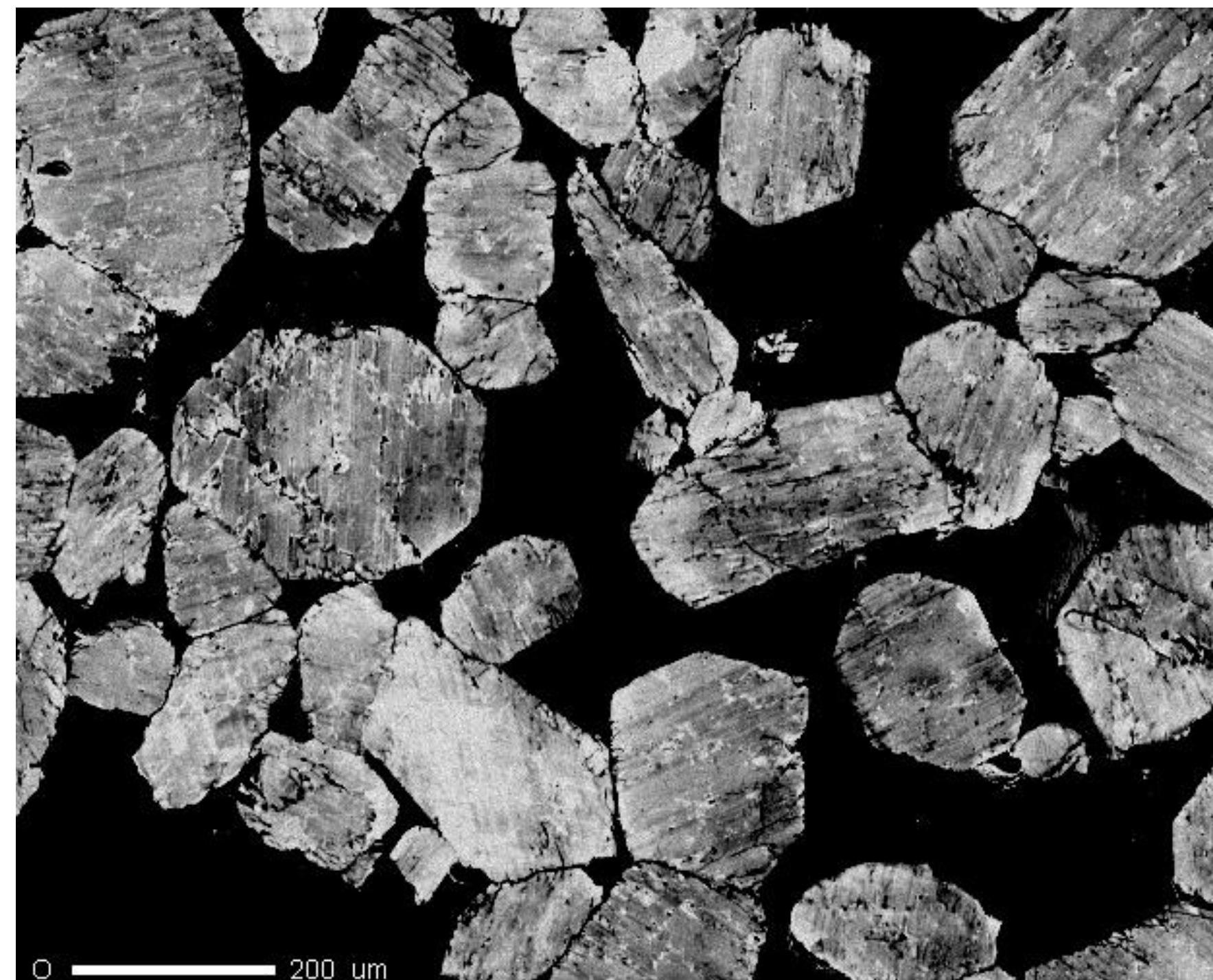
Accel Voltage: 15.0 kV

Beam Current: 9.976e-008 A

Dwell Time: 10.0

Image Size: 623 x 503

O 200 um



O

Cts  
- 2,764

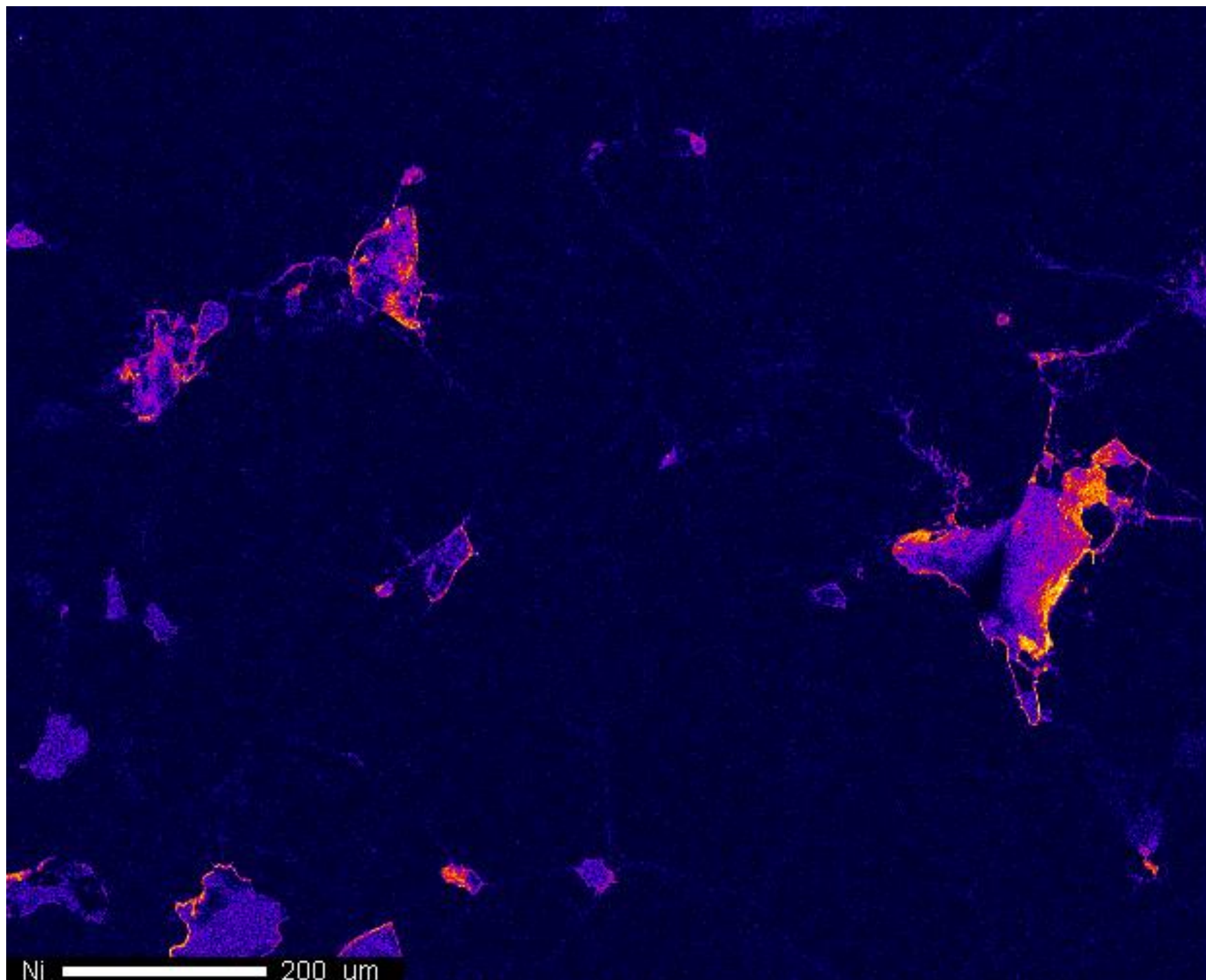


2,059

Project: September\_17\_2015  
Comment: Zak\_map01\_2um  
Date: 2015/09/17  
Accel Voltage: 15.0 kV  
Beam Current: 9.976e-008 A  
Dwell Time: 10.0  
Image Size: 623 x 503

O 200 um

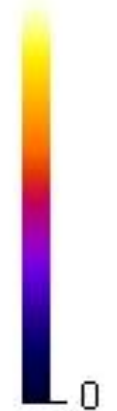




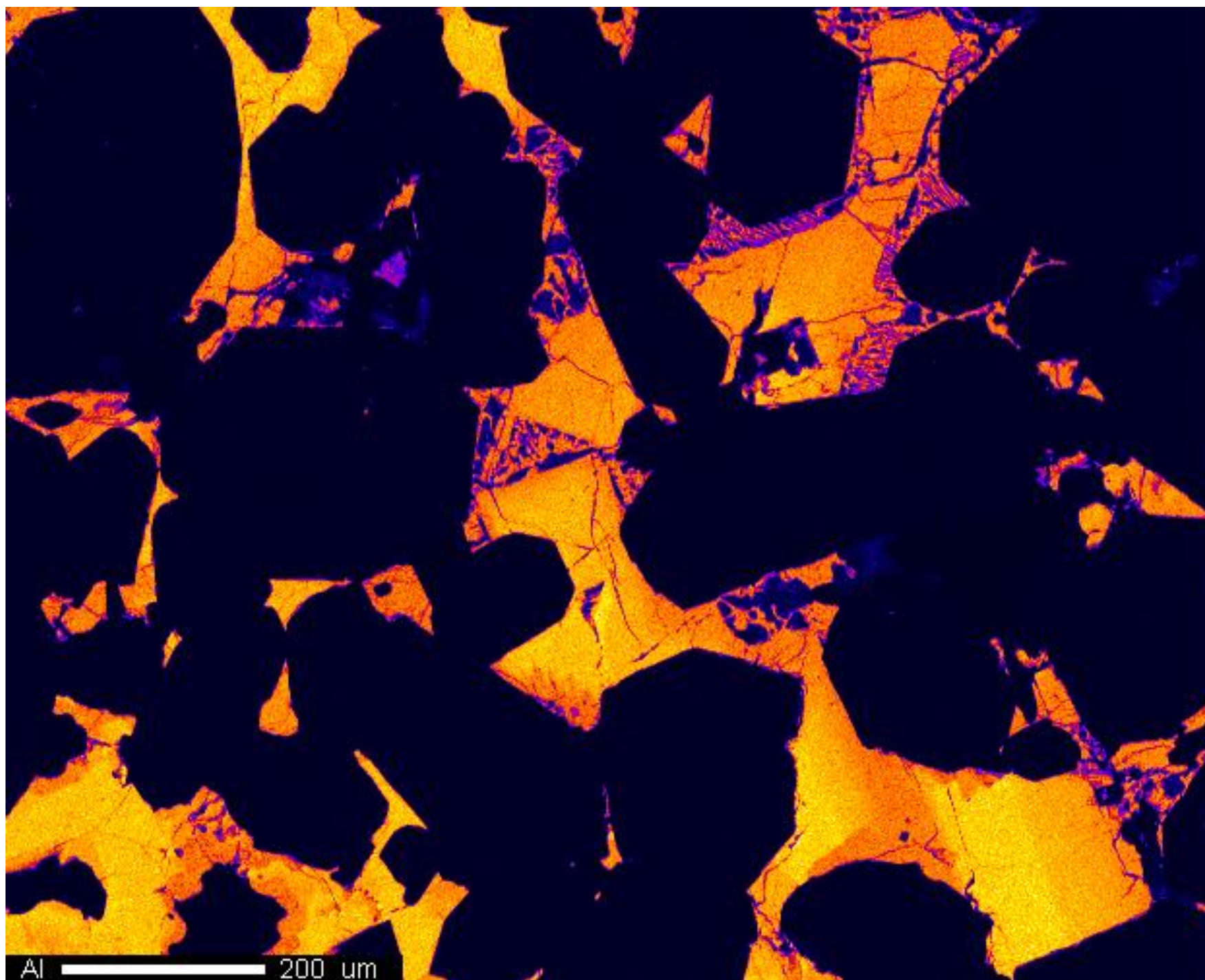
Ni

Cts

- 69



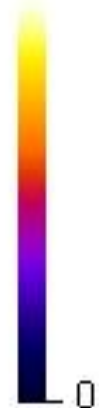
Project: September\_17\_2015  
Comment: Zak\_map01\_2um  
Date: 2015/09/17  
Accel Voltage: 15.0 kV  
Beam Current: 5.001e-008 A  
Dwell Time: 10.0  
Image Size: 623 x 503



Al

Cts

- 327



Project: September\_17\_2015

Comment: Zak\_map01\_2um

Date: 2015/09/17

Accel Voltage: 15.0 kV

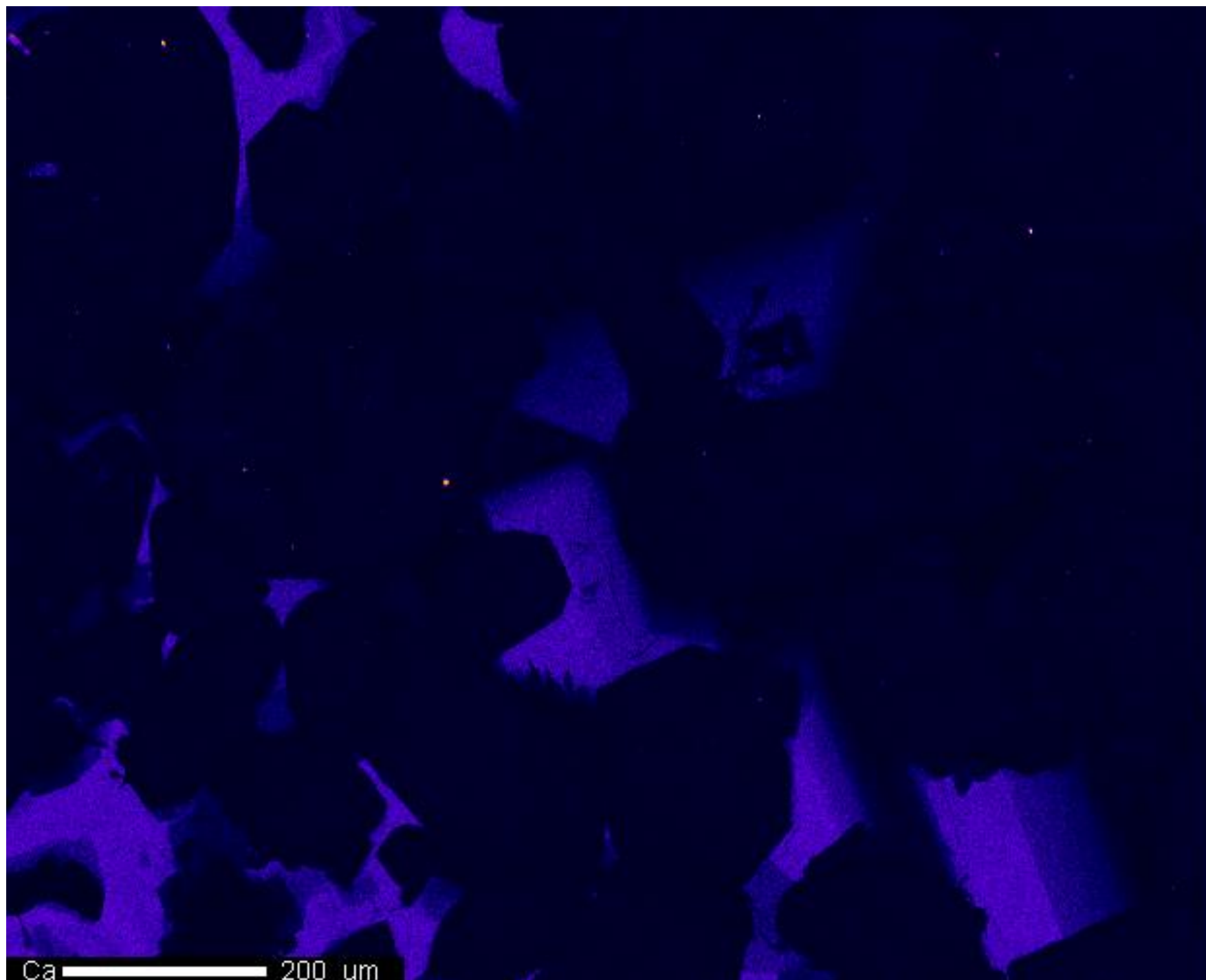
Beam Current: 9.976e-008 A

Dwell Time: 10.0

Image Size: 623 x 503

Al 200 um





Ca

Cts

- 367



0

Project: September\_17\_2015

Comment: Zak\_map01\_2um

Date: 2015/09/17

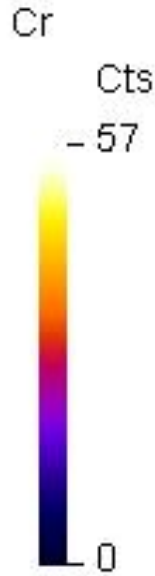
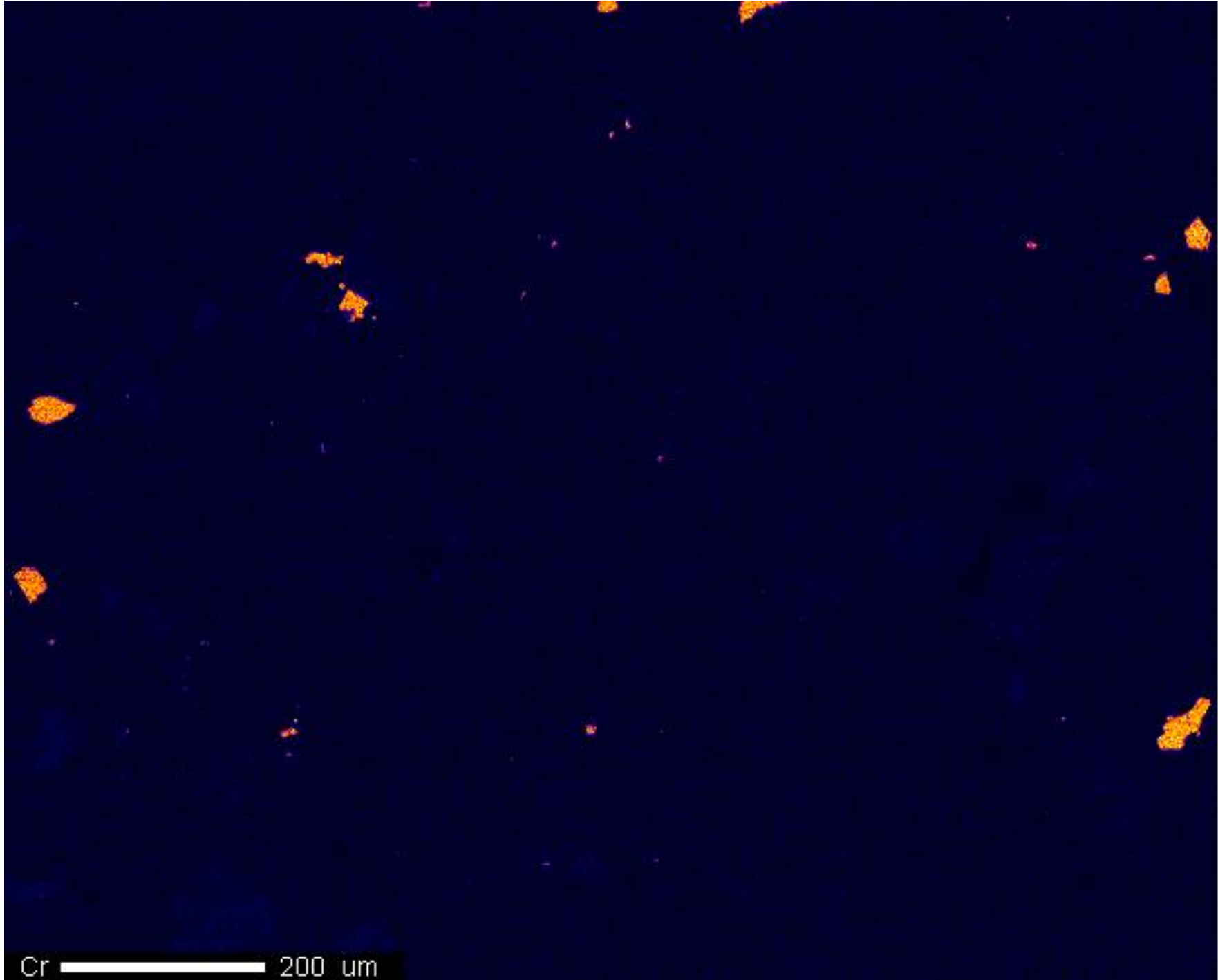
Accel Voltage: 15.0 kV

Beam Current: 9.976e-008 A

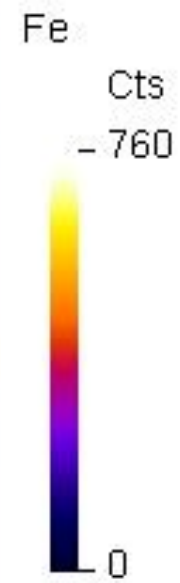
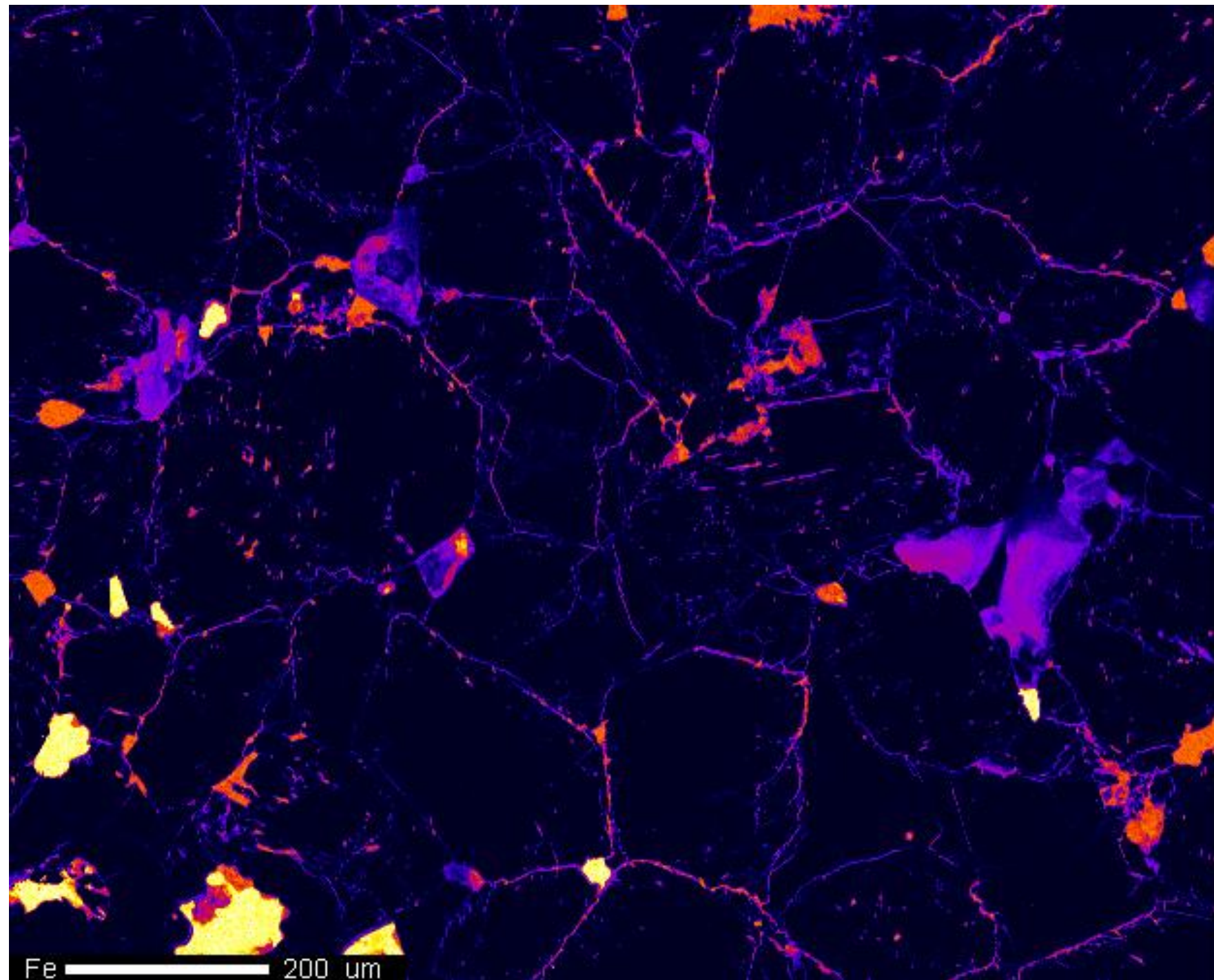
Dwell Time: 10.0

Image Size: 623 x 503

Ca 200 um

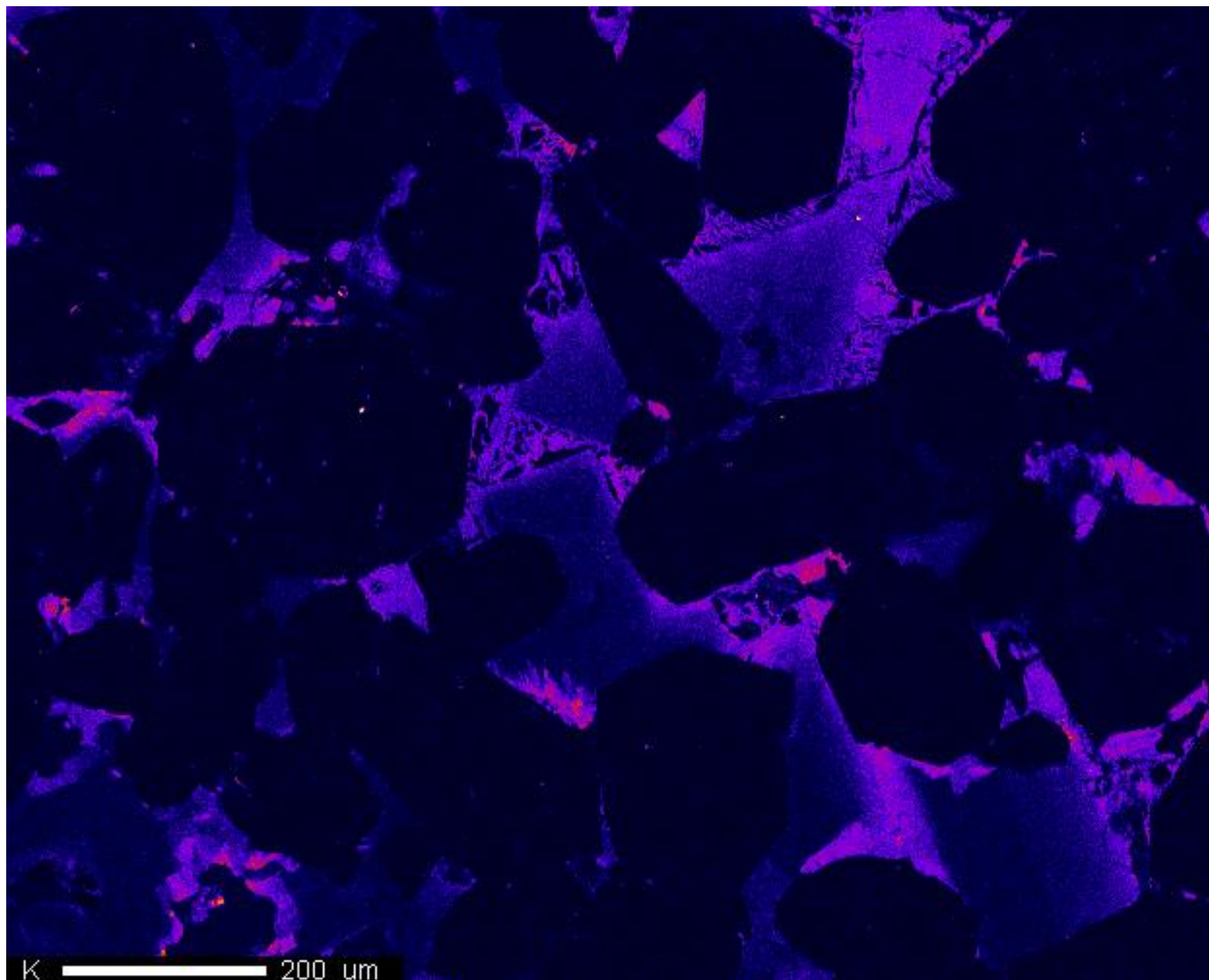


Project: September\_17\_2015  
Comment: Zak\_map01\_2um  
Date: 2015/09/17  
Accel Voltage: 15.0 kV  
Beam Current: 9.976e-008 A  
Dwell Time: 10.0  
Image Size: 623 x 503



Project: September\_17\_2015  
Comment: Zak\_map01\_2um  
Date: 2015/09/17  
Accel Voltage: 15.0 kV  
Beam Current: 9.976e-008 A  
Dwell Time: 10.0  
Image Size: 623 x 503





K

Cts

- 151



0

Project: September\_17\_2015

Comment: Zak\_map01\_2um

Date: 2015/09/17

Accel Voltage: 15.0 kV

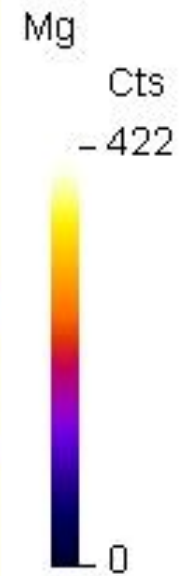
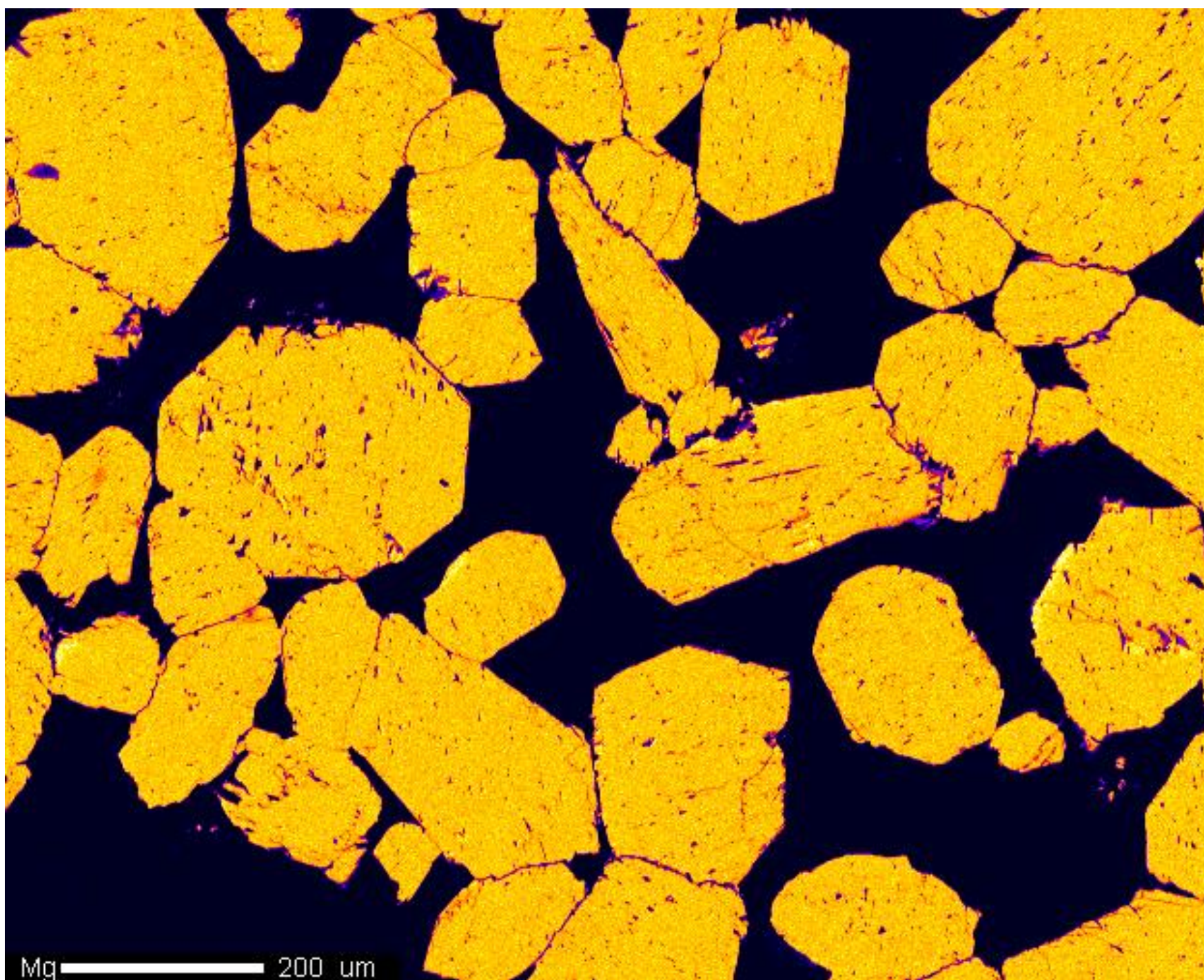
Beam Current: 9.976e-008 A

Dwell Time: 10.0

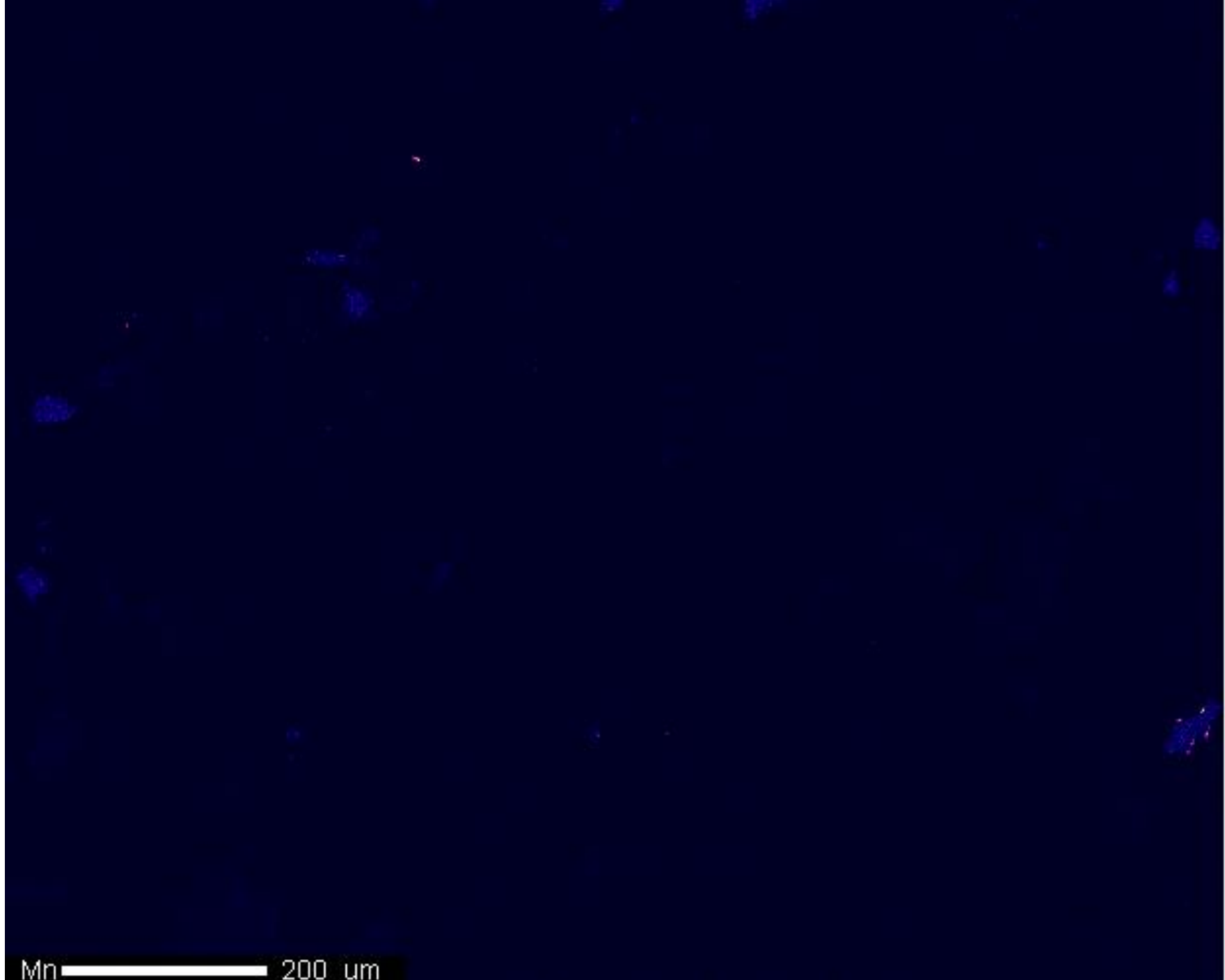
Image Size: 623 x 503

K  200 um





Project: September\_17\_2015  
Comment: Zak\_map01\_2um  
Date: 2015/09/17  
Accel Voltage: 15.0 kV  
Beam Current: 9.976e-008 A  
Dwell Time: 10.0  
Image Size: 623 x 503



Mn

Cts

- 162



0

Project: September\_17\_2015

Comment: Zak\_map01\_2um

Date: 2015/09/17

Accel Voltage: 15.0 kV

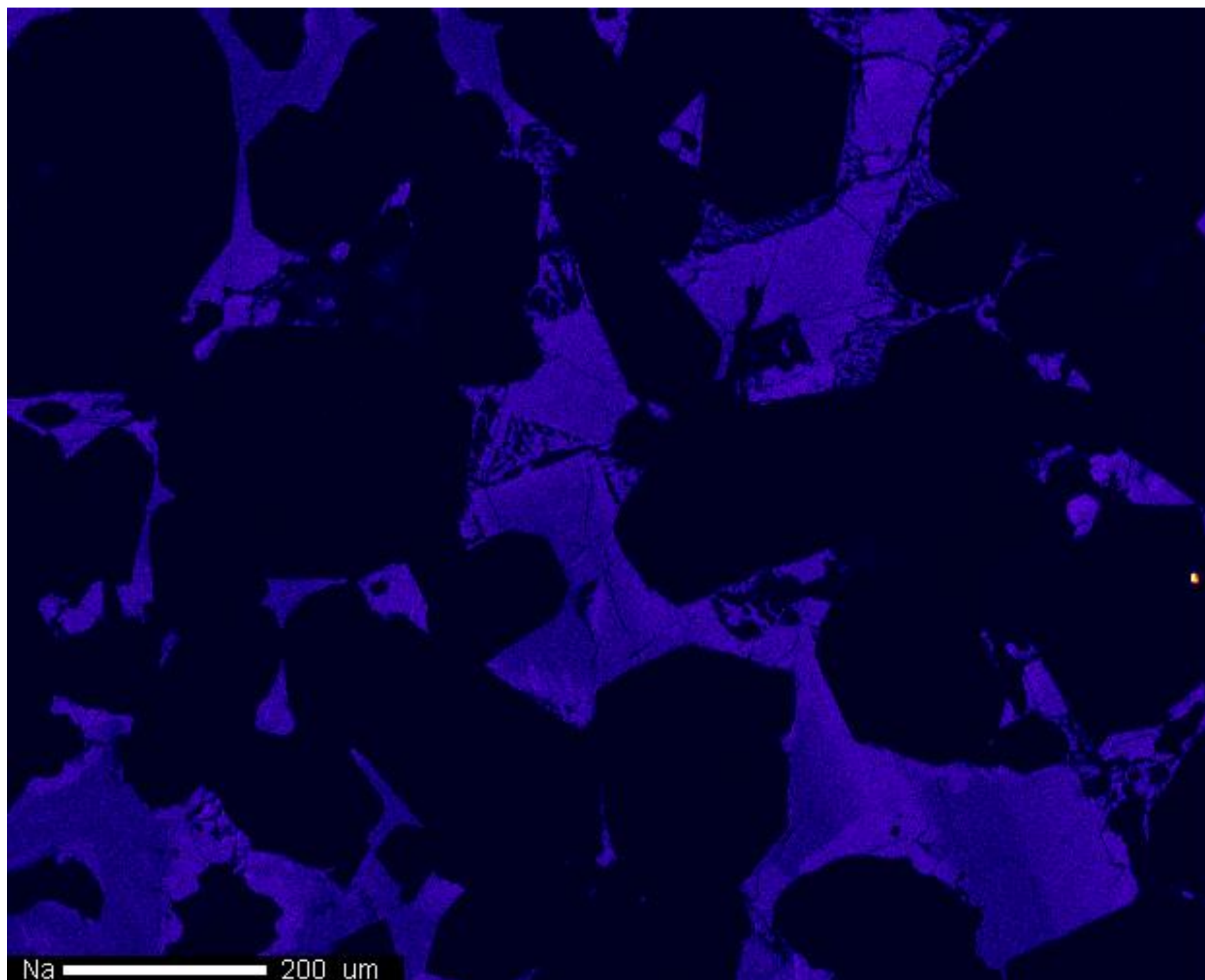
Beam Current: 9.976e-008 A

Dwell Time: 10.0

Image Size: 623 x 503

Mn  200 um





Na

Cts

- 406



Project: September\_17\_2015

Comment: Zak\_map01\_2um

Date: 2015/09/17

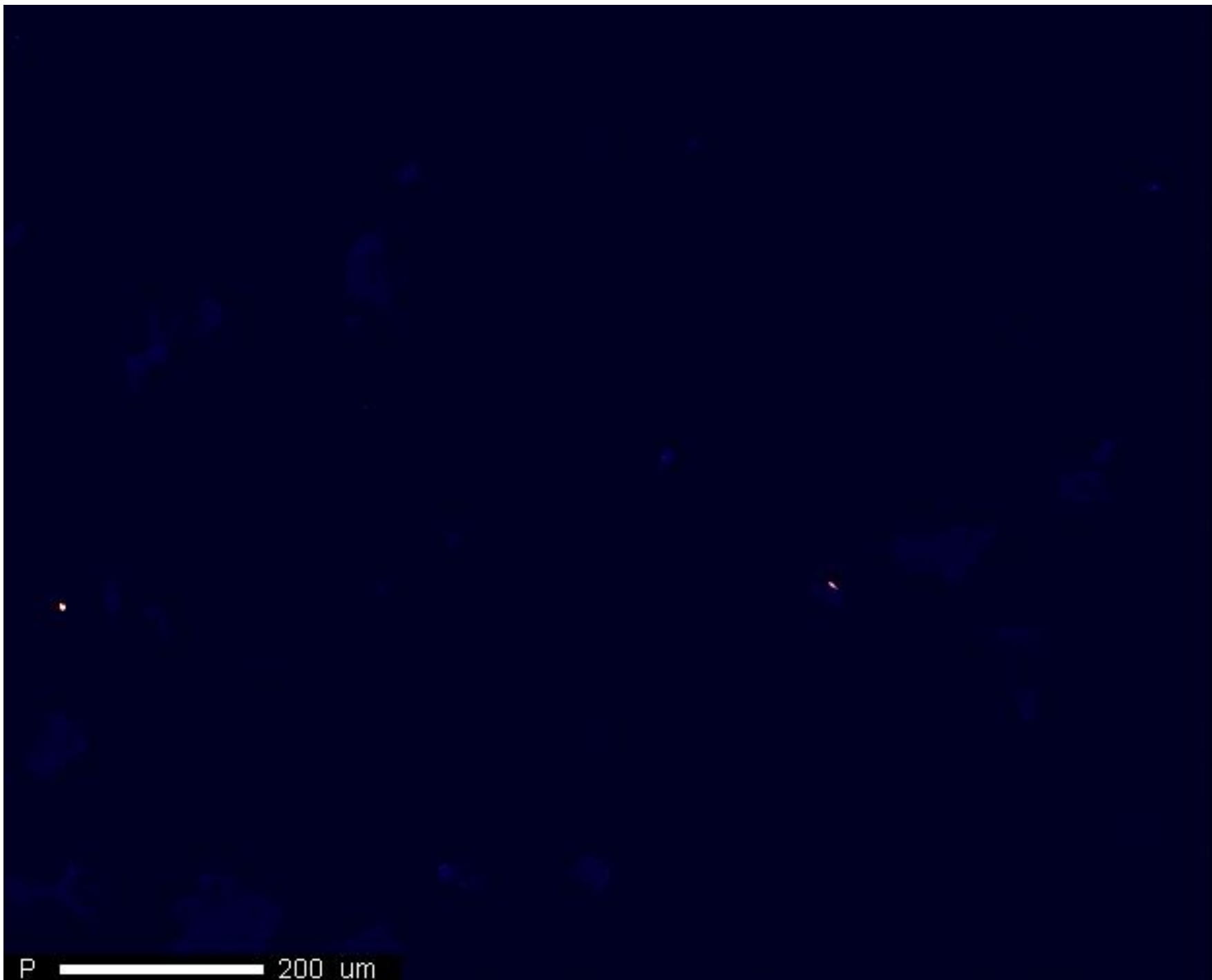
Accel Voltage: 15.0 kV

Beam Current: 9.976e-008 A

Dwell Time: 10.0

Image Size: 623 x 503

Na 200 um



P

Cts  
- 120

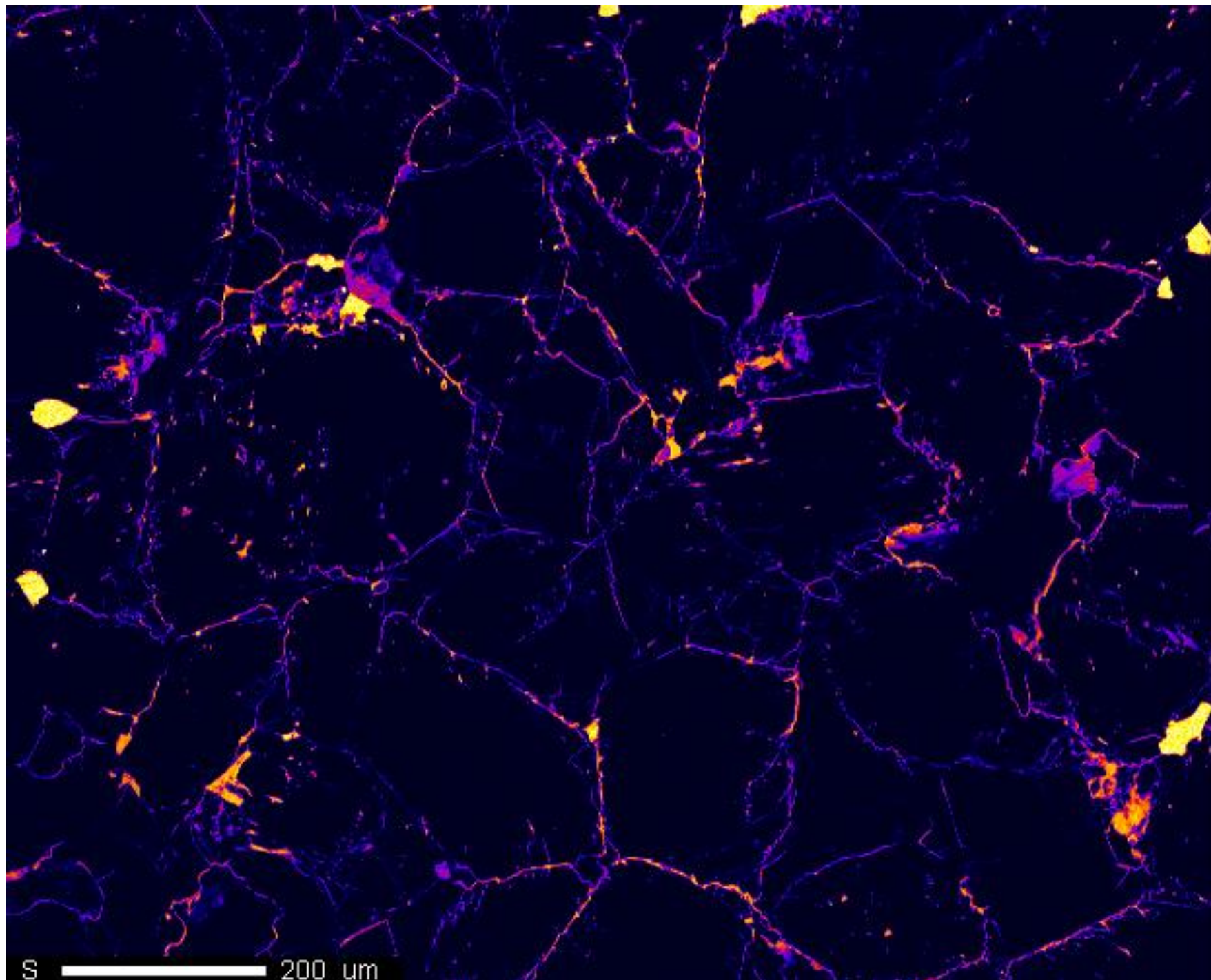


0

Project: September\_17\_2015  
Comment: Zak\_map01\_2um  
Date: 2015/09/17  
Accel Voltage: 15.0 kV  
Beam Current: 9.976e-008 A  
Dwell Time: 10.0  
Image Size: 623 x 503

P  200 um





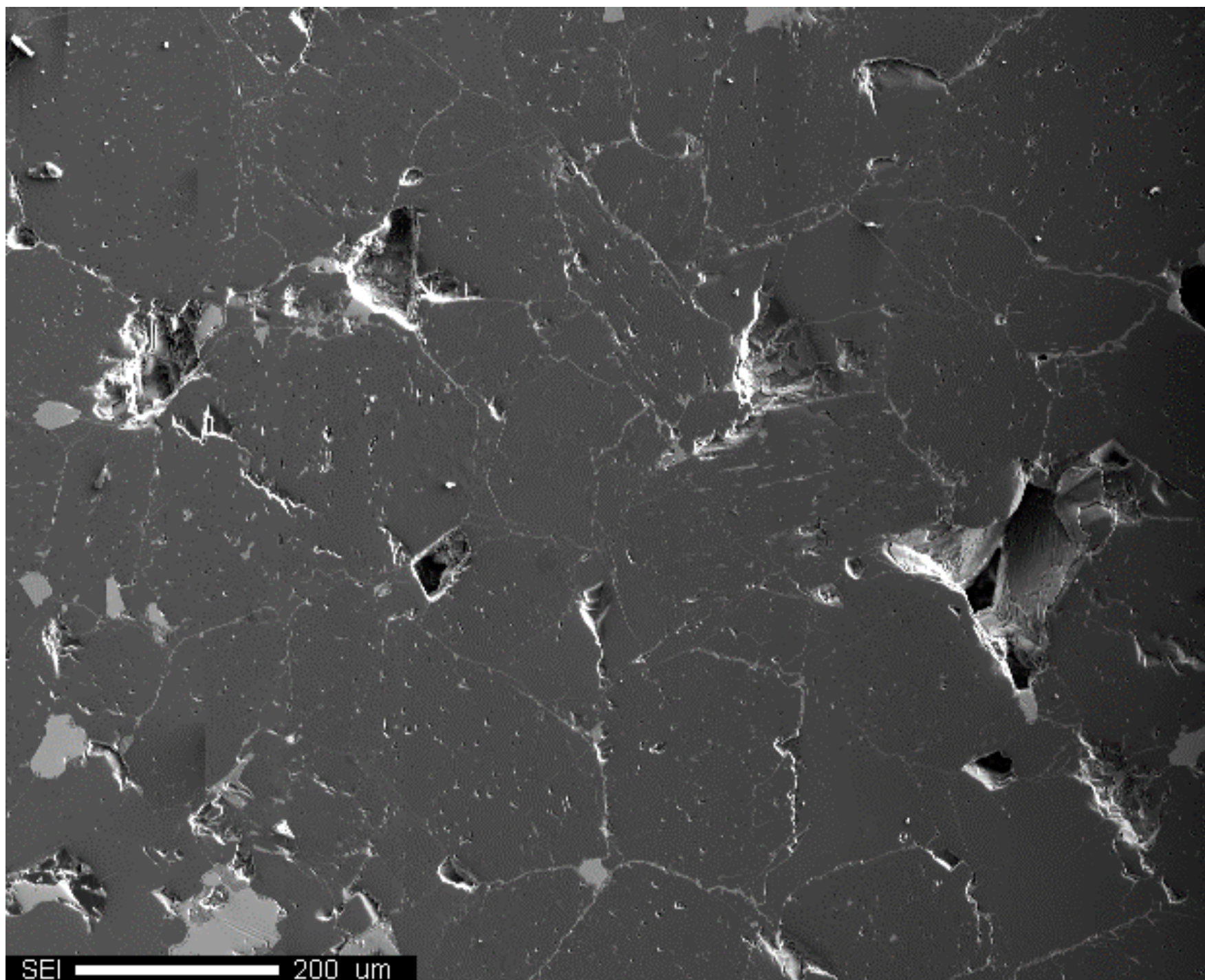
S

Cts  
- 538



Project: September\_17\_2015  
Comment: Zak\_map01\_2um  
Date: 2015/09/17  
Accel Voltage: 15.0 kV  
Beam Current: 9.976e-008 A  
Dwell Time: 10.0  
Image Size: 623 x 503





SEI

Cts

- 4,095

0

Project: September\_17\_2015

Comment: Zak\_map01\_2um

Date: 2015/09/17

Accel Voltage: 15.0 kV

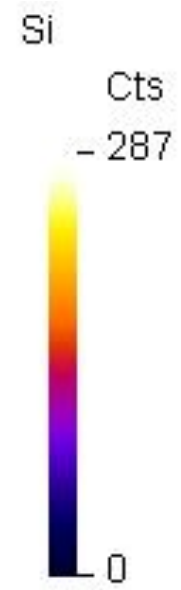
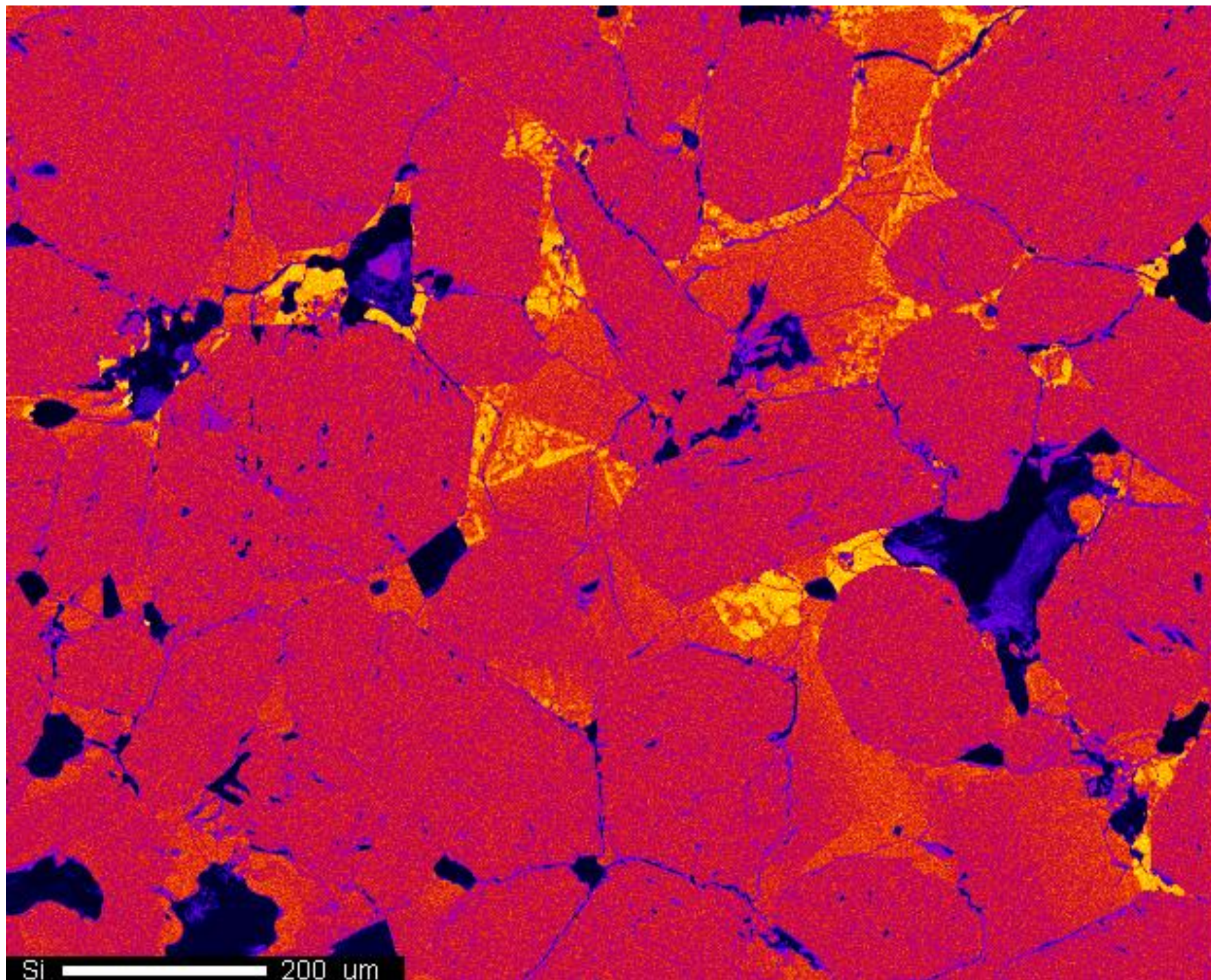
Beam Current: 9.976e-008 A

Dwell Time: 10.0

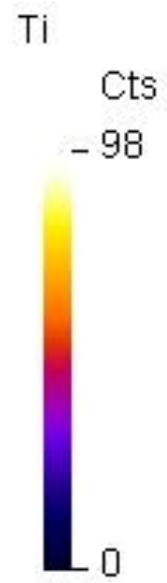
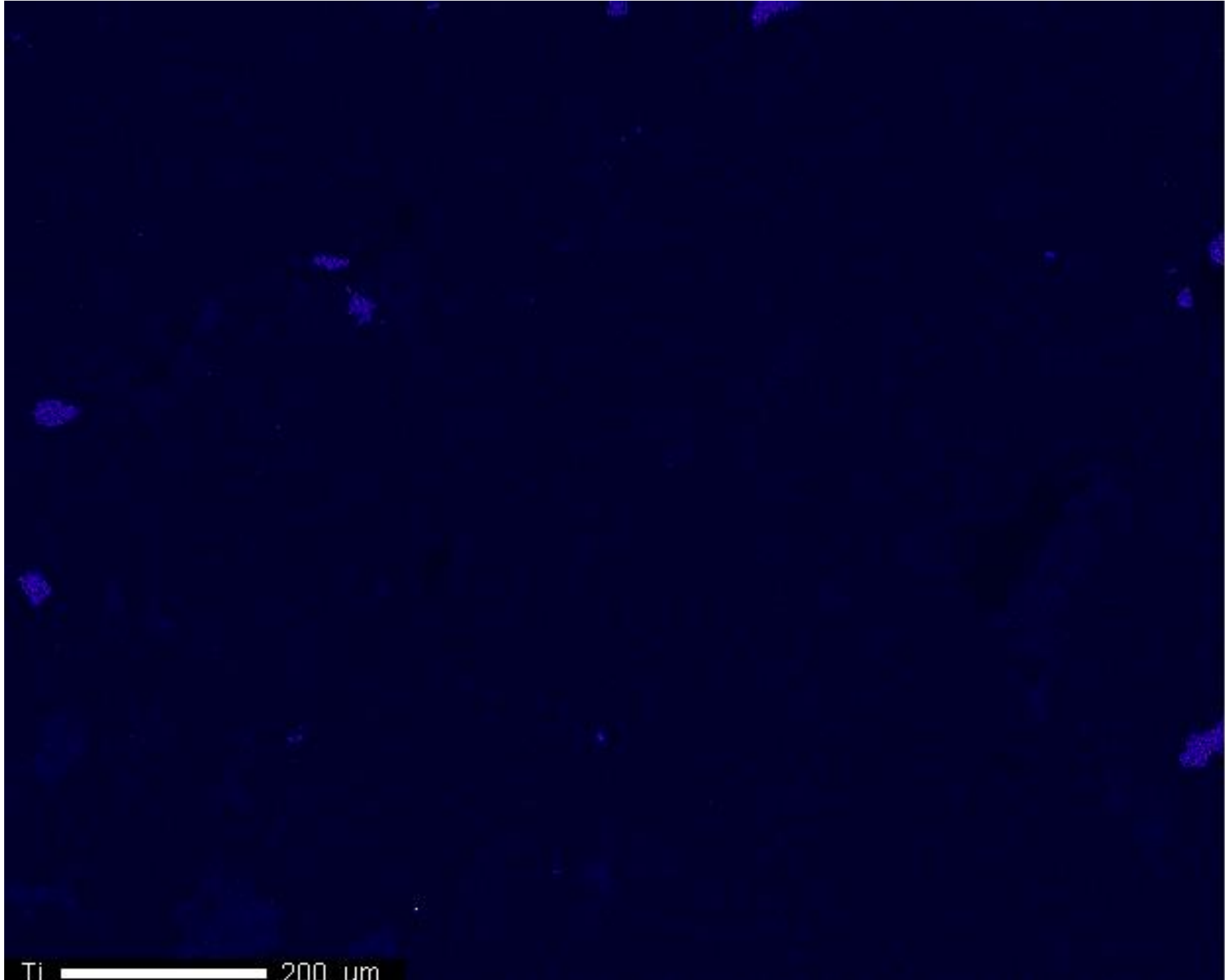
Image Size: 623 x 503

SEI 200 um





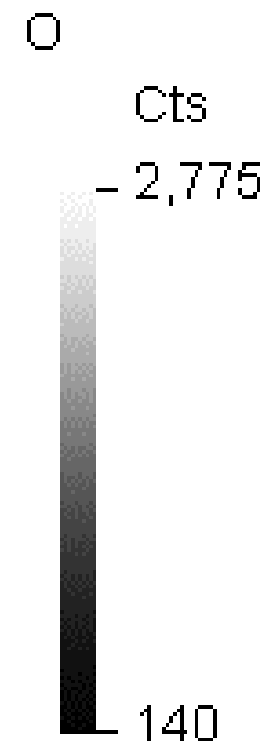
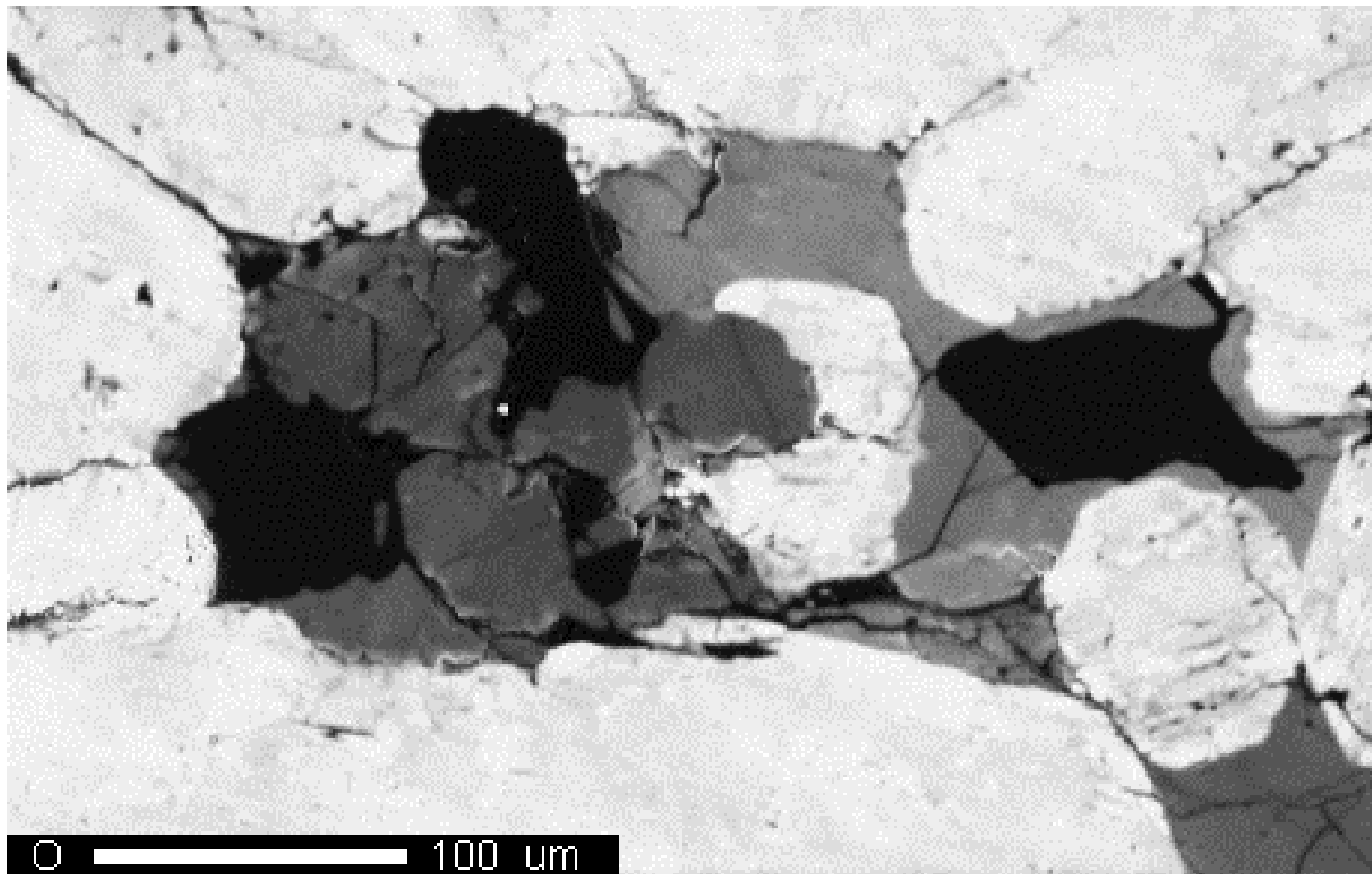
Project: September\_17\_2015  
Comment: Zak\_map01\_2um  
Date: 2015/09/17  
Accel Voltage: 15.0 kV  
Beam Current: 9.976e-008 A  
Dwell Time: 10.0  
Image Size: 623 x 503



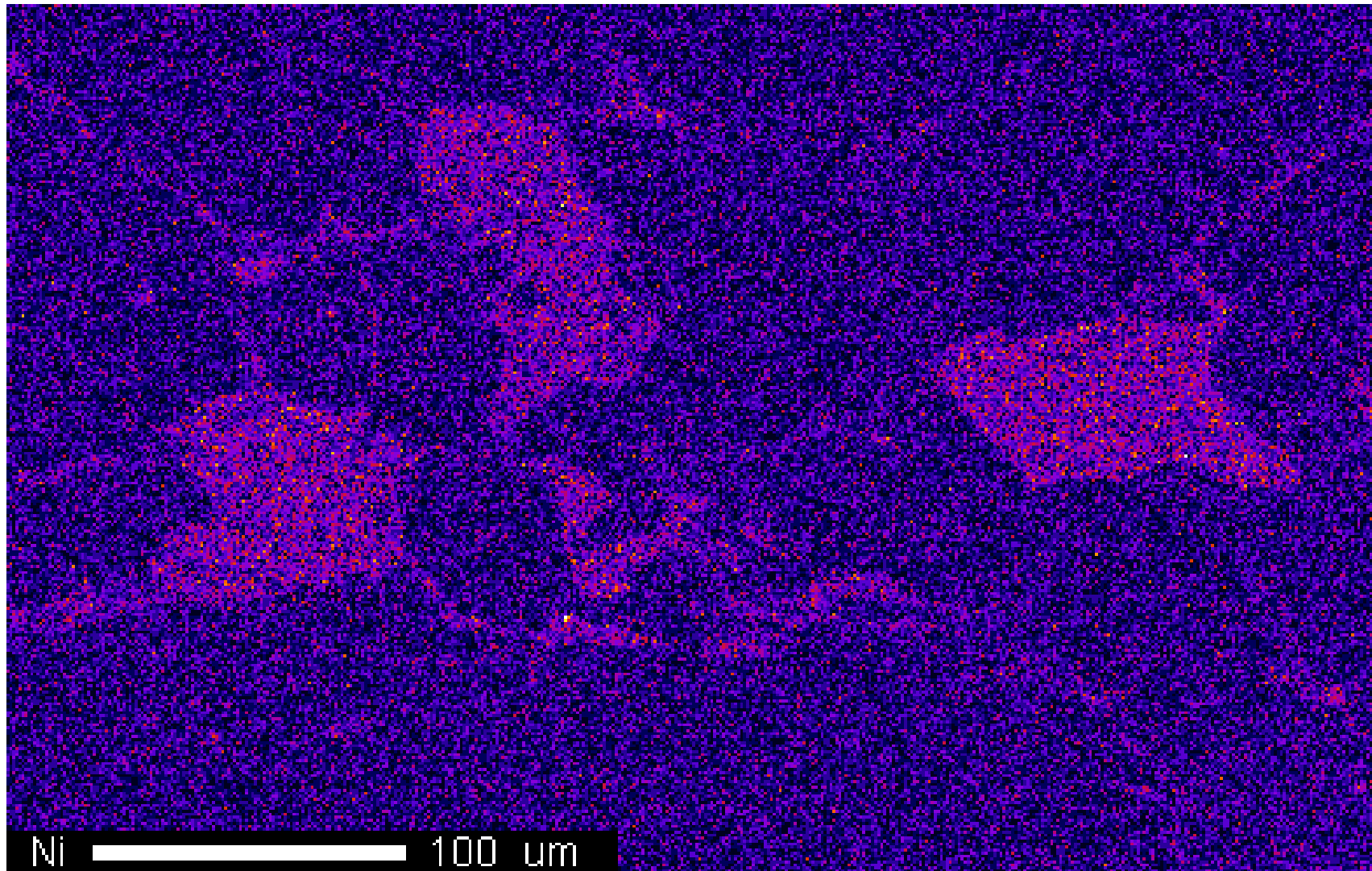
Project: September\_17\_2015  
Comment: Zak\_map01\_2um  
Date: 2015/09/17  
Accel Voltage: 15.0 kV  
Beam Current: 9.976e-008 A  
Dwell Time: 10.0  
Image Size: 623 x 503

Ti  200 um





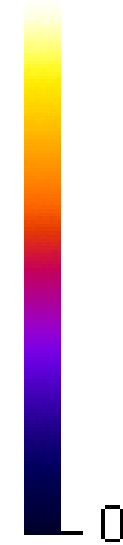
Project: September\_17\_2015  
Comment: Zak\_map02\_1um  
Date: 2015/09/17  
Accel Voltage: 15.0 kV  
Beam Current: 9.973e-008 A  
Dwell Time: 10.0  
Image Size: 460 x 291



Ni

Cts

- 17



0

Project: September\_17\_2015

Comment: Zak\_map02\_1um

Date: 2015/09/17

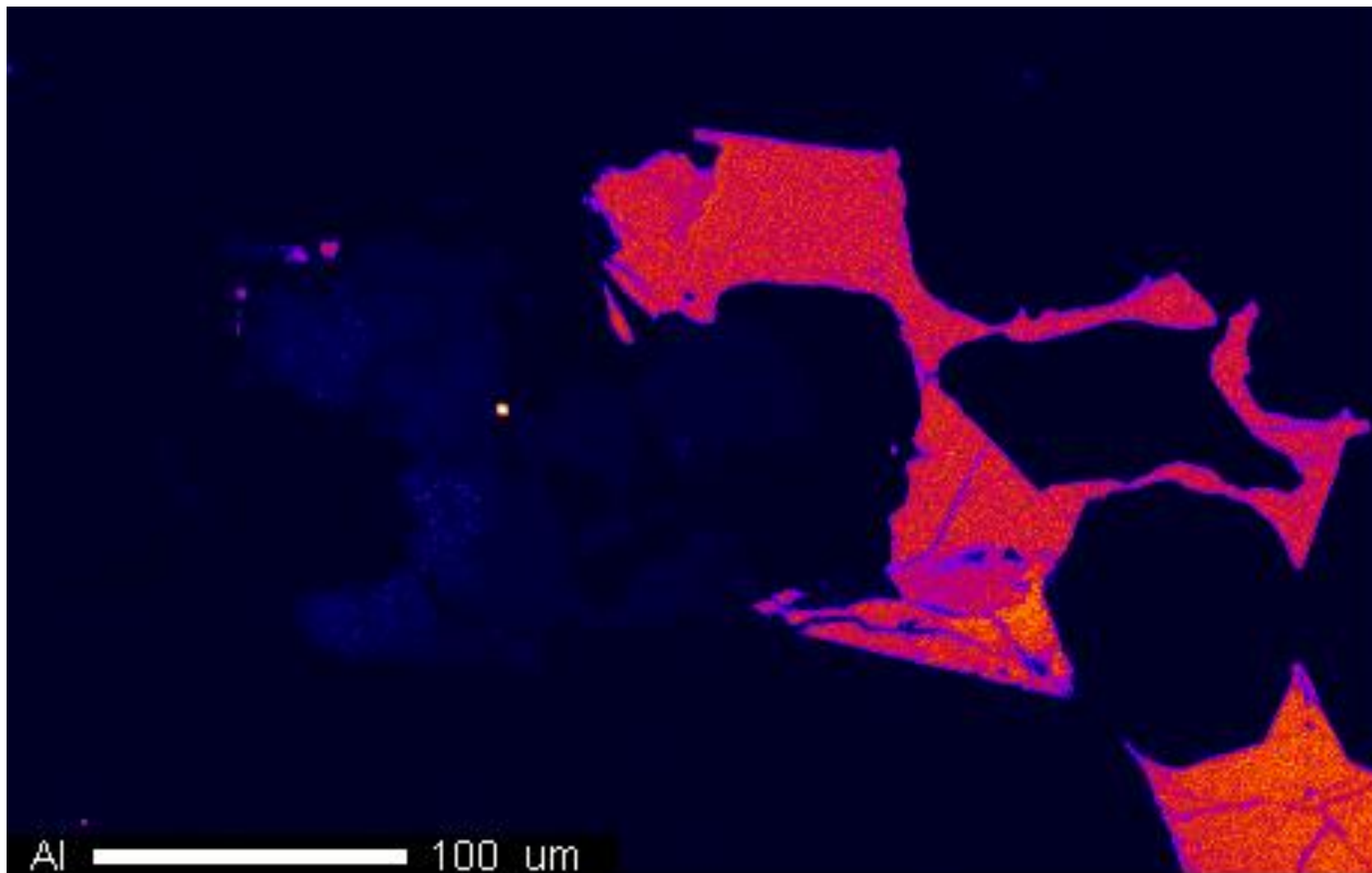
Accel Voltage: 15.0 kV

Beam Current: 9.959e-008 A

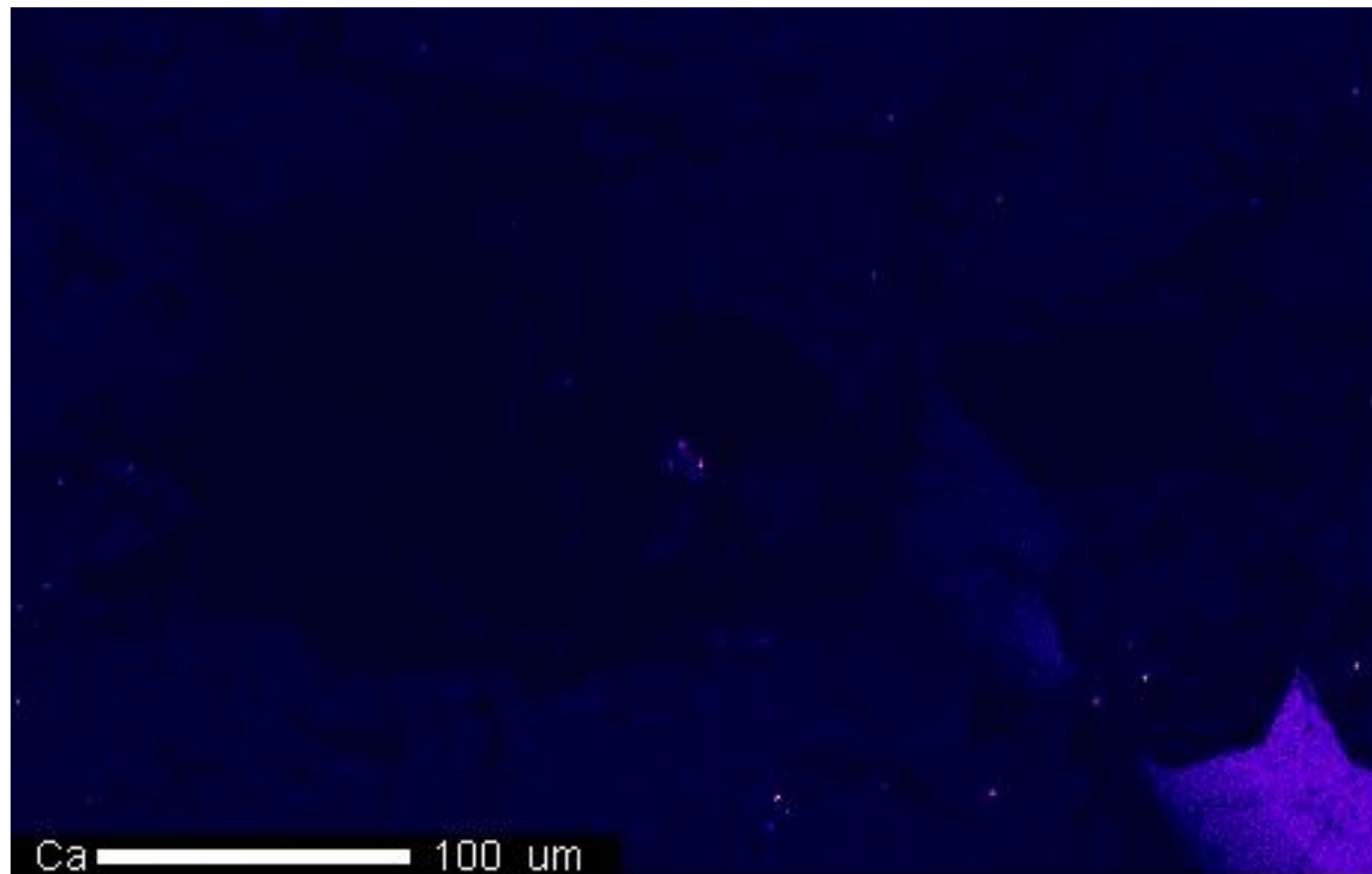
Dwell Time: 10.0

Image Size: 460 x 291

Ni 100 um

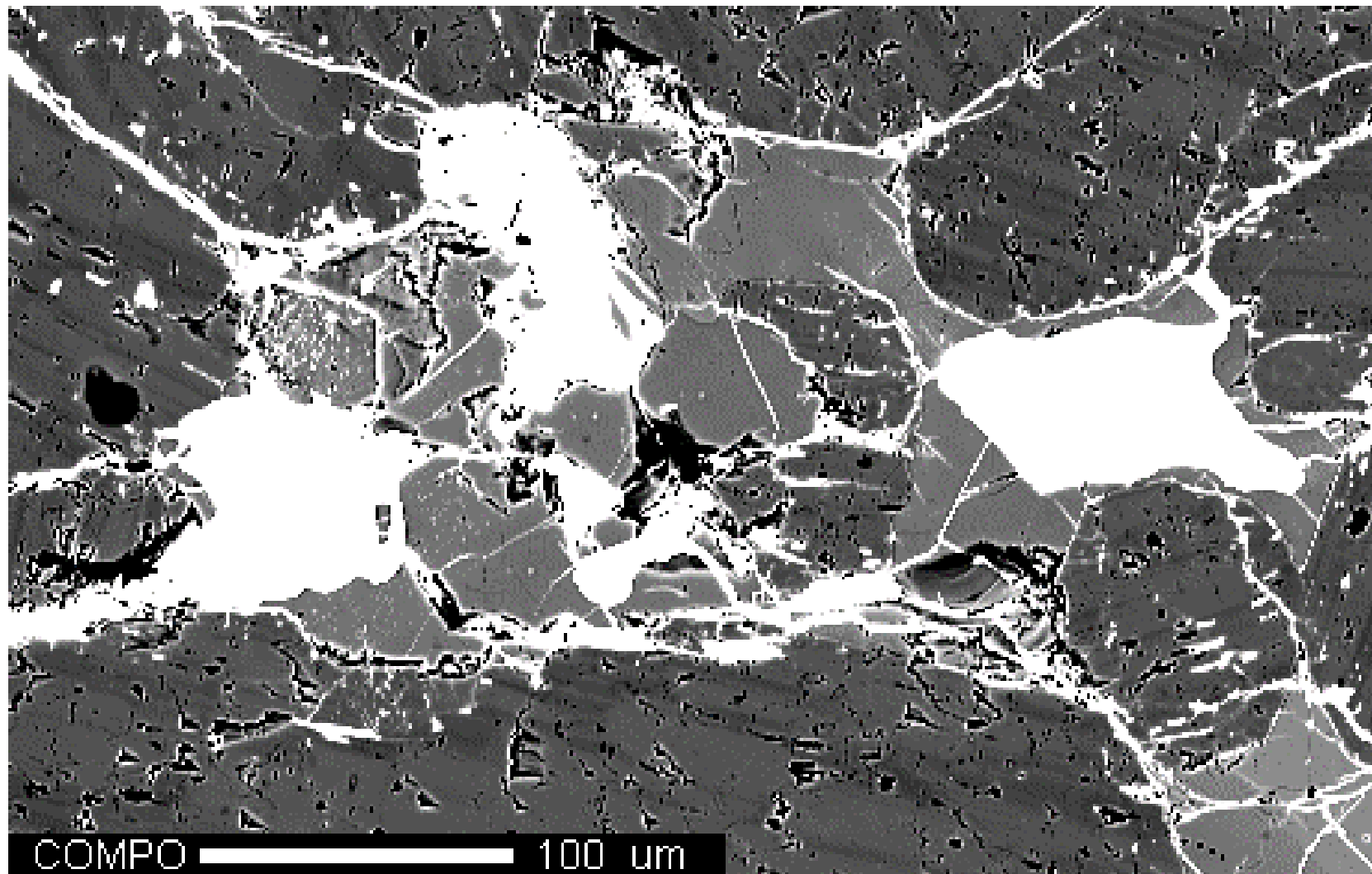


Project: September\_17\_2015  
Comment: Zak\_map02\_1um  
Date: 2015/09/17  
Accel Voltage: 15.0 kV  
Beam Current: 9.973e-008 A  
Dwell Time: 10.0  
Image Size: 460 x 291



Project: September\_17\_2015  
Comment: Zak\_map02\_1um  
Date: 2015/09/17  
Accel Voltage: 15.0 kV  
Beam Current: 9.973e-008 A  
Dwell Time: 10.0  
Image Size: 460 x 291





COMPO

Cts

- 4,095



0

Project: September\_17\_2015

Comment: Zak\_map02\_1um

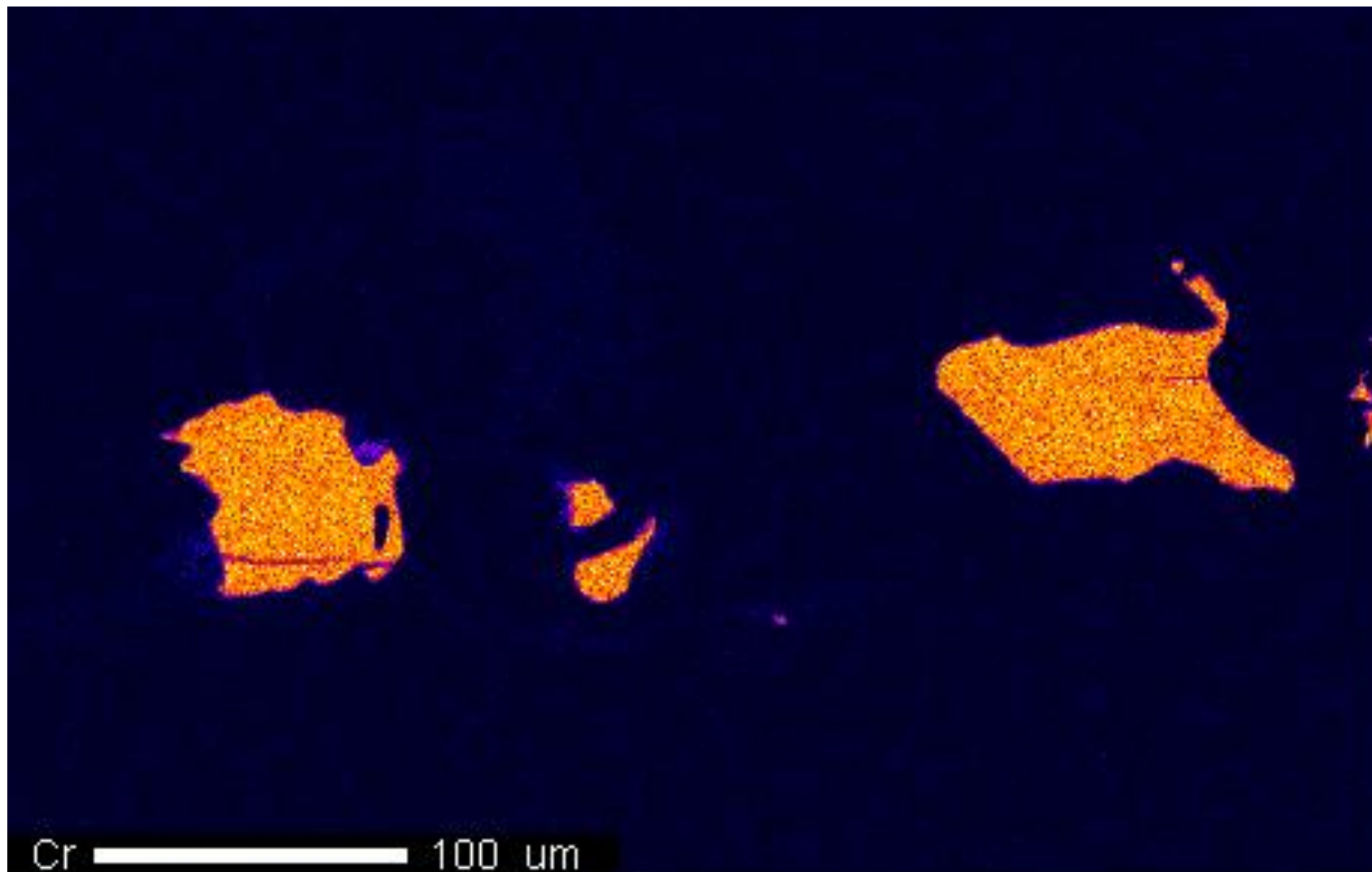
Date: 2015/09/17

Accel Voltage: 15.0 kV

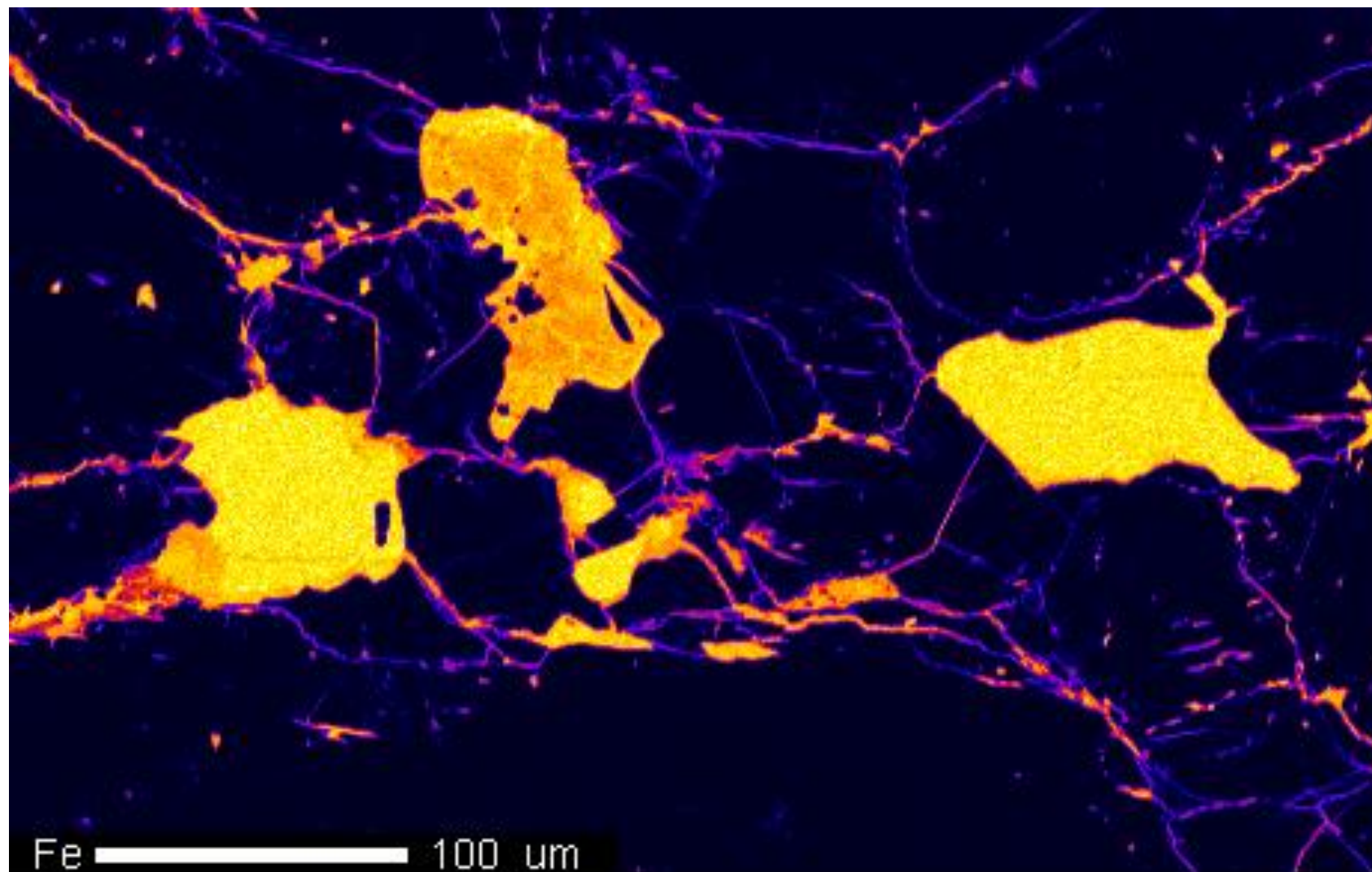
Beam Current: 9.973e-008 A

Dwell Time: 10.0

Image Size: 460 x 291



Project: September\_17\_2015  
Comment: Zak\_map02\_1um  
Date: 2015/09/17  
Accel Voltage: 15.0 kV  
Beam Current: 9.973e-008 A  
Dwell Time: 10.0  
Image Size: 460 x 291



Fe

Cts

- 466



0

Project: September\_17\_2015

Comment: Zak\_map02\_1um

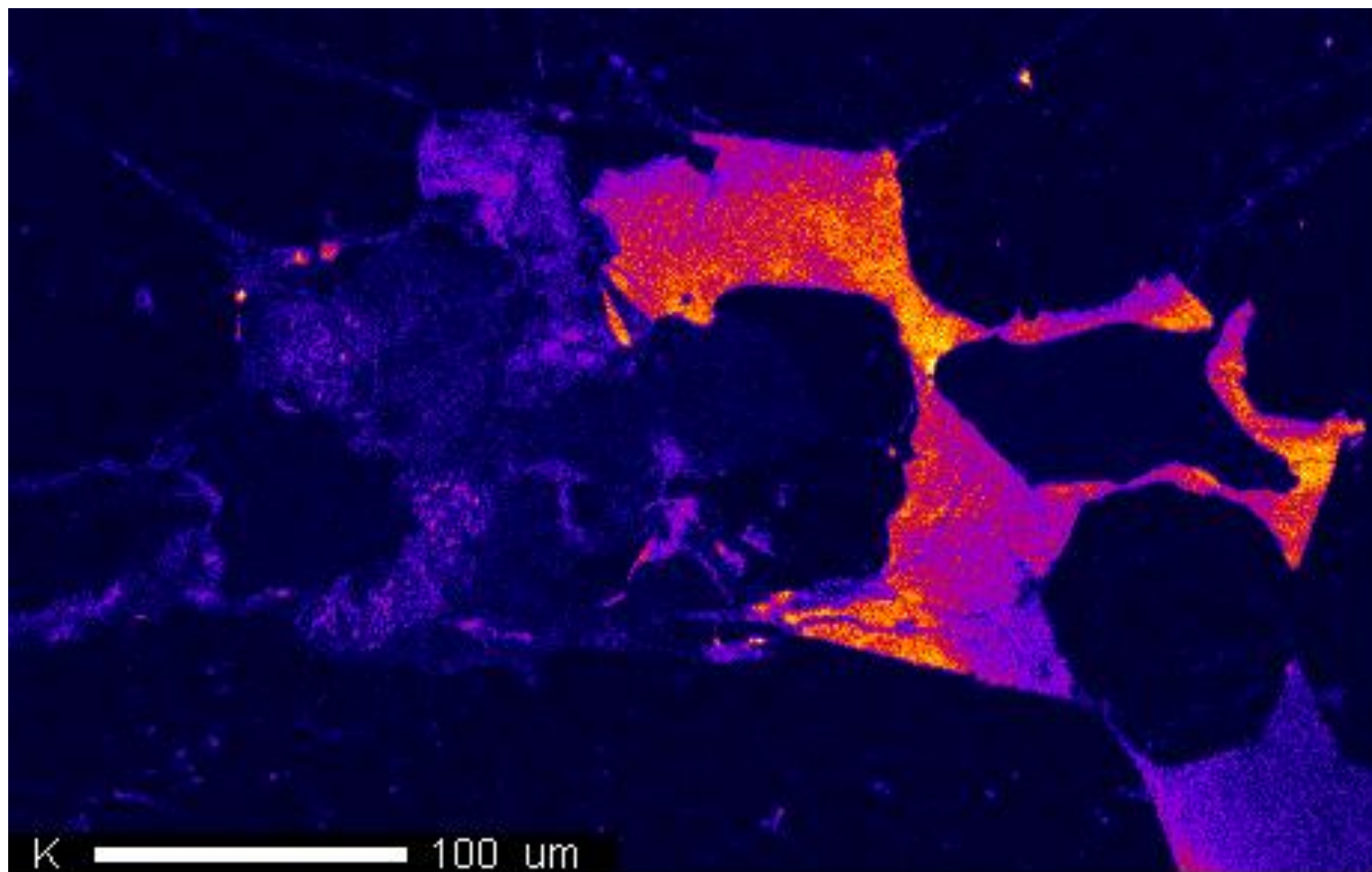
Date: 2015/09/17

Accel Voltage: 15.0 kV

Beam Current: 9.973e-008 A

Dwell Time: 10.0

Image Size: 460 x 291



K

Cts

- 96



0

Project: September\_17\_2015

Comment: Zak\_map02\_1um

Date: 2015/09/17

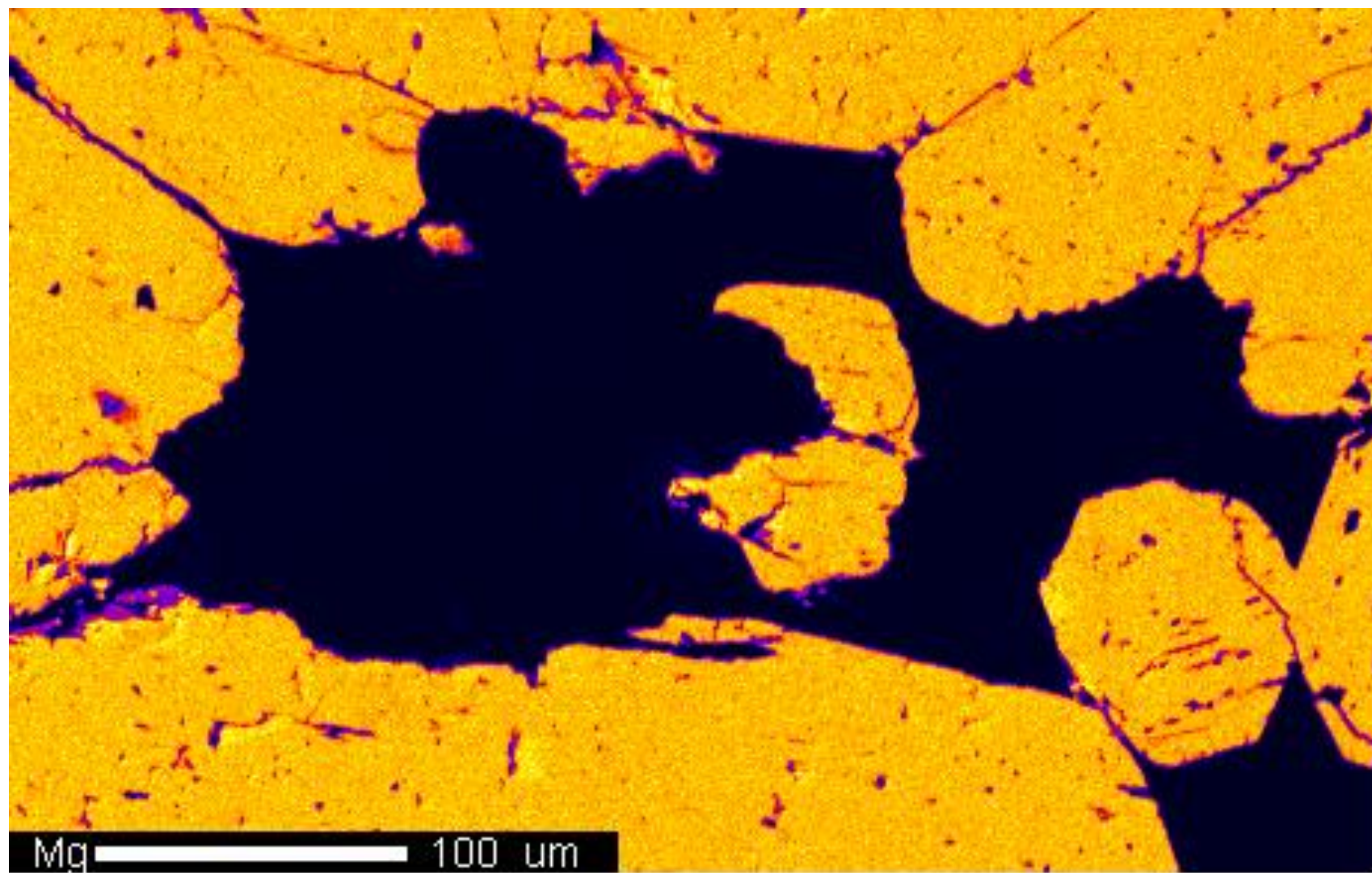
Accel Voltage: 15.0 kV

Beam Current: 9.973e-008 A

Dwell Time: 10.0

Image Size: 460 x 291

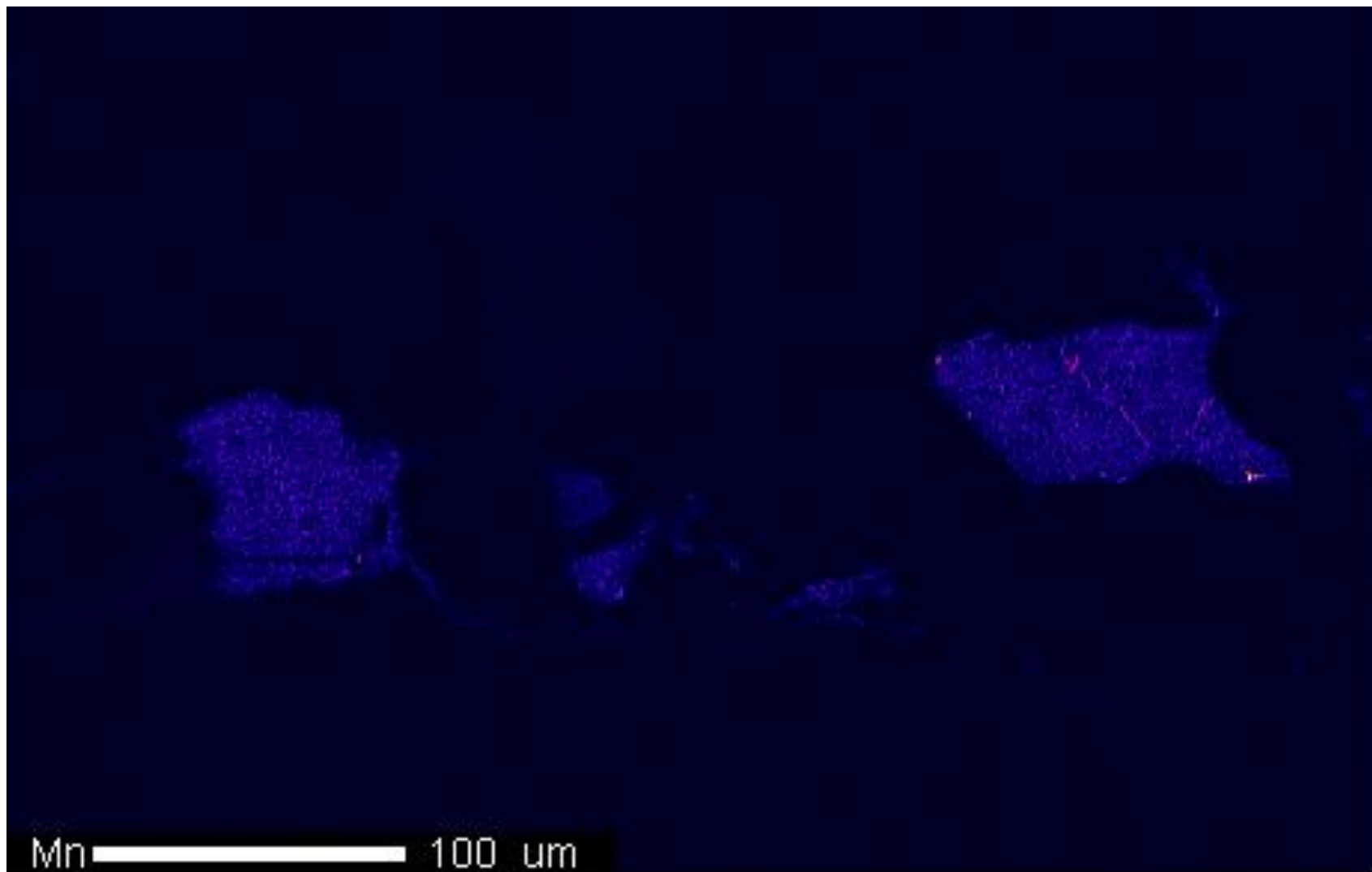




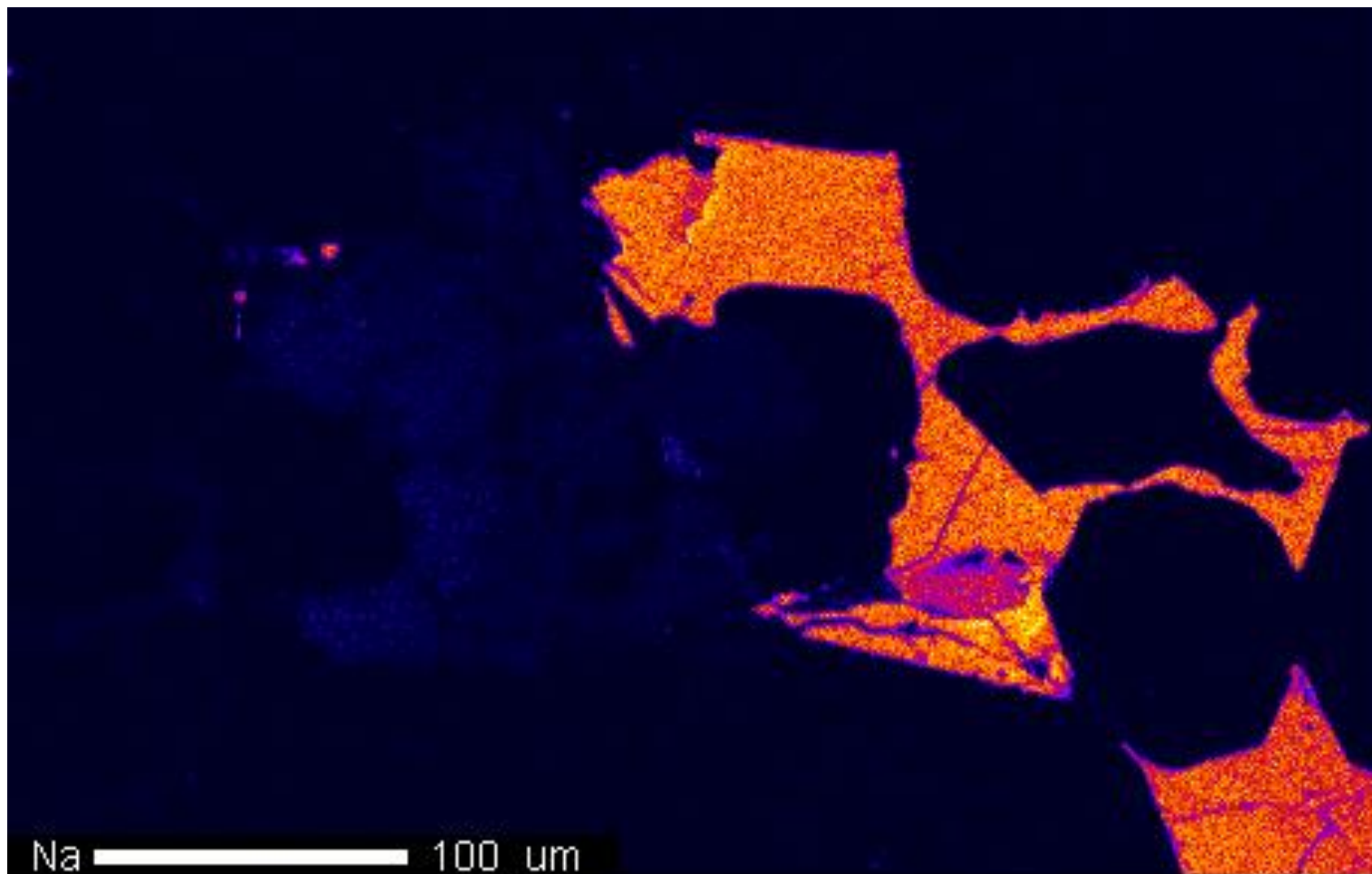
Mg  
Cts  
- 392



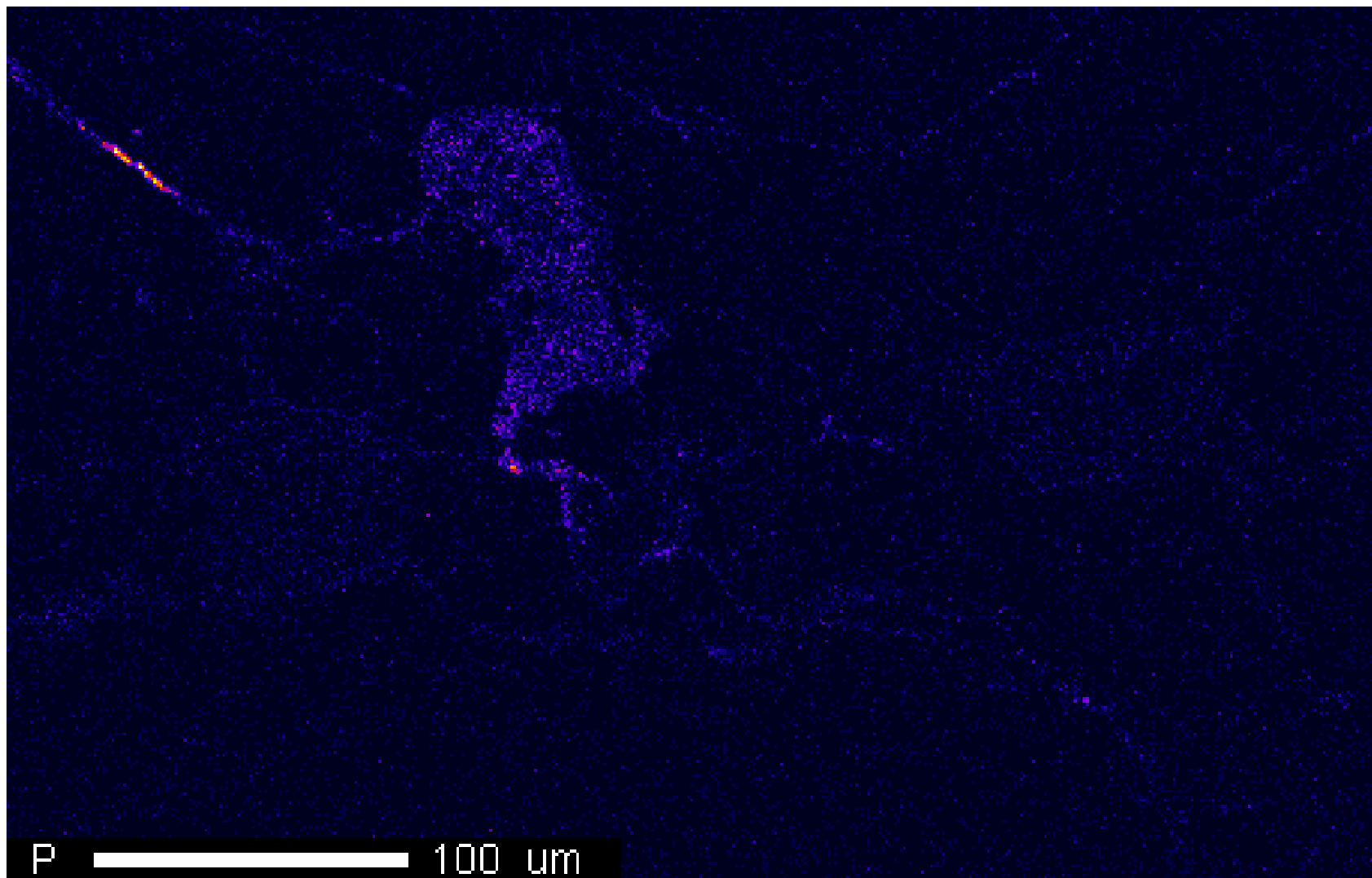
Project: September\_17\_2015  
Comment: Zak\_map02\_1um  
Date: 2015/09/17  
Accel Voltage: 15.0 kV  
Beam Current: 9.973e-008 A  
Dwell Time: 10.0  
Image Size: 460 x 291



Project: September\_17\_2015  
Comment: Zak\_map02\_1um  
Date: 2015/09/17  
Accel Voltage: 15.0 kV  
Beam Current: 9.973e-008 A  
Dwell Time: 10.0  
Image Size: 460 x 291

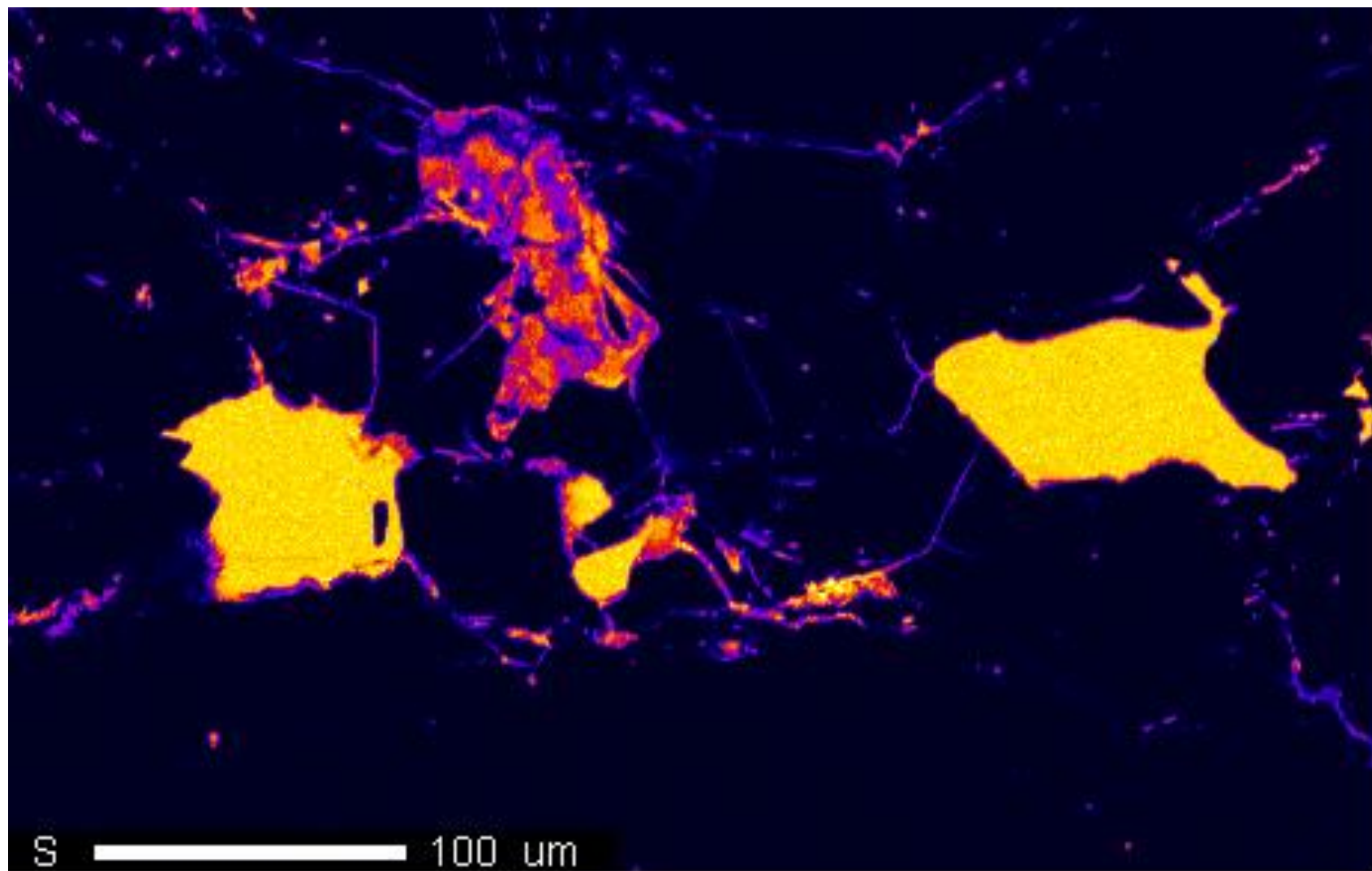


Project: September\_17\_2015  
Comment: Zak\_map02\_1um  
Date: 2015/09/17  
Accel Voltage: 15.0 kV  
Beam Current: 9.973e-008 A  
Dwell Time: 10.0  
Image Size: 460 x 291



Project: September\_17\_2015  
Comment: Zak\_map02\_1um  
Date: 2015/09/17  
Accel Voltage: 15.0 kV  
Beam Current: 9.973e-008 A  
Dwell Time: 10.0  
Image Size: 460 x 291



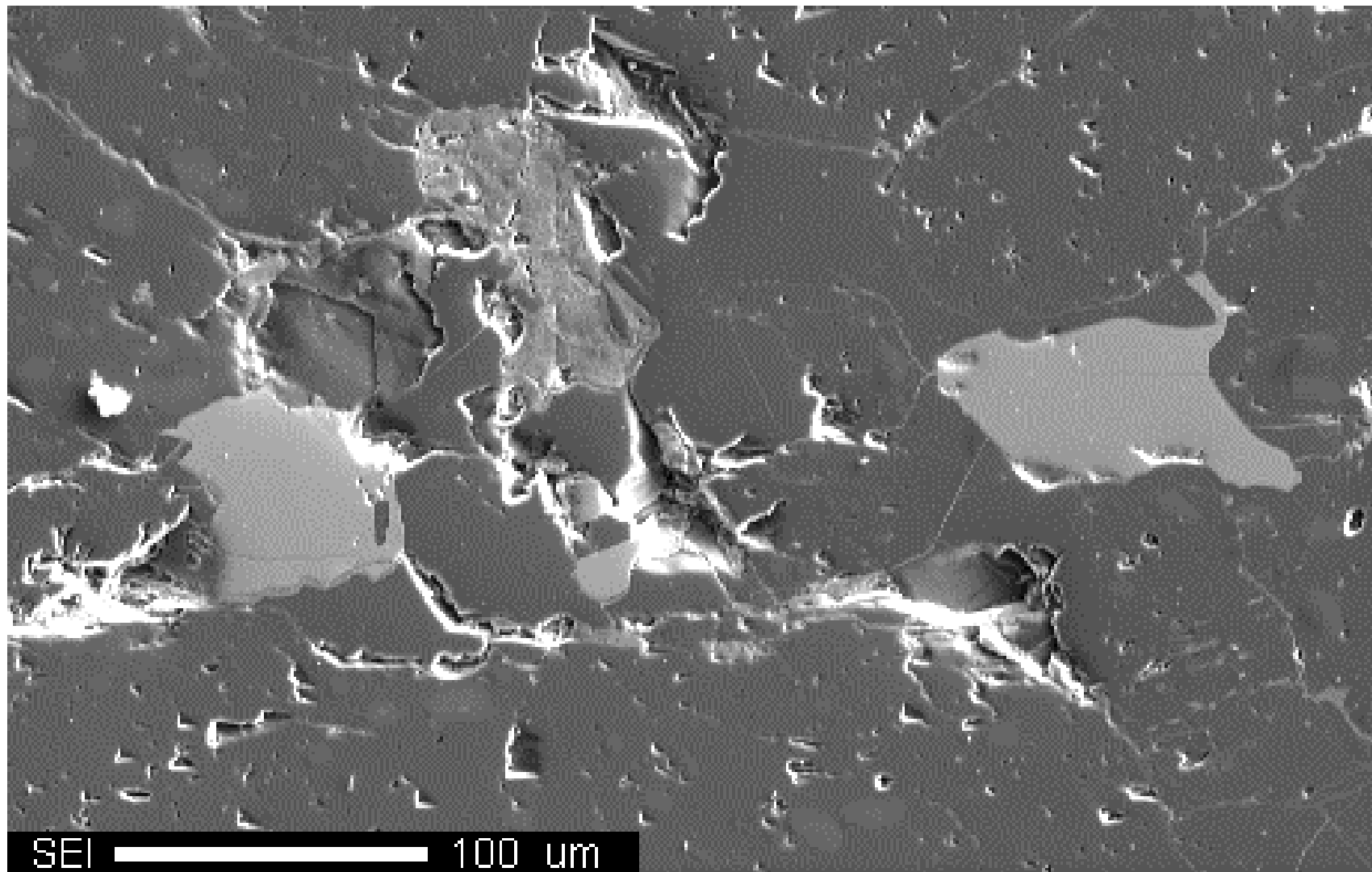


S

Cts  
- 602



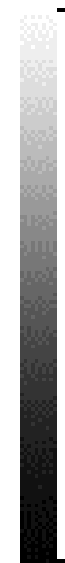
Project: September\_17\_2015  
Comment: Zak\_map02\_1um  
Date: 2015/09/17  
Accel Voltage: 15.0 kV  
Beam Current: 9.973e-008 A  
Dwell Time: 10.0  
Image Size: 460 x 291



SEI

Cts

- 4,095



252

Project: September\_17\_2015

Comment: Zak\_map02\_1um

Date: 2015/09/17

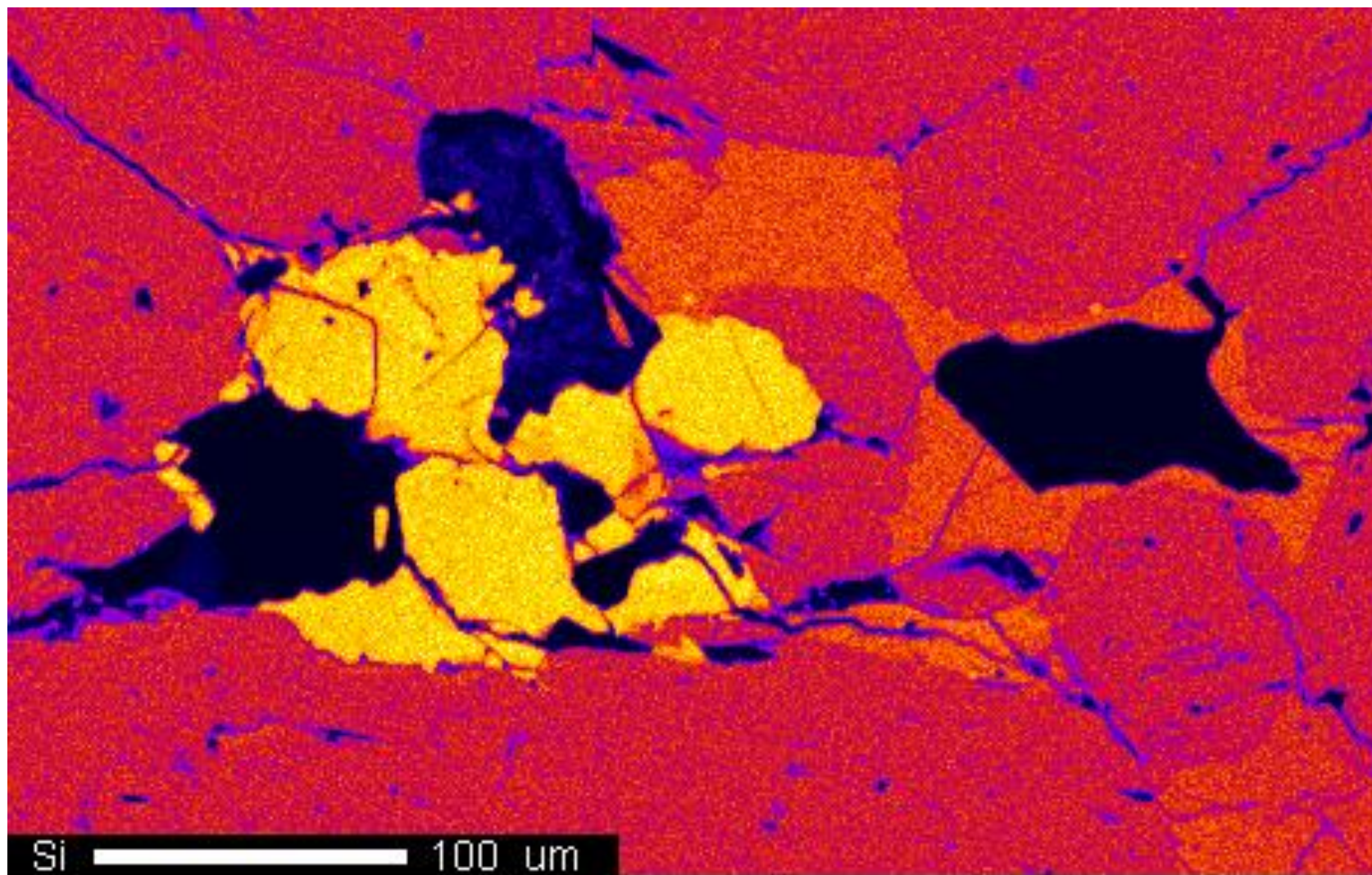
Accel Voltage: 15.0 kV

Beam Current: 9.973e-008 A

Dwell Time: 10.0

Image Size: 460 x 291

SEI 100 um



Si

Cts

- 281



Project: September\_17\_2015

Comment: Zak\_map02\_1um

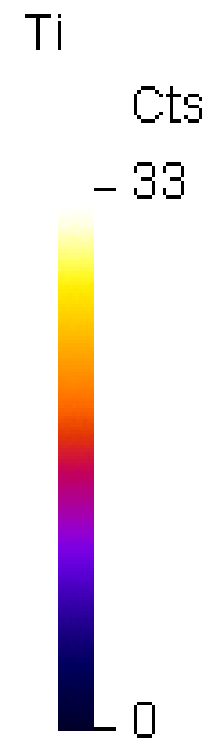
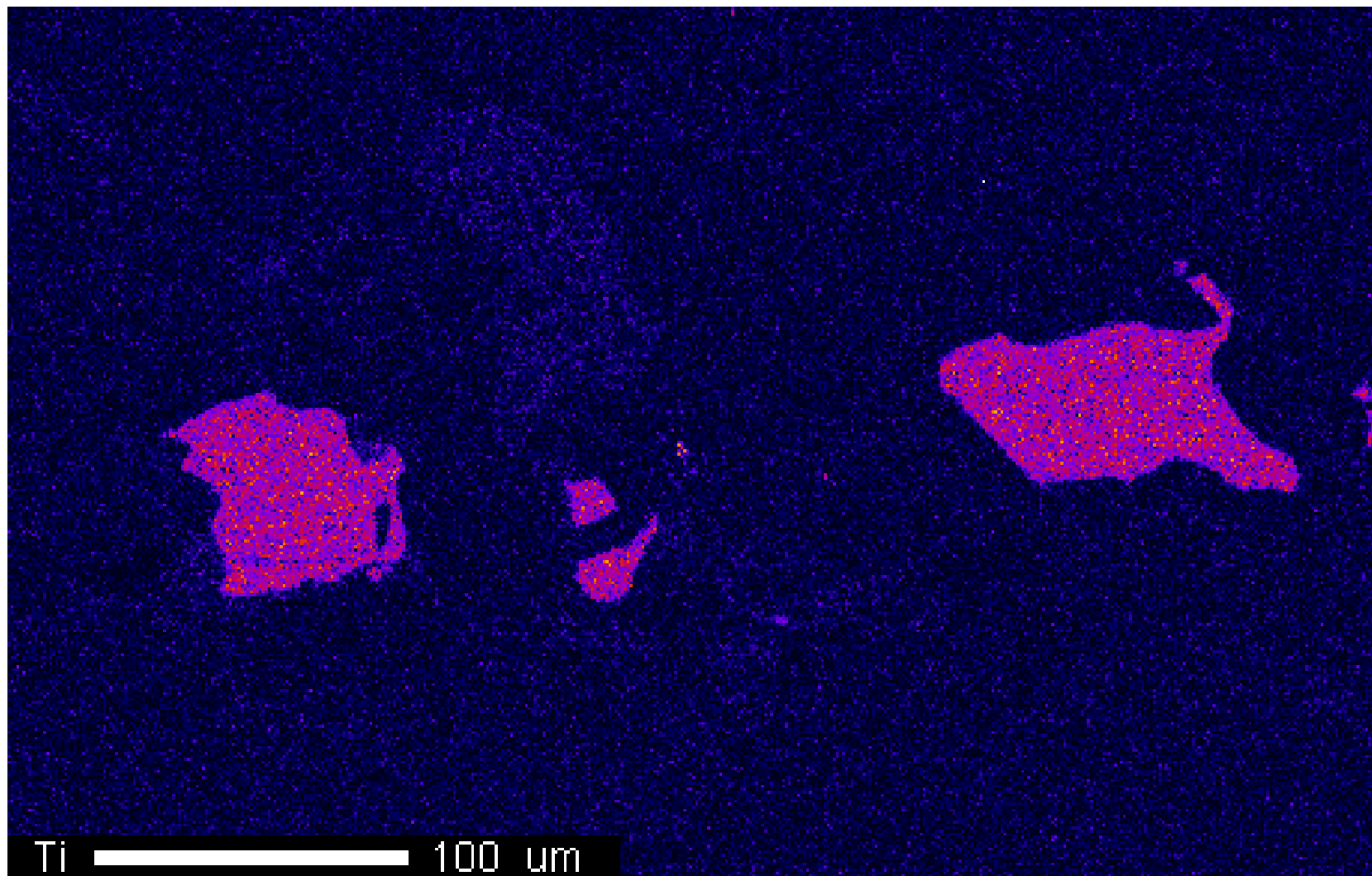
Date: 2015/09/17

Accel Voltage: 15.0 kV

Beam Current: 9.973e-008 A

Dwell Time: 10.0

Image Size: 460 x 291

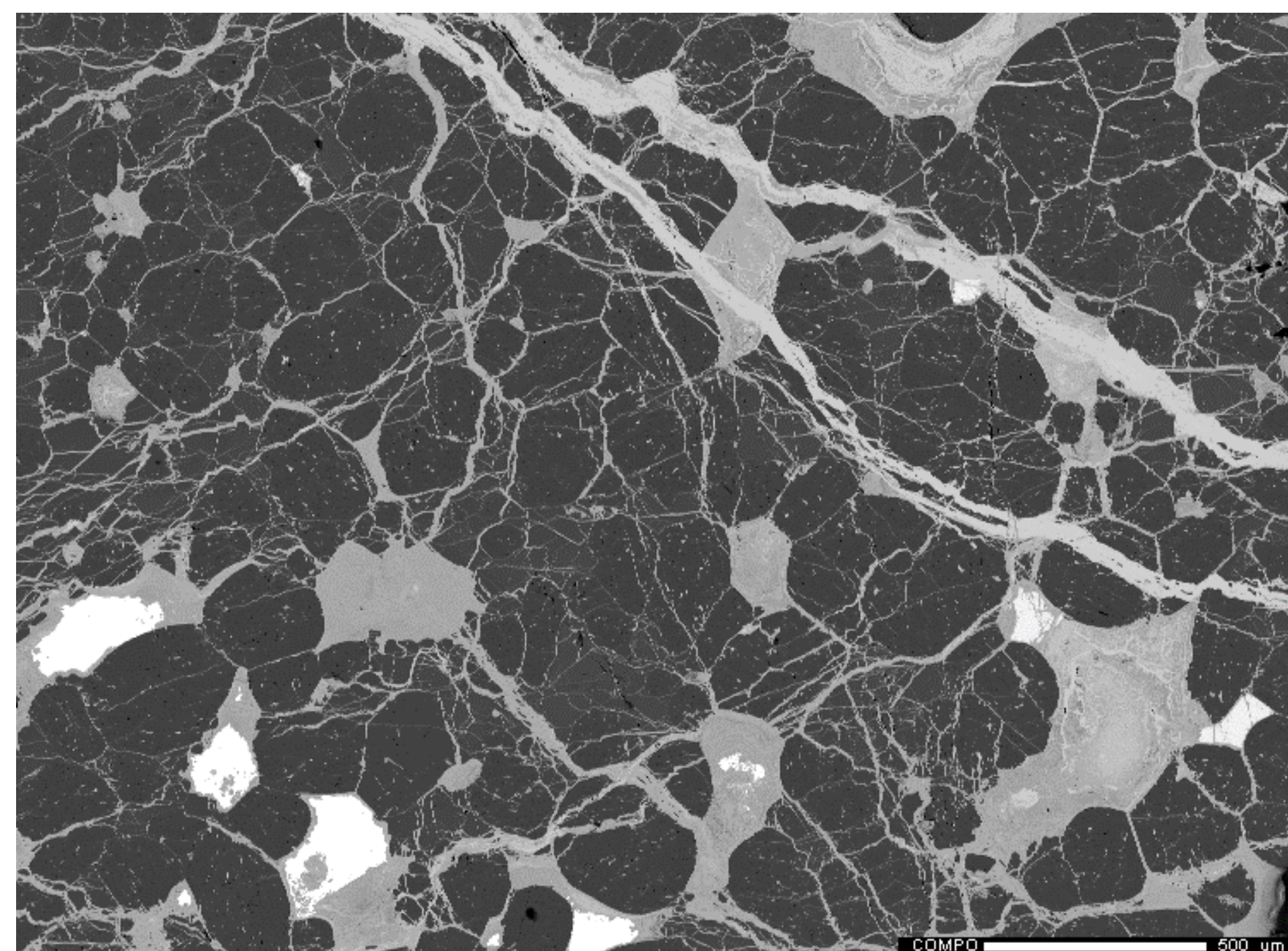


Project: September\_17\_2015  
Comment: Zak\_map02\_1um  
Date: 2015/09/17  
Accel Voltage: 15.0 kV  
Beam Current: 9.973e-008 A  
Dwell Time: 10.0  
Image Size: 460 x 291



# Appendix 4.2

X-Ray Elemental maps of NWA 4301



COMPO

Cts

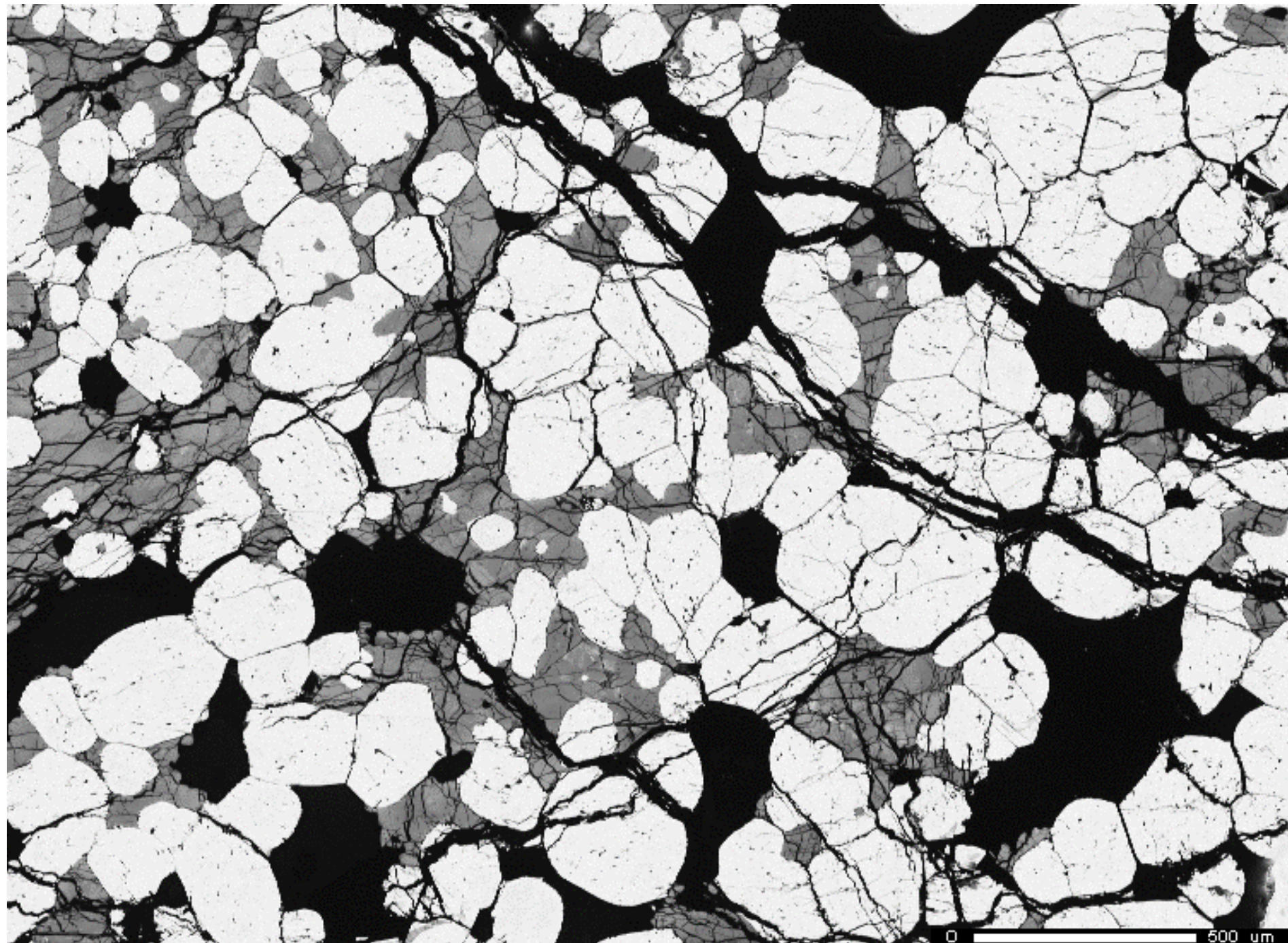
- 4,095



Project: June\_25\_2015  
Comment: NWA4301\_map01\_4um  
Date: 2015/06/28  
Accel Voltage: 15.0 kV  
Beam Current: 9.974e-008 A  
Dwell Time: 10.0  
Image Size: 750 x 550

COMPO 500 um

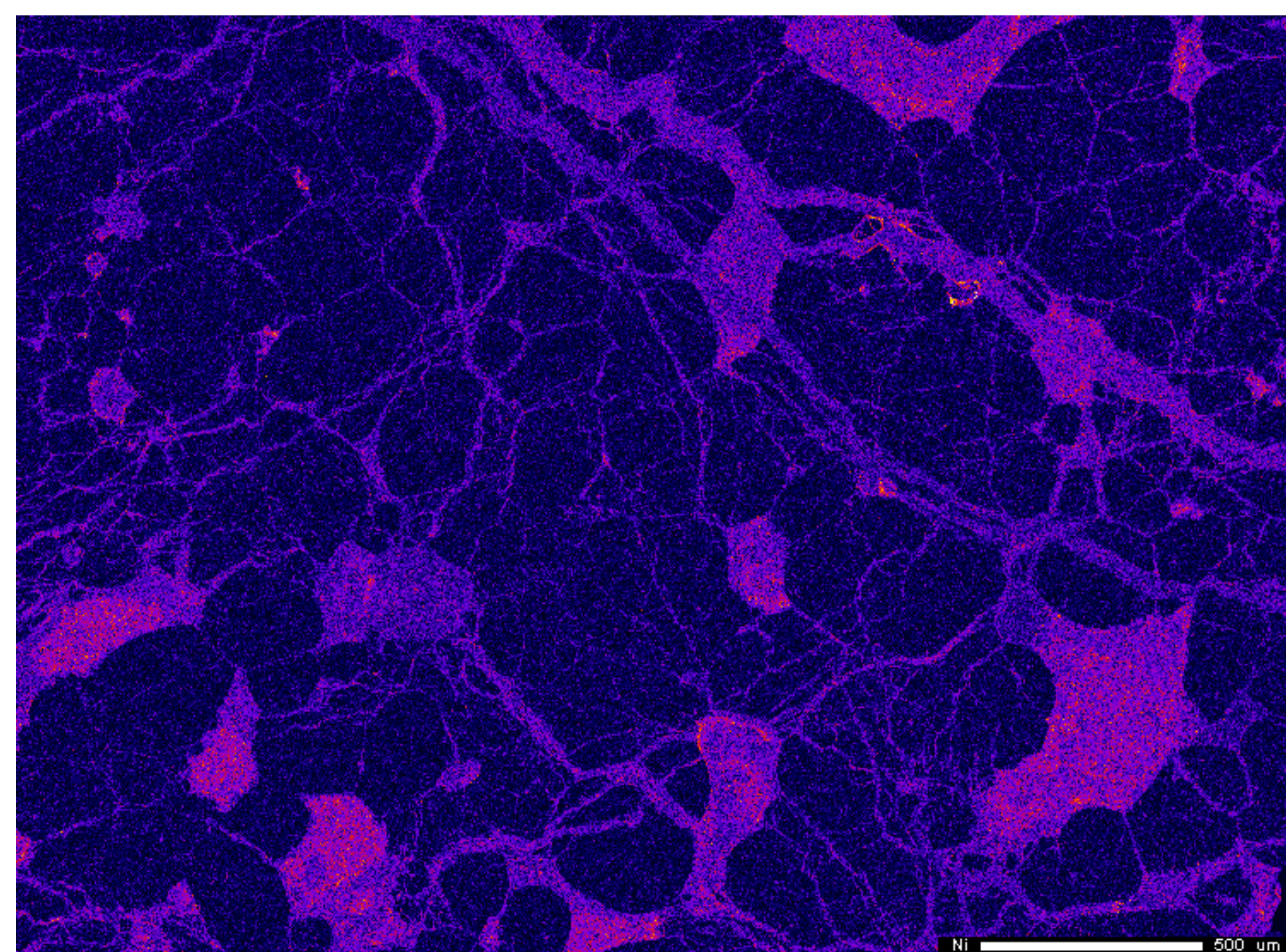




Project: June\_25\_2015  
Comment: NWA4301\_map01\_4um  
Date: 2015/06/28  
Accel Voltage: 15.0 kV  
Beam Current: 9.974e-008 A  
Dwell Time: 10.0  
Image Size: 750 x 550

0 500  $\mu\text{m}$

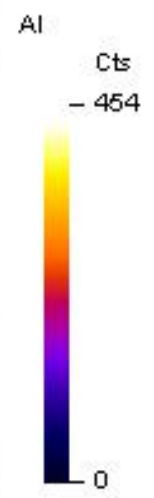
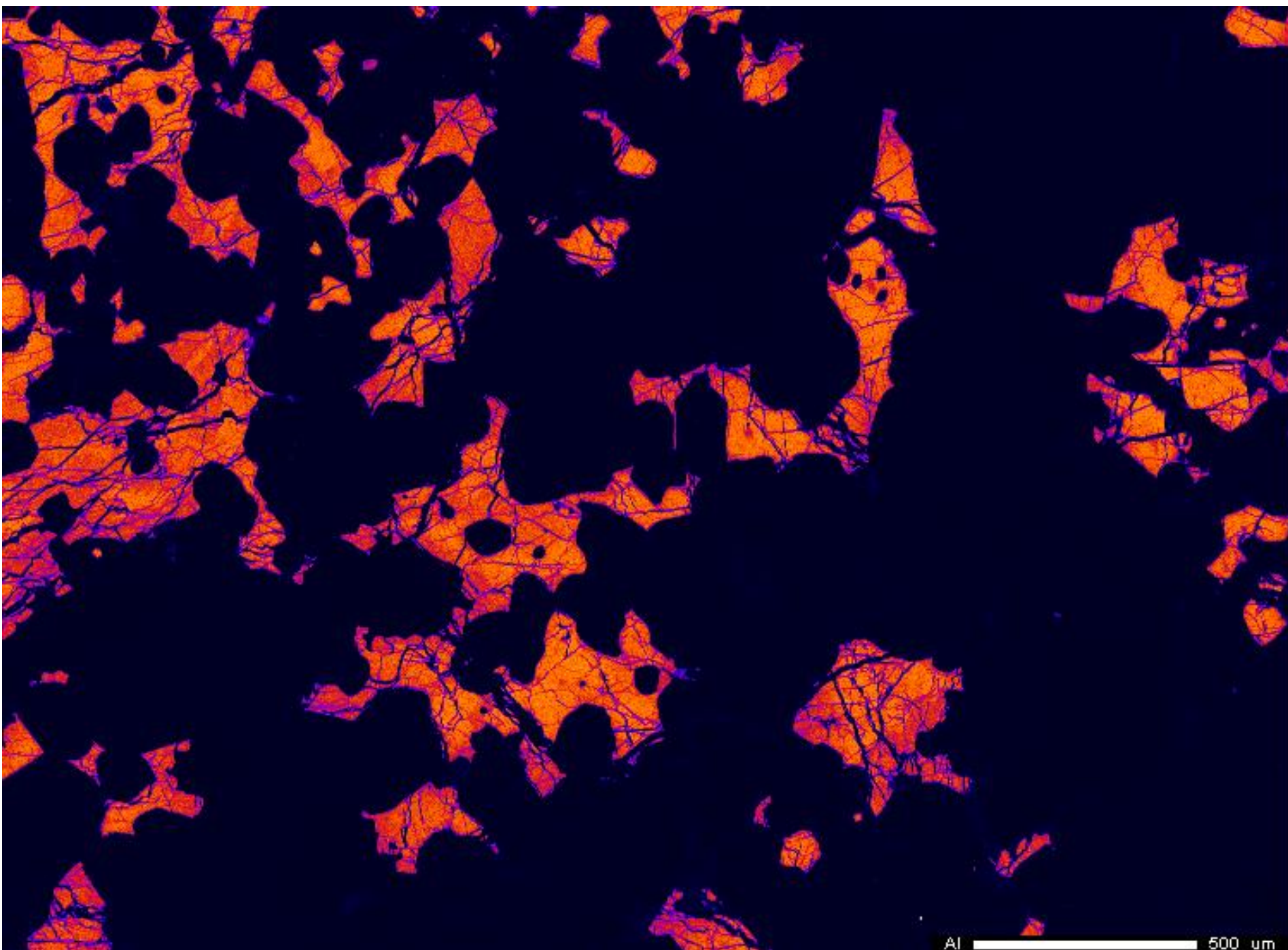




Project: June\_25\_2015  
Comment: NWA4301\_map01\_4um  
Date: 2015/06/28  
Accel Voltage: 15.0 kV  
Beam Current: 9.956e-008 A  
Dwell Time: 10.0  
Image Size: 750 x 550

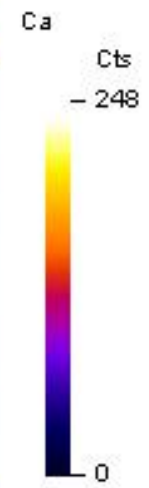
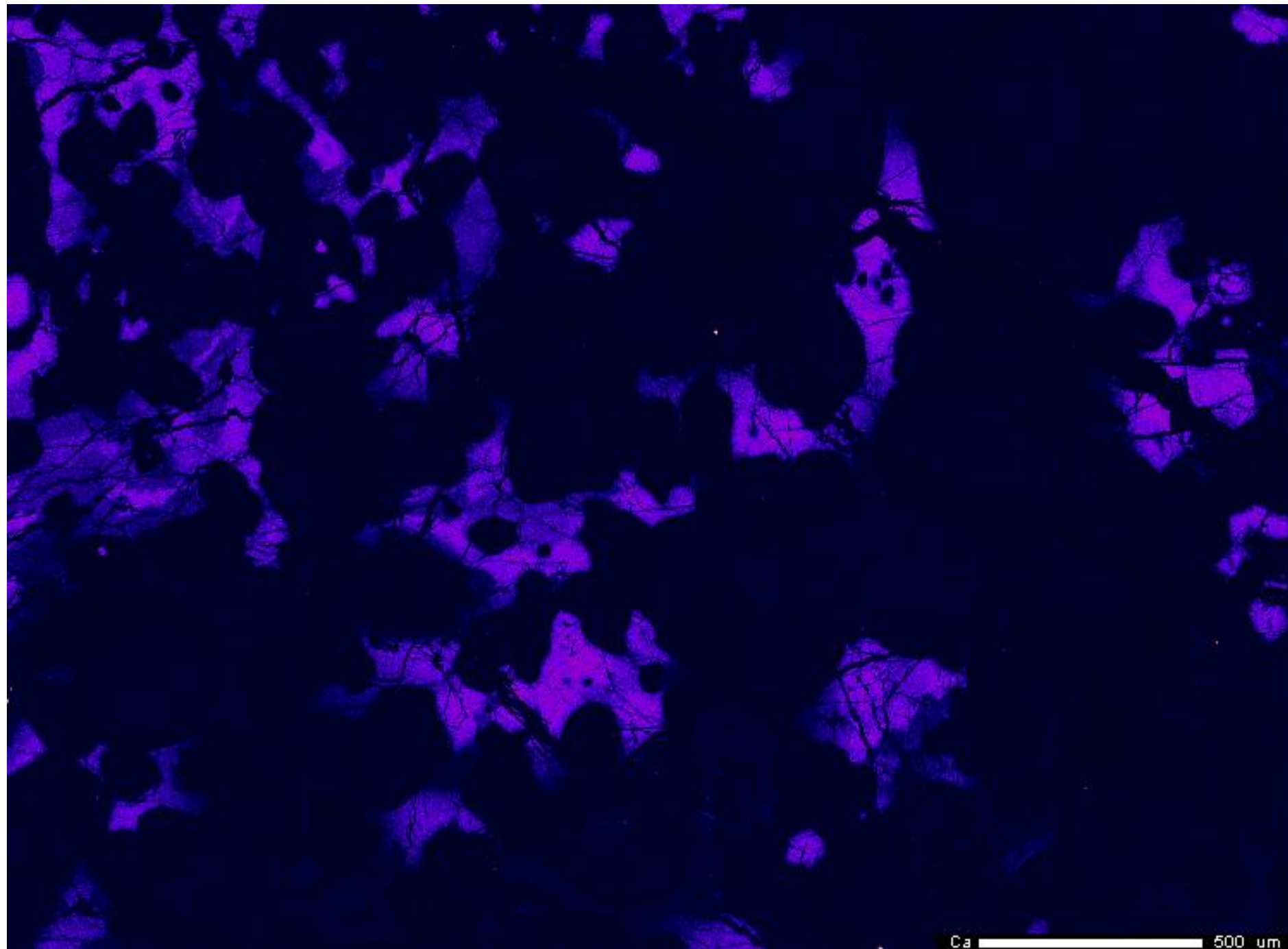
Ni 500 um





Project: June\_25\_2015  
Comment: NWA4301\_map01\_4um  
Date: 2015/06/28  
Accel Voltage: 15.0 kV  
Beam Current: 9.974e-008 A  
Dwell Time: 10.0  
Image Size: 750 x 550

Al 500 um



Project: June\_25\_2015  
Comment: NWA4301\_map01\_4um  
Date: 2015/06/28  
Accel Voltage: 15.0 kV  
Beam Current: 9.974e-008 A  
Dwell Time: 10.0  
Image Size: 750 x 550

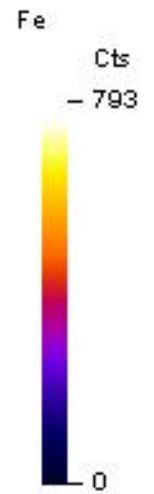
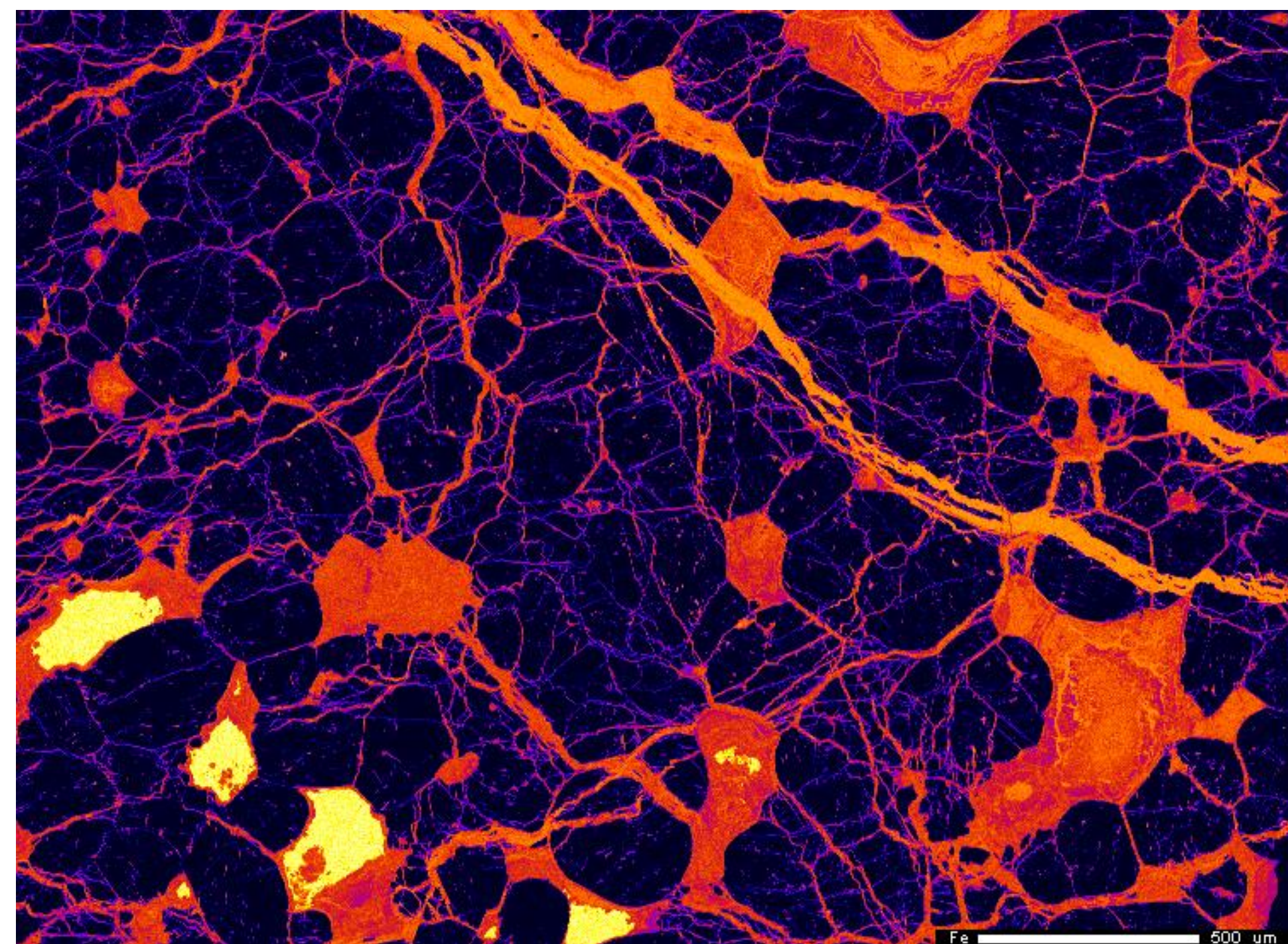
Ca 500 um



Project: June\_25\_2015  
Comment: NWA4301\_map01\_4um  
Date: 2015/06/28  
Accel Voltage: 15.0 kV  
Beam Current: 9.974e-008 A  
Dwell Time: 10.0  
Image Size: 750 x 550

Cr 500 um





Project: June\_25\_2015  
Comment: NWA4301\_map01\_4um  
Date: 2015/06/28  
Accel Voltage: 15.0 kV  
Beam Current: 9.974e-008 A  
Dwell Time: 10.0  
Image Size: 750 x 550

Fe 500 um



K

Cts

- 456



Project: June\_25\_2015

Comment: NW/A4301\_map01\_4um

Date: 2015/06/28

Accel Voltage: 15.0 kV

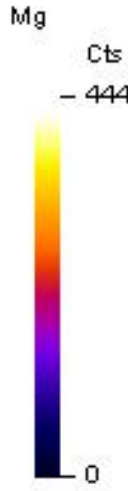
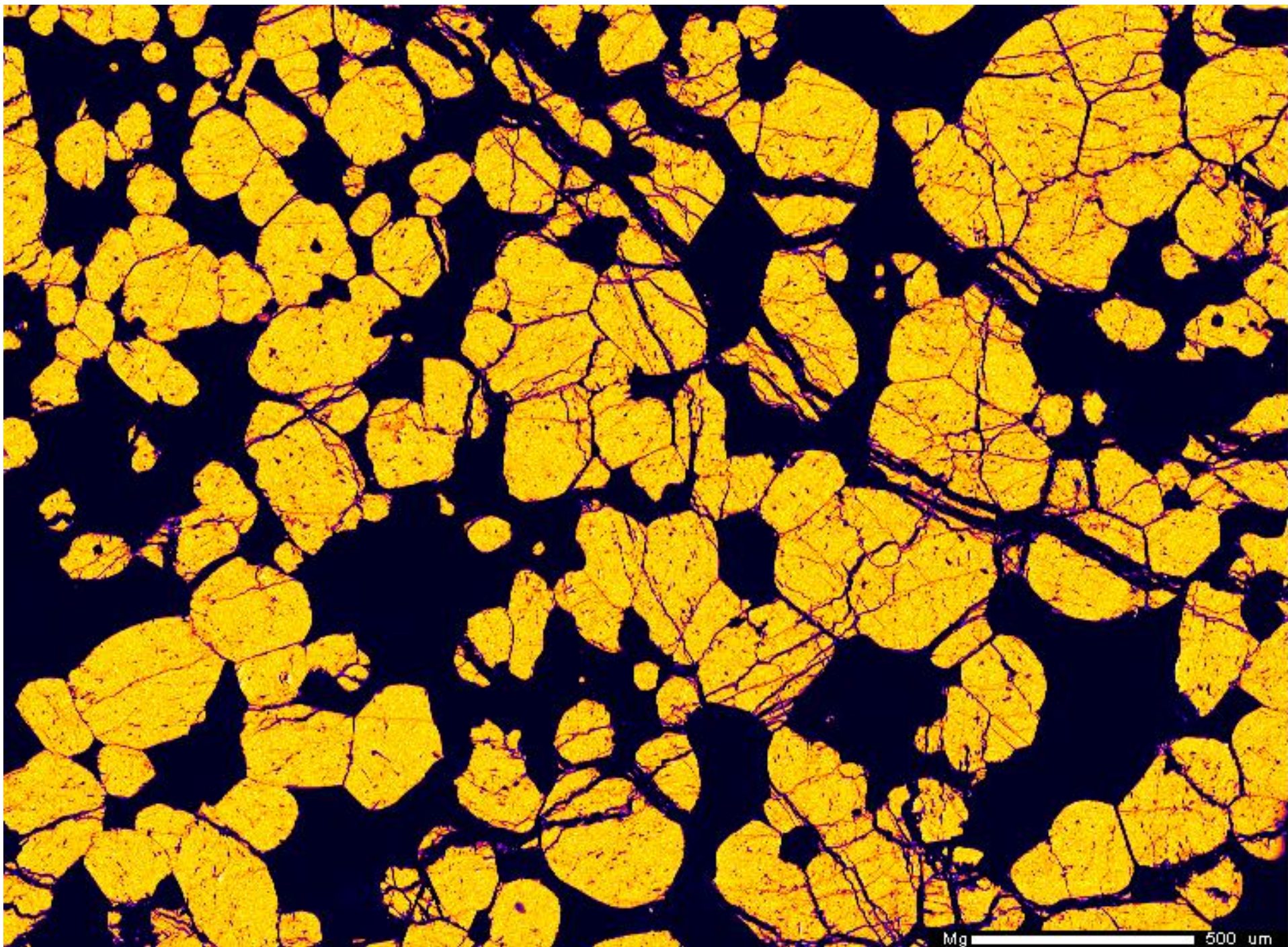
Beam Current: 9.974e-008 A

Dwell Time: 10.0

Image Size: 750 x 550

K  500 um





Project: June\_25\_2015  
Comment: NWA4301\_map01\_4um  
Date: 2015/06/28  
Accel Voltage: 15.0 kV  
Beam Current: 9.974e-008 A  
Dwell Time: 10.0  
Image Size: 750 x 550



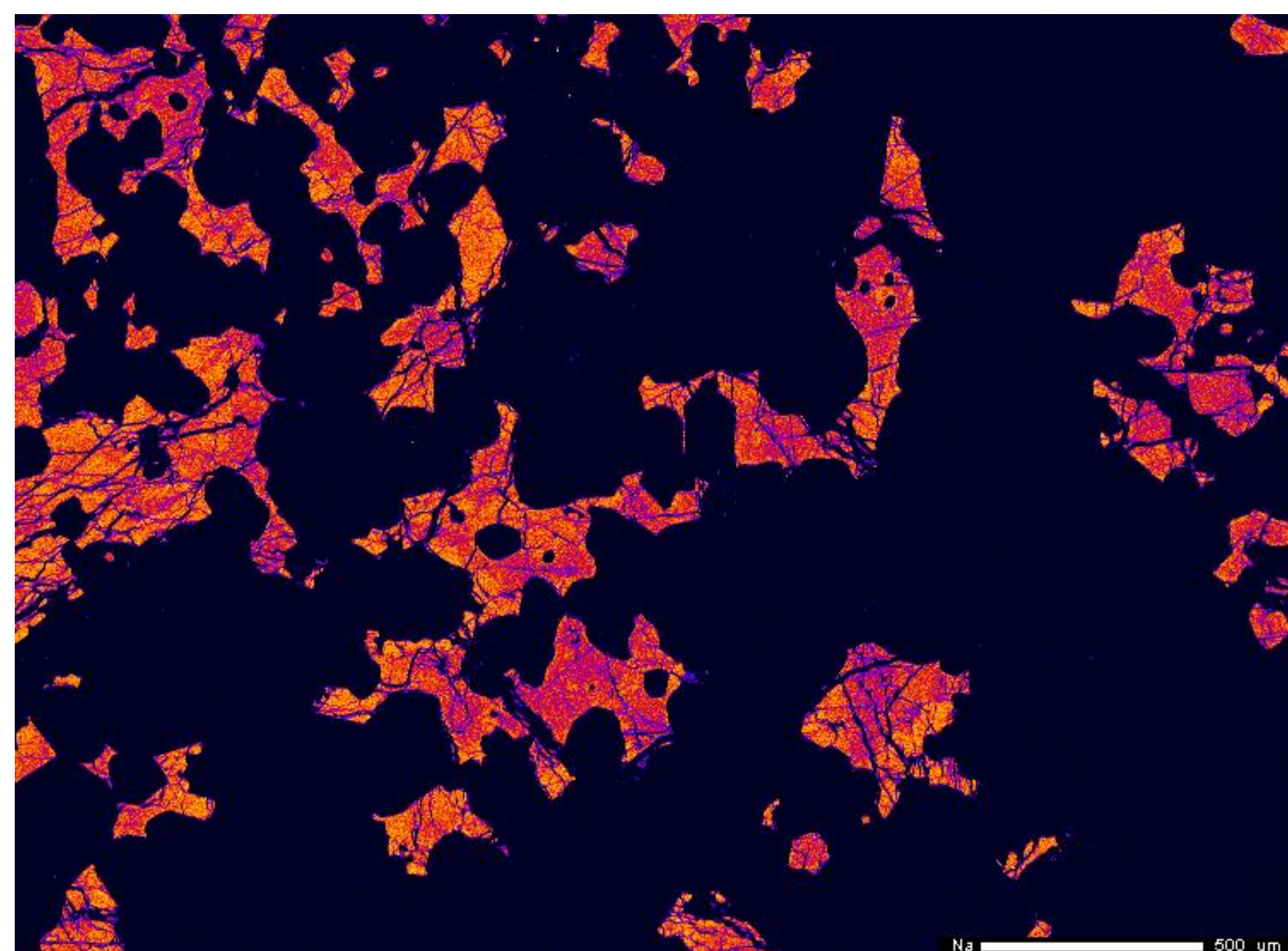


Project: June\_25\_2015  
Comment: NWA4301\_map01\_4um  
Date: 2015/06/28  
Accel Voltage: 15.0 kV  
Beam Current: 9.974e-008 A  
Dwell Time: 10.0  
Image Size: 750 x 550

Mn 500 um

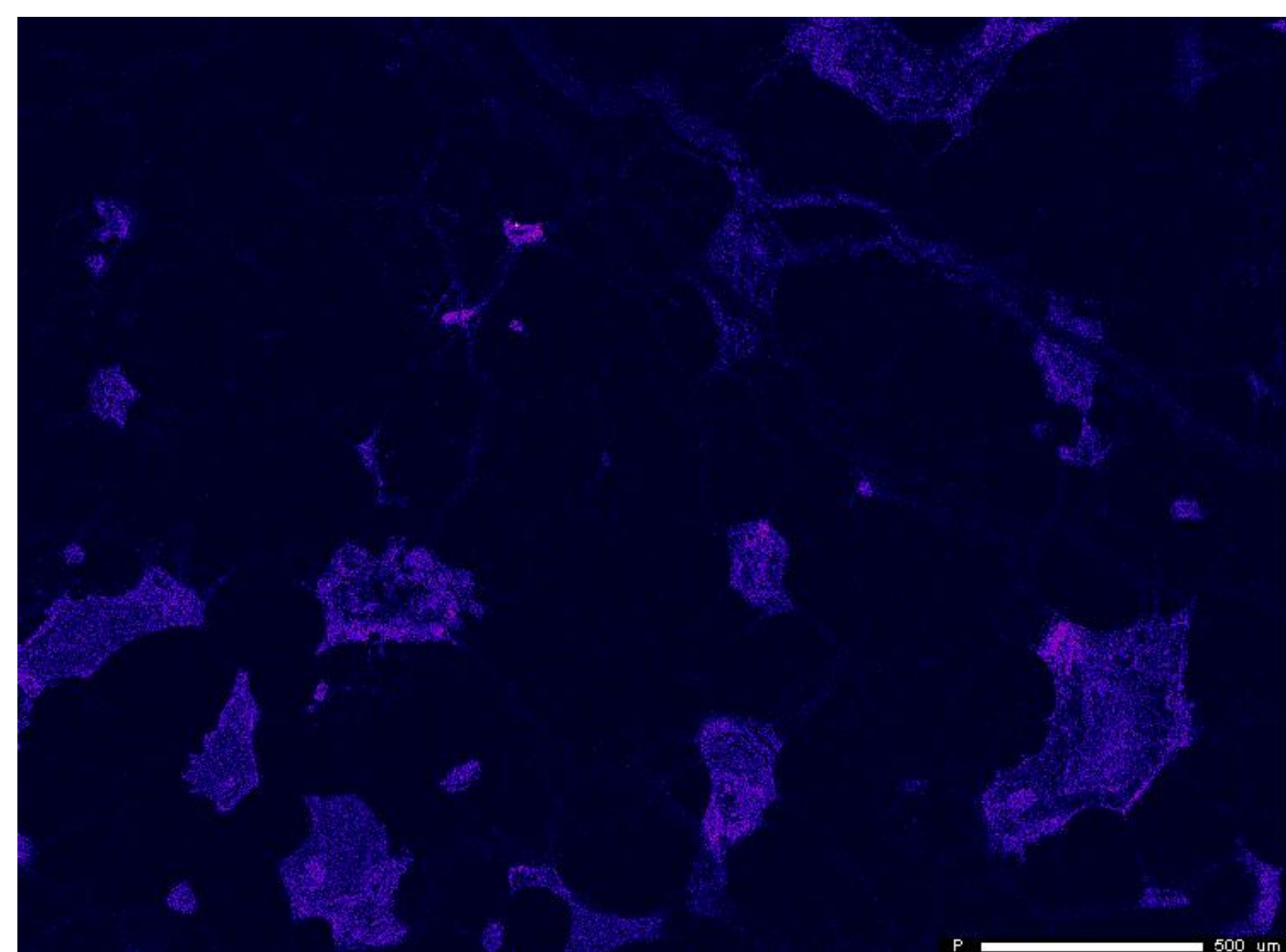
A horizontal scale bar at the bottom right of the image, labeled "500 um". The bar is white with a black outline. The text "Mn" is positioned to the left of the bar, and "500 um" is to the right.





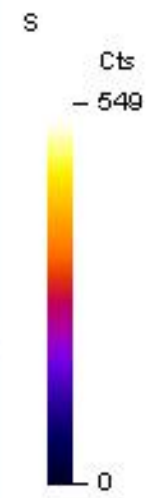
Project: June\_25\_2015  
Comment: NWA4301\_map01\_4um  
Date: 2015/06/28  
Accel Voltage: 15.0 kV  
Beam Current: 9.974e-008 A  
Dwell Time: 10.0  
Image Size: 750 x 550

Na 500 um

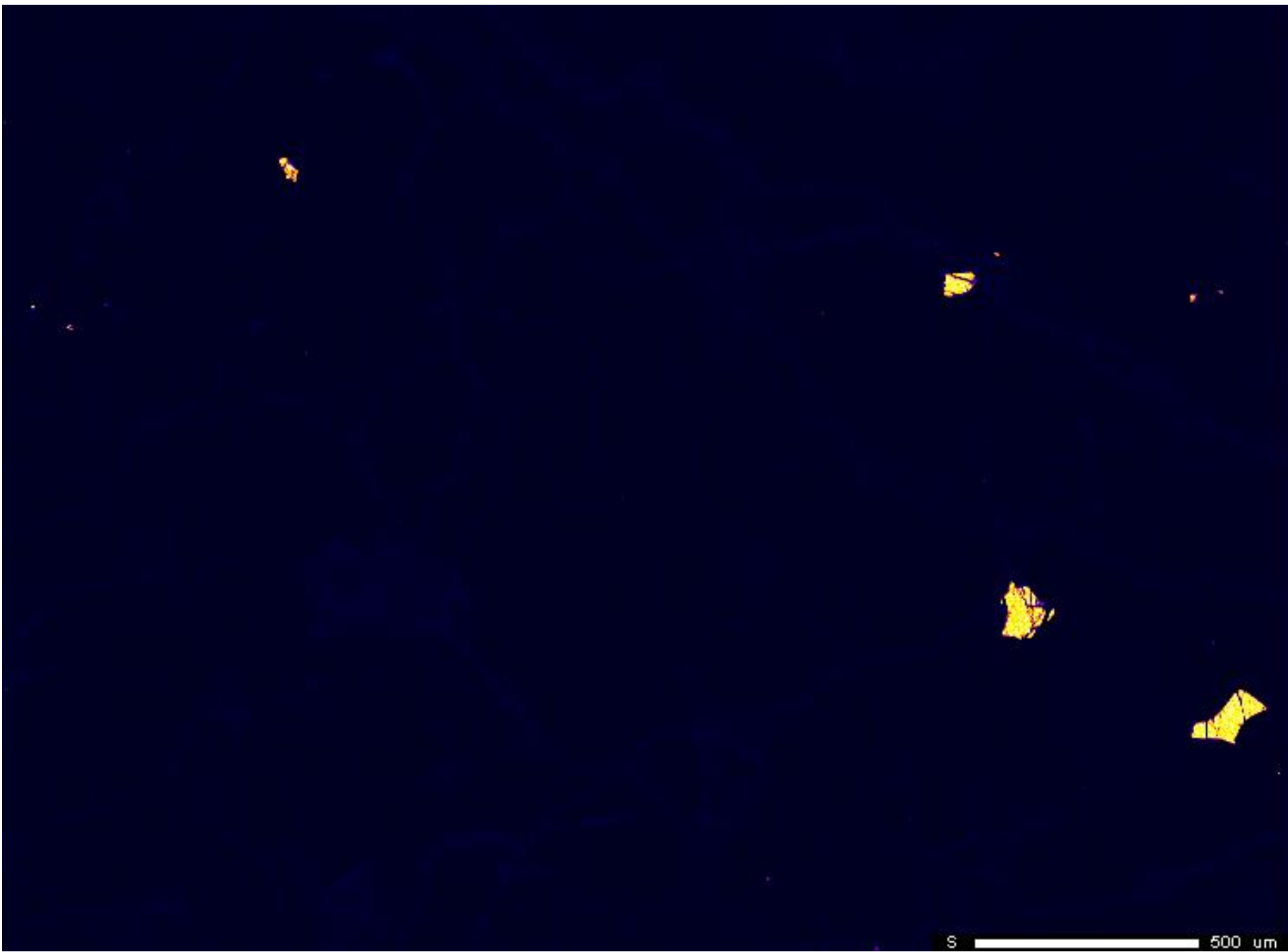


Project: June\_25\_2015  
Comment: NWA4301\_map01\_4um  
Date: 2015/06/28  
Accel Voltage: 15.0 kV  
Beam Current: 9.974e-008 A  
Dwell Time: 10.0  
Image Size: 750 x 550

P  500 um

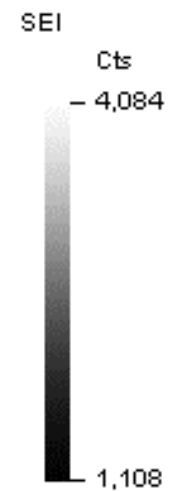
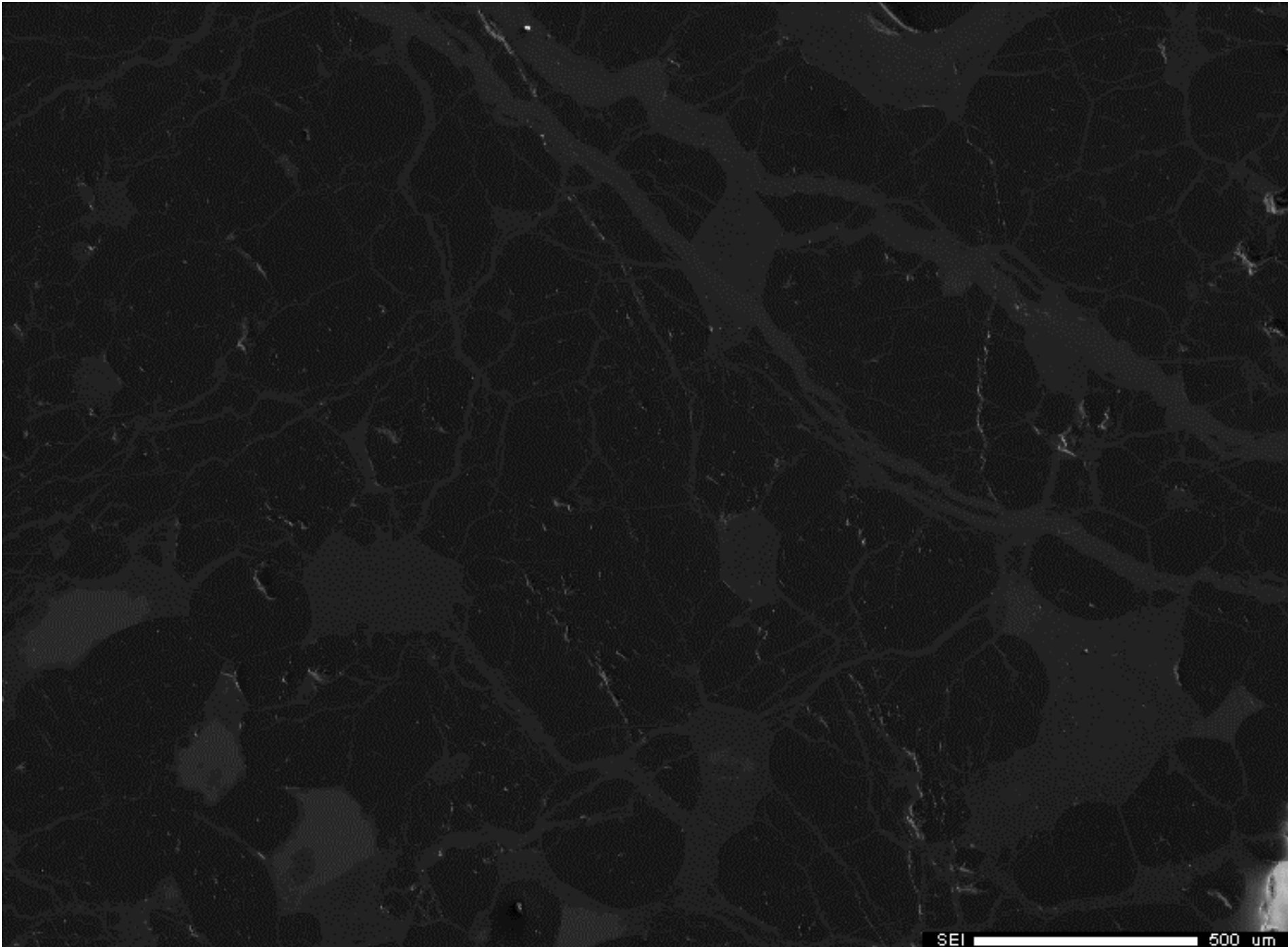


Project: June\_25\_2015  
Comment: NWA4301\_map01\_4um  
Date: 2015/06/28  
Accel Voltage: 15.0 kV  
Beam Current: 9.974e-008 A  
Dwell Time: 10.0  
Image Size: 750 x 550



S 500 um

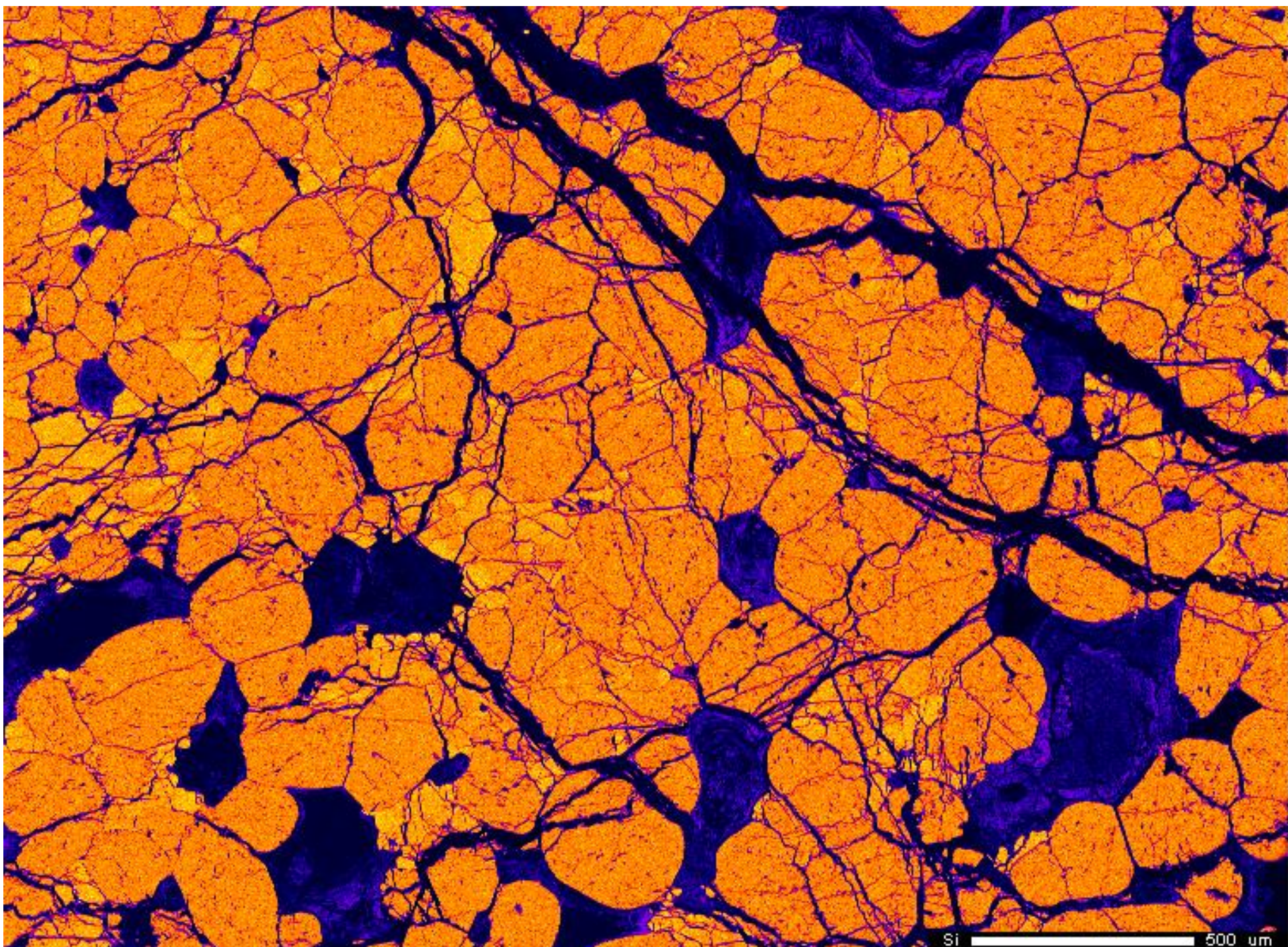




Project: June\_25\_2015  
Comment: NWA4301\_map01\_4um  
Date: 2015/06/28  
Accel Voltage: 15.0 kV  
Beam Current: 9.974e-008 A  
Dwell Time: 10.0  
Image Size: 750 x 550

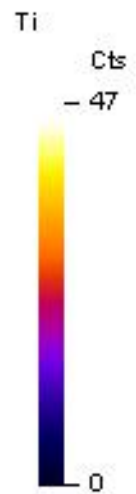
SEI 500 um





Project: June\_25\_2015  
Comment: NWA4301\_map01\_4um  
Date: 2015/06/28  
Accel Voltage: 15.0 kV  
Beam Current: 9.974e-008 A  
Dwell Time: 10.0  
Image Size: 750 x 550

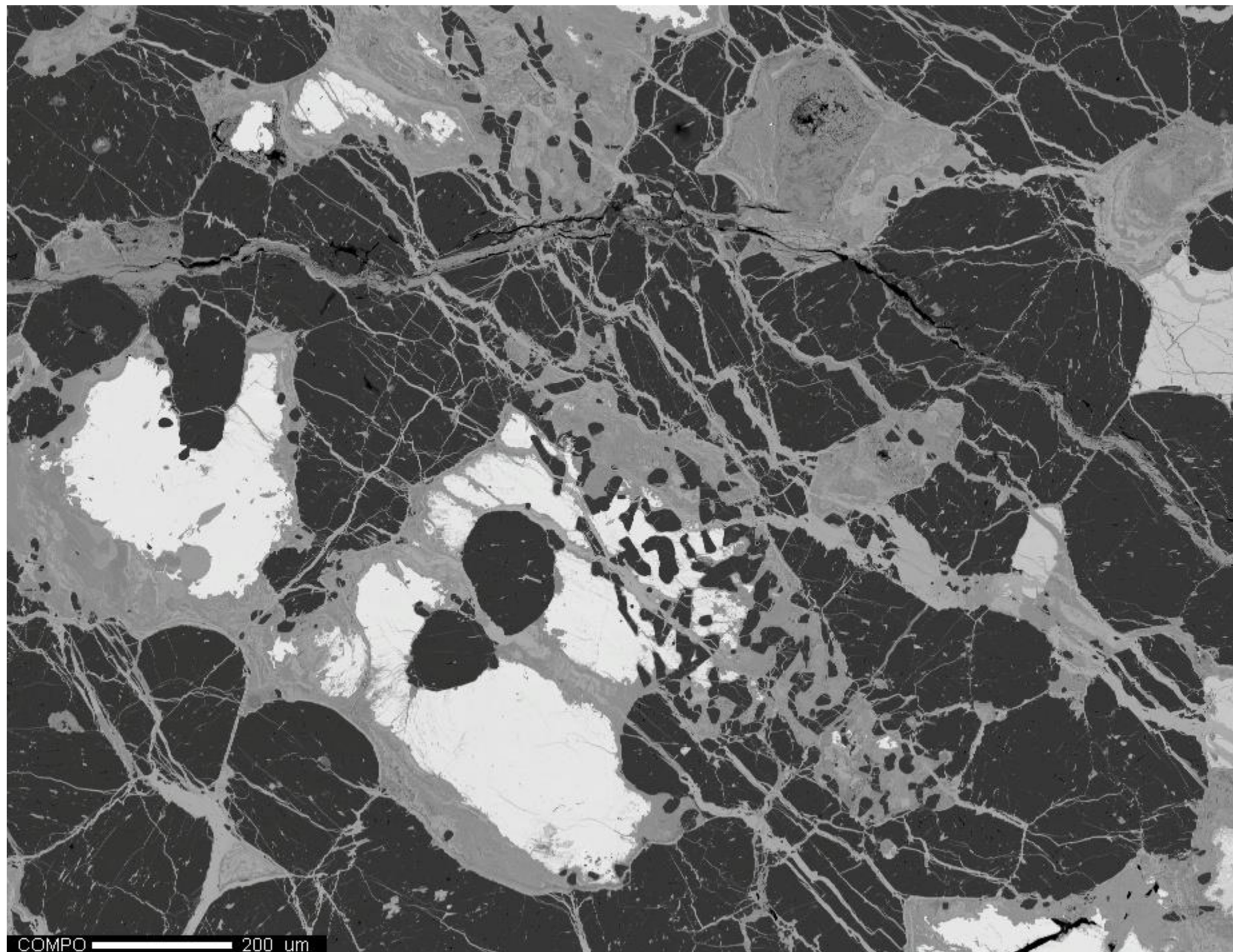




Project: June\_25\_2015  
Comment: NW/A4301\_map01\_4um  
Date: 2015/06/28  
Accel Voltage: 15.0 kV  
Beam Current: 9.974e-008 A  
Dwell Time: 10.0  
Image Size: 750 x 550

Ti 500 um

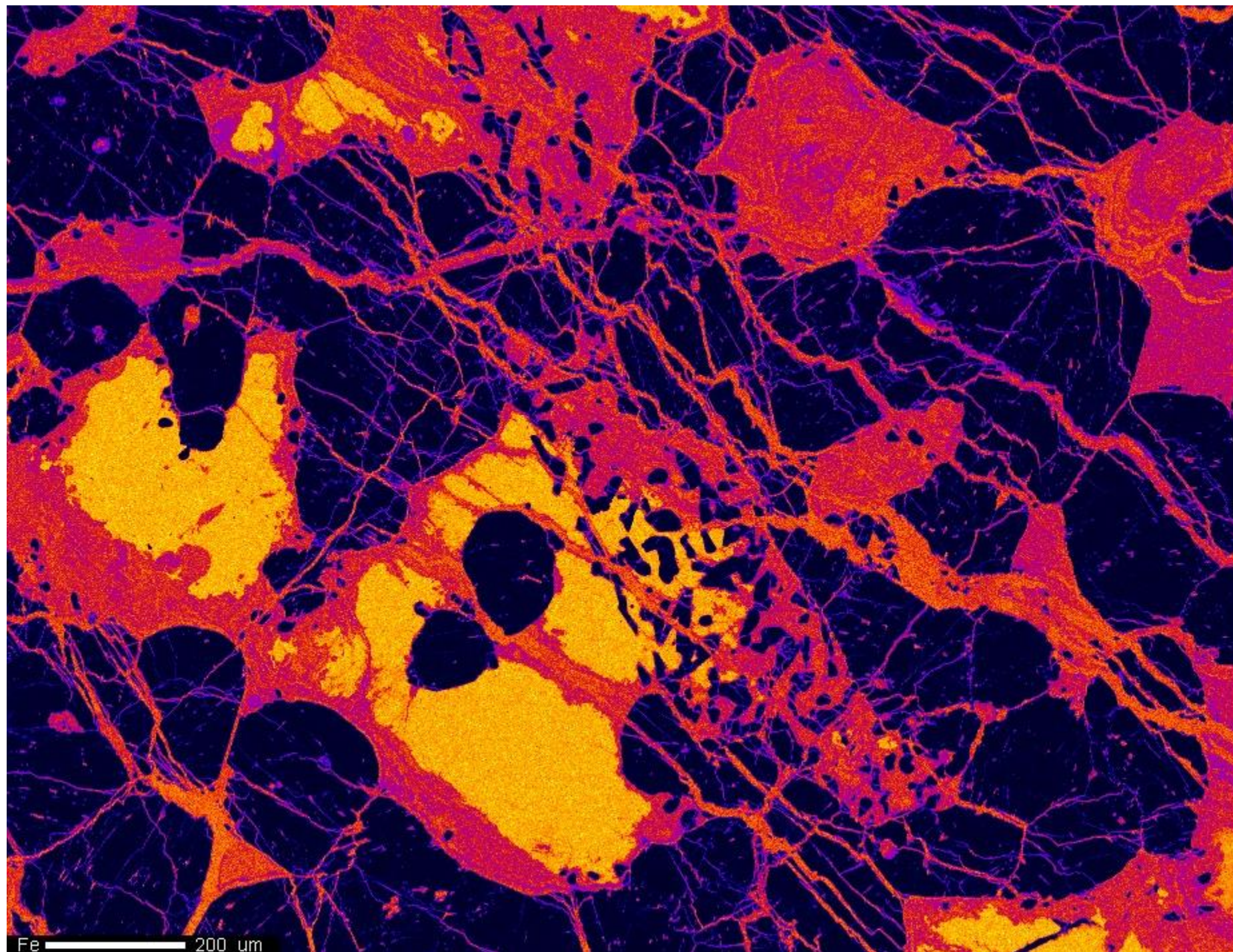




Project: March\_2\_2016  
Comment: NWA4301\_map02\_2um  
Date: 2016/03/04  
Accel Voltage: 15.0 kV  
Beam Current: 9.922e-008 A  
Dwell Time: 10.0  
Image Size: 927 x 711

COMPO 200 um





Fe

Cts

- 194

0

Project: March\_2\_2016

Comment: NWA4301\_map02\_2um

Date: 2016/03/04

Accel Voltage: 15.0 kV

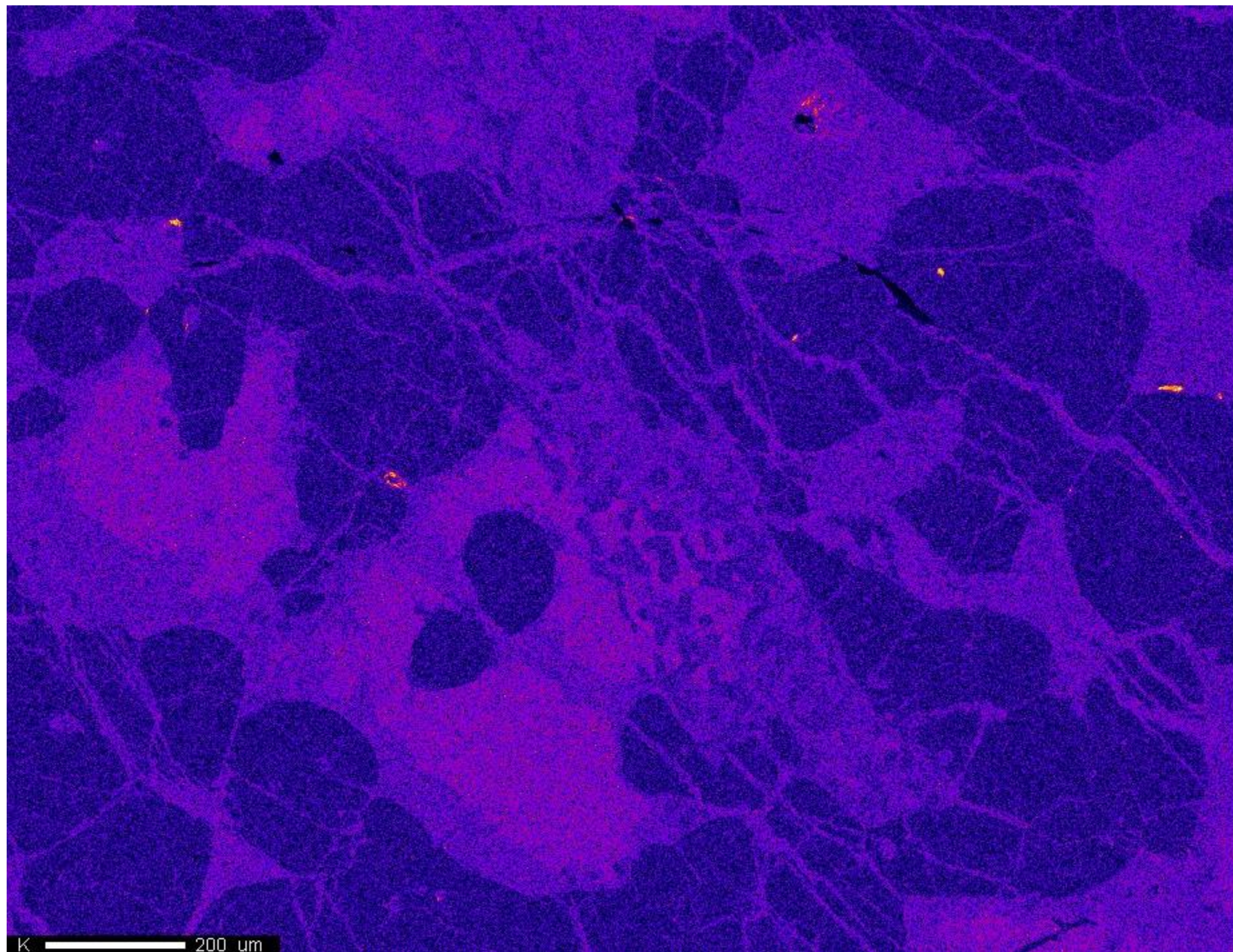
Beam Current: 5.002e-008 A

Dwell Time: 10.0

Image Size: 927 x 711

Fe 200 um





K

Cts

- 50



Project: March\_2\_2016

Comment: NWA4301\_map02\_2um

Date: 2016/03/04

Accel Voltage: 15.0 kV

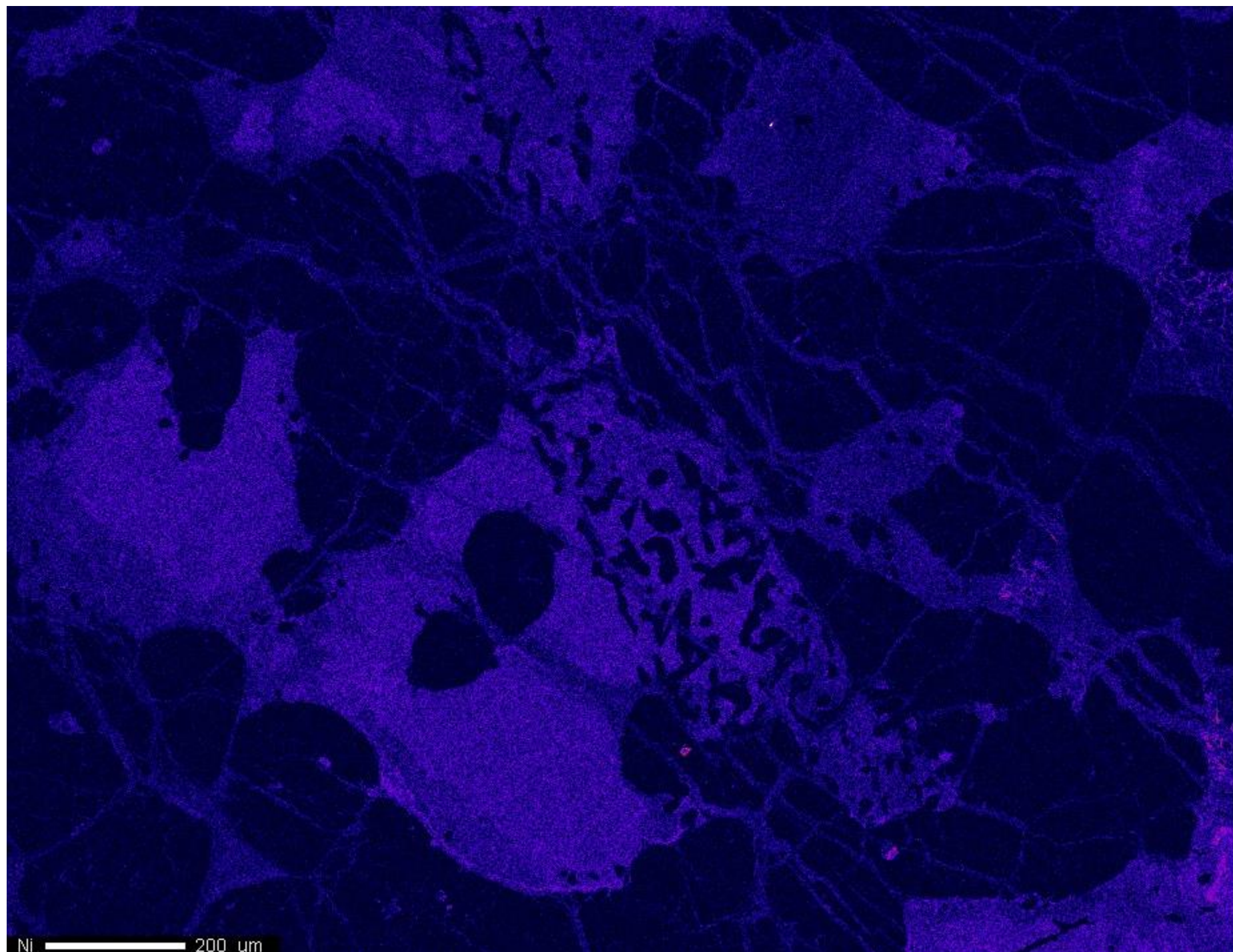
Beam Current: 5.002e-008 A

Dwell Time: 10.0

Image Size: 927 x 711

K 200 um





Ni

Cts

- 76



0

Project: March\_2\_2016

Comment: NWA4301\_map02\_2um

Date: 2016/03/04

Accel Voltage: 15.0 kV

Beam Current: 5.002e-008 A

Dwell Time: 10.0

Image Size: 927 x 711

Ni 200 um



Al

Cts

- 656



0

Project: March\_2\_2016

Comment: NWA4301\_map02\_2um

Date: 2016/03/04

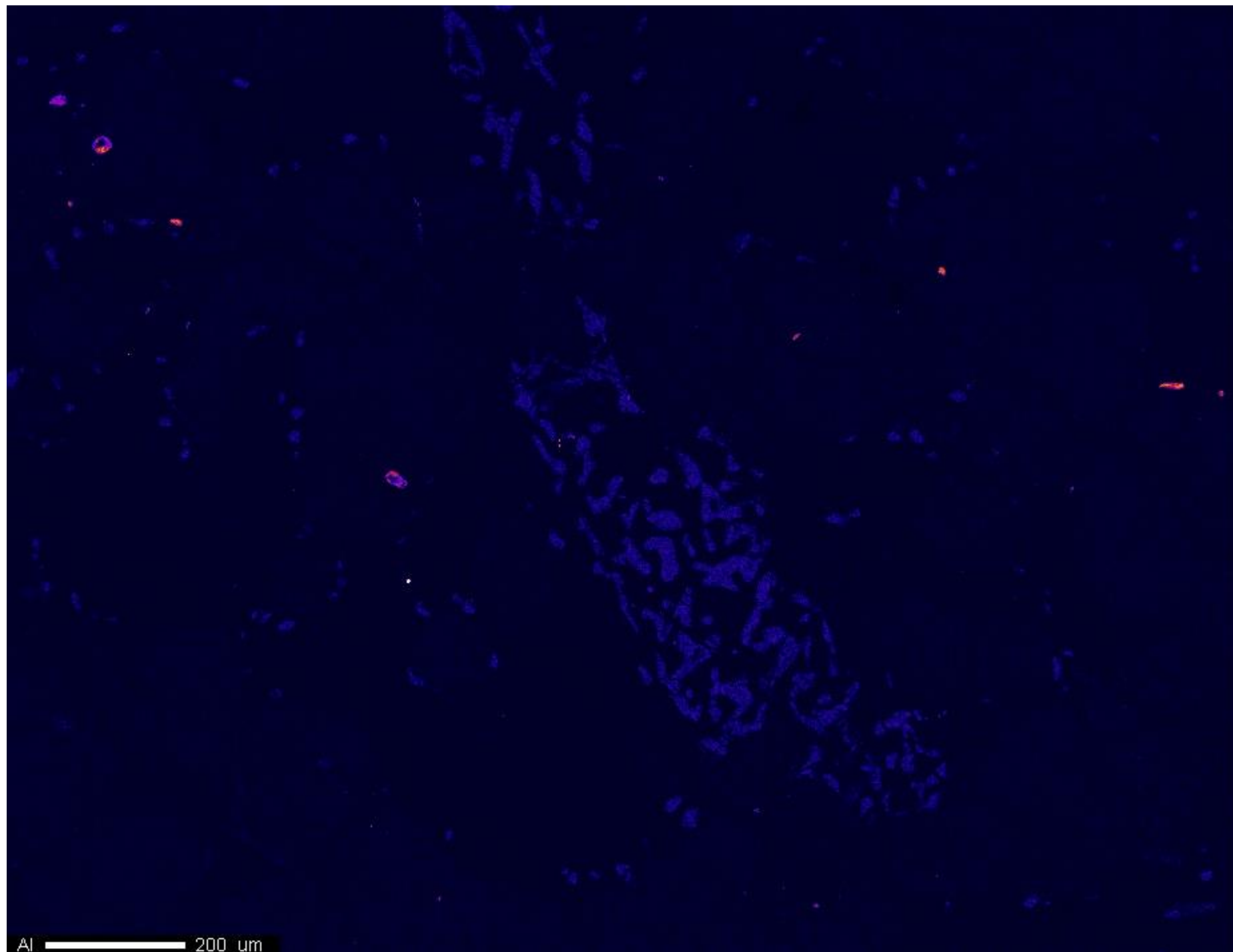
Accel Voltage: 15.0 kV

Beam Current: 9.922e-008 A

Dwell Time: 10.0

Image Size: 927 x 711

Al 200 um



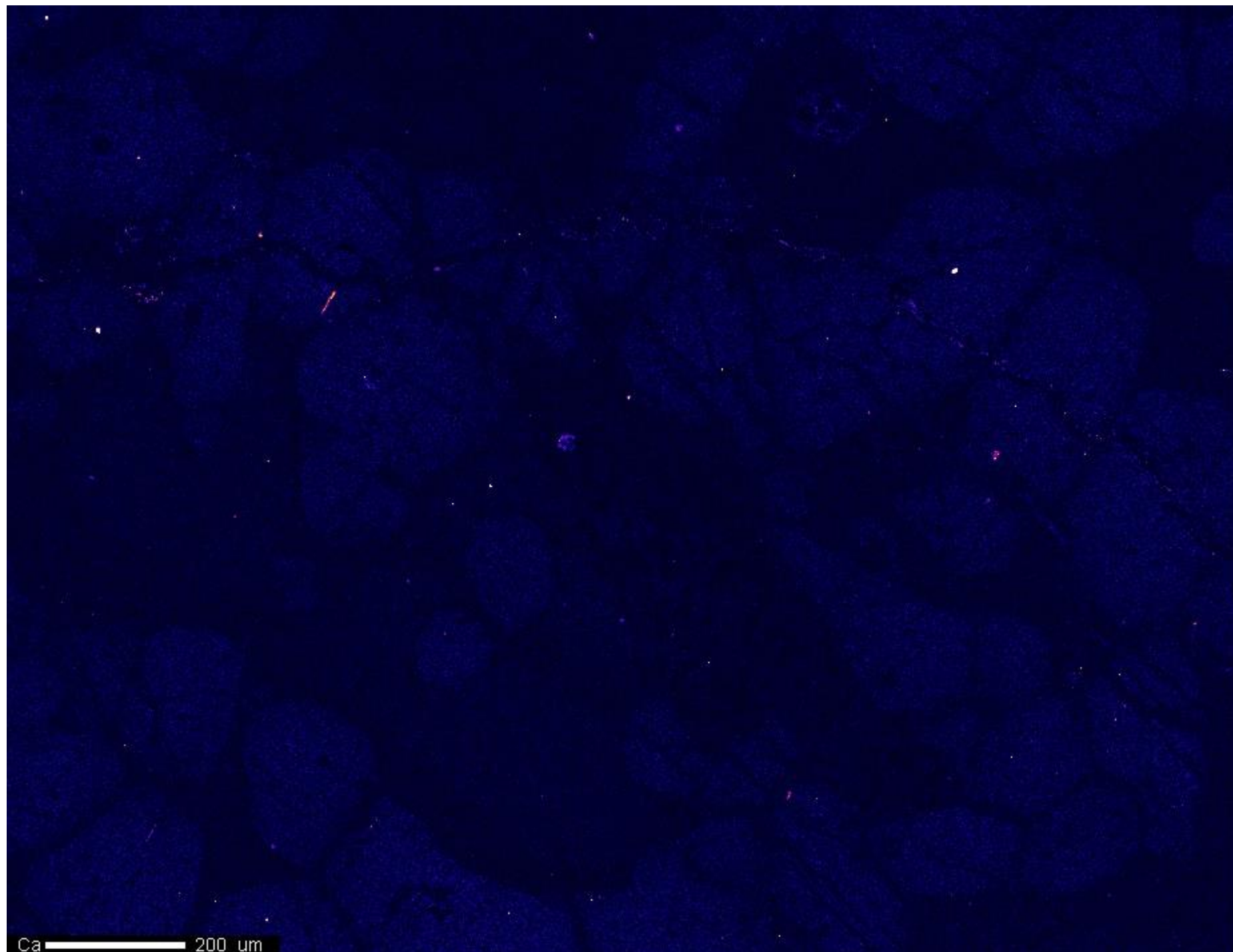
Project: March\_2\_2016  
Comment: NWA4301\_map02\_2um  
Date: 2016/03/04  
Accel Voltage: 15.0 kV  
Beam Current: 9.922e-008 A  
Dwell Time: 10.0  
Image Size: 927 x 711

Al 200 um



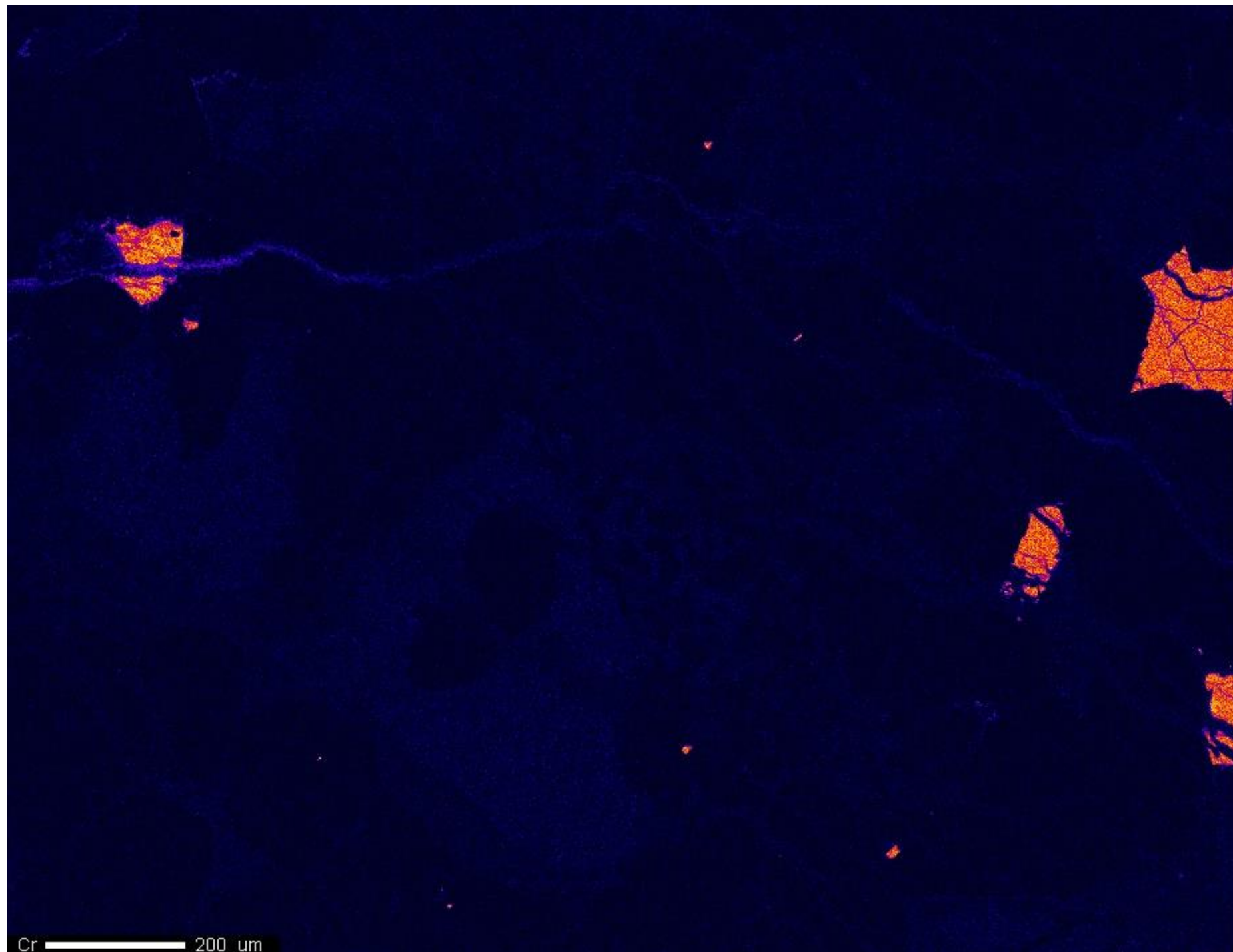


Project: March\_2\_2016  
Comment: NWA4301\_map02\_2um  
Date: 2016/03/04  
Accel Voltage: 15.0 kV  
Beam Current: 9.922e-008 A  
Dwell Time: 10.0  
Image Size: 927 x 711



Project: March\_2\_2016  
Comment: NWA4301\_map02\_2um  
Date: 2016/03/04  
Accel Voltage: 15.0 kV  
Beam Current: 9.922e-008 A  
Dwell Time: 10.0  
Image Size: 927 x 711

Ca 200 um



Cr

Cts

- 53



Project: March\_2\_2016

Comment: NWA4301\_map02\_2um

Date: 2016/03/04

Accel Voltage: 15.0 kV

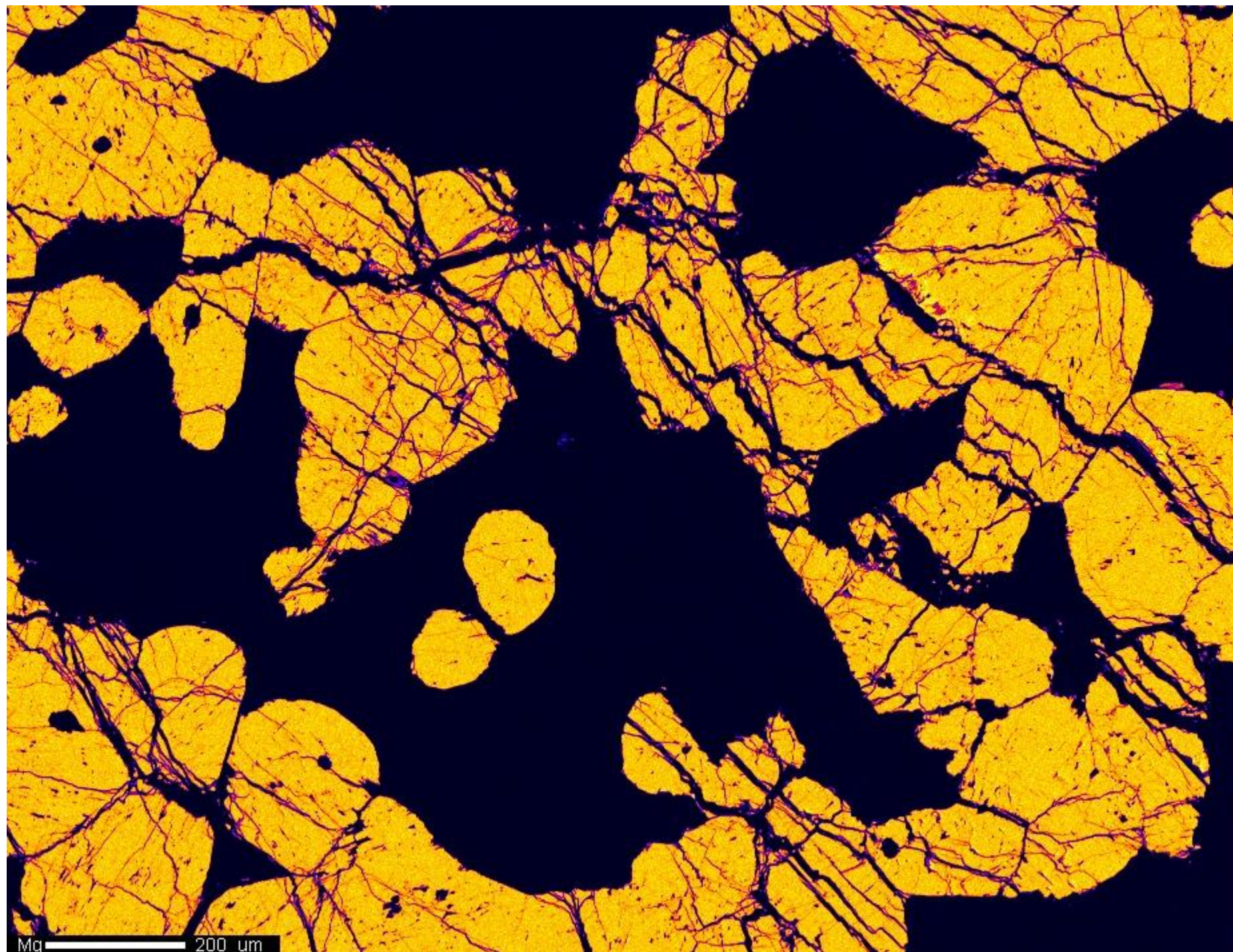
Beam Current: 9.922e-008 A

Dwell Time: 10.0

Image Size: 927 x 711

Cr 200 um





Project: March\_2\_2016  
Comment: NWA4301\_map02\_2um  
Date: 2016/03/04  
Accel Voltage: 15.0 kV  
Beam Current: 9.922e-008 A  
Dwell Time: 10.0  
Image Size: 927 x 711

Mg 200 um



Project: March\_2\_2016  
Comment: NWA4301\_map02\_2um  
Date: 2016/03/04  
Accel Voltage: 15.0 kV  
Beam Current: 9.922e-008 A  
Dwell Time: 10.0  
Image Size: 927 x 711

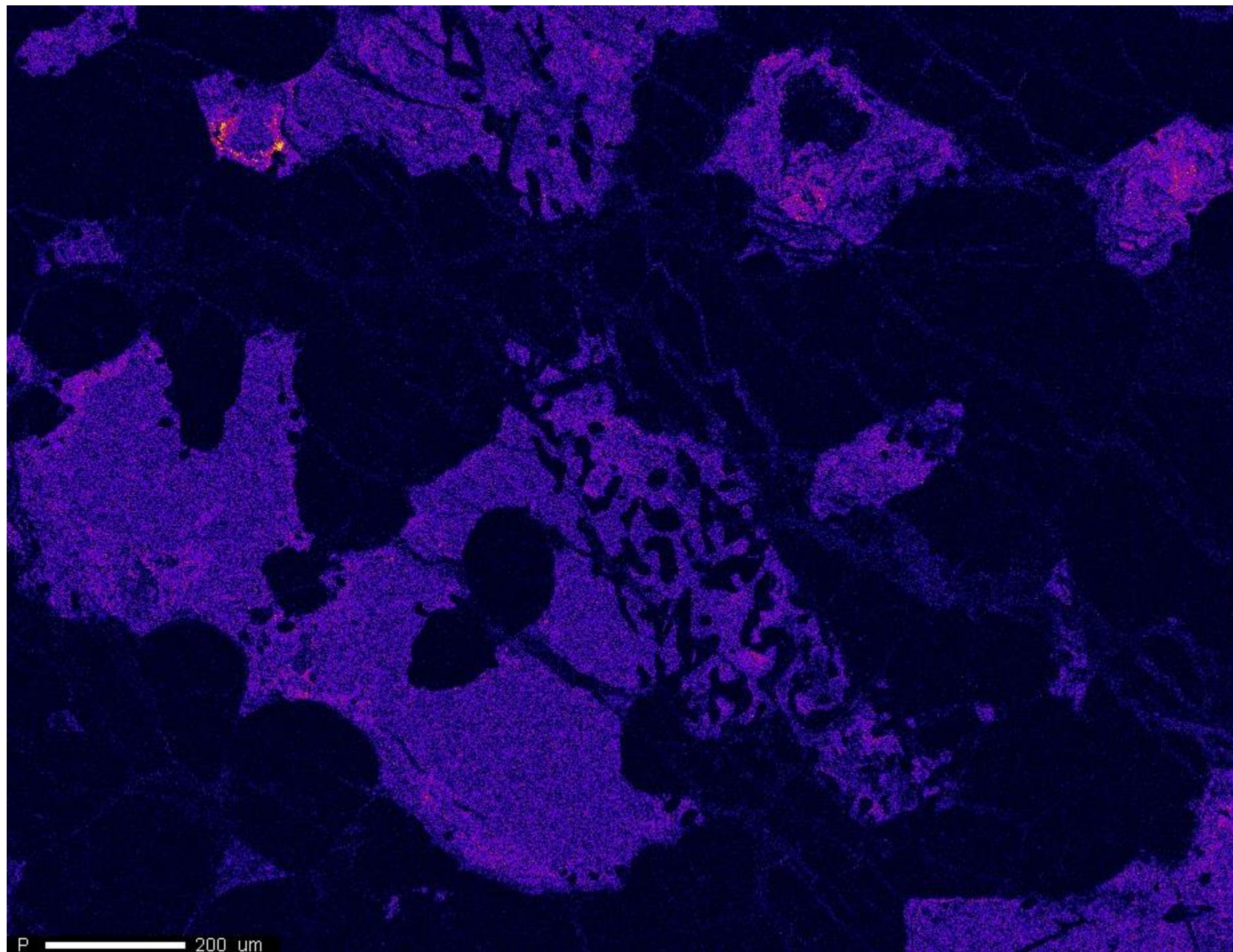
Mn 200 um



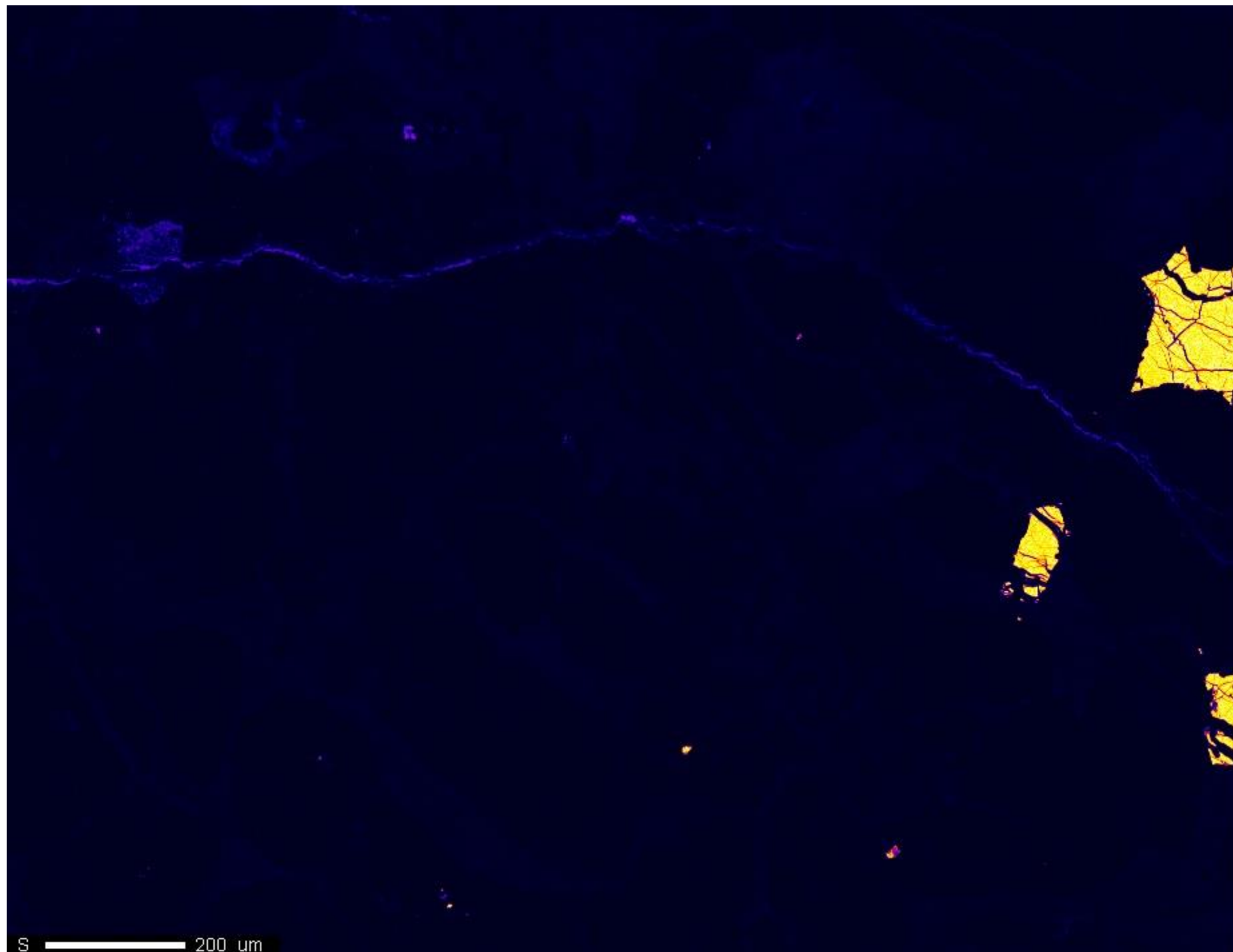
Project: March\_2\_2016  
Comment: NWA4301\_map02\_2um  
Date: 2016/03/04  
Accel Voltage: 15.0 kV  
Beam Current: 9.922e-008 A  
Dwell Time: 10.0  
Image Size: 927 x 711

Na 200 um





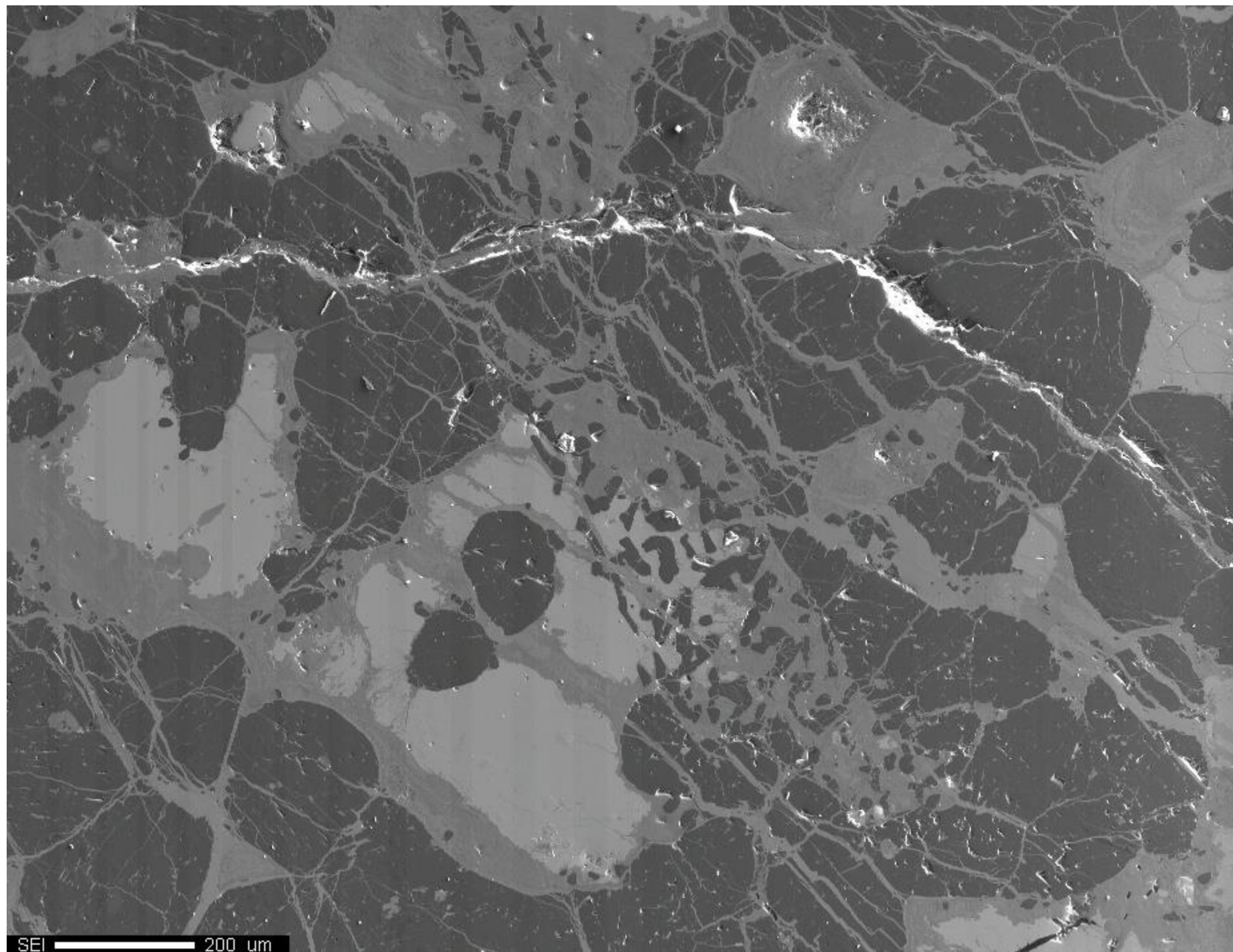
P  
Cts  
- 21  
0  
Project: March\_2\_2016  
Comment: NWA4301\_map02\_2um  
Date: 2016/03/04  
Accel Voltage: 15.0 kV  
Beam Current: 9.922e-008 A  
Dwell Time: 10.0  
Image Size: 927 x 711



S  
Cts  
- 556  
0  
Project: March\_2\_2016  
Comment: NWA4301\_map02\_2um  
Date: 2016/03/04  
Accel Voltage: 15.0 kV  
Beam Current: 9.922e-008 A  
Dwell Time: 10.0  
Image Size: 927 x 711

S 200 um





SEI

Cts

- 4,095

504

Project: March\_2\_2016

Comment: NWA4301\_map02\_2um

Date: 2016/03/04

Accel Voltage: 15.0 kV

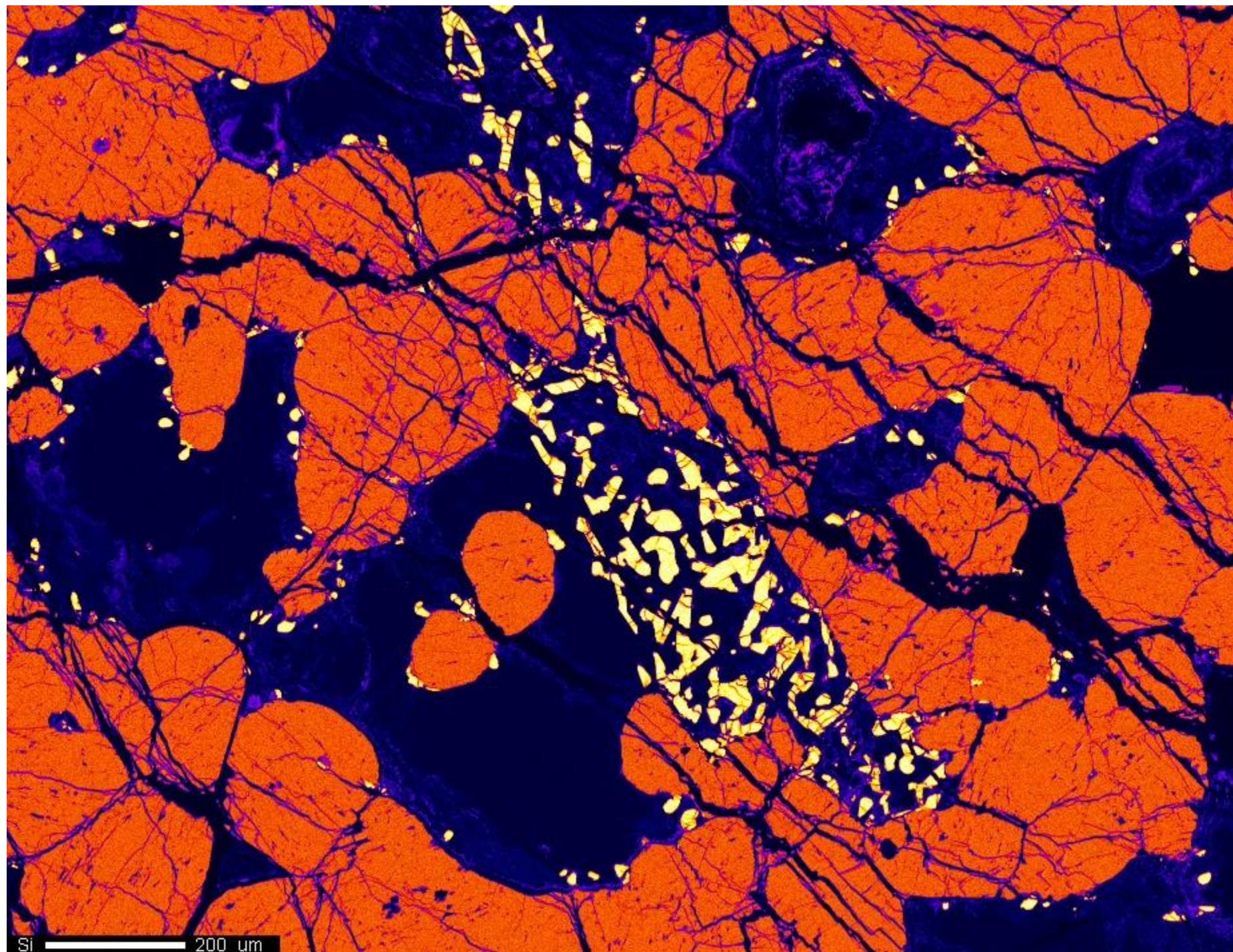
Beam Current: 9.922e-008 A

Dwell Time: 10.0

Image Size: 927 x 711

SEI 200 um

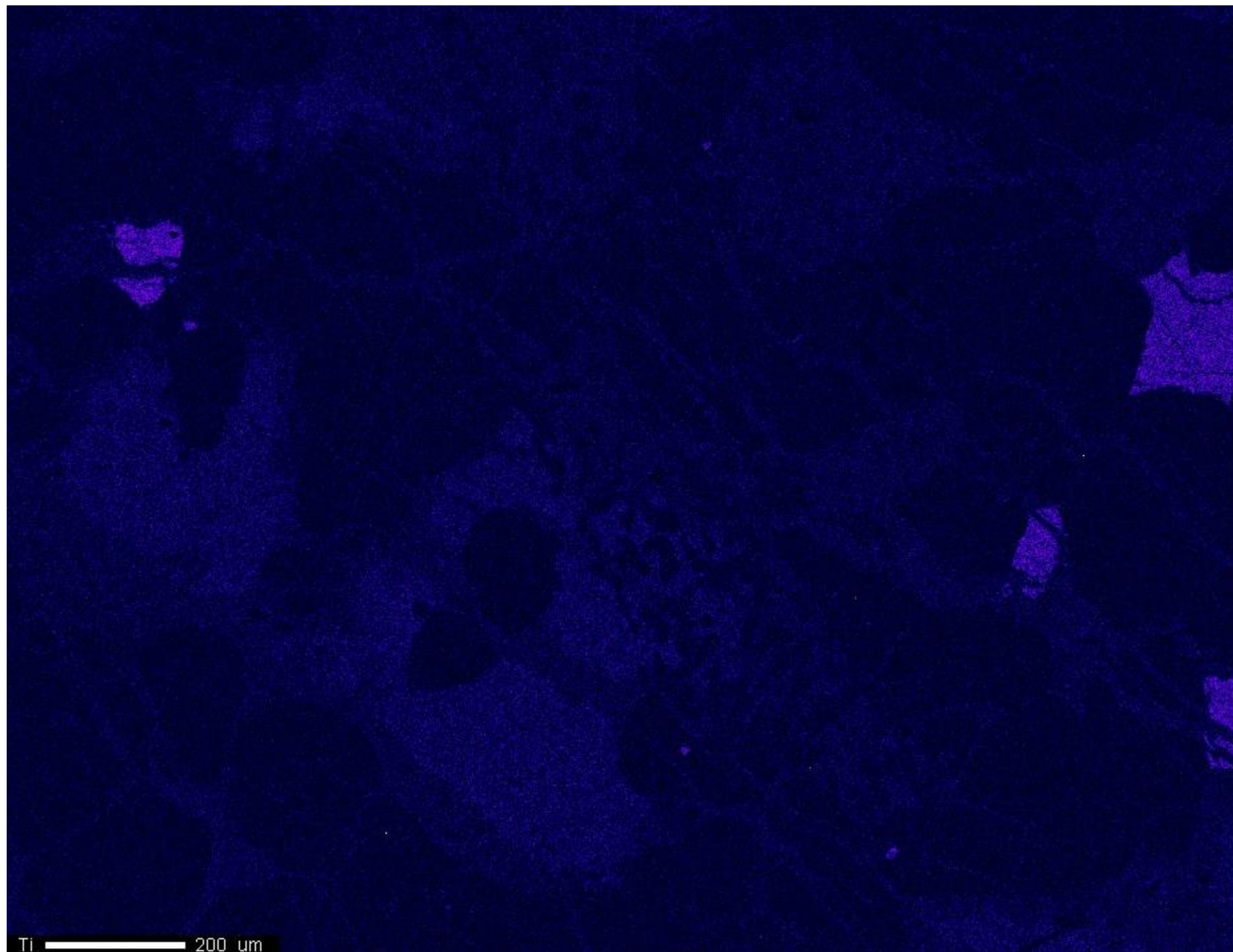




Project: March\_2\_2016  
Comment: NWA4301\_map02\_2um  
Date: 2016/03/04  
Accel Voltage: 15.0 kV  
Beam Current: 9.922e-008 A  
Dwell Time: 10.0  
Image Size: 927 x 711

Si 200 um





Ti

Cts

- 50



0

Project: March\_2\_2016

Comment: NWA4301\_map02\_2um

Date: 2016/03/04

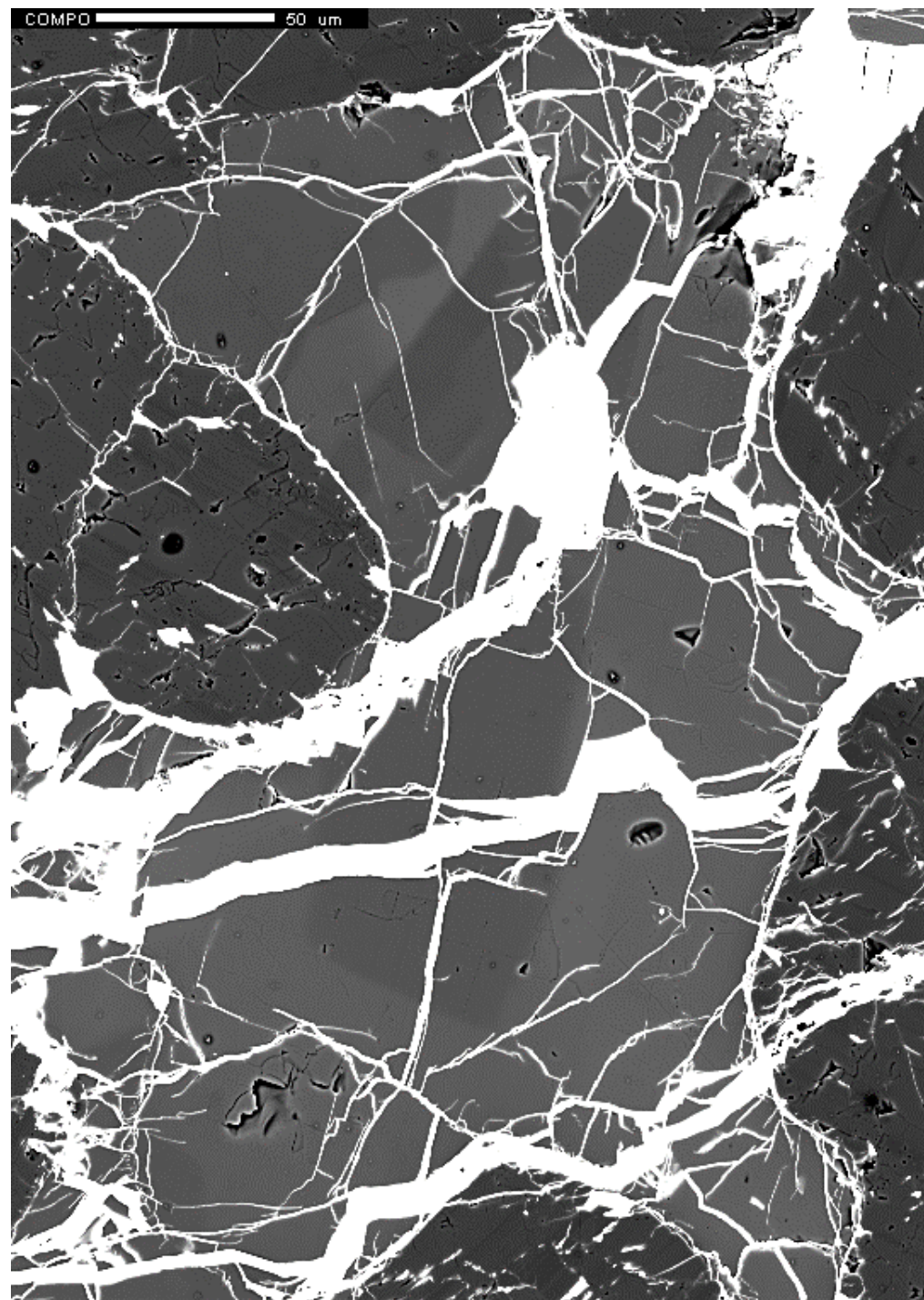
Accel Voltage: 15.0 kV

Beam Current: 9.922e-008 A

Dwell Time: 10.0

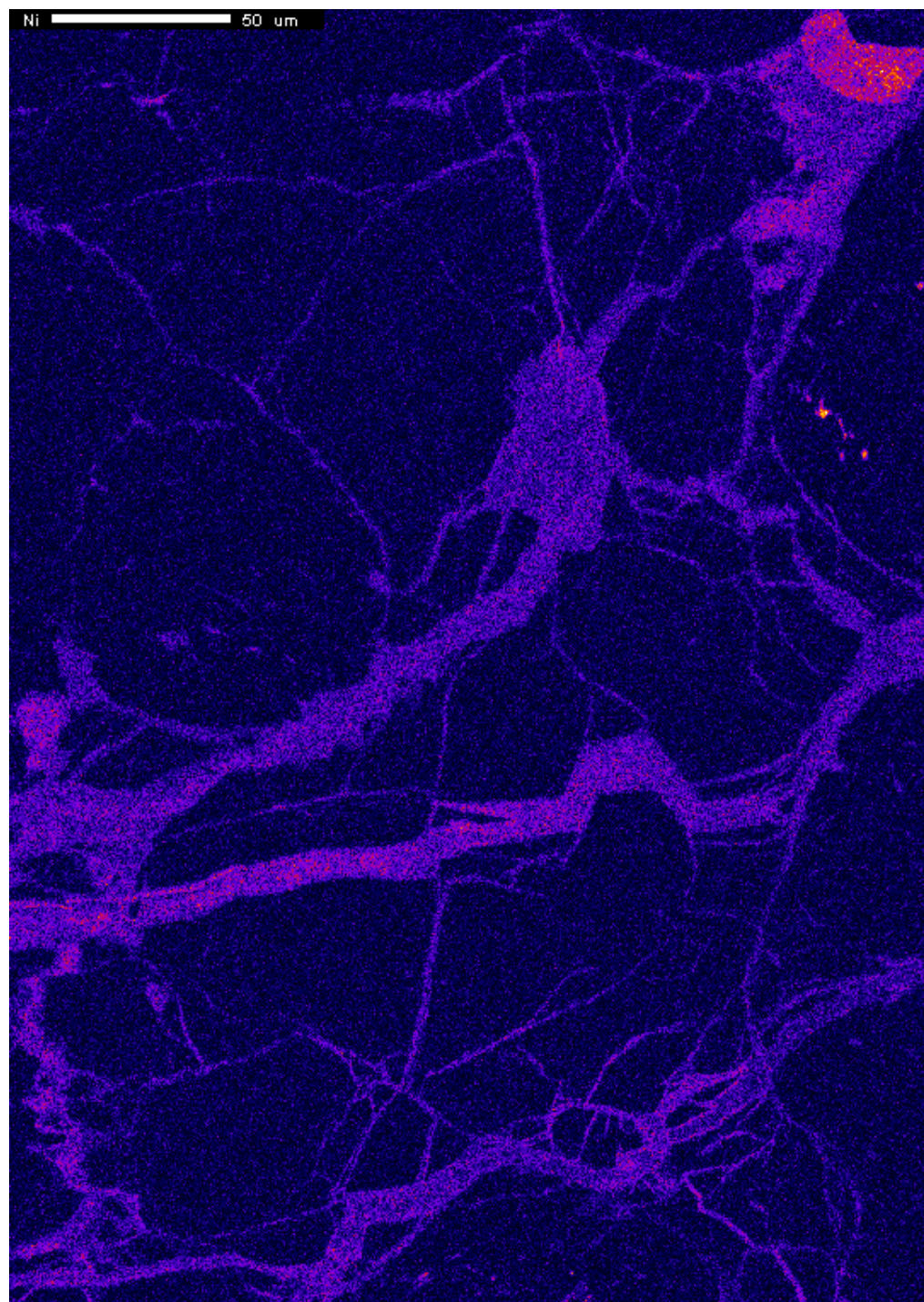
Image Size: 927 x 711

Ti 200 um



Project: August\_4\_2015  
Comment: NWA4301\_map01\_0p5um  
Date: 2015/08/05  
Accel Voltage: 15.0 kV  
Beam Current: 1.007e-007 A  
Dwell Time: 10.0  
Image Size: 541 x 760





Ni

Cts

- 41

0

Project: August\_4\_2015

Comment: NWA4301\_map01\_0p5um

Date: 2015/08/05

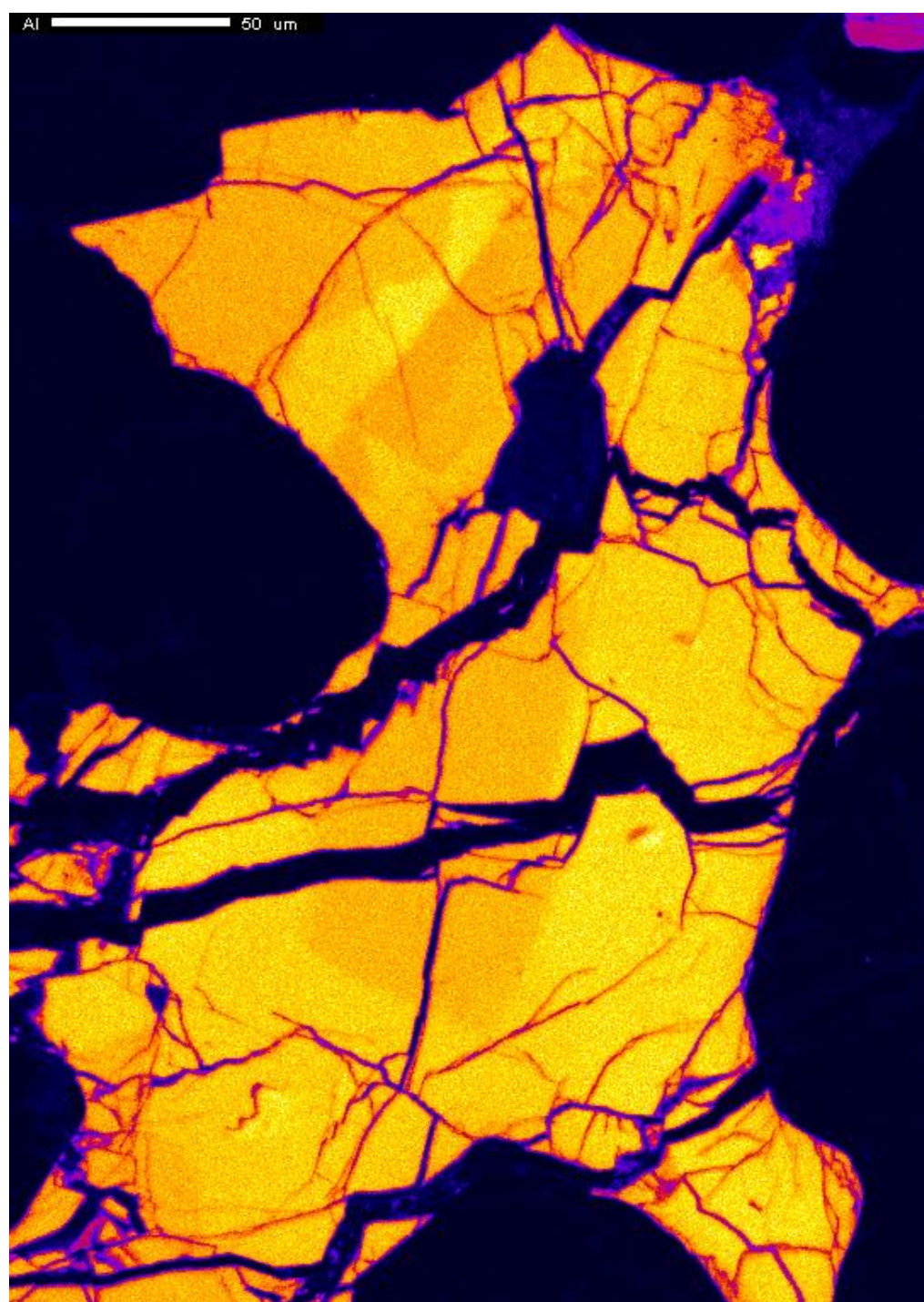
Accel Voltage: 15.0 kV

Beam Current: 5.005e-008 A

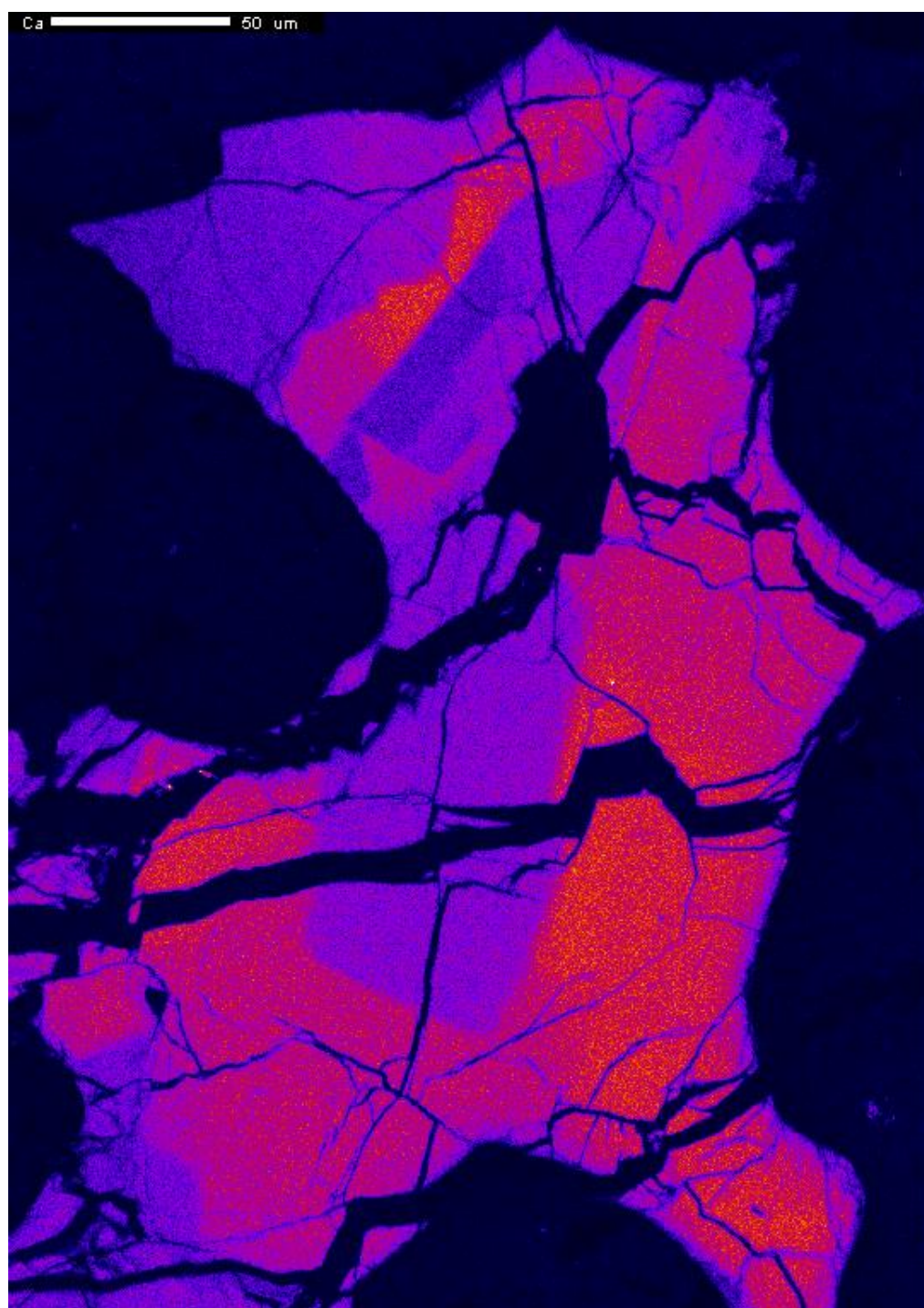
Dwell Time: 10.0

Image Size: 541 x 760



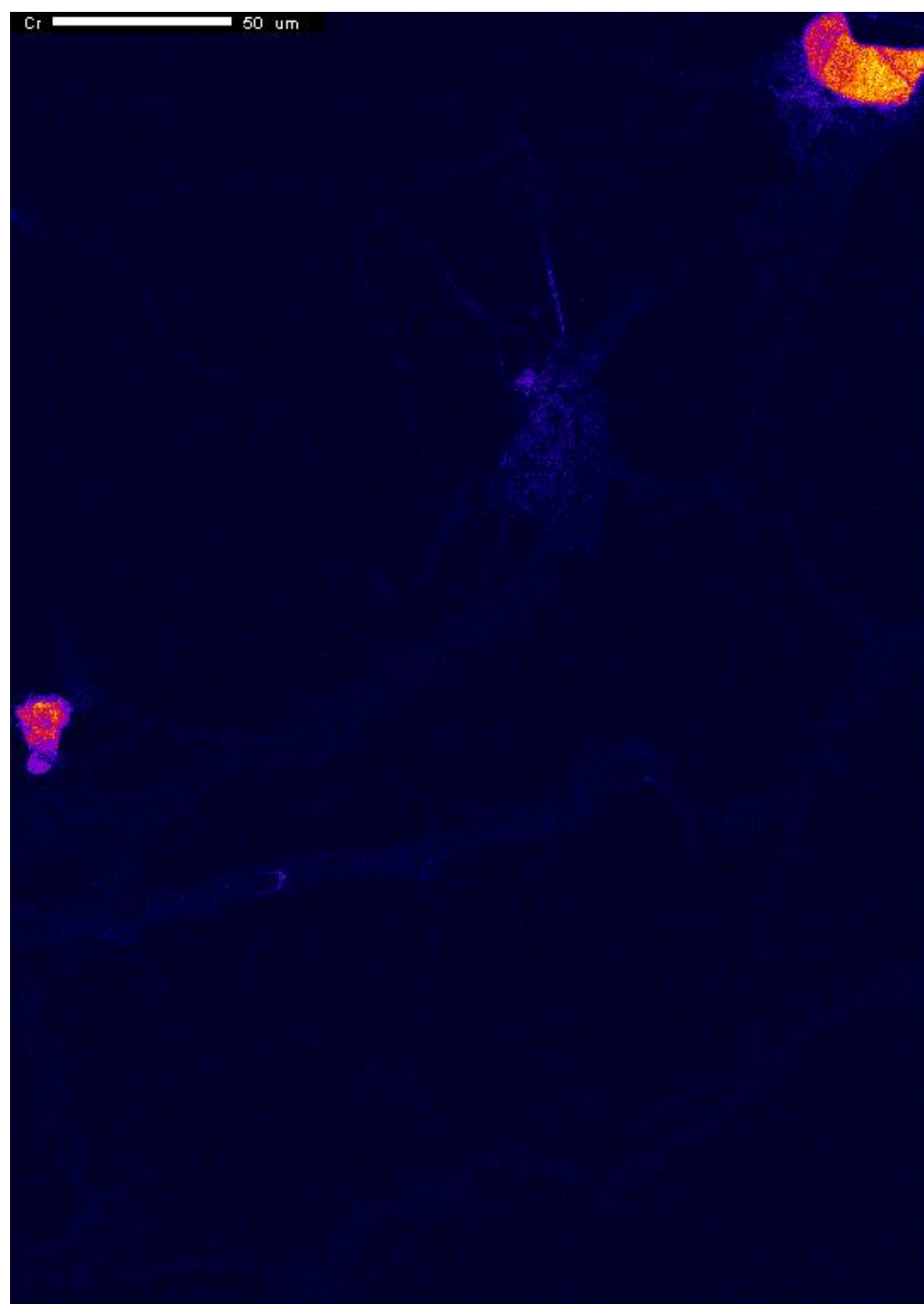


Project: August\_4\_2015  
Comment: NWA4301\_map01\_0p5um  
Date: 2015/08/05  
Accel Voltage: 15.0 kV  
Beam Current: 1.007e-007 A  
Dwell Time: 10.0  
Image Size: 541 x 760

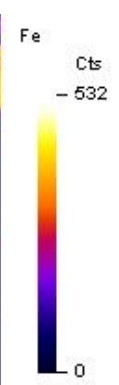
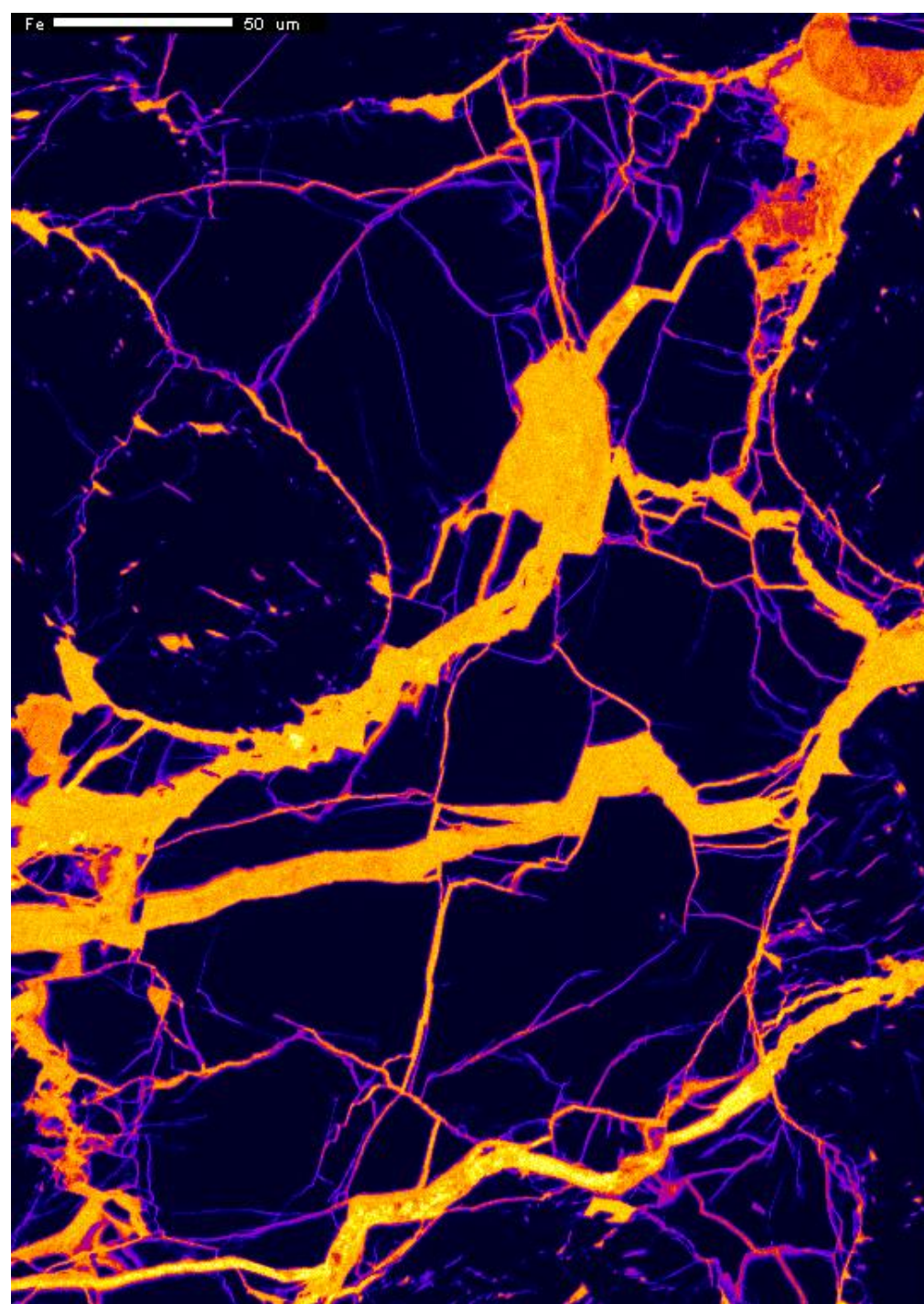


Project: August\_4\_2015  
Comment: NWA4301\_map01\_0p5um  
Date: 2015/08/05  
Accel Voltage: 15.0 kV  
Beam Current: 1.007e-007 A  
Dwell Time: 10.0  
Image Size: 541 x 760

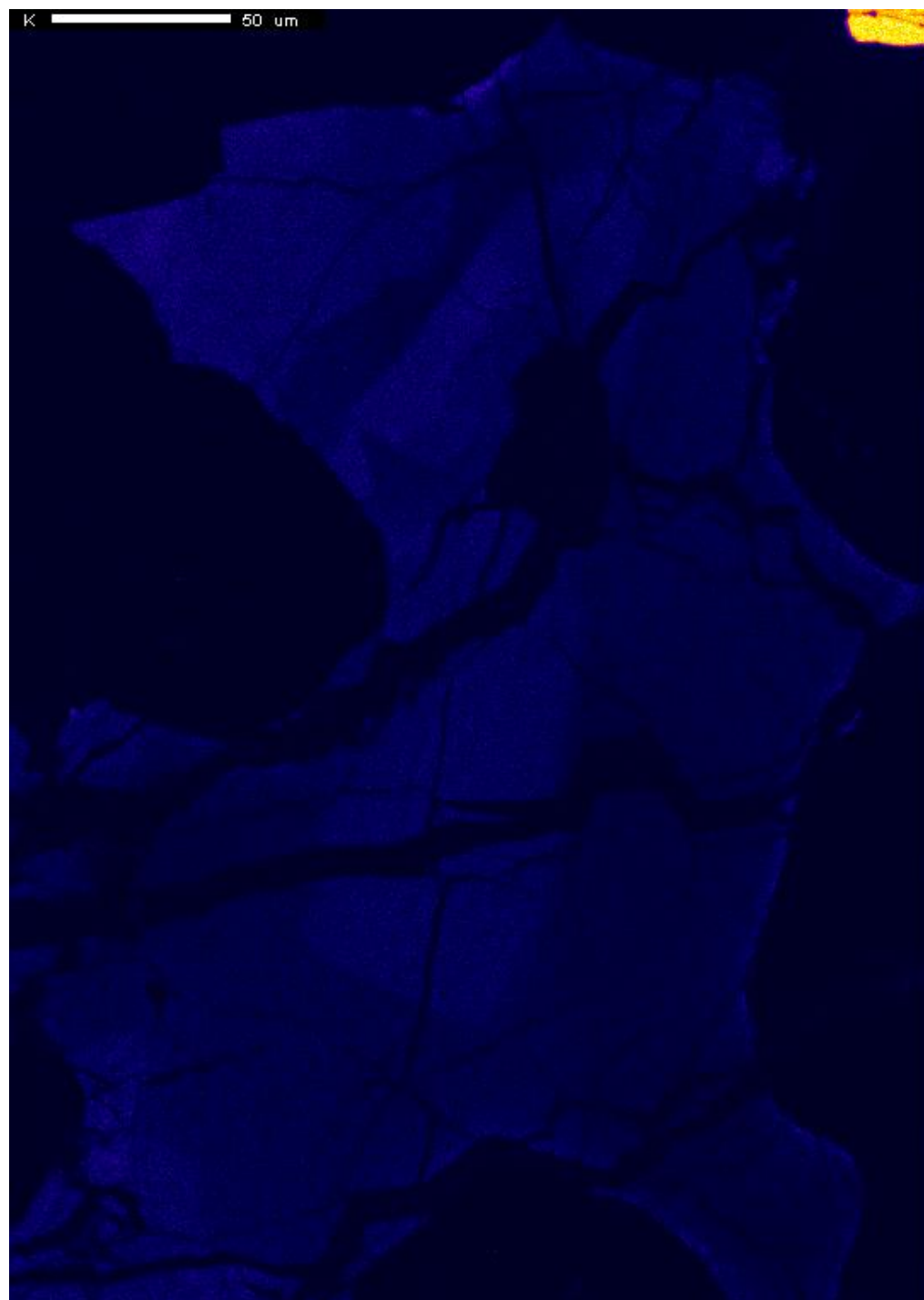




Project: August\_4\_2015  
Comment: NWA4301\_map01\_0p5um  
Date: 2015/08/05  
Accel Voltage: 15.0 kV  
Beam Current: 1.007e-007 A  
Dwell Time: 10.0  
Image Size: 541 x 760

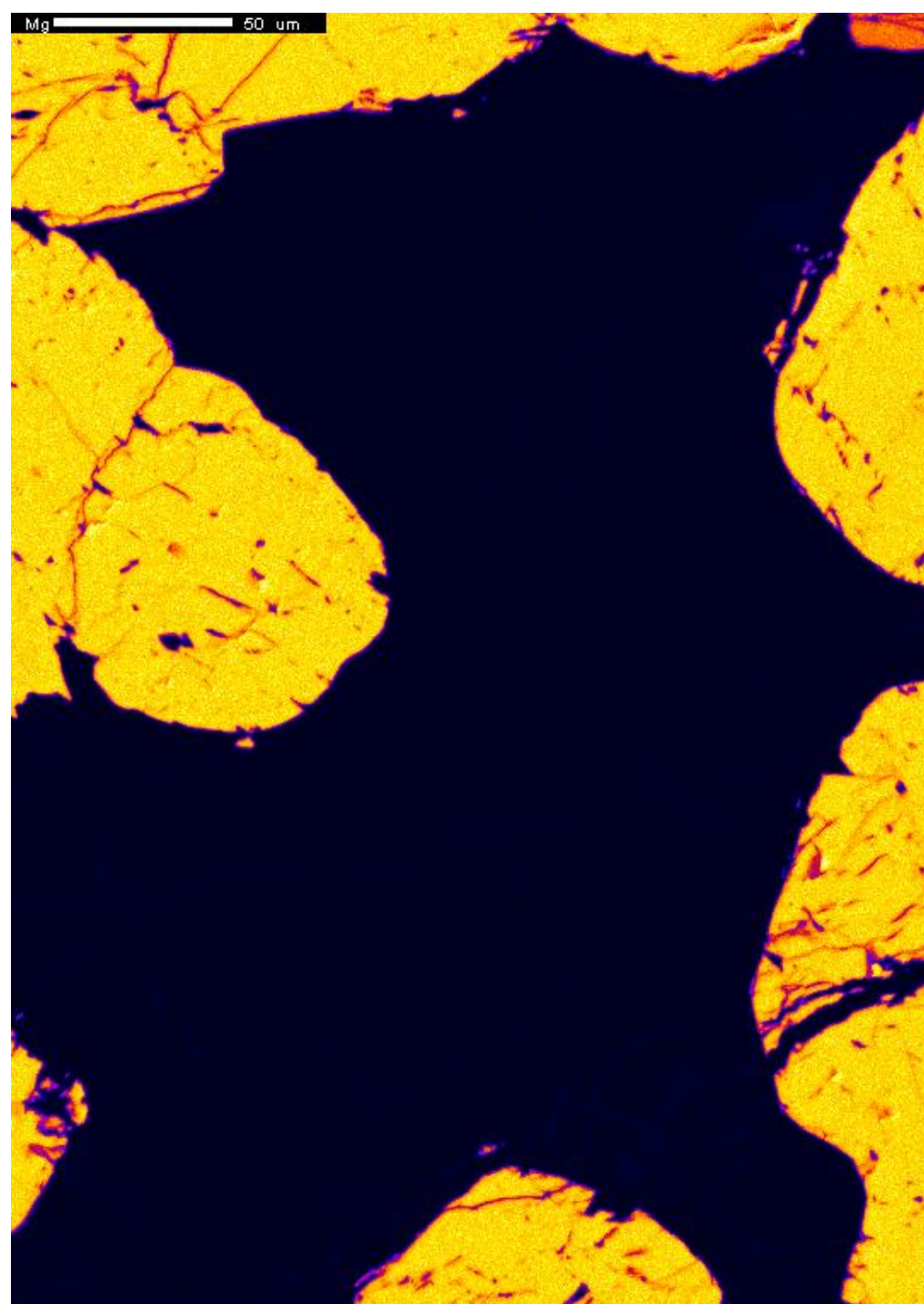


Project: August\_4\_2015  
Comment: NWA4301\_map01\_0p5um  
Date: 2015/08/05  
Accel Voltage: 15.0 kV  
Beam Current: 1.007e-007 A  
Dwell Time: 10.0  
Image Size: 541 x 760

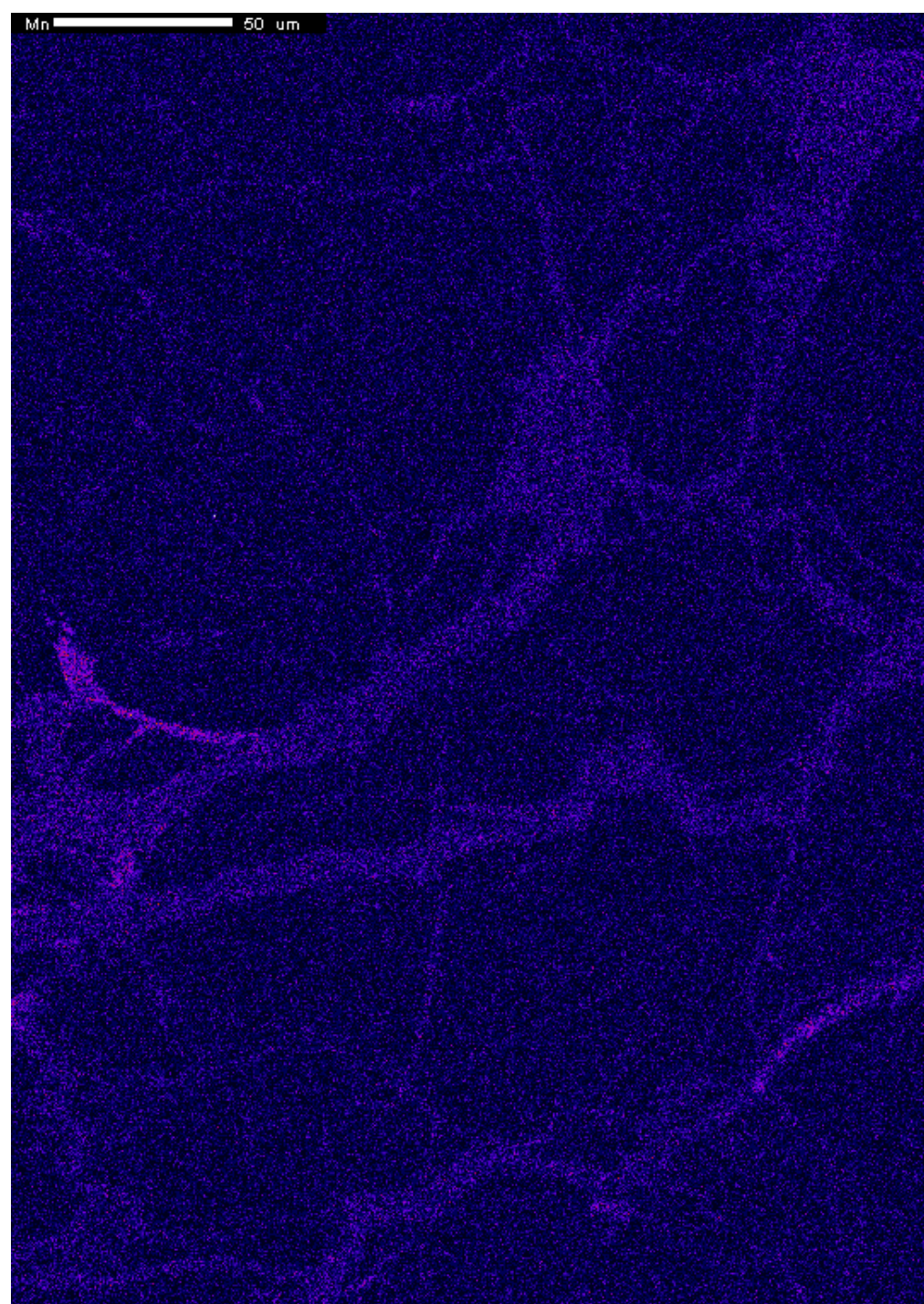


Project: August\_4\_2015  
Comment: NWA4301\_map01\_0p5um  
Date: 2015/08/05  
Accel Voltage: 15.0 kV  
Beam Current: 1.007e-007 A  
Dwell Time: 10.0  
Image Size: 541 x 760



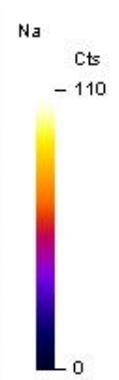
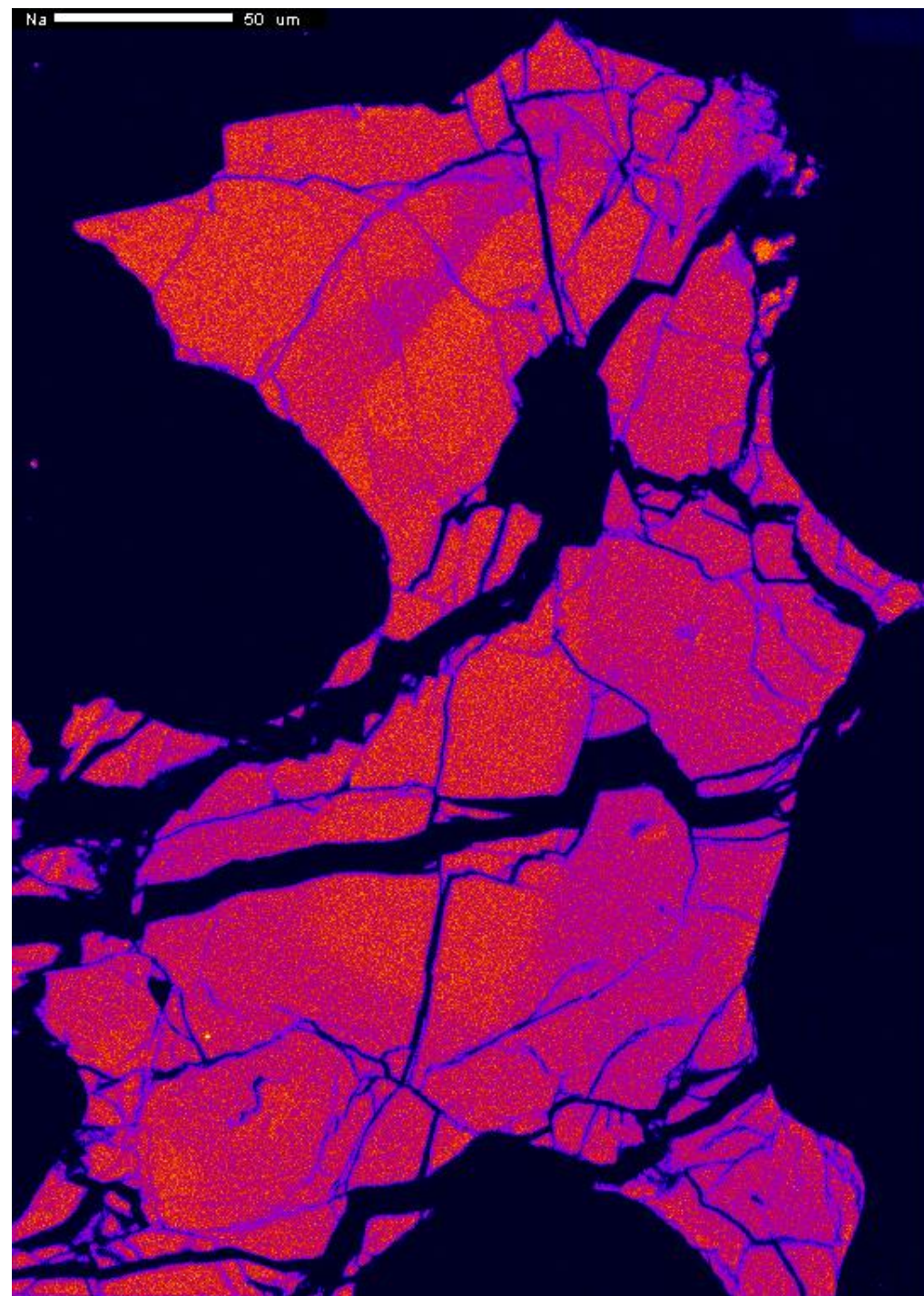


Project: August\_4\_2015  
Comment: NWA4301\_map01\_0p5um  
Date: 2015/08/05  
Accel Voltage: 15.0 kV  
Beam Current: 1.007e-007 A  
Dwell Time: 10.0  
Image Size: 541 x 760



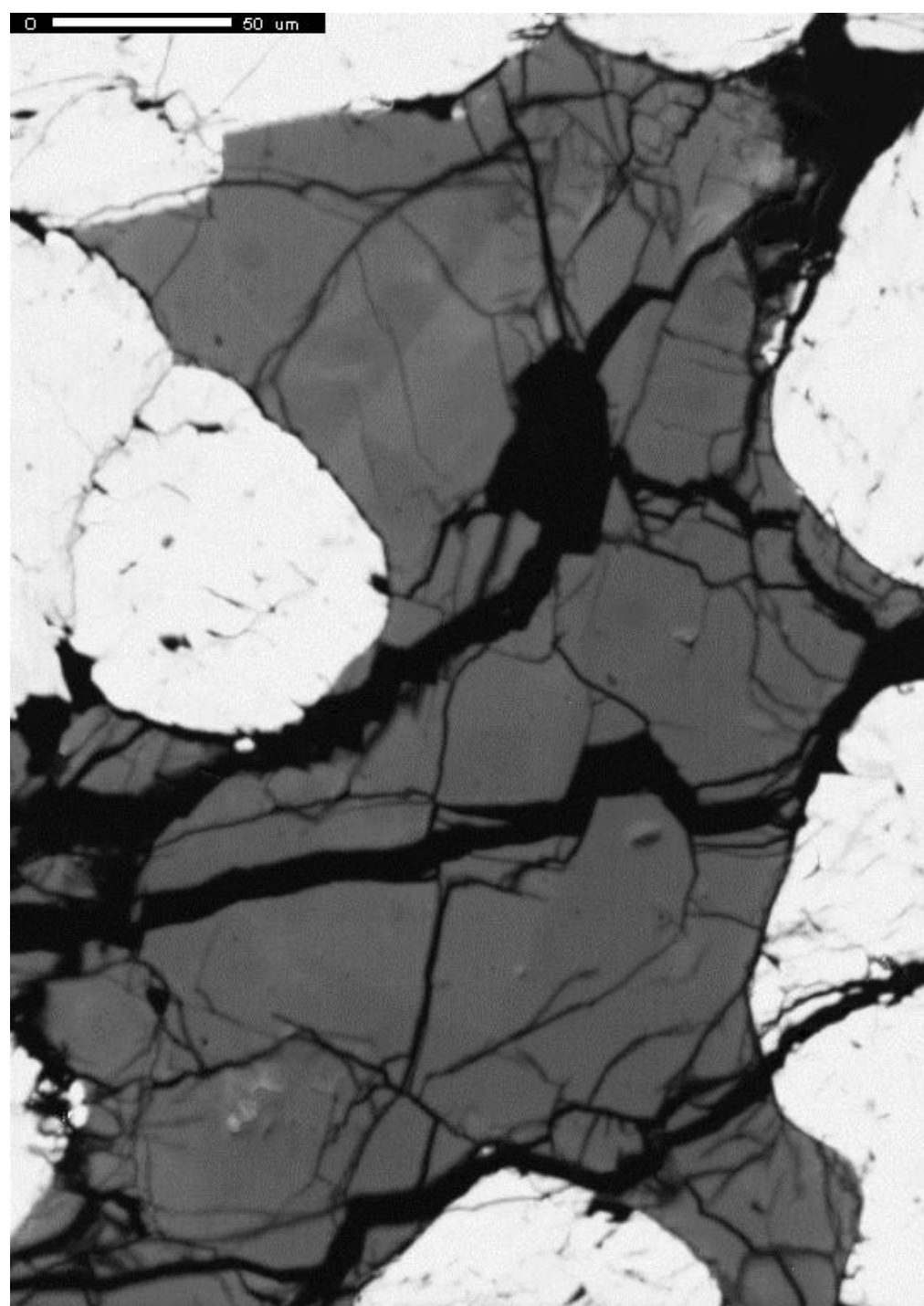
Project: August\_4\_2015  
Comment: NWA4301\_map01\_0p5um  
Date: 2015/08/05  
Accel Voltage: 15.0 kV  
Beam Current: 1.007e-007 A  
Dwell Time: 10.0  
Image Size: 541 x 760



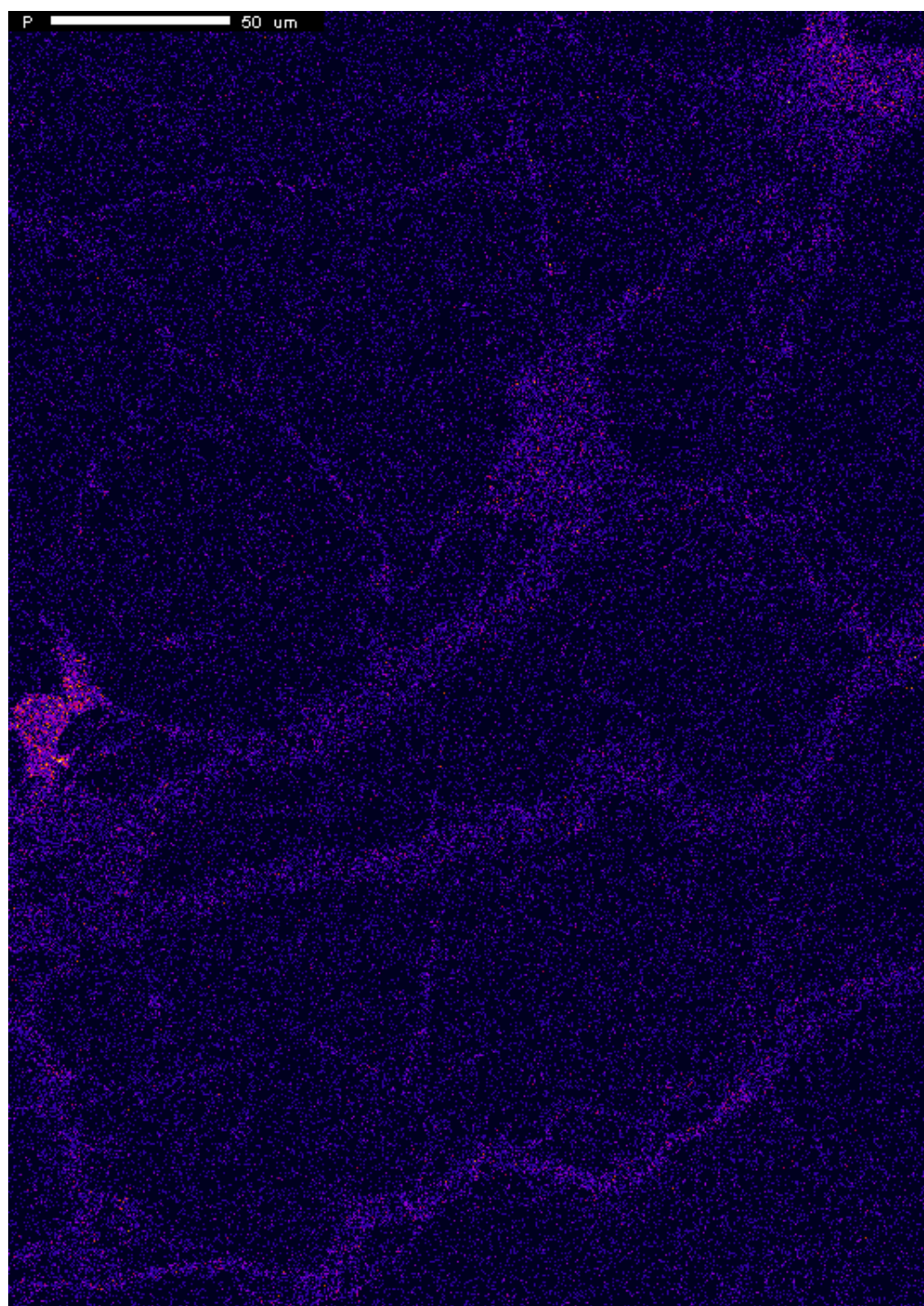


Project: August\_4\_2015  
Comment: NWA4301\_map01\_0p5um  
Date: 2015/08/05  
Accel Voltage: 15.0 kV  
Beam Current: 1.007e-007 A  
Dwell Time: 10.0  
Image Size: 541 x 760

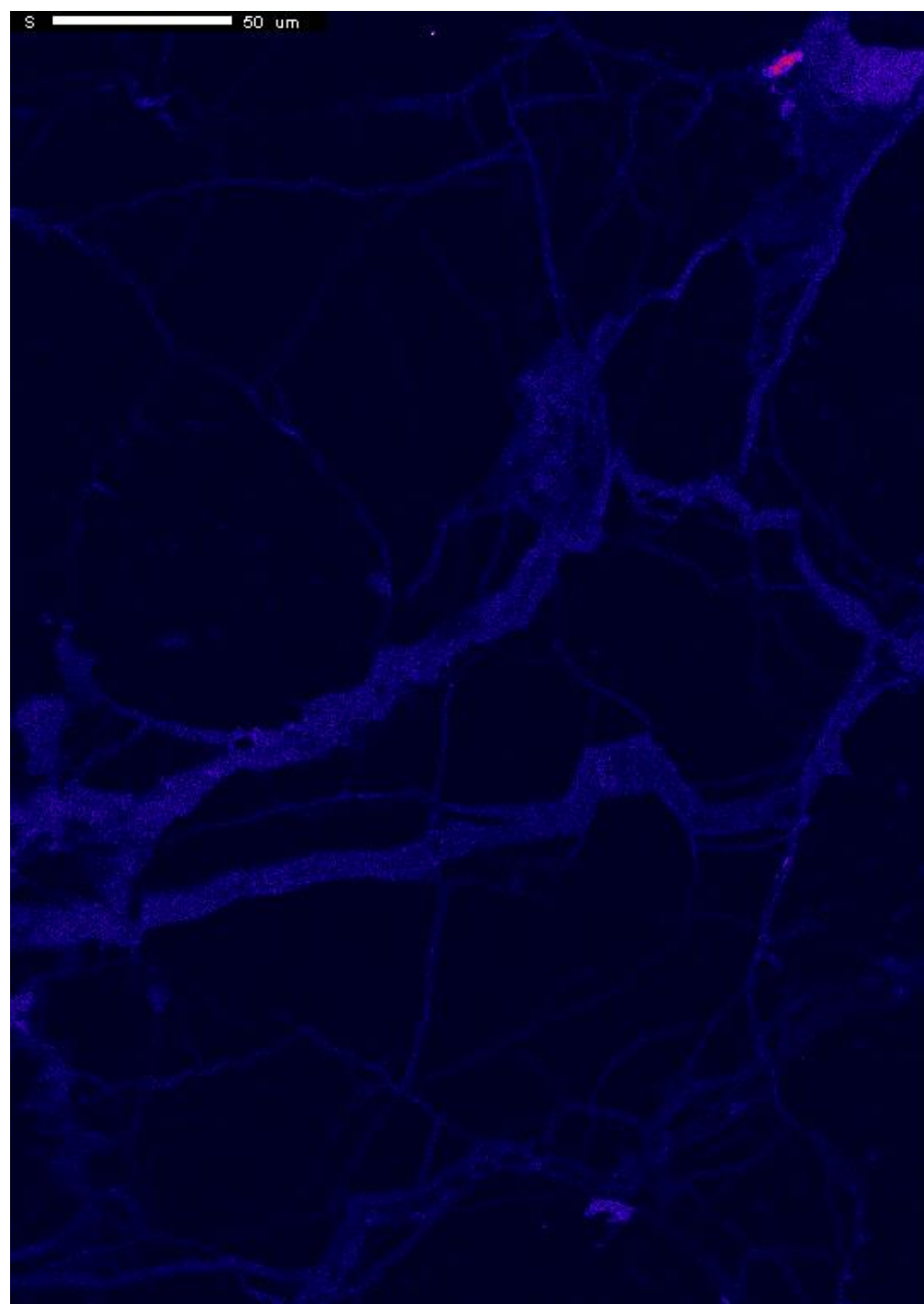




Project: August\_4\_2015  
Comment: NWA4301\_map01\_0p5um  
Date: 2015/08/05  
Accel Voltage: 15.0 kV  
Beam Current: 1.007e-007 A  
Dwell Time: 10.0  
Image Size: 541 x 760

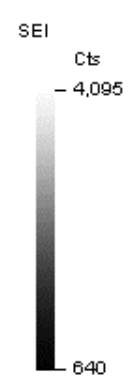
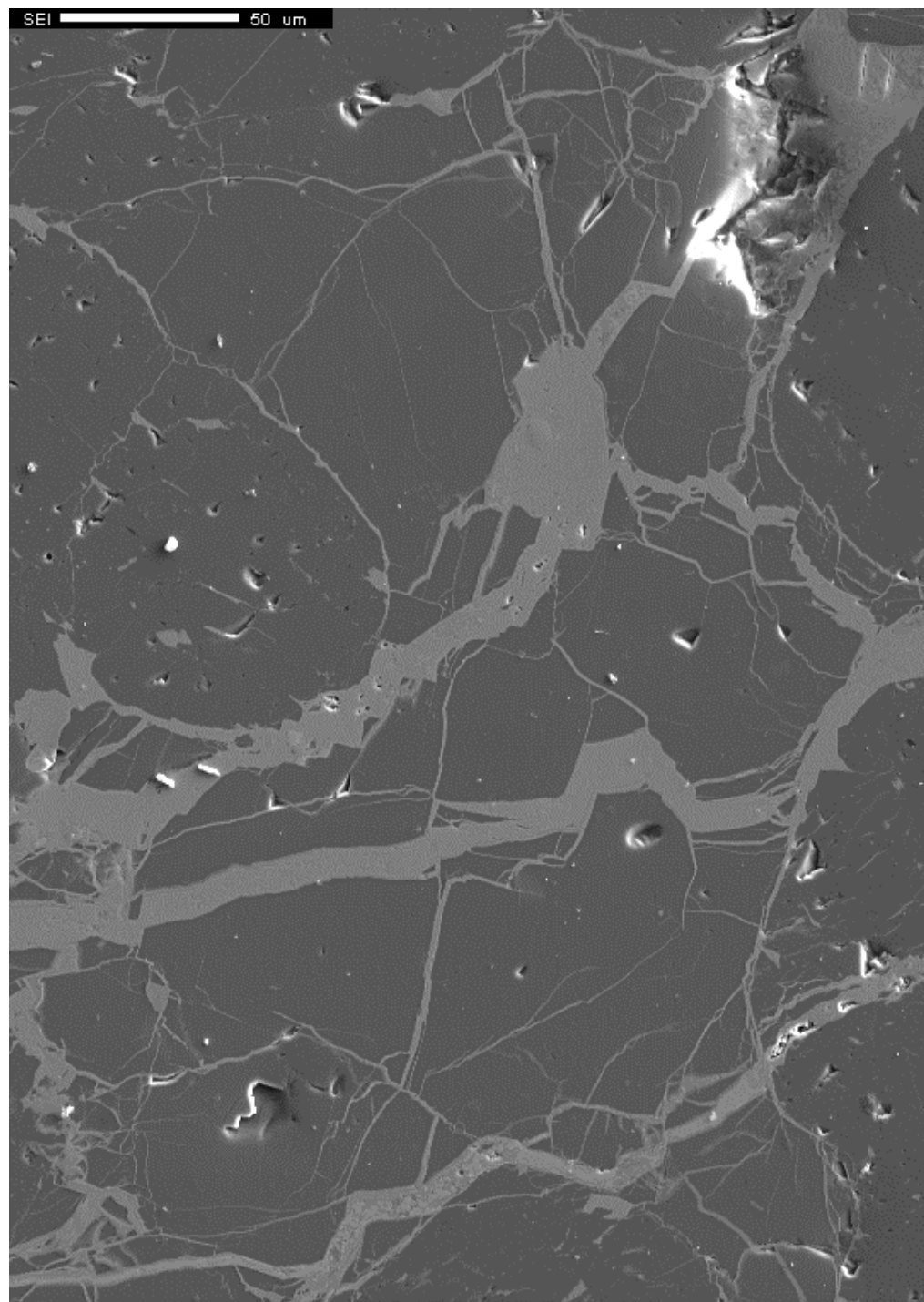


Project: August\_4\_2015  
Comment: NWA4301\_map01\_0p5um  
Date: 2015/08/05  
Accel Voltage: 15.0 kV  
Beam Current: 1.007e-007 A  
Dwell Time: 10.0  
Image Size: 541 x 760

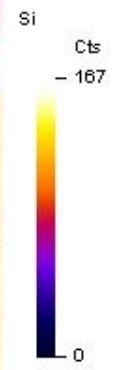
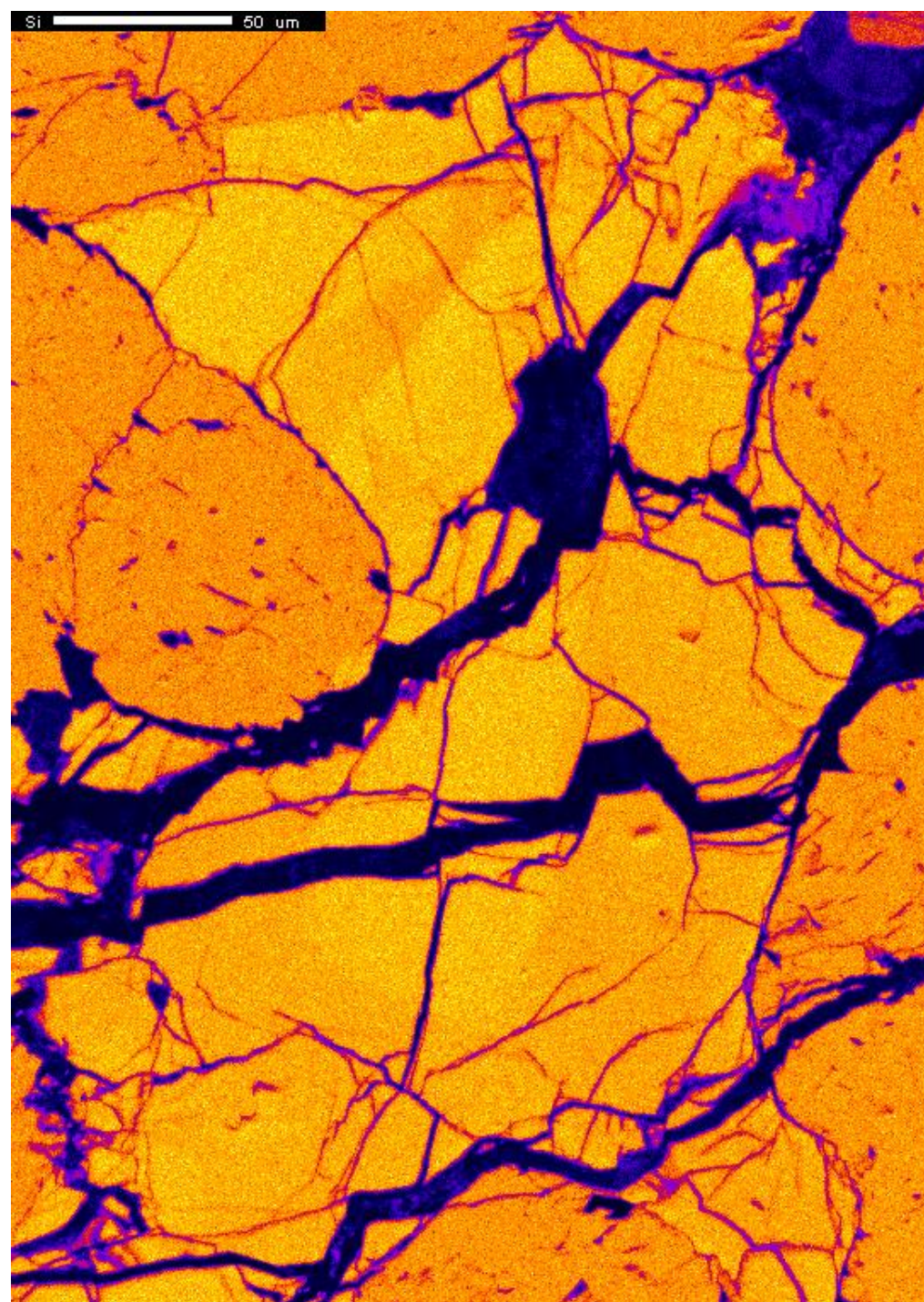


Project: August\_4\_2015  
Comment: NWA4301\_map01\_0p5um  
Date: 2015/08/05  
Accel Voltage: 15.0 kV  
Beam Current: 1.007e-007 A  
Dwell Time: 10.0  
Image Size: 541 x 760



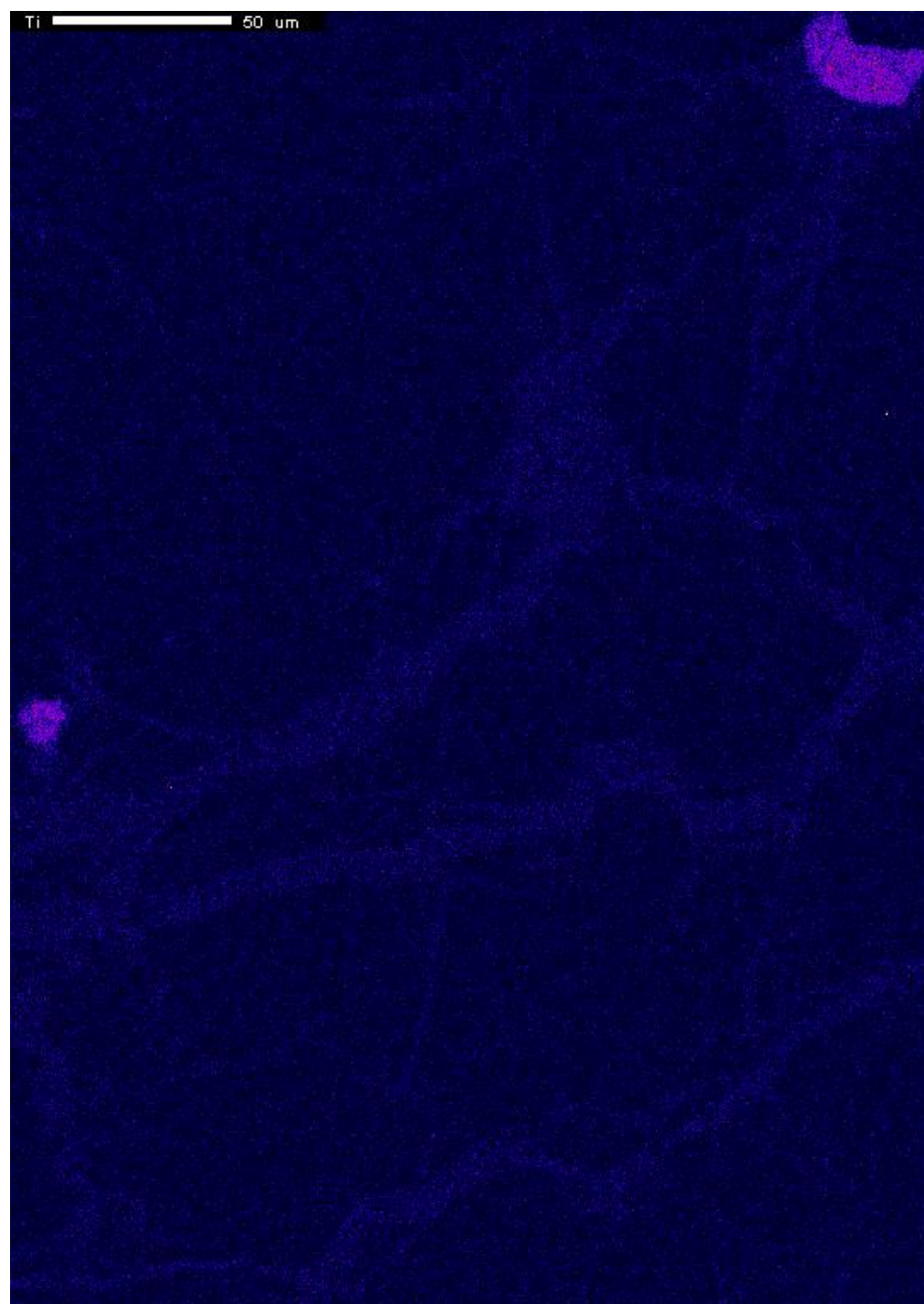


Project: August\_4\_2015  
Comment: NWA4301\_map01\_0p5um  
Date: 2015/08/05  
Accel Voltage: 15.0 kV  
Beam Current: 1.007e-007 A  
Dwell Time: 10.0  
Image Size: 541 x 760



Project: August\_4\_2015  
Comment: NWA4301\_map01\_0p5um  
Date: 2015/08/05  
Accel Voltage: 15.0 kV  
Beam Current: 1.007e-007 A  
Dwell Time: 10.0  
Image Size: 541 x 760





Project: August\_4\_2015  
Comment: NWA4301\_map01\_0p5um  
Date: 2015/08/05  
Accel Voltage: 15.0 kV  
Beam Current: 1.007e-007 A  
Dwell Time: 10.0  
Image Size: 541 x 760



## Curriculum Vitae

**Name:** Diego Uribe

**Post-secondary Education and Degrees:** The University of Western Ontario  
London, Ontario, Canada  
2010-2014 B.Sc.

The university of Western Ontario  
London, Ontario, Canada  
2014-present

**Honours and Awards:** 3<sup>rd</sup> place Canada region, Imperial Barrel Award (IBA) (2015)

Hodder travel Award 2015

ASTRO Travel Grant 2015

Dean's Honor List 2013-2014

Robert Lumsden Award 2013

Meteoritical Society undergrad travel award 2013

Canadian Space Agency-ASTRO undergrad research award 2013

Canadian Space Agency -ASTRO grad research incentive 2014

**Related Work Experience** Teaching Assistant  
The University of Western Ontario  
2014-2016

Research Assistant  
The University of Western Ontario  
2011-2016

### Abstracts

LPSC # 2537 *Chemical Microanalysis of Anomalous Enstatite Achondrites via Electron Backscatter Diffraction (EBSD)*

D.D. Uribe, P.J.A. McCausland, M.R.M. Izawa, R.L. Flemming, I. Barker, D. Moser

LPSC # 3071 *A comparative study of the Zaklodzie and NWA 4301 anomalous enstatite achondrite.*

D. D. Uribe , P. J. A. McCausland, M .R. M. Izawa, R. L. Flemming

LPSC # 2797 Mineralogy, Petrology and mineral chemistry of NWA 8173: An anomalous enstatite achondrite with evidence for high-temperature silicate sulphidation.

D. D. Uribe ,M.R.M. Izawa, P. J. A. McCausland, M .R. M. Izawa, P.J.A. McCausland, R. L. Flemming,

LPSC # 2817 *Comparative Non-destructive study of the Zaklodzie and NWA 4301 Enstatite Achondrites via Micro-Computed Tomography.*

D. D. Uribe , P. J. A. McCausland, M .R. M. Izawa, R. L. Flemming, J. U. Umoh, D. W. Holdsworth.

GAC-MAC #36015 *3D petrography of Enstatite achondrites via micro computed tomography scanning ( $\mu$ CT).*

D. D. Uribe , P. J. A. McCausland, M .R. M. Izawa, R. L. Flemming, J. U. Umoh, D. W. Holdsworth.